Mechanical Simulation of the Passive Confinement of Reinforced Concrete for Design

by

Xinkai Hao

A Thesis Submitted for the Degree of Doctor of Philosophy

School of Civil, Environmental and Mining Engineering, the University of Adelaide

October 2019

Table of Contents

Abstract

Reinforcement that acts to passively confine concrete, such as stirrups, steel tubes, FRP (fibre reinforced polymer) wraps or a combination of the above can enhance the strength and, more importantly, the ductility of concrete members, allowing for greater absorption of energy and consequently ductile failure. Research to quantify the stress-strain response of confined concrete has largely resulted in empirical or semi-empirical modification factors that are applied to the stress-strain relationships for unconfined or actively confined concrete. These approaches appear, however, to be the result of seemingly disparate research conducted to develop safe approaches for design purposes. As a result, the approaches often yield conservative predictions of performance within the bounds of the dataset from which they were calibrated, but poor performance when extended outside these bounds. This presents a particular challenge for the application of new types of confinement reinforcement material as expensive member tests for different size and concrete strength specimens are required and the whole procedure has to be repeated for each type of new material..

In this thesis, a generic mechanics-based model is proposed for the passive stress/strain of concrete that can incorporate: any type of confinement reinforcement; rectangular or circular cross-sections; different specimen sizes; and different concrete strengths. This approach is based on the direct application of fundamental partial-interaction shear-friction and bond-slip mechanics rather than the empirical modification of unconfined material properties. The benefit of this approach is that it is based directly on fundamental material properties that are obtained from simple material tests and, therefore, it can rapidly and inexpensively be extended to new types of confinement without the need for member level calibration testing. Additionally, simplified closed-form solutions for the proposed approach are developed for use in the design of members.

This thesis first investigates the confinement reinforcement behaviour including debonding, yielding, fracture or a combination of the above and the corresponding closed-form equations are proposed. Then the shear friction material properties are derived from actively confined cylinder tests as well as shear-sliding tests and are simplified to a linear form. After which the bond-slip material properties for different types of confinement reinforcement are

summarised. Having gathered all these fundamental material properties, the stress/strain response of confined concrete is quantified and corresponding simplified closed-form solutions are proposed for rectangular and circular cross-section members respectively. Next, closed-form solutions of the passive stress/strain of concentrically loaded specimens are simplified to rectangular stress blocks for flexural analysis. From which the closed-form solution based on the segmental analysis approach is used to quantify the beam ductility by deriving the moment/rotation of a hinge. Finally, the above proposed approach is extended to steel tube confined concrete for which the passive stress/strain incorporates shrinkage and the results are simplified to rectangular stress blocks that can be used in flexural analyses.

Declaration

I certify that this work contains no material which has been accepted for the award of any other degree or diploma in my name in any university or other tertiary institution and, to the best of my knowledge and belief, contains no material previously published or written by another person, except where due reference has been made in the text. In addition, I certify that no part of this work will, in the future, be used in a submission in my name for any other degree or diploma in any university or other tertiary institution without the prior approval of the University of Adelaide and where applicable, any partner institution responsible for the joint award of this degree.

The author acknowledges that copyright of published works contained within this thesis resides with the copyright holder(s) of those works. I give permission for the digital version of my thesis to be made available on the web, via the University's digital research repository, the Library Search and also through web search engines, unless permission has been granted by the University to restrict access for a period of time.

Date: 25/10/2019

Xinkai Hao

List of Publication

Hao, X, Visintin, P and Oehlers, DJ (2018) Simulating the Passive Confinement of Rectangular Concrete Prisms Allowing for Size Effect. Submitted to *Proceedings of Institution of Civil Engineers-Structures and Buildings*

Hao, X, Visintin, P and Oehlers, DJ (2019) Simulating the Passive Confinement of Circular Concrete Cylinders Allowing for Size Effect. Submitted to *Composite Structures*

Hao, X, Visintin, P and Oehlers, DJ (2019) Closed Form Solutions for Quantifying the Ductility of Concrete Beams with Passively Restrained Concrete. Submitted to *Journal of Structural Engineering*

Hao, X, Visintin, P and Oehlers, DJ (2019) Passive Stress/Strain Relationship for the Design of Steel Tube Confined Concrete. Submitted to *Journal of Constructional Steel Research*

Acknowledgements

I would like to thank my supervisors A/Prof. Phillip Visintin and Professor Deric John Oehlers sincerely with their knowledge and patience. Their excellent supervision and support help me finish this thesis. I am so lucky to be supervised by them.

I also would like to thank my families and friends for their supports and advice which motivates me and helps me to overcome obstacles.

Introduction and General Overview

Concrete members reinforced by passive confinement through the use of either internal stirrups or external FRP wraps, or FRP tubes, or steel tubes or a combination of the above have received much research interest as these confinement reinforcements can significantly enhance both the strength and, more importantly, the ductility of concrete members. Previous research relies on empirical or semi-empirical factors to define the stress-strain behaviour for confined concrete and these approaches often yield conservative results. Furthermore, these approaches may only be accurate within the bounds of the regressed databases and should not be extended beyond these bound. As a result, expensive member tests have to be repeated for new types of confinement reinforcement reinforced concrete with different sizes and concrete strengths to derive corresponding empirical or semi-empirical approaches.

To aid in addressing the limitations of empirical and semi-empirical approaches, a generic fundamental mechanics-based approach is proposed to predict the passive stress/strain response and flexural behaviour of concrete members. This approach is generic in that it can be applied to rectangular or circular cross-sections, different specimen heights, different concrete strengths and various confinement reinforcement types such as stirrups, FRP wraps, steel tubes or a combination of the above. Based on fundamental partial-interaction shear-friction and bond-slip material properties, the proposed approach and the corresponding closed-form solutions for design purposes are developed to predict the passive stress/strain response and flexural behaviour. As only partial-interaction material properties are required, they can be extracted from simple material tests instead of member level testing, such that the proposed approach can be extended to new types of confinement reinforcement at low cost.

The Chapters in this thesis are comprised of a series of school reports which provide full details of the development of the approach and then these have then been condensed to journal papers.

Chapter 1 contains a school report which describes the mechanics of the confinement reinforcement which includes debonding, yielding, fracture, or a combination of the these. Based on the bond-slip fundamental material property, three scenarios that may occur to the confinement reinforcement are described and the mechanics equations for the confinement reinforcement behaviour are proposed for both rectangular cross-sections and circular cross-sections.

Chapter 2 contains two school reports on two partial-interaction material properties that govern the confinement mechanism. These material properties are used in this research, however, the mechanics does not depend directly on these specific properties such that they could be replaced by any more convenient or appropriate models. Firstly, the shear-friction material properties are derived from both actively confined cylinder tests and shear-sliding tests from a large dataset. These shear friction properties are then simplified to a linear approximation that can be used in the closed-form solutions of the proposed approach. Then active stress/strains are constructed based on the linearized shear friction material properties to validate this linear approximation. Secondly, bond-slip properties for available reinforcement including steel and FRP rebars as well as steel and FRP plates are summarised and simplified to a bilinear model for ease of application in the proposed approach.

In Chapter 3, a passively confined stress-strain relationship for rectangular and circular cross-sections is derived based on the application of the material properties and mechanics equations described in the first two chapters. As a result, this approach does not rely on member tests and can predict the behaviour of concrete specimens with different properties. Closed-form solutions are given for design purpose which allows for the different scenarios that can occur to the confinement reinforcement including intermediate crack debonding, yield, fracture or a combination of these. In this chapter, two submitted journal papers are included. The first paper describes the proposed approach in detail for rectangular cross-sections; the second paper investigates how the mechanics varies for circular cross-sections from the rectangular ones as well as a parametric study to show the importance of the specimen size on the passive stress/strain behaviour.

The traditional flexural analysis relies on empirically calibrated hinge lengths to quantify beam ductility and ignores the size-effect of the passively confined concrete stress/strain response as well as the confinement effect. Ignoring the confinement effect may underestimate the strength and, more significantly, the ultimate strain of the concrete. Hence in Chapter 4, one submitted journal paper is included to describe the application of the proposed passive stress/strain in flexural analyses which is mechanics-based and size-dependent and can allow for confinement effect. The reason why the passive stress/strain derived from prisms can be applied in flexural analyses is first explained, then the passive stress/strain derived in Chapter 3 is simplified to a rectangular stress block. Based on the well-established segmental analysis, closed-form solutions are derived to quantify the beam ductility by quantifying moment/rotation of a hinge which can be used in design.

In Chapter 5, the fundamental mechanics is extended to steel tube confined concrete prisms in a submitted journal paper. As a result, the passive stress/strain response allowing for the shrinkage effect is quantified and simplified to a rectangular stress block which can be used in flexural analyses. Then a parametric study is conducted to investigate the effect of shrinkage on the passive stress/strain behaviour.

Chapter 6 concludes this thesis and provides possible future research.

Chapter 1— Confinement Reinforcement Behaviour

Introduction

This Chapter contains the school report below which describes the fundamental mechanism of the confinement reinforcement and gives the quantification of the confinement that includes the cases of IC debonding, yielding, fracture or a combination of these.

List of Manuscripts

Hao, X., Oehlers, D., and Visintin, P. (2017) Mechanics Closed Form Equations for the Confinement. *School Report*, School of Civil, Environmental and Mining Engineering, The University of Adelaide, Australia.

Mechanics Closed Form Equations for Confinement

Introduction

The lateral confinement of the concrete due to transverse reinforcement in the form of stirrups, steel tubes, FRP wraps or combinations of them can enhance the axial strength and ductility of concrete columns (Basset & Uzumeri 1986; Bresler & Gilbert 1961; Lam & Teng 2003; Sakino et al. 2004; Visintin et al. 2012). The confinement due to the transverse reinforcement is a passive confinement as it depends on the lateral deformation, such that if there is no lateral deformation then the confinement effect is zero. In this report, the mechanics of the confinement due to the transverse reinforcement will be described and quantified.

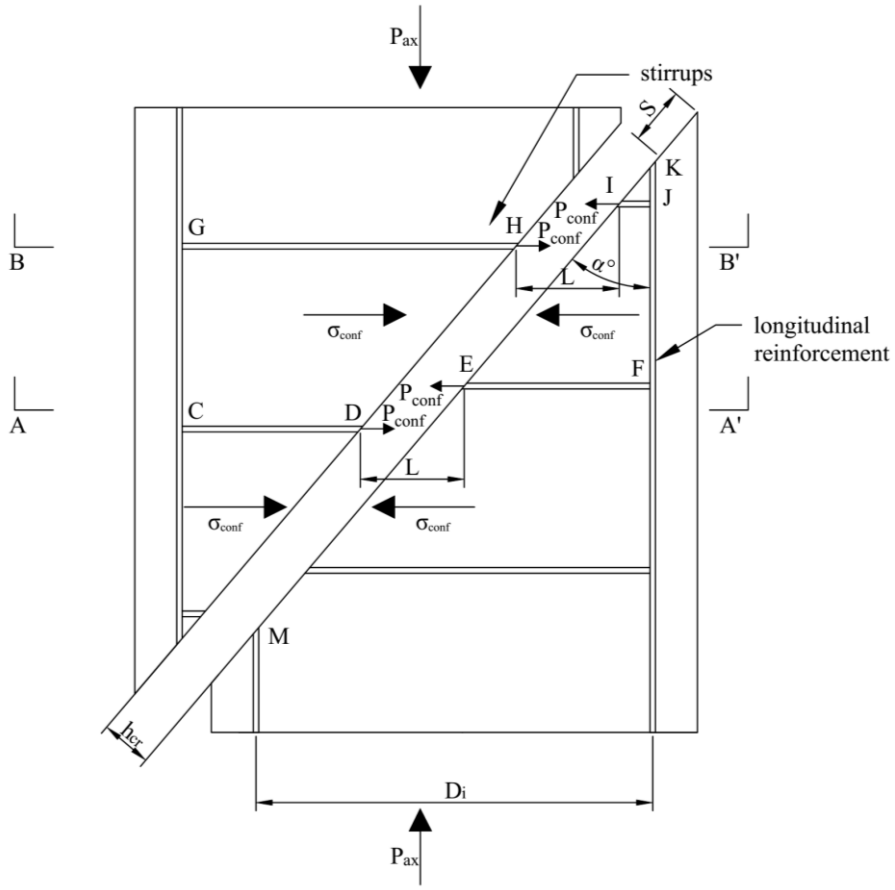

Fig. 1 Stirrups reinforced concrete column under axial load

It is assumed in this report that both the stirrup reinforced concrete column in Fig. 1 and the plated concrete column in Fig. 2 that are under concentric loads P_{ax} will fail because of sliding along a single sliding plane at an angle of α as shown (Chen, Visintin & Oehlers 2015a; Chen et al. 2015). It should be noted that the sections of the columns in Figs. 1 and 2 can be either rectangular or circular and we will consider the rectangular case first, where D_i is the width of the transverse reinforcement as shown. For a column whose slenderness ratio is equal to or more than three, sliding most likely occurs across a single sliding plane as in Figs. 1 and 2 (Ali, Oehlers & Griffith 2010; Visintin, Chen & Oehlers 2015). For slenderness ratios less than three such as in standard cylinder tests where the slenderness ratio is two, circumferential sliding planes are the most common form of failure (Chen, Visintin & Oehlers 2015a, 2015b; Chen et al. 2015; Oehlers, Deric J et al. 2017) and which occur at higher axial loads. As most columns in structures have a slenderness of more than three and as the strength of a single sliding plane is a lower bound to that due to circumferential sliding planes, only the single sliding plane failure type will be considered in this investigation.

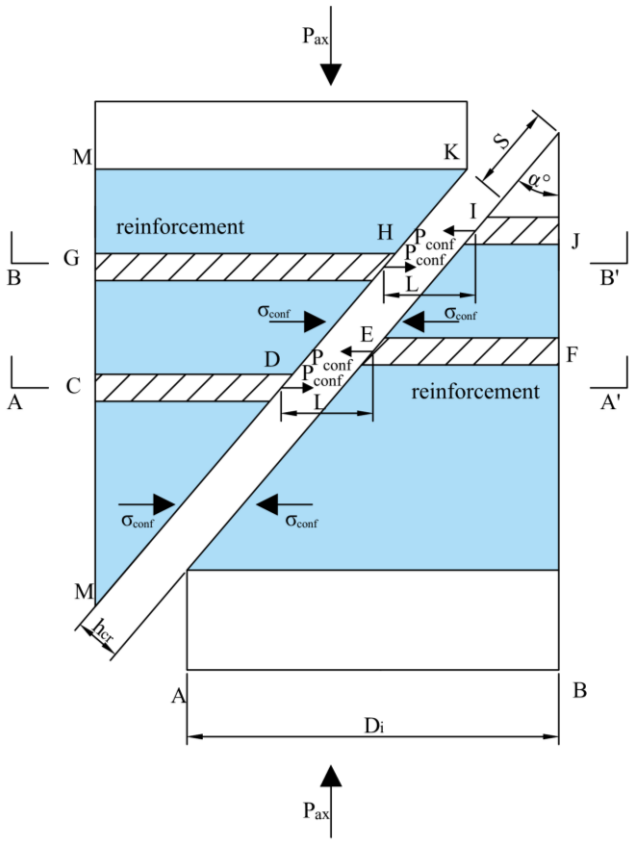

Fig. 2 Plate reinforced concrete column under axial load

In Figs. 1 and 2, the slip due to sliding S and the crack opening h_{cr} will cause the crack width L across the sliding plane as shown and subsequently the confinement force P_{conf} as shown. As the crack opening h_{cr} is an order of magnitude smaller than the slip S (Birkeland & Birkeland 1966; Chen, Visintin & Oehlers 2015a; Haskett, M et al. 2010; Haskett, Matthew et al. 2011), the effect of h_{cr} on the crack width L is ignored in this research which is a further conservative approach. Section A-A' from Fig. 2 can be either a rectangular or a circular section and the rectangular case is shown in Fig. 3 as an example. The crack width L is comprised of the crack face slips Δ of both sides of reinforcement such as Δ_D and Δ_E in Fig. 3, which will induce the confinement force P_{conf} and subsequent confining stress σ_{conf} as in Fig. 2 (Muhamad et al. 2012).

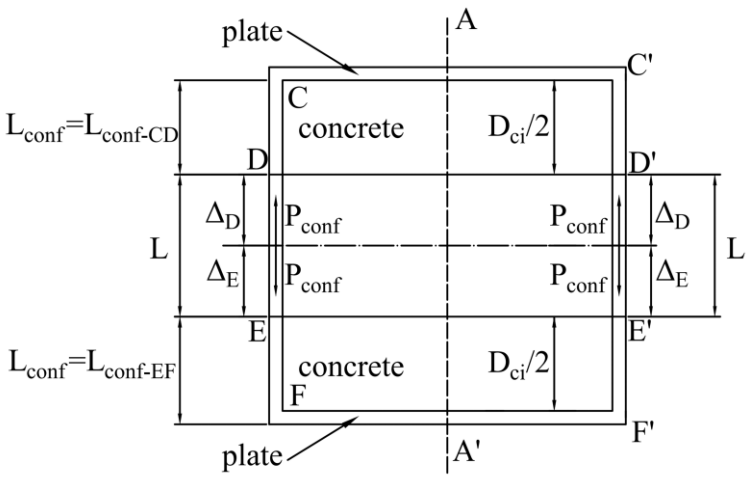

Fig. 3 Rectangular Section A-A' from Fig. 2

In this report, the reinforcement behaviours that includes debonding, yielding, fracture and combinations of these behaviours, will be investigated first. Then all the mechanics details of the relationships between the transverse confinement force P_{conf} and the crack width L in Fig. 3 will be investigated.

Bond-Slip Relationship

For the stirrup reinforced concrete column in Fig. 1 and the plated concrete column in Fig. 2 under concentric loads, the slip S is constant along the shear failure plane. The components of the slip are shown in Fig. 4. The lateral component L is an effective crack width as it is

equivalent to a real crack width of L that would cause forces in the lateral reinforcement that induce confinement as shown in Fig. 3. The longitudinal or axial or vertical component V when divided by specimen height L_{prsm} gives the additional effective axial strain due to sliding. Furthermore, this can be written as that shown in square brackets in Fig. 4 such that the vertical axial deformation that controls the axial behaviour of the member such as under flexure is directly related to the lateral deformation that controls confinement. The horizontal component of the slip S, the effective crack width L, and which is equal to $S\sin\alpha$ is constant along the shear failure plane and this is shown in Figs. 1 and 2.

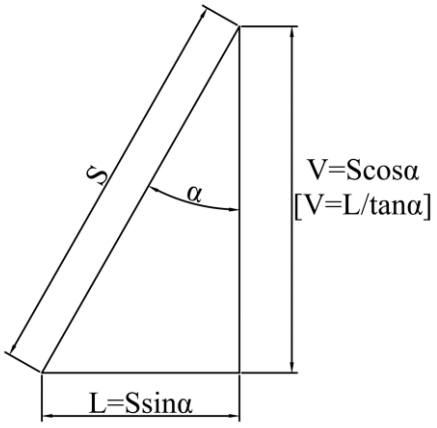

Fig. 4 Vertical component V of slip S and horizontal component L of slip S

Let us consider the mechanics that control confinement across a sliding plane, that is the mechanical relationships between the deformations and the forces in Fig. 3 that induce confinement. It will be shown that the confinement force P_{conf} depends directly on the bond-slip characteristics in Fig. 5, which describes the relationship between the bond stress τ_B and the slip δ between reinforcement and adjacent concrete as explained next.

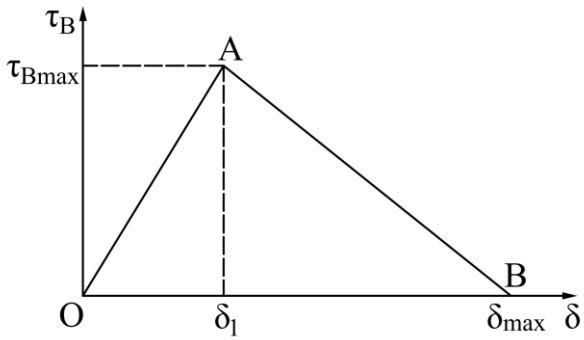

Fig. 5 Bilinear bond-slip relationship for stirrups and plate reinforcement

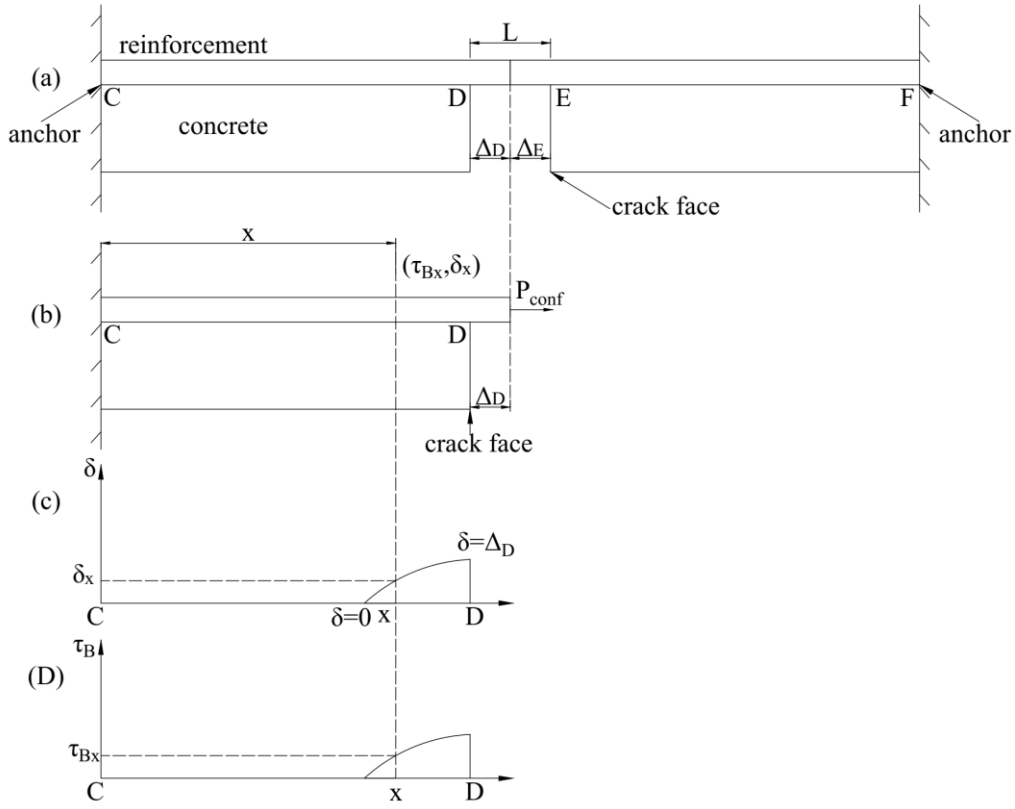

Fig. 6 Reinforcements CD and EF from Fig. 3

Consider the reinforcements CD and EF in Fig. 3 are shown in Fig. 6(a) as an example. The reinforcement ends are anchored because of the right angle bends at points C and F in Fig. 3. At a distance x from point C in Fig. 6(b), the confinement force in the reinforcement P_{conf} will induce the slip δ_x between concrete and reinforcement and subsequently the bond stress τ_{Bx} between them as shown. The distributions of slip δ and bond stress τ_B along the reinforcement CD are shown in Figs. 6(c) and (d) respectively. The relationship between δ and τ_B, that is the material bond property, can be idealised as a bilinear model; this is comprised of the ascending branch OA and the descending branch AB in Fig 5 and the expressions can be written as follows (Haskett, Matthew, Oehlers & Ali 2008; Visintin et al. 2013)

$$\tau_B = \tau_{B\max}\frac{\delta}{\delta_1} \qquad if \quad \delta \le \delta_1 \tag{1}$$

$$\tau_B = \tau_{B\max}\frac{\delta_{\max}-\delta}{\delta_{\max}-\delta_1} \qquad if \quad \delta_1 \le \delta \le \delta_{\max} \tag{2}$$

$$\tau_B = 0 \qquad if \quad \delta \geq \delta_{\max} \tag{3}$$

where τ_{Bmax} is the peak bond stress, δ_1 is the slip between the reinforcement and adjacent concrete at τ_{Bmax} and δ_{max} is the slip between the reinforcement and adjacent concrete when the bond stress τ_B reduces to zero. The slip δ specifically at the crack face is referred to as the crack face slip Δ as shown in Fig. 6(a) and crack face slips of both sides of the confinement reinforcement that is Δ_D and Δ_E make up the crack width L as shown. In the following section, the relationship between the confinement force P_{conf} and the crack width L will be investigated for both rectangular-section columns and circular-section columns.

Reinforced Concrete Column with Rectangular Sections

The case of a rectangular column will first be considered and the results will then be used in the analysis of circular column sections. The mechanics for both the stirrup reinforced column in Fig. 1 and the plated column in Fig. 2 are almost identical so only the latter case in Fig. 2 will be described here.

Displacement

The width of the transverse reinforcement in Fig. 2 is equal to D_i. The Sections A-A' and B-B' through the rectangular-section column in Fig. 2 are shown in Figs. 3 and 7 respectively. In the former case in Fig. 3, the crack is at the centre and in the latter one in Fig. 7 the crack is off-centre. As a result, the length of the confinement reinforcement L_{conf} for the former case in Fig. 3 is equal to $D_i/2$. However, for the latter one in Fig. 7: L_{conf} of the reinforcement IJ is referred to as $L_{conf\text{-}IJ}$ and has a length x; such that L_{conf} of the reinforcement GH $L_{conf\text{-}GH}$ is equal to D_i-x. The crack width L in both Figs. 3 and 7 equals the sum of the reinforcement crack face slips of both sides as follows

$$L = \Delta_D + \Delta_E = \Delta_H + \Delta_I \tag{4}$$

where Δ_D and Δ_E in Fig. 3 as well as Δ_H and Δ_I in Fig. 7 are the reinforcement slips at the crack faces. It should be noted that at the crack face, the confinement forces P_{conf} in both

sides are equal and the reinforcement ends are anchored because of the right angle bends such as points C, C', F and F' in Fig. 3 and G, G', J and J' in Fig. 7. The anchored confinement reinforcement may either debond, or yield or fracture or be subjected to a combination of these effects and the behaviour will be investigated in the following section.

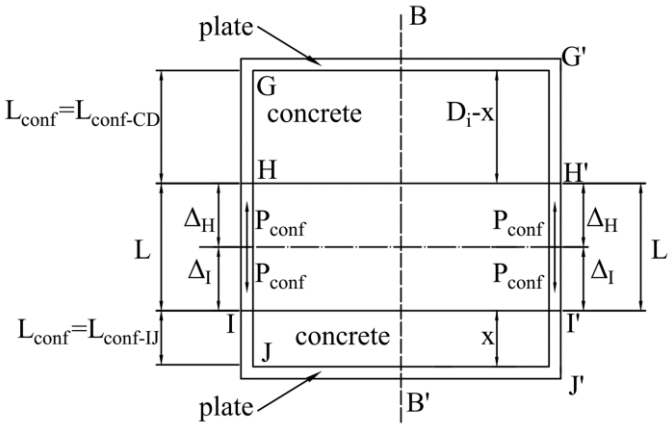

Fig. 7 Section B-B' from Fig. 2

Confinement Behaviour

The behaviour of the confinement reinforcement will be investigated in this section. The debonding procedure in Fig. 8 will be described first. When the bond stress distribution in Fig. 5 is fully developed along the confinement reinforcement as in Fig. 8(c), the bond force reaches its maximum value and consequently the force in the confinement reinforcement reaches its maximum value that is when only restrained by the bond stresses. This is referred to as the intermediate crack (IC) debonding resistance P_{IC} which is the maximum bond force and is given by (Ali et al. 2008; Oehlers, Deric John et al. 2008; Seracino, Raizal Saifulnaz & Oehlers 2007; Yuan et al. 2004)

$$P_{IC} = \sqrt{\tau_{B\max}\delta_{\max}}\sqrt{L_{per}E_rA_r} \tag{5}$$

where E_r is the modulus of the reinforcement, L_{per} and A_r in Fig. 9 are the total length of the potential debonding failure planes and the total cross-section area of the reinforcement respectively as shown. As shown in Fig. 8(c), the length of confinement reinforcement required to develop P_{IC} is L_{crt} which can be expressed as (Seracino, Raizal Saifulnaz & Oehlers 2007)

$$L_{crt} = \frac{\pi}{2\lambda} \tag{6}$$

where the parameter λ can be expressed as

$$\lambda = \sqrt{\frac{\tau_{B\max} L_{per}}{\delta_{\max} E_r A_r}} \tag{7}$$

where δ_{max} and τ_{Bmax} are shown in Fig. 5.

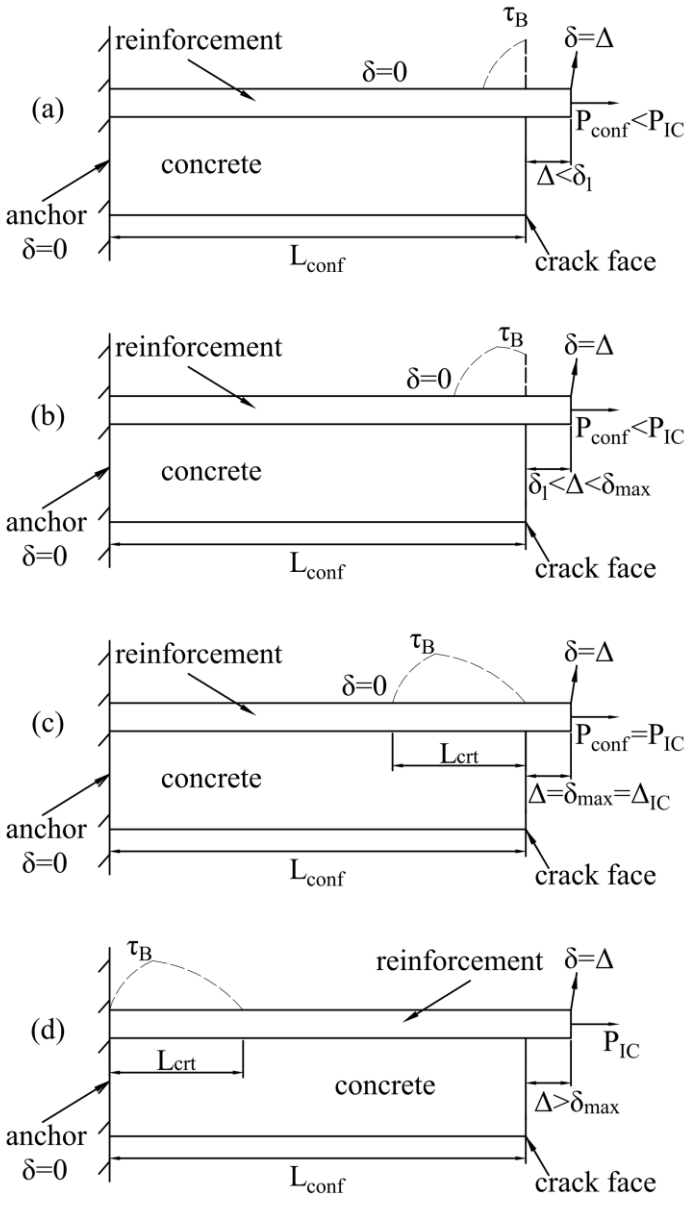

Fig. 8 Procedure of confinement debonding when $L_{conf}>L_{crt}$

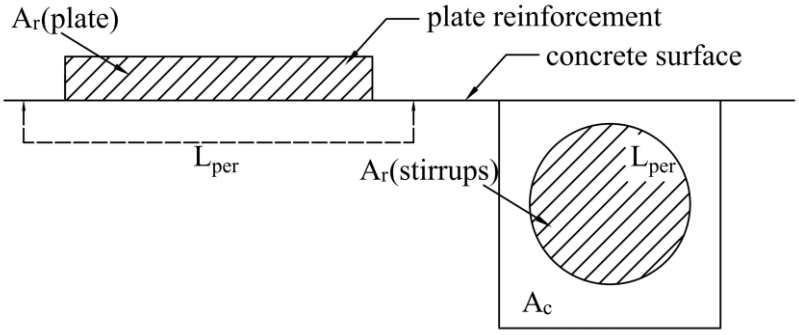

Fig. 9 Debonding of stirrups or plate confinement

The behaviour of the reinforcement is determined by the relationship between the critical length L_{crt} from Eq. (6) and the length of the confinement reinforcement L_{conf} which is shown in Figs. 3 and 7. The case when L_{crt} is smaller than L_{conf} will be described first and this is then followed by the case when L_{crt} is larger.

The case when L_{crt} is smaller than L_{conf}

When L_{crt} is smaller than L_{conf}, the confinement reinforcement behaviour depends on the relative values between the debonding force P_{IC}, the yield force P_{yld} and the fracture force P_{frac}, such that the debonding of the confinement reinforcement may either occur or not. The case where debonding occurs prior to yielding or fracture will be described first.

Debonding occurs prior to yielding or fracture

When the debonding force P_{IC} is smaller than the yield force P_{yld} or fracture force P_{frac}, the confinement reinforcement will debond first then yield or fracture. The relationship between the confinement force P_{conf} and the crack face slip Δ is shown in Fig. 10 where for ease of analysis this relationship is assumed to be piecewise linear. The whole debonding process is shown in Fig. 8. Firstly, when the reinforcement slip at the crack face Δ in Fig. 8(a) is less than δ_1 in Fig. 5, then the confinement force P_{conf} is less than P_{IC} as shown in Fig. 8(a). Increasing the reinforcement slip Δ at the crack face such that Δ is larger than δ_1 but smaller than δ_{max} in Fig. 5 gives Fig. 8(b). When the crack face slip Δ reaches δ_{max} in Fig. 8(c) that is also referred to as Δ_{IC}, the confinement force will reach P_{IC} at point A in Fig. 10; the stress distribution at which this occurs is labelled τ_B in Fig. 8(c) and occurs over the critical length

L_{crt}. Any further increase in Δ will now cause debonding as the bond stress block τ_B will move along the length of the confinement reinforcement L_{conf} towards the reinforcement end as in Fig. 8(d). Meanwhile, the confinement force P_{conf} will remain the same at P_{IC} and the reinforcement slip at the crack face Δ will increase until the bond stress distribution reaches the confinement reinforcement end at a crack face slip Δ_{deb}, that is point B in Fig. 10, where Δ_{deb} can be written as

$$\Delta_{deb} = \Delta_{IC} + \varepsilon_{IC}(L_{conf} - L_{crt}) \tag{8}$$

where ε_{IC} is the strain in the confinement reinforcement when the confinement force is P_{IC} that is ε_{IC} is $P_{IC}/(E_r A_r)$ and L_{crt} can be obtained from Eq. (6). A further increase of the crack face slip Δ in Fig. 8(d) will lead to a reduction of the component of the confinement force due to bond and an increase of the component due to anchorage. However, for convenience it will be assumed that the confinement force P_{conf} is kept constant at P_{IC} until Δ reaches the following Δ_{IC2} at point C in Fig. 10 which can be written as

$$\Delta_{IC2} = \varepsilon_{IC} L_{conf} \tag{9}$$

after which, an increase in the reinforcement slip at the crack face will increase the confinement reinforcement strain. Subsequently, the confinement force due to the anchorage of the confinement reinforcement end will after completely debonding at point C: either yield at (Δ_{yld}, P_{yld}) that is point D in Fig. 10 then fracture at (Δ_{frac}, P_{frac}) that is point E in Fig. 10; or directly fracture at point E. The corresponding crack face slip when the reinforcement yields or fractures, that is Δ_{yld} or Δ_{frac} respectively, can be written as follows

$$\Delta_{yld} = \varepsilon_{yld} L_{conf} \tag{10}$$

$$\Delta_{frac} = \varepsilon_{frac} L_{conf} \tag{11}$$

where ε_{yld} and ε_{frac} are the yield and fracture strains respectively.

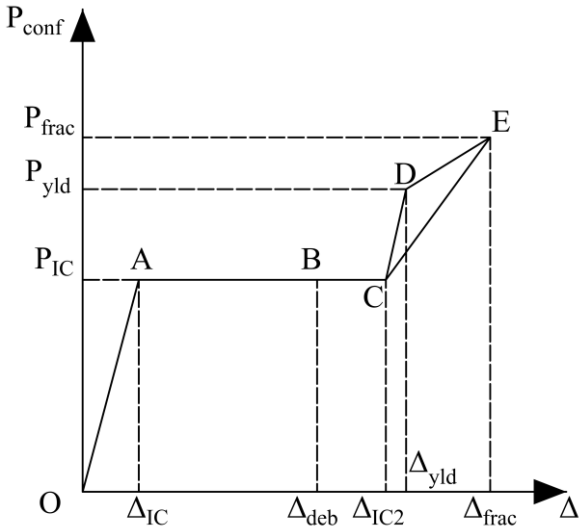

Fig. 10 The relationship between confinement force P_{conf} and crack face slip Δ when debonding occurs prior to yielding or fracture and $L_{conf}>L_{crt}$

From the above analyses, the relationship between the crack width L and the confinement force P_{conf} will be described next. When L_{crt} is less than L_{conf} on both sides of the crack face as may occur in Figs. 3 and 7 when all values of L_{conf} are larger than L_{crt}, then at the commencement of IC debonding as in Fig. 8(c) the confinement force is P_{IC} and the width of the crack at the start of IC debonding L_{IC} is

$$L_{IC} = 2\Delta_{IC} \tag{12}$$

Furthermore, when the bond stress distribution reaches the reinforcement end as in Fig. 8(d), the confinement force remains at P_{IC} and the following crack width L_{deb} can be obtained from Eq. (8)

$$L_{deb} = 2\Delta_{IC} + \varepsilon_{IC}(D_i - 2L_{crt}) \tag{13}$$

where L_{crt} can be obtained from Eq. (6) and D_i is shown in Fig. 2. After which at the end of debonding but still at P_{IC}, the width of the crack L_{IC2} can be derived from Eq. (9) as

$$L_{IC2} = \varepsilon_{IC} D_i \tag{14}$$

A further increase in the crack width L will cause a direct increase in the confinement reinforcement strain and consequently an increase in the confinement force due to anchorage of the confinement reinforcement ends. When the confinement reinforcement either yields then fractures or directly fractures, the crack width L_{yld} at P_{yld} and L_{frac} at P_{frac} can be obtained from Eqs. (10) and (11)

$$L_{yld} = \varepsilon_{yld} D_i \tag{15}$$

$$L_{frac} = \varepsilon_{frac} D_i \tag{16}$$

It is worth noting that L_{crt} may be less than L_{conf} on one side but not on the other as might occur in Fig. 7. In which case at the attainment of P_{IC} that is on the commencement of debonding on one side, the crack width L_{IC} is less than $2\Delta_{IC}$; this is because on one side the crack face slip is Δ_{IC} but on the other side it is less due to the anchorage. Hence Eq. (12) will at worst give a conservative estimate in analysis when applied throughout the sliding plane. However at the end of debonding, Eqs. (13), (14), (15) and (16) still apply, that is these equations are always correct throughout the sliding plane in Figs. 1 and 2.

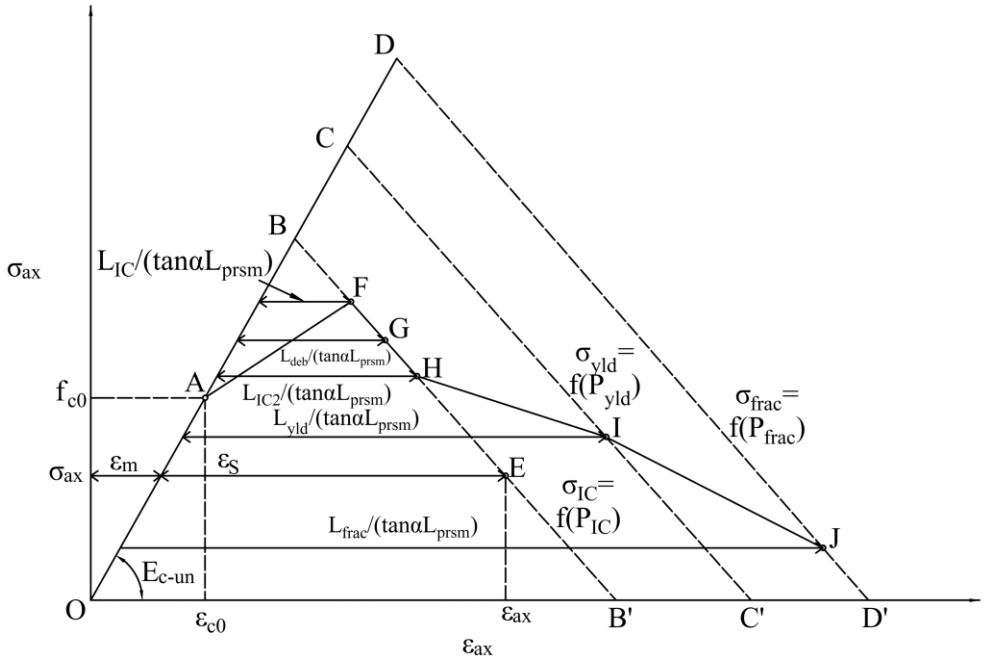

Fig. 11 The closed form solution of stress-strain relationship of passively confined concrete columns when debonding occurs prior to yielding or fracture and $L_{conf}>L_{crt}$

The relationship between the confinement force P_{conf} and the crack width L is employed to derive the closed form solution of the stress-strain relationship of passively confined concrete columns. Full details of the derivation are shown elsewhere (Hao 2017). Let us consider the stress-strain relationship in Fig. 11 of the passively confined concrete when debonding occurs prior to yielding or fracture and for the case where $L_{conf}>L_{crt}$. The ascending branch O-A-B-C-D in Fig. 11 and the descending branches B-B', C-C' and D-D' are idealised as linear. The positions of these falling branches are determined by the confining stresses σ_{conf} from the confinement reinforcement, which is a function of the confinement force P_{conf}. For instance, the confining stress σ_{IC} of the falling branch B-B', σ_{yld} of the falling branch C-C' and σ_{frac} of the falling branch D-D' are the functions of the debonding force P_{IC}, yield force P_{yld} and fracture force P_{frac} respectively.

To summarise Fig. 11 (Hao 2017). The ascending branch of the concrete stress-strain O-A-B-C-D is a material property that can be obtained directly from compression tests. The descending branch B-B' is due to sliding, as shown in Figs. 1 and 2, when an active confining stress σ_{conf} is of magnitude σ_{IC} that is when the force in the confining reinforcement is P_{IC}. Path B-B' can be obtained from the shear friction properties (Hao 2017). Similarly the descending branch C-C' is the descending branch which can be obtained from the shear friction properties when there is an active confinement of σ_{yld} that is when the reinforcement is at yield at P_{yld}. Finally, the descending branch D-D' applies when the reinforcement is about to fracture that is when the force in the reinforcement is P_{frac} such that the active confinement is σ_{frac}. On application of a load such as P_{ax} in Fig. 1, the stress in a concrete element follows the path of the ascending branch O-A in Fig. 11 of the unconfined concrete until at f_{c0} a sliding plane occurs such that the path diverges from O-A at point A. When there is sufficient sliding that the confinement reinforcement force is at P_{IC} such that the confining stress is σ_{IC}, then the path is somewhere along B-B' and it is a question of determining what part of B-B' or what point on B-B' is on the stress path. When there is sufficient sliding to cause yield such that the confining stress is σ_{yld}, then it is a question of determining which part or point of C-C' lies on the stress path and similarly for D-D' at fracture. Let us consider how this is achieved.

As an example, consider point E in Fig. 11 on the descending branch B-B'; any point on any of the descending branches could have been used. The axial strain ε_{ax} in Fig. 11 of point E is comprised of the material strain ε_m and sliding strain ε_s caused by sliding as follows

$$\varepsilon_{ax} = \varepsilon_m + \varepsilon_S \tag{17}$$

where ε_m as shown in Fig. 11 is $\sigma_{ax}/E_{c\text{-}un}$ in which σ_{ax} is the axial stress and $E_{c\text{-}un}$ is the material modulus, and ε_s can be expressed as

$$\varepsilon_s = \frac{V}{L_{prsm}} \tag{18}$$

where L_{prsm} is the height of the concrete column and V shown in Fig. 4 is the vertical component of the slip S such that V is also a function of the crack width L as from Fig. 4 the lateral deformation L=Ssinα. Hence

$$V = S\cos\alpha = \frac{L}{\tan\alpha} \tag{19}$$

Substituting V from Eq. (19) into Eq. (18) gives the following sliding strain ε_s

$$\varepsilon_s = \frac{L}{\tan\alpha L_{prsm}} \tag{20}$$

To derive a closed form solution for the stress-strain relationship of a passively confined concrete, the axial stress σ_{ax} and strain ε_{ax} of key points such as the points that the confinement reinforcements debond, yield or fracture are required; these are shown as points F to J in Fig. 11.

The crack widths L and consequently the strain ε_s, which can be obtained by substituting the crack width L into Eq. (20), and the confinement forces P_{conf} and consequently the confinement stresses σ_{conf} can be obtained for the key points in Fig. 11 as follows.

- At point A in Fig. 11, sliding is about to start at the coordinates (ε_{c0}, f_{c0}) where f_{c0} and ε_{c0} are the unconfined concrete strength and strain at f_{c0} respectively.

- As sliding occurs after point A, debonding commences at point F in Fig. 11; at point F the crack width equals L_{IC} from Eq. (12) and the confinement force is P_{IC} such that the confining stress is σ_{IC} and consequently on the falling branch B-B' which was derived for a confinement of σ_{IC}. The position of point F is fixed by ensuring that the horizontal distance between the ascending branch O-A-B-C-D and the descending branch B-B' is equal to the sliding strain ε_s obtained by substituting L_{IC} from Eq. (12) into Eq. (20) that is $L_{IC}/(\tan\alpha L_{prsm})$ as shown in Fig. 11. Point F can occur above or below point A. To simplify the derivation of closed form solutions, it has been assumed that there is a linear variation between points A and F.
- After point F in Fig. 11 and on further sliding, the crack width will increase to L_{deb} from Eq. (13) whilst the confining stress remains at σ_{IC}. Hence the sliding strain is obtained by substituting L_{deb} from Eq. (13) into Eq. (20) that is $L_{deb}/(\tan\alpha L_{prsm})$. Point G is fixed by finding the position where the horizontal distance between O-A-B-C-D and B-B' is equal to $L_{deb}/(\tan\alpha L_{prsm})$ as shown.
- Using the same procedure as outlined above. Point H in Fig. 11 lies on the falling branch B-B' as the confining stress remains at σ_{IC}. Point H is fixed by finding the position where the sliding strain between the ascending branch O-A-B-C-D and B-B' is $L_{IC2}/(\tan\alpha L_{prsm})$ as shown where the crack width L_{IC2} is obtained from Eq. (14).
- After a further increase in sliding, the crack width L may cause yield of the confinement reinforcement at the confinement force P_{yld} and confining stress σ_{yld} and, therefore, the next point I must lie on C-C' where the confinement stress is σ_{yld}. Point I is fixed by finding the position where the sliding strain between the ascending branch O-A-B-C-D and C-C' is $L_{yld}/(\tan\alpha L_{prsm})$ as shown where the crack width L_{yld} is obtained from Eq.(15). To ease the complexity of finding closed form solutions, it has been assumed that there is a linear variation between points H and I.
- After yielding, fracture of the reinforcement at the confinement force P_{frac} and confinement stress σ_{frac} lies somewhere along D-D' which was obtained for a confinement of σ_{frac}. The crack width L_{frac} is given by Eq. (16) which can be used to fix point J as shown using the sliding strain $L_{frac}/(\tan\alpha L_{prsm})$. Once again, a linear interpolation between points I and J is assumed to help in the derivation of closed form solutions.

- For reinforcements that do not yield, the reinforcement may directly fracture at point J in Fig. 11 after completely debonding at point H that is there is a linear load path H to J as shown.

As stated previously, for convenience and in order to develop closed form solutions, the stress-strain path in Fig. 11 is assumed to be linear between critical points as shown. It is also worth noting that if a solution cannot be found, this simple means that there is insufficient sliding capacity. For example, for fracture to occur a sliding strain of $L_{frac}/(\tan\alpha L_{prsm})$ is required as shown. If this strain exceeds O-D', then this simply means that the sliding capacity is not sufficient to fracture the reinforcement.

Yielding or fracture occurs prior to debonding

Consider the case when yielding or fracture precedes debonding and when the critical length L_{crt} is smaller than the confinement reinforcement length L_{conf} as in Fig. 8(c). The assumed relationship between the confinement force P_{conf} and crack face slip Δ is shown in Fig. 12. Point D, at P_{IC} and Δ_{IC} and which can be derived through mechanics, is therefore fixed through mechanics. Yield or fracture may happen when the bond stress is not fully developed as shown in Figs. 8 (a) and (b). However as point D is fixed and for ease of analysis, it is assumed that there is a linear variation in Fig. 12 from the origin to point D. The fracture force P_{frac} and yield force P_{yld} are smaller than the debonding force P_{IC} such that the confinement reinforcement may either directly fracture at (Δ_{frac2}, P_{frac}) at point B or yield at (Δ_{yld2}, P_{yld}) at point A. As we are assuming a linear variation O-A-B-D in Fig. 12, the stiffness of this linear variation is $E_1 = P_{IC}/\Delta_{IC}$ such that Δ_{yld2} and Δ_{frac2} can be expressed as

$$\Delta_{yld\,2} = \Delta_{IC}\frac{P_{yld}}{P_{IC}} \tag{21}$$

$$\Delta_{frac\,2} = \Delta_{IC}\frac{P_{frac}}{P_{IC}} \tag{22}$$

where P_{IC} is obtained from Eq. (5) and Δ_{IC} can be obtained through mechanics (Ali et al. 2008; Lu et al. 2005).

After yielding of the confinement reinforcement that is at point A in Fig. 12, the confinement force is assumed to be kept constant at P_{yld}; the effect of strain hardening on the IC debonding resistance (Haskett, Matthew et al. 2009) is ignored in this research to achieve a simple yet conservative solution for design purpose. It will be assumed that as yielding progresses along L_{conf}, the bond stress in Fig. 8 is gradually destroyed (Shima, Chou & Okamura 1987). Hence when yielding is complete along L_{conf} and the confinement force is still maintained at P_{yld} then point C in Fig. 12 is given by the crack face slip Δ_{yld} which can be obtained from Eq. (10) and P_{yld}. After which, a further increase in the crack face slip will cause the fracture of the confinement reinforcement at P_{frac} that is point E in Fig. 12 and the crack face slip Δ_{frac} can be obtained from Eq. (11).

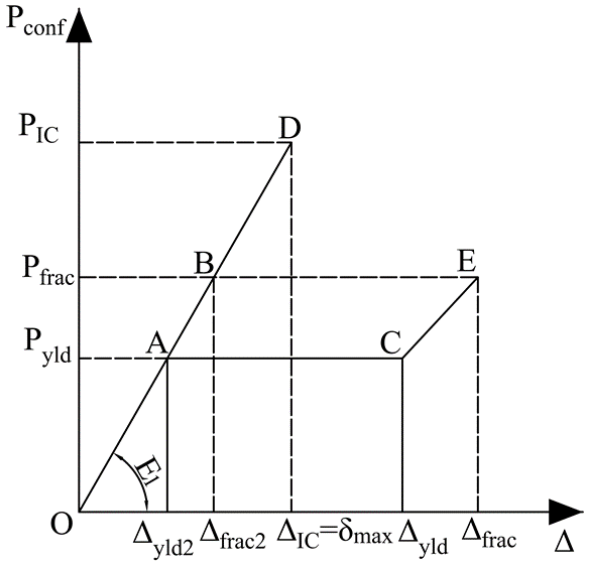

Fig. 12 The relationship between confinement force P_{conf} and crack face slip Δ when yielding or fracture occur prior to debonding and $L_{conf}>L_{crt}$

From the above analyses, when L_{crt} from Eq. (6) is less than L_{conf} on both sides of the crack face and $P_{IC}>P_{frac}$ or $P_{IC}>P_{yld}$, the confinement reinforcement may fracture directly and at the commencement of fracture the following width of the crack L_{frac2} can be written as

$$L_{frac2} = 2\Delta_{frac2} \tag{23}$$

where Δ_{frac2} can be achieved from Eq. (22). The confinement reinforcement may also yield. At the commencement of yielding the following width of the crack L_{yld2} can be written as

$$L_{yld2} = 2\Delta_{yld2} \tag{24}$$

where Δ_{yld2} can be obtained from Eq. (21). After which, when the reinforcement is completely yielded the crack width L_{yld} can be obtained from Eq. (15). Then a further increase in the crack width will cause the fracture of the confinement reinforcement when the crack width L_{frac} can be obtained from Eq. (16).

Similar to the case when debonding occurs first and $L_{crt}<L_{conf}$. The critical length L_{crt} may be less than L_{conf} on one side of the crack face but not on the other as might occur in Fig. 7. Then at the commencement of yielding or fracture, the crack widths L_{frac2} and L_{yld2} may be less than $2\Delta_{frac2}$ or $2\Delta_{yld2}$ respectively from Eqs. (23) or (24) because on one side the crack face slip is Δ_{frac2} or Δ_{yld2} but on the other side it may be less due to the anchorage. Hence these crack widths will give a conservative estimate in analysis when applied throughout the sliding plane. However Eqs. (15) and (16) at the completion of yield or fracture still apply, that is they are always correct throughout the sliding plane.

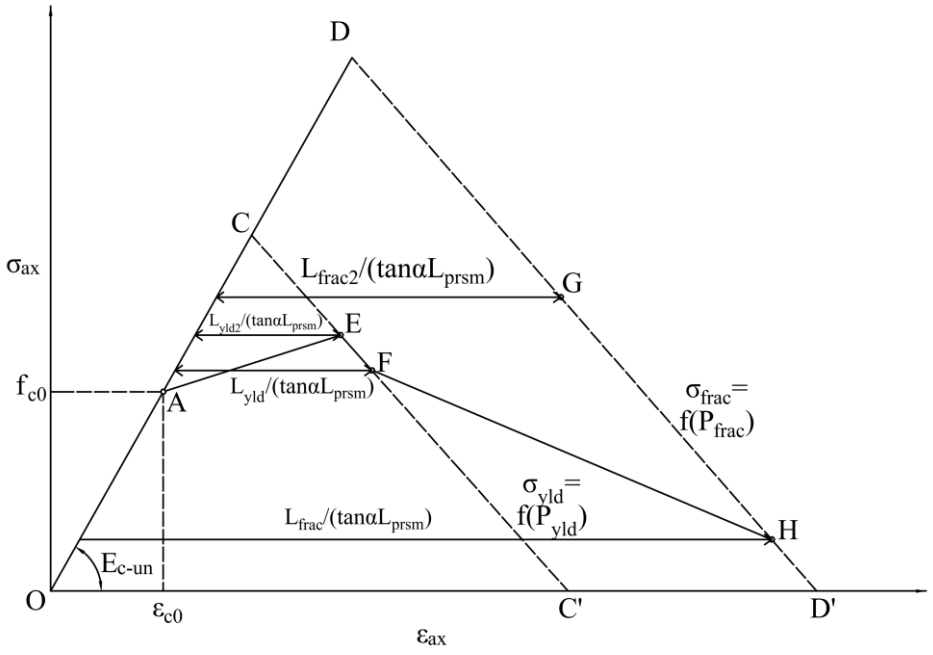

Fig. 13 The closed form solution of stress-strain relationship of passively confined concrete columns when yielding or fracture occurs prior to debonding and $L_{conf}>L_{crt}$

Consider the construction of the passive stress-strain relationship for the case when $L_{crt}<L_{conf}$ and P_{IC} is larger than P_{yld} or P_{frac} as shown in Fig. 13. Equations. (23), (24), (15) and (16) can be used in the construction of the stress-strain relationship of passively confined concrete as in Fig. 13 where: should yield occur before fracture then the path is O-A-E-F-H; or should fracture occur before yield then the path is O-A-G. This case when $L_{crt}<L_{conf}$ and P_{IC} is larger than P_{yld} or P_{frac} is similar to the previous case in Fig. 11, where $L_{crt}<L_{conf}$ and P_{IC} is smaller than P_{yld} or P_{frac}. However, IC debonding does not occur such that B-B' in Fig. 11 does not exist as shown in Fig. 13.

In summary. For the fracture case where yielding does not occur, the confinement reinforcement will fracture at point G in Fig. 13, where the crack width equals L_{frac2} from Eq. (23) instead of L_{frac} from Eq. (16) and the confinement force is P_{frac} such that the confining stress is σ_{frac} and consequently on the falling branch D-D'. The position of point G is fixed by finding the position where the horizontal distance between O-A-C-D and D-D' is equal to the sliding strain derived by substituting L_{frac2} from Eq. (23) into Eq. (20) that is $L_{frac2}/(\tan\alpha L_{prsm})$ as shown. In addition, for the yield case, yielding commences at point E, where the crack width equals L_{yld2} from Eq. (24) instead of L_{yld} from Eq. (15) and the confinement force is P_{yld} such that the confining stress is σ_{yld} and consequently on the falling branch C-C'. The position of point E is fixed by finding the position where the horizontal distance between O-A-C-D and C-C' is equal to the sliding strain derived by substituting L_{yld2} from Eq. (24) into Eq. (20) that is $L_{yld2}/(\tan\alpha L_{prsm})$ as shown. It is worth noting that the position of completely yielding at point F in Fig. 13 is the same as that of yield point I in Fig. 11. The other procedures are the same.

The case when L_{crt} is larger than L_{conf}

Confinement reinforcement behaviour

When the critical length L_{crt} in Fig. 8(c) is larger than the confinement length L_{conf}, the bond distribution labelled τ_B cannot be fully developed. Consequently the relationship between the confinement force P_{conf} and crack face slip Δ shown in Figs. 8, 10 and 12 and given by their associated equations above are not applicable.

The case where $L_{conf}<L_{crt}$ is shown in Figs. 14(a-c) where the anchor to the reinforcement is on the left and the crack face on the right. The variation in slip δ is shown in Fig. 14(b) where, because of the anchor, the slip on the left δ is zero and that on the right at the crack face is the crack face slip Δ as shown. The variation in the bond shear stress τ_B is shown in Fig. 14(a). The variations in Figs. 14(a), (b) and (c) are identical to that which occurs in a multi-crack analysis (Oehlers, D et al. 2012; Zhang, Visintin & Oehlers 2015; Zhang, Visintin & Oehlers 2017; Zhang et al. 2014) with a crack spacing S_p of $2L_{conf}$ in Figs 14(d) and (e) where by symmetry the slip midway between cracks is zero. Hence the relationship between the confinement force P_{conf} and the crack face slip Δ from a multi-crack analysis is directly applicable.

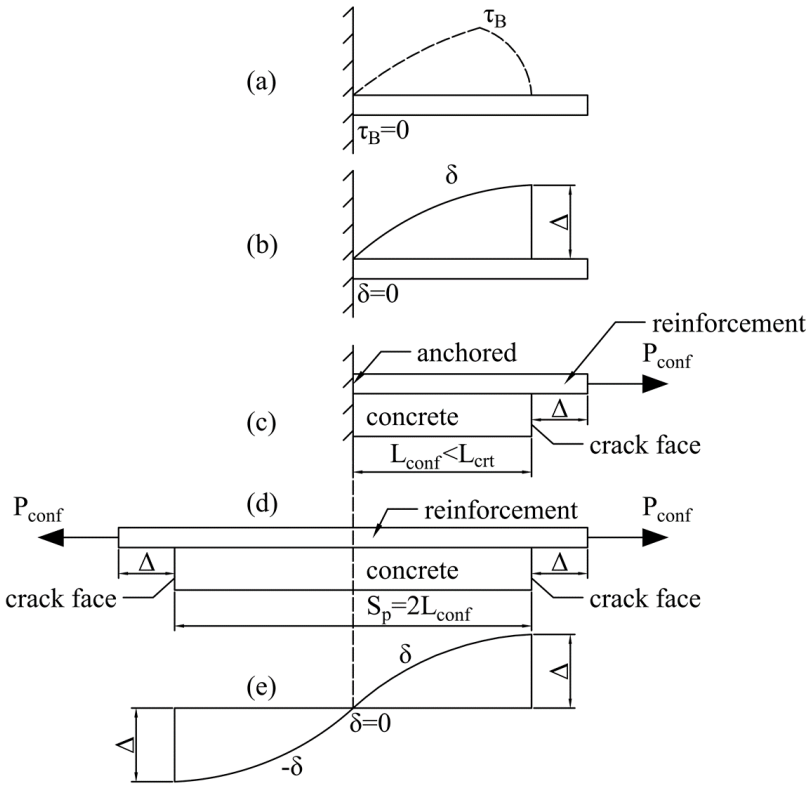

Fig. 14 Analysis of the case when $L_{conf}<L_{crt}$ (a-c) and multi-crack analysis (d and e)

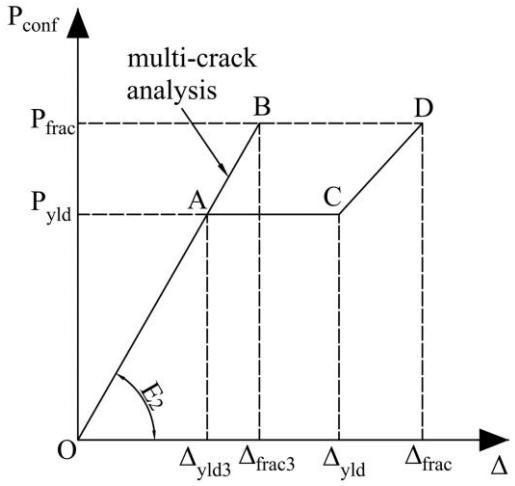

Fig. 15 The relationship between confinement force P_{conf} and crack face slip Δ when $L_{conf}<L_{crt}$

The P_{conf}/Δ relationship from a multi-crack analysis is shown as O-A-B in Fig. 15 with stiffness E_2 as shown. Let us first consider the fracture case, that is the reinforcement fractures directly without showing yielding behaviour. The confinement reinforcement will fracture at (Δ_{frac3}, P_{frac}) that is point B in Fig. 15. With regard to the yield case, the confinement reinforcement will firstly yield at (Δ_{yld3}, P_{yld}) at point A in Fig. 15. After the start of yielding and as yielding progresses, the bond in Fig. 14(a) is gradually destroyed (Shima, Chou & Okamura 1987). Consequently when yielding is complete and still at P_{yld}, the crack face slip is Δ_{yld} from Eq. (10) that is point C in Fig. 15. After which, the confinement reinforcement will fracture at (Δ_{frac}, P_{frac}) at point D, where Δ_{frac} can be derived from Eq. (11). With regard to Δ_{frac3} and Δ_{yld3}, they can be derived from multi-crack analysis. Closed form solutions to quantify Δ_{frac3} or Δ_{yld3} as proposed by Sturm, Visintin and Oehlers (2018) can be written as follows

$$\Delta_{frac3} = \frac{P_{frac}}{\lambda E_r A_r} \tanh\left(\frac{\lambda S_p}{2}\right) \tag{25}$$

$$\Delta_{yld3} = \frac{P_{yld}}{\lambda E_r A_r} \tanh\left(\frac{\lambda S_p}{2}\right) \tag{26}$$

where S_p is the primary crack spacing that is equal to $2L_{conf}$ as shown in Fig. 14(d), and λ is the variation in the slip parameter which can be written as follows

$$\lambda = \sqrt{\beta k} \tag{27}$$

where the prism parameter β and bond-slip stiffness k can be expressed as

$$\beta = L_{per}\left(\frac{1}{E_r A_r} + \frac{1}{E_c A_c}\right) \tag{28}$$

$$k = \frac{\tau_{B\max}}{\delta_1} \tag{29}$$

It should be noted that for a plate reinforcement the area of the reinforcement A_r is much smaller than that of the concrete A_c such that Eq. (28) can be simplified as follows (Ali et al. 2008)

$$\beta = \frac{L_{per}}{E_r A_r} \tag{30}$$

Relationship between confinement force P_{conf} and crack width L

In this section the crack width L will be quantified at different confinement forces P_{conf} including P_{frac} and P_{yld} in Fig. 15. It is worth noting that when $L_{crt}>L_{conf}$ the confinement reinforcement slips at the crack face Δ_{frac3} and Δ_{yld3} in Fig. 15 can be quantified from Eqs. (25) and (26) respectively, where S_p is equal to $2L_{conf}$ as in Fig. 14(d). This means that the length of the confinement reinforcement L_{conf} will affect the confinement reinforcement slip Δ_{frac3} and Δ_{yld3} at the crack face and, subsequent, the corresponding crack width L_{frac3} and L_{yld3}, which will be derived below.

Consider the cross section B-B' in Fig. 7 which can be a yield case or fracture case and in which L_{crt} is larger than L_{conf}. The yield case will be discussed first. For reinforcements GH and IJ in Fig. 7, the lengths of the confinement reinforcements L_{conf} are referred to as $L_{conf\text{-}GH}$ and $L_{conf\text{-}IJ}$, and are assumed to have lengths of D_i-x and x respectively as shown. As a result, the following crack width L'_{yld3}, when the confinement reinforcement starts to yield, can be derived from Eqs. (4) and (26) by substituting $L_{conf\text{-}GH}=D_i$-x, $L_{conf\text{-}IJ}=x$ and $S_p=2L_{conf}$

$$L'_{yld} = \frac{P_{yld}}{\lambda E_r A_r}\tanh(\frac{2\lambda x}{2}) + \frac{P_{yld}}{\lambda E_r A_r}\tanh[\frac{2\lambda(D_i - x)}{2}] \quad (31)$$

rearranging Eq. (31) gives

$$L'_{yld} = \frac{P_{yld}}{\lambda E_r A_r}\frac{\sinh(D_i\lambda)}{\cosh(\lambda x)\cosh[\lambda(D_i - x)]} = \frac{P_{yld}}{\lambda E_r A_r}\frac{\sinh(D_i\lambda)}{\frac{1}{2}\cosh(D_i\lambda) + \frac{1}{2}\cosh(D_i\lambda - 2\lambda x)} \quad (32)$$

simplifying Eq. (32) gives

$$L'_{yld3} = \frac{P_{yld}}{\lambda E_r A_r}\{\frac{2\sinh(D_i\lambda)}{\cosh(D_i\lambda) + \cosh[\lambda(D_i - 2x)]}\} \quad (33)$$

when $L_{conf\text{-}IJ}=x$ in Fig. 7 varies, only $\cosh[\lambda(D_i\text{-}2x)]$ in Eq. (33) is not a constant. This hyperbolic cosine function $y=\cosh x$ in Fig. 16 will reach the lowest value at point A in Fig. 16 at $x=0$ (Oldham, Myland & Spanier 2010). This means that when $D_i\text{-}2x=0$ then $\cosh[\lambda(D_i\text{-}2x)]$ in Eq. (33) will reach the lowest value such that the crack width L'_{yld3} will reach the following highest value L_{yld3} which can be obtained by substituting $D_i\text{-}2x=0$ into Eq. (33)

$$L_{yld3} = \frac{P_{yld}}{\lambda E_r A_r}\{\frac{2\sinh(D_i\lambda)}{\cosh(D_i\lambda) + 1}\} \quad (34)$$

For this case, $D_i\text{-}2x=0$ can be arranged to $x = D_i/2$ and this is the case in Fig. 3 in which the crack is at the mid-width of the cross-section. Consequently, when $L_{crt}>L_{conf}$, L will reach the highest value L_{yld3} for the case in Fig. 3 compared with that in Fig. 7 where the crack is off centre. As a result, it is only necessary to consider the former case in Fig. 3 as this gives a conservative solution compared with the latter one in Fig. 7; this simplifies the analysis considerably and consequently will be applied in the following research to derive the closed form solution of the stress-strain relationship of reinforced concrete columns (Hao 2017). It will be assumed that as yielding progresses, the bond stress in Fig. 8 is gradually destroyed (Shima, Chou & Okamura 1987). Consequently, when yielding is complete and still at P_{yld}

the crack width L_{yld} can be obtained from Eq. (15). Finally at the fracture force P_{frac}, the crack width L_{frac} can be obtained from Eq. (16).

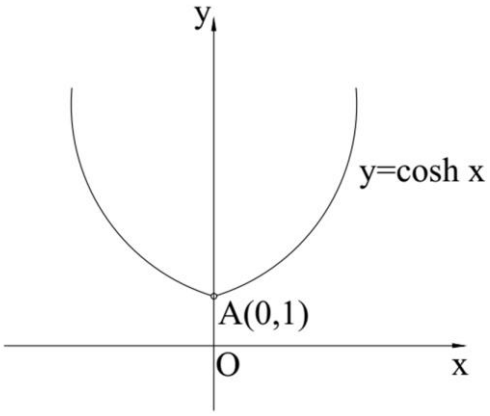

Fig. 16 Shape of hyperbolic cosine function y=cosh(x)

With regard to the fracture case, that is when the confinement reinforcement fractures directly and does not yield, the following crack width L_{frac3} when the confinement reinforcement starts to fracture can be derived by substituting P_{frac} for P_{yld} in Eq. (34) as follows

$$L_{frac3} = \frac{P_{frac}}{\lambda E_r A_r}\{\frac{2\sinh(D_i\lambda)}{\cosh(D_i\lambda)+1}\} \tag{35}$$

From the above analysis and for the case where $L_{crt}>L_{conf}$, Eqs. (15), (16), (34) and (35) can be used in the construction of the stress-strain relationship of passively confined concrete as in Fig. 13. The only difference between this case of $L_{crt}>L_{conf}$ and the previous case in Fig. 13, where $L_{crt}<L_{conf}$ and P_{IC} is larger than P_{yld} or P_{frac}, is that the confinement reinforcement starts to yield or fracture at points E or G in Fig. 13 at the crack width L_{yld3} or L_{frac3} from Eqs. (34) or (35) respectively instead of L_{yld2} or L_{frac2} from Eqs. (24) and (23). Consequently, point E or G can be fixed by the distance between O-A-C-D and falling branch C-C' or D-D' that equals $L_{yld3}/(\tan\alpha L_{prsm})$ or $L_{frac3}/(\tan\alpha L_{prsm})$ respectively which is derived by substituted the crack width L_{yld3} or L_{frac3} into Eq. (20).

In conclusion, the relationships between the crack width L and the confinement force P_{conf} are shown in Fig. 17. When the critical length L_{crt} from Eq. (6) is less than the length of the confinement reinforcement L_{conf} and debonding force P_{IC} is less than yield force P_{yld} or

fracture force P_{frac} as in Fig. 17(a), the confinement reinforcement will: debond at (L_{IC}, P_{IC}); during a further increase in the crack width to L_{deb}, the force is maintained at P_{IC}; then the confinement reinforcement will be fully debonded at (L_{IC2}, P_{IC}); after which the confinement reinforcement may either directly fracture at (L_{frac}, P_{frac}); or yield at (L_{yld}, P_{yld}) first and then fracture at (L_{frac}, P_{frac}). When L_{crt}<L_{conf} and P_{IC} is larger than P_{yld} or P_{frac} as in Fig. 17(b): the confinement reinforcement may either fracture directly at (L_{frac2}, P_{frac}); or yield at (L_{yld2}, P_{yld}); then reach (L_{yld}, P_{yld}); and fracture at (L_{frac}, P_{frac}) without showing debonding behaviour. When L_{crt} is larger than the length of the confinement reinforcement L_{conf}: then the reinforcement may either directly rupture at (L_{frac3}, P_{frac}); or yield at (L_{yld3}, P_{yld}) in Fig. 17(c); then reach (L_{yld}, P_{yld}); and fracture at (L_{frac}, P_{frac}) without showing debonding behaviour.

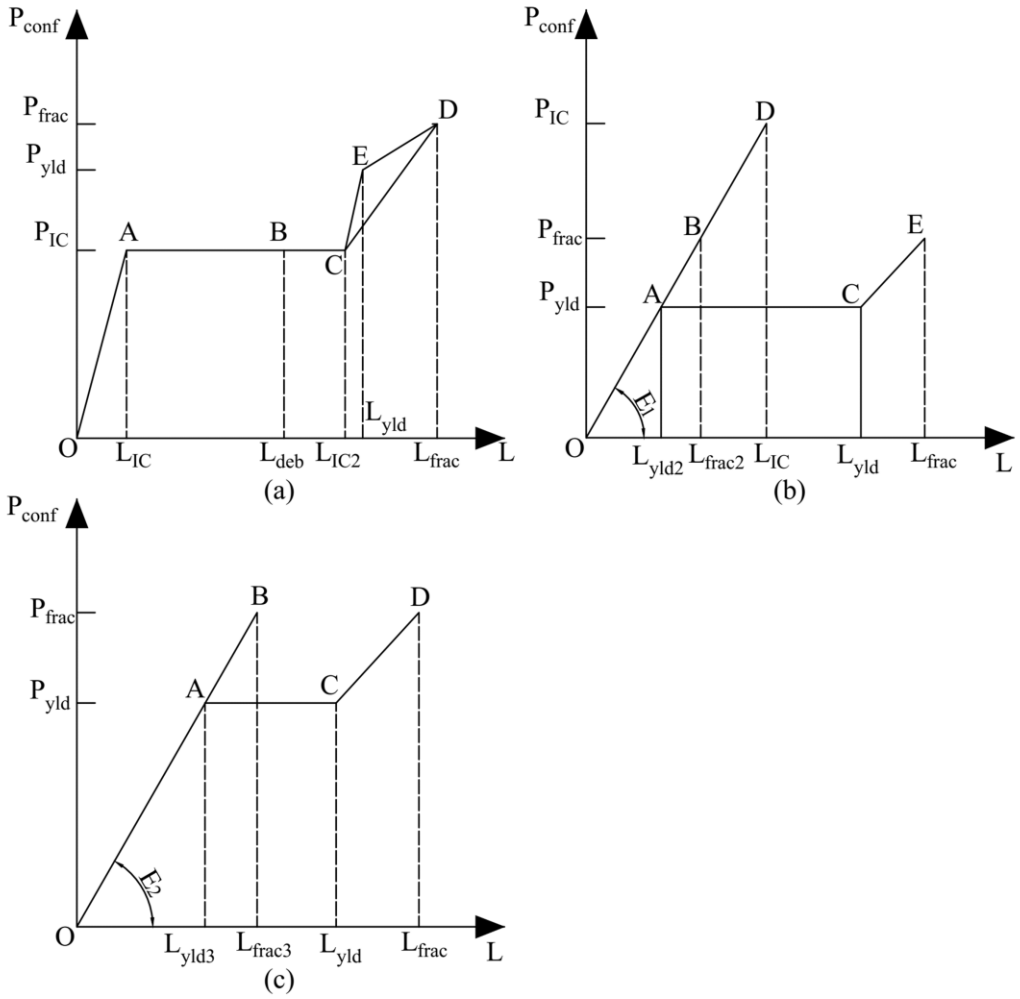

Fig. 17 Behaviour of reinforcement: (a) debonding occurs prior to fracture or yield when L_{crt}<L_{conf}; (b) fracture or yield occurs prior to debonding when L_{crt}<L_{conf}; (c) fracture or yield occurs when L_{crt}>L_{conf}

Reinforced Concrete Column with Circular Sections

The governing equations for rectangular sections have been derived above. Now let us consider the confinement of a circular column. The circular column in Fig. 18(a) has the sliding plane at the centre and that in Fig. 18(b) off-centre; these are equivalent to the sections in Figs. 3 and 7 for a rectangular section. It can be shown through the resolution of forces (Kyle et al. 2015) that for a given confinement force P_{conf} across the sliding plane as shown in Figs. 18(a) and (b), the lateral confinement stress across the sliding plane σ_{conf} is the same as shown. For example when P_{conf} has the same magnitude in Figs. 18(a) and (b), then the confinement stress σ_{conf} is the same in both cases even though the confinement force in Fig. 18(b) is inclined to the sliding plane. This is very important for columns with circular sections as it shows that the confinement stress and consequently confinement is constant which simplifies the mechanics considerably.

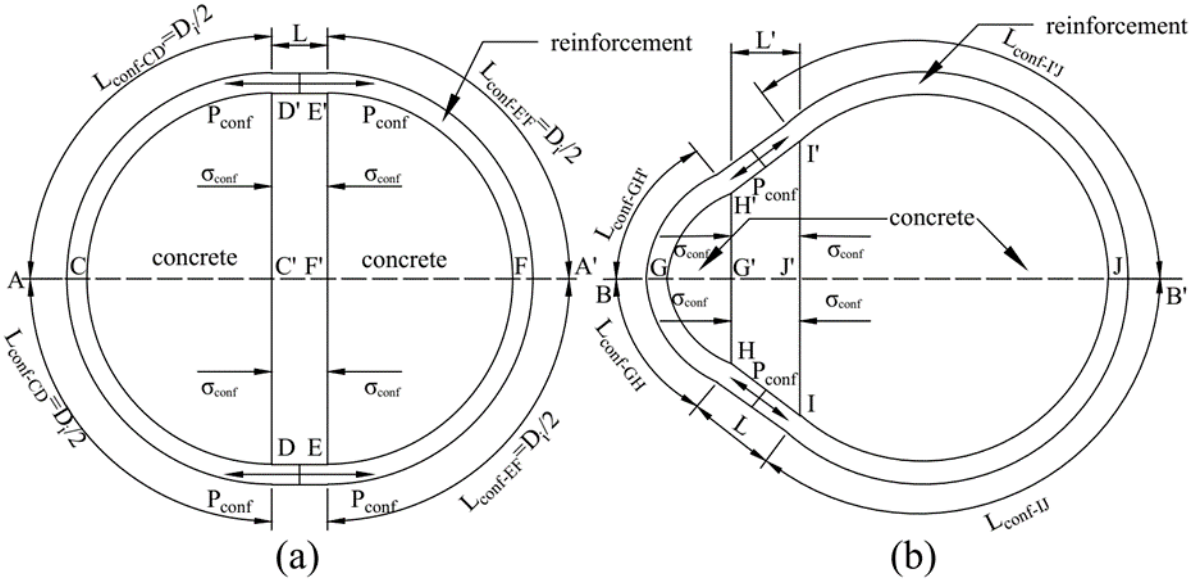

Fig. 18 Section A-A' (a) and B-B' (b) for a circular-section case from Fig. 1 or 2

Let us first consider Fig. 18(a) where the sliding plane is at the centre. Let us also start with IC debonding. Equation (5) for IC debonding is for a flat plate and, therefore, should be on the conservative side when there is a radius as in a circular column. Debonding will then progress to points C or F in Fig. 18(a) which by symmetry are the anchor points. Hence the sum of the confinement lengths $L_{conf\text{-}CD}$ and $L_{conf\text{-}EF}$ is equal to the D_i of the rectangular section and each of them equals $D_i/2$. Consequently equations (12), (13), (14), (15), (16)

with D_i defined in Fig. 18(a) can be applied directly. Similarly for the case when debonding does not occur, equations (23), (24), (34) and (35) can be applied directly with D_i defined in Fig. 18(a).

The case when the sliding plane is eccentric is shown in Fig. 18(b). In this case, it can be seen that the crack widening measured along the circumference and shown as L is not the same as the crack width L' of the sliding plane. Hence L from the above equations will overestimate L' required for the shear friction analysis which will give a safe and conservative analysis. Consequently equations (12), (13), (14), (15), (16), (23) and (24) can also be applied directly with D_i defined in Fig. 18(a).

Conclusion

In this report, the relationship between the confinement force P_{conf} and the crack width L is investigated. It is shown that it depends on the critical length L_{crt} and the length of the confinement reinforcement L_{conf} as well as the relative value between debonding force P_{IC}, yield force P_{yld} and fracture force P_{frac}. If L_{crt} is smaller than L_{conf} and debonding force P_{IC} is smaller than yield force P_{yld} or fracture force P_{frac}: the confinement reinforcement will debond first then fracture; or yield then fracture. When $L_{crt}<L_{conf}$ and debonding force P_{IC} is larger than yield force P_{yld} or fracture force P_{frac}: the confinement reinforcement may either directly fracture; or yield then fracture. When $L_{crt}>L_{conf}$, the confinement reinforcement may either directly fracture or yield then fracture, too. The crack face slips and crack widths of the confinement reinforcement for different confinement forces are derived based on mechanics. The relationships between confinement forces and crack widths will be employed to derive the closed form solution of the stress-strain relationship of confined concrete columns in future research.

Notation

A_c = cross-section area of concrete which interacts with reinforcement in tension stiffening analysis
A_r = total cross-section area of reinforcement in tension stiffening analysis
D_i = width of a rectangular prism

E_c = elastic modulus of concrete

$E_{c\text{-}un}$ = elastic modulus of material strain

E_r = elastic modulus of reinforcement

E_1 = stiffness of P_{conf}/Δ relationship that is equal to P_{IC}/Δ_{IC}

E_2 = stiffness of P_{conf}/Δ relationship from multi-crack analysis

f_{c0} = unconfined concrete strength

h_{cr} = crack widening of sliding plane

k = bond-slip stiffness in tension stiffening analysis

L = crack width which is also horizontal component of slip S

L_{conf} = length of confinement reinforcement

L_{crt} = critical length which is the minimum length required to achieve the maximum debond force

L_{deb} = crack width when debond developed to plate ends

L_{frac} = crack width when confinement reinforcement starts to fracture when $L_{crt}<L_{conf}$ and $P_{IC}<P_{frac}$

L_{frac2} = crack width when confinement reinforcement starts to fracture when $L_{crt}<L_{conf}$ and $P_{IC}>P_{frac}$

L_{frac3} = crack width when confinement reinforcement starts to fracture when $L_{crt}>L_{conf}$

L_{IC} = crack width at commencement of IC debonding

L_{IC2} = crack width when confinement reinforcement is fully debonded

L_{per} = total length of potential debonding failure plane of reinforcement in tension stiffening analysis

L_{prsm} = height of concrete column

L_{yld} = crack width when reinforcement starts to yield when $L_{crt}<L_{conf}$ and $P_{IC}<P_{yld}$

L_{yld2} = crack width when reinforcement starts to yield when $L_{crt}<L_{conf}$ and $P_{IC}>P_{yld}$

L_{yld3} = crack width when reinforcement starts to yield when $L_{crt}>L_{conf}$

P_{ax} = axial load

P_{conf} = force in confinement reinforcement

P_{frac} = fracture force of confinement reinforcement

P_{IC} = debond force of confinement reinforcement

P_{yld} = yield force of confinement reinforcement

S = slip displacement

S_p = primary crack spacing

V = vertical component of slip S

α = failure angle of concrete column

β = prism parameter in tension stiffening analysis

Δ = slip of confinement reinforcement at crack face

Δ_{deb} = slip of confinement reinforcement at crack face when debond developed to plate ends

Δ_{frac} = slip of confinement reinforcement at crack face when confinement reinforcement starts to fracture when $L_{crt}<L_{conf}$ and $P_{IC}<P_{frac}$

Δ_{frac2} = slip of confinement reinforcement at crack face when confinement reinforcement starts to fracture when $L_{crt}<L_{conf}$ and $P_{IC}>P_{frac}$

Δ_{frac3} = slip of confinement reinforcement at crack face when confinement reinforcement starts to fracture when $L_{crt}>L_{conf}$

Δ_{IC} = slip of confinement reinforcement at crack face when debond starts

Δ_{IC2} = slip of confinement reinforcement at crack face when confinement reinforcement is fully debonded

Δ_{yld} = slip of confinement reinforcement at crack face when confinement reinforcement starts to yield when $L_{crt}<L_{conf}$ and $P_{IC}<P_{yld}$

Δ_{yld2} = slip of confinement reinforcement at crack face when confinement reinforcement starts to yield when $L_{crt}<L_{conf}$ and $P_{IC}>P_{yld}$

Δ_{yld3} = slip of confinement reinforcement at crack face when confinement reinforcement starts to yield when $L_{crt}>L_{conf}$

δ = slip between reinforcement and adjacent concrete

δ_1 = slip between reinforcement and adjacent concrete at τ_{Bmax}

δ_{max} = slip between reinforcement and adjacent concrete when bond stress τ_B reduces to zero

ε_{ax} = axial strain

ε_{c0} = axial strain at f_{c0}

ε_{frac} = strain when force in confinement reinforcement equals P_{frac}

ε_{IC} = strain when force in confinement reinforcement equals P_{IC}

ε_m = material strain

ε_s = sliding strain caused by slip

ε_{yld} = strain when force in confinement reinforcement equals P_{yld}

λ = variation in slip parameter

σ_{ax} = axial strain at ε_{ax}

σ_{conf} = lateral confining stress from confinement reinforcement

σ_{frac} = lateral confining stress from confinement reinforcement when confinement force equals fracture force P_{frac}

σ_{IC} = lateral confining stress from confinement reinforcement when confinement force equals debond force P_{IC}

σ_{yld} = lateral confining stress from confinement reinforcement when confinement force equals yield force P_{yld}

τ_B = bond stress existing between reinforcement and concrete

τ_{Bmax} = peak bond stress

References

Ali, MM, Oehlers, D & Griffith, M 2010, 'The residual strength of confined concrete', *Advances in Structural Engineering*, vol. 13, no. 4, pp. 603-618.

Ali, MM, Oehlers, D, Griffith, M & Seracino, R 2008, 'Interfacial stress transfer of near surface-mounted FRP-to-concrete joints', *Engineering Structures*, vol. 30, no. 7, pp. 1861-1868.

Basset, R & Uzumeri, S 1986, 'Effect of confinement on the behaviour of high-strength lightweight concrete columns', *Canadian Journal of Civil Engineering*, vol. 13, no. 6, pp. 741-751.

Birkeland, PW & Birkeland, HW 1966 'Connections in precast concrete construction', *Journal Proceedings*, vol. 63, no. 3, pp. 345-368.

Bresler, B & Gilbert, P 1961, 'Tie requirements for reinforced concrete columns', in *Journal Proceedings*, vol. 58, pp. 555-570.

Chen, Y, Visintin, P & Oehlers, D 2015a, 'Concrete shear-friction material properties: Derivation from actively confined compression cylinder tests', *Advances in Structural Engineering*, vol. 18, no. 8, pp. 1173-1185.

Chen, Y, Visintin, P & Oehlers, D 2015b, 'Extracting Size-Dependent Stress–Strain Relationships from FRP-Confined Concrete Cylinders for Varying Diameters and Heights', *Journal of Materials in Civil Engineering*, vol. 28, no. 5, p. 04015182.

Chen, Y, Zhang, T, Visintin, P & Oehlers, D 2015, 'Concrete shear-friction material properties: application to shear capacity of RC beams of all sizes', *Advances in Structural Engineering*, vol. 18, no. 8, pp. 1187-1198.

Hao, X 2017, 'Generation of stress-strain relationship of passively reinforced concrete' *School Report*, School of Civil, Environmental and Mining Engineering, The University of Adelaide, Australia.

Haskett, M, Oehlers, D, Ali, MM & Sharma, S 2010, 'The shear friction aggregate interlock resistance across sliding planes in concrete', *Magazine of Concrete Research*, vol. 62, no. 12, pp. 907-924.

Haskett, M, Oehlers, DJ & Ali, MM 2008, 'Local and global bond characteristics of steel reinforcing bars', *Engineering Structures*, vol. 30, no. 2, pp. 376-383.

Haskett, M, Oehlers, DJ, Ali, MM & Sharma, SK 2011, 'Evaluating the shear-friction resistance across sliding planes in concrete', *Engineering Structures*, vol. 33, no. 4, pp. 1357-1364.

Haskett, M, Oehlers, DJ, Mohamed Ali, M & Wu, C 2009, 'Yield penetration hinge rotation in reinforced concrete beams', *Journal of Structural Engineering*, vol. 135, no. 2, pp. 130-138.

Kyle, B, Harrison, S, Alexander, S & Philip, S 2015, 'A mechanics-based approach to quantifying the ductility of reinforced concrete members with passive confinement of stirrups and FRP wraps', *School Report*, School of Civil, Environmental and Mining Engineering, The University of Adelaide, Australia.

Lam, L & Teng, J 2003, 'Design-oriented stress–strain model for FRP-confined concrete', *Construction and Building Materials*, vol. 17, no. 6, pp. 471-489.

Lu, X, Teng, J, Ye, L & Jiang, J 2005, 'Bond–slip models for FRP sheets/plates bonded to concrete', *Engineering Structures*, vol. 27, no. 6, pp. 920-937.

Muhamad, R, Ali, MM, Oehlers, DJ & Griffith, M 2012, 'The tension stiffening mechanism in reinforced concrete prisms', *Advances in Structural Engineering*, vol. 15, no. 12, pp. 2053-2069.

Oehlers, D, Visintin, P, Zhang, T, Chen, Y & Knight, D 2012, 'Flexural rigidity of reinforced concrete members using a deformation based analysis', *Concrete in Australia*, vol. 38, no. 4, pp. 50-56.

Oehlers, DJ, Haskett, M, Wu, C & Seracino, R 2008, 'Embedding NSM FRP plates for improved IC debonding resistance', *Journal of Composites for Construction*, vol. 12, no. 6, pp. 635-642.

Oehlers, DJ, Visintin, P, Chen, J-F, Seracino, R, Wu, Y & Lucas, W 2017, 'Reinforced Concrete Behavior, Research, Development, and Design through Partial-Interaction Mechanics', *Journal of Structural Engineering*, vol. 143, no. 7, p. 02517002.

Oldham, KB, Myland, J & Spanier, J 2010, *An atlas of functions: with equator, the atlas function calculator*, Springer Science & Business Media.

Sakino, K, Nakahara, H, Morino, S & Nishiyama, I 2004, 'Behavior of centrally loaded concrete-filled steel-tube short columns', *Journal of Structural Engineering*, vol. 130, no. 2, pp. 180-188.

Seracino, R, Raizal Saifulnaz, M & Oehlers, D 2007, 'Generic debonding resistance of EB and NSM plate-to-concrete joints', *Journal of Composites for Construction*, vol. 11, no. 1, pp. 62-70.

Shima, H, Chou, L-L & Okamura, H 1987, 'Micro and macro models for bond in reinforced concrete', *Journal of the Faculty of Engineering*, vol. 39, no. 2, pp. 133-194.

Sturm, AB, Visintin, P & Oehlers, DJ 2017, 'Time-dependent serviceability behavior of reinforced concrete beams: Partial interaction tension stiffening mechanics', *Structural Concrete*, vol. 19, no. 2, pp. 508-523.

Visintin, P, Chen, Y & Oehlers, D 2015, 'Simulating the behavior of FRP-confined cylinders using the shear-friction mechanism', *Journal of Composites for Construction*, vol. 19, no. 6, p. 04015014.

Visintin, P, Oehlers, D, Haskett, M & Wu, C 2012, 'Mechanics-based hinge analysis for reinforced concrete columns', *Journal of Structural Engineering*, vol. 139, no. 11, pp. 1973-1980.

Visintin, P, Oehlers, D, Muhamad, R & Wu, C 2013, 'Partial-interaction short term serviceability deflection of RC beams', *Engineering Structures*, vol. 56, pp. 993-1006.

Yuan, H, Teng, J, Seracino, R, Wu, Z & Yao, J 2004, 'Full-range behavior of FRP-to-concrete bonded joints', *Engineering Structures*, vol. 26, no. 5, pp. 553-565.

Zhang, T, Visintin, P & Oehlers, DJ 2015, 'Shear strength of RC beams with steel stirrups', *Journal of Structural Engineering*, vol. 142, no. 2, p. 04015135.

Zhang, T, Visintin, P & Oehlers, DJ 2017, 'Partial-interaction tension-stiffening properties for numerical simulations', *Advances in Structural Engineering*, vol. 20, no. 5, pp. 812-821.

Zhang, T, Visintin, P, Oehlers, DJ & Griffith, MC 2014, 'Presliding shear failure in prestressed RC beams. I: Partial-Interaction mechanism', *Journal of Structural Engineering*, vol. 140, no. 10, p. 04014069.

Chapter 2— Material Properties

Introduction

This Chapter contains the two school reports below. These two school reports provide the shear-friction and bond-slip material properties required for the proposed approach given later. In the first school report, the shear friction material properties are derived from actively confined cylinder tests and are simplified to a linear form that can be used to derive closed-form solutions of the proposed approach. In the second school report, the bond-slip material properties are simplified to a bilinear form and then summarised for different confinement reinforcements including rebars and plates of FRP or steel.

List of Manuscripts

Hao, X., Oehlers, D., and Visintin, P. (2017) Mechanics of Extracting Shear-Friction Properties from Actively Confined Cylinder Tests. *School Report*, School of Civil, Environmental and Mining Engineering, The University of Adelaide, Australia.

Hao, X., Oehlers, D., and Visintin, P. (2017) Provide Partial Interaction Bond-Slip Relationship for Mechanical Properties. *School Report*, School of Civil, Environmental and Mining Engineering, The University of Adelaide, Australia.

Mechanics of Extracting Shear-Friction Properties from Actively Confined Cylinder Tests

Abstract

Shear friction properties are used to quantify the shear resistance to concrete sliding by giving the relationship between the shear stress parallel to the shear-sliding plane, normal stress transverse to the shear-sliding plane and slip displacement along the shear-sliding plane. These shear friction properties are derived primarily from simple and inexpensive actively confined cylinder compression tests and where there are gaps in the results with the results from relatively expensive complex shear-sliding tests. Approximations of these shear friction properties are proposed. This is then applied inversely to construct the stress-strain relationships of actively confined concrete to validate the simulation and with good correlation.

Keywords

Shear friction properties; actively confined concrete; Shear-sliding tests; approximation; size effect;

Introduction

Shear friction properties are used to quantify the shear resistance to sliding. They were first derived from shear-sliding tests as shown in Figs. 1(a) and (b) where the shear stress τ can be obtained for a given normal confining stress σ_N, crack widening h_{cr} and slip S along the shear sliding plane as shown. It is worth noting that, the normal stress σ_N can be supplied by either external loading in Fig. 1(a) (Zhang 2014) or internal reinforcement in Fig. 1(b) (Birkeland & Birkeland 1966; Johal 1975; Mattock 1974; Mattock & Hawkins 1972). The latter type of shear sliding tests is widely used as it is simpler. The difference between these two types of experiments has be described elsewhere (Chen, Y et al. 2015) and summarised later.

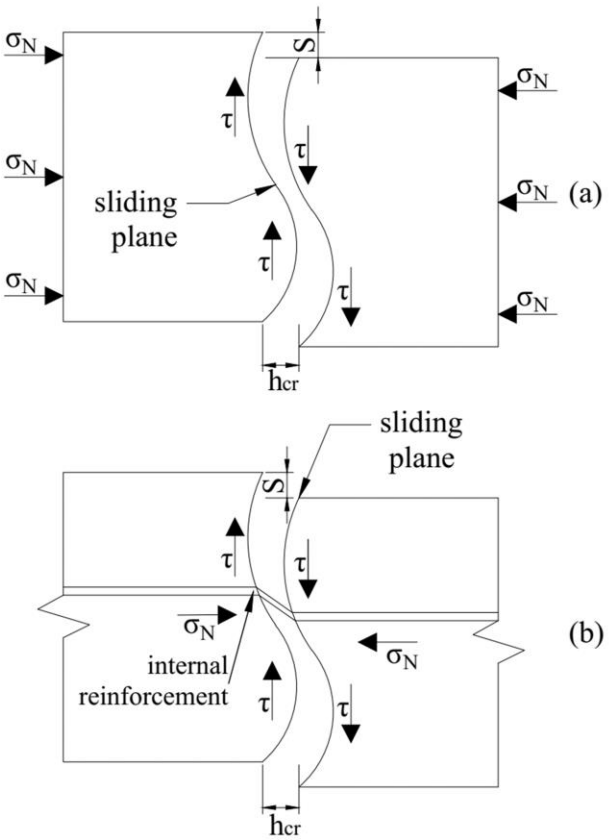

Fig. 1 Mechanism of shear sliding tests with (a) external confinement; (b) normal stress σ_N supplied by internal reinforcement

Mattock investigated the relationship between the maximum shear stress along the sliding plane and normal stress transverse to the sliding plane from shear-sliding tests as in Fig. 1(b) for both initially cracked concrete and uncracked concrete (Johal 1975; Mattock 1974;

Mattock & Hawkins 1972). It is found that the confining stress σ_N normal to the sliding plane is a significant factor that affects the resistance to sliding. After only investigating the shear friction properties at the ultimate stage (Johal 1975; Mattock 1974; Mattock & Hawkins 1972), Walraven and Reinhardt (1981) developed these properties for the whole loading spectrum, by quantifying the relationships between the shear stress τ parallel to the shear-sliding plane, the confining stress σ_N normal to the sliding plane, slip displacement S along the shear-sliding plane and crack widening h_{cr} across the shear-sliding plane as follows

$$\tau = -\frac{f_{c0-cube}}{30} + [1.8h_{cr}^{-0.8} + (0.234h_{cr}^{-0.707} - 0.2)\, f_{c0-cube}]S \quad (1)$$

$$\sigma_N = \frac{f_{c0-cube}}{20} - [1.35h_{cr}^{-0.63} + (0.191h_{cr}^{-0.552} - 0.15)\, f_{c0-cube}]S \quad (2)$$

where the unit of stress is in MPa, $f_{c0\text{-}cube}$ is the unconfined concrete strength from concrete cube tests, slip S and crack widening h_{cr} are in mm. These shear friction properties are only for initially cracked concrete and were derived from shear-sliding tests as shown in Fig. 1(b). Haskett, Matthew et al. (2011) combined Mattock and Walraven's approaches (Mattock 1974; Mattock & Hawkins 1972; Walraven & Reinhardt 1981) such that the shear friction properties for both initially cracked concrete and uncracked concrete can be predicted. Furthermore, the shear friction properties are derived in the form which gives the relationship between the shear stress τ and slip S for the constant normal stress σ_N for easier application (Haskett, M et al. 2010). However, these shear friction properties are only obtained from experiments with low normal stress σ_N.

Shear friction properties can also be extracted from actively confined cylinder compression tests (Chen, Y, Visintin & Oehlers 2015a; Chen, Y et al. 2015; Haskett, Matthew et al. 2011). By employing this method, high-cost shear sliding tests are not required and the shear friction properties with high confining stress σ_N can be obtained. However, in this work (Chen, Y, Visintin & Oehlers 2015a; Chen, Y et al. 2015; Haskett, Matthew et al. 2011), it was assumed that slip will occur before the peak stresses are attained of both unconfined concrete columns and actively confined concrete columns. This assumption is now felt not to simulate the behaviour accurately as it would entail the formation of numerous hinges that does not occur in practice. Instead this approach is modified by assuming that slip only happens after the peak stress is achieved as this ensures the formation of a single plastic

hinge. Furthermore, the form of the previous approach (Chen, Y, Visintin & Oehlers 2015a; Chen, Y et al. 2015) is comprised of power functions and rational functions which are not easy to apply.

In this research, the derivation of these shear friction properties from actively confined cylinder tests will be described. Furthermore, approximations of these properties will be proposed and some of them are more simple and accurate. Moreover, these approximations will be applied inversely to construct the stress-strain relationships of the actively confined concrete to validate the approximations.

Shear Sliding Mechanism

An actively confined concrete column under a concentric load is assumed to fail due to sliding at an angle of α as shown in Fig. 2 (Rutland & Wang 1997). It should be noted that the cross-section of this column can be either rectangular, or square, or circular. For a slender prism whose aspect ratio is equal to or more than three, sliding mostly occurs across a single sliding plain as shown in Figs. 2 and 3 (Chen, Y, Visintin & Oehlers 2015b; Oehlers, D et al. 2012; Oehlers, DJ et al. 2017). For slenderness ratios less than three such as standard cylinder tests where the slenderness ratio is two, circumferential sliding planes are the most common form of failure as shown in Fig. 4 and which occur at higher axial loads.

Let us consider a concrete column with a single sliding plane in Fig. 2 first. Along the potential sliding plane OQ in Fig. 2, the following confining stress σ_N and shear stress τ can be expressed as (Chen, Y et al. 2015)

$$\sigma_N = \frac{N}{A_{sl}} = \frac{P_{ax}\sin\alpha + C_l\cos\alpha}{A_{sl}} \tag{3}$$

$$\tau = \frac{T}{A_{sl}} = \frac{P_{ax}\cos\alpha - C_l\sin\alpha}{A_{sl}} \tag{4}$$

where A_{sl} is the area of the sliding plane, T and N are the forces along and normal to the potential shear failure plane resolved from the axial load P_{ax} and lateral confining force C_l.

It is assumed that the following axial load P_{ax} is distributed uniformly along the cross-section and can be written as follows

$$P_{ax} = \sigma_{ax} A_{in} \tag{5}$$

where σ_{ax} is the axial stress of the confined concrete and A_{in} is the cross-section area of the confined concrete. The next step is to quantify the lateral confining force C_l for columns with rectangular, square and circular sections.

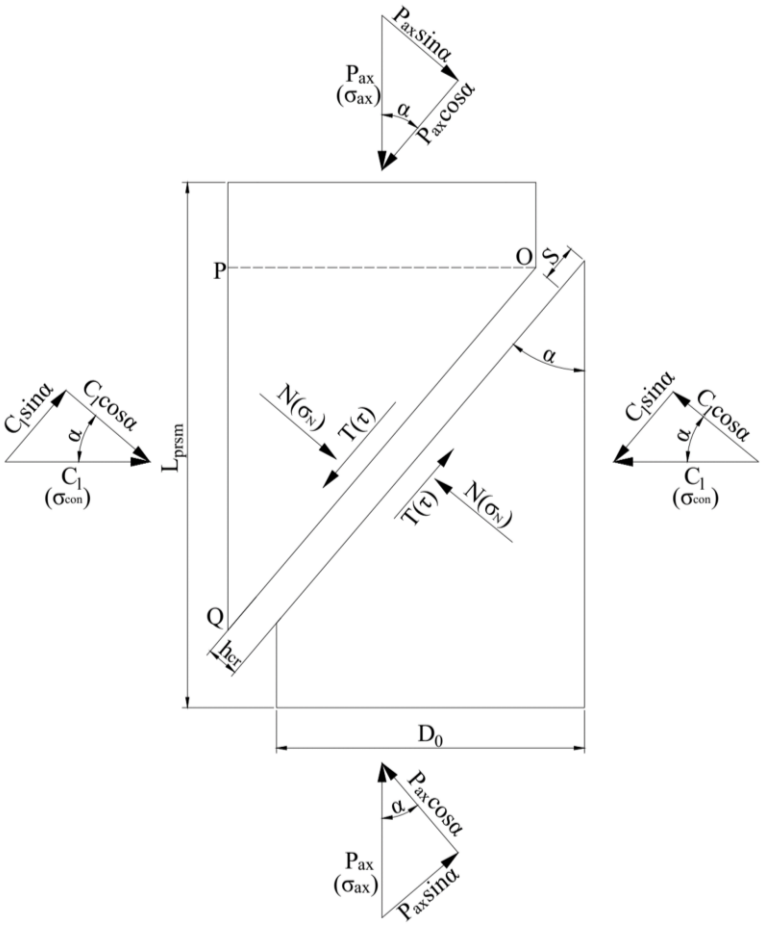

Fig. 2 The forces and stresses of an actively confined column with a single sliding plane under a concentric compressive load

Fig. 3 A column fail due to concentric load with a single sliding plane

Fig. 4 A column fail due to concentric load with a circumferential wedge

Confinement Force

Consider the free body OPQ in Fig. 2 that contains the whole shear sliding plane of an actively confined rectangular-section column and is shown in Fig. 5. The following lateral confining force C_{rec} applied on this free body can be expressed as

$$C_{rec} = \sigma_{con} \frac{D_{02} D_0}{\tan \alpha} \tag{6}$$

where σ_{con} is the active lateral confining stress and D_0 and D_{02} are the width and depth of the rectangular prism respectively.

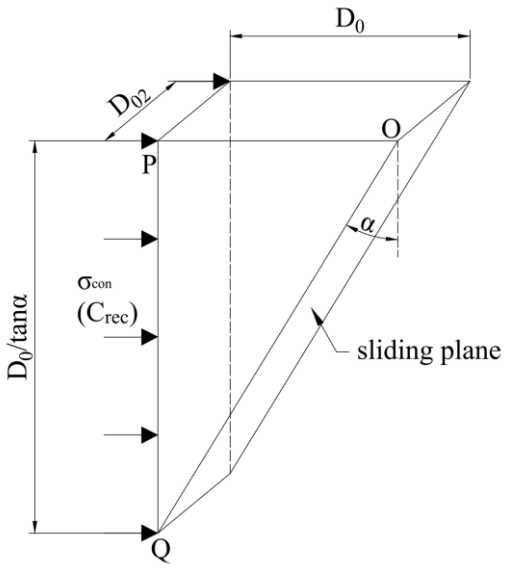

Fig. 5 Lateral confining force applied on a rectangular-section column

For a square-section column, the width D_0 and depth D_{02} of the cross-section are equivalent such that Eq. (6) becomes

$$C_{sq} = \sigma_{con} \frac{D_0^2}{\tan \alpha} \tag{7}$$

The method to quantify the lateral confining force of a circular-section column C_{cir} proposed by Chen, Y et al. (2015) will be described as below.

The free body OPQ in Fig. 2 that contains the whole sliding plane of an actively confined concrete column with a circular section is shown in Fig. 6(a). The diameter of the cylinder

equals D_0. The height of the cylinder wedge PQ that equals $D_0/\tan\alpha$ is cut into n small slices. The cross-section of the i_{-th} slice DE is shown in Fig. 6(b) as an example. The distance DQ in Fig. 6(a) that is x_i can be expressed as

$$x_i = \frac{i_{-th} D_0}{n \tan \alpha} \tag{8}$$

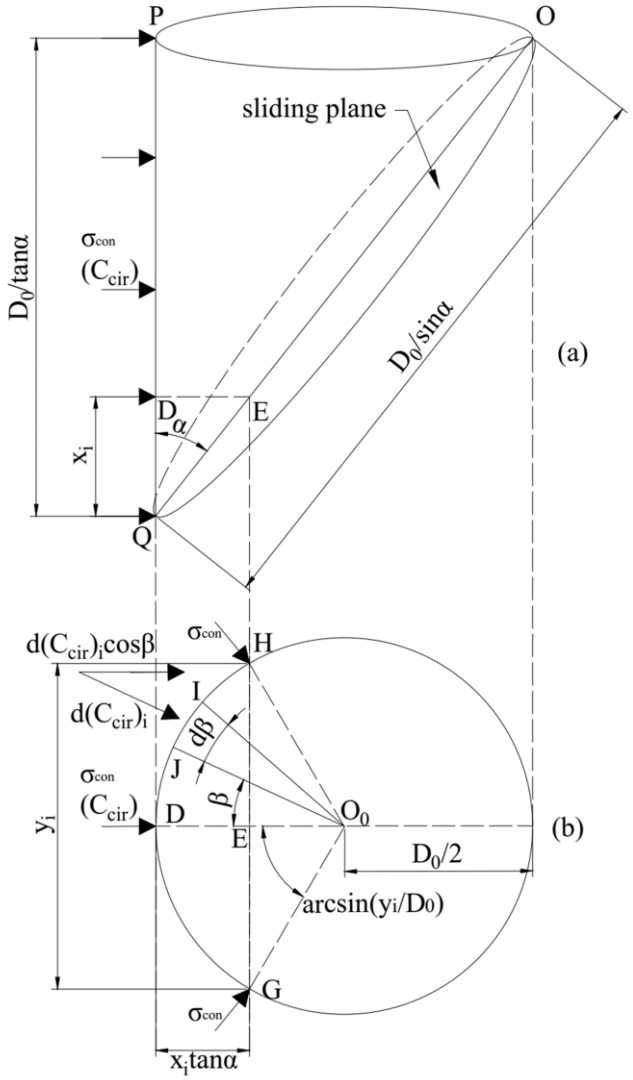

Fig. 6 (a) Lateral confining force of the free body OPQ in Fig. 2; (b) Lateral confining force of the cross-section containing slice DE in Fig. 6(a)

The length of chord HG in Fig. 6(b) y_i can be written as follows

$$y_i = 2(\sqrt{(\frac{D_0}{2})^2 - (\frac{D_0}{2} - x_i \tan\alpha)^2} \tag{9}$$

Substituting Eq. (8) into Eq. (9) yields

$$y_i = 2D_0(\sqrt{\frac{i_{-th}}{n} - (\frac{i_{-th}}{n})^2} \tag{10}$$

Taking line O_0D in Fig. 6(b) as the baseline, the sector O_0HDG is cut into small sectors. The horizontal component of the force $d(C_{cir})_i\cos\beta$ applied on the element O_0IJ can be written as follows

$$d(C_{cir})_i \cos\beta = \cos\beta\sigma_{con}\frac{D_0}{n\tan\alpha}\frac{D_0}{2}d\beta \tag{11}$$

where β is the angle between the sector O_0IJ and the baseline O_0D. The total horizontal lateral confining force can be derived by integrating forces acting on all elements along the arc HDG

$$(C_{cir})_i = \int_{-\arcsin(\frac{yi}{D_0})}^{\arcsin(\frac{yi}{D_0})} \cos\beta\sigma_{con}\frac{D_0}{n\tan\alpha}\frac{D_0}{2}d\beta \tag{12}$$

Substituting Eq. (10) into Eq. (12) yields

$$(C_{cir})_i = \sigma_{con}\frac{D_0}{n\tan\alpha}[2D_0\sqrt{\frac{i_{-th}}{n} - (\frac{i_{-th}}{n})^2}] \tag{13}$$

Then the force acting on element DE in Fig. 6(a) will be integrated along the vertical height of the sliding plane PQ and gives

$$C_{cir} = \frac{\pi}{4}\sigma_{con}\frac{D_0}{\tan\alpha}D_0 \tag{14}$$

Stress Equilibrium

For circular, square and rectangular section columns respectively, combining Eqs. (3), (5), (6), (7) and (14) gives the resultant stress normal to the sliding plane $(\sigma_N)_{cir}$, $(\sigma_N)_{sq}$ and $(\sigma_N)_{rec}$ as

$$(\sigma_N)_{cir} = \frac{P_{ax}\sin\alpha + C_{cir}\cos\alpha}{A_{sl}} = \frac{\sigma_{ax}\dfrac{\pi D_0^2}{4}\sin\alpha + \sigma_{con}\dfrac{\pi D_0^2}{4\tan\alpha}\cos\alpha}{\dfrac{\pi D_0^2}{4\sin\alpha}} = \sigma_{ax}\sin^2\alpha + \sigma_{con}\cos^2\alpha \quad (15)$$

$$(\sigma_N)_{sq} = \frac{P_{ax}\sin\alpha + C_{sq}\cos\alpha}{A_{sl}} = \frac{\sigma_{ax}D_0^2\sin\alpha + \sigma_{con}\dfrac{D_0^2}{\tan\alpha}\cos\alpha}{\dfrac{D_0^2}{\sin\alpha}} = \sigma_{ax}\sin^2\alpha + \sigma_{con}\cos^2\alpha \quad (16)$$

$$(\sigma_N)_{rec} = \frac{P_{ax}\sin\alpha + C_{rec}\cos\alpha}{A_{sl}} = \frac{\sigma_{ax}D_0D_{02}\sin\alpha + \sigma_{con}\dfrac{D_0D_{02}}{\tan\alpha}\cos\alpha}{\dfrac{D_0D_{02}}{\sin\alpha}} = \sigma_{ax}\sin^2\alpha + \sigma_{con}\cos^2\alpha \quad (17)$$

where D_0 is either the diameter of a circular column, or the side length of a square prism, or the width of a rectangular prism and D_{02} is the depth of the rectangular prism.

Similarly for the circular, square and rectangular section columns respectively, combining Eqs. (4), (5), (6), (7) and (14) gives the resultant stresses along the sliding plane τ_{cir}, τ_{sq} and τ_{rec} as

$$\tau_{cir} = \frac{P_{ax}\cos\alpha - C_{cir}\sin\alpha}{A_{sl}} = \frac{\sigma_{ax}\dfrac{\pi D_0^2}{4}\cos\alpha - \sigma_{con}\dfrac{\pi D_0^2}{4\tan\alpha}\sin\alpha}{\dfrac{\pi D_0^2}{4\sin\alpha}} = (\sigma_{ax} - \sigma_{con})\sin\alpha\cos\alpha \quad (18)$$

$$\tau_{sq} = \frac{P_{ax}\cos\alpha - C_{sq}\sin\alpha}{A_{sl}} = \frac{\sigma_{ax}D_0^2\cos\alpha - \sigma_{con}\dfrac{D_0^2}{\tan\alpha}\sin\alpha}{\dfrac{D_0^2}{\sin\alpha}} = (\sigma_{ax} - \sigma_{con})\sin\alpha\cos\alpha \quad (19)$$

$$\tau_{rec} = \frac{P_{ax}\cos\alpha - C_{rec}\sin\alpha}{A_{sl}} = \frac{\sigma_{ax}D_0D_{02}\cos\alpha - \sigma_{con}\dfrac{D_0D_{02}}{\tan\alpha}\sin\alpha}{\dfrac{D_0D_{02}}{\sin\alpha}} = (\sigma_{ax} - \sigma_{con})\sin\alpha\cos\alpha \quad (20)$$

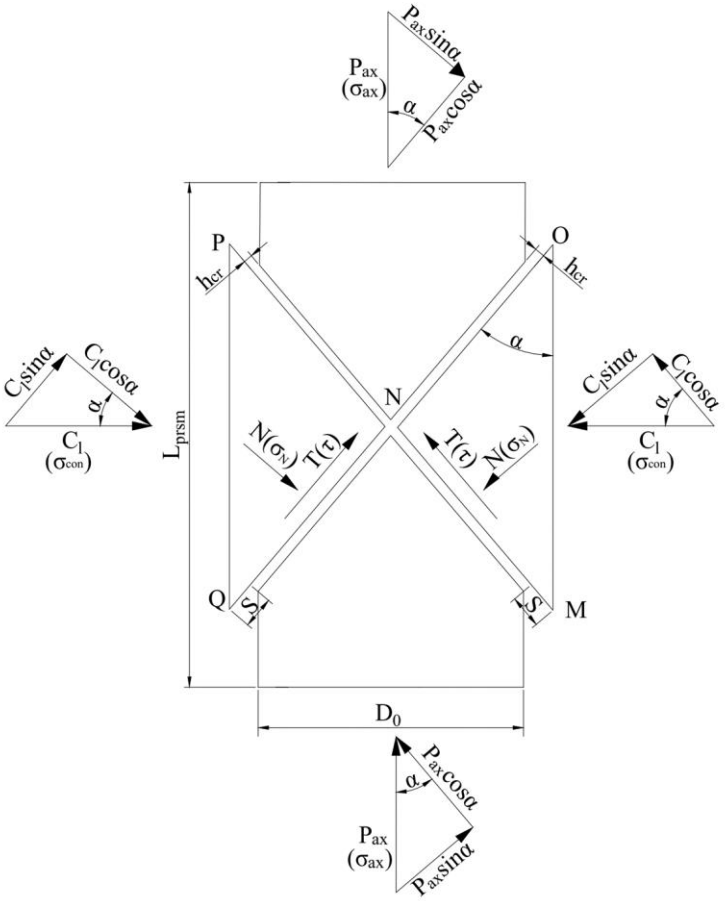

Fig. 7 The force and stress of a column with a circumferential wedge under concentric compressive load

From Eqs. (15), (16) and (17), it can be concluded that the expressions of the resultant stresses normal to the shear failure plane σ_N are the same for circular, rectangular or square section columns and consequently can be expressed in the following generic

$$\sigma_N = \sigma_{ax} \sin^2 \alpha + \sigma_{con} \cos^2 \alpha \tag{21}$$

With regard to the shear stress along the shear failure plane τ, from Eqs. (18), (19) and (20), expressions are the same for columns with different cross-sections such that the generic form is as follows

$$\tau = (\sigma_{ax} - \sigma_{con}) \sin \alpha \cos \alpha \tag{22}$$

As the shear friction properties will be derived from standard cylinder tests where the aspect ratios of all the test specimens are equal to two, the concrete columns will slide as in Fig. 4 where the circumferential wedge will form (Chen, Yongjian 2015). The shear stress τ and normal stress σ_N along and normal to the shear failure plane will be changed as in Fig. 7 and can be expressed as (Chen, Y, Visintin & Oehlers 2015a, 2015b; Chen, Y et al. 2015)

$$\sigma_N = \sigma_{ax} \sin^2 \alpha + 2\sigma_{con} \cos^2 \alpha \tag{23}$$

$$\tau = (\sigma_{ax} - 2\sigma_{con}) \sin \alpha \cos \alpha \tag{24}$$

Size Dependent Stress-Strain Relationship

Typical stress-strain relationships for unconfined and actively confined concrete columns proposed by Chen, Y et al. (2013) are shown in Fig. 8, where it is assumed that 200 mm is the standard height of a standard test specimen L_{prsm} as this is the height of most test specimens. The stress-strain behaviour of concrete columns is governed by the height of test specimen L_{prsm} in Fig. 2 (Jamet, Millard & Nahas 1984; Jansen & Shah 1997; Sangha & Dhir 1972; Smith et al. 1989); it will be shown how to derive a size-dependent stress-strain relationship for a non-standard specimen (Chen, Y et al. 2013; Visintin, Chen & Oehlers 2015) which is shown in Fig. 8 as $L_{prsm} > 200$ mm. It is worth noting that the size-dependent stress-strain relationship does not need the same aspect ratio of 2:1 for non-standard specimens.

Unconfined Concrete Column

The following stress-strain relationship of unconfined concrete columns whose height is equal to 200 mm can be written as (Chen, Y et al. 2013)

$$\sigma_{ax} = f_{c0} \frac{\frac{\varepsilon_{ax-200}}{\varepsilon_{c0}} r}{r - 1 + (\frac{\varepsilon_{ax-200}}{\varepsilon_{c0}})^r} \tag{25}$$

where the unit of stress is in MPa, σ_{ax} is the axial stress when the axial strain is equal to ε_{ax}, $\varepsilon_{ax\text{-}200}$ is the axial strain in a standard specimen that is of length 200 mm, f_{c0} is the peak stress of unconfined concrete, ε_{c0} is the strain at the peak stress f_{c0} and r is the ductility factor which can be expressed as

$$r = \frac{E_c}{E_c - \frac{f_{c0}}{\varepsilon_{c0}}} \tag{26}$$

where the unit of stress is in MPa and E_c is the elastic modulus of concrete. It will be shown how to adjust this stress-strain relationship to that of a specimen with a different height L_{prsm} > 200 mm in Fig. 8.

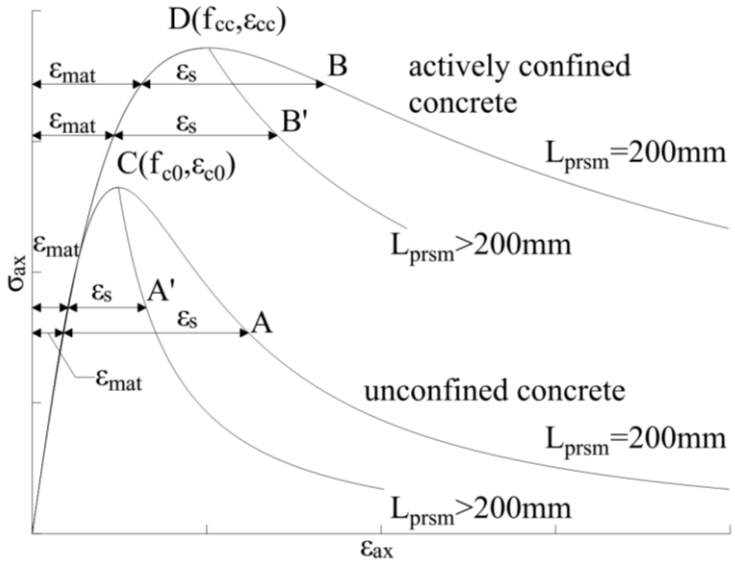

Fig. 8 Stress-strain relationships of both unconfined and actively confined concrete column with different specimen heights

Before the stress reaches the unconfined concrete peak stress f_{c0} that is point C in Fig. 8, the axial deformation is defined as the material strain ε_{mat} which is size-independent. However after this point C, concrete starts to slide along the shear failure plane and the total axial deformation is comprised of: the size-independent material strain ε_{mat}, caused by material deformation as shown in Fig. 8 and size-dependent strain ε_S caused by the slip S also shown in Fig. 8; and the size-dependent strain caused by the crack widening h_{cr}. However, the crack widening dimension h_{cr} is an order magnitude smaller than the slip S (Chen, Y, Visintin &

Oehlers 2015a; Haskett, M et al. 2010; Haskett, Matthew et al. 2011) such that h_{cr} can be ignored. Hence the size-dependent strain is only that due to slip S in Fig. 2 and is given by the vertical component of the slip S divided by the length of the prism L_{prsm} that is

$$\varepsilon_S = \frac{S\cos\alpha}{L_{prsm}} \tag{27}$$

Consider an arbitrary point on the falling branch of the stress-strain relationship in Fig. 8; this can be point A for the standard specimen and point A' for the non-standard specimen where the axial stress is equal to σ_{ax}. The total axial strain ε_{ax} can be expressed as

$$\varepsilon_{ax} = \varepsilon_{mat} + \varepsilon_S \ = \varepsilon_{mat} + \frac{S\cos\alpha}{L_{prsm}} \tag{28}$$

Rearranging Eq. (28) gives the slip S as

$$S = \frac{(\varepsilon_{ax} - \varepsilon_{mat})L_{prsm}}{\cos\alpha} \tag{29}$$

The axial strain ε_{ax} of a specimen with the height equal to L_{prsm} can be adjusted to the following strain $\varepsilon_{ax\text{-}200}$ of a standard specimen (Chen, Y et al. 2013)

$$\varepsilon_{ax-200} = \varepsilon_{mat} + \frac{L_{prsm}}{200}(\varepsilon_{ax} - \varepsilon_{mat}) \tag{30}$$

Consequently from Eq. (30), the strain ε_{ax} of the non-standard specimen can be adjusted to the strain $\varepsilon_{ax\text{-}200}$ of the standard specimen. Substituting the strain $\varepsilon_{ax\text{-}200}$ from Eq. (30) into the stress-strain relationship Eq. (25) for standard unconfined concrete specimen gives the axial stress σ_{ax} as a function of the strain ε_{ax} of the non-standard specimen. This relationship is referred to as size-dependent stress-strain relationship (Chen, Y et al. 2013).

Confined Concrete Column

The stress-strain relationship of actively confined concrete columns proposed by Visintin, Chen and Oehlers (2015) for a standard specimen is shown as follows

$$\sigma_{ax} = f_{cc} \frac{\frac{\varepsilon_{ax-200}}{\varepsilon_{cc}} r_c}{r_c - 1 + (\frac{\varepsilon_{ax-200}}{\varepsilon_{cc}})^{r_c}} \tag{31}$$

where the unit of stress is in MPa, f_{cc} and ε_{cc} are the peak stress of the confined concrete and strain at f_{cc}, and r_c is the ductility factor which can be expressed as

$$r_c = \frac{E_c}{E_c - \frac{f_{cc}}{\varepsilon_{cc}}} \tag{32}$$

where the unit of stress is in MPa. Similar to the case of the unconfined concrete column, the axial strain ε_{ax} and strain ε_S caused by slip S can be obtained from Eqs. (28) and (27) respectively that is the point B or B' in Fig. 8. The stress-strain relationship of a specimen with the height equal to L_{prsm} > 200 mm can be obtained by substituting Eq. (30) into Eq. (31) as shown in Fig. 8 (Visintin, Chen & Oehlers 2015). Furthermore, the slip S can be derived from Eq. (29).

Material Properties

It is shown in tests that the natural angle of the sliding plane α as shown in Fig. 2 can be assumed to be constant at 26^O (Chen, Yongjian 2015; Chen, Y, Visintin & Oehlers 2015a).

With regard to the material properties of concrete, the strain ε_{c0} at the unconfined concrete strength f_{c0} can be given by (Chen, Y et al. 2013)

$$\varepsilon_{c0} = 1.74 \times 10^{-6} f_{c0} + 2.41 \times 10^{-3} \tag{33}$$

where the unconfined concrete strength f_{c0} is in MPa. The material properties of confined concrete of strength f_{cc} and strain ε_{cc} at f_{cc} as in Fig. 8 can be expressed as (Visintin, Chen & Oehlers 2015)

$$f_{cc} = f_{c0}[1 + A_0(\frac{\sigma_{con}}{f_{c0}})] \tag{34}$$

$$\varepsilon_{cc} = \varepsilon_{c0}[1 + B_0(\frac{\sigma_{con}}{f_{c0}})] \tag{35}$$

where the unit of stress is in MPa, A_0 and B_0 are the coefficients derived from regression analyses and are taken as 5.34 and 13.9 respectively.

Concrete elastic modulus E_c can be written as follows (Chen, Y, Visintin & Oehlers 2015a)

$$E_c = 3320\sqrt{f_{c0}} + 6900 \tag{36}$$

where the unconfined concrete strength f_{c0} is in MPa.

Extracting Shear Friction Properties from Size-Dependent Stress-Strain Relationship of Actively Confined Column

As in Fig. 2 and ignoring the crack widening h_{cr}, the shear friction properties are the relationships between the shear stress τ and slip S for different normal stresses σ_N for a specific concrete strength f_{c0}. Shear friction properties for 40 MPa concrete and 80 MPa concrete are shown in Figs. 9 and 10 as two examples. Let us start with 40 MPa-strength concrete as an example to show the derivation of the shear friction properties. The stress-strain relationships of actively confined concrete columns with different lateral confining stresses σ_{con} are shown in Fig. 11. At the coordinate (f_{c0}, ε_{c0}) of the unconfined concrete stress-strain relationship that is the point A in Fig. 11, the shear stress V_{u0} and the normal stress σ_{N0} are the shear stress τ and normal stress σ_N at the onset of sliding. They can be derived by substituting $\sigma_{ax} = f_{c0}$ and $\sigma_{con} = 0$ at point A into Eqs. (23) and (24) as follows

$$\sigma_{N0} = f_{c0}\sin^2\alpha \tag{37}$$

$$V_{u0} = f_{c0} \sin\alpha \cos\alpha \tag{38}$$

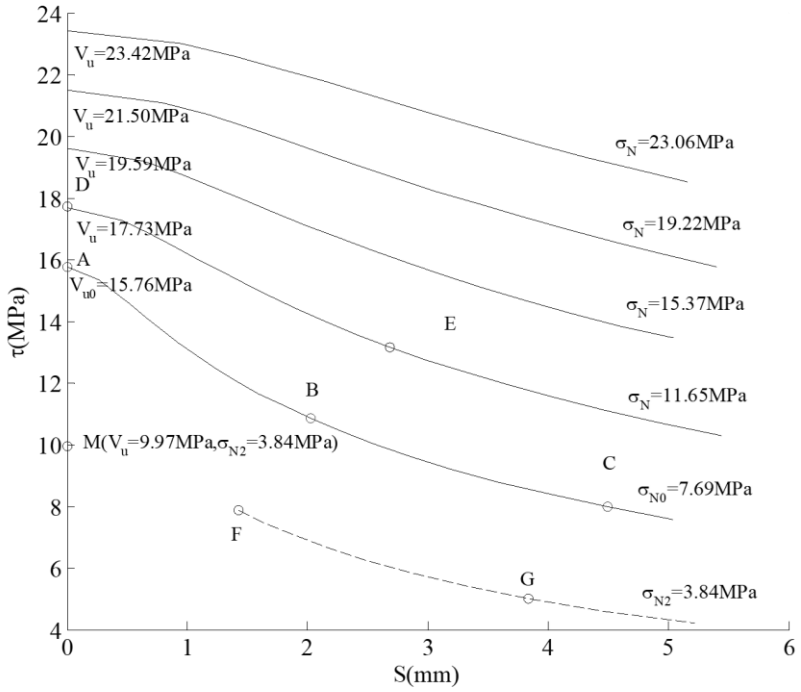

Fig. 9 Shear friction properties derived from stress-strain relationship for 40MPa concrete

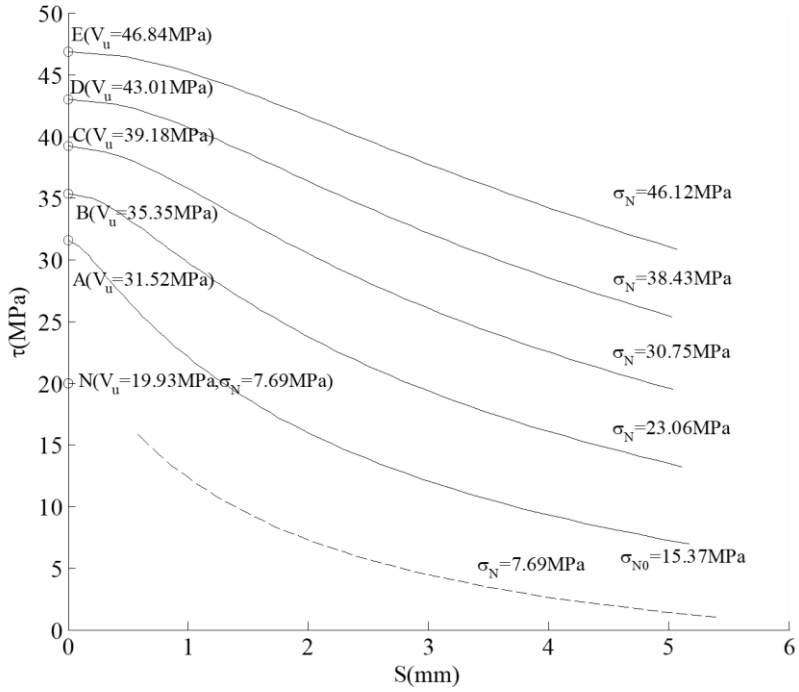

Fig. 10 Shear friction properties derived from stress-strain relationship for 80MPa concrete

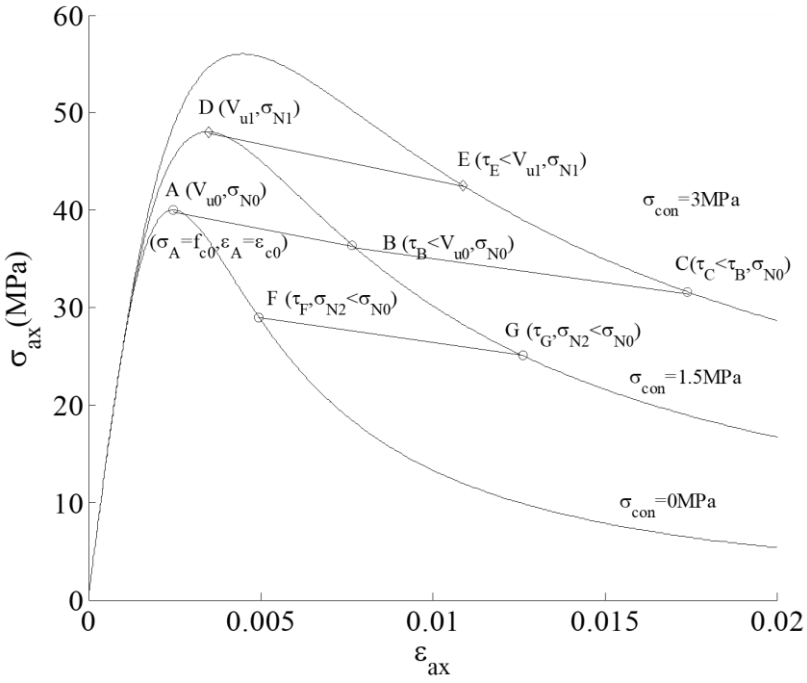

Fig. 11 Extracting shear friction properties from stress-strain relationships of actively confined concrete columns with different lateral confining stresses (unconfined concrete strength f_{c0} = 40MPa)

Points can be extracted from the falling branches of the stress-strain relationships with different lateral confining stresses σ_{con} in Fig. 11. From mechanics, the shear friction properties that is the shear stress τ, normal stress σ_N and slip S can be obtained from Eqs. (24), (23) and (29) respectively for these points. Then from this population of results, the points with the same normal confining stress σ_N can be extracted. For example, points A, B and C in Fig. 11 may have been found from the population set to have the same normal stress σ_{N0} of 7.69 MPa. Hence these can be plotted as points A, B, C in Fig. 9 where the ordinate is the shear stress τ_{exp} and the abscissa is the slip S which, as shown previously, have been obtained from Eqs. (23), (24) and (29). Similarly, the points D and E with the same normal stress σ_{N1} of 11.65 MPa in Fig. 11 can be extracted; and at these points the slip S and shear stress τ_{exp} can be derived from Eqs. (23), (24) and (29) such that points D and E can be plotted in Fig. 9.

Repeating this procedure gives the shear friction properties for 40MPa concrete in Fig. 9 and 80MPa concrete in Fig. 10 for different normal stresses σ_N as shown. This procedure can be duplicated for different unconfined concrete strengths from 20 MPa to 100 MPa. Approximations will be proposed to simulate all these shear friction properties later.

Shear Stress V_u at the Commencement of Sliding from Mechanics

It is worth noting that at the peak point of the actively confined concrete stress-strain relationship such as point D in Fig. 11, the shear stress τ is referred to as V_u as it is the shear stress at the onset of sliding. Furthermore, V_u is also the maximum shear stress for a specific normal stress σ_N for an unconfined concrete strength f_{c0}, such as that as shown in Fig. 10. Being at the onset of sliding, it is obvious that the slips S at these peak points equal zero and the peak stresses equal f_{cc}; these can be substituted into Eqs. (24) and (23) respectively to derive the shear stress V_u and normal stress σ_N at the peak point of the actively confined concrete stress-strain relationship as follows

$$V_u = (f_{cc} - 2\sigma_{con})\sin\alpha\cos\alpha \tag{39}$$

$$\sigma_N = f_{cc}\sin^2\alpha + 2\sigma_{con}\cos^2\alpha \tag{40}$$

substituting the peak stress f_{cc} from Eq. (34) and the natural angle of the sliding plane α = 26^{O} (Chen, Yongjian 2015; Chen, Y, Visintin & Oehlers 2015a) into Eqs. (39) and (40) respectively and rearranging gives

$$V_u = 0.394 f_{c0} + 1.182\sigma_{con} \tag{41}$$

$$\sigma_N = 0.192 f_{c0} + 2.642\sigma_{con} \tag{42}$$

combining Eqs. (41) and (42) gives the following shear stress V_u as a function of the normal stress σ_N and unconfined concrete strength f_{c0}

$$V_u = 0.298 f_{c0} + 0.498\sigma_N \tag{43}$$

It is worth noting that for some points, the normal stress σ_N is less than the peak normal stress in the unconfined concrete σ_{N0} obtained from Eq. (37), such as points F and G in Fig. 11. The slip S of point F obtained from Eq. (29) is larger than zero and is plotted as point F in Fig. 9 at σ_{N2} = 3.84 MPa. Hence there is now a gap, or an absence of experimental data between the y-axis and point F for σ_{N2} = 3.84 MPa as shown. To fill this gap, the intercept of the plot at σ_{N2} = 3.84 MPa with the y-axis, that is V_u at σ_{N2} = 3.84 MPa, can be derived from shear sliding tests as shown in Figs. 1 and will be explained next.

Shear Stress V_u at the Commencement of Sliding from Shear Sliding Tests

The relationship between shear stress V_u over concrete strength f_{c0} and normal stress σ_N over f_{c0} is plotted in Fig. 12. Let us start with point A in Fig. 12. When the natural angle of the sliding plane α as shown in Fig. 2 is substituted with 26^{O} (Chen, Yongjian 2015; Chen, Y, Visintin & Oehlers 2015a), σ_N is equal to σ_{N0} from Eq. (37) which becomes 0.192f_{c0}, which is also the abscissa of the point A. Consequently, when $\sigma_N/f_{c0} \geq 0.192$ then $\sigma_N \geq 0.192 f_{c0}$ and $\sigma_N \geq \sigma_{N0}$ such that shear stress V_u can be derived from Eq. (43). The variation A–B in Fig. 12 can be obtained from Eq. (43) by substituting unconfined concrete strength f_{c0} and normal stress σ_N and can be expressed as

$$\frac{V_u}{f_{c0}} = 0.298 + 0.498\frac{\sigma_N}{f_{c0}} \qquad (\sigma_N \geq \sigma_{N0}) \tag{44}$$

where σ_{N0} is obtained from Eq. (37) and this variation has been labelled 'cylinder' in Fig. 12 as it has been derived from the analysis of cylinder tests.

When σ_N/f_{c0} is smaller than 0.192 in Fig. 12 that is $\sigma_N < \sigma_{N0}$, there is a gap in the data set such as that shown in Fig. 9 between point F and y-axis such that cylinder tests cannot provide experimental data for this region. Consequently, the shear stress V_u can only be obtained from shear sliding tests that have external prestressed reinforcement that is the confinement is active; these are plotted as X mark points in Fig. 12 from the work of Zhang (2014). To make the shear stress V_u as a continuous function of the normal stress σ_N, point A in Fig. 12 is fixed and the dashed line CA in Fig. 12 taken through the centroid of Zhang's test results marked X as shown which gives the following equation

$$\frac{V_u}{f_{c0}} = 0.105 + 1.50\frac{\sigma_N}{f_{c0}} \qquad (\sigma_N < \sigma_{N0}) \tag{45}$$

where σ_{N0} is obtained from Eq. (37). The shear stress V_u can also be obtained from shear friction tests with internal unprestressed reinforcement that is with passive confinement such that the confinement force gradually increases with slip through aggregate interlock. The experimental database of these passive confinement tests of initially uncracked concrete by Chen, Y et al. (2015) as plotted as dot points in Fig. 12. It can be seen that Chen's test results from passively confined tests lie in general below the line C–A from actively confined tests. The reason is as follows.

Let us consider the relationship between the shear stress τ and slip S in Fig. 13 which is from an initially uncracked specimen with internal reinforcement in the shear sliding test, that is a passively confined shear friction test; the results in Fig. 13 are specimen G2 (Mattock, Li & Wang 1976). The test results follow the path O–A–C. The normal stress σ_N in Fig. 1(b) at the start point O in Fig. 13 (S = 0 mm) is equal to zero as the internal reinforcement in Fig. 1(b) has no deformation and hence, no confining stress. As the slip S increases, the deformation of the internal reinforcement will increase through the aggregate interlock mechanism and, subsequently, the normal confining stress will reach σ_{N1} at the peak point A

($S = S_0$) in Fig. 13 (Chen, Y et al. 2015; Mattock, Li & Wang 1976) where the transverse reinforcement has yielded and, consequently, provides the greatest confinement. The maximum shear stress τ_A at point A will be recorded as V_u in the experiment. On a further increase in slip, the reinforcement force remains at its yield strength so the confinement stays constant at its maximum but interface slip causes a reduction in the shear strength, as can be seen in Figs. 9 and 10, producing the gradual reduction A–C in Fig. 13. This is an example of passive confinement as the normal stress builds up over O–A and then is constant afterwards along A–C.

If the transverse reinforcement had yielded as soon as slip occurred that is at B in Fig. 13, then the specimen would behave as actively confined. In which case, the variation would be B–A that is $\sigma_N = \sigma_{N1}$ throughout giving the dashed line in the Fig. 13. The maximum shear stress V_u equals τ_B at point B. Hence the variation B–A–C is due to active confinement. The reduction from B-A to O-A is due to the difference between active and passive confinement tests and explains why most of Chen's points in Fig. 12 which were from passively confined tests are below A–C which is based on active confinement.

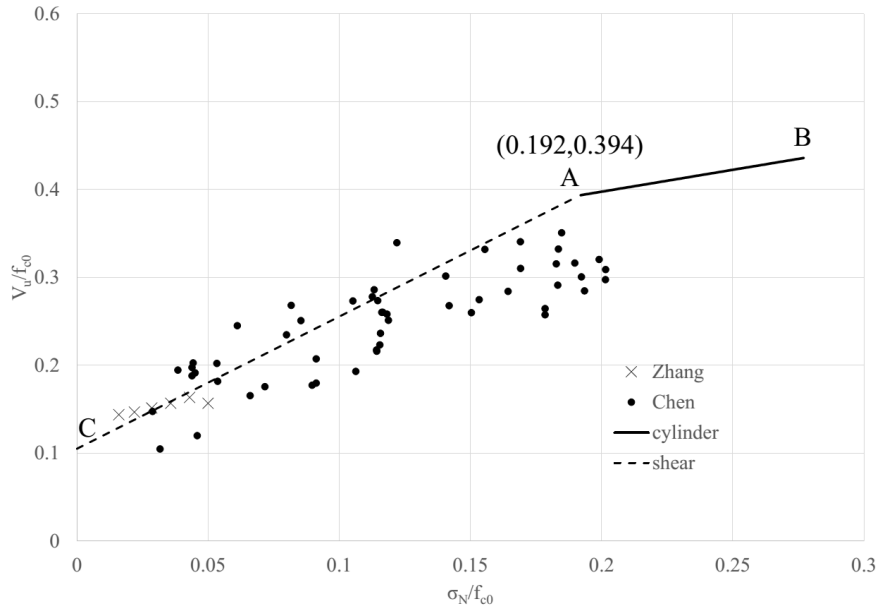

Fig. 12 Shear stress V_u over concrete strength f_{c0} against normal stress σ_N over f_{c0}

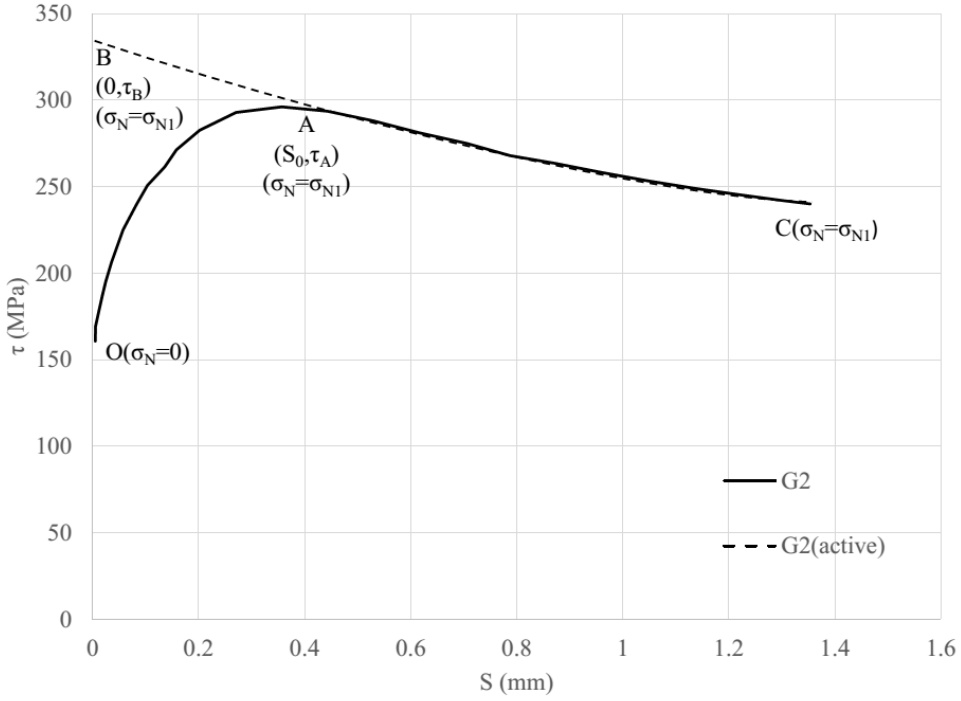

Fig. 13 Shear stress τ against slip S from the shear sliding test with internal reinforcement for specimen G2

In summary, for variations in Fig. 9 where the normal stress σ_N is less than σ_{N0} as obtained from Eq. (37) such as σ_{N2} in Fig. 9, the shear stress V_u at the commencement of sliding can be obtained from Eq. (45). Examples are point M in Fig. 9 ($\sigma_N = \sigma_{N2} = 3.84$ MPa) and point N in Fig. 10 ($\sigma_N = 7.69$ MPa). When the normal stress σ_N is equal to or higher than σ_{N0} as obtained from Eq. (37) such as solid lines AB ($\sigma_N = 7.69$ MPa) and DE ($\sigma_N = 11.65$ MPa) in Fig. 9, the shear stress V_u can be obtained from Eq. (43). Consequently from Eqs. (44) and (45) the shear stress V_u can be written as follows

$$\begin{aligned} V_u &= 0.105 f_{c0} + 1.50\sigma_N \qquad (\sigma_N < \sigma_{N0}) \\ V_u &= 0.298 f_{c0} + 0.498\sigma_N \qquad (\sigma_N \geq \sigma_{N0}) \end{aligned} \tag{46}$$

where σ_{N0} can be obtained from Eq. (37).

Derivation of Shear Stress $\tau_{2.5}$ at S = 2.5 mm

In this section, the approximations to simulate the shear friction properties derived from the actively confined concrete stress-strain relationship, such as the lines in Figs. 9 and 10, will be proposed. It should be noted that the maximum slip is restricted to around 5 mm as shown, which is taken based on that of previous approach (Chen, Y, Visintin & Oehlers 2015a). It will be shown later how this affects the application.

Consider the shear friction properties of 80 MPa concrete as shown in Fig. 14. The shear stresses V_u at the commencement of sliding at points A to G can be obtained from Eq. (46) and the slips at these points are equal to zero. Consequently one point at $S = 0$ is fixed for each dashed line in Fig. 14. Let us consider the shear stress $\tau_{2.5}$ where the slip equals 2.5 mm such as points H to N in Fig. 14. The shear stresses $\tau_{2.5}$ at $S = 2.5$ mm at points H to N can be obtained for the normal stresses $\sigma_{N\text{-}H}$, $\sigma_{N\text{-}I}$, $\sigma_{N\text{-}J}$, $\sigma_{N\text{-}K}$, $\sigma_{N\text{-}L}$, $\sigma_{N\text{-}M}$ and $\sigma_{N\text{-}N}$ as shown. This procedure can be duplicated for 20 to 100MPa concrete. Consequently the shear stresses $\tau_{2.5}$ at $S = 2.5$ mm for the range of 20 MPa $\leq f_{c0} \leq$ 100 MPa can be plotted against normal stress σ_N as shown in Fig. 15. Four approaches to quantify the shear stress $\tau_{2.5}$ as a function of the normal stress σ_N and unconfined concrete strength f_{c0} will be described in this section.

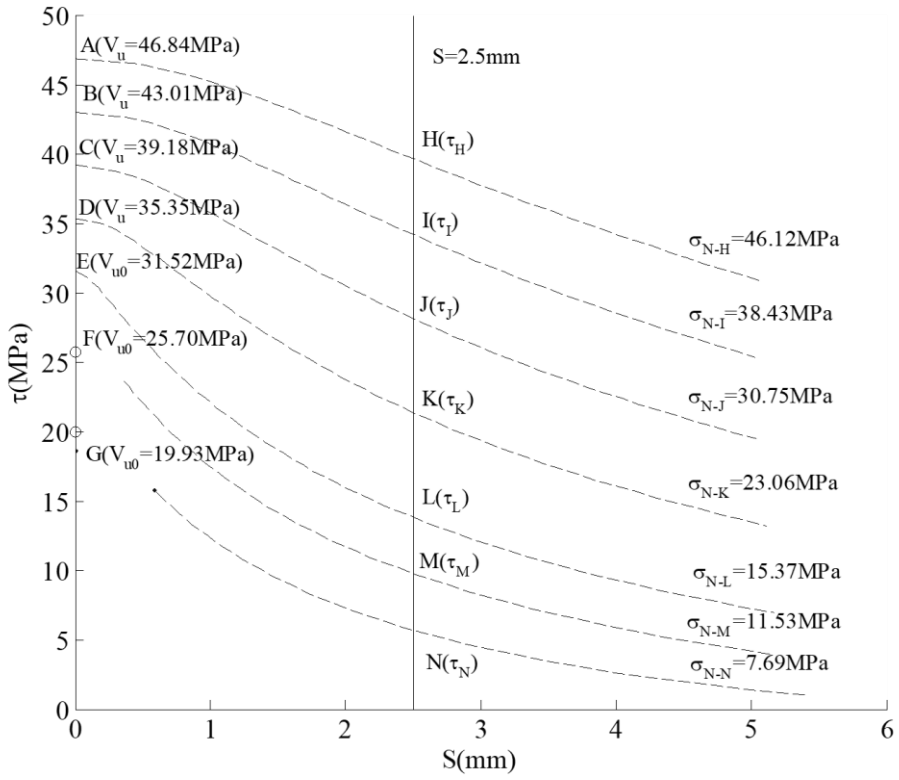

Fig. 14 Derivation of the shear stress at $S = 2.5$mm when $f_{c0} = 80$MPa

Approach 1: Parabolic Approach

Let us consider the shear stress $\tau_{2.5}$ at S = 2.5 mm against normal stress σ_N for different concrete strengths f_{c0} as shown in Fig. 15. As an example, shear stress $\tau_{2.5}$ for concrete strength f_{c0} = 100 MPa is plotted as hexagram marks. From these results, the three points A, B and C that have the normal stresses σ_{N1}, σ_{N2} and $(\sigma_{N1}+\sigma_{N2})/2$ respectively can be extracted and their shear stresses can be determined. Through these three points, $\tau_{2.5}$ can be simulated as a parabolic function of the normal stress σ_N as follows

$$\tau_{2.5} = a\sigma_N^2 + b\sigma_N + c \tag{47}$$

where the parameters a, b and c for 100MPa concrete can be derived. This procedure can be duplicated for points in Fig. 15 with different concrete strengths and a, b and c can be derived for different concrete strengths as plotted as points in Figs. 16 to 18. These points can be simulated as quadratic polynomials as a function of the concrete strength f_{c0} as below

$$\begin{aligned} a &= -0.00000336f_{c0}^2 + 0.000619f_{c0} - 0.0333 \\ b &= -0.0000447f_{c0}^2 + 0.00744f_{c0} + 0.902 \\ c &= -0.00161f_{c0}^2 + 0.0660f_{c0} + 1.87 \end{aligned} \tag{48}$$

where the unconfined concrete strength f_{c0} is in MPa. Substituting Eq. (48) into Eq. (47) gives the shear stress $\tau_{2.5}$ at S = 2.5 mm.

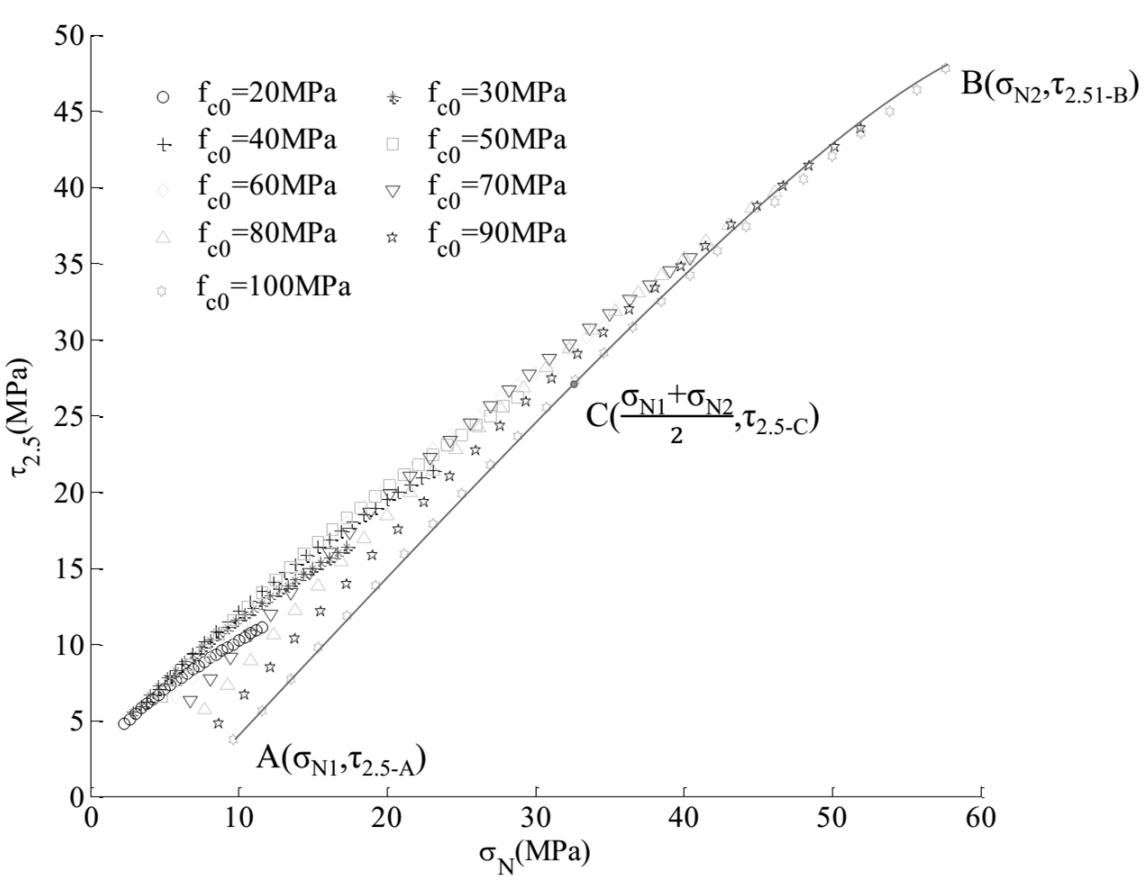

Fig. 15 Shear stresses $\tau_{2.5}$ at S = 2.5mm within the range of 20 MPa ≤ f_{c0} ≤ 100 MPa

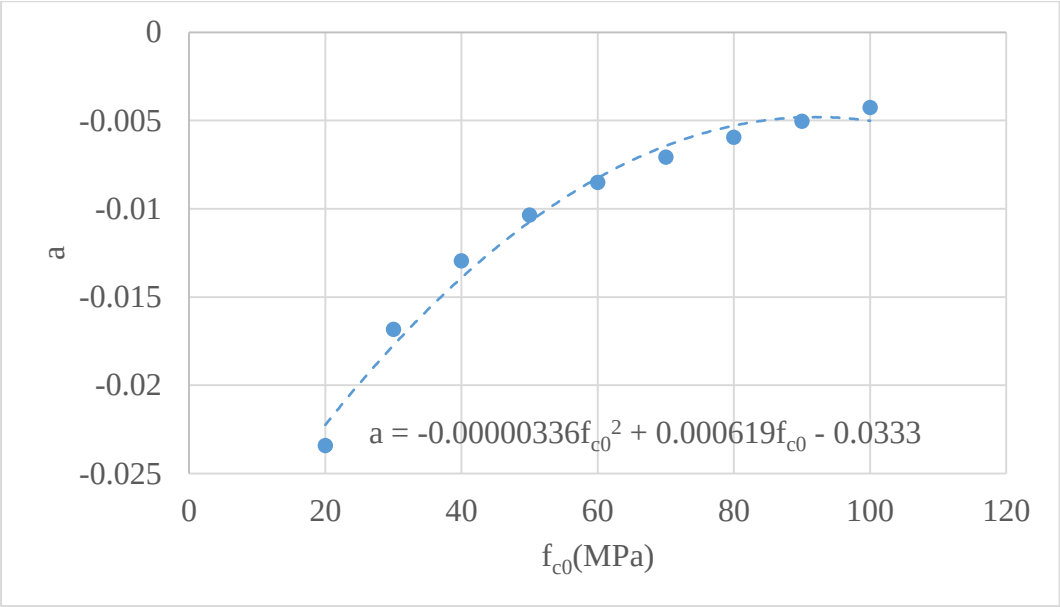

Fig. 16 Parameter a as a function of unconfined concrete strength f_{c0} from approach 1

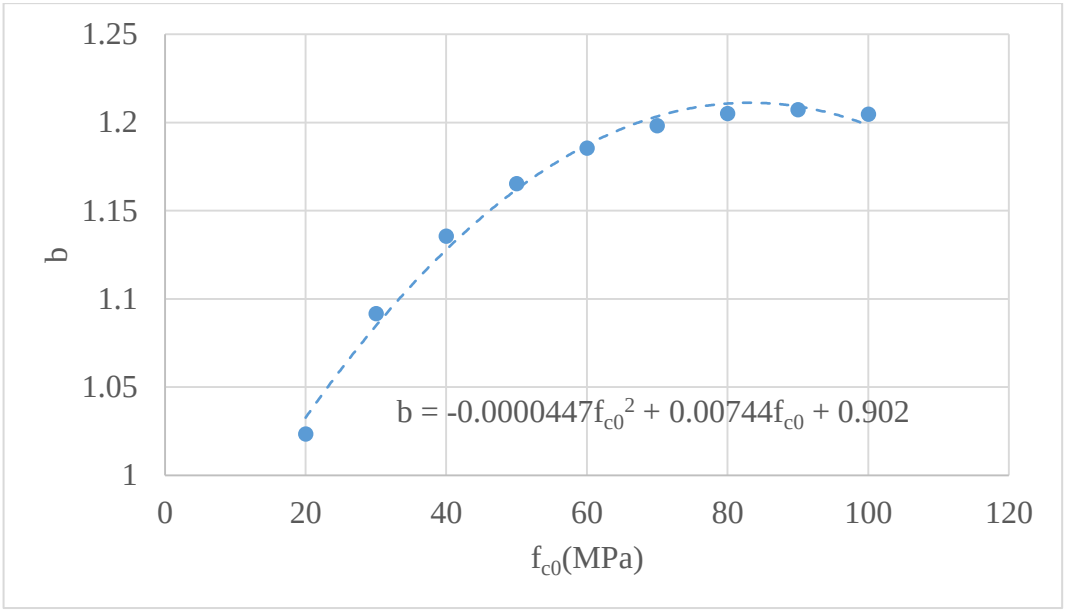

Fig. 17 Parameter *b* as a function of unconfined concrete strength f_{c0} from approach 1

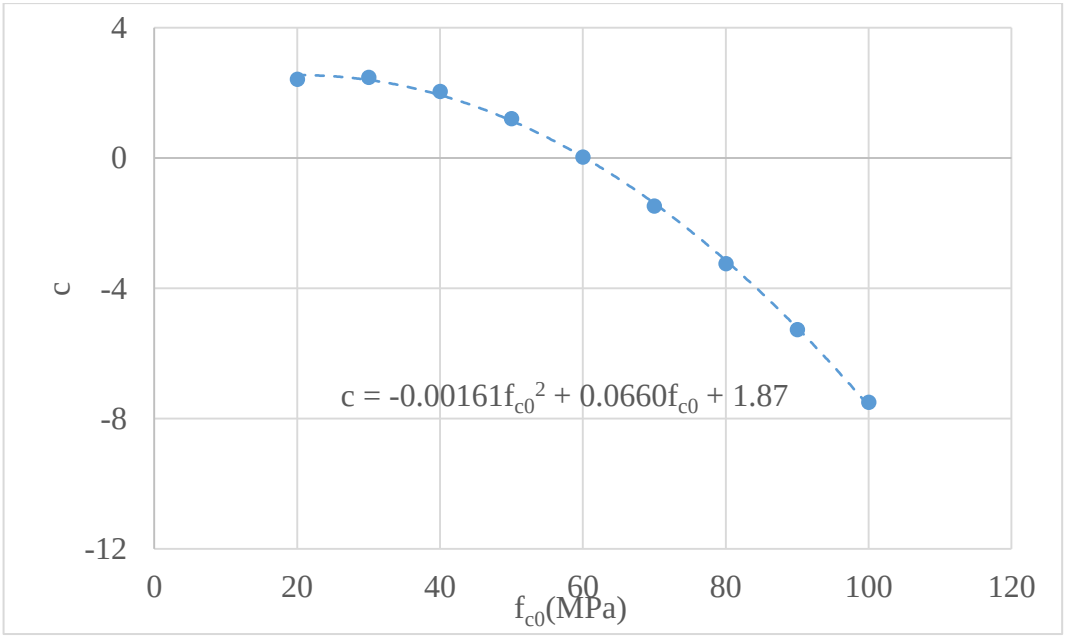

Fig. 18 Parameter *c* as a function of unconfined concrete strength f_{c0} from approach 1

Approach 2: Three-Stage Approach

The parameters *a*, *b* and *c* that are plotted as points in Figs. 16 to 18 can also be simulated as three-stage linear functions as shown in Figs. 19 to 21, which can be written as follows

$$
\begin{aligned}
a_1 &= 0.000524\,f_{c0} - 0.0334 \qquad (20MPa \le f_{c0} < 40MPa) \\
a_2 &= 0.000196\,f_{c0} - 0.0208 \qquad (40MPa \le f_{c0} < 70MPa) \\
a_3 &= 0.0000935\,f_{c0} - 0.0135 \qquad (70MPa \le f_{c0} \le 100MPa) \\
b_1 &= 0.00561\,f_{c0} + 0.915 \qquad (20MPa \le f_{c0} < 40MPa) \\
b_2 &= 0.00209\,f_{c0} + 1.05 \qquad (40MPa \le f_{c0} < 70MPa) \\
b_3 &= 0.000217\,f_{c0} + 1.19 \qquad (70MPa \le f_{c0} \le 100MPa) \\
c_1 &= -0.0184\,f_{c0} + 2.87 \qquad (20MPa \le f_{c0} < 40MPa) \\
c_2 &= -0.117\,f_{c0} + 6.91 \qquad (40MPa \le f_{c0} < 70MPa) \\
c_3 &= -0.201\,f_{c0} + 12.7 \qquad (70MPa \le f_{c0} \le 100MPa)
\end{aligned}
\tag{49}
$$

where the unconfined concrete strength f_{c0} is in MPa. Hence for a specific concrete strength f_{c0}, the associated parameters a, b and c can be derived from Eq. (49), which can be substituted into Eq. (47) to derive the shear stress $\tau_{2.5}$ at S = 2.5 mm.

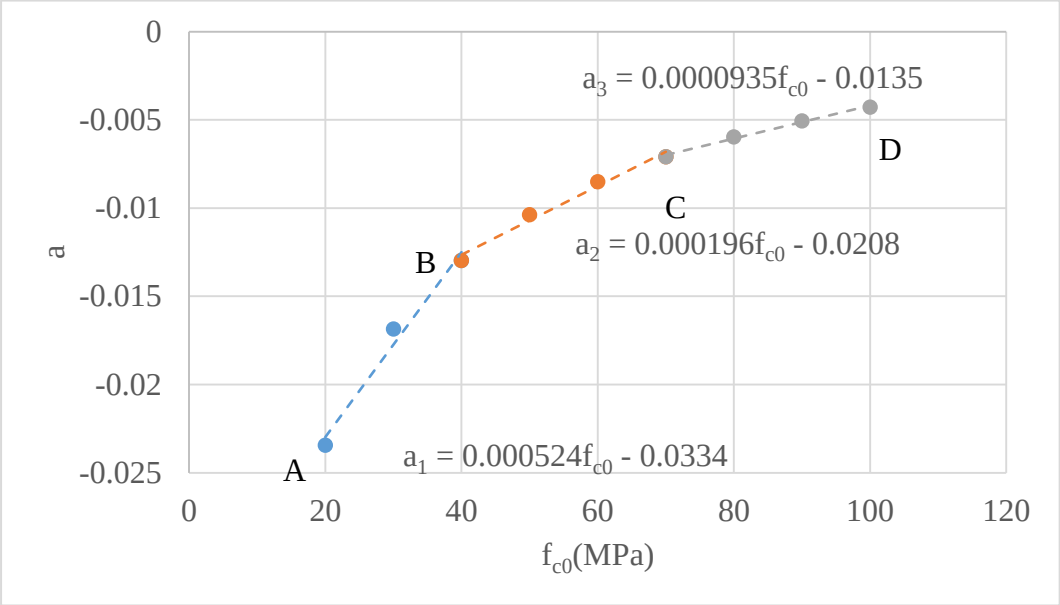

Fig. 19 Parameter a as a function of unconfined concrete strength f_{c0} from approach 2

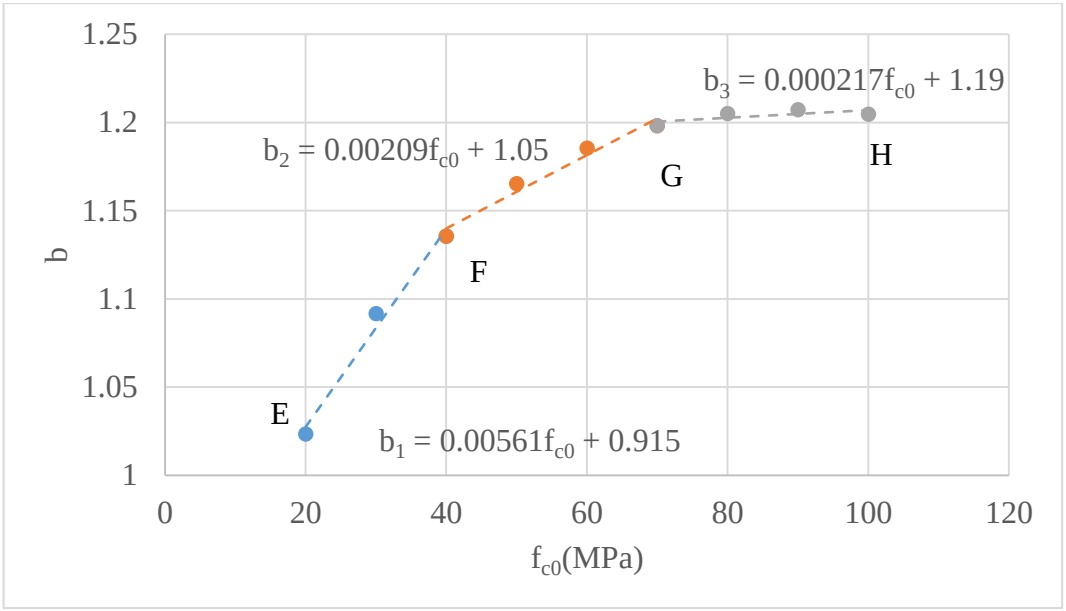

Fig. 20 Parameter *b* as a function of unconfined concrete strength f_{c0} from approach 2

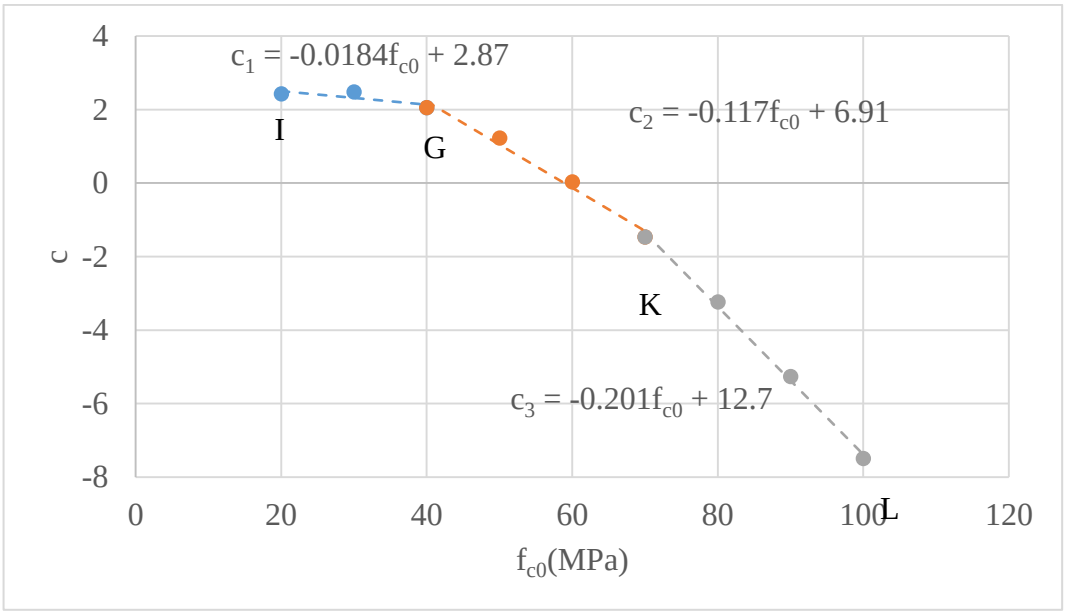

Fig. 21 Parameter *c* as a function of unconfined concrete strength f_{c0} from approach 2

Approach 3: Linear-Form Approach

This approach is similar to approach 1. The difference is that the shear stress $\tau_{2.5}$ at S = 2.5 mm in Fig. 15 is simulated as a linear function instead of the parabolic function of the normal stress σ_N for different concrete strengths as follows

$$\tau_{2.5} = a\sigma_N + b \tag{50}$$

where the slope a and y-intercept b for different concrete strength is shown in Figs. 22 and 23 and can be expressed as follows

$$\begin{aligned} a &= 0.00281 f_{c0} + 0.657 \\ b &= -0.00196 f_{c0}^2 + 0.143 f_{c0} + 1.39 \end{aligned} \tag{51}$$

where the unconfined concrete strength f_{c0} is in MPa. Substituting Eq. (51) into Eq. (50) gives the shear stress $\tau_{2.5}$ at S = 2.5 mm.

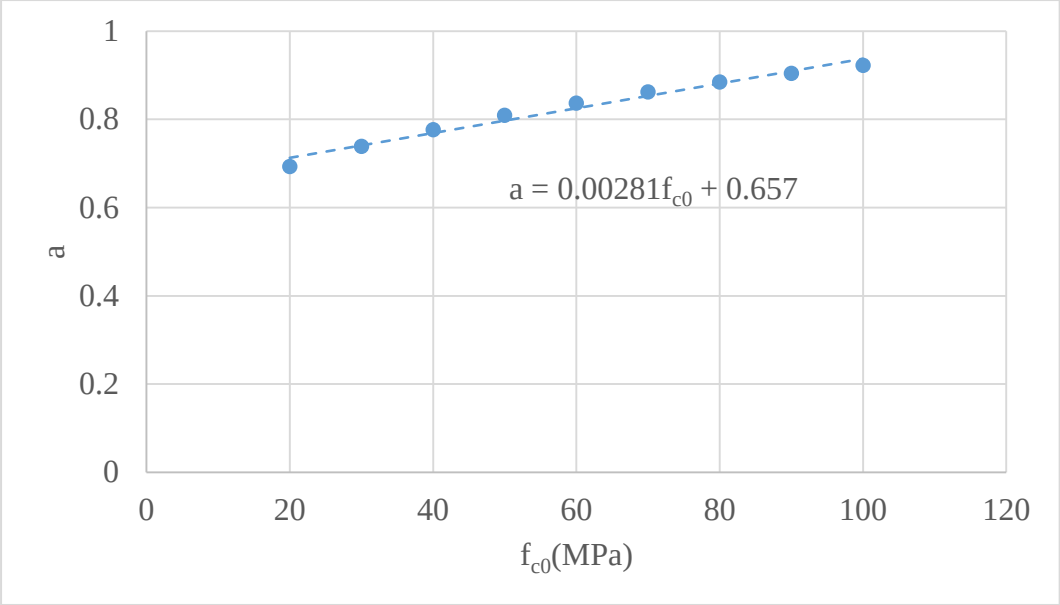

Fig. 22 Parameter a as a function of unconfined concrete strength f_{c0} from approach 3

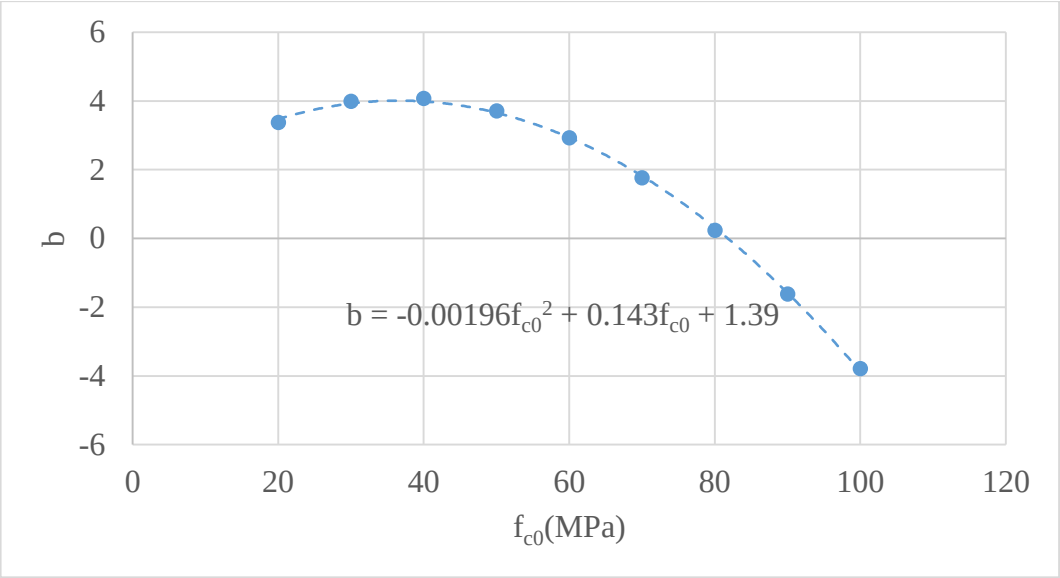

Fig. 23 Parameter *b* as a function of unconfined concrete strength f_{c0} from approach 3

Approach 4: Statistical Approach

The shear stress $\tau_{2.5}$ at S = 2.5 mm for a given normal stress σ_N and unconfined concrete strength f_{c0} are shown in Fig. 15. First consider only the points whose concrete strengths are in the range of 20MPa ≤ f_{c0} < 50MPa. The shear stress $\tau_{2.5}$ at S = 2.5 mm, normal stress σ_N and unconfined concrete strength f_{c0} can be determined for every extracted point. Based on these data points and applying a multivariable linear regression analysis, the shear stresses $\tau_{2.5}$ at S = 2.5 mm can be simulated as a linear function of the normal stress σ_N and unconfined concrete strength f_{c0} as follows

$$\tau_{2.5} = 0.779\sigma_N - 0.0470\, f_{c0} + 2.01 \tag{52}$$

When only the points whose concrete strengths are in the range of 50MPa ≤ f_{c0} ≤ 100MPa are extracted from Fig. 15, the shear stress $\tau_{2.5}$ at S = 2.5 mm can also be simulated as a linear function of the normal stress σ_N and unconfined concrete strength f_{c0} as follows

$$\tau_{2.5} = 0.886\sigma_N - 0.0996\, f_{c0} + 7.81 \tag{53}$$

In summary, Eqs. (52) and (53) give the following shear stress $\tau_{2.5}$ at S = 2.5 mm

$$\tau_{2.5} = 0.779\sigma_N - 0.0470 f_{c0} + 2.01 \qquad (f_{c0} < 50MPa)$$
$$\tau_{2.5} = 0.886\sigma_N - 0.0996 f_{c0} + 7.81 \qquad (f_{c0} \geq 50MPa) \tag{54}$$

where the unit of stress is in MPa. This approach gives two equations near the boundary point f_{c0} = 50MPa and it will be shown later how the boundary point affects the accuracy of the shear friction properties.

The shear stress $\tau_{2.5}$ at S = 2.5 mm have been obtained from four approaches described in this section. The mean, standard derivation and coefficient of variation of the ratio of $\tau_{2.5}$ derived from experimental data $\tau_{2.5\text{-}exp}$ over that derived from the approximations $\tau_{2.5\text{-}theo}$ are shown in Table 1. This ratio is also shown in Figs. 24 to 27 against σ_N/σ_{N0} where σ_{N0} can be obtained from Eq. (37). It can be concluded that the second approach is the most accurate one but complex. By contrast, the third approach is accurate and simple, but less accurate than the second approach.

	approach1	approach 2	approach 3	approach 4
mean	0.999	1.006	0.994	0.996
SD	0.028	0.022	0.050	0.057
CoV	0.028	0.022	0.050	0.057

Table. 1 Mean, standard derivation (S.D) and coefficient of variations (COV) of $\tau_{2.5\text{-}exp}/\tau_{2.5\text{-}theo}$ from four approaches

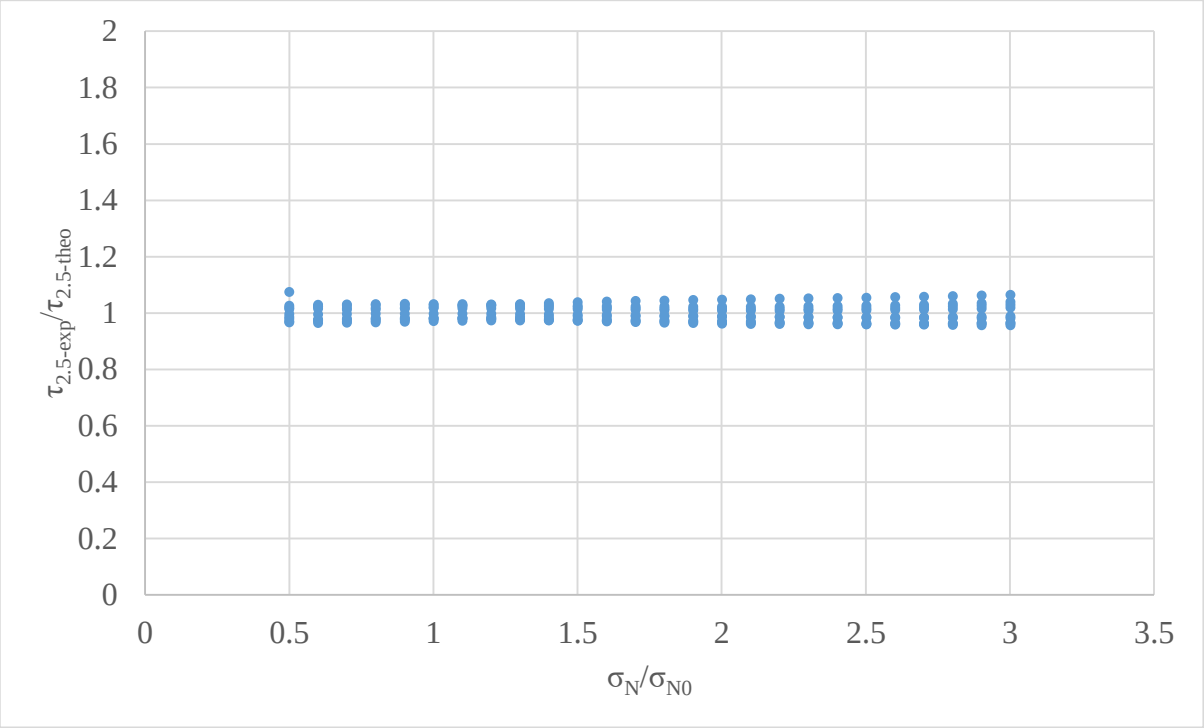

Fig. 24 Ratio of shear stress $\tau_{2.5\text{-}exp}$ from experimental data over that from approach 1 $\tau_{2.5\text{-}theo}$

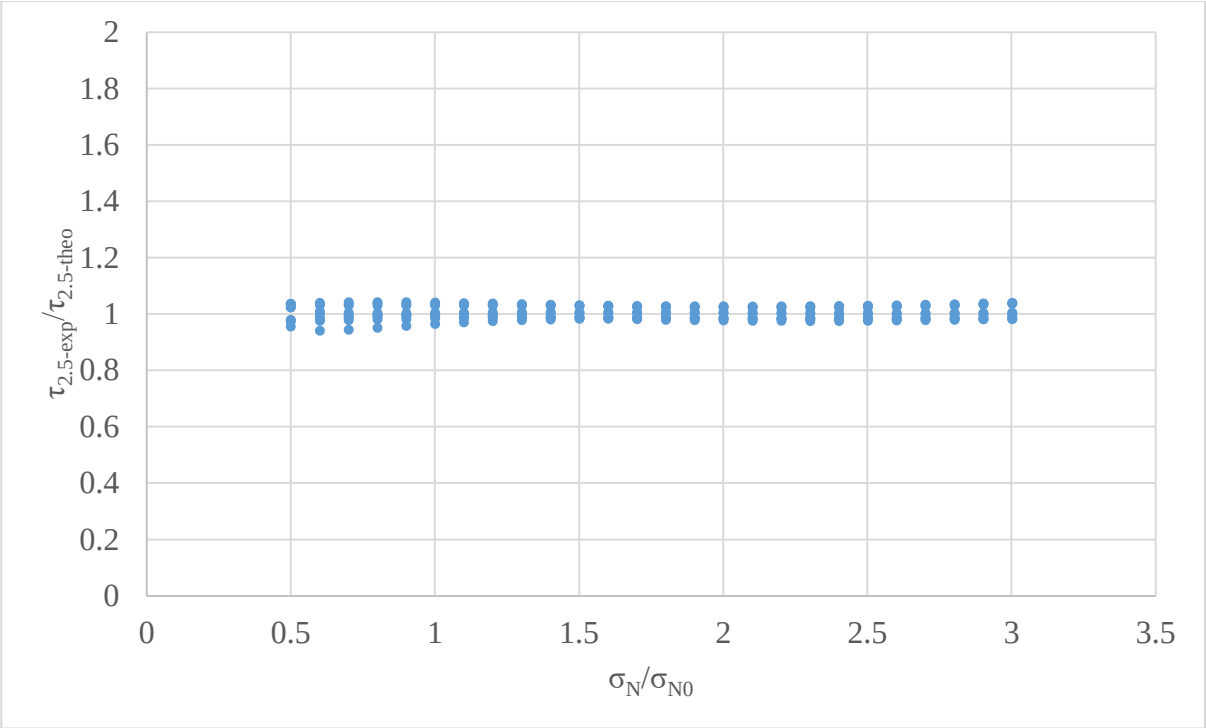

Fig. 25 Ratio of shear stress $\tau_{2.5\text{-}exp}$ from experimental data over that from approach 2 $\tau_{2.5\text{-}theo}$

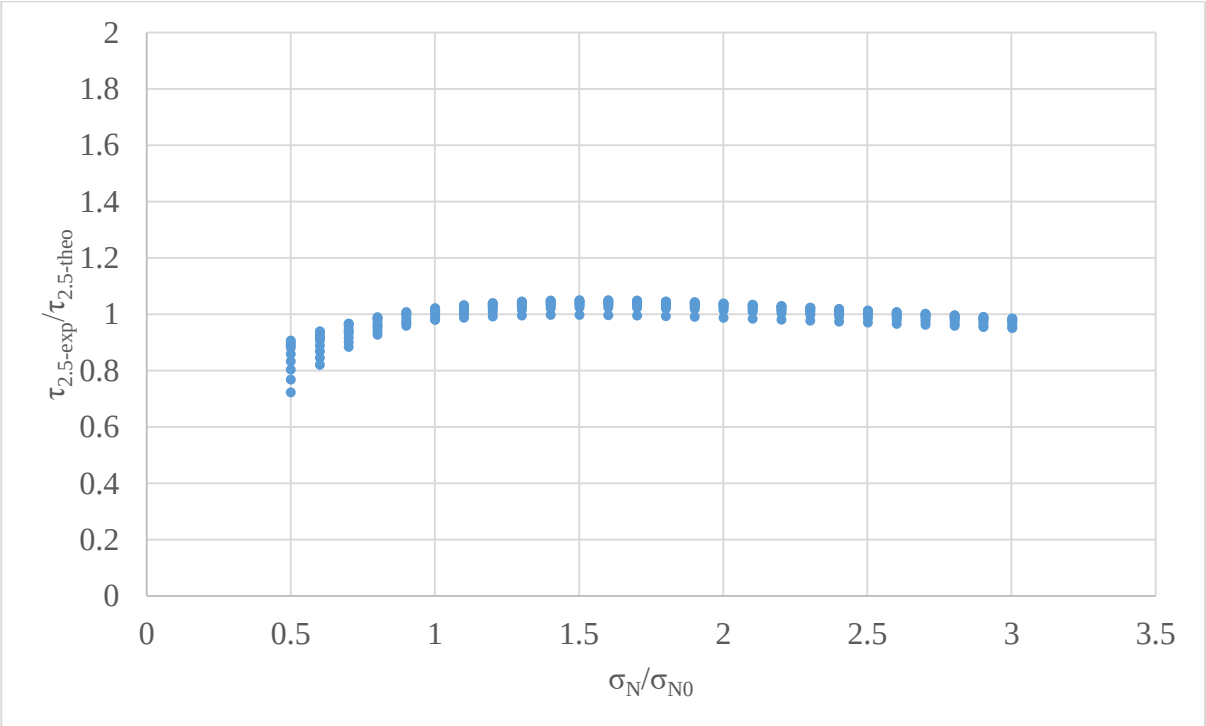

Fig. 26 Ratio of shear stress $\tau_{2.5\text{-}exp}$ from experimental data over that from approach 3 $\tau_{2.5\text{-}theo}$

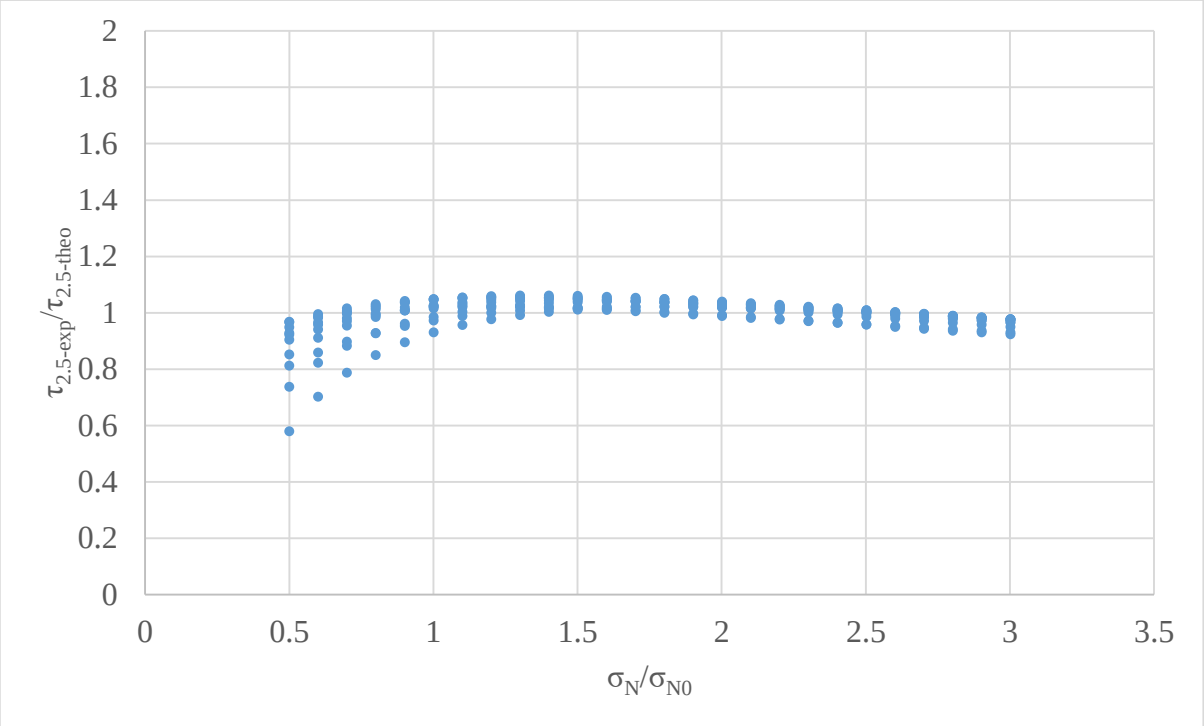

Fig. 27 Ratio of shear stress $\tau_{2.5\text{-}exp}$ from experimental data over that from approach 4 $\tau_{2.5\text{-}theo}$

Derivation of $\tau_{2.5}$ at High σ_N

In Fig. 15, the range of normal stress σ_N is $\sigma_N < 3\sigma_{N0}$ and in practise, this normal stress may be higher. Consequently in this section, the shear stress at $S = 2.5$ for higher normal stress σ_N will be described.

Let us take the shear friction properties of 40 MPa concrete as an example as shown in Fig. 28. The normal stresses $\tau_{2.5}$ at 2.5 mm for normal stress $\sigma_N = 3\sigma_{N0}$ and $\sigma_N = 10\sigma_{N0}$ can be extracted and are referred to as $\tau_{2.5\text{-}3\sigma N0}$ and $\tau_{2.5\text{-}10\sigma N0}$ respectively as shown. Furthermore, $\tau_{2.5\text{-}10\sigma N0}$ can be extracted for different concrete strengths including 20 MPa to 100 MPa concrete as shown in Fig. 29 and can be written as follows

$$\tau_{2.5\text{–}10\sigma N0} = 1.229 f_{c0} \tag{55}$$

For simplification, it is assumed when $\sigma_N > 3\sigma_{N0}$ the shear stress $\tau_{2.5}$ is a linear function of σ_N as shown in Fig. 30 and can be expressed as

$$\tau_{2.5} = \frac{\tau_{2.5-10\sigma N0} - \tau_{2.5-3\sigma N0}}{7\sigma_{N0}}(\sigma_N - 3\sigma_{N0}) + \tau_{2.5-3\sigma N0} \qquad (\sigma_N > 3\sigma_{N0}) \tag{56}$$

where σ_{N0} can be obtained from Eq. (37), $\tau_{2.5\text{-}3\sigma N0}$ in Fig. 30 can be derived by substituting $\sigma_N = 3\sigma_{N0}$ into Eq. (46), (47), (48), (49), (50), (51) or (54) and $\tau_{2.5\text{-}10\sigma N0}$ can be derived from Eq. (55).

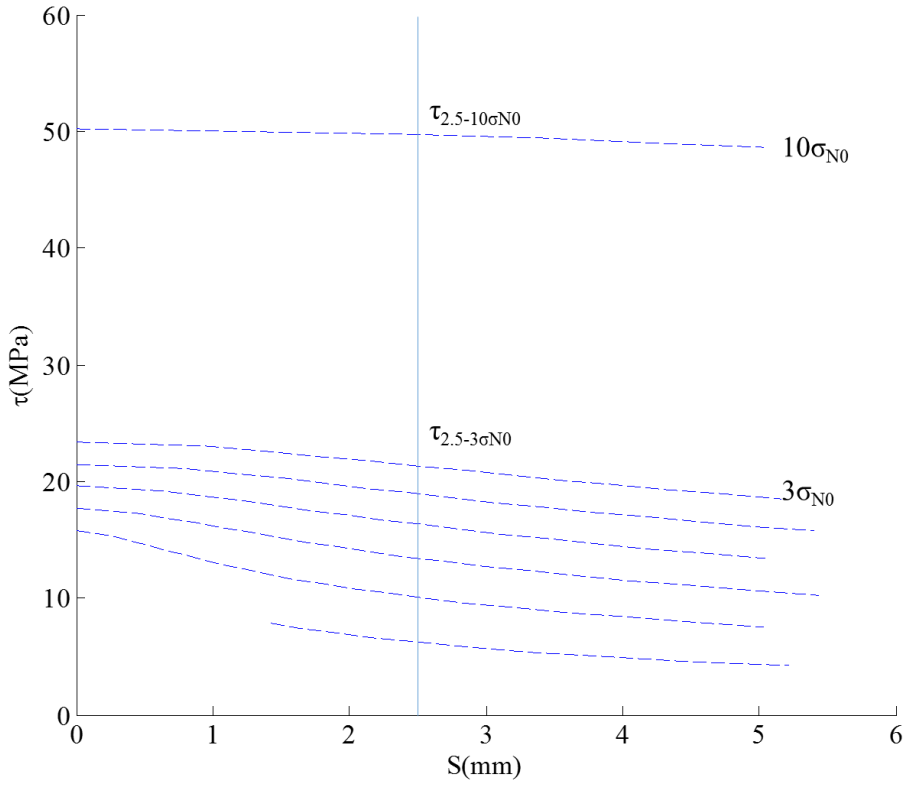

Fig. 28 Shear stress $\tau_{2.5}$ for different normal stress $3\sigma_{N0}$ and $10\sigma_{N0}$ for 40MPa concrete

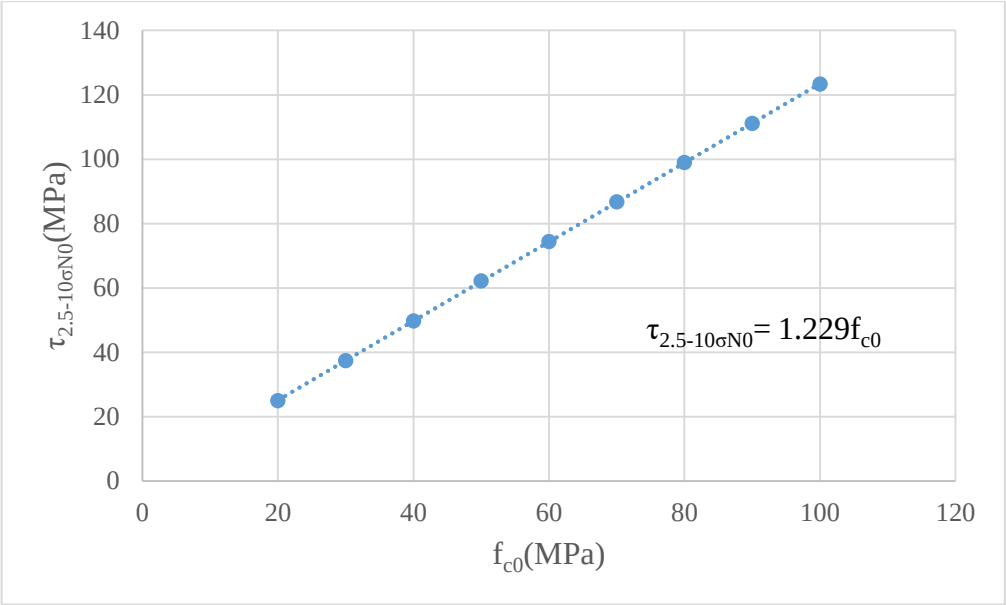

Fig. 29 Shear stress $\tau_{2.5\text{-}10\sigma N0}$ for different concrete strength f_{c0}

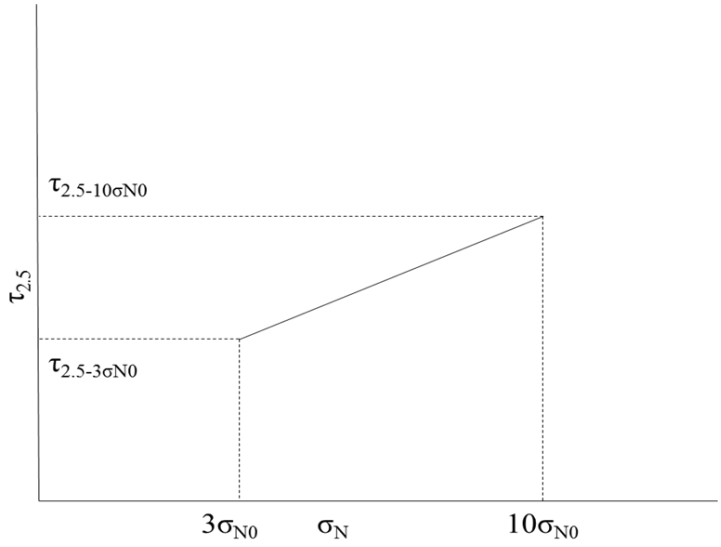

Fig. 30 Shear stress $\tau_{2.5}$ for different normal stress $3\sigma_{N0}$ and $10\sigma_{N0}$

Shear Friction Property Equations

The shear friction properties can be derived by linking the shear stress V_u at $S = 0$ and shear stress $\tau_{2.5}$ at $S = 2.5$ mm derived from four approaches in this section as follows

$$\frac{\tau - V_u}{\tau_{2.5} - V_u} = \frac{S - 0}{2.5 - 0} \tag{57}$$

which can be rearranged to

$$\tau = \frac{\tau_{2.5} - V_u}{2.5} S + V_u \tag{58}$$

substituting $\tau_{2.5}$ from Eqs. (47), (48), (49), (50), (51) and (54) and V_u obtained from Eq. (46) into Eq. (58) gives the shear friction properties. In the next section, the accuracy of these approximations will be validated.

It is worth noting that substituting $\tau_{2.5}$ from Eq. (50) (approach 3) and Eq. (56) and V_u obtained from Eq. (46) into Eq. (58) and simplifying gives equations as follows

When $\sigma_N < \sigma_{N0}$

$$\tau_m = [(0.00112 f_{c0} - 0.337)\sigma_N - 0.000784 f_{c0}^2 + 0.0152 f_{c0} + 0.556]S + 1.50\sigma_N + 0.105 f_{c0} \tag{59}$$

where σ_{N0} can be obtained from Eq. (37).

and when $\sigma_{N0} \leq \sigma_N < 3\sigma_{N0}$, then

$$\tau_m = [(0.00112 f_{c0} + 0.0636)\sigma_N - 0.000784 f_{c0}^2 - 0.0620 f_{c0} + 0.556]S + 0.498\sigma_N + 0.298 f_{c0} \tag{60}$$

and when $\sigma_N > 3\sigma_{N0}$, then

$$\tau_m = [(\frac{A_H}{2.5} - 0.199)\sigma_N + \frac{B_H}{2.5} - 0.119 f_{c0}]S + 0.498\sigma_N + 0.298 f_{c0} \tag{61}$$

where the parameters A_H and B_H can be written as

$$A_H = (1.229 f_{c0} - 0.577 f_{c0} A_\tau - B_\tau) / (1.345 f_{c0}) \tag{62}$$

$$B_\tau = -0.00196 f_{co}^2 + 0.143 f_{c0} + 1.39 \quad (63)$$

where the parameters *a* and *b* can be obtained from Eq. (51).

Validation of Approaches

Figures 31 to 50 show the shear friction properties derived from the stress-strain relationship of the actively confined concrete (the dashed lines) and the approximations obtained from the four approaches derived by substituting Eqs. (46), (47), (48), (49), (50), (51) and (54) into Eq. (58) (the solid lines) for 20 to 100 MPa concrete. Furthermore, the shear stress τ_{exp} derived from experimental data is plotted against the curve fits τ_{theo} obtained from the four approaches in section 6 as shown in Figs. 51 to 54. In these results, the unconfined concrete strength f_{c0} varies from 20 MPa to 100 MPa and slip S varies from 0 mm to 5 mm. The mean, standard derivation and the coefficient of variation of the ratio τ_{theo}/τ_{exp} are shown in Table 2. It is found that these four approaches can simulate the shear friction properties well generally. Nevertheless, it is shown that the accuracy of the approximations will decrease when the shear stress τ is low enough as shown in Figs. 51 to 54; and this is the main reason why the standard derivations in Table 2 are not low. However, the approximations mostly give conservative prediction when the shear stress τ is low. The influence of the error between the approximations and shear friction properties from experimental data will be investigated in the next section.

	approach1	approach2	approach3	approach4
mean	1.042	1.050	1.048	1.054
SD	0.158	0.168	0.165	0.197
CoV	0.151	0.160	0.157	0.187

Table. 2 Mean, standard derivation (S.D) and coefficient of variations (COV) of τ_{exp}/τ_{theo} from four approaches

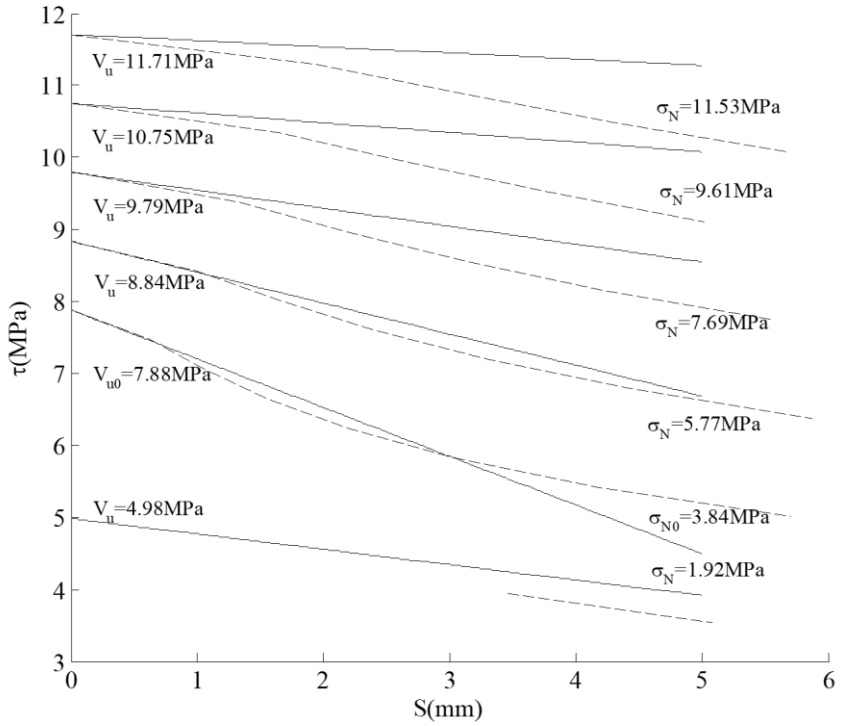

Fig. 31 Shear friction properties derived from stress-strain relationship (dashed lines) and approximation from approach 1 (solid lines) for 20MPa concrete

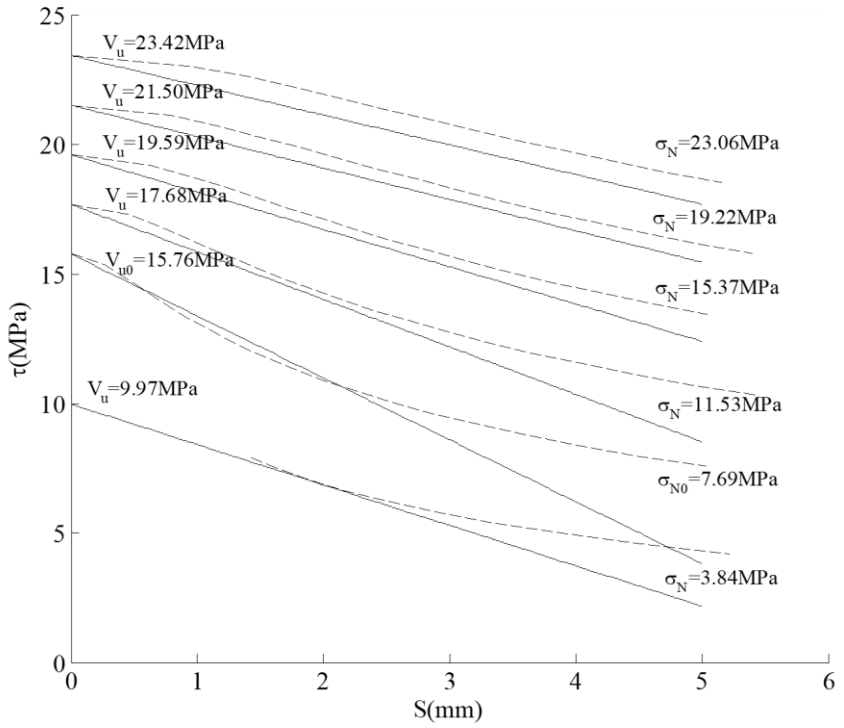

Fig. 32 Shear friction properties derived from stress-strain relationship (dashed lines) and approximation from approach 1 (solid lines) for 40MPa concrete

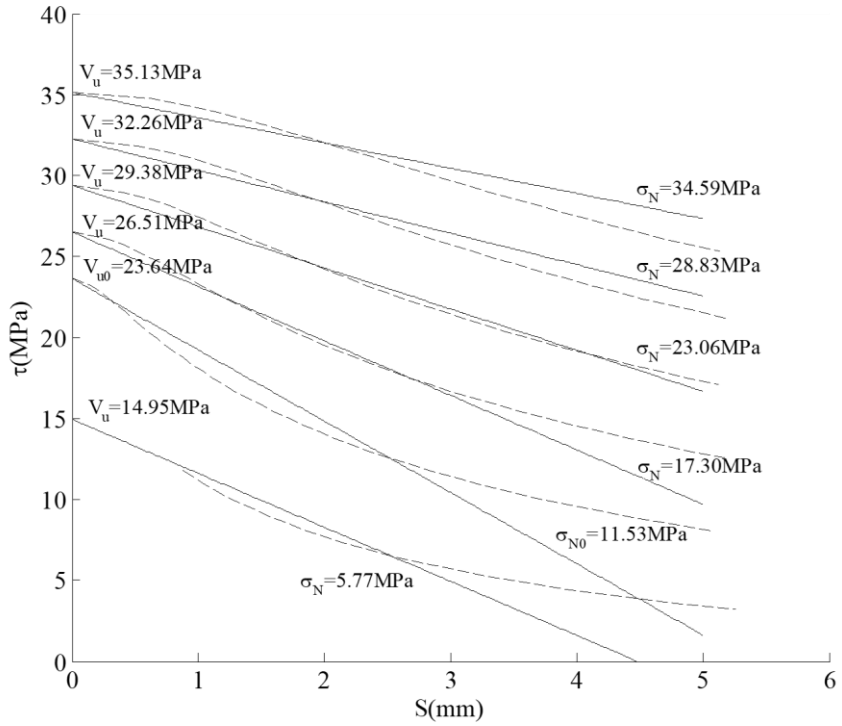

Fig. 33 Shear friction properties derived from stress-strain relationship (dashed lines) and approximation from approach 1 (solid lines) for 60MPa concrete

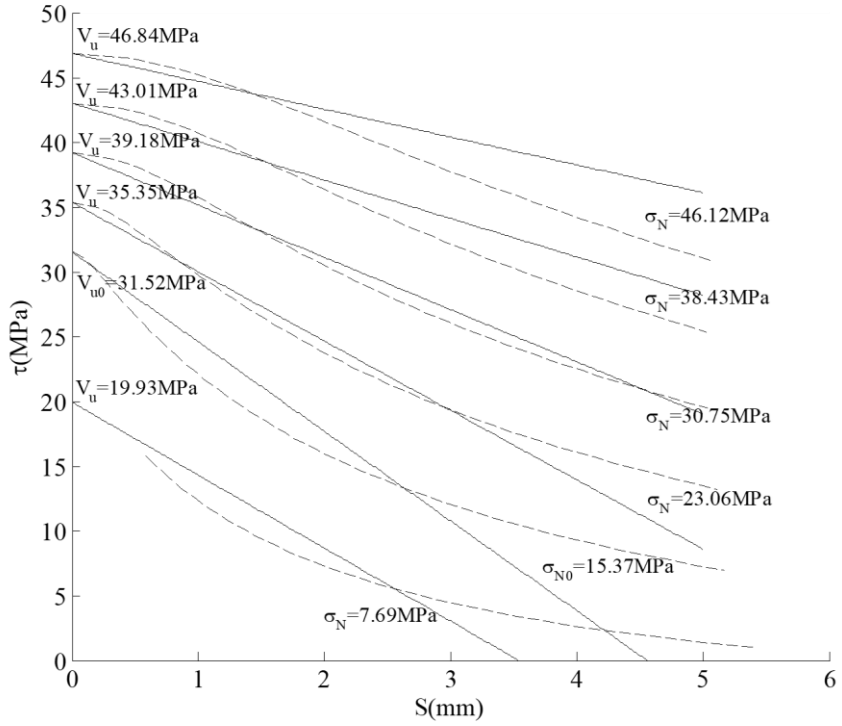

Fig. 34 Shear friction properties derived from stress-strain relationship (dashed lines) and approximation from approach 1 (solid lines) for 80MPa concrete

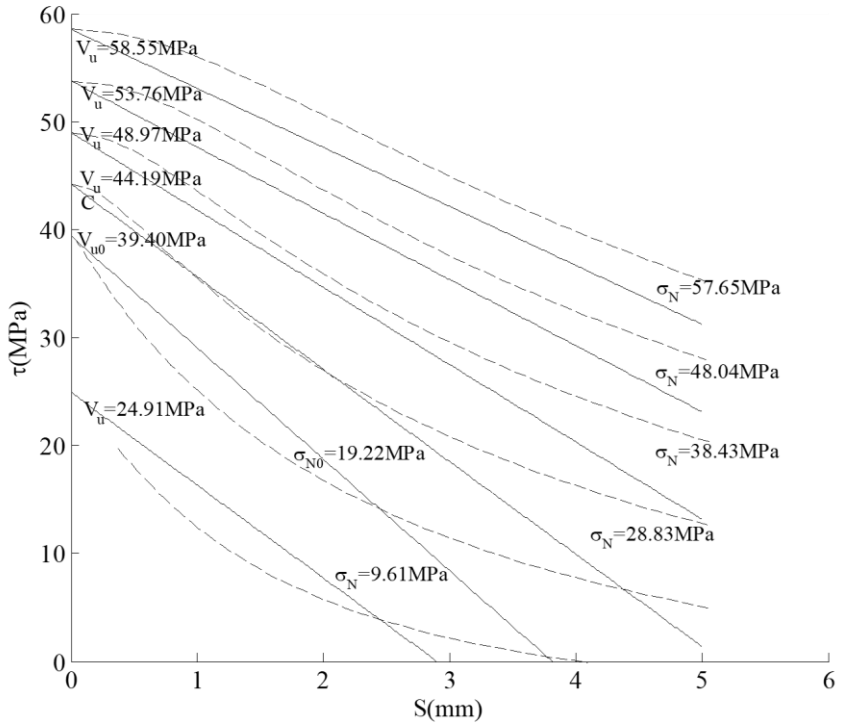

Fig. 35 Shear friction properties derived from stress-strain relationship (dashed lines) and approximation from approach 1 (solid lines) for 100MPa concrete

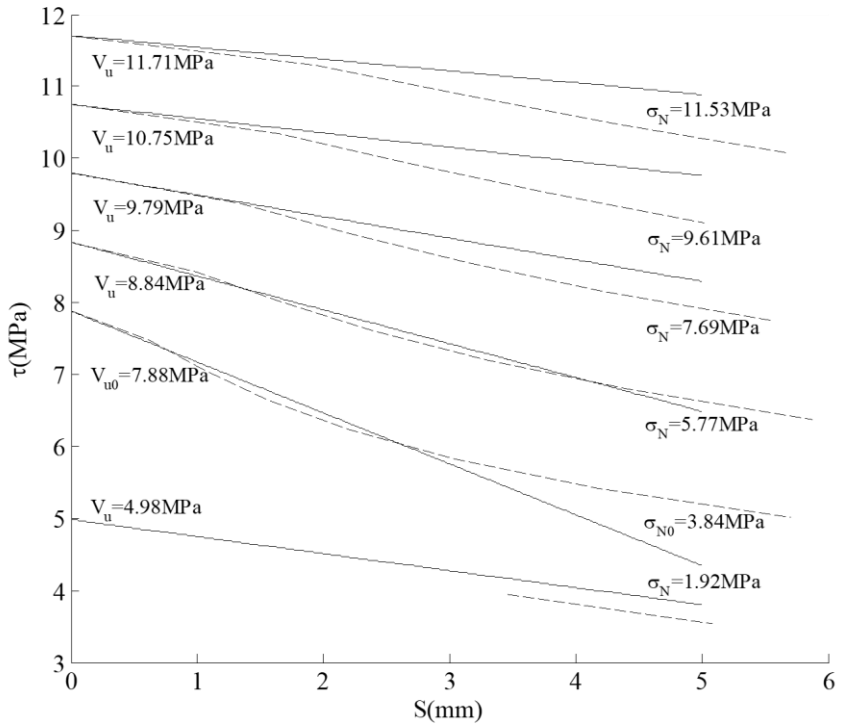

Fig. 36 Shear friction properties derived from stress-strain relationship (dashed lines) and approximation from approach 2 (solid lines) for 20MPa concrete

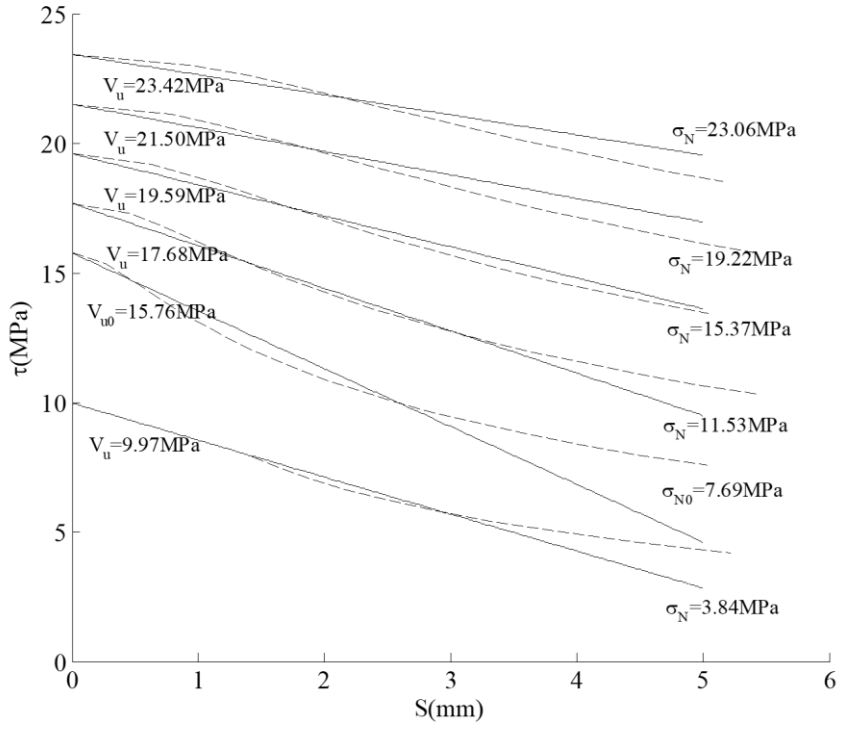

Fig. 37 Shear friction properties derived from stress-strain relationship (dashed lines) and approximation from approach 2 (solid lines) for 40MPa concrete

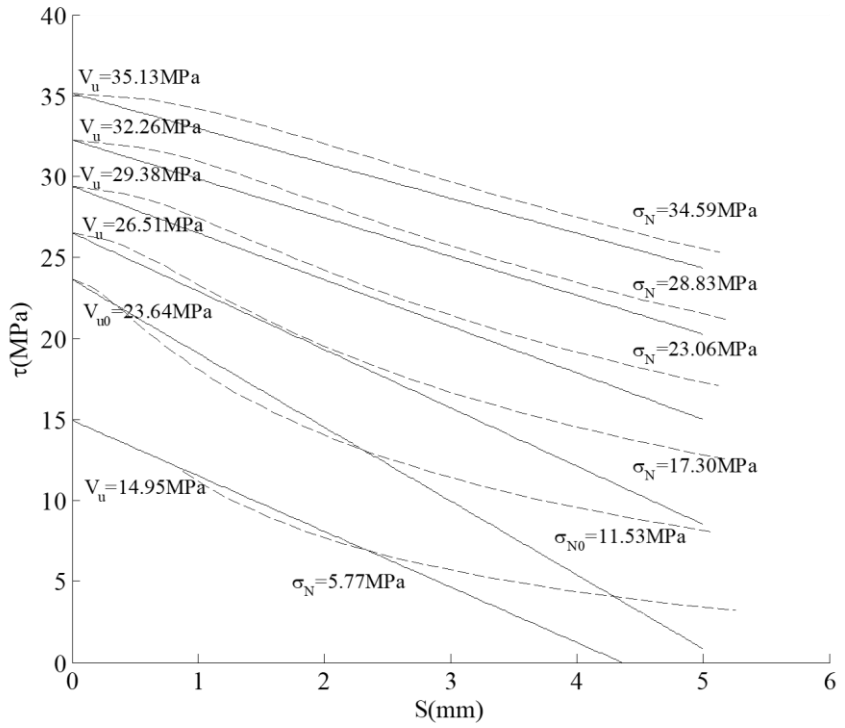

Fig. 38 Shear friction properties derived from stress-strain relationship (dashed lines) and approximation from approach 2 (solid lines) for 60MPa concrete

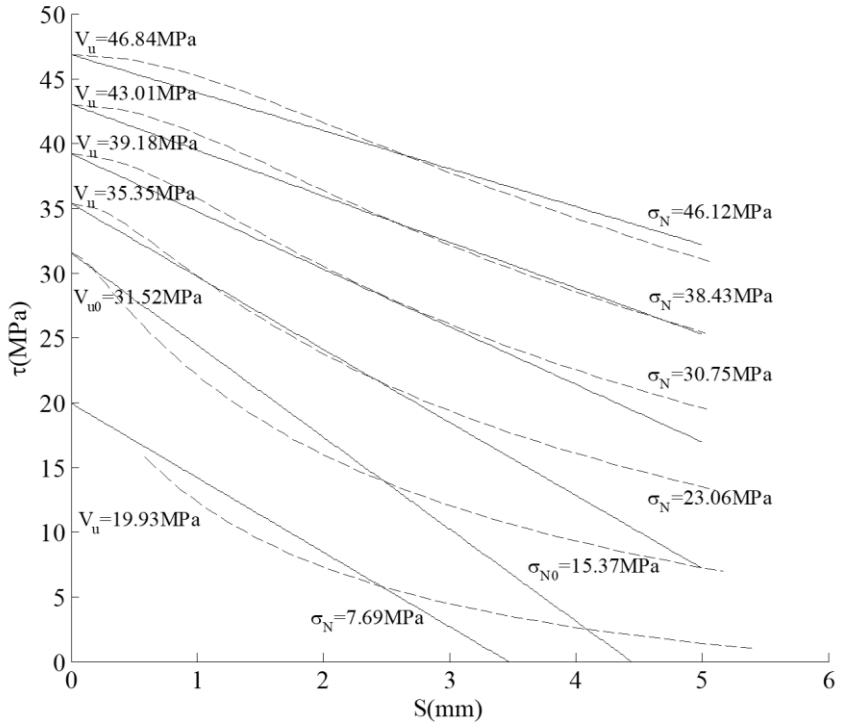

Fig. 39 Shear friction properties derived from stress-strain relationship (dashed lines) and approximation from approach 2 (solid lines) for 80MPa concrete

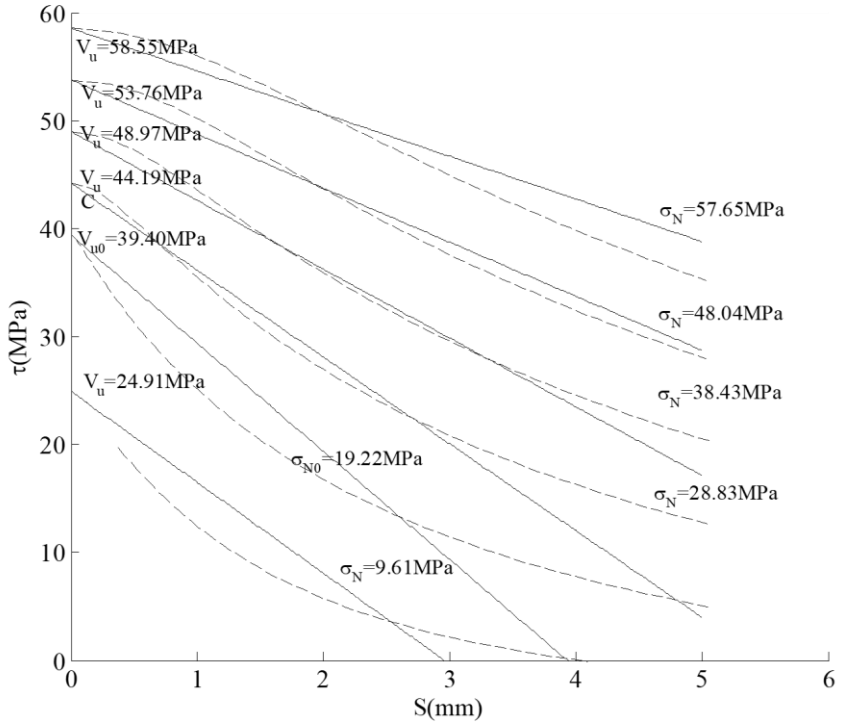

Fig. 40 Shear friction properties derived from stress-strain relationship (dashed lines) and approximation from approach 2 (solid lines) for 100MPa concrete

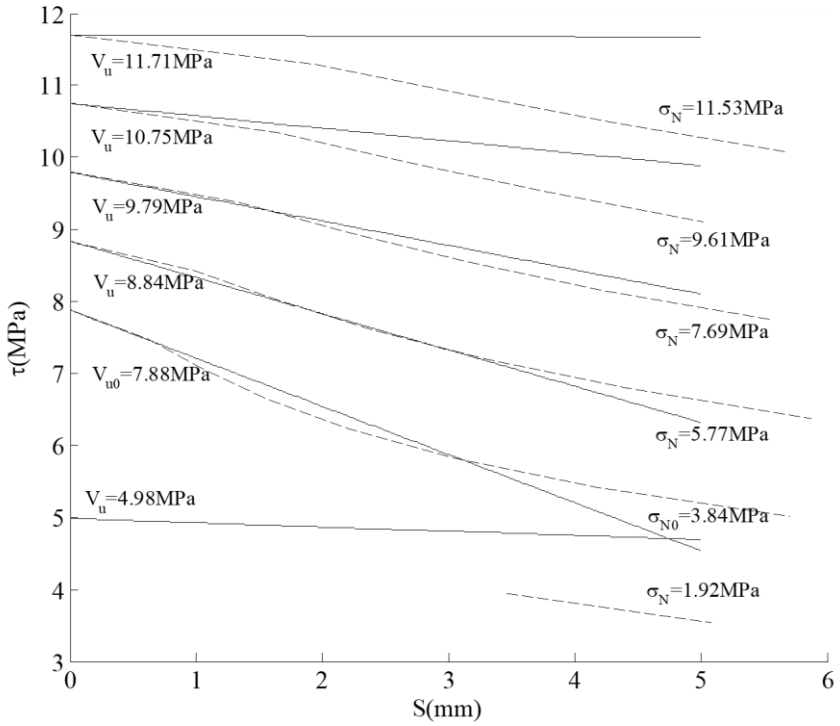

Fig. 41 Shear friction properties derived from stress-strain relationship (dashed lines) and approximation from approach 3 (solid lines) for 20MPa concrete

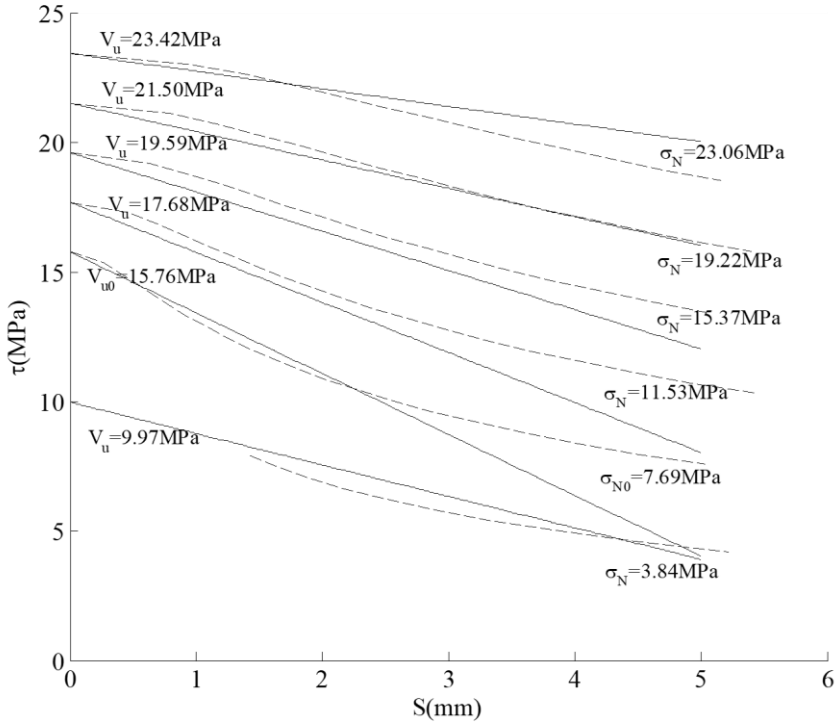

Fig. 42 Shear friction properties derived from stress-strain relationship (dashed lines) and approximation from approach 3 (solid lines) for 40MPa concrete

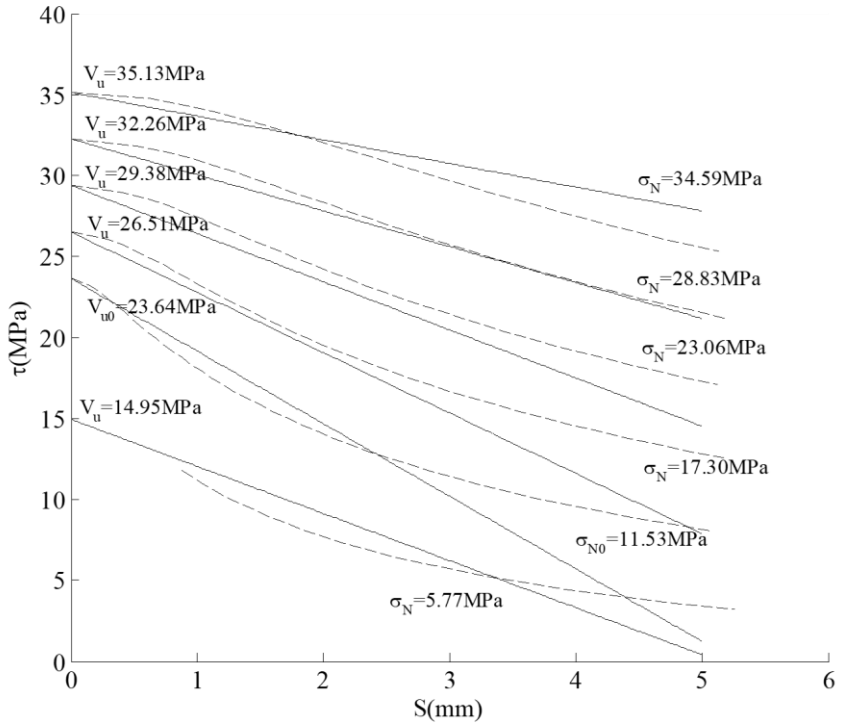

Fig. 43 Shear friction properties derived from stress-strain relationship (dashed lines) and approximation from approach 3 (solid lines) for 60MPa concrete

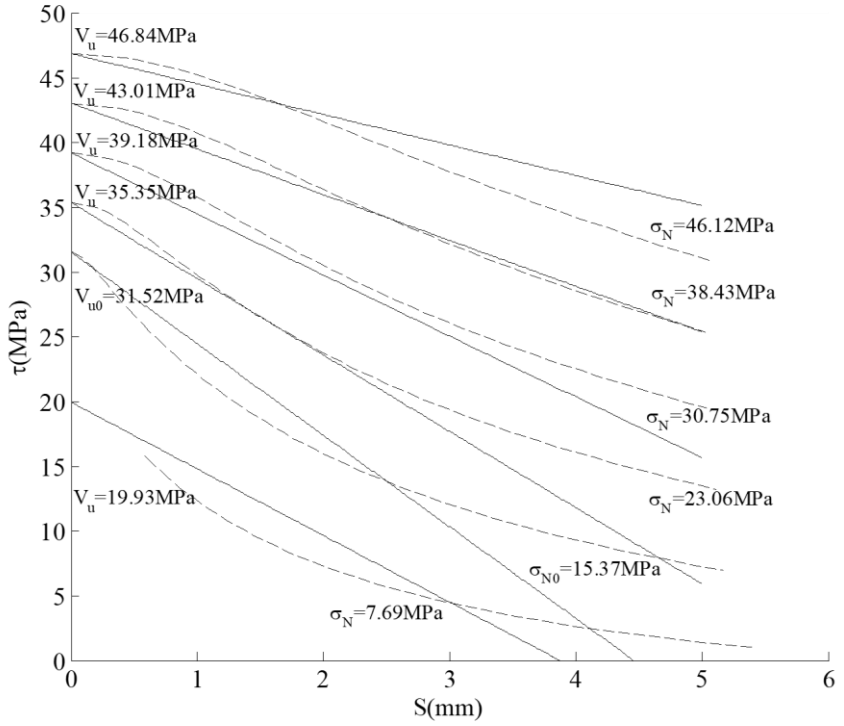

Fig. 44 Shear friction properties derived from stress-strain relationship (dashed lines) and approximation from approach 3 (solid lines) for 80MPa concrete

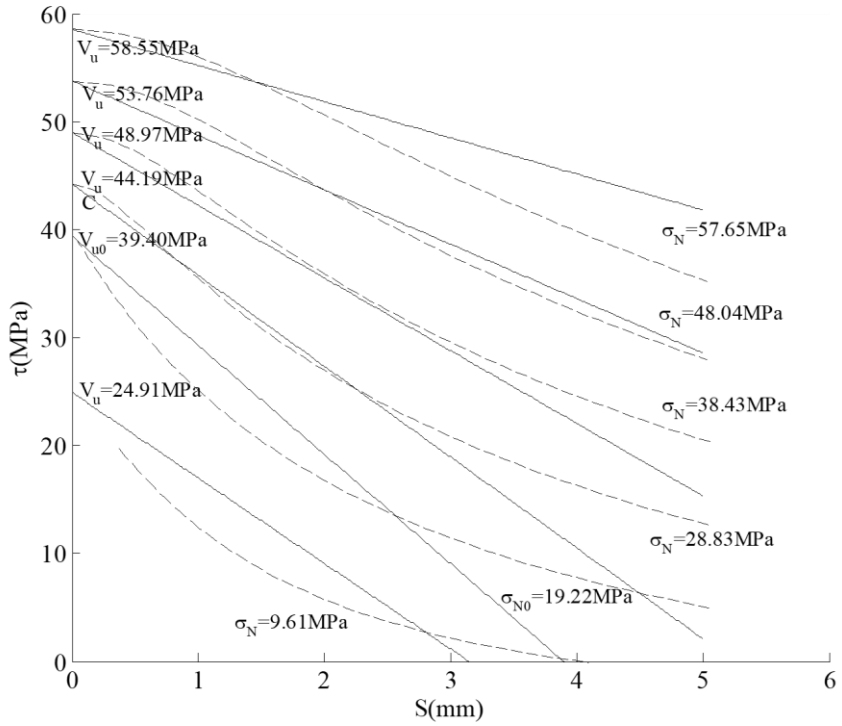

Fig. 45 Shear friction properties derived from stress-strain relationship (dashed lines) and approximation from approach 3 (solid lines) for 100MPa concrete

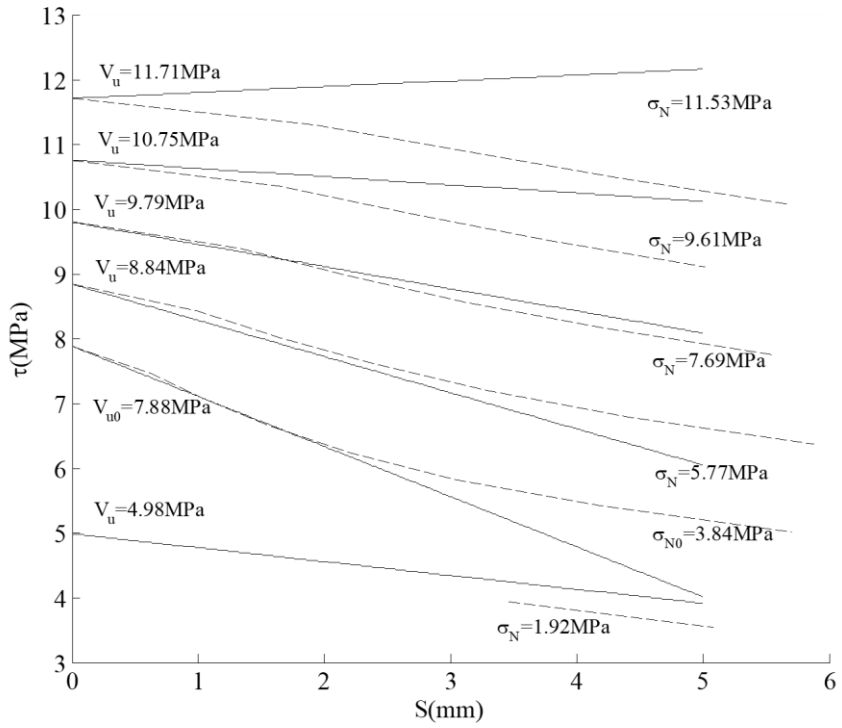

Fig. 46 Shear friction properties derived from stress-strain relationship (dashed lines) and approximation from approach 4 (solid lines) for 20MPa concrete

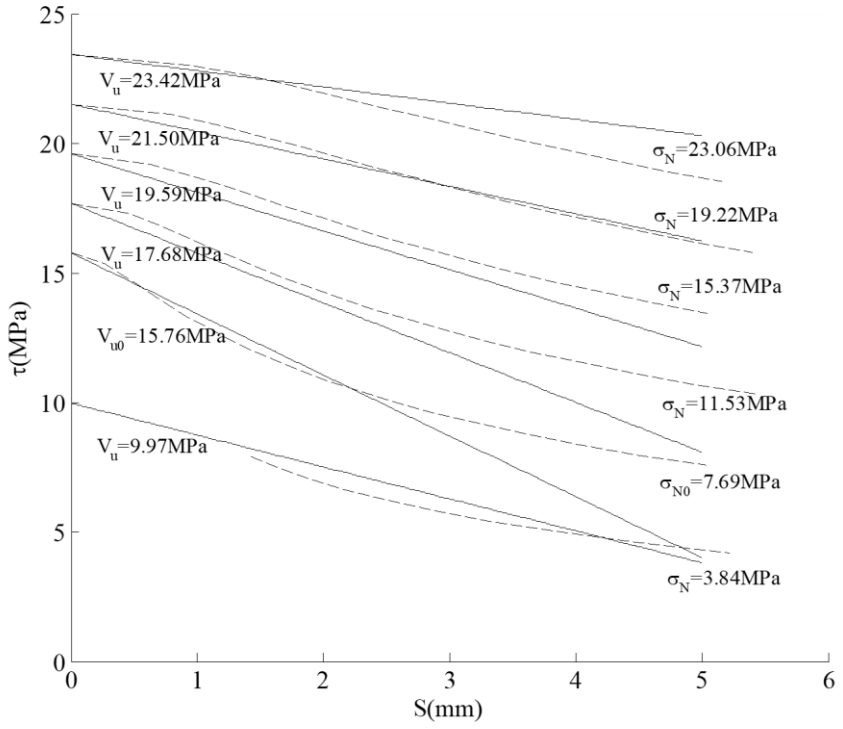

Fig. 47 Shear friction properties derived from stress-strain relationship (dashed lines) and approximation from approach 4 (solid lines) for 40MPa concrete

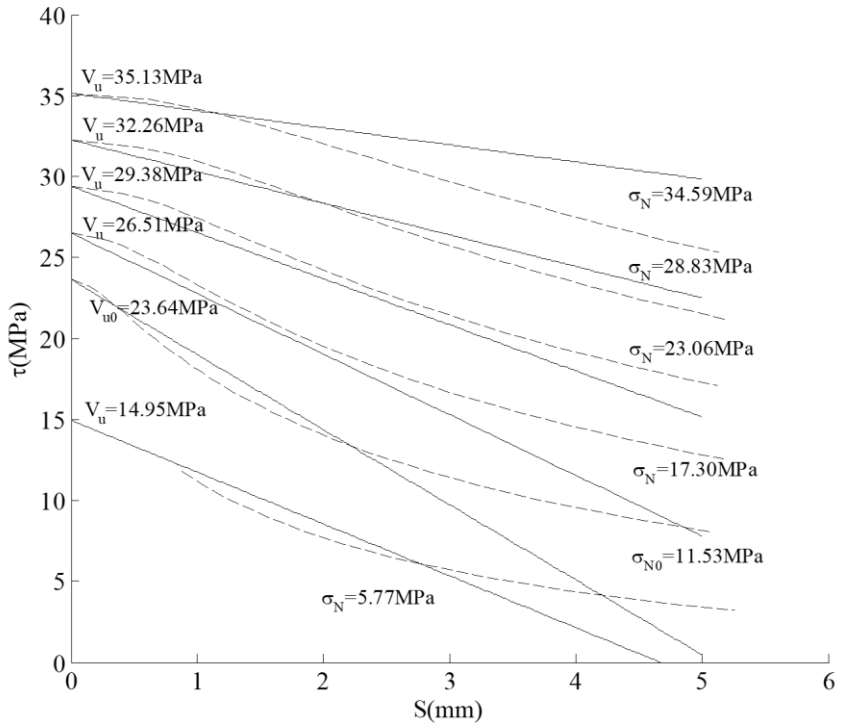

Fig. 48 Shear friction properties derived from stress-strain relationship (dashed lines) and approximation from approach 4 (solid lines) for 60MPa concrete

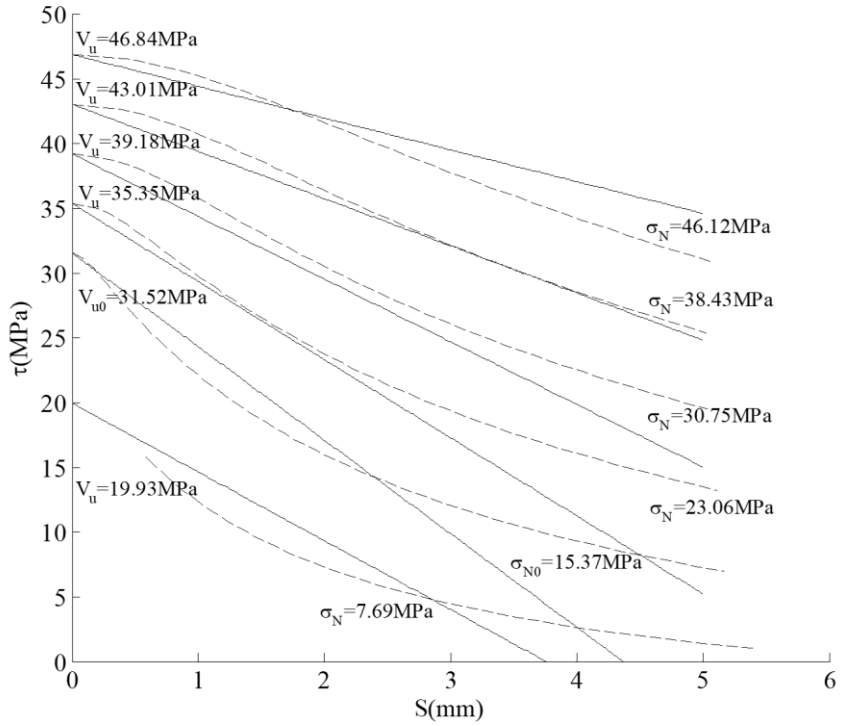

Fig. 49 Shear friction properties derived from stress-strain relationship (dashed lines) and approximation from approach 4 (solid lines) for 80MPa concrete

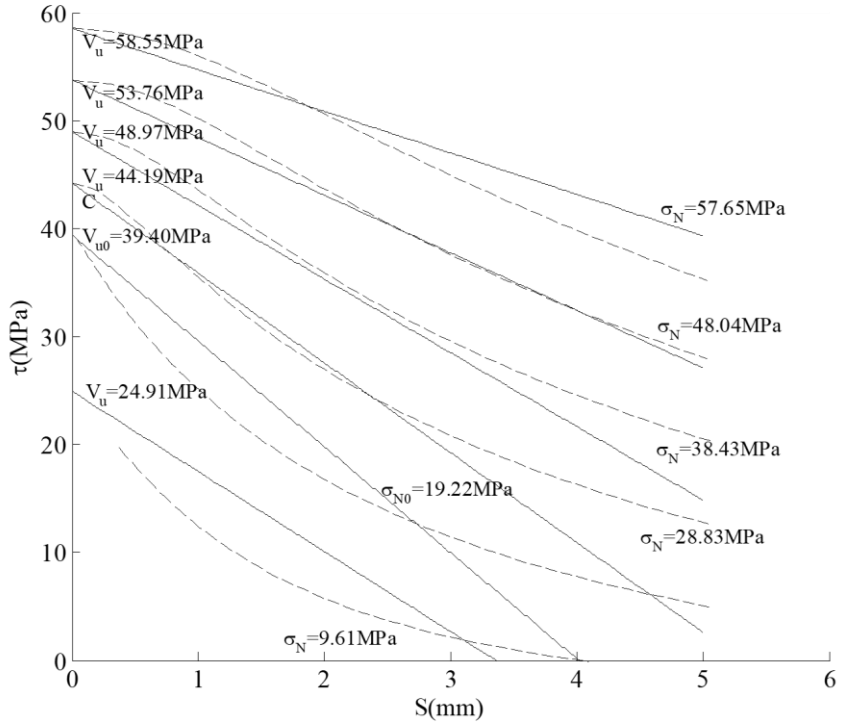

Fig. 50 Shear friction properties derived from stress-strain relationship (dashed lines) and approximation from approach 4 (solid lines) for 100MPa concrete

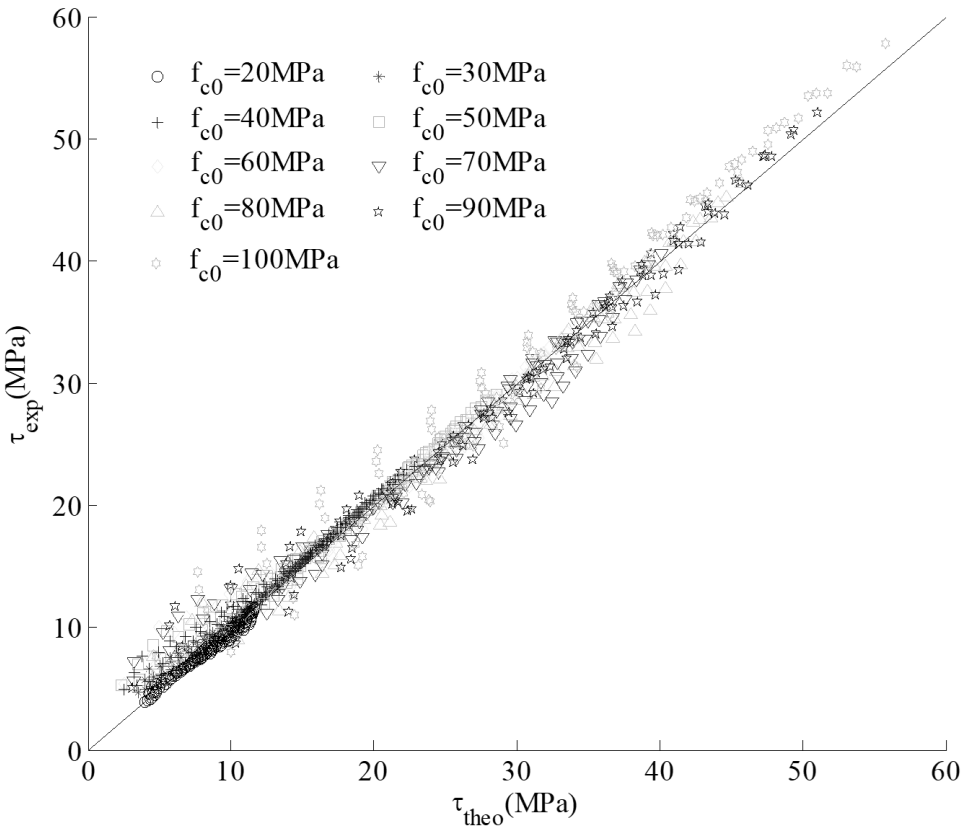

Fig. 51 Relationship between τ_{exp} from experimental data and τ_{theo} from method 1 for different unconfined concrete strengths f_{c0}

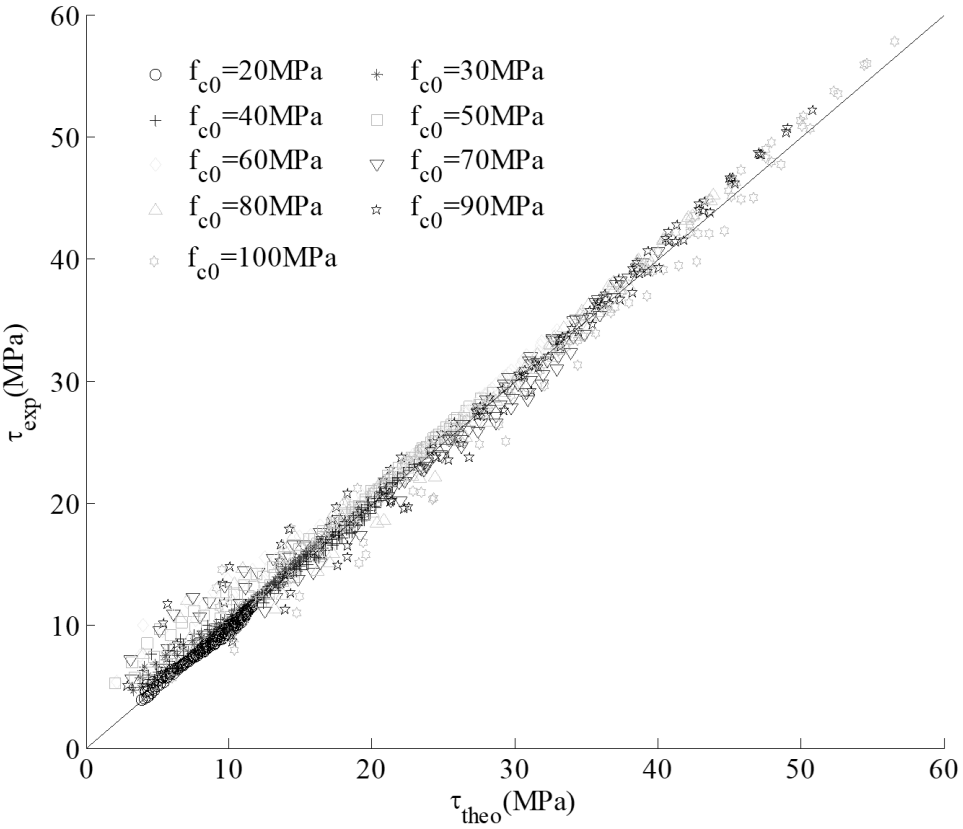

Fig. 52 Relationship between τ_{exp} from experimental data and τ_{theo} from method 2 for different unconfined concrete strengths f_{c0}

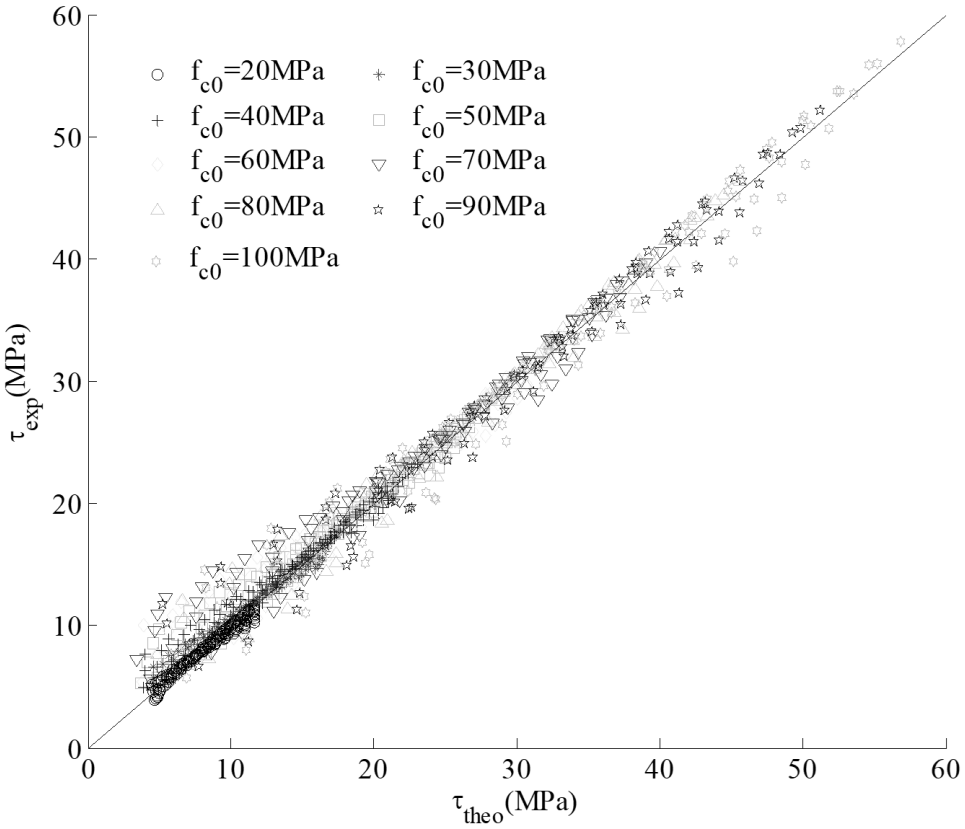

Fig. 53 Relationship between τ_{exp} from experimental data and τ_{theo} from method 3 for different unconfined concrete strengths f_{c0}

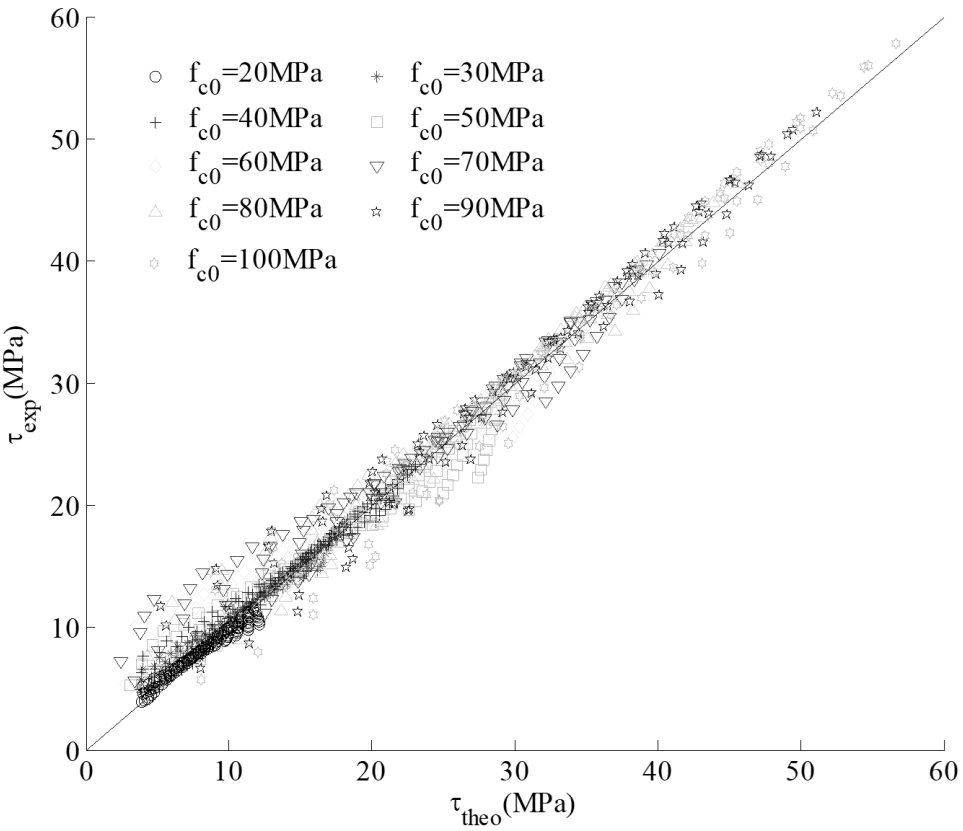

Fig. 54 Relationship between τ_{exp} from experimental data and τ_{theo} from method 4 for different unconfined concrete strengths f_{c0}

Construction of the Stress-Strain Relationships of Actively Confined Cylinders

In this report, the shear friction properties have been extracted from the stress-strain relationships of the actively confined cylinder tests and are simulated by four approaches in section 6. In this section, based on these approximations from the four approaches, the stress-strain relationships of the actively confined concrete will be constructed in this section to check the accuracy of these approximations.

Consider a standard specimen (specimen height L_{prsm} = 200 mm) with a concrete strength f_{c0} and lateral confining stress σ_{con}. The shear friction properties derived from actively confined cylinder tests such as the solid lines in Figs. 31 to 50 are shown in Fig. 55. It is worth noting that sliding is assumed to occur after the peak point of the stress/strain relationship such as point D in Fig. 8; the shear friction properties are dealing with the stage after the

commencement of sliding so that only the falling branches will be derived in this section. Let us consider the stress/strain relationship in Fig. 56 which will be derived from the approximations of the shear friction properties. The ascending branch OA of the stress-strain relationship will be obtained from Eq. (31) as this is a material property. The following procedure to find points on the falling branch will be described.

1. The shear stress V_u at the first point A in Fig. 55 is obtained from Eq. (46); this is also the shear stress of the peak point A in Fig. 56 where the axial stress and strain equal f_{cc} and ε_{cc} respectively and which are obtained from Eqs. (34) and (35) respectively.
2. The slip S_1 of the next point B in Fig. 55 can be fixed at any arbitrary positive value. The axial stress at point B which is generally below that at A due to sliding is guessed and is referred to as $\sigma_{ax1\text{-}g}$. The shear stress τ_1 at point B can be derived from mechanics that is from Eq. (24) by substituting in both this guessed axial stress $\sigma_{ax1\text{-}g}$ and lateral confining stress σ_{con}.
3. Next the shear capacity τ_m at point B in Fig. 55 is now derived from the material properties; this is the material resistance to the applied guessed axial stress $\sigma_{ax1\text{-}g}$. Hence the shear friction material properties will be applied to quantify τ_m which can be obtained from the approximations; that is substituting Eqs. (47), (48), (49), (50), (51) and (54) and V_u obtained from Eq. (46) into Eq. (58). This requires the unconfined concrete strength f_{c0} and also the normal stress σ_{N1} at point B in Fig. 55 which is derived as follows.
4. The normal stress σ_{N1} at point B in Fig. 55 will be obtained by substituting the guessed axial stress $\sigma_{ax1\text{-}g}$ and lateral confining stress σ_{con} into Eq. (23). This is the normal stress when the guessed axial stress $\sigma_{ax1\text{-}g}$ is imposed.
5. The normal stress σ_{N1} and unconfined concrete strength f_{c0} can be substituted into Eqs. (46), (47), (48), (49), (50), (51), (54) and (58) to derive the shear capacity τ_m from shear friction material properties.
6. If the shear capacity τ_m derived from Step 5 is equal to the shear stress τ_1 derived from Step 2, the axial stress σ_{ax1} at point B in Fig. 56 can be taken as the guessed axial stress $\sigma_{ax1\text{-}g}$.
7. If the shear stress τ_1 derived from Step 2 is not equal to the shear capacity τ_m derived from Step 5, then the guessed axial stress $\sigma_{ax1\text{-}g}$ in Step 2 will be changed. This procedure will be iterated until the shear capacity τ_m derived from Step 5 is equal to

the shear stress τ_1 derived from Step 2. If a solution cannot be found, this simply means that there is not enough capacity to resist the applied loads.

8. The axial stress σ_{ax1} at point B in Fig. 56 can be taken as the guessed axial stress $\sigma_{ax1\text{-}g}$ after the end of the iteration Steps 2 to 7. At this point, the axial strain ε_{ax1} can be obtained from Eq. (28) as the slip S is known and this is illustrated in Fig. 56.

The above procedure can be duplicated to derive the axial stress σ_{ax} and strain ε_{ax} for any point on the descending branch such as point C in Fig. 56. In this report, the interval of the imposed slips S of these points within a range of $0 \leq S \leq 5$ (mm) is set as 0.01 mm.

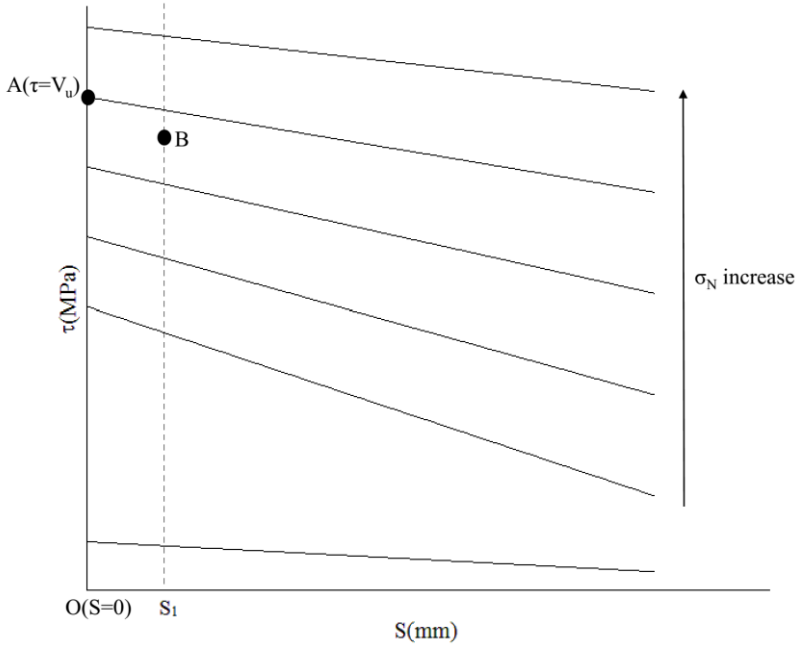

Fig. 55 The linear approximation of the shear friction properties

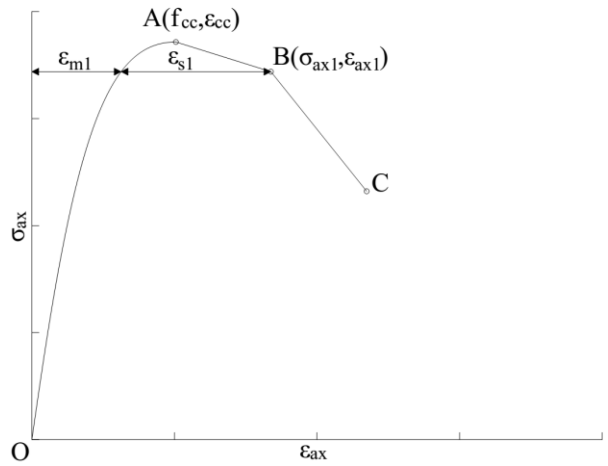

Fig. 56 Stress-strain relationship of actively confined concrete columns derived from approximation of the shear friction properties

Comparison of the Stress-Strain Relationships Derived from the Closed Form Solutions and Cylinder Tests

The procedure to construct the stress-strain relationship of actively confined concrete columns based on the approximations of the shear friction properties in Section 6 has been described. In Figs 57 to 76, are shown comparisons between the experimental stress/strain relationships (solid lines as shown) and the constructed stress/strain relationships (dashed lines as shown) based on the approximations; the approximations from the four approaches in Section 6 were derived by substituting Eqs. (47), (48), (49), (50), (51) and (54) and V_u obtained from Eq. (46) into Eq. (58). Details extracted from these comparisons are shown as follows:

- The simulated standard specimens with specimen heights L_{prsm} = 200 mm cover a range of: $0 \leq S \leq 5$ (mm), $0 \leq \sigma_{con}/f_{c0} \leq 0.15$ and $20 \leq f_{c0} \leq 100$ (MPa). It can be seen for this range of slip, the axial strain ε_{ax} is large enough or the axial stress σ_{ax} is small enough at S = 5 mm in Figs 57 to 76 such that nearly overall shapes of the stress/strain relationships are given. Furthermore, as the mechanism of the derivation of the shear friction properties has been described in this report, it is easy to extend either the range of the slip S, or lateral confining stress σ_{con}, or unconfined concrete strength f_{c0} for shear friction properties.

- It should be noted that for 20MPa concrete in Figs. 67 and 72, the predictions can overestimate the axial stress for $\sigma_{con} = 0.15f_{c0}$. However, this may not be important as the usage of 20MPa concrete is decreasing in the last few decades (Kurniawan 2011).
- Most of the stress-strain relationships derived from the approximations give conservative result compared with that derived from experimental data.
- In approach 4, the shear stress $\tau_{2.5}$ from Eq. (54) at $S = 2.5$ mm will be obtained from two different equations when the unconfined concrete strength $f_{c0} \geq 50$MPa and $f_{c0} <$ 50MPa. To check the difference of these equations near the bound point $f_{c0} = 50$MPa, the stress-strain relationships of actively confined concrete are plotted in Fig. 77; these relationships are derived from experimental data (solid line) and derived based on shear friction properties obtained from approach 4 for $f_{c0} = 50$MPa (dotted line) and $f_{c0} = 49.9$MPa (dashed line). It can be seen that for high lateral confining stresses at $\sigma_{con} = 0.15f_{c0}$ the difference is large but for the remaining confinements the difference is relatively small.

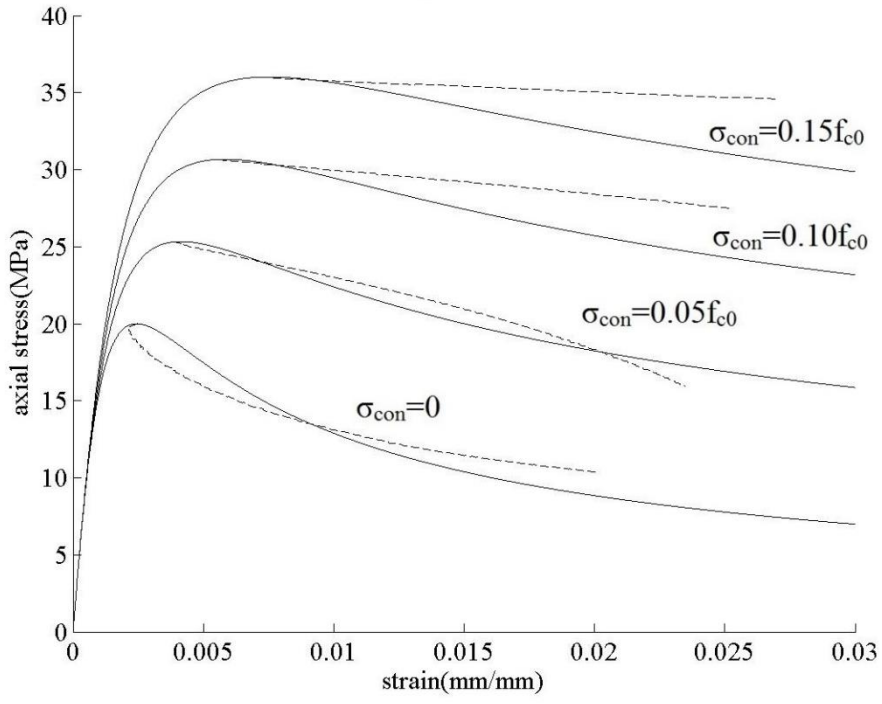

Fig. 57 The stress-strain relationship of actively confined concrete derived from experimental data (solid line) and that derived from shear friction properties from approach 1 (dashed line) when $f_{c0} = 20$MPa

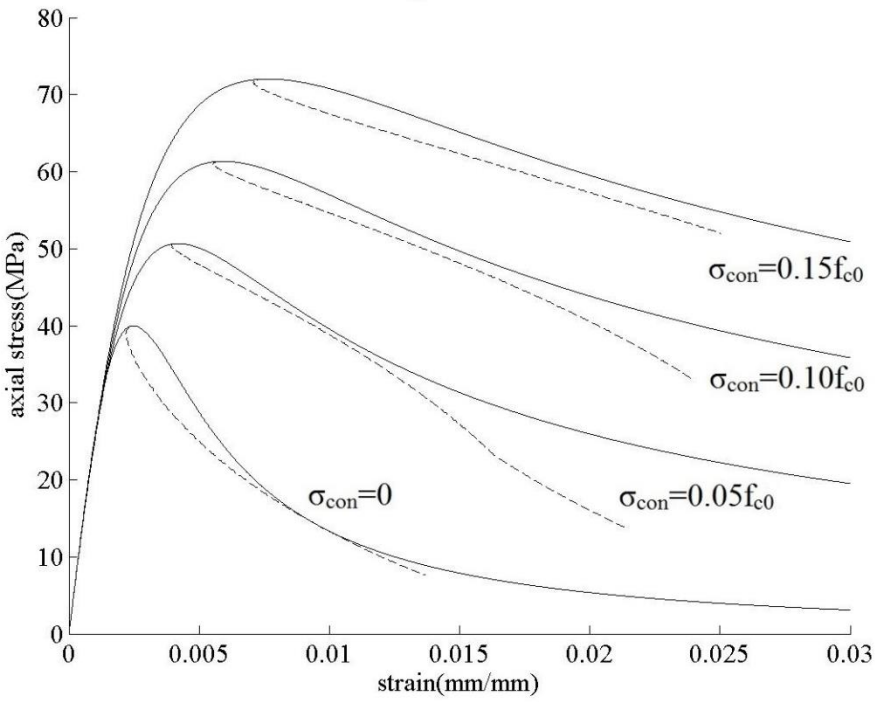

Fig. 58 The stress-strain relationship of actively confined concrete derived from experimental data (solid line) and that derived from shear friction properties from approach 1 (dashed line) when f_{c0} = 40MPa

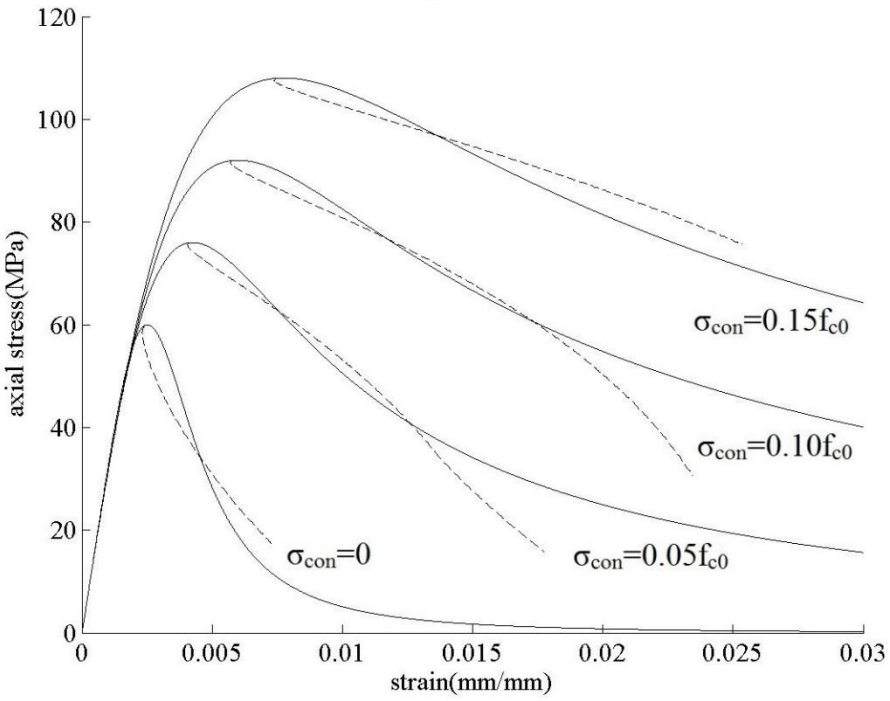

Fig. 59 The stress-strain relationship of actively confined concrete derived from experimental data (solid line) and that derived from shear friction properties from approach 1 (dashed line) when f_{c0} = 60MPa

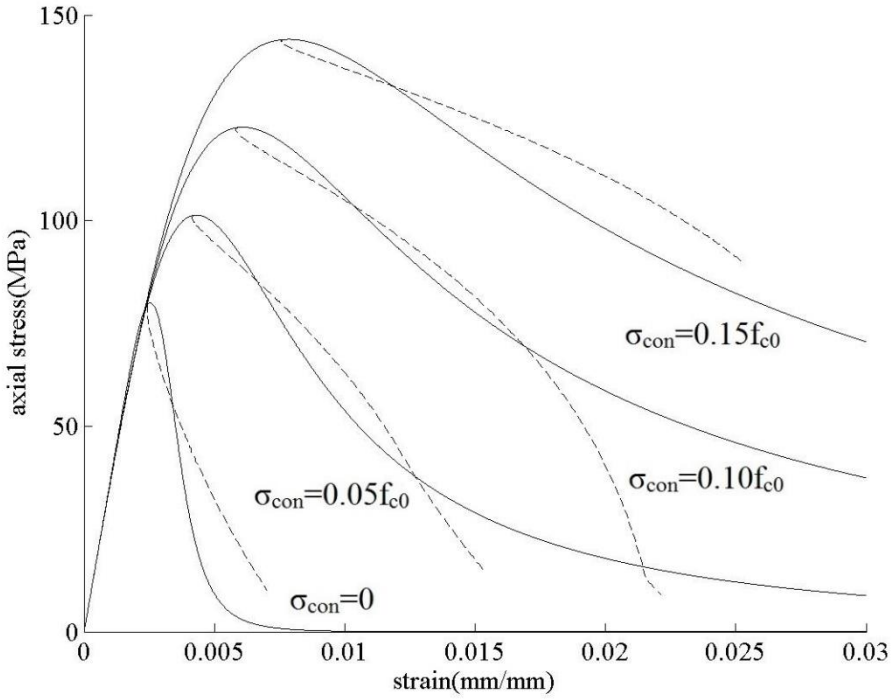

Fig. 60 The stress-strain relationship of actively confined concrete derived from experimental data (solid line) and that derived from shear friction properties from approach 1 (dashed line) when f_{c0} = 80MPa

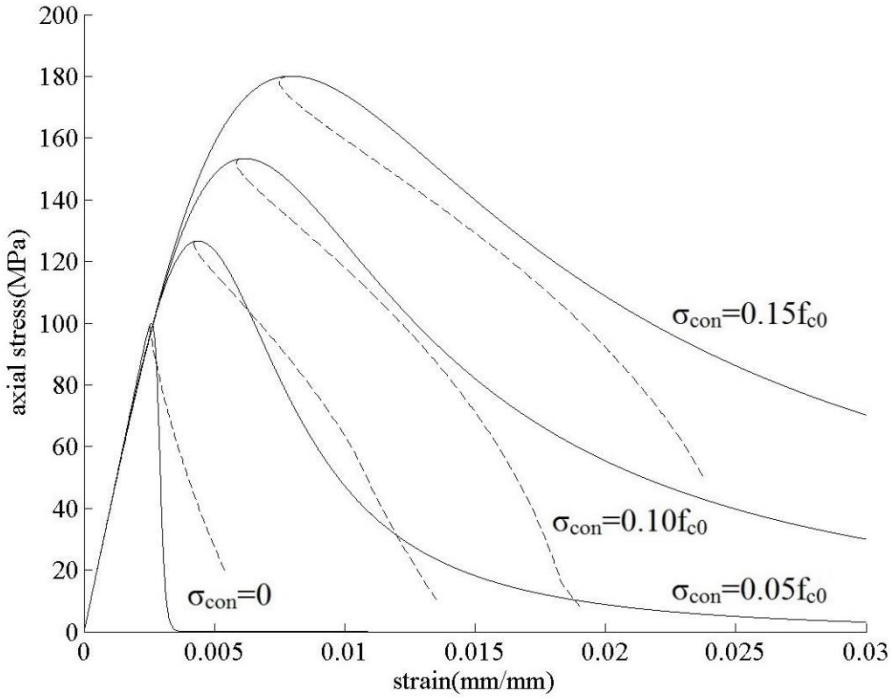

Fig. 61 The stress-strain relationship of actively confined concrete derived from experimental data (solid line) and that derived from shear friction properties from approach 1 (dashed line) when f_{c0} = 100MPa

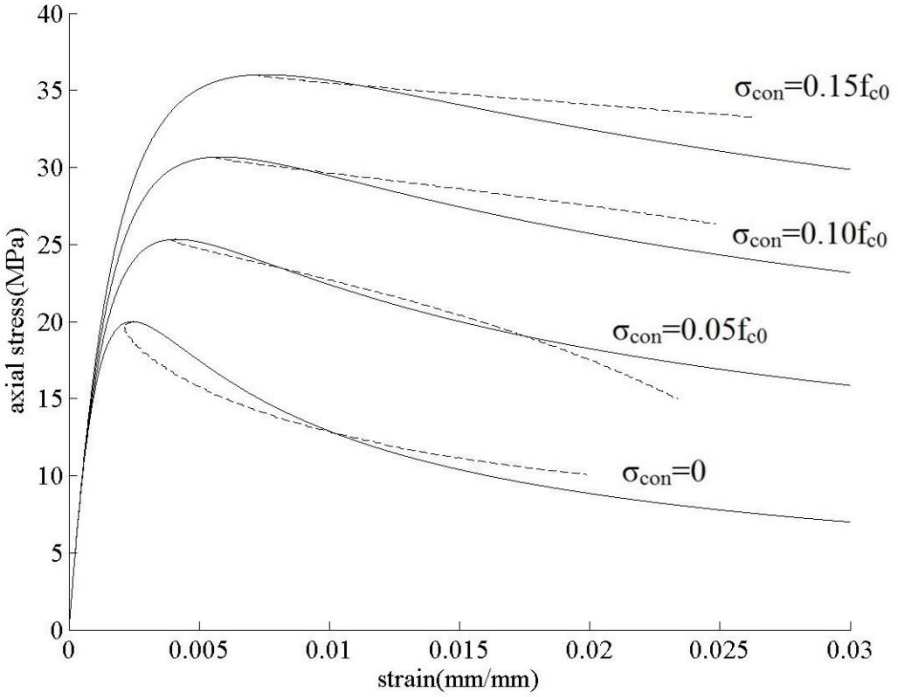

Fig. 62 The stress-strain relationship of actively confined concrete derived from experimental data (solid line) and that derived from shear friction properties from approach 2 (dashed line) when f_{c0} = 20MPa

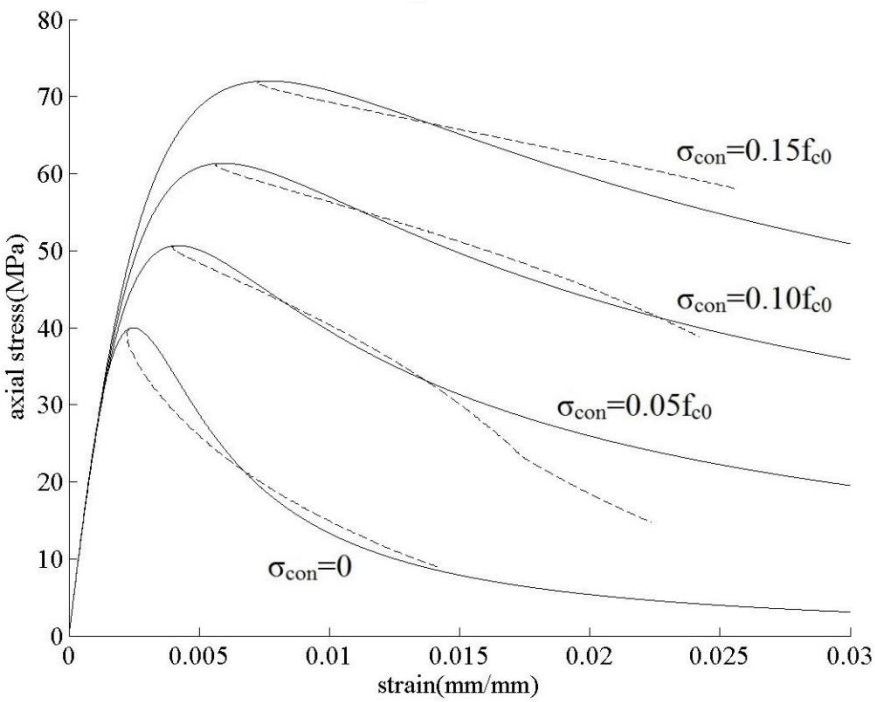

Fig. 63 The stress-strain relationship of actively confined concrete derived from experimental data (solid line) and that derived from shear friction properties from approach 2 (dashed line) when f_{c0} = 40MPa

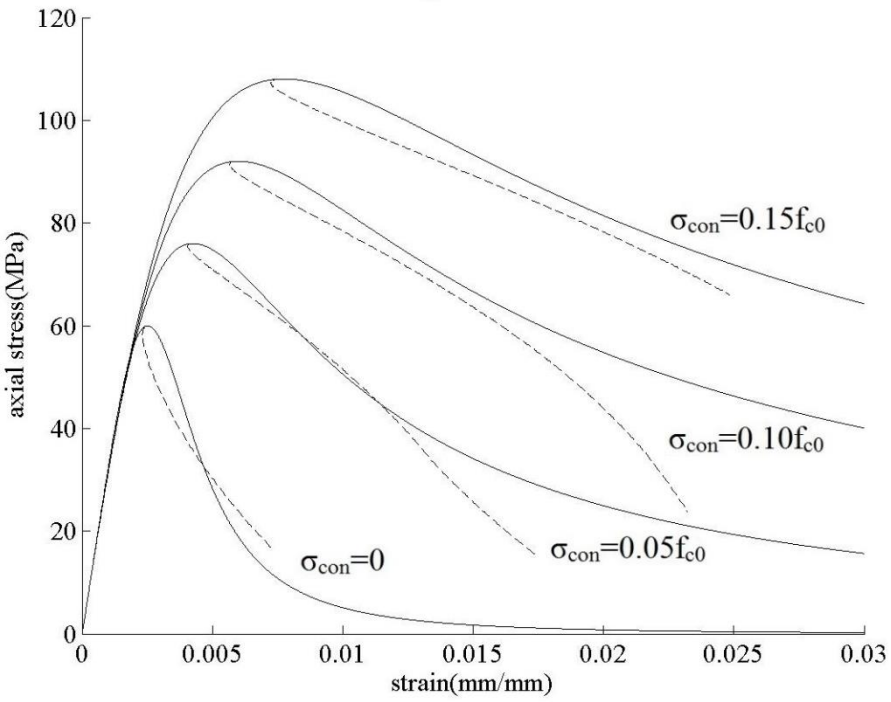

Fig. 64 The stress-strain relationship of actively confined concrete derived from experimental data (solid line) and that derived from shear friction properties from approach 2 (dashed line) when f_{c0} = 60MPa

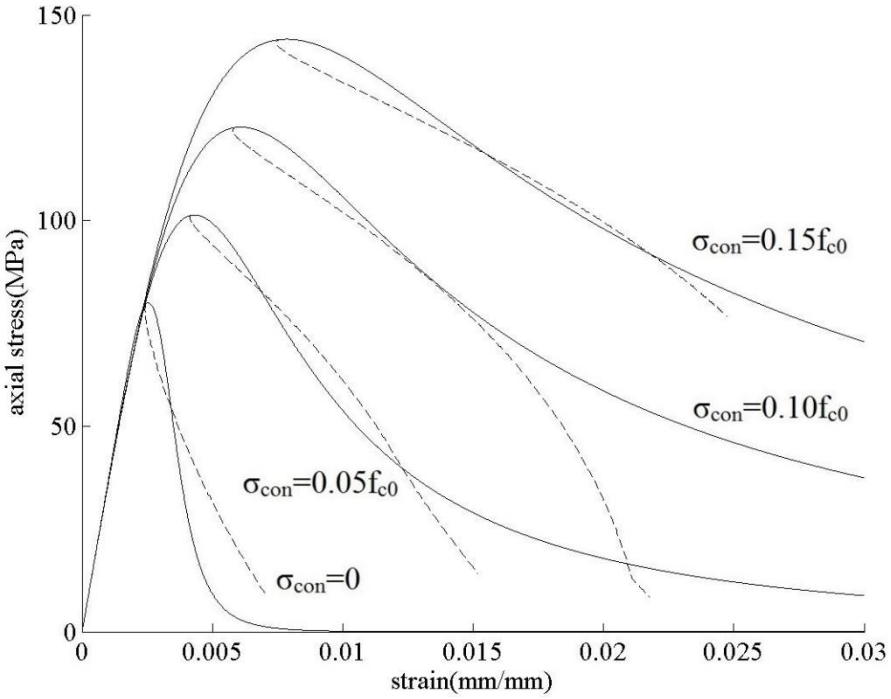

Fig. 65 The stress-strain relationship of actively confined concrete derived from experimental data (solid line) and that derived from shear friction properties from approach 2 (dashed line) when f_{c0} = 80MPa

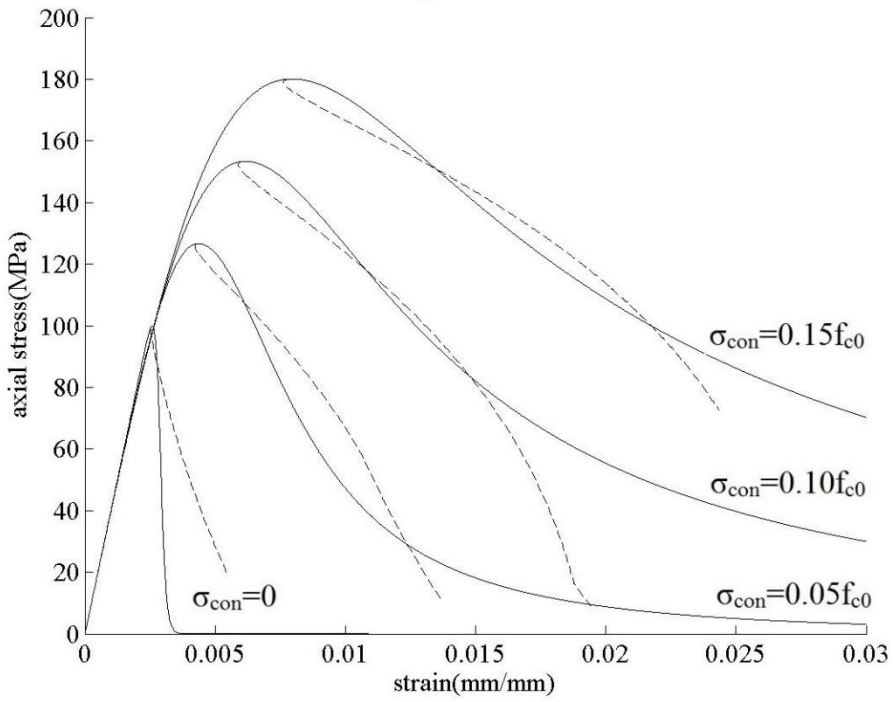

Fig. 66 The stress-strain relationship of actively confined concrete derived from experimental data (solid line) and that derived from shear friction properties from approach 2 (dashed line) when f_{c0} = 100MPa

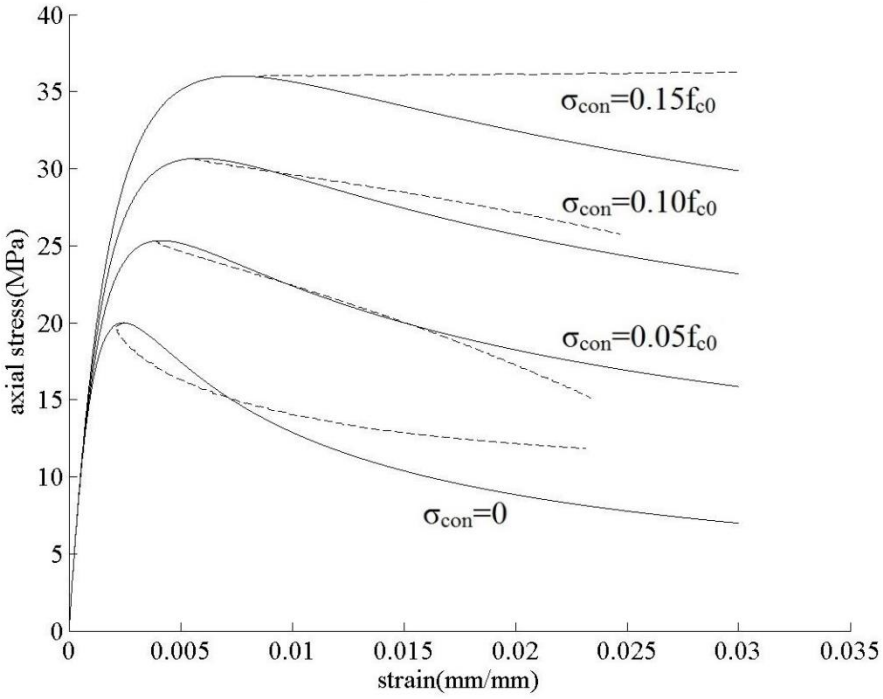

Fig. 67 The stress-strain relationship of actively confined concrete derived from experimental data (solid line) and that derived from shear friction properties from approach 3 (dashed line) when f_{c0} = 20MPa

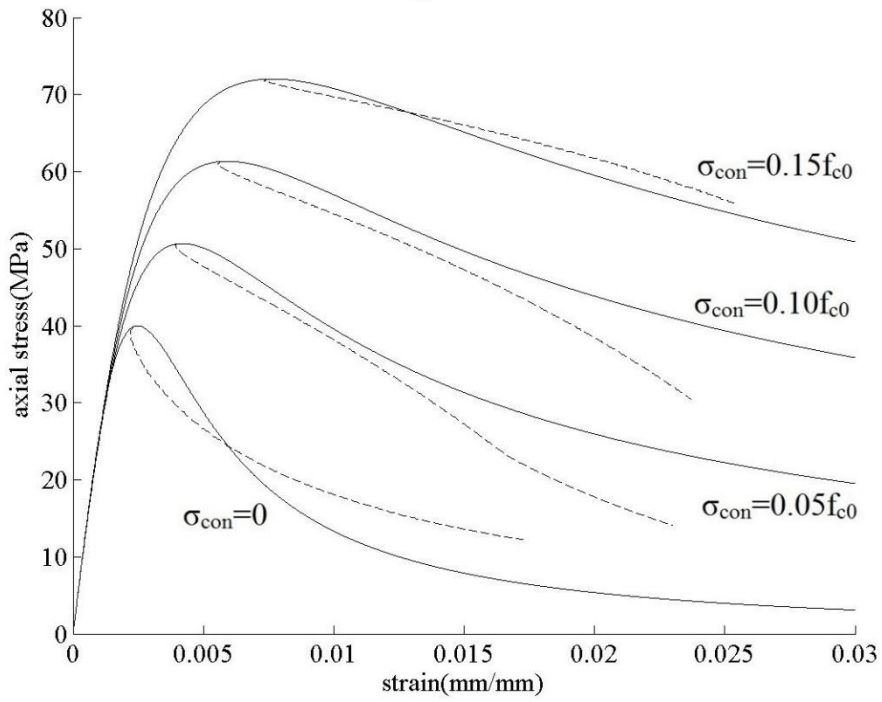

Fig. 68 The stress-strain relationship of actively confined concrete derived from experimental data (solid line) and that derived from shear friction properties from approach 3 (dashed line) when f_{c0} = 40MPa

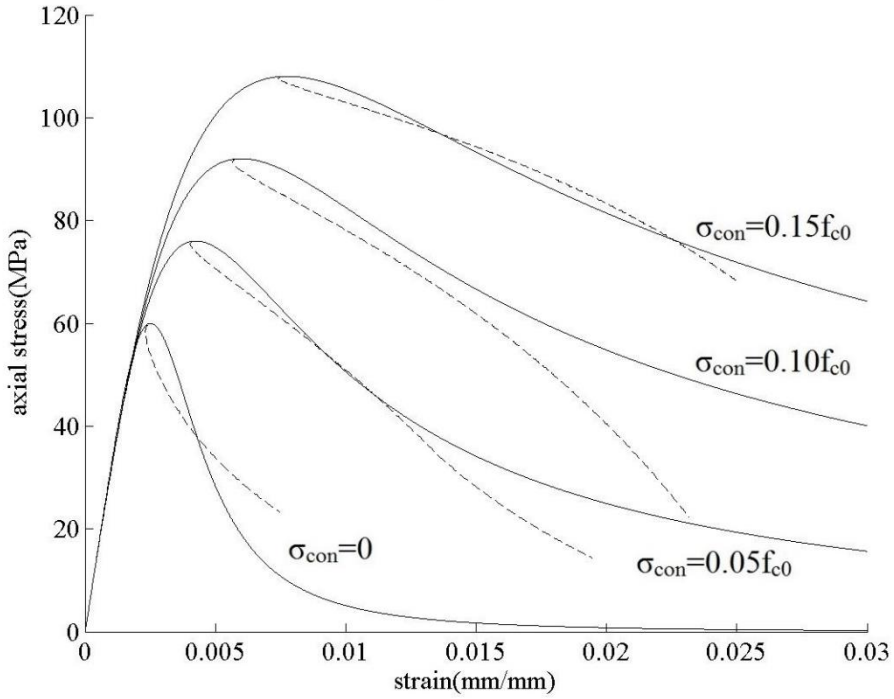

Fig. 69 The stress-strain relationship of actively confined concrete derived from experimental data (solid line) and that derived from shear friction properties from approach 3 (dashed line) when f_{c0} = 60MPa

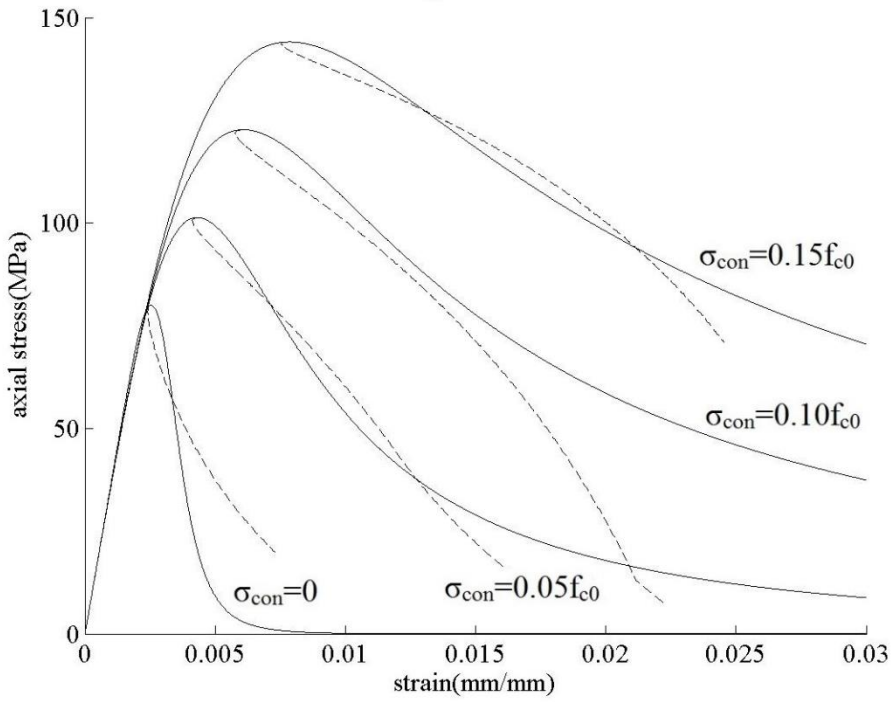

Fig. 70 The stress-strain relationship of actively confined concrete derived from experimental data (solid line) and that derived from shear friction properties from approach 3 (dashed line) when f_{c0} = 80MPa

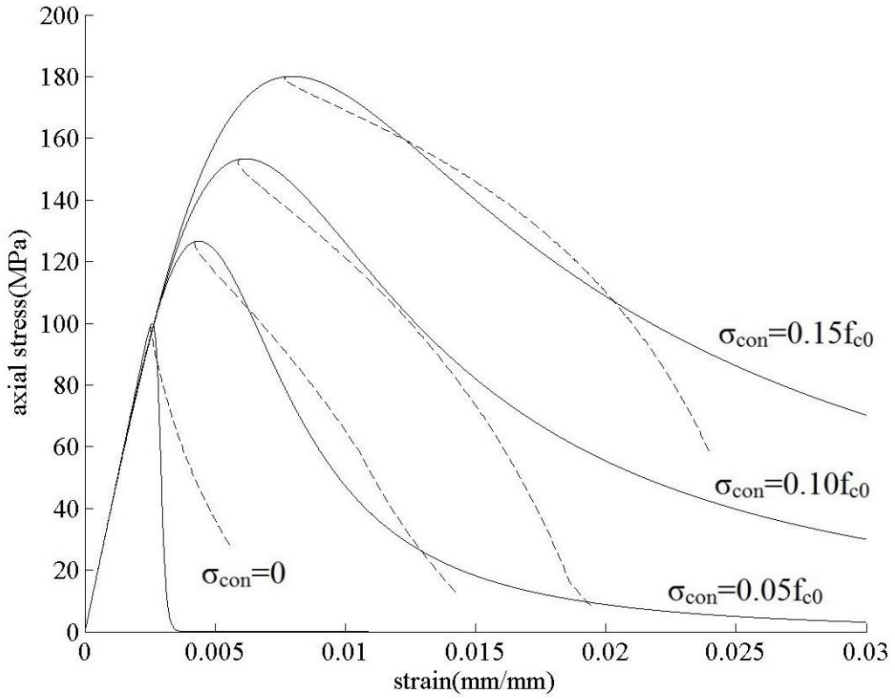

Fig. 71 The stress-strain relationship of actively confined concrete derived from experimental data (solid line) and that derived from shear friction properties from approach 3 (dashed line) when f_{c0} = 100MPa

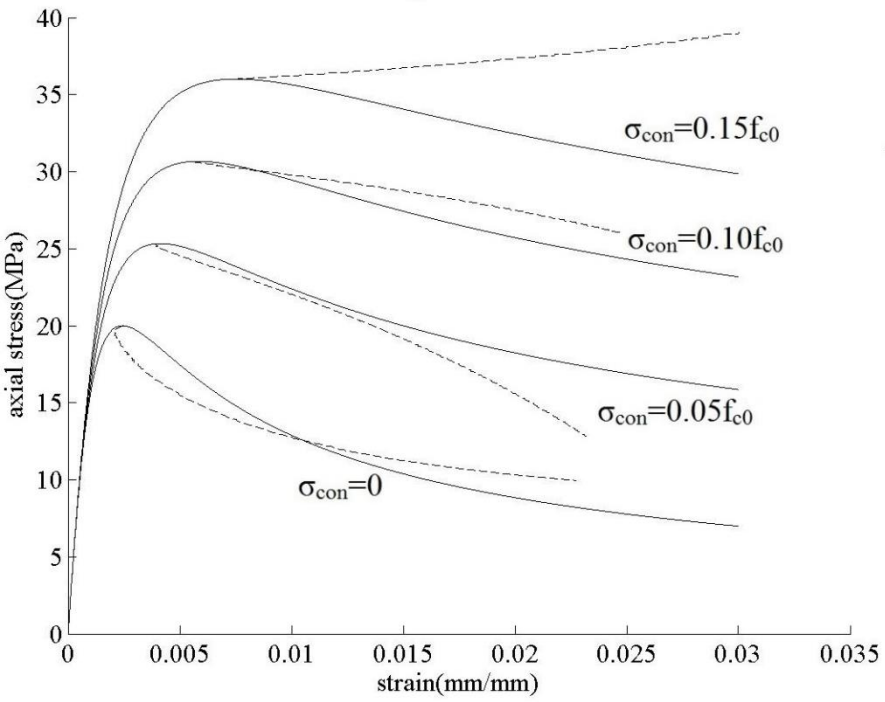

Fig. 72 The stress-strain relationship of actively confined concrete derived from experimental data (solid line) and that derived from shear friction properties from approach 4 (dashed line) when f_{c0} = 20MPa

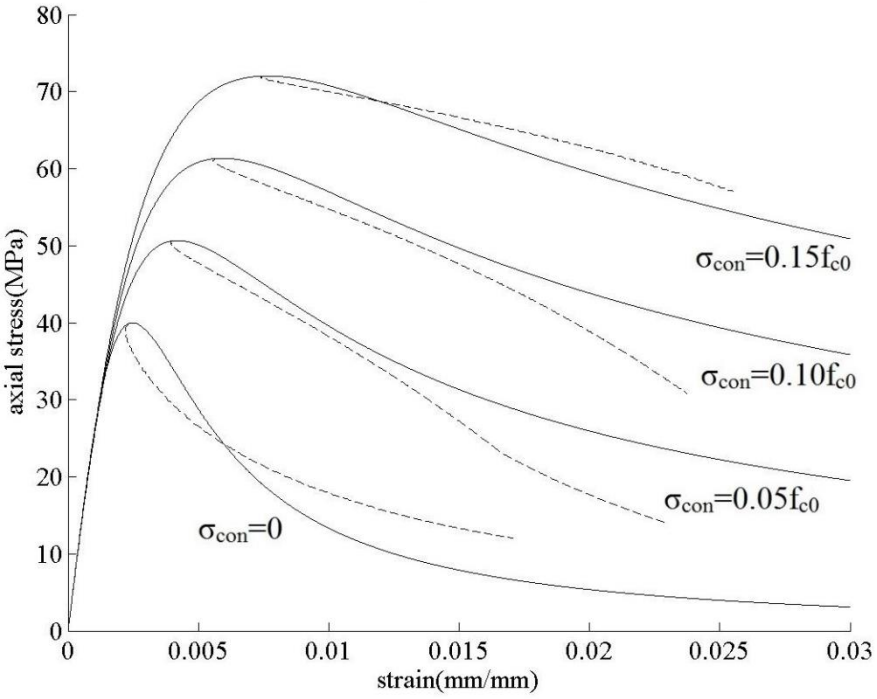

Fig. 73 The stress-strain relationship of actively confined concrete derived from experimental data (solid line) and that derived from shear friction properties from approach 4 (dashed line) when f_{c0} = 40MPa

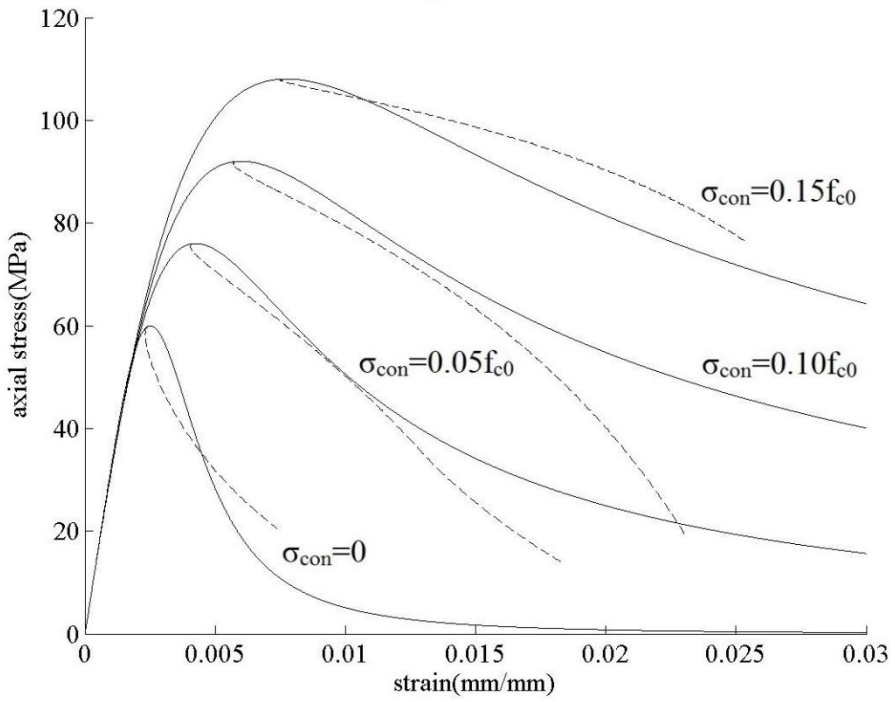

Fig. 74 The stress-strain relationship of actively confined concrete derived from experimental data (solid line) and that derived from shear friction properties from approach 4 (dashed line) when f_{c0} = 60MPa

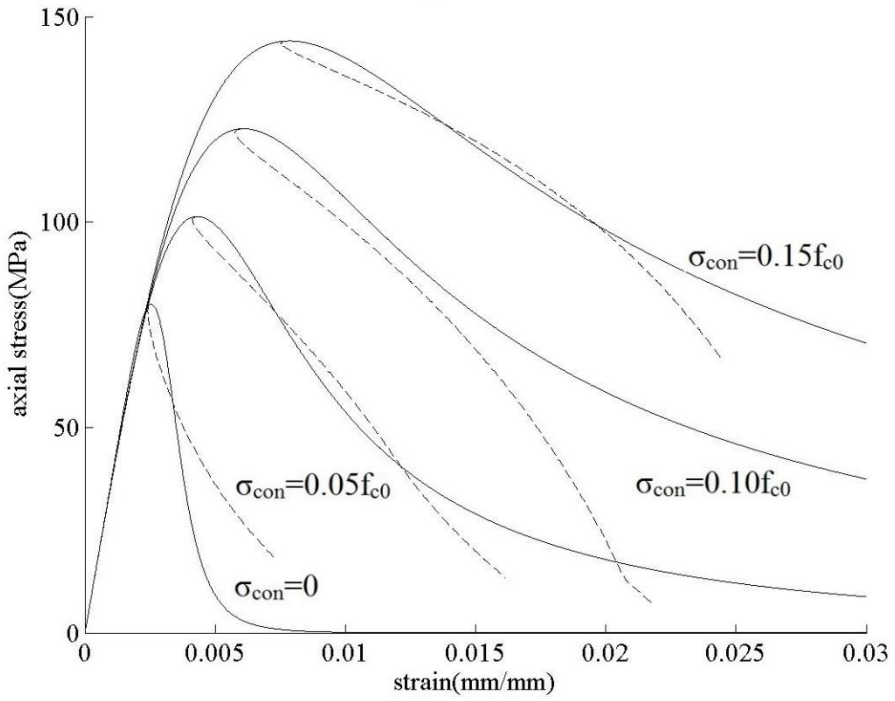

Fig. 75 The stress-strain relationship of actively confined concrete derived from experimental data (solid line) and that derived from shear friction properties from approach 4 (dashed line) when f_{c0} = 80MPa

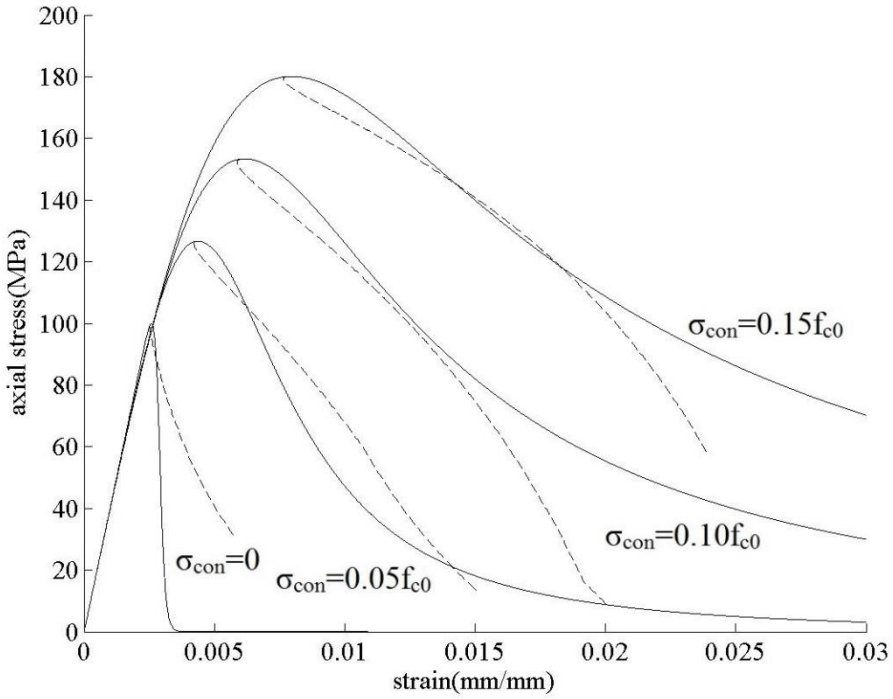

Fig. 76 The stress-strain relationship of actively confined concrete derived from experimental data (solid line) and that derived from shear friction properties from approach 4 (dashed line) when f_{c0} = 100MPa

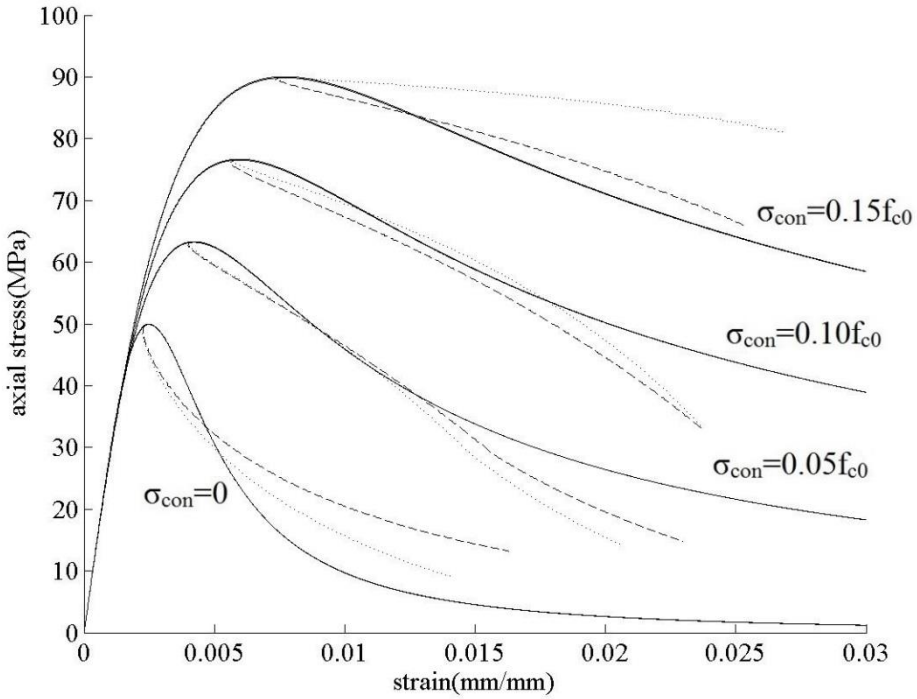

Fig. 77 The stress-strain relationship of actively confined concrete derived from experimental data (solid line) and that derived from shear friction properties from approach 4 when f_{c0} = 50MPa (dotted line) and f_{c0} = 49.9MPa (dashed line)

Conclusion

It is shown how the shear friction properties are derived primarily from simple actively confined cylinder compression tests; where there are gaps in the results they are then obtained from the results from relatively expensive shear-sliding tests. For design purpose, these shear friction properties are simulated by approximations which defines that, for a specific unconfined concrete strength f_{c0} and confining stress normal to the shear failure plane σ_N, the shear stress along the shear failure plane τ is a function of the slip S. These approximations can simulate the shear friction properties derived from actively confined cylinder tests well and are applied inversely to construct the stress-strain relationships of actively confined concrete with good correlation.

Notation

A_{in} = area of confined concrete
A_{sl} = area of sliding plane
C_l = confining force
C_{cir} = confining force of circular-section column
C_{rec} = confining force of rectangular-section column
C_{sq} = confining force of square-section column
D_0 = diameter of circular column, side length of square prism or width of rectangular prism
D_{02} = depth of a rectangular-section prism
E_c = elastic modulus of concrete
f_{c0} = peak strength of unconfined concrete from cylinder tests
$f_{c0\text{-}cube}$ = peak strength of unconfined concrete from cube tests
f_{cc} = peak strength of actively confined concrete
h_{cr} = crack widening of sliding plane
L_{prsm} = height of specimen
N = resultant force normal to shear-sliding plane
P_{ax} = axial load applied to confined concrete
r = ductility factor in unconfined concrete stress-strain relationship
r_c = ductility factor in confined concrete stress-strain relationship
S = slip displacement

T = resultant force along shear-sliding plane

V_u = shear stress at the commencement of crack widening

V_{u0} = shear stress at the commencement of crack widening for unconfined concrete column

α = failure angle of concrete column

ε_{ax} = axial strain

$\varepsilon_{ax\text{-}200}$ = axial strain of a specimen whose height is equal to 200 mm

$\varepsilon_{c0} = \varepsilon_{ax}$ at f_{c0} for unconfined concrete

$\varepsilon_{cc} = \varepsilon_{ax}$ at f_{cc} for confined concrete

ε_{mat} = material strain of concrete column

ε_S = strain caused by slip

σ_{ax} = axial stress applied to concrete

$\sigma_{ax\text{-}g}$ = guessed axial stress applied to concrete

σ_{con} = transverse confining stress

σ_N = resultant stress normal to shear-sliding plane

$(\sigma_N)_{cir}$ = resultant stress normal to shear-sliding plane of a circular-section column

$(\sigma_N)_{rec}$ = resultant stress normal to shear-sliding plane of a rectangular-section column

$(\sigma_N)_{sq}$ = resultant stress normal to shear-sliding plane of a square-section column

σ_{N0} = normal stress at the commencement of crack widening for unconfined concrete column

τ = resultant stress along shear-sliding plane

τ_{cir} = resultant stress along shear-sliding plane of a circular-section column

τ_m = shear capacity from material properties

τ_{rec} = resultant stress along shear-sliding plane of a rectangular-section column

τ_{sq} = resultant stress along shear-sliding plane of a square-section column

τ_{exp} = shear stress derived from stress-strain relationship of actively confined concrete columns

τ_{theo} = shear stress from approximations

$\tau_{2.5}$ = shear stress at S = 2.5 mm

$\tau_{2.5\text{-}exp}$ = shear stress at S = 2.5 mm derived from experimental data

$\tau_{2.5\text{-}theo}$ = shear stress at S = 2.5 mm derived from approximations

$\tau_{2.5\text{-}3\sigma N0} = \tau_{2.5}$ when σ_N equals $3\sigma_{N0}$

$\tau_{2.5\text{-}10\sigma N0} = \tau_{2.5}$ when σ_N equals $10\sigma_{N0}$

References

Birkeland, PW & Birkeland, HW 1966 'Connections in precast concrete construction', *Journal Proceedings*, vol. 63, no. 3, pp. 345-368.

Chen, Y 2015, 'Quantifying the compressive ductility of concrete in RC members through shear friction mechanics'. Ph.D. dissertation, The University of Adelaide.

Chen, Y, Visintin, P & Oehlers, D 2015a, 'Concrete shear-friction material properties: Derivation from actively confined compression cylinder tests', *Advances in Structural Engineering*, vol. 18, no. 8, pp. 1173-1185.

Chen, Y, Visintin, P & Oehlers, D 2015b, 'Extracting Size-Dependent Stress–Strain Relationships from FRP-Confined Concrete Cylinders for Varying Diameters and Heights', *Journal of Materials in Civil Engineering*, vol. 28, no. 5, p. 04015182.

Chen, Y, Visintin, P, Oehlers, D & Alengaram, U 2013, 'Size-dependent stress-strain model for unconfined concrete', *Journal of Structural Engineering*, vol. 140, no. 4, p. 04013088.

Chen, Y, Zhang, T, Visintin, P & Oehlers, D 2015, 'Concrete shear-friction material properties: application to shear capacity of RC beams of all sizes', *Advances in Structural Engineering*, vol. 18, no. 8, pp. 1187-1198.

Haskett, M, Oehlers, D, Ali, MM & Sharma, S 2010, 'The shear friction aggregate interlock resistance across sliding planes in concrete', *Magazine of Concrete Research*, vol. 62, no. 12, pp. 907-924.

Haskett, M, Oehlers, DJ, Ali, MM & Sharma, SK 2011, 'Evaluating the shear-friction resistance across sliding planes in concrete', *Engineering Structures*, vol. 33, no. 4, pp. 1357-1364.

Jamet, P, Millard, A & Nahas, G 1984, *Triaxial behaviour of a micro-concrete complete stress-strain curves for confining pressures ranging from 0 to 100 MPa*, CEA Centre d'Etudes Nucleaires de Saclay.

Jansen, DC & Shah, SP 1997, 'Effect of length on compressive strain softening of concrete', *Journal of Engineering Mechanics*, vol. 123, no. 1, pp. 25-35.

Johal, L 1975, 'Shear transfer in reinforced concrete with moment or tension acting across the shear plane', *PCI Journal*, pp. 76-93.

Kurniawan, DP 2011, 'Shear Behavior of Reinforced Concrete Columns with High Strength Steel and Concrete under Low Axial Load'. Master Paper, National Taiwan University of Science and Technology

Mattock, AH 1974, 'Shear transfer in concrete having reinforcement at an angle to the shear plane', *Special Publication*, vol. 42, pp. 17-42.

Mattock, AH & Hawkins, NM 1972, 'Shear transfer in reinforced concrete-recent research', *PCI Journal*, vol. 17, no. 2. pp. 55-75

Mattock, AH, Li, W & Wang, T 1976, 'Shear transfer in lightweight reinforced concrete', *PCI Journal*, vol. 21, no. 1, pp. 20-39.

Oehlers, D, Visintin, P, Zhang, T, Chen, Y & Knight, D 2012, 'Flexural rigidity of reinforced concrete members using a deformation based analysis', *Concrete in Australia*, vol. 38, no. 4, pp. 50-56.

Oehlers, DJ, Visintin, P, Chen, J-F, Seracino, R, Wu, Y & Lucas, W 2017, 'Reinforced Concrete Behavior, Research, Development, and Design through Partial-Interaction Mechanics', *Journal of Structural Engineering*, vol. 143, no. 7, p. 02517002.

Rutland, CA & Wang, ML 1997, 'The effects of confinement on the failure orientation in cementitious materials experimental observations', *Cement and Concrete Composites*, vol. 19, no. 2, pp. 149-160.

Sangha, C & Dhir, R 1972, 'Strength and complete stress-strain relationships for concrete tested in uniaxial compression under different test conditions', *Matériaux et Construction*, vol. 5, no. 6, pp. 361-370.

Smith, SS, Willam, KJ, Gerstle, KH & Sture, S 1989, 'Concrete over the top--or, is there life after peak?', *Materials Journal*, vol. 86, no. 5, pp. 491-497.

Visintin, P, Chen, Y & Oehlers, D 2015, 'Size dependent axial and lateral stress strain relationships for actively confined concrete', *Advances in Structural Engineering*, vol. 18, no. 1, pp. 1-20.

Walraven, J & Reinhardt, H 1981, 'Theory and experiments on the mechanical behaviour of cracks in plain and reinforced concrete subjected to shear loading', *HERON*, 26 (1A), pp. 5-68

Zhang, T 2014, 'A generic mechanics approach for predicting shear strength of reinforced concrete beams'. Ph.D. dissertation, The University of Adelaide.

Partial Interaction Bond-Slip Relationship for Mechanical Properties

Introduction

Transverse reinforcement in the form of stirrups, steel tubes, FRP (fibre reinforced polymer) wraps or combination of them can significantly enhance both the axial strength and ductility of reinforced concrete columns (Basset & Uzumeri 1986; Chung et al. 2002; Giakoumelis & Lam 2004; Han 2000; Lam & Teng 2003; Pessiki & Pieroni 1997; Price 1951; Toutanji et al. 2009; Turgay et al. 2009). The bond behaviour between reinforcements and concrete plays a significant part in reinforced concrete columns and has received much research interest in the last few decades (Ali et al. 2008; Haskett et al. 2009; Lu et al. 2005; Seracino, Raizal Saifulnaz & Oehlers 2007; Visintin, Oehlers & Haskett 2013).

In a companion report (Hao 2017a), the confinement mechanism in reinforced concrete has been investigated. In this report, all the partial interaction bond-slip material properties required for the partial interaction mechanical properties in the companion report (Hao 2017a) will be described.

Bond-Slip Mechanics Properties

Let us start by considering the anchored confinement reinforcement AB in Fig. 1 which is pulled out from the concrete as shown. A confinement force P_{conf} in Fig. 1(a) will result in the slip δ between the reinforcement and adjacent concrete. Consider point C in Fig. 1(a); any point between points A and B in Fig. 1(a) could have been used. It is assumed that the distance between point C and point A equals x. At point C, the bond stress and slip are referred to as τ_{Bx} and δ_x respectively. The distributions of bond stress τ_B and slip δ are shown in Figs. 1(b) and (c) respectively. The slip δ at the crack face is referred to as the crack face slip Δ. In this report, the relationship between bond stress τ_B and slip δ in Fig. 1 which is a material property and which can also be referred to as the bond-slip model will be described in this report.

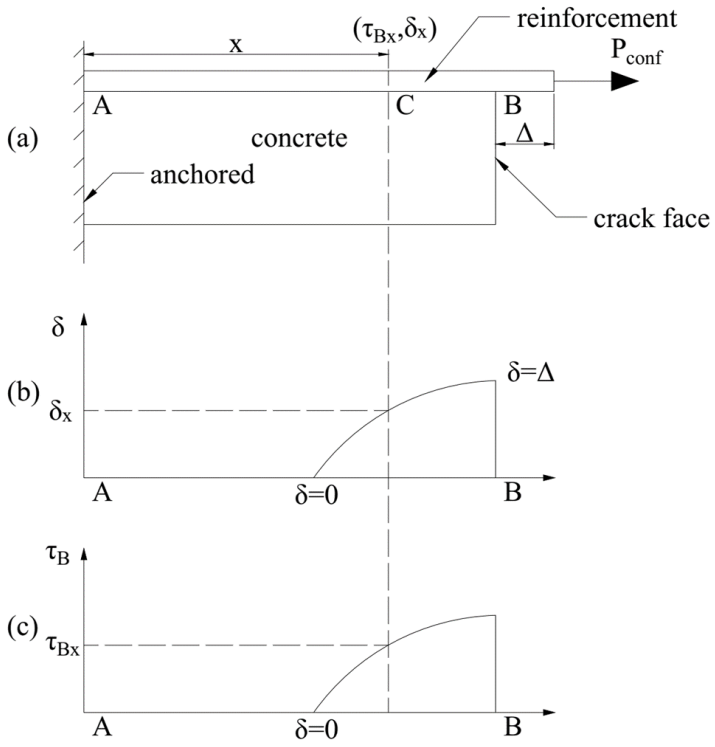

Fig. 1 Analysis of an anchored reinforcement

Shapes of Current Bond-Slip Models for Steel Rebars

Eligehausen, Popov and Bertero (1982) proposed the most widely used model for steel rebars as shown in Fig. 2 and which was accepted by the International Federation for Structural Concrete (CEB-FIP 1993; Fib. 2010). This model is referred to as 'B.E.P. Model' and can be expressed as

$$\tau = \tau_{B\max SR}\left(\frac{\delta}{\delta_1}\right)^{\alpha} \qquad if \quad 0 \le \delta \le \delta_{1SR} \tag{1}$$

$$\tau = \tau_{B\max SR} \qquad if \quad \delta_{1SR} < \delta \le \delta_{2SR} \tag{2}$$

$$\tau = \tau_{B\max SR} - (\tau_{B\max SR} - \tau_f)\frac{\delta - \delta_{2SR}}{\delta_{3SR} - \delta_{2SR}} \qquad if \quad \delta_{2SR} < \delta \le \delta_{3SR} \tag{3}$$

$$\tau = \tau_f \qquad if \quad \delta_{3SR} < \delta \tag{4}$$

where the parameter α is equal to 0.4, τ_{BmaxSR} is the peak bond stress for steel rebars, τ_f is the frictional component of the bond stress, δ_{1SR} is the slip between the steel rebars and adjacent concrete when the bond stress first reaches τ_{BmaxSR}, δ_{2SR} is the slip when the bond stress starts to decrease and δ_{3SR} is the slip when the bond stress first reaches τ_f.

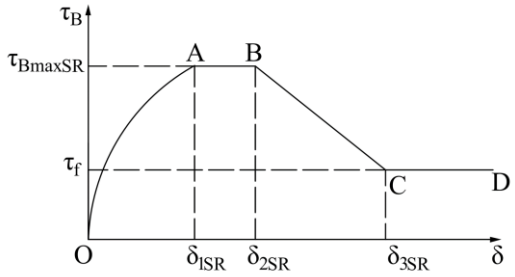

Fig. 2 Eligehausen's bond-slip model for steel rebars

Most approaches have similar shapes as the 'B.E.P. Model' for steel reinforcements as shown in Fig 2 (Harajli, Hout & Jalkh 1995; Soroushian & Choi 1989). Furthermore, Yankelevsky (1985) simplified the 'B.E.P. Model' as a linear relationship as shown in Fig. 3.

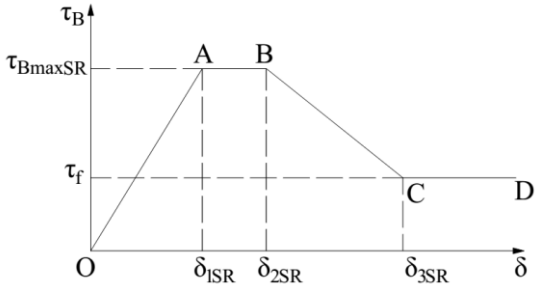

Fig. 3 Simplified Eligehausen's bond-slip model for steel rebars

Haskett et al. (2009) proposed a bond-slip model for steel rebars as shown in Fig. 4. Based on a partial interaction mechanism, the values of the parameters δ_{1SR} and δ_{maxSR} in Fig. 4 were derived. Then this model was validated by experimental data with good correlation. Furthermore, this model ignores the frictional component of the bond stress CD in Fig. 3 to achieve a conservative solution.

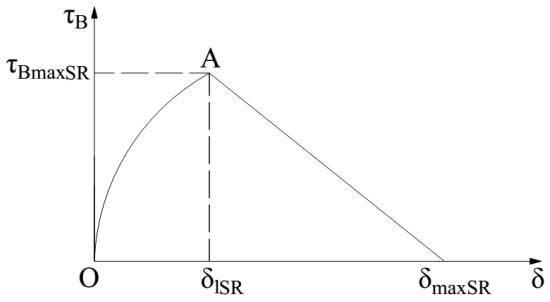

Fig. 4 Haskett's bond-slip model for steel rebars

Shapes of Current Bond-Slip Models for FRP Rebars

With regard to FRP rebars, Cosenza, Edoardo, Manfredi and Realfonzo (1997) removed the platform AB of the 'B.E.P. Model' in Fig. 2 as shown in Fig. 5; this model is applied by the International Federation for Structural Concrete (Fib. 2010). Another widely used model as shown in Fig. 6 only gives the expression for ascending branch as follows (Cosenza, E, Manfredi & Realfonzo 1995)

$$\tau = \tau_{B\max FR}[1-\exp(\frac{\delta}{\delta_{1FR}})]^{\beta} \tag{5}$$

where β is a parameter, τ_{BmaxFR} is the peak bond stress for FRP rebars and δ_{1FR} is the slip between the FRP rebars and adjacent concrete when the bond stress first reaches τ_{BmaxFR}. These two approaches are widely used and parameters including δ_{1FR}, δ_{2FR}, τ_f, τ_{BmaxFR} in the former approach (Cosenza, Edoardo, Manfredi & Realfonzo 1997) and β, δ_{1FR} and τ_{BmaxFR} in the latter approach (Cosenza, E, Manfredi & Realfonzo 1995) are empirically derived for each individual item of research (Baena et al. 2009; Focacci, Nanni & Bakis 2000; Lin & Zhang 2014; Malvar, Cox & Cochran 2003; Pecce et al. 2001; Tighiouart, Benmokrane & Gao 1998). However, these parameters are more likely to be only accurate for the experiments from which they were derived. Consequently, this requires further research.

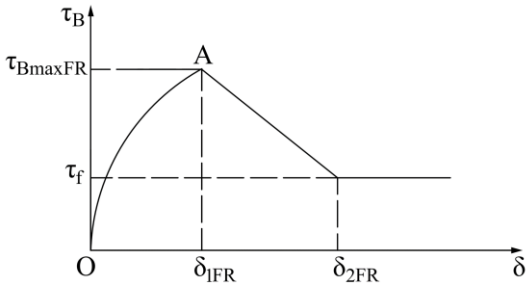

Fig. 5 Cosenza's bond-slip model for FRP rebars

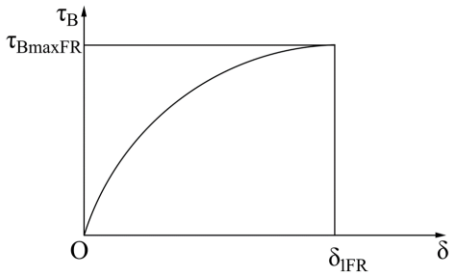

Fig. 6 Cosenza's ascending bond-slip model for FRP rebars

Shapes of Current Bond-Slip Models for Bonded FRP or Steel Plates

Lu et al. (2005) developed a database for bonded FRP plates and different models were reviewed. Most of the models give the shape as shown in Figs. 7 and 8. Based on the database, they also derive the values of the parameters δ_{1P}, δ_{maxP} and τ_{BmaxP} in the models in Figs. 7 and 8. Seracino, Raizal Saifulnaz and Oehlers (2007) also proposed a bilinear model as in Fig. 8 for externally bonded (EB) and near-surface mounted (NSM) steel or FRP plates. This approach also gives the values of parameters δ_{1P}, δ_{maxP} and τ_{BmaxP} in Fig. 8 and will be described later.

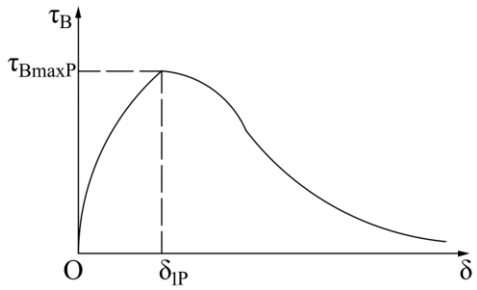

Fig. 7 Lu's non-linear bond-slip relationship for FRP sheets and plates

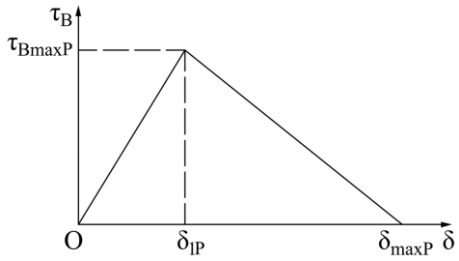

Fig. 8 Lu's bilinear bond-slip relationship for FRP sheets and plates

Shapes of Current Bond-Slip Models for Unbonded FRP Plate or Steel Plate

For unbonded FRP plates or steel plates such as that in concrete filled FRP tubes or steel tubes, there is no adhesive between the concrete and FRP tube or steel tube. Consequently, it is assumed there is no bond between concrete and FRP tube or steel tube as this gives a conservative solution in the analysis.

Simplified Bond-Slip Model

In order to derive a closed-form solution, several simplified bond-slip models are proposed. The three main models include the bilinear model, linear ascending model and linear descending model as shown in Figs. 9, 10 and 11 respectively (Yuan, Wu & Yoshizawa 2001). The bilinear bond-slip model is the closest to reality. By contrast, the linear ascending bond-slip model in Fig. 10 can apply when δ_1 in Fig. 9 is big enough such that the bond stress between reinforcement and concrete may be not able to reach the maximum bond stress τ_{Bmax}. This is most likely to happen in steel reinforced concrete columns as the steel reinforcement is likely to yield before the crack face slip Δ in Fig. 1(a) reaches δ_1 in Fig. 9 (Sturm, Visintin & Oehlers 2018). When δ_1 in Fig. 9 is small enough and can be ignored (Seracino, Raizal Saifulnaz & Oehlers 2007), the bilinear bond-slip model can be simplified to the linear descending model as shown in Fig. 11.

In this research, the bilinear model in Fig. 9 will be applied in order to derive simple closed-form solutions of the stress-strain relationships of passively reinforced concrete columns

(Hao 2017b). Next, the material properties in this bilinear model for different types of reinforcement will be described.

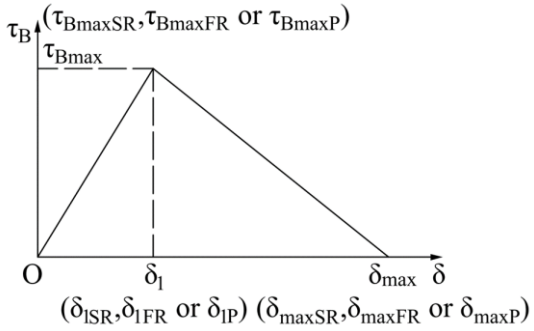

Fig. 9 Bilinear bond-slip relationship

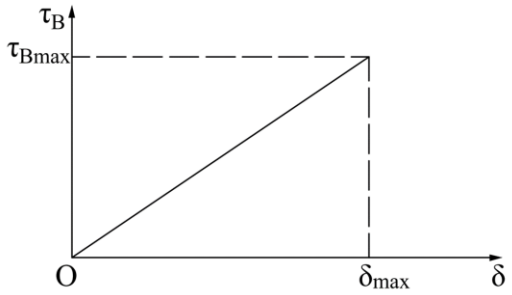

Fig. 10 Linear ascending bond-slip relationship

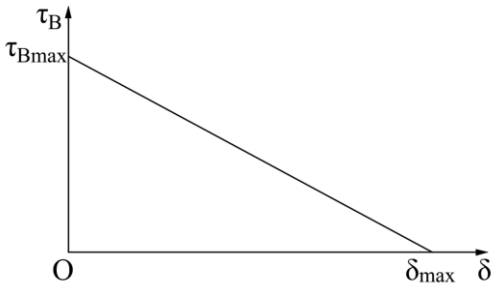

Fig. 11 Linear descending bond-slip relationship

Bond-Slip Material Properties

Bilinear Bond-Slip Model for Steel and FRP Rebars

For steel rebars, slips δ_{1SR} and δ_{maxSR} in Fig. 9 can be expressed as

$$\delta_{1SR} = 1.5mm \tag{6}$$

$$\delta_{\max SR} = 15mm \tag{7}$$

Furthermore, the maximum bond stress τ_{BmaxSR} at δ_{1SR} can be expressed as (Haskett et al. 2009)

$$\tau_{B\max SR} = 2.5\sqrt{f_{c0}} \tag{8}$$

where f_{c0} is the unconfiend concrete strength. With regard to the bilinear bond-slip model for FRP rebars, slips δ_{1FR} and δ_{maxFR} in Fig. 9 can be expressed as (Focacci, Nanni & Bakis 2000)

$$\delta_{1FR} = 1mm \tag{9}$$

$$\delta_{\max FR} = 16.9mm \tag{10}$$

Furthermore, τ_{BmaxFR} in Fig. 9 can be taken as (Okelo & Yuan 2005)

$$\tau_{B\max FR} = 14.7\frac{\sqrt{f_{c0}}}{d_0} \tag{11}$$

where d_0 is the diameter of the FRP rebar.

Bilinear Bond-Slip Model for Bonded Steel and FRP Plates

The parameters τ_{BmaxP} , δ_{1P} and δ_{maxP} in Fig. 9 for bonded steel and FRP plates proposed by Seracino, Raizal Saifulnaz and Oehlers (2007) can be expressed as

$$\tau_{B\max P} = (0.802 + 0.078\phi_f) f_{c0}^{0.6} \tag{12}$$

$$\delta_{1P} = 0 \tag{13}$$

$$\delta_{\max P} = \frac{0.976\phi_f^{0.526}}{0.802 + 0.078\phi_f} \tag{14}$$

where f_{c0} is the unconfined concrete strength, δ_{1P} is assumed to be zero as it is an order of magnitude smaller than δ_{maxP} and the aspect ratio of the interface failure plane φ_f can be expressed as

$$\phi_f = \frac{d_f}{b_{f2}} \tag{15}$$

where d_f and b_{f2} are the thickness of the failure plane and the length of the failure plane parallel to the concrete surface as shown in Fig. 12, and which are equal to 1 mm and b_f + 2 mm (b_f is the width of reinforcement plate as shown in Fig. 12) respectively. Furthermore, the intermediate crack (IC) debonding resistance P_{IC} can be expressed as (Seracino, Raizal Saifulnaz & Oehlers 2007)

$$P_{IC} = 0.85\phi_f^{0.25} f_{c0}^{0.33} \sqrt{L_{per} E_p A_p} \tag{16}$$

where L_{per} is the length of the potential failure plane in Fig. 12 and is equal to b_f + 4 mm, E_p and A_p are the modulus and cross-section area of the reinforcement plate. It is worth noting that the IC debonding resistance P_{IC} should be less than either the rupture force for the FRP plates or yield force for steel plates. When the confinement force first reaches the IC debonding resistance P_{IC}, the crack face slip Δ_{IC} can be expressed as (Hao 2017a)

$$\Delta_{IC} = \delta_{\max P} \tag{17}$$

where δ_{maxP} can be obtained from Eq. (14). The reinforcement length required to develop P_{IC} is referred to as the critical length L_{crt} and can be expressed as (Seracino, Raizal Saifulnaz & Oehlers 2007)

$$L_{crt} = \frac{\pi}{2\lambda} \tag{18}$$

where the parameter λ can be expressed as

$$\lambda = \sqrt{\frac{\tau_{B\max P} L_{per}}{\delta_{\max P} E_p A_p}} \tag{19}$$

where τ_{BmaxP} and δ_{maxP} can be obtained from Eqs. (12) and (14) respectively.

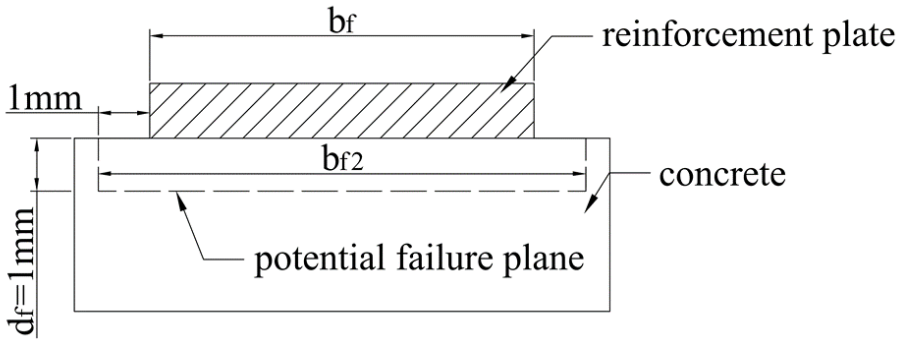

Fig. 12 Debonding failure of FRP plate bonded to concrete

Conclusion

In this report, the partial interaction bond-slip relationships for the mechanics properties required in a companion report are described. A brief review of available bond-slip models for steel rebars, FRP rebars, bonded steel and FRP plates are described. In future research, the simplified bilinear model will be employed to derive the closed form solution of the stress-strain relationship for passively confined concrete. Furthermore, bond-slip material properties required to do quantitative analysis have been described in this report.

Notation

A_P = total cross-section area of reinforcement plate
b_f = width of reinforcement plate
b_{f2} = length of failure plane parallel to concrete surface
d_f = thickness of failure plane
d_0 = diameter of FRP rebar.

E_P = elastic modulus of reinforcement plate

f_{c0} = unconfined concrete strength

L_{crt} = critical length that is reinforcement length required to develop P_{IC}

L_{per} = total length of potential debonding failure plane of reinforcement in tension stiffening analysis

P_{conf} = force in confinement reinforcement

P_{IC} = IC debonding resistance

Δ = slip of confinement reinforcement at crack face

Δ_{IC} = crack face slip when confinement force first reaches IC debonding resistance P_{IC}

δ = slip between reinforcement and adjacent concrete

δ_1 = slip between reinforcement and adjacent concrete at τ_{Bmax}

δ_{1FR} = slip between FRP rebars and adjacent concrete at τ_{BmaxFR}

δ_{1P} = slip between plate reinforcement and adjacent concrete at τ_{BmaxP}

δ_{1SR} = slip between steel rebars and adjacent concrete at τ_{BmaxSR}

δ_{2FR} = slip between FRP rebars and adjacent concrete when τ_B starts to decrease

δ_{2SR} = slip between steel rebars and adjacent concrete when τ_B starts to decrease

δ_{3SR} = slip when the bond stress first reaches τ_f for steel rebars

δ_{max} = slip between confinement reinforcement and adjacent concrete when bond stress τ_B reduces to zero

δ_{maxFR} = slip between FRP rebars and adjacent concrete when bond stress τ_B reduces to zero

δ_{maxP} = slip between plate reinforcement and adjacent concrete when bond stress τ_B reduces to zero

δ_{maxSR} = slip between steel rebars and adjacent concrete when bond stress τ_B reduces to zero

τ_B = bond stress existing between reinforcement and concrete

τ_{Bmax} = peak bond stress for confinement reinforcement

τ_{BmaxFR} = peak bond stress for FRP rebars

τ_{BmaxP} = peak bond stress for plates

τ_{BmaxSR} = peak bond stress for steel rebars

τ_f = frictional component of the bond stress

φ_f = aspect ratio of interface failure plane

References

Ali, MM, Oehlers, D, Griffith, M & Seracino, R 2008, 'Interfacial stress transfer of near surface-mounted FRP-to-concrete joints', *Engineering Structures*, vol. 30, no. 7, pp. 1861-1868.

Baena, M, Torres, L, Turon, A & Barris, C 2009, 'Experimental study of bond behaviour between concrete and FRP bars using a pull-out test', *Composites Part B: Engineering*, vol. 40, no. 8, pp. 784-797.

Basset, R & Uzumeri, S 1986, 'Effect of confinement on the behaviour of high-strength lightweight concrete columns', *Canadian Journal of Civil Engineering*, vol. 13, no. 6, pp. 741-751.

CEB-FIP 1993, *CEB-FIP Model Code 1990: Design Code*, Thomas Telford.

Chung, H-S, Yang, K-H, Lee, Y-H & Eun, H-C 2002, 'Strength and ductility of laterally confined concrete columns', *Canadian Journal of Civil Engineering*, vol. 29, no. 6, pp. 820-830.

Fib. (The International Federation for Structural Concrete) (2010) 'Model Code 2010–Final draft', *Thomas Thelford, Lausanne, Switzerland*.

Cosenza, E, Manfredi, G & Realfonzo, R 1995, '20 Analytical modelling of bond between frp reinforcing bars and concrete', in *Non-Metallic (FRP) Reinforcement for Concrete Structures: Proceedings of the Second International RILEM Symposium*, CRC Press, vol. 29, p. 164.

Cosenza, E, Manfredi, G & Realfonzo, R 1997, 'Behavior and modeling of bond of FRP rebars to concrete', *Journal of Composites for Construction*, vol. 1, no. 2, pp. 40-51.

Eligehausen, R, Popov, EP & Bertero, VV 1982, 'Local bond stress-slip relationships of deformed bars under generalized excitations', *Proceedings of the 7th European Conference on Earthquake Engineering*, vol. 4, pp. 69-80

Focacci, F, Nanni, A & Bakis, CE 2000, 'Local bond-slip relationship for FRP reinforcement in concrete', *Journal of Composites for Construction*, vol. 4, no. 1, pp. 24-31.

Giakoumelis, G & Lam, D 2004, 'Axial capacity of circular concrete-filled tube columns', *Journal of Constructional Steel Research*, vol. 60, no. 7, pp. 1049-1068.

Han, L-H 2000, 'The influence of concrete compaction on the strength of concrete filled steel tubes', *Advances in Structural Engineering*, vol. 3, no. 2, pp. 131-137.

Hao, X 2017a, 'Mechanics closed-form equations for the confinement forces and displacesments', *School Report*, School of Civil, Environmental and Mining Engineering, The University of Adelaide, Australia.

Hao, X 2017b, 'Generation of stress-strain relationship of passively reinforced concrete' *School Report*, School of Civil, Environmental and Mining Engineering, The University of Adelaide, Australia.

Harajli, M, Hout, M & Jalkh, W 1995, 'Local bond stress-slip behavior of reinforcing bars embedded in plain and fiber concrete', *Materials Journal*, vol. 92, no. 4, pp. 343-353.

Haskett, M, Oehlers, DJ, Mohamed Ali, M & Wu, C 2009, 'Yield penetration hinge rotation in reinforced concrete beams', *Journal of Structural Engineering*, vol. 135, no. 2, pp. 130-138.

Lam, L & Teng, J 2003, 'Design-oriented stress–strain model for FRP-confined concrete', *Construction and Building Materials*, vol. 17, no. 6, pp. 471-489.

Lin, X & Zhang, Y 2014, 'Evaluation of bond stress-slip models for FRP reinforcing bars in concrete', *Composite Structures*, vol. 107, pp. 131-141.

Lu, X, Teng, J, Ye, L & Jiang, J 2005, 'Bond–slip models for FRP sheets/plates bonded to concrete', *Engineering Structures*, vol. 27, no. 6, pp. 920-937.

Malvar, L, Cox, J & Cochran, KB 2003, 'Bond between carbon fiber reinforced polymer bars and concrete. I: Experimental study', *Journal of Composites for Construction*, vol. 7, no. 2, pp. 154-163.

Okelo, R & Yuan, RL 2005, 'Bond strength of fiber reinforced polymer rebars in normal strength concrete', *Journal of Composites for Construction*, vol. 9, no. 3, pp. 203-213.

Pecce, M, Manfredi, G, Realfonzo, R & Cosenza, E 2001, 'Experimental and analytical evaluation of bond properties of GFRP bars', *Journal of Materials in Civil Engineering*, vol. 13, no. 4, pp. 282-290.

Pessiki, S & Pieroni, A 1997, 'Axial load behavior of large-scale spirally-reinforced high-strength concrete columns', *ACI Structural Journal*, vol. 94, no. 3, pp. 304-314.

Price, WH 1951, 'Factors influencing concrete strength', *ACI journal*, vol. 47, no. 2, pp. 417-432.

Seracino, R, Raizal Saifulnaz, M & Oehlers, D 2007, 'Generic debonding resistance of EB and NSM plate-to-concrete joints', *Journal of Composites for Construction*, vol. 11, no. 1, pp. 62-70.

Soroushian, P & Choi, K-B 1989, 'Local bond of deformed bars with different diameters in confined concrete', *Structural Journal*, vol. 86, no. 2, pp. 217-222.

Sturm, AB, Visintin, P & Oehlers, DJ 2018, 'Time-dependent serviceability behavior of reinforced concrete beams: Partial interaction tension stiffening mechanics', *Structural Concrete*, vol. 19, no. 2, pp. 508-523.

Tighiouart, B, Benmokrane, B & Gao, D 1998, 'Investigation of bond in concrete member with fibre reinforced polymer (FRP) bars', *Construction and Building Materials*, vol. 12, no. 8, pp. 453-462.

Toutanji, H, Han, M, Gilbert, J & Matthys, S 2009, 'Behavior of large-scale rectangular columns confined with FRP composites', *Journal of Composites for Construction*, vol. 14, no. 1, pp. 62-71.

Turgay, T, Köksal, H, Polat, Z & Karakoc, C 2009, 'Stress–strain model for concrete confined with CFRP jackets', *Materials & Design*, vol. 30, no. 8, pp. 3243-3251.

Visintin, P, Oehlers, D & Haskett, M 2013, 'Partial-interaction time dependent behaviour of reinforced concrete beams', *Engineering Structures*, vol. 49, pp. 408-420.

Yankelevsky, DZ 1985, 'New finite element for bond-slip analysis', *Journal of Structural Engineering*, vol. 111, no. 7, pp. 1533-1542.

Yuan, H, Wu, Z & Yoshizawa, H 2001, 'Theoretical solutions on interfacial stress transfer of externally bonded steel/composite laminates', *Doboku Gakkai Ronbunshu*, vol. 2001, no. 675, pp. 27-39.

Chapter 3— Passive Stress/Strain Behaviour

Introduction

In this chapter, a mechanics-based approach to predict the passive stress/strain for passively confined concrete prisms under concentric load are described in the two journal papers below. These two journal papers condense the information in the school reports in the first two chapters in a form suitable for a journal.

In the first paper, a mechanics-based approach for rectangular cross-sections is derived from the confinement mechanics equations in Chapter 1 and material properties in Chapter 2. Then in the second paper, the proposed approach is extended to the circular sections and the effect of the section shape on confinement is described. This is followed by a parametric study to describe the effect of specimen size on the passive stress/strain response.

List of Manuscripts

Hao, X, Visintin, P and Oehlers, DJ (2018) Simulating the Passive Confinement of Rectangular Concrete Prisms Allowing for Size Effect. Submitted to *Proceedings of Institution of Civil Engineers-Structures and Buildings*

Hao, X, Visintin, P and Oehlers, DJ (2019) Simulating the Passive Confinement of Circular Concrete Cylinders Allowing for Size Effect. Submitted to *Composite Structures*

Statement of Authorship

Statement of Authorship

Title of Paper	Simulating the Passive Confinement of Rectangular Concrete Prisms Allowing for Size Effect
Publication Status	☐ Published ☐ Accepted for Publication ☑ Submitted for Publication ☐ Unpublished and Unsubmitted work written in manuscript style
Publication Details	Hao, X, Visintin, P and Oehlers, DJ (2018) "Simulating the Passive Confinement of Rectangular Concrete Prisms Allowing for Size Effect". Submitted to *Proceedings of Institution of Civil Engineers-Structures and Buildings*

Principal Author

Name of Principal Author (Candidate)	Xinkai Hao		
Contribution to the Paper	Developed the model, interpreted data, wrote manuscript		
Overall percentage (%)	70%		
Certification:	This paper reports on original research I conducted during the period of my Higher Degree by Research candidature and is not subject to any obligations or contractual agreements with a third party that would constrain its inclusion in this thesis. I am the primary author of this paper.		
Signature		Date	20/10/2019

Co-Author Contributions

By signing the Statement of Authorship, each author certifies that:

i. the candidate's stated contribution to the publication is accurate (as detailed above);

ii. permission is granted for the candidate in include the publication in the thesis; and

iii. the sum of all co-author contributions is equal to 100% less the candidate's stated contribution.

Name of Co-Author	Phillip Visintin		
Contribution to the Paper	Supervised work progress, help modelling and revising manuscript		
Signature		Date	21/10/2019

Name of Co-Author	Deric John Oehlers		
Contribution to the Paper	Supervised work progress, help modelling and revising manuscript		
Signature		Date	21/10/19

Please cut and paste additional co-author panels here as required.

Simulating the Passive Confinement of Rectangular Concrete Prisms Allowing for Size Effect

X. Hao[1], P. Visintin[2] and D. J. Oehlers[3]

Abstract

Tests have shown that providing passive confinement to concrete, either through the use of internal stirrups, external fibre reinforced polymer (FRP) wraps, FRP tubes or steel tubes, can increase the concrete strength and, in particular, the concrete ductility, thereby allowing greater absorption of energy and consequently ductile failure. The problem of including the benefits of passive confinement in design is in generalising the effect of passive confinement because it varies with member size, confining reinforcement configuration and material properties. In this paper, the fundamental mechanics of passive concrete confinement are explained both qualitatively and quantitatively through the use of shear-friction and bond-slip mechanics. An analysis oriented procedure is described for quantifying the passive stress/strain of concrete for rectangular sections. The mechanics model is found to have good correlation with tests and, consequently, can be used in the design of a member to allow for the benefits of confinement.

Keywords: concrete; concrete confinement; active confinement; passive confinement; partial interaction; RC members; IC debonding; shear sliding.

Introduction

Passive confinement may be applied to concrete members through the use of either internal stirrups or external FRP (fibre reinforced polymer) wraps, or FRP tubes or steel tubes. The changes in concrete strength and ductility arising from this passive confinement has received much research attention (Hognestad, 1951, Jiang and Teng, 2007, Mander et al., 1988, Plevris and Triantafillou, 1994, Popovics, 1973, Richart et al., 1928, Sakino et al., 2004, Teng et al., 2009). Means of predicting the impact of passive confinement on the stress/strain relationship of concrete can be split into two broad categories: *design oriented* or *analysis oriented*.

The design oriented approach generally treat passively confined concrete as a new material, and develops stress/strain models for each specific confinement based on empirical observations. The general shapes of passive stress/strain relationships for concrete confined by stirrups or wraps/tubes are compared in Fig. 1 (Lam and Teng, 2003, Mander et al., 1988, Shams and Saadeghvaziri, 1997). These are generally comprised of a non-linear ascending branch (O-A or O-C) followed by either an ascending or descending secondary branch depending on the level of confinement (A-B or C-D). Design oriented approaches such as that proposed by Lam and Teng (2003) provide a stress/strain model for FRP reinforced concrete based on the regression of a large database of test observations and have been routinely updated as new test data covering a broader range of parameters have become available (Teng et al., 2009, Wei and Wu, 2012, Youssef et al., 2007). For concrete confined by stirrups, Mander et al. (1988) derived the peak stress f_{cc} and strain ε_{cc} at f_{cc} semi-empirically and substituted them into stress/strain models of actively confined concrete proposed by Popovics (1973). This approach is similar to that accepted by CEB-FIB Model (Fib., 2010).

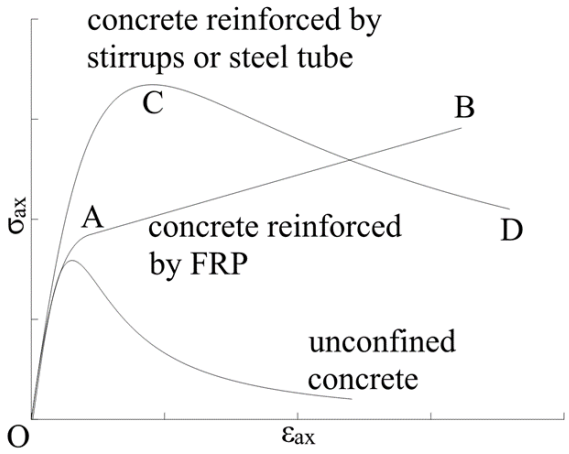

Fig. 1 Empirical stress/strain of passively confined concrete

The primary benefit of design oriented approaches is their ease of use, that is, because they are based on the regressed data, simple expressions for the key points of the stress/strain relationship can be easily defined. Care in the application of design oriented approaches is however required, because the empirical basis that makes them easy to apply, may also limit accuracy if used to predict the behaviour of concrete with parameters outside the range of

the regressed database. An important example of this is in the prediction of the behaviour of full size columns which have overall dimensions much larger than the majority of specimens in the compiled databases. The issue of member size is significant because previous research has shown passive confinement to be size dependent (Du et al., 2017, Jin et al., 2017, Thériault et al., 2004, Wang et al., 2012). Also of importance is the consideration of member slenderness, as experimental work has shown the slenderness ratio to have a significant impact on both the failure mode and degree of confinement (Visintin et al., 2015a). Although empirically derived approaches based on the regression of the database of large-size concrete members do exist (Wang et al., 2011b) as do approaches that consider different slenderness ratios (Silva and Rodrigues, 2006). However, the largest diameter and slenderness ratio of concrete members in these database are 305 mm and 5, respectively; these ranges are smaller than a significant proportion of columns constructed in practice.

In analysis-oriented approaches, the behaviour of confined concrete is based on the interaction between the concrete and lateral reinforcement. For analysis, a family of curves representing the actively confined stress/strain relationships of the concrete are first generated. Then, depending on the interaction relationship between the concrete and lateral reinforcement, the lateral confining stress is derived either from the radial dilation (Becque et al., 2003, Fam and Rizkalla, 2001, Jiang and Teng, 2007, Mirmiran and Shahawy, 1996, Spoelstra and Monti, 1999, Teng et al., 2007) or from the slip along the shear failure plane (Harmon et al., 1998, Visintin et al., 2015a), from which the axial strain and axial stress can be derived. Each point of the loading path on the family of curves of the generated active stress/strain can then be determined.

Although a more detailed analysis than the design oriented approach, these analysis-oriented approaches suffer from the same limitations in that if the actively confined stress/strain relationships, from which the passive stress/strain behaviour is derived, are not size dependent then the passive relationship will not be size dependent. Again, this issue does not appear to be easy to solve with current empirical data as the vast majority of actively confined stress/strain relationships have been developed from triaxial test results on small scale specimens with an aspect ratio of 2. There is, therefore, a need to develop approaches to predict the passively confined stress/strain relationship of concrete that is independent of size and that are not based on size independent stress/strain relationships. In this paper, we seek to address this issue by developing an approach for constructing the stress/strain

relationship for concrete passively confined by stirrups, wraps or tubes using fundamental shear friction and partial interaction mechanics.

The shear-friction and bond-slip partial interaction mechanics that control the fundamental mechanics of the passive confinement of concrete is first described in qualitative terms. The fundamental mechanics is then quantified with the use of mechanics equations and material properties. The quantitative analysis is then validated with comparison with test results.

Qualitative Description of the Confinement Mechanism

To understand the mechanisms that control the passive confinement of concrete, it is necessary to first consider the behaviour of actively confined concrete as the passive behaviour stems from these active properties.

Actively Confined Concrete

Consider the concrete prism in Fig. 2 that is subjected to an axial stress σ_{ax} and an active confinement pressure σ_{conf}. Prior to the formation of the sliding plane, the axial stress σ_{ax} induces a material strain in the concrete ε_m which is uniform throughout the concrete and independent of the length of the prism L_{def}.

On gradually increasing σ_{ax}, eventually a sliding plane forms as in Fig. 2 at an inclination α and slip S occurs across the sliding plane. The axial component of the slip S_{ax} as shown in Fig. 2 causes contraction of the prism such that the axial strain increases by an equivalent strain of ε_S equal to S_{ax}/L_{def}; this is an equivalent strain as it is not a material property since it involves both local and non-local deformations and is therefore size dependent. The total axial strain in the prism ε_{ax} is, therefore, the sum of the material component ε_m and the sliding component ε_S. The lateral component of the slip S_{lat} in Fig. 2 would be resisted by any lateral reinforcement such as stirrups or wraps should they be present. This tensile resistance of the lateral reinforcement is balanced by compression across the sliding plane and therefore acts in addition to the confinement stress σ_{conf}.

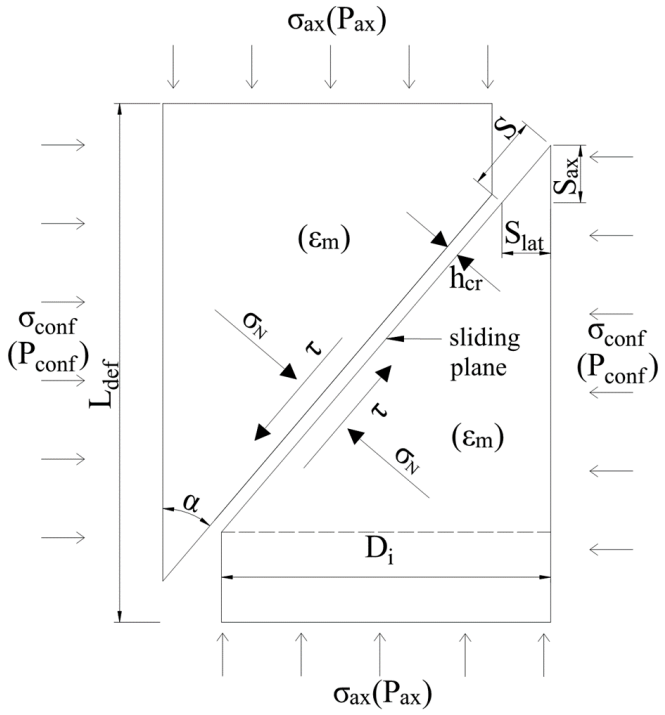

Fig. 2 Actively confined prism

As slip occurs across the sliding plane in Fig. 2, aggregate interlock causes the interface surfaces to separate by h_{cr} as shown. The magnitude of this crack width h_{cr} (Haskett et al., 2010, Haskett et al., 2011) is at least one order of magnitude smaller than either S_{ax} or S_{lat}, therefore, for simplicity it will be ignored to give a slightly conservative design. The forces induced on the sliding plane due to the axial stress σ_{ax} and the confinement stress σ_{conf} can be resolved along the sliding plane to determine the shear stress τ along the sliding plane and the normal stress to the sliding plane σ_N. The parameters τ_m, σ_N and S are the shear-friction material properties of the concrete as illustrated in Fig. 3 where: V_u is the shear capacity at the onset of sliding; and τ_m is the shear capacity for a specific combination of a normal stress σ_N and slip S. It can be seen that for a given normal stress across the interface σ_N the shear capacity τ_m reduces with slip S.

The behaviour of the prism in Fig. 2 is shown as the active stress/strain ($\sigma_{ax}/\varepsilon_{ax}$) relationship in Fig. 4 where σ_{ax} is the applied axial stress and ε_{ax} is the total strain that is the material strain ε_m plus the equivalent sliding strain ε_S should it occur. For the unconfined concrete O-

A-B, the peak strength f_{co} at strain ε_{co} occurs at the onset of sliding. For the confined concrete such as O-C-D or O-E-F, at the onset of sliding the peak strength is f_{cc} at a strain ε_{cc}.

Prior to the formation of the sliding plane in Fig. 2, the axial stress/strain ($\sigma_{ax}/\varepsilon_{ax}$) in Fig. 4 follows an ascending branch which depends on the active confinement pressure σ_{conf} and which is a material property that can be determined directly from tests. Eventually a sliding plane forms after which the axial stress reduces due to interface slip as shown by the descending branch in Fig. 4. The descending branches in Fig. 4 can be determined from the concrete shear-friction properties in Fig. 3. That is, for a given axial stress σ_{ax} and confinement pressure σ_{conf} in Fig. 2, the shear friction properties τ_{mx} and σ_{Nx} in Fig. 3 can be determined. From these values, can be determine the interface slip S_x and from S_x can be determined the equivalent strain due to slip. That is one point on the descending branch for its construction. It is also worth noting that the peak strengths f_{cc} in Fig. 4 occur at the shear capacities V_u in Fig. 3.

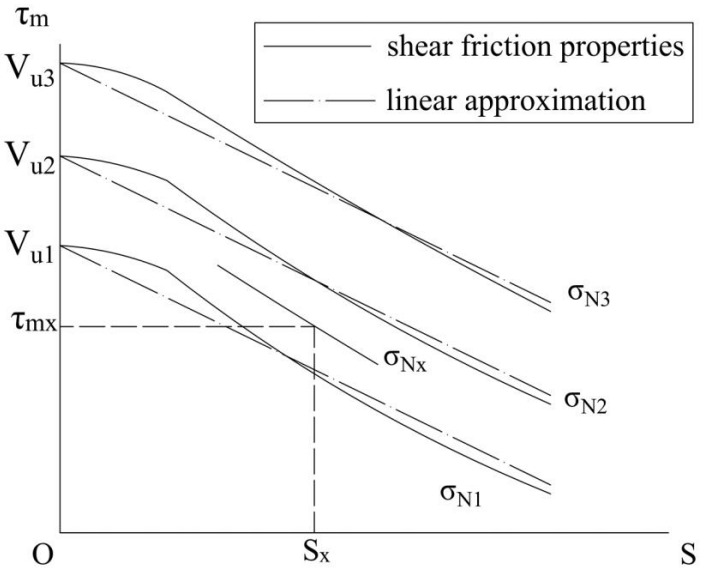

Fig. 3 Shear-Friction material properties

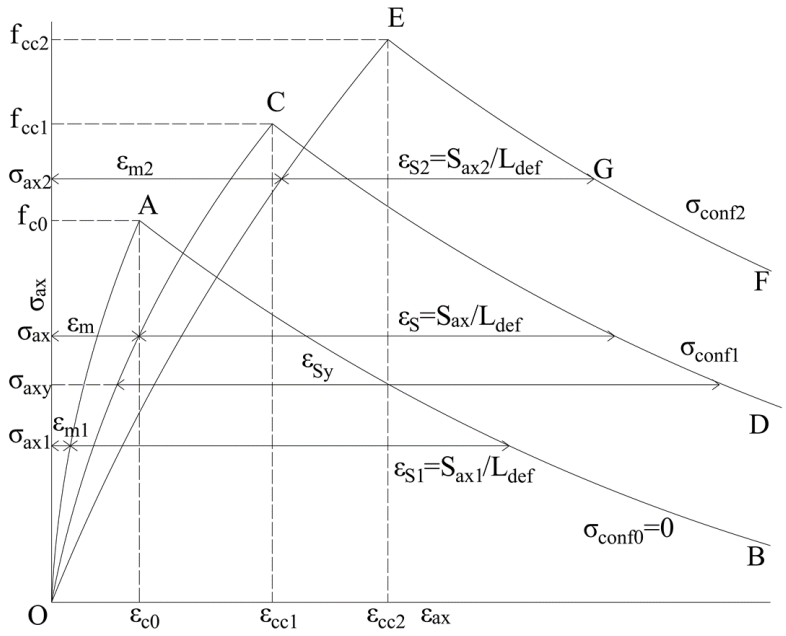

Fig. 4 Theoretical stress/strain of actively confined concrete

To summarise, take for example the $\sigma_{ax}/\varepsilon_{ax}$ relationship O-E-F in Fig. 4 in which the active confinement is σ_{conf2}. At an axial stress σ_{ax2}, the material strain is ε_{m2} and the equivalent sliding strain is ε_{S2} which is equal to S_{ax2}/L_{def} that is the axial component of the slip divided by the length of the prism.

Passively Confined Concrete

Let us now add lateral reinforcement to the prism in Fig. 2 as shown in Fig. 5; this lateral reinforcement could be internal stirrups encasing the concrete within the width D_i, or external wraps or external tubes encasing the section of width D_i. The confinement pressure shown as σ_{conf} is now not acting on the external surface of the prism but across the interface of the sliding plane. As shown, the interface slip S induces a lateral expansion S_{lat} which causes the lateral or confinement reinforcement to go into tension which is shown as force P_{conf}. These tensile forces in the reinforcement are balanced by internal compression across the interface σ_{conf}.

The lateral movement S_{lat} in Fig. 5 can be visualised as the opening of a crack by 2Δ in the lateral direction which induces a reinforcement force P_{conf}. The relationship between P_{conf} and Δ (P_{conf}/Δ) where Δ is the half crack width in the lateral direction can be determined from the partial-interaction mechanics of intermediate-crack (IC) debonding (Lu et al., 2005, Seracino et al., 2007) which depends on the bond-slip property (τ_B/δ) between the reinforcement and the adjacent concrete (Azizinamini et al., 1993, Darwin and Graham, 1993, Yao et al., 2005). Hence, for a given slip S in Fig. 5, Δ is known, such that P_{conf} can be derived from the P_{conf}/Δ properties, and further from P_{conf} can be derived the passive confining pressure σ_{conf}. Consequently σ_{conf} in Fig. 4 is known, and as ε_S is also known, it is a simple question of finding σ_{ax} at which this occurs. For example, if the confinement pressure is σ_{conf1} in Fig. 4 such that O-C-D is the active stress/strain. Then for a specific slip S, ε_{Sy} is known and it is a question of finding σ_{axy} at which this occurs that is where the horizontal dimension ε_{Sy} fits within O-C-D as shown.

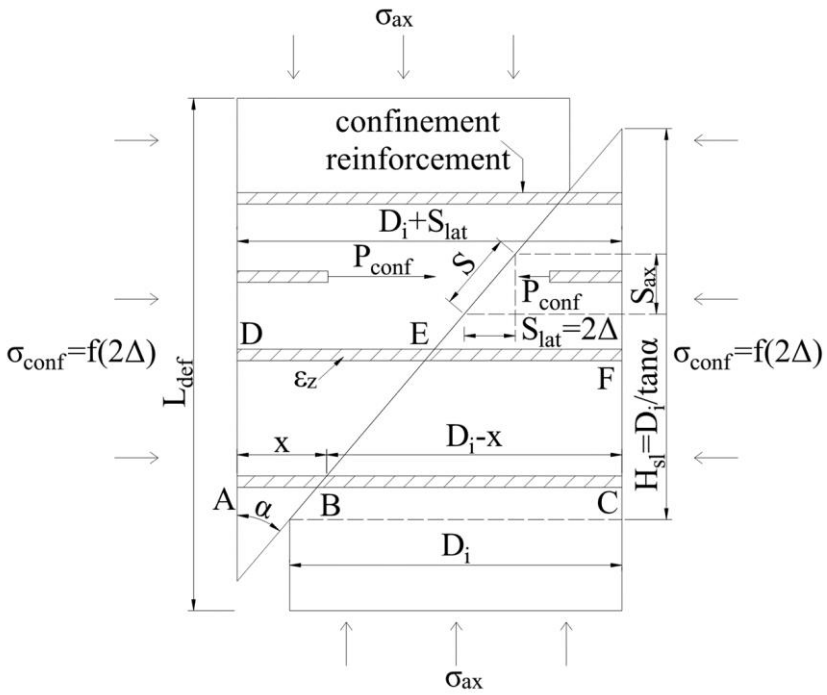

Fig. 5 Confinement force and deformation of passively confined concrete

When debonding is complete, or when there is no bond, then the strain in the reinforcement in Fig. 5 is constant. Hence for a given strain such as ε_z for the reinforcement D-E-F, S_{lat} is

equal to $\varepsilon_z D_i$ where D_i is the length of the unbonded confinement reinforcement and the analysis proceeds as above that is substituting ε_z for ε_{Sy} in the above example.

Construction of the passive stress/strain for a prism such as in Fig. 5 with specific dimensions, reinforcement arrangements and material properties is illustrated in Fig. 6 where the descending branches are shown as linear for ease of explanation. To construct the passively confined stress/strain relationship, firstly the actively confined stress/strain relationships are constructed as described previously. Let O-A-B represent the stress/strain when the concrete is unconfined that is σ_{conf0} is zero. The active confinement variation O-C-D is when the force in the reinforcement is the IC debonding force P_{IC}, at a confinement reinforcement strain ε_{IC} (Yuan et al., 2001), such that the confinement is σ_{confIC}. The active confinement O-E-F is when the reinforcement is in yield at a force P_{yld} which starts at a strain ε_{yld2} and completes at a strain ε_{yld}. Finally O-G-H is when the reinforcement is about to fracture at a force P_{fr} and a strain ε_{fr}.

On applying the axial stress to the prism in Fig. 5, the stress/strain path follows O-A in Fig. 6 because prior to cracking the lateral reinforcement is to all intents and purposes ineffective in providing confinement. When a sliding plane occurs at Point A, the half crack width Δ at the commencement of IC debonding can be determined from partial-interaction theory (Yuan et al., 2001) as well as the IC debonding force P_{IC} and consequently the confinement σ_{confIC} and the reinforcement strain at which this occurs ε_{IC}. Consequently $S_{lat} = 2\Delta_{IC}$ is known so that ε_{SIC} is known. From O-C-D and ε_{SIC} can be determined the level of stress σ_{SIC} at which this occurs and hence Point I along the descending branch C-D is known. During IC debonding the reinforcement force P_{IC} and the strain in the unbonded bar ε_{IC} remain constant (Yuan et al., 2001). When IC debonding is complete, S_{lat} equals $\varepsilon_{IC} D_i$ so ε_{SIC2} can be determined and consequently point J also along C-D as the confinement has not changed that is σ_{SIC2} can be determined. At the commencement of yield P_{yld} and consequently $\sigma_{confyld}$ at a strain ε_{yld2}, S_{lat} equals $\varepsilon_{yld2} D_i$ from which can be determined ε_{Syld2} and consequently point K which now lies along E-F where the confinement is $\sigma_{confyld}$ and the stress is σ_{Syld2}. Substituting the yield strain at the end of yielding ε_{yld}, gives point L. Finally, at fracture P_{fr} and the fracture strain ε_{fr} can be determined point M. It is worth noting that the sliding strain

such as ε_{Sfr} may be larger than OH. This simply means that the prism has already failed before reaching this point.

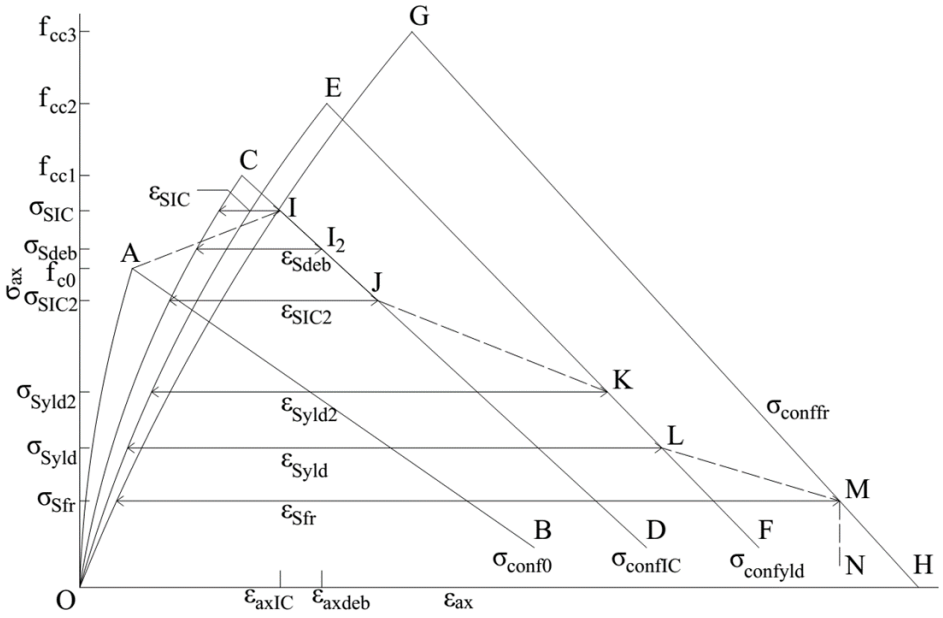

Fig. 6 Theoretical stress-strain of passively confined concrete

From Fig. 6, and for the specific specimen in Fig. 5, the passive confinement stress/strain is given by O-A-I-J-K-L-M-N in Fig. 6. If yielding does not occur such as with FRP reinforcement, then the passive stress/strain is O-A-I-J-M-N. If there is no bond, then it is O-A-K-L-M-N and so on. The analysis can be made more accurate by using intermediate confinement stresses such as at $P_{IC}/2$ or $P_{yld}/2$. It is worth noting that the lateral expansion of concrete will cause the confining stress between the concrete and confinement reinforcement which may enhance the bond between them (Chen et al., 2018). This enhancement has been ignored in this research to give a conservative solution.

Quantification of Confinement

In this section, the quantification of the stress/strain is described. The family of the active stress/strain relationships in Fig. 6 are first derived, then the sliding strains ε_S of all the key points in Fig. 6, after which the axial stresses σ_S. Let us start with the ascending branch of the active stress/strain.

Quantification of the Ascending Branch

The ascending branches of the active stress/strain in Figs. 4 and 6 depend on the peak stress f_{cc} and the strain ε_{cc} at f_{cc}, which are functions of the lateral confining stress σ_{conf}. The strain ε_{cc} at f_{cc} for confined concrete can be written as follows (Chen et al., 2013)

$$\varepsilon_{cc} = \varepsilon_{c0}\left[1 + A_0\left(\frac{\sigma_{conf}}{f_{c0}}\right)\right] \tag{1}$$

where A_0 is a coefficient derived from regression analyses and can be taken as 13.9, ε_{c0} is the strain at f_{c0} for unconfined concrete and can be written as (Chen et al., 2013)

$$\varepsilon_{c0} = 1.74\times10^{-6} f_{c0} + 2.41\times10^{-3} \tag{2}$$

where f_{c0} is in MPa. The peak stress of the confined concrete f_{cc} can be either derived from experimental data or shear-friction material properties. In this research, the latter approach will be applied as follows. Here peak strain model of Chen et al. (Chen et al., 2013) is applied as it has been made independent of specimen size during the regression of terms.

The active stress/strain behaviour is affected by the failure type as shown in Fig. 7. For a slender column with an aspect ratio equal to or more than three, sliding mostly occurs across a single failure plane as shown in Fig. 7(b). For a column whose slenderness is equal to two such as standard cylinder tests, a circumferential sliding plane is the most common failure form as shown in Fig. 7(a) and which, for a given concrete mix, occurs at higher axial loads than those for the single sliding plane (Visintin et al., 2015a). In practical structures the former case, that is the single sliding plane, is more common, and as the circumferential sliding plane can give an unsafe solution as it always represents an upper bound to the confinement, the single sliding plane, also shown in Figs. 2 and 5, will be used in this research and in the validation of test results both the results from the single sliding plane and circumferential sliding plane will be presented to give an indication of scatter.

(a) (b)

Fig. 7 Concentrically loaded concrete column failure: (a) circumferential wedge (b) single sliding plane

From the resolution of the axial load P_{ax} and lateral confining force P_{conf} in Fig. 2, the shear stress τ and normal stress σ_N along and normal to the single shear sliding plane can be written as follows (Ali et al., 2010, Hao, 2017, Visintin et al., 2015b)

$$\tau = \left(\sigma_{ax} - \sigma_{conf}\right)\sin\alpha\cos\alpha \tag{3}$$

$$\sigma_N = \sigma_{ax}\sin^2\alpha + \sigma_{conf}\cos^2\alpha \tag{4}$$

where α is the angle of the shear failure plane as shown in Figs. 2 and 5 and as an example can be assumed to be constant at 26^o (Chen et al., 2015a).

From the shear-friction material properties in Fig. 3, the shear-stress material property τ_m shown as the unbroken lines can be written in the following linear form plotted as dash-dot lines, as follows

$$\tau_m = (A\sigma_N + B)S + C\sigma_N + D \tag{5}$$

where A, B, C and D are coefficients of the unconfined concrete strength f_{c0}. As an example, the linear approximation of the shear-friction material properties derived by Hao (Hao, 2017) are used as follows, although these can be replaced with any model deemed more appropriate or accurate.

When $\sigma_N < \sigma_{N0}$

$$\tau_m = [(0.00112 f_{c0} - 0.337)\sigma_N - 0.000784 f_{c0}^2 + 0.0152 f_{c0} + 0.556]S + 1.50\sigma_N + 0.105 f_{c0} \quad (6)$$

and when $\sigma_{N0} \leq \sigma_N < 3\sigma_{N0}$, then

$$\tau_m = [(0.00112 f_{c0} + 0.0636)\sigma_N - 0.000784 f_{c0}^2 - 0.0620 f_{c0} + 0.556]S + 0.498\sigma_N + 0.298 f_{c0} \quad (7)$$

where, σ_{N0} is the normal stress at the peak axial stress f_{c0} of unconfined concrete and is given as

$$\sigma_{N0} = f_{c0} \sin^2 \alpha \quad (8)$$

It is worth noting that the fundamental mechanics does not depend directly on the material properties so any experimental values of the shear-friction material properties could have been used.

Setting the shear stress from mechanical equilibrium τ from Eq. (3) to the shear-friction material capacity τ_m from Eq. (5) and substituting σ_N from Eq. (4) gives the variation of the axial stress σ_{ax} in Fig. 2 with the interface slip S as

$$\sigma_{ax} = \frac{\sigma_{conf} \sin\alpha \cos\alpha + AS\sigma_{conf} \cos^2\alpha + BS + C\sigma_{conf} \cos^2\alpha + D}{\sin\alpha \cos\alpha - AS \sin^2\alpha - C \sin^2\alpha} \quad (9)$$

Actively confined concrete will reach the peak stress f_{cc} at the onset of sliding. Hence substituting $S = 0$ into Eq. (9) gives the following peak stress f_{cc} of confined concrete as derived from the shear-friction material properties

$$f_{cc} = \frac{\sigma_{conf} \sin\alpha \cos\alpha + C\sigma_{conf} \cos^2\alpha + D}{\sin\alpha \cos\alpha - C \sin^2\alpha} \tag{10}$$

After the quantification of the peak stress f_{cc} and strain ε_{cc}, the ascending branch can be derived from the active stress/strain relationship (Popovics, 1973)

$$\sigma_{ax} = f_{cc} \frac{\frac{\varepsilon_{ax}}{\varepsilon_{cc}} r_c}{r_c - 1 + \left(\frac{\varepsilon_{ax}}{\varepsilon_{cc}}\right)^{r_c}} \tag{11}$$

where f_{cc} and ε_{cc} can be obtained from Eqs. (10) and (1) and r_c is the ductility factor which can be expressed as

$$r_c = \frac{E_c}{E_c - \frac{f_{cc}}{\varepsilon_{cc}}} \tag{12}$$

where the concrete elastic modulus E_c is a material property and can be expressed in MPa as (ACI 1992)

$$E_c = 3320\sqrt{f_{c0}} + 6900 \tag{13}$$

Thus, for a specific lateral confining stress σ_{conf}, the ascending branch of the active stress/strain can be generated from Eq. (11). As an example and for ease of analysis, the ascending branch of the active stress/strain can be linearized as

$$\varepsilon_{ax} = \sigma_{ax} \frac{\varepsilon_{cc}}{f_{cc}} \tag{14}$$

where f_{cc} and ε_{cc} can be obtained from Eqs. (10) and (1).

Quantification of the Descending Branch

The vertical component S_{ax} of the slip S in Fig. 2 divided by L_{def} is the equivalent strain due to slip ε_S that is

$$\varepsilon_S = \frac{S\cos\alpha}{L_{def}} \tag{15}$$

Bearing in mind that there is also the additional material strain ε_m in Fig. 4 then the total axial strain is given by (Visintin et al., 2015a)

$$\varepsilon_{ax} = \varepsilon_m + \varepsilon_S = \varepsilon_m + \frac{S\cos\alpha}{L_{def}} \tag{16}$$

where, as an example, the material strain ε_m can also be obtained from Eq. (14) which can be substituted into Eq. (16) as follows

$$\varepsilon_{ax} = \sigma_{ax}\frac{\varepsilon_{cc}}{f_{cc}} + \frac{S\cos\alpha}{L_{def}} \tag{17}$$

Substituting S from Eq. (17) into Eq. (9) gives the relationship between σ_{ax} and the axial strain ε_{ax} in Fig. 4. The descending branch can now be constructed.

As an example, let us take the active stress/strain in Fig. 4 shown as O-E-G-F. First fix the slip S at a specific value S_{ax2} and the confinement σ_{conf} at σ_{conf2}. The axial stress σ_{ax2} can be derived from Eq. (9) by substituting σ_{conf2} and S_{ax2} to give point G. The material strain ε_{m2} is fixed by finding the point from the ascending branch O-E whose axial stress equals σ_{ax2}. The axial strain ε_{ax2} at point G is given by Eq. (17).

Linking points E and G in Fig. 4, that is assuming a linear falling branch EG, gives the falling branch of the active stress/strain for the lateral confining stress σ_{conf2} as follows

$$\frac{\sigma_{ax} - \sigma_{ax2}}{f_{cc} - \sigma_{ax2}} = \frac{\varepsilon_{ax} - \varepsilon_{ax2}}{\varepsilon_{cc} - \varepsilon_{ax2}} \tag{18}$$

where σ_{ax2}, ε_{ax2}, f_{cc} and ε_{cc} can be obtained from Eqs. (9), (17), (10) and (1).

Quantification of the Equivalent Strain ε_S

In order to derive the equivalent strain ε_S in Fig. 4 which is equal to S_{ax}/L_{def} as shown, the axial component of the slip S_{ax} is required, which is also a function of the lateral component of slip S_{lat} as shown in Fig. 5. Let us start with the derivation of S_{lat} and consider the passive confinement reinforcement A-B in Fig. 5 as an example, which is shown in Fig. 8 in detail. The reinforcement is assumed to be anchored at point A due to the reinforcement angle bend between A-C and A-B, where A-C is the reinforcement perpendicular to the plane in Fig. 5.

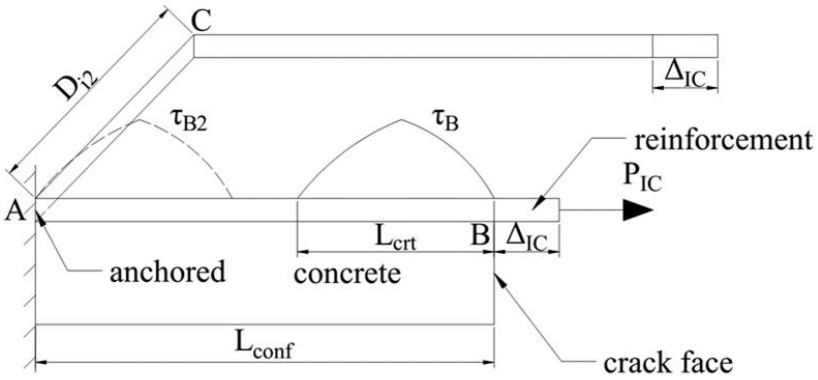

Fig. 8 Bond force first reaches IC debonding resistance P_{IC}

Bond-Slip

The confinement across the sliding plane in Figs. 5 and 8 depends on the bond-slip (τ_B/δ) between the confinement reinforcement A-B and the adjacent concrete which is a material property and can be any shape. As an example, the bilinear bond-slip material properties in Fig. 9 for plate reinforcement have the following parameters τ_{Bmax}, δ_1 and δ_{max} as shown which can be written as (Seracino et al., 2007)

$$\tau_{B\max} = \left(0.802 + 0.078\phi_f\right) f_{c0}^{0.6} \tag{19}$$

$$\delta_1 = 0 \tag{20}$$

$$\delta_{\max} = \frac{0.976\phi_f^{0.526}}{0.802 + 0.078\phi_f} \tag{21}$$

in which the units are in mm and N and where φ_f is the aspect ratio of the interface failure plane as shown in Fig. 10 and which can be written as

$$\phi_f = \frac{d_f}{b_{f2}} \tag{22}$$

where d_f and b_{f2} are the thickness of the failure plane and the length of the failure plane parallel to the concrete surface as shown, and which are equal to 1 mm and b_f + 2 mm (where b_f is the width of the reinforcement plate as shown) respectively.

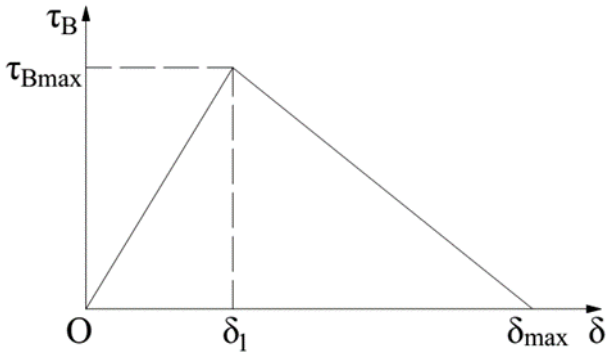

Fig. 9 Bond-slip material properties

IC debonding

When the bond stress τ_B in Fig. 9 is fully developed along the confinement reinforcement length L_{conf} as shown in Fig. 8, the confinement force P_{conf} will reach its maximum value P_{IC} at a crack face slip Δ_{IC}, where P_{IC} and Δ_{IC} can be written as follows (Seracino et al., 2007, Yuan et al., 2004, Yuan et al., 2001)

$$P_{IC} = \sqrt{\tau_{B\max}\delta_{\max}}\sqrt{L_{per}E_rA_r} \tag{23}$$

$$\Delta_{IC} = \delta_{\max} \tag{24}$$

where, τ_{Bmax} and δ_{max} are shown in Fig. 9 which can be obtained from Eqs. (19) and (21) respectively, E_r is the modulus of the reinforcement, and L_{per} and A_r are the total length of the potential debonding failure plane and the total cross-section area of the reinforcement respectively. As an example, the IC debonding resistance P_{IC} for the plate reinforcement can be written as (Seracino et al., 2007)

$$P_{IC} = 0.85\phi_f^{0.25} f_{c0}^{0.33} \sqrt{L_{per} E_r A_r} \tag{25}$$

where φ_f can be obtained from Eq. (22) and L_{per} is shown in Fig. 10. The length of reinforcement required to develop P_{IC} is referred to as L_{crt} as shown in Fig. 8, which can be written as (Seracino et al., 2007)

$$L_{crt} = \frac{\pi}{2\lambda} \tag{26}$$

where the parameter λ can be expressed as

$$\lambda = \sqrt{\frac{\tau_{B\max} L_{per}}{\delta_{\max} E_r A_r}} \tag{27}$$

It is worth noting that the maximum width b_f in Fig. 10 of the plate reinforced specimens in the database by Seracino et al. (Seracino et al., 2007) to derive P_{IC} equals 100 mm. The width b_f of the plate reinforcement along the shear failure plane may be outside this range of b_f such that the reinforcement plate will be cut into plates with width $b_f \leq 100$ mm. The IC debonding resistance P_{IC} can be obtained by adding P_{IC} of all cut plates. For instance, if H_{sl} in Fig. 5 is assumed to be 350 mm and the plate along the shear failure plane will be cut into three 100-mm width plates and one 50-mm width plate. The IC debonding resistance P_{IC} can be derived for each of these four plates which are added to obtain P_{IC} for reinforcement along the whole shear failure plane.

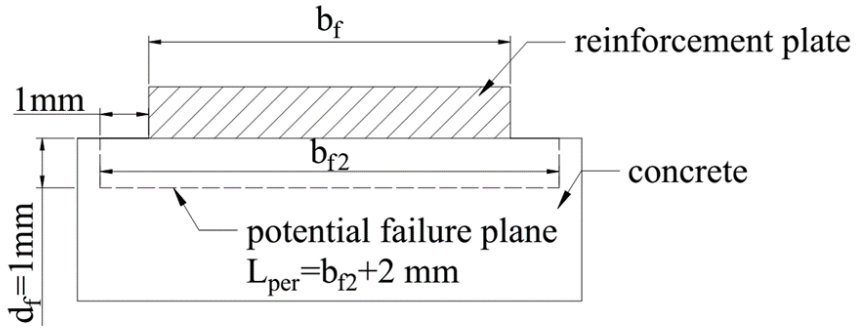

Fig. 10 Failure plane of FRP plate bonded to concrete

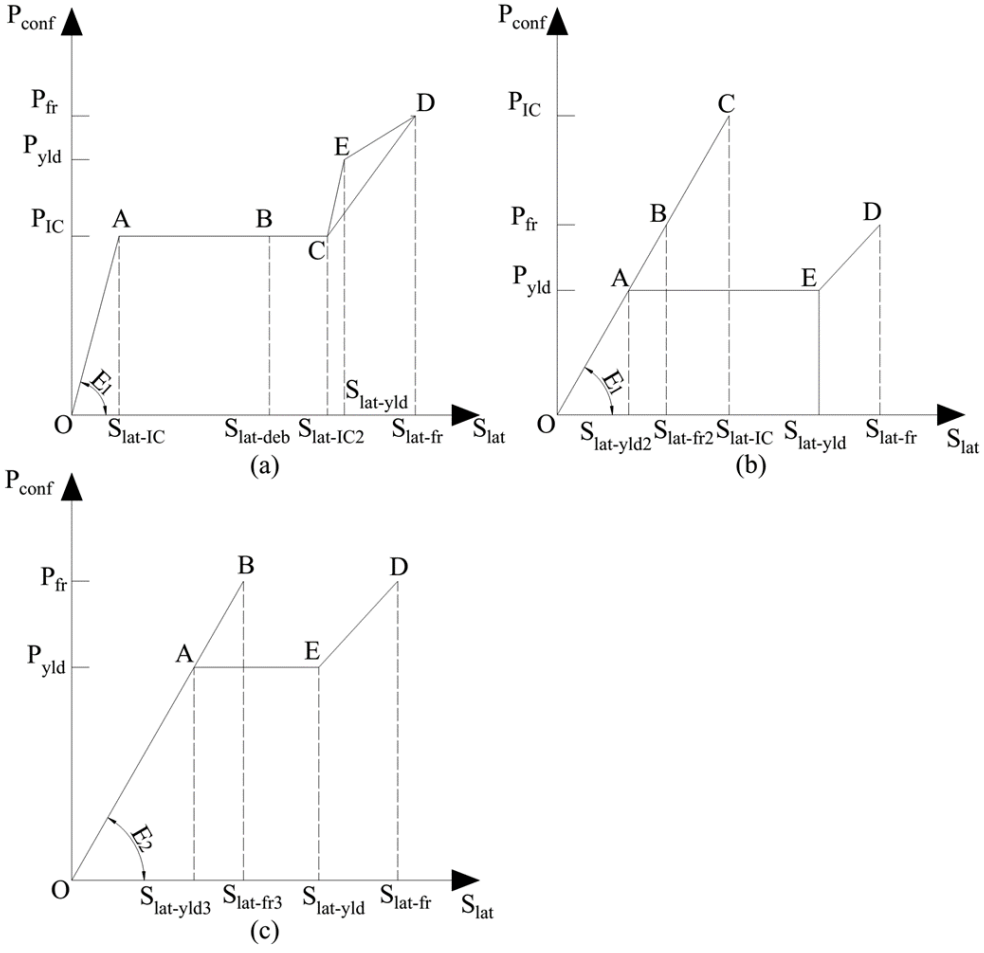

Fig. 11 P_{conf} and S_{lat} relationship for: (a) debonding prior to fracture or yield and $L_{crt} \leq L_{conf}$; (b) fracture or yield without debonding and $L_{crt} \leq L_{conf}$; (c) $L_{crt} > L_{conf}$

The confinement behaviour is determined by the relative values between L_{crt} and L_{conf} in Fig. 8 as well as that between the IC debonding resistance P_{IC}, the yield capacity P_{yld} and the fracture capacity P_{fr}. In Fig. 11, the relationships between P_{conf} and S_{lat} are shown. It is necessary to derive the relationship between P_{conf} and S_{lat} to quantify confinement as follows.

Debonding occurs prior to yielding or fracture when $L_{conf} \geq L_{crt}$

When P_{IC} is less than P_{yld} or P_{fr} and $L_{conf} \geq L_{crt}$ in Fig. 8, then debonding occurs prior to yielding or fracture which is the case shown in Fig. 11(a). Debonding starts at point A in Fig. 11(a) when from Eq. (24) the crack face slip reaches $\Delta_{IC} = \delta_{max}$ which can be obtained from Eq. (21). Adding the crack face slips from both crack faces gives the horizontal component of slip $S_{lat\text{-}IC}$ as

$$S_{lat-IC} = 2\Delta_{IC} \tag{28}$$

A further increase in the crack face slip Δ above Δ_{IC} will cause the bond stress distribution to move towards the plate end until it reaches the plate end which is plotted as the dashed line in Fig. 8. The confinement force P_{conf} along the unbonded reinforcement is constant at P_{IC} and subsequently at a strain ε_{IC}; this is point B in Fig. 11(a) such that Δ_{deb} equals $\Delta_{IC} + \varepsilon_{IC}$ ($L_{conf} - L_{crt}$). Adding the crack face slips at both sides of the crack face gives the lateral expansion $S_{lat\text{-}deb}$ as

$$S_{lat-deb} = 2\Delta_{IC} + \varepsilon_{IC}\left(D_i - 2L_{crt}\right) \tag{29}$$

A further increase in Δ and consequently S_{lat} will cause a reduction of the confinement force due to bond and an increase of that due to anchorage. For convenience, the confinement force P_{conf} is assumed to be kept constant at P_{IC} until P_{IC} is fully developed at a strain ε_{IC}, which is point C in Fig. 11(a), where the crack face slip Δ_{IC2} equals $\varepsilon_{IC}L_{conf}$ and $S_{lat\text{-}IC2}$ is

$$S_{lat-IC2} = \varepsilon_{IC} D_i \tag{30}$$

Further increasing Δ and consequently S_{lat} will cause an increase in reinforcement strain and consequently an increase in P_{conf} due to anchorage. The confinement reinforcement may

either directly fracture at a strain ε_{fr}, point D in Fig. 11(a), or yield at a strain ε_{yld} at point E and then fracture at point D. The crack face slip Δ_{yld} at point E and Δ_{fr} at point D equal $\varepsilon_{yld}L_{conf}$ and $\varepsilon_{fr}L_{conf}$ respectively such that the lateral component of slips $S_{lat\text{-}yld}$ and $S_{lat\text{-}fr}$ can be written as follows

$$S_{lat-yld} = \varepsilon_{yld} D_i \tag{31}$$

$$S_{lat-fr} = \varepsilon_{frac} D_i \tag{32}$$

It is worth noting in Fig. 11(a) that in the example and for ease of analysis it is assumed all the relationships between P_{conf} and S_{lat} are piecewise linear.

Yielding or fracture occurs prior to debonding when $L_{conf} \geq L_{crt}$

When P_{IC} is larger than P_{fr} or P_{yld} and $L_{conf} \geq L_{crt}$, debonding does not occur as the confinement reinforcement will either yield or fracture before the bond stress is fully developed. However, point C in Fig. 11(b) is fixed and a linear variation O-A-B-C is assumed, for ease of analysis, with a stiffness $E_1 = P_{IC}/(2\Delta_{IC})$. Subsequently, when the confinement reinforcement yields or fractures at points A and B, S_{lat} can be written as

$$S_{lat-yld2} = 2\Delta_{IC} \frac{P_{yld}}{P_{IC}} \tag{33}$$

$$S_{lat-fr2} = 2\Delta_{IC} \frac{P_{fr}}{P_{IC}} \tag{34}$$

where, from Eq. (24), Δ_{IC} equals δ_{max} which can be obtained from Eq. (21) and P_{IC} can be obtained from Eq.(25). Consequently from Eqs. (33) and (34), the crack face slip at both sides of the crack face at points A and B in Fig. 11(b) can be written as $\Delta_{yld2} = \Delta_{IC}P_{yld}/P_{IC}$ and $\Delta_{fr2} = \Delta_{IC}P_{fr}/P_{IC}$. The confinement reinforcement may either directly fracture at point B, or yield at point A then complete yielding at point E and then ultimately fracture at point D. At points E and D, P_{conf}, Δ and S_{lat} are equal to that of points E and D in Fig. 11(a) such that $S_{lat\text{-}yld}$ and $S_{lat\text{-}fr}$ at these two points can be obtained from Eqs. (31) and (32) respectively.

The critical length L_{crt} may be less than L_{conf} on one side but not on the other. For instance, L_{crt} may be less than the confinement reinforcement length BC in Fig. 5 and larger than the confinement reinforcement length AB. At the commencement of debonding, yielding or fracture, $S_{lat\text{-}IC}$, $S_{lat\text{-}yld2}$ or $S_{lat\text{-}fr2}$ from Eqs. (28), (33) and (34) may be less than $2\Delta_{IC}$, $2\Delta_{yld2}$ or $2\Delta_{fr2}$ because on one side the crack face slip is Δ_{IC}, Δ_{yld2} or Δ_{fr2} but on the other side it may be less due to the end anchor. Hence these S_{lat} values can be used as they give a conservative solution. However, the lateral expansions S_{lat} of the other points B, C, E and D in Fig. 11(a) and points E and D in Fig. 11(b) from Eqs. (29), (30), (31) and (32) still apply directly.

Yielding or fracture occurs prior to debonding when $L_{conf} < L_{crt}$

The case where $L_{conf} < L_{crt}$ is shown in Fig. 12(c) where the anchor to the reinforcement is on the left and the crack face on the right as shown. The variations in bond stress τ_B and slip δ are shown in Figs. 12(a) and (b) respectively. The slip δ on the left is zero due to the anchor such that the bond stress there is also zero. These variations are identical to that which occurs in a multi-crack analysis (Muhamad et al., 2012, Oehlers et al., 2010) with a crack spacing S_p of $2L_{conf}$ in Figs. 12(d) and (e) where by symmetry the midway slip between crack faces equals zero. Hence the P_{conf}/Δ relationship from a multi-crack analysis is directly applicable.

Let us first take the yield case as an example. The crack face slip Δ_{yld3} at point A in Fig. 11(c) when the confinement reinforcement first reaches P_{yld} can be derived through the following mechanics proposed by Sturm et al. (Sturm et al., 2018) where

$$\Delta_{yld3} = \frac{P_{yld}}{\lambda E_r A_r} \tanh\left(\frac{\lambda S_p}{2}\right) \tag{35}$$

where S_p is the primary crack spacing that equals $2L_{conf}$ as shown in Fig. 12(d) and which will be quantified later, and where λ is the variation in the slip parameter which can be written as follows

$$\lambda = \sqrt{\beta k} \tag{36}$$

where the prism parameter β and bond-slip stiffness k can be expressed as

$$\beta = L_{per}\left(\frac{1}{E_r A_r} + \frac{1}{E_c A_c}\right) \tag{37}$$

$$k = \frac{\tau_{B\max}}{\delta_1} \tag{38}$$

where L_{per} has already been defined through Fig. 10 and where A_c is the cross-section area of concrete which interacts with the reinforcement in the tension stiffening analysis. It should be noted that for plate reinforcement, the area of the reinforcement A_r is much smaller than that of the concrete A_c such that $1/E_cA_c$ in Eq. (37) can be assumed to be zero (Ali et al., 2008).

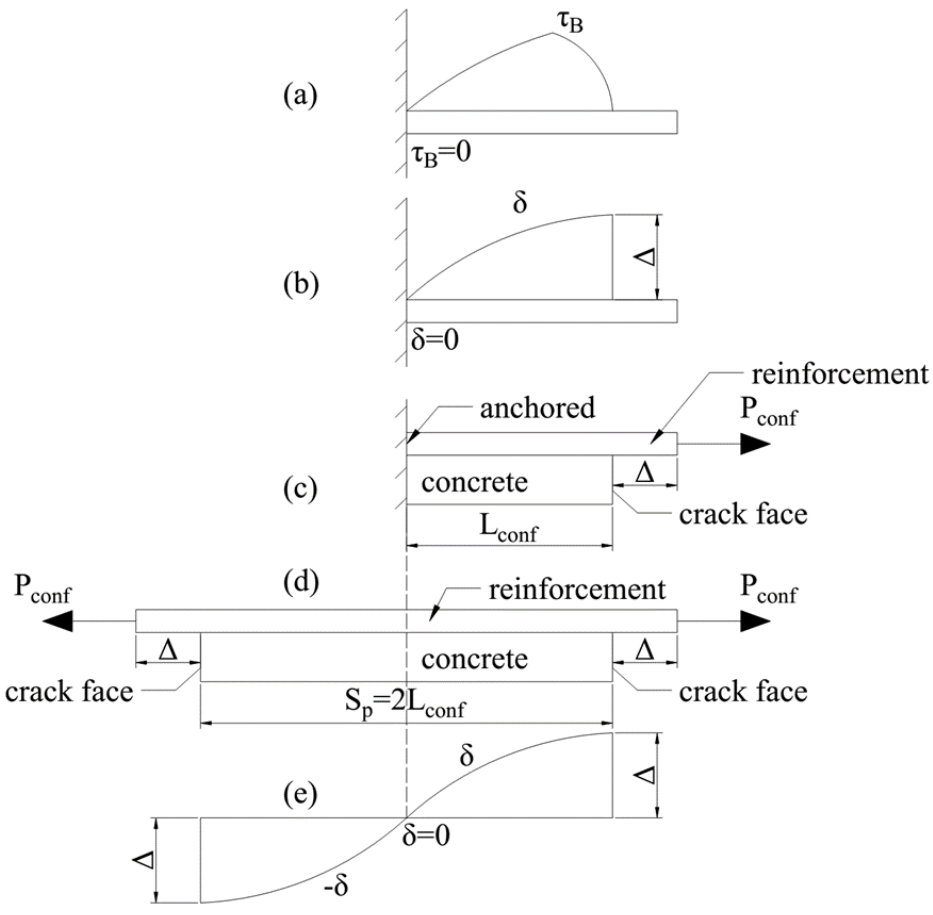

Fig. 12 (a) to (c) $L_{conf}<L_{crt}$ and (d) to (e) multi-crack analysis

Consider an arbitrary plane crossing the sliding plane, such as A-B-C in Fig. 5 where the crack face is x from the nearest anchor. Adding the crack face slips Δ_{yld3} at point A in Fig. 11 (c) from both sides of the crack face gives the lateral component of slip $S_{lat\text{-}yld3}$ at point A as follows (Sturm et al., 2018)

$$S_{lat-yld3} = \frac{P_{yld}}{\lambda E_r A_r} \tanh\left(\frac{2\lambda x}{2}\right) + \frac{P_{yld}}{\lambda E_r A_r} \tanh\left[\frac{2\lambda\left(D_i - x\right)}{2}\right] \tag{39}$$

where x is the confinement reinforcement length AB in Fig. 5. Rearranging and simplifying Eq. (39) gives

$$S_{lat-yld3} = \frac{P_{yld}}{\lambda E_r A_r}\left\{\frac{2\sinh\left(D_i\lambda\right)}{\cosh\left(D_i\lambda\right) + \cosh\left[\lambda\left(D_i - 2x\right)\right]}\right\} \tag{40}$$

The value of $S_{lat\text{-}yld3}$ in Eq. (40) will reach its maximum at $x = D_i/2$ (Oldham et al., 2010) which means the crack is in the middle of the length D_i such as in the plane D-E-F in Fig. 5. Only considering this case gives a conservative solution and simplifies the analysis. Hence substituting $x = D_i/2$ into Eq. (40) gives

$$S_{lat-yld3} = \frac{P_{yld}}{\lambda E_r A_r}\left[\frac{2\sinh\left(D_i\lambda\right)}{\cosh\left(D_i\lambda\right) + 1}\right] \tag{41}$$

which is the crack width at the onset of yielding.

After yielding at point A in Fig. 11(c), the confinement reinforcement will completely yield at point E and then fracture at point D. Furthermore, S_{lat} at these points are the same as that of points E and D in Fig. 11(a) such that $S_{lat\text{-}yld}$ and $S_{lat\text{-}fr}$ can be obtained from Eqs. (31) and (32) respectively.

Similarly for the fracture case, $S_{lat\text{-}fr3}$ at P_{fr} that is point B in Fig. 11(c) can be derived by substituting P_{fr} for P_{yld} in Eq. (41) as follows

$$S_{lat-fr3} = \frac{P_{fr}}{\lambda E_r A_r}\left[\frac{2\sinh\left(D_i\lambda\right)}{\cosh\left(D_i\lambda\right)+1}\right] \tag{42}$$

Equivalent strain ε_S

The lateral expansions S_{lat} of all the key points in Fig. 6 have been quantified above and can be employed to derive the sliding strain ε_S as follows

$$\varepsilon_S = \frac{S\cos\alpha}{L_{def}} = \frac{S_{lat}}{\tan\alpha L_{def}} \tag{43}$$

In summary, for the fracture case in Fig. 11(a), the loading path will follow O-A-I-I_2-J-M-N in Fig. 6, and S_{lat} at the key points I, I_2, J and M can be obtained from Eqs. (28), (29), (30) and (32) respectively. For the yield case in Fig. 11(a), the loading path will follow O-A-I-I_2-J-L-M-N in Fig. 6, and S_{lat} at the key points I, I_2, J, L and M can be obtained from Eqs. (28), (29), (30), (31) and (32). For the fracture case in Fig. 11(b), debonding does not occur and the falling branch C-D in Fig. 6 does not exist such that the loading path will follow O-A-M-N in Fig. 6 where S_{lat} at point M can be obtained from Eq. (34). For the yield case in Fig. 11(b) the loading path will follow O-A-K-L-M-N in Fig. 6 where S_{lat} at points K, L and M can be obtained from Eqs. (33), (31) and (32) respectively. The case in Fig. 11(c) is similar to the case in Fig. 11(b), the only difference is that the S_{lat} at point M in Fig. 6 for the fracture case and S_{lat} at point K for the yielding case can be obtained from Eqs. (42) and (41) respectively.

Quantification of the Stress σ_S

The analysis of the confining stress from stirrups σ_{const} and plates σ_{conpl} are shown in Fig. 13 as these are required to derive the axial stress σ_s in Fig. 6. Consider the rectangular-section column reinforced by stirrups in Figs. 13(a) and (c). The crack width S_{lat} will cause the confinement force P_{st} in the stirrups. The total tensile force in the stirrup legs crossing the crack face $2P_{st}$ is balanced by the compressive force from concrete across the crack face $P_{st\text{-}comp}$ and is of equal magnitude. It is assumed that the cover concrete acts as unconfined concrete and that the lateral confining stress σ_{const} will act within the stirrups that is within

the width D_{i2} in Fig. 13(a). As shown in Fig. 13(c), the confinement reinforcement force acts along the region within a height equal to the stirrups spacing S_s such that the confining stress due to stirrups is

$$\sigma_{const} = \frac{2P_{st}}{S_s D_{i2}} \tag{44}$$

Similarly, the analysis of a plated concrete column is shown in Figs. 13(b) and (d). All the concrete is encased, such that the confinement force P_{pl} from a plate is acting on all the concrete within the width D_{i2}. In addition, P_{pl} is acting along the whole sliding plane that is over a depth $H_{sl} = D_i/\tan\alpha$ as shown in Fig. 5. Hence the confining stress due to the plate is

$$\sigma_{conpl} = \frac{2P_{pl}\tan\alpha}{D_i D_{i2}} \tag{45}$$

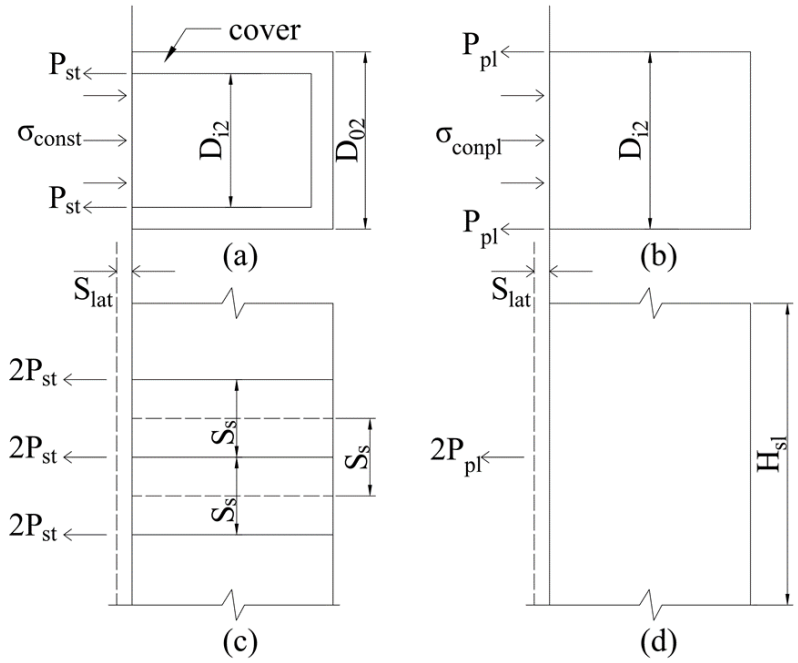

Fig. 13 (a) and (c) stirrup confined concrete and (b) and (d) plated concrete members

The key points in Fig. 6 can now be fixed by fitting the horizontal dimension that is the sliding strain ε_S within the specific ascending branch and descending branch already derived.

For instance, fitting ε_{SIC} between ascending branch O-C and descending branch C-D in Fig. 6 gives the point I.

The following axial stress σ_S can be derived by substituting $S = S_{lat}/\sin\alpha$ and lateral confining stress σ_{conf} from Eq. (44) or (45) into Eq. (9)

$$\sigma_S = \frac{\sigma_{conf} \sin\alpha\cos\alpha + \left(A\frac{S_{lat}}{\sin\alpha} + C\right)\sigma_{conf}\cos^2\alpha + B\frac{S_{lat}}{\sin\alpha} + D}{\sin\alpha\cos\alpha - \sin^2\alpha\left(A\frac{S_{lat}}{\sin\alpha} + C\right)} \tag{46}$$

Substituting S_{lat} for all the key points in Fig. 6 gives the axial stress σ_S of these points, which can be substituted into Eq. (43) to derive sliding strain ε_S. Adding the addition material strain from ε_m from Eq. (14) gives the total axial strain ε_{ax} as follows

$$\varepsilon_{ax} = \sigma_S \frac{\varepsilon_{cc}}{f_{cc}} + \frac{S_{lat}}{\tan\alpha L_{def}} \tag{47}$$

where f_{cc} and ε_{cc} can be obtained from Eqs. (10) and (1). After deriving the axial stress and strain of all the key points, linking adjacent key points gives the passive stress/strain.

The flowchart of the whole procedure is shown in Fig. 14 and will be described by taking stage I-I_2 in Fig. 6 as an example, where debonding starts at point I and is completed at I_2 as illustrated in Fig. 8; this is the path A-B in Fig. 11(a). (1) First derive the lateral confining stress σ_{confIC} at P_{IC} from Eq. (44) or (45). (2) Substitute σ_{confIC} into Eqs. (10) and (1) to derive f_{cc} and ε_{cc}. (3) Substitute σ_{confIC} as well as $S_{lat\text{-}IC}$ and $S_{lat\text{-}deb}$ from Eqs. (28) and (29) respectively into Eq. (46) gives the axial stress σ_{SIC} and σ_{Sdeb}. (4) Substitute f_{cc}, ε_{cc}, $S_{lat\text{-}IC}$ and $S_{lat\text{-}deb}$ as well as the derived axial stress σ_{SIC} and σ_{Sdeb} into Eq. (47) gives the axial strain ε_{axIC} and ε_{axdeb}. (5) Linking two points (ε_{axIC}, σ_{SIC}) and (ε_{axdeb}, σ_{Sdeb}) gives the passive stress/strain I-I_2 as follows

$$\frac{\sigma_{ax} - \sigma_{SIC}}{\sigma_{Sdeb} - \sigma_{SIC}} = \frac{\varepsilon_{ax} - \varepsilon_{axIC}}{\varepsilon_{axdeb} - \varepsilon_{axIC}} \tag{48}$$

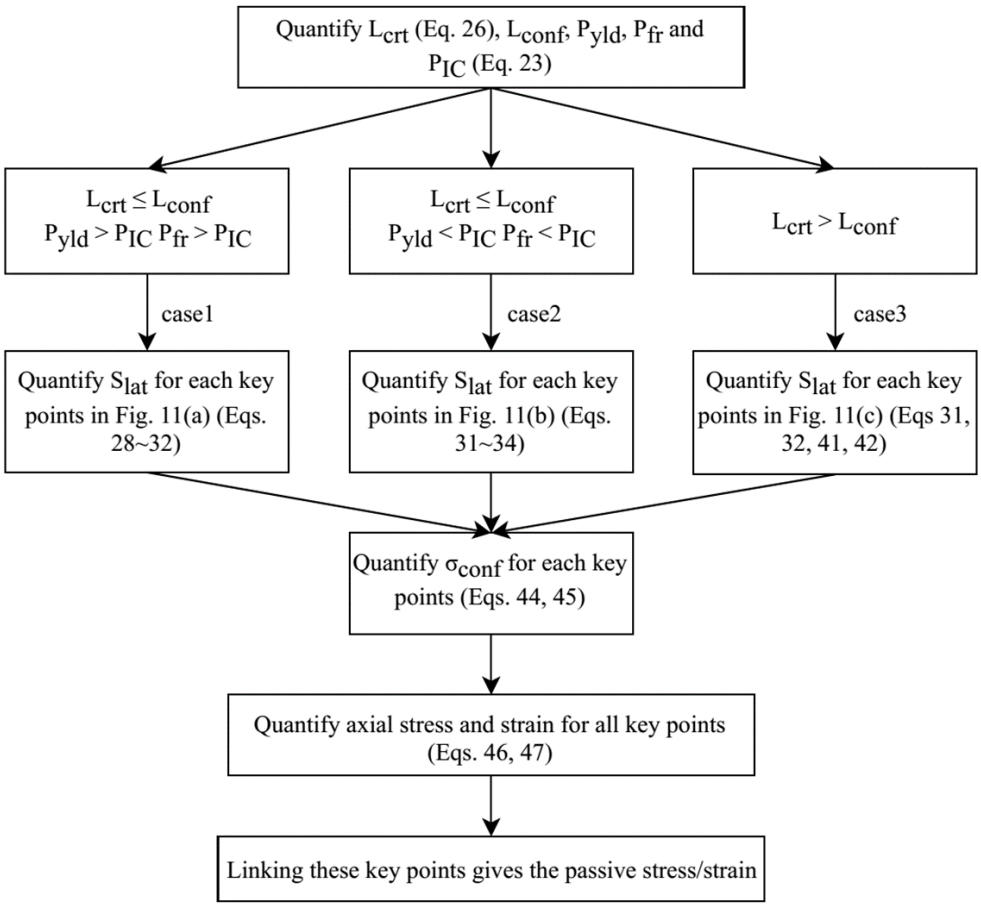

Fig. 14 Flowchart describing the generation of the passive stress/strain

Validation of Confinement Model

To validate the approach consider the FRP wrapped rectangular concrete prisms that were tested under concentric load by Abbasnia and Ziaadiny (2015), Carrazedo and de Hanai (2016), Lam and Teng (2003), Wang et al. (2012), Wang et al. (2011a) and Wu and Wei (2010) in Fig. 15, Fig. 16, Fig. 17, Fig. 18 and Fig. 19, and the rectangular prisms confined by stirrups shown in Fig. 20 (Basset and Uzumeri, 1986, Li et al., 2001). The results of these tests have been simulated using both the single sliding plane and the circumferential wedge and are compared with approaches to predict FRP (Wei and Wu, 2012, Youssef et al., 2007) and stirrup (Mander et al., 1988) confined stress/strain relationships. Full details of the simulated specimens are given in Appendix 2 but importantly the validation covers a range of specimen slenderness. It is worth noting that the gauge length over which the strains were

measured was referred to as L_{gl} which is, therefore, substituted for L_{def} in Eq. (47) to derive the stress/strain.

Derivation of Stress/Strain from Theoretical Approach

As an example, Fig. 15 compares the experimentally derived passive stress/strain relationship for specimen G2L1 with the proposed theoretical approach. Let us consider the steps in the theoretical analysis:

1. From Eq. (26) L_{crt} equals 44.3 mm, and $D_i/2$ equals 62.5 mm. From Eq. (25), P_{IC} equals 41790 N and at P_{IC} the confinement reinforcement strain ε_{IC} equals 0.00400. The fracture capacity of the plate reinforcement along the shear failure plane P_{fr} equals $f_p t_{FRP} H_{sl}$ = 185800 N, where the FRP fracture stress f_p equals 4340 MPa, the FRP thickness t_{FRP} equals 0.167 mm and the height of the plate reinforcement along the shear failure plane H_{sl} in Fig. 5 equals 256.3 mm. As $L_{crt} < D_i/2$ and $P_{IC} < P_{fr}$, then the variation in Fig. 11(a) applies so the loading path will follow O-A-I-I_2-J-M in Fig. 6 as shown in Fig. 15.
2. Let us start with the active stress/strain O-C-I-I_2-J for σ_{confIC} as shown in Figs. 6 and 15. Substituting P_{IC} into Eq. (45) gives the lateral confining stress at P_{IC} σ_{confIC} = 2.61 MPa, which can be substituted into Eqs. (1) and (10) to derive $\varepsilon_{cc\text{-}C}$ = 0.00609 and $f_{cc\text{-}C}$ = 31.4 MPa at point C. The crack width $S_{lat\text{-}IC}$, $S_{lat\text{-}deb}$ and $S_{lat\text{-}IC2}$ at points I, I_2 and J can be obtained by substituting Δ_{IC} = 0.107 mm from Eqs. (21) and (24) as well as ε_{IC} = 0.00400, D_i = 125 mm and L_{crt} = 44.3 mm into Eqs. (28), (29) and (30). Consequently $S_{lat\text{-}IC}$, $S_{lat\text{-}deb}$ and $S_{lat\text{-}IC2}$ equal 0.214, 0.359 and 0.500 mm respectively which, as well as $\varepsilon_{cc\text{-}C}$ and $f_{cc\text{-}C}$, can be substituted into Eqs. (46) and (47) to derive the axial stresses σ_S as 30.2 MPa, 29.4 MPa and 28.5 MPa and the axial strains ε_{ax} as 0.00937, 0.0116 and 0.0138 at points I ,I_2 and J respectively. Linking points O, C, I, I_2 and J gives the active stress/strain O-C-I-I_2-J for σ_{confIC}.
3. Then comes the active stress/strain O-G-M for σ_{confFr} as shown in Figs. 6 and 15. Let us start with the confinement reinforcement force at fracture. In the experiments (Wang et al., 2012, Wang et al., 2011a), concrete prisms will fail before the confinement reinforcement strain reaches material rupture strain ε_{fr} = 0.0178 due to stress concentraction at the section corner. Consequently at failure

the average lateral fracture strain of reinforcement recorded in the experiments ε_{fr2} = 0.00459 will be substituted for ε_{fr} in Eq. (32) to obtain $S_{lat\text{-}fr2}$ = 0.574. As ε_{fr2} is larger than ε_{IC} = 0.00400 at point C in Fig. 11(a), the confinement reinforcement has completely debonded. Hence the confinement reinforcement stress σ_{fr2} equals $E_{FRP}\varepsilon_{fr2}$ = 1122 MPa where E_{FRP} is the elastic modulus of FRP and subsequently confinement force along the shear failure plane P_{fr2} equals $\sigma_{fr2}t_{FRP}H_{sl}$ = 48040 N. Substituting P_{fr2} into Eq. (45) gives the lateral confining stress at P_{fr2} σ_{conffr} = 3.00 MPa, which can be substituted into Eqs. (1) and (10) to derive $\varepsilon_{cc\text{-}G}$ = 0.00663 and $f_{cc\text{-}G}$ = 32.4 MPa at point G in Figs. 6 and 15. Substituting $S_{lat\text{-}fr2}$, $\varepsilon_{cc\text{-}G}$ and $f_{cc\text{-}G}$ into Eqs. (46) and (47) gives the axial stress σ_S = 29.3 MPa and the axial strain ε_{ax} = 0.0154 respectively at point M. Linking points O, G and M gives the active stress/strain O-G-M for σ_{conffr}.

4. At point A in Figs. 6 and 15, the axial stress f_{c0} equals 24.4 MPa and the axial strain ε_{c0} = 0.00245 can be obtained from Eq. (2). Linking points O-A-I-I_2-J-M gives the passive stress-strain.

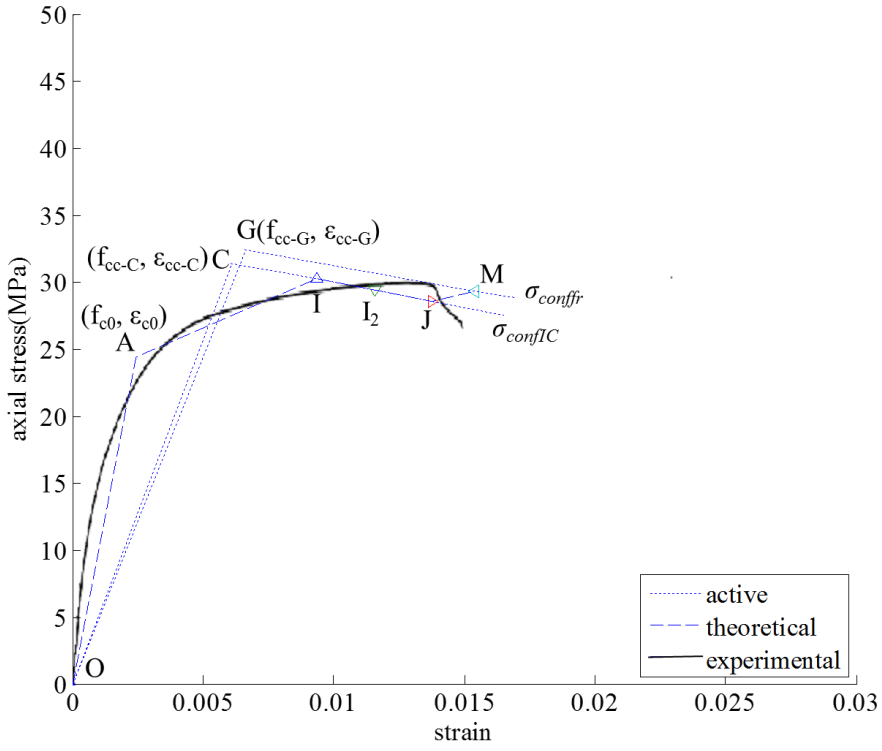

Fig. 15 Theoretical analysis of specimen G2L1

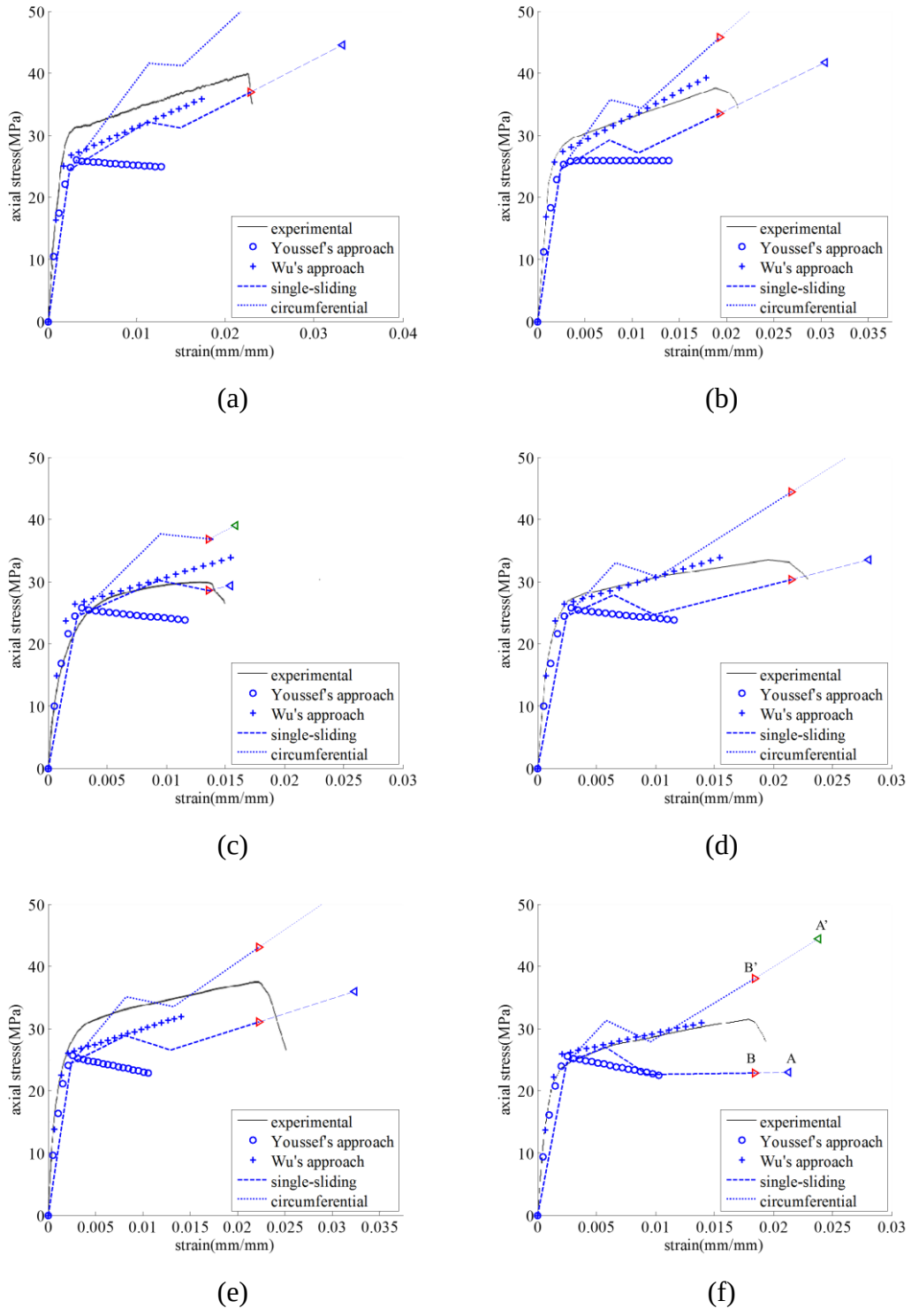

Fig. 16 Validation with FRP reinforced specimens (aspect ratio ≥ 3): (a) G1L1; (b) G1L2; (c) G2L1; (d) G2L2; (e) G3L1; (f) G3L2;

With regard to the stirrups reinforced concrete prisms in Fig. 20, the case in Fig. 11(c) applies as $L_{crt} > L_{conf}$. The passive stress/strain will follow O-A-K-F in Fig. 6 and is described as

follows. Sliding occurs at point A as shown and then the confinement reinforcement yields at point K. The strain hardening effect of stirrups is ignored for stirrups reinforced concrete prisms to achieve a conservative solution. Hence, after yielding the confinement reinforcement force P_{conf} is assumed to be constant at P_{yld} and subsequently the confinement $\sigma_{confyld}$ and consequently the falling branch K-F. This is also shown as O-A-K-F in Fig. 20(a) as an example.

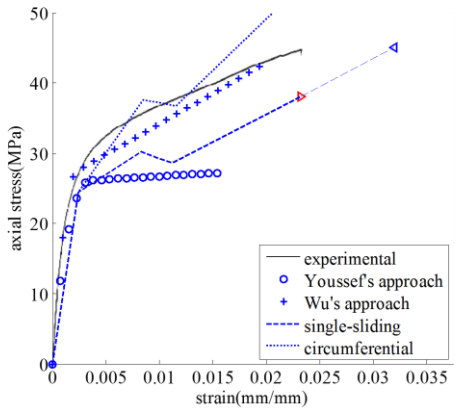

(a)

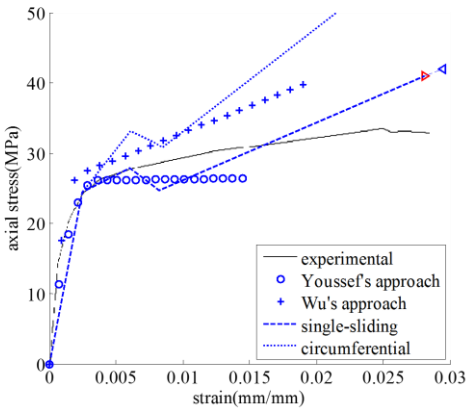

(b)

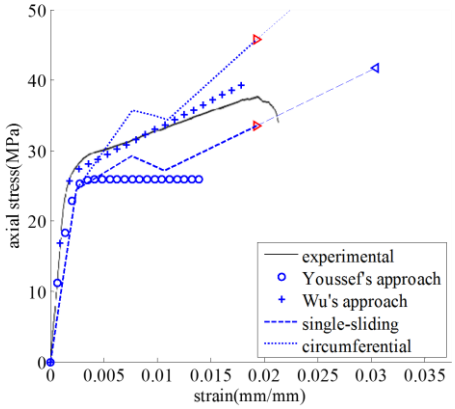

(c)

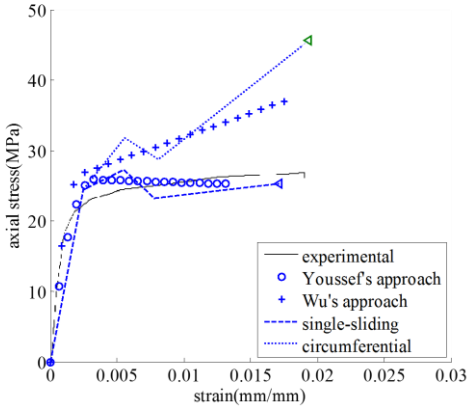

(d)

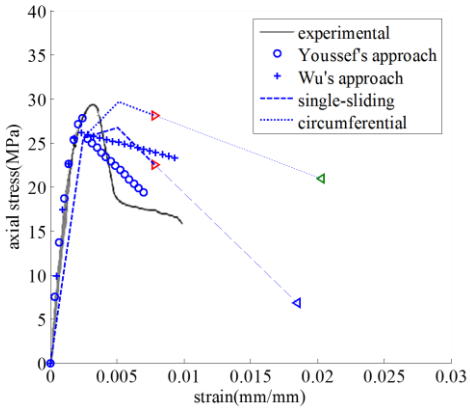

(e)

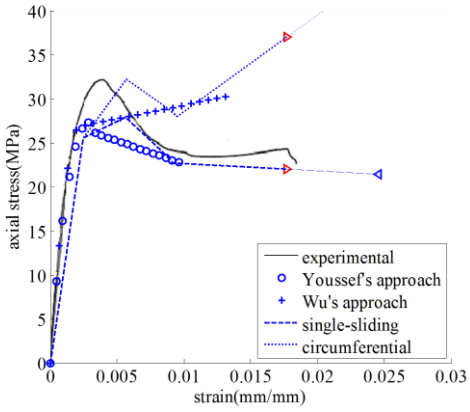

(f)

Fig. 17 Validation with FRP reinforced specimens (aspect ratio ≥ 3): (a) G4L2; (b) G4L4; (c) G5L2; (d) G5L4; (e) S1H0L1M; (f) S1H0L2M;

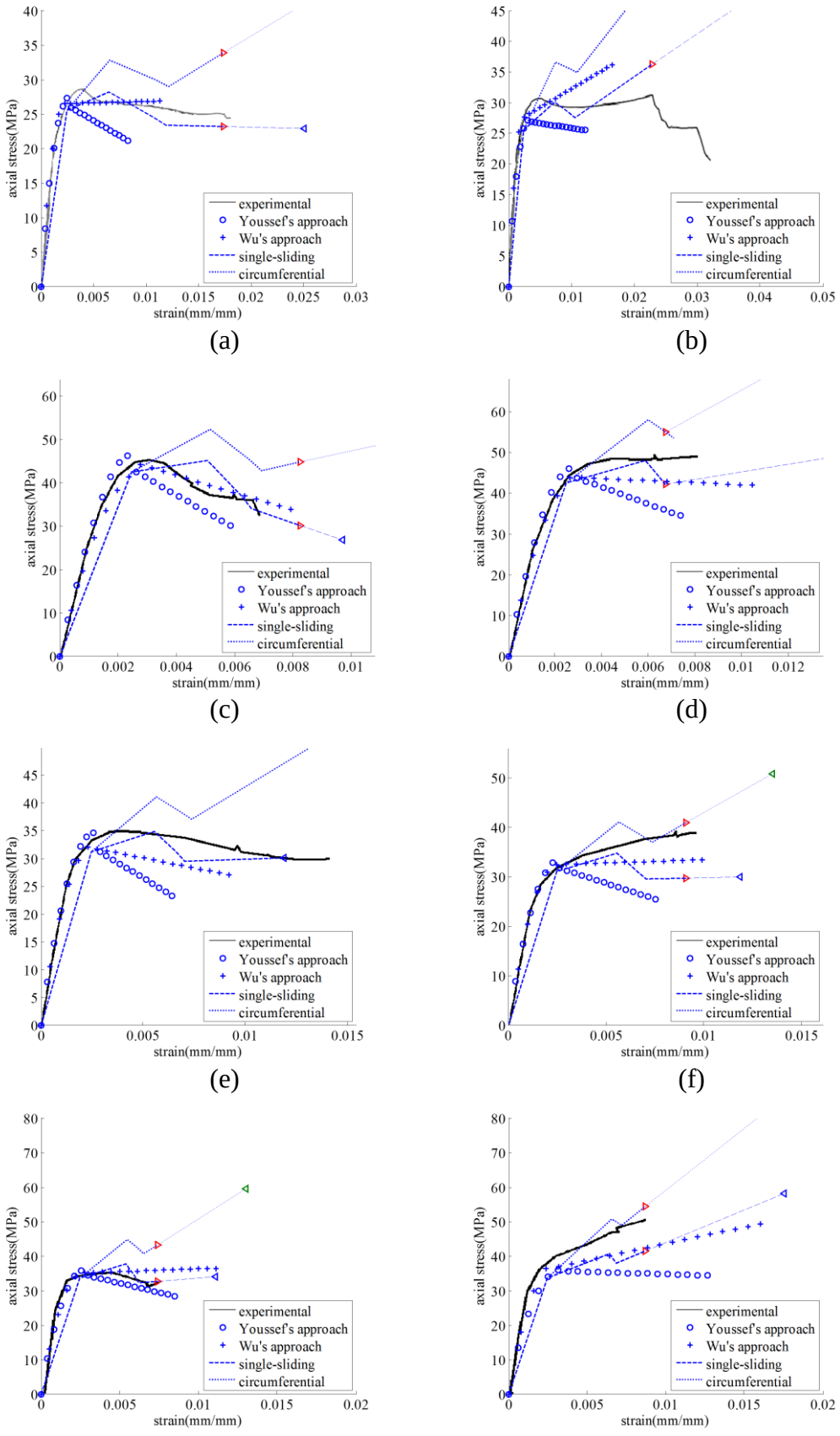

Fig. 18 Validation with FRP reinforced specimens (aspect ratio ≥ 3): (a) S2H0L1M; (b) S2H0L2M; (c) S10r1; (d) S20r1; (e) X10r1; (f) X20r3; (g) S1R25; (h) S2R25;

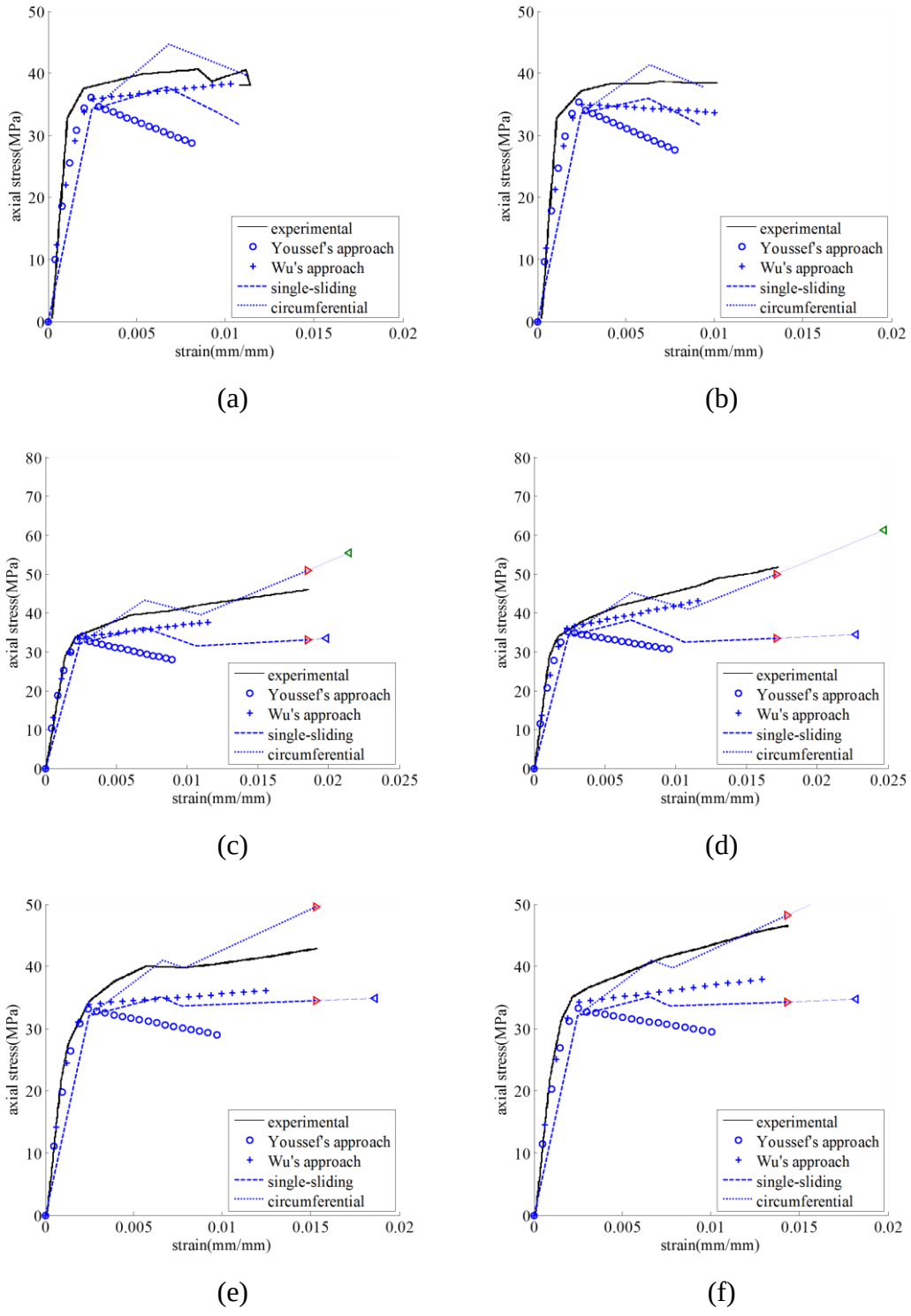

Fig. 19 Validation with stirrups reinforced specimens (aspect ratio =2): (a) 1S-1; (b) 1R-1.25; (c) A2; (d) A3; (e) A6; (f) A7;

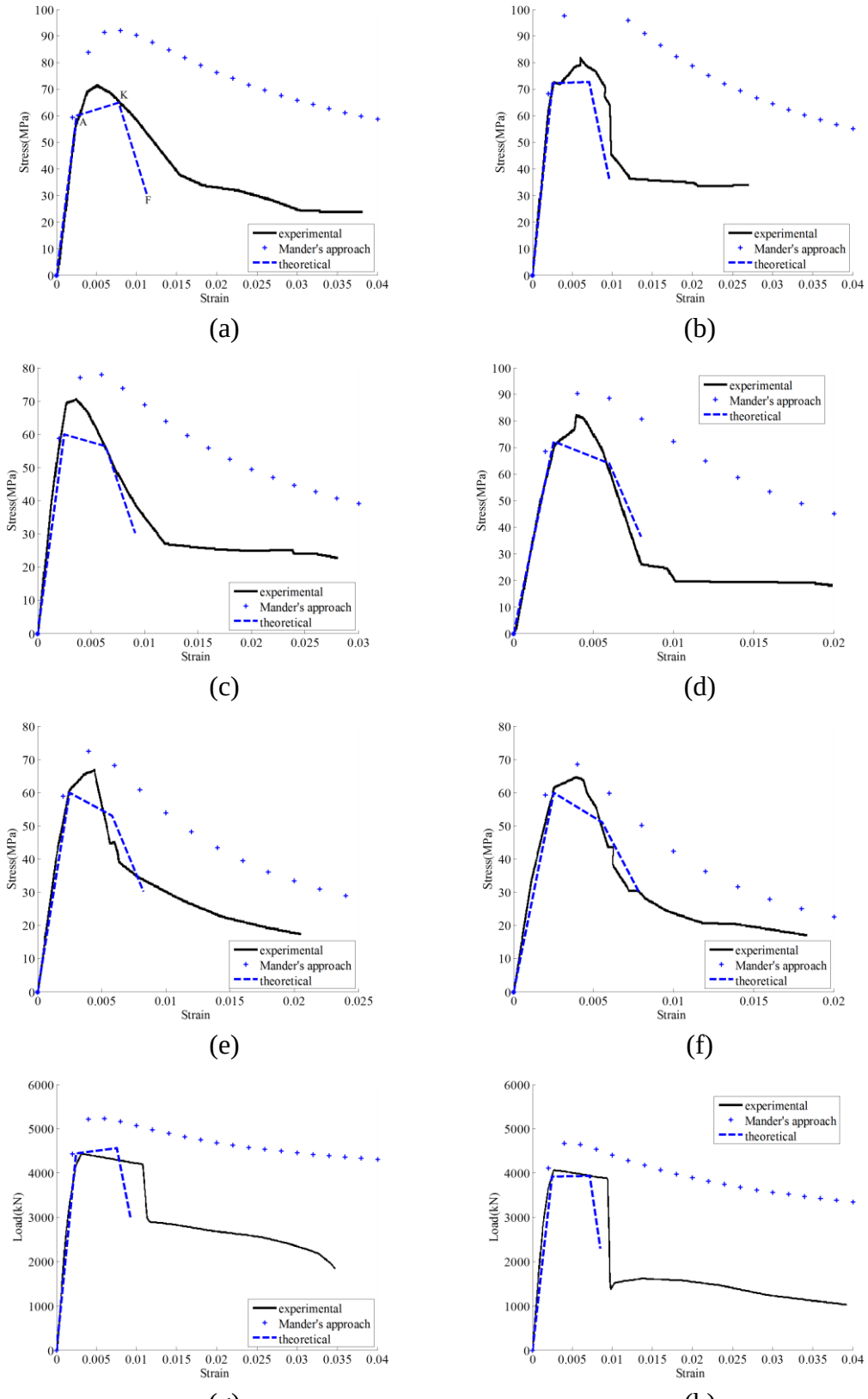

Fig. 20 Validation with stirrups reinforced specimens (aspect ratio ≥ 3): (a) 1A; (b) 1B; (c) 4A; (d) 4B; (e) 7A; (f)10A; (g)10; (h)15;

Ultimate Strain of FRP Reinforced Prisms

It has been described in the last section that the average lateral fracture strain of reinforcement recorded in the experiments ε_{fr2} can be substituted for ε_{fr} in Eq. (32) to quantify the axial stress and strain at fracture. This fracture point is plotted as left-pointing triangle as shown in Figs. 16 to 19 such as point A and A' for single-sliding and circumferential failure type respectively as shown in Fig. 16(f). However, the theoretical axial strain at fracture ε_{axfr} is normally larger than the ultimate strain ε_{cu} recorded experimentally. The theoretical axial stress corresponding to the experimentally measured rupture strain is plotted as right-pointing triangle as shown in Figs. 16 to 19 and this is plotted as points B and B' in Fig. 16(f) for single-sliding and circumferential failure type respectively as an example. The difference in result arises because the average lateral fracture strain ε_{fr2} at facture overestimates the practical rupture strain of the confinement reinforcement which is also influenced by stress concentrations (Wang et al., 2012) and this requires further research.

Validation of Theoretical Stress/Strain Approach

In this paper, the fundamental mechanics of the single-sliding failure type in Fig. 7(b) has been described because, as explained previously, this is the mode by which most full size prisms will fail. In this section, the other circumferential failure type in Fig. 7(a) is described as many lab scale test specimens can often fail in this mode (Wu et al., 2009). This circumferential failure will change the resultant shear stress τ and normal stress σ_N from Eqs. (3) and (4) to τ_{cir} and σ_{Ncir} as follows (Ali et al., 2010, Chen et al., 2015a, Chen et al., 2015b)

$$\tau_{cir} = \left(\sigma_{ax} - 2\sigma_{conf}\right)\sin\alpha\cos\alpha \tag{49}$$

$$\sigma_{Ncir} = \sigma_{ax}\sin^2\alpha + 2\sigma_{conf}\cos^2\alpha \tag{50}$$

Setting the circumferential-wedge failure plane shear stress τ_{cir} from Eq. (49) to the shear-friction material capacity τ_m from Eq. (5) and substituting σ_{Ncir} from Eq. (50) as well as S =

$S_{lat}/\sin\alpha$, which is similar to the way to derive σ_S in Eq. (46), gives the variation of the axial stress σ_{Scir} as follows

$$\sigma_{Scir} = \frac{2\sigma_{conf}\sin\alpha\cos\alpha + \left(A\frac{S_{lat}}{\sin\alpha} + C\right)2\sigma_{conf}\cos^2\alpha + B\frac{S_{lat}}{\sin\alpha} + D}{\sin\alpha\cos\alpha - \sin^2\alpha\left(A\frac{S_{lat}}{\sin\alpha} + C\right)} \tag{51}$$

The other procedures are the same as that of the single-sliding failure. The passive stress/strains of the single-sliding failure and circumferential failure gives a lower bound and upper bound respectively and are compared with the experimental data in Figs. 16 to 19 with good correlation both in magnitude and shape. The accuracy of the simulation can be improved by developing more accurate material properties but the fundamental mechanics always applies. For concrete prisms reinforced by high level of confinement reinforcement such as that shown in Fig. 18(b), the high lateral confining stress may cause the stress concentration at the section corner which may cause premature failure (Tastani et al., 2013) and this requires further research in the future.

It is worth noting that for specimens whose aspect ratio is less than three, circumferential failure is more likely to occur and as shown in Fig. 19, the proposed approach (by assuming this failure type) gives good correlation with experimental results. Furthermore, for FRP wrapped specimens with D_i < 300 mm such as specimens in Fig. 17(a), (b) and (c), the empirical approach proposed by Wei and Wu (Wei and Wu, 2012) can predict the passive stress/strain well; however, for large specimen with $D_i \geq 300$ mm such as specimens in Figs. 17(b), (d), (e) and (f), proposed approach gives an improved prediction. The reason is that empirical approach is normally derived from small-size specimens (D_i < 300 mm).

Conclusions

In this paper a theoretical model based on partial interaction shear-friction mechanics of concrete and bond-slip of reinforcement (internal or external) to concrete through intermediate-crack debonding have been used to quantify both the stress/strain of actively confined concrete and, consequently, the stress/strain of passively confined concrete. The theoretically derived passive stress/strain has been compared with FRP wrapped and stirrups

reinforced specimens with good correlation both in their shape and magnitude. It has been shown that the single sliding plane failure mode should be used in design as it is more likely to occur in full size specimens. The fundamental mechanics has been described specifically for members with rectangular RC sections although the mechanics applies to RC sections with any shape, size and configuration. This procedure can be used to derive the passive stress/strain of concrete for a particular member which can then be used to derive its strength and ductility. This new mechanics approach which is based only on fundamental material properties, provides structural engineers with the tools to incorporate the benefits of concrete confinement in their designs.

Appendix 1. Notation

The following symbols are used in this paper:

A_c = cross-section area of concrete which interacts with reinforcement in tension stiffening analysis

A_r = total cross-section area of reinforcement in tension stiffening analysis

b_f = width of reinforcement plate

b_{f2} = length of failure plane parallel to concrete surface

c = concrete cover

D_i = height within confined area of rectangular prism

D_{i2} = width within confined area of rectangular prism

D_0 = height within the whole area including concrete cover of rectangular prism

D_{02} = width within the whole area including concrete cover of rectangular prism

d_f = thickness of failure plane

d_l = longitudinal reinforcement diameter

E_c = elastic modulus of concrete

E_{FRP} = elastic modulus of FRP

E_r = elastic modulus of reinforcement plate

E_1 = stiffness of P_{conf}/S_{lat} relationship that is equal to $P_{IC}/(2\Delta_{IC})$

E_2 = stiffness of P_{conf}/S_{lat} relationship from multi-crack analysis

f_{c0}	=	peak strength of unconfined concrete from cylinder tests
f_{cc}	=	peak strength of confined concrete from cylinder tests
f_p	=	fracture stress of FRP
$f_{y\text{-}l}$	=	yield capacity of longitudinal reinforcement
$f_{y\text{-}s}$	=	yield capacity of stirrups
h_{cr}	=	separation of shear-sliding plane interface
H_{sl}	=	height of sliding plane
k	=	bond-slip stiffness in tension stiffening analysis
L_{conf}	=	length of confinement reinforcement
L_{crt}	=	critical length which is the minimum length required to achieve the maximum debond force
L_{def}	=	height of specimen
L_{gl}	=	gauge length
L_{per}	=	total length of potential debonding failure plane of reinforcement in tension stiffening analysis
P_{ax}	=	axial load applied to concrete column
P_{conf}	=	confinement force from confinement reinforcement
P_{exp}	=	maximum axial load from experiments
P_{fr}	=	fracture capacity of confinement reinforcement
P_{fr2}	=	confinement force at ε_{fr2}
P_{IC}	=	debond force of confinement reinforcement
P_{pl}	=	confinement force from plate reinforcement along the shear failure plane
P_{st}	=	confinement force from one leg of stirrups
$P_{st\text{-}comp}$	=	compressive force from concrete across the crack face balanced by P_{st} or P_{pl}
P_{yld}	=	yield capacity of confinement reinforcement
r_c	=	ductility factor of confined concrete
S	=	slip displacement
S_{ax}	=	vertical component of slip S
S_{lat}	=	lateral component of slip S
$S_{lat\text{-}deb}$	=	lateral component of slip when debond developed to plate ends

$S_{lat\text{-}fr}$ = lateral component of slip when confinement reinforcement starts to fracture when $L_{crt}<L_{conf}$ and $P_{IC}<P_{fr}$

$S_{lat\text{-}fr2}$ = lateral component of slip when confinement reinforcement starts to fracture when $L_{crt}<L_{conf}$ and $P_{IC}>P_{fr}$

$S_{lat\text{-}fr3}$ = lateral component of slip when confinement reinforcement starts to fracture when $L_{crt}>L_{conf}$

$S_{lat\text{-}IC}$ = lateral component of slip at commencement of IC debonding

$S_{lat\text{-}IC2}$ = lateral component of slip when confinement reinforcement is fully debonded

$S_{lat\text{-}yld}$ = lateral component of slip when reinforcement starts to yield when $L_{crt}<L_{conf}$ and $P_{IC}<P_{yld}$

$S_{lat\text{-}yld2}$ = lateral component of slip when reinforcement starts to yield when $L_{crt}<L_{conf}$ and $P_{IC}>P_{yld}$

$S_{lat\text{-}yld3}$ = lateral component of slip when confinement reinforcement starts to yield when $L_{crt}>L_{conf}$

S_p = primary crack spacing

S_s = stirrups spacing

$S\#$ = specimen reference number

t_{FRP} = FRP thickness

V_u = shear stress at the commencement of crack widening

α = failure angle of concrete column

β = prism parameter in tension stiffening analysis

Δ = slip of confinement reinforcement at crack face

Δ_{deb} = slip of confinement reinforcement at crack face when bond stress develops to plate end

Δ_{fr} = slip of confinement reinforcement at crack face when confinement reinforcement starts to fracture when $L_{crt}<L_{conf}$ and $P_{IC}<P_{fr}$

Δ_{fr2} = slip of confinement reinforcement at crack face when confinement reinforcement starts to fracture when $L_{crt}<L_{conf}$ and $P_{IC}>P_{fr}$

Δ_{IC} = slip of confinement reinforcement at crack face when debond starts

Δ_{IC2} = slip of confinement reinforcement at crack face when confinement reinforcement is fully debonded

Δ_{yld} = slip of confinement reinforcement at crack face when confinement reinforcement starts to yield when $L_{crt}<L_{conf}$ and $P_{IC}<P_{yld}$

Δ_{yld2} = slip of confinement reinforcement at crack face when confinement reinforcement starts to yield when $L_{crt}<L_{conf}$ and $P_{IC}>P_{yld}$

Δ_{yld3} = slip of confinement reinforcement at crack face when confinement reinforcement starts to yield when $L_{crt}>L_{conf}$

δ = slip between reinforcement and adjacent concrete

δ_1 = δ at τ_{Bmax}

δ_{max} = δ when τ_B reduces to zero

ε_{ax} = axial strain when axial stress is equal to σ_{ax}

ε_{axdeb} = axial strain at S_{deb}

ε_{axfr} = axial strain at fracture

ε_{axIC} = axial strain at S_{IC}

ε_{c0} = strain at f_{c0} for unconfined concrete

ε_{cc} = strain at f_{cc} for confined concrete

ε_{cu} = ultimate strain for confined concrete

ε_{fr} = confinement reinforcement strain at P_{fr}

ε_{fr2} = average lateral fracture strain of reinforcement recorded in the experiments

ε_{IC} = confinement reinforcement strain at P_{IC}

ε_m = material strain of concrete

ε_S = sliding strain caused by slip S

ε_{Sdeb} = sliding strain at $S_{lat\text{-}deb}$

ε_{Sfr} = sliding strain at $S_{lat\text{-}fr}$

ε_{SIC} = sliding strain at $S_{lat\text{-}IC}$

ε_{SIC2} = sliding strain at $S_{lat\text{-}IC2}$

ε_{Syld} = sliding strain at $S_{lat\text{-}yld}$

ε_{Syld2} = sliding strain at $S_{lat\text{-}yld2}$

ε_{yld} = confinement reinforcement strain at $S_{lat\text{-}yld}$

ε_{yld2} = confinement reinforcement strain at $S_{lat\text{-}yld2}$

ε_z = confinement reinforcement strain when debonding is complete or when there is no bond

λ = variation in slip parameter

σ_{ax} = axial stress applied to concrete

σ_{axfr} = axial stress at fracture

σ_{conf} = lateral confining stress applied on concrete

σ_{conffr} = lateral confining stress from confinement reinforcement at P_{fr}

σ_{confIC} = lateral confining stress from confinement reinforcement at P_{IC}

$\sigma_{confyld}$ = lateral confining stress from confinement reinforcement at P_{yld}

σ_{conf0} = lateral confining stress of unconfined concrete and equals zero

σ_{const} = lateral confining stress of from stirrups

σ_{conpl} = lateral confining stress of from plate reinforcement

σ_{fr2} = confinement reinforcement stress at ε_{fr2}

σ_N = confining stress normal to single-sliding plane

σ_{Ncir} = confining stress normal to circumferential-sliding plane

σ_{N0} = normal stress at f_{c0} for unconfined concrete

σ_S = axial stress of passively confined concrete by assuming single-sliding failure

σ_{Scir} = axial stress of passively confined concrete by assuming circumferential failure

σ_{Sdeb} = axial stress at $S_{lat\text{-}deb}$

σ_{Sfr} = axial stress at $S_{lat\text{-}fr}$

σ_{SIC} = axial stress at $S_{lat\text{-}IC}$

σ_{SIC2} = axial stress at $S_{lat\text{-}IC2}$

σ_{Syld} = axial stress at $S_{lat\text{-}yld}$

σ_{Syld2} = axial stress at $S_{lat\text{-}yld2}$

τ = shear stress along single-sliding plane

τ_{cir} = shear stress along circumferential-sliding plane

τ_B = bond stress existing between reinforcement and concrete

τ_{Bmax} = maximum τ_B

τ_m = shear-friction material capacity

φ_f = aspect ratio of interface failure plane

Appendix 2. Specimens Details

Table 2.1 FRP wrapped specimens

S#	Ref.	L_{def} (mm)	D_i (mm)	D_{i2} (mm)	f_{c0} (MPa)	t_{FRP} (mm)	L_{gl} (mm)	E_{frp} (MPa)	f_p (MPa)	ε_{fr2}
G1L1	Wang et al 2012	300	100	100	24.4	0.167	100	244000	4340	0.00973
G1L2	Wang et al 2012	600	200	200	24.4	0.334	200	244000	4340	0.00897
G2L1	Wang et al 2012	375	125	125	24.4	0.167	125	244000	4340	0.00459
G2L2	Wang et al 2012	750	250	250	24.4	0.334	250	244000	4340	0.00927
G3L1	Wang et al 2012	450	150	150	24.4	0.167	150	244000	4340	0.01109
G3L2	Wang et al 2012	900	300	300	24.4	0.334	300	244000	4340	0.00776
G4L2	Wang et al 2012	525	175	175	24.4	0.334	175	244000	4340	0.00897
G4L4	Wang et al 2012	1050	350	350	24.4	0.668	350	244000	4340	0.00832
G5L2	Wang et al 2012	600	200	200	24.4	0.334	200	244000	4340	0.00897
G5L4	Wang et al 2012	1200	400	400	24.4	0.668	400	244000	4340	0.00542
S1H0L1M	Wang et al 2011	915	305	305	25.5	0.167	305	240000	4340	0.00843
S1H0L2M	Wang et al 2011	915	305	305	25.5	0.334	305	240000	4340	0.00951
S2H0L1M	Wang et al 2011	612	204	204	25.5	0.167	204	240000	4340	0.00986
S2H0L2M	Wang et al 2011	612	204	204	25.5	0.334	204	240000	4340	0.01212
S10r1	Carrazedo et al 2016	450	150	150	42.5	0.17	450	209000	2720	0.00973
S20r1	Carrazedo et al 2016	450	150	150	42.5	0.34	450	209000	2720	0.00973
X10r1	Carrazedo et al 2016	450	150	150	31.1	0.17	450	209000	2720	0.00973
X20r3	Carrazedo et al 2016	450	150	150	31.1	0.17	450	209000	2720	0.00973
S1R25	Lam et al 2003	600	150	150	33.7	0.165	600	257000	4519	0.0105
S2R25	Lam et al 2003	600	150	150	33.7	0.33	600	257000	4519	0.0108
1S-1	Wu et al 2010	300	150	150	34.1	0.167	200	230000	3400	0.0207
1R-1.25	Wu et al 2010	300	150	188	33.6	0.167	200	230000	3400	0.0214
A2	Abbasnia et al 2013	300	150	150	32.0	0.176	200	241000	3943.5	0.0091
A3	Abbasnia et al 2013	300	150	150	34.0	0.176	200	241000	3943.5	0.0109
A6	Abbasnia et al 2013	300	120	180	32.0	0.176	200	241000	3943.5	0.0102
A7	Abbasnia et al 2013	300	120	180	32.0	0.176	200	241000	3943.5	0.0099

where *S#* is the specimen reference number.

Table 2.2 stirrups reinforced specimens

S#	Ref.	L_{def}	D_0	D_{02}	f_{c0}	d_l	L_{gl}	f_{y-l}	d_s	S_s	f_{y-s}
		(mm)	(mm)	(mm)	(MPa)	(mm)	(mm)	(MPa)	(mm)	(mm)	(MPa)
1A	Li et al 2001	720	240	240	60.0	12.0	300	443	6.00	20.0	445
1B	Li et al 2001	720	240	240	72.3	12.0	300	443	6.00	20.0	445
4A	Li et al 2001	720	240	240	60.0	12.0	300	443	6.00	35.0	445
4B	Li et al 2001	720	240	240	72.3	12.0	300	443	6.00	35.0	445
7A	Li et al 2001	720	240	240	60.0	12.0	300	443	6.00	50.0	445
10A	Li et al 2001	720	240	240	60.0	12.0	300	443	6.00	65.0	445
10	Basset et al 1986	1956	305	305	34.0	29.9	610	491	7.94	50.8	533
15	Basset et al 1986	1956	305	305	37.2	19.5	610	418	7.94	50.8	533

where D_0 is the height within the whole area including concrete cover of rectangular prism, D_{02} is the width within the whole area including concrete cover of rectangular prism, c is the concrete cover, d_l is the longitudinal reinforcement diameter, d_s is the stirrups diameter, f_{y-l} is the yield capacity of longitudinal reinforcement and f_{y-s} is the yield capacity of stirrups.

Acknowledgements

The first author would like to acknowledge the financial support of the China Scholarship Council.

References

Abbasnia, R. & Ziaadiny, H. (2015) Experimental investigation and strength modeling of CFRP-confined concrete rectangular prisms under axial monotonic compression. *Materials and Structures* **48(1-2)**:485-500.

Ali, M. M., Oehlers, D. & Griffith, M. (2010) The residual strength of confined concrete. *Advances in Structural Engineering* **13(4)**:603-618.

Ali, M. M., Oehlers, D., Griffith, M. & Seracino, R. (2008) Interfacial stress transfer of near surface-mounted FRP-to-concrete joints. *Engineering Structures* **30(7)**:1861-1868.

American Concrete Institute. (1992) State-of-the-art report on high-strength concrete. *American Concrete Institute, Farmington Hills, Michigan*.

Azizinamini, A., Stark, M., Roller, J. J. & Ghosh, S. K. (1993) Bond performance of reinforcing bars embedded in high-strength concrete. *Structural Journal* **90(5)**:554-561.

Basset, R. & Uzumeri, S. (1986) Effect of confinement on the behaviour of high-strength lightweight concrete columns. *Canadian Journal of Civil Engineering* **13(6)**:741-751.

Becque, J., Patnaik, A. K. & Rizkalla, S. H. (2003) Analytical models for concrete confined with FRP tubes. *Journal of Composites for Construction* **7(1)**:31-38.

Carrazedo, R. & De Hanai, J. B. (2016) Concrete Prisms and Cylinders Wrapped by FRP Loaded in Compression with Small Eccentricities. *Journal of Composites for Construction* **21(4)**:04016115.

Fib. (The International Federation for Structural Concrete) (2010) CEB-FIB Model Code 2010–Final draft. *Thomas Thelford, Lausanne, Switzerland*.

Chen, C., Sui, L., Xing, F., Li, D., Zhou, Y. & Li, P. (2018) Predicting bond behavior of HB FRP strengthened concrete structures subjected to different confining effects. *Composite Structures* **187**:212-225.

Chen, Y., Visintin, P. & Oehlers, D. (2015a) Concrete shear-friction material properties: Derivation from actively confined compression cylinder tests. *Advances in Structural Engineering* **18(8)**:1173-1185.

Chen, Y., Visintin, P. & Oehlers, D. (2015b) Extracting Size-Dependent Stress–Strain Relationships from FRP-Confined Concrete Cylinders for Varying Diameters and Heights. *Journal of Materials in Civil Engineering* **28(5)**:04015182.

Chen, Y., Visintin, P., Oehlers, D. & Alengaram, U. (2013) Size-dependent stress-strain model for unconfined concrete. *Journal of Structural Engineering* **140(4)**:04013088.

Darwin, D. & Graham, E. K. (1993) *Effect of deformation height and spacing on bond strength of reinforcing bars*. *ACI Structural Journal* **90(6)**: 646-657

Du, M., Jin, L., Du, X. & Li, D. (2017) Size effect tests of stocky reinforced concrete columns confined by stirrups. *Structural Concrete* **18(3)**:454-465.

Fam, A. Z. & Rizkalla, S. H. (2001) Confinement model for axially loaded concrete confined by circular fiber-reinforced polymer tubes. *Structural Journal* **98(4)**:451-461.

Hao, X. (2017) Mechanics of extracting shear-friction properties from actively confined cylinder tests. *School report, School of Civil, Environmental and Mining Engineering, The University of Adelaide, Australia.*

Harmon, T. G., Ramakrishnan, S. & Wang, E. H. (1998) Confined concrete subjected to uniaxial monotonic loading. *Journal of Engineering Mechanics* **124(12)**:1303-1309.

Haskett, M., Oehlers, D., Ali, M. M. & Sharma, S. (2010) The shear friction aggregate interlock resistance across sliding planes in concrete. *Magazine of Concrete Research* **62(12)**:907-924.

Haskett, M., Oehlers, D. J., Ali, M. M. & Sharma, S. K. (2011) Evaluating the shear-friction resistance across sliding planes in concrete. *Engineering Structures* **33(4)**:1357-1364.

Hognestad, E. (1951) Study of combined bending and axial load in reinforced concrete members. *Technical Reports, Bulletin no. 399, University of Illinois, Engineering Experiment Station.*.

Jiang, T. & Teng, J. (2007) Analysis-oriented stress–strain models for FRP–confined concrete. *Engineering Structures* **29(11)**:2968-2986.

Jin, L., Du, M., Li, D., Du, X. & Xu, H. (2017) Effects of cross section size and transverse rebar on the behavior of short squared RC columns under axial compression. *Engineering Structures* **142**:223-239.
Lam, L. & Teng, J. (2003) Design-oriented stress-strain model for FRP-confined concrete in rectangular columns. *Journal of Reinforced Plastics and Composites* **22(13)**:1149-1186.
Li, B., Park, R. & Tanaka, H. (2001) Stress-strain behavior of high-strength concrete confined by ultra-high-and normal-strength transverse reinforcements. *ACI Structural Journal* **98(3)**:395-406.
Lu, X., Teng, J., Ye, L. & Jiang, J. (2005) Bond–slip models for FRP sheets/plates bonded to concrete. *Engineering Structures* **27(6)**:920-937.
Mander, J. B., Priestley, M. J. & Park, R. (1988) Theoretical stress-strain model for confined concrete. *Journal of Structural Engineering* **114(8)**:1804-1826.
Mirmiran, A. & Shahawy, M. (1996) A new concrete-filled hollow FRP composite column. *Composites Part B: Engineering* **27(3-4)**:263-268.
Muhamad, R., Ali, M. M., Oehlers, D. J. & Griffith, M. (2012) The tension stiffening mechanism in reinforced concrete prisms. *Advances in Structural Engineering* **15(12)**:2053-2069.
Oehlers, D. J., Mohamed Ali, M., Haskett, M., Lucas, W., Muhamad, R. & Visintin, P. (2010) FRP-reinforced concrete beams: unified approach based on IC theory. *Journal of Composites for Construction* **15(3)**:293-303.
Oldham, K. B., Myland, J. & Spanier, J. (2010) *An atlas of functions: with equator, the atlas function calculator*. Springer Science & Business Media.
Plevris, N. & Triantafillou, T. C. (1994) Time-dependent behavior of RC members strengthened with FRP laminates. *Journal of Structural Engineering* **120(3)**:1016-1042.
Popovics, S. (1973) A numerical approach to the complete stress-strain curve of concrete. *Cement and Concrete Research* **3(5)**:583-599.
Richart, F. E., Brandtzaeg, A. & Brown, R. L. (1928) A study of the failure of concrete under combined compressive stresses. *University of Illinois Bulletin; v. 26, no. 12*.
Sakino, K., Nakahara, H., Morino, S. & Nishiyama, I. (2004) Behavior of centrally loaded concrete-filled steel-tube short columns. *Journal of Structural Engineering* **130(2)**:180-188.
Seracino, R., Raizal Saifulnaz, M. & Oehlers, D. (2007) Generic debonding resistance of EB and NSM plate-to-concrete joints. *Journal of Composites for Construction* **11(1)**:62-70.
Shams, M. & Saadeghvaziri, M. A. (1997) State of the art of concrete-filled steel tubular columns. *Structural Journal* **94(5)**:558-571.
Silva, M. A. & Rodrigues, C. C. (2006) Size and relative stiffness effects on compressive failure of concrete columns wrapped with glass FRP. *Journal of Materials in Civil Engineering* **18(3)**:334-342.
Spoelstra, M. R. & Monti, G. (1999) FRP-confined concrete model. *Journal of Composites for Construction* **3(3)**:143-150.
Sturm, A. B., Visintin, P. & Oehlers, D. J. (2018) Time-dependent serviceability behavior of reinforced concrete beams: Partial interaction tension stiffening mechanics. *Structural Concrete* **19(2)**:508-523.
Tastani, S., Balafas, I., Dervisis, A. & Pantazopoulou, S. (2013) Effect of core compaction on deformation capacity of FRP-jacketed concrete columns. *Construction and Building Materials* **47**:1078-1092.

Teng, J., Huang, Y., Lam, L. & Ye, L. (2007) Theoretical model for fiber-reinforced polymer-confined concrete. *Journal of Composites for Construction* **11(2)**:201-210.
Teng, J., Jiang, T., Lam, L. & Luo, Y. (2009) Refinement of a design-oriented stress–strain model for FRP-confined concrete. *Journal of Composites for Construction* **13(4)**:269-278.
Thériault, M., Neale, K. W. & Claude, S. (2004) Fiber-reinforced polymer-confined circular concrete columns: Investigation of size and slenderness effects. *Journal of Composites for Construction* **8(4)**:323-331.
Visintin, P., Chen, Y. & Oehlers, D. (2015a) Simulating the behavior of FRP-confined cylinders using the shear-friction mechanism. *Journal of Composites for Construction* **19(6)**:04015014.
Visintin, P., Chen, Y. & Oehlers, D. (2015b) Size dependent axial and lateral stress strain relationships for actively confined concrete. *Advances in Structural Engineering* **18(1)**:1-20.
Wang, Z., Wang, D. & Smith, S. T. (2012) Size effect of square concrete columns confined with CFRP wraps. In *Proceedings of the 3rd Asia-Pacific Conference on FRP in Structures, Hokkaido University, Sapporo, Japan*, pp. 2-4.
Wang, Z., Wang, D., Smith, S. T. & Lu, D. (2011a) CFRP-confined square RC columns. I: Experimental investigation. *Journal of Composites for Construction* **16(2)**:150-160.
Wang, Z., Wang, D., Smith, S. T. & Lu, D. (2011b) CFRP-confined square RC columns. II: Cyclic axial compression stress-strain model. *Journal of Composites for Construction* **16(2)**:161-170.
Wei, Y.-Y. & Wu, Y.-F. (2012) Unified stress–strain model of concrete for FRP-confined columns. *Construction and Building Materials* **26(1)**:381-392.
Wu, H.-L., Wang, Y.-F., Yu, L. & Li, X.-R. (2009) Experimental and computational studies on high-strength concrete circular columns confined by aramid fiber-reinforced polymer sheets. *Journal of Composites for Construction* **13(2)**:125-134.
Wu, Y.-F. & Wei, Y.-Y. (2010) Effect of cross-sectional aspect ratio on the strength of CFRP-confined rectangular concrete columns. *Engineering Structures* **32(1)**:32-45.
Yao, J., Teng, J. & Chen, J. (2005) Experimental study on FRP-to-concrete bonded joints. *Composites Part B: Engineering* **36(2)**:99-113.
Youssef, M. N., Feng, M. Q. & Mosallam, A. S. (2007) Stress–strain model for concrete confined by FRP composites. *Composites Part B: Engineering* **38(5-6)**:614-628.
Yuan, H., Teng, J., Seracino, R., Wu, Z. & Yao, J. (2004) Full-range behavior of FRP-to-concrete bonded joints. *Engineering Structures* **26(5)**:553-565.
Yuan, H., Wu, Z. & Yoshizawa, H. (2001) Theoretical solutions on interfacial stress transfer of externally bonded steel/composite laminates. *Doboku Gakkai Ronbunshu* **2001(675)**:27-39.

Statement of Authorship

Statement of Authorship

Title of Paper	Simulating the Passive Confinement of Circular Concrete Cylinders Allowing for Size Effect
Publication Status	☐ Published ☐ Accepted for Publication ☑ Submitted for Publication ☐ Unpublished and Unsubmitted w ork w ritten in manuscript style
Publication Details	Hao, X, Visintin, P and Oehlers, DJ (2019) Simulating the Passive Confinement of Circular Concrete Cylinders Allowing for Size Effect. Submitted to *Composite Structures*

Principal Author

Name of Principal Author (Candidate)	Xinkai Hao		
Contribution to the Paper	Developed the model, interpreted data, wrote manuscript		
Overall percentage (%)	70%		
Certification:	This paper reports on original research I conducted during the period of my Higher Degree by Research candidature and is not subject to any obligations or contractual agreements with a third party that would constrain its inclusion in this thesis. I am the primary author of this paper.		
Signature		Date	20/10/2019

Co-Author Contributions

By signing the Statement of Authorship, each author certifies that:

i. the candidate's stated contribution to the publication is accurate (as detailed above);

ii. permission is granted for the candidate in include the publication in the thesis; and

iii. the sum of all co-author contributions is equal to 100% less the candidate's stated contribution.

Name of Co-Author	Phillip Visintin		
Contribution to the Paper	Supervised work progress, help modelling and revising manuscript		
Signature		Date	21/10/2019

Name of Co-Author	Deric John Oehlers		
Contribution to the Paper	Supervised work progress, help modelling and revising manuscript		
Signature		Date	21/10/19

Please cut and paste additional co-author panels here as required.

Simulating the Passive Confinement of Circular Concrete Cylinders Allowing for Size Effect

X. Hao[1], P. Visintin[2] and D. J. Oehlers[3]

Abstract

There are innumerable tests on small stocky circular cylinders with either internal passive encasement of the concrete with circular stirrups or spirals, or external passive encasement through fibre reinforced polymer (FRP) wrapping or through the use of FRP tubes or steel tubes. These tests have shown that passive confinement can increase the strength but, in particular, can substantially increase the ductility of concrete cylinders. Because of these important benefits, the effect of passive confinement on the concrete stress/strain in a particular cylinder section is invariably derived from tests such that substantial member testing is required. In this paper, it is shown how the passive stress/strain of the concrete for a particular circular member can theoretically be determined directly from their partial-interaction shear-friction and partial-interaction bond-slip material properties for any reinforcement arrangement and geometry of the circular cylinder. This procedure provides the tools for designing for the benefits of passive confinement directly without the need for member testing.

Keywords: concrete; concrete confinement; passive confinement; partial interaction; RC members; circular cylinders; shear sliding.

Introduction

The improvement in the concrete ductility of passively constrained RC cylinders through the use of stirrups [1, 2] or wraps [3-6] is well documented. Most current approaches for predicting the stress/strain of passively confined concrete cylinders are either design-oriented or analysis-oriented.

The former, that is the design-oriented approaches, treat the passively confined concrete simply as a new material in which the key properties of the passive stress/strain (σ/ε) are the: peak stress σ_{max}; strain $\varepsilon_{cc\text{-}max}$ at σ_{max}; ultimate stress f_{cu}; and the ultimate strain ε_{cu}. These

properties are derived empirically and separately for rectangular and circular cylinders [1, 7, 8]. For instance, Mander et al. [2] proposed a semi-empirical approach to quantify the peak stress of concrete cylinders reinforced by stirrups that assumed that the rectangular or circular sections were not fully confined as shown in Figs. 1 (a), (b). An arching-effect coefficient k_e was derived for rectangular or circular sections respectively and employed to reduce the lateral confining stress from the confinement reinforcement and subsequently the reduction of the peak strength and ductility. This approach was then extended to FRP wrapped concrete cylinders where it was assumed that circular cylinders reinforced by tubes are fully confined as in Fig. 1(c), whereas, rectangular cylinders are ineffectively confined as in Fig. 1(d) [8-12] such that the arching-effect coefficient k_e was employed.

The main benefit of these design-oriented approaches is their simplicity in defining the key points of the passive stress/strain. They are accurate within the bounds from which they were derived but should not be extrapolated beyond the ranges of their regressed databases which may severely limit their application to full size structures. For example, research has shown that the behaviour of passively confined concrete members is significantly dependent on size [13-15]. As most current design-oriented approaches are derived from databases where the specimens are small, having a diameter normally less than 200 mm [8, 16], application of these design-oriented approaches to much larger practical concrete members may limit their accuracy. Also of importance is the effect of the slenderness ratio as this affects the failure mode and strength significantly [17]. The aspect ratio of most specimens in databases [8, 16] equals two which is generally much less than that which occurs in practical concrete members. Empirically derived approaches based on the regression of databases of specimens with large sizes [18] or slenderness ratios [19] have been proposed but the derived approaches do not incorporate both the effects of size and slenderness ratio and the databases are small.

With regard to analysis-oriented models, the passive stress/strain is derived from the interaction between the concrete and lateral reinforcement. The general procedure is summarised as follows. First a family of curves of the active stress/strain are generated and, similarly to the cases in Fig. 1, the arching-effect coefficient k_e is employed. Then based on the interaction between the concrete and lateral confinement reinforcement, the lateral confining stress can be determined based either on the radial dilation [20-25] or the slip along

the shear failure plane [26]. From which, the axial stress and axial strain can be derived such that the loading path on the family of curves of the active stress/strain can be derived.

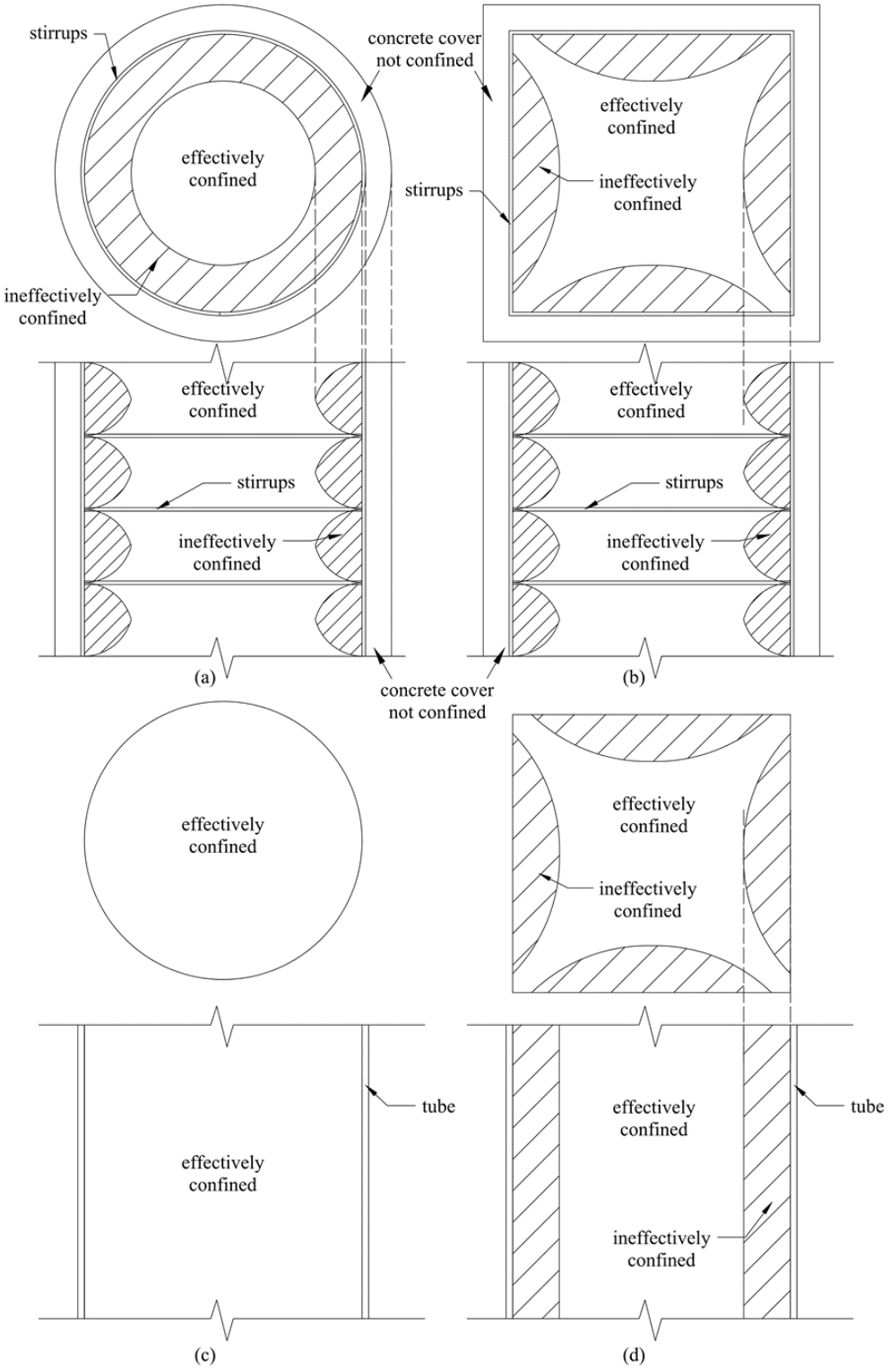

Fig. 1 Effectiveness of concrete confinement: (a) stirrup reinforced circular section (b) stirrup reinforced rectangular section (c) tube reinforced circular section (d) tube reinforced rectangular section

Although analysis-oriented approaches are more detailed than design-oriented, these analysis-oriented approaches have the same limitation. That is, these passive stress/strains are derived from active stress/strains that may not incorporate a size effect, such that the derived passive stress/strain is not size dependent. Hence, an approach that is independent of size and is not based on size independent stress/strain relationships is required. In this paper, a fundamental partial-interaction mechanics approach that quantifies the σ/ε for passively restrained circular concrete cylinders is described. The approach uses the partial-interaction shear-friction [27-31] and bond-slip [32-34] material properties to quantify the passive σ/ε of the concrete for design; this approach only requires the material properties and does not rely on member testing.

The fundamental mechanics for quantifying the passive concrete σ/ε of passively restrained rectangular sections has been described elsewhere [35] where the results gave good correlation with tests. As the resolution of the passive restraints in circular cylinders differs markedly from those in rectangular prisms, this paper describes these differences in detail, and derives the fundamental mechanics allowing for these differences. The passive confinement pressure throughout the circular section is first quantified. This is followed by a qualitative description of the passive confinement mechanism in circular cylinders. Having described the fundamental mechanics, closed form solutions are then derived for the concrete passive σ/ε and a parametric study is conducted to highlight the main parameters that control the ductility of concrete through lateral passive confinement. This is then followed by the comparison between the published test data and the theoretical approaches.

Confinement Pressure in Circular Sections

Consider the tube infilled with concrete in Fig. 2 that has the cross-section in Fig. 3(a). The sliding plane in Fig. 2 has formed in the concrete at an angle α and the interface slip across the sliding plane is S. When the cylinder is subjected to active hydraulic pressure σ_{conf}, which is shown on the left and right hand sides of Fig. 2, then this active pressure induces an interface pressure across the sliding plane which is shown as σ_{conf} along the sliding plane. Similarly, slip across the sliding plane interface would cause any lateral reinforcement, which in this case is the tube, to go into tension through its passive resistance to sliding; this

tension is balanced by compression σ_{conf} across the sliding plane. Hence the interface pressure σ_{conf} across the sliding plane can be induced by either passive resistance of the lateral reinforcement or active hydraulic pressure. It is this interface confinement pressure across the sliding plane σ_{conf} that needs to be determined as it controls the strength and ductility of the sliding plane through its shear friction properties.

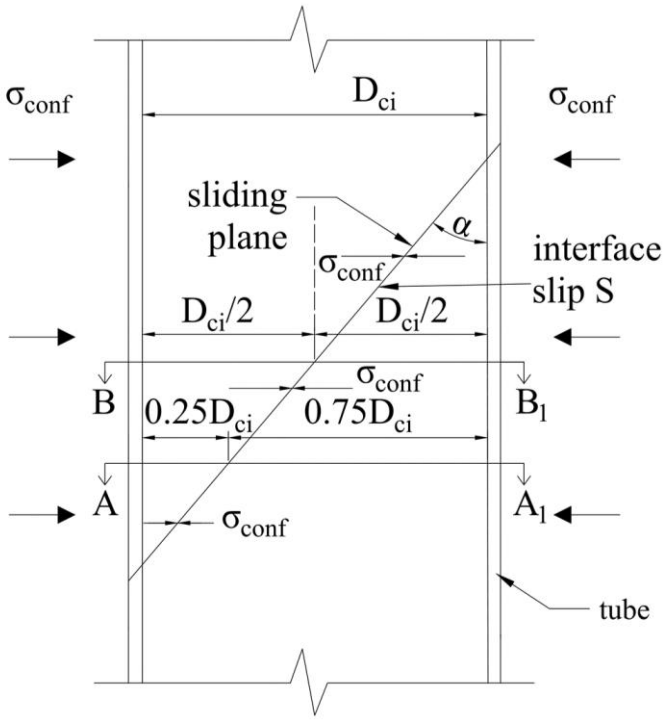

Fig. 2 Prism subjected to active hydraulic pressure σ_{conf}

The confinement mechanism in circular sections is compared with that in rectangular sections in Fig. 3. Let us first consider the square section in Fig. 3(b) of width and depth D_{ci} [35] which could be a section of the cylinder in Fig. 2. Section B-B_1 in Fig. 2 is taken where the sliding plane is at the centre of the section. This is shown in Fig. 3(b) with the sliding plane at B-B_1 and where the lateral component of the interface slip S is S_{lat}. This lateral movement of the sliding plane S_{lat} is resisted by lateral tension in the tube P_{conf} which induces a lateral compressive force across the sliding plane of equal magnitude from which the confinement stress σ_{conf} can be derived. When the sliding plane is at A-A_1 in Fig. 2, then the sliding plane is at $0.75D_{ci}$ in Fig. 3(b). The slip component S_{lat} is the same as in the previous example so that P_{conf} is the same such that σ_{conf} is the same. Hence the confinement stress σ_{conf} across the sliding plane in Fig. 2 is constant for a rectangular section as the confinement force P_{conf} and the lateral movement S_{lat} is constant.

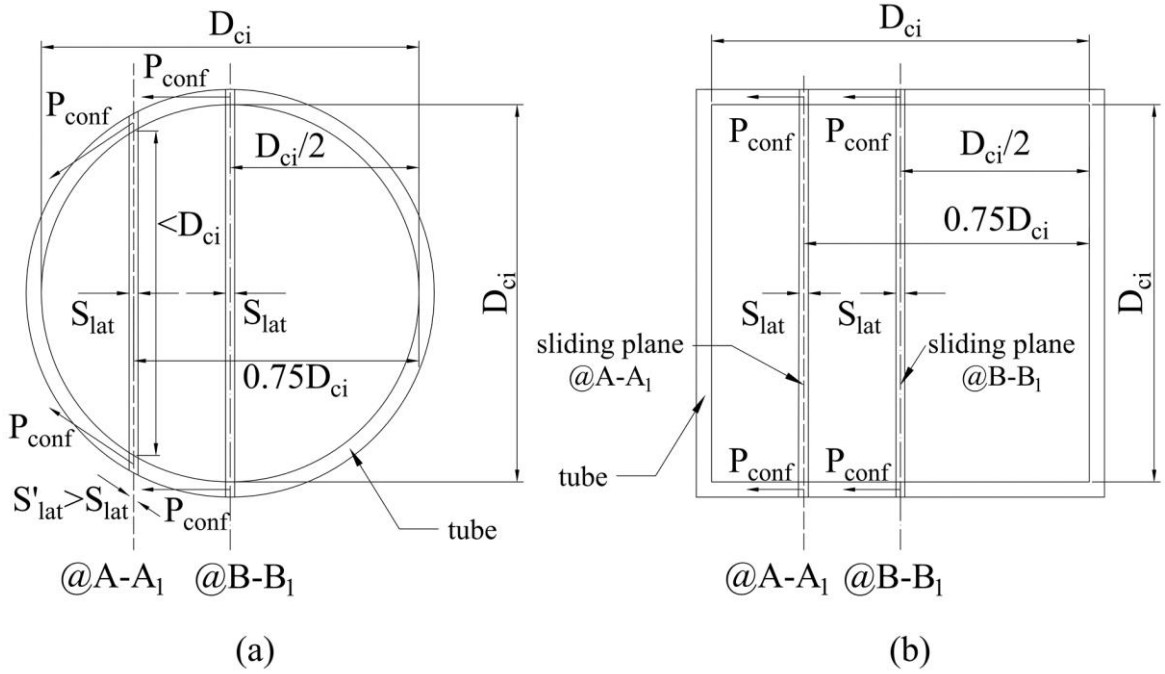

Fig. 3 Confinement mechanism in circular and rectangular sections

The above description of confinement for a rectangular section is applied to the confinement mechanism in a circular section in Fig. 3(a). At B-B_1 in Fig. 2, the analysis for the rectangular section in Fig. 3(b) is exactly the same as in the circular section in Fig. 3(a): P_{conf} and S_{lat} are the same and the width over which P_{conf} acts that is the depth D_{ci} is the same ensuring σ_{conf} is the same. However at A-A_1 in Fig. 2: the lateral component of P_{conf} in Figs. 3(a) and 3(b) are not the same; the concrete compression zone is not the same being D_{ci} in the rectangular section and $<D_{ci}$ in the circular section; and the tangential component of S_{lat}, shown as S'_{lat} and which induces the forces in the tube are not the same. Let us now consider the effect of these differences.

Section A-A_1 in Fig. 2 is shown in Fig. 4(a) where the sliding plane is to the left. The circumferential force in the tube, which is the confining reinforcement, is shown as P_{conf} and being a circumferential force it is tangential to the tube. Let us assume that the thickness of the tube t is much less than the internal diameter D_{ci} and the intercept of the sliding plane with the tube occurs at θ as shown. From the geometry in Fig. 4(a), it can be seen that the component of the circumferential force that is perpendicular to the sliding plane is $P_{conf}\sin\theta$ as also shown in Fig. 4(b). Hence the total tensile force is $2P_{conf}\sin\theta$ and this is balanced by a compressive force across the sliding plane of width $2r\sin\theta$ and of equal magnitude. If P_{conf}

is the force per unit depth of tube that is the depth into the paper in Fig. 3, then the confinement pressure is given by

$$\sigma_{conf} = \frac{2P_{conf}\sin\theta}{2r\sin\theta} = \frac{P_{conf}}{r} \tag{1}$$

which is the confinement pressure in Fig. 2 due to the passive lateral restraint. It can be seen in Eq. (1) that the confinement pressure is independent of θ that is it is independent of the level of the sliding plane in Fig. 2 for a specific confinement force P_{conf}. This is very important in deriving mechanics solutions as it means that the confinement pressure can be assumed to be constant along the sliding plane when P_{conf} is constant.

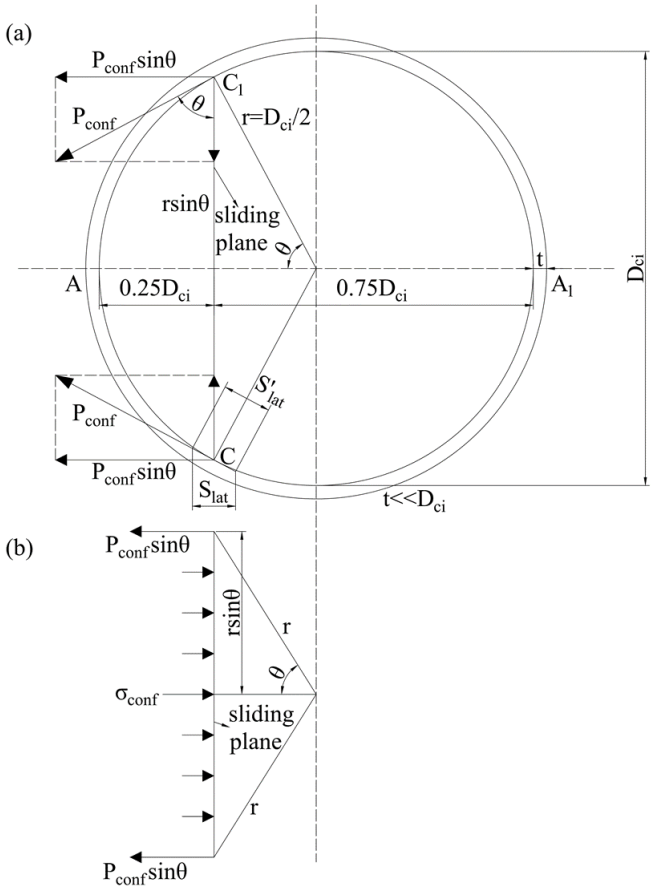

Fig. 4 Confinement force in a circular cylinder

From the above analysis, it can be seen that when P_{conf} is the same in the rectangular section in Fig. 3(b) and in the circular section in Fig. 3(a), then the confinement stress is the same in both cases. The confinement force P_{conf} could be limited by intermediate crack (IC)

debonding P_{IC} [36-38], yield of the tube P_{yld} should the material be ductile or fracture of the tube P_{fr}. The IC debonding resistance P_{IC} depends on the bond-slip material characteristics between the lateral reinforcement and the adjacent concrete. Hence P_{IC} in the rectangular section in Fig. 3(b) will be the same as in the circular section in Fig. 3(a). Hence when P_{conf} equals P_{IC} then σ_{conf} will be the same in both the circular and rectangular sections.

The IC debonding resistance P_{IC} depends on the tangential component of S_{lat} that is S'_{lat} for the circular section in Fig. 3(a). For the rectangular section in Fig. 3(b) S'_{lat} equals S_{lat}. Hence for a specific interface slip S in Figs. 3(a) and (b) S'_{lat} is constant in the rectangular section in Fig. 3(b) but varies in the circular section in Fig. 3(a). Consequently both systems in Fig. 3 have the same value of P_{IC} but the onset of P_{IC}, that is the interface slip at which they occur, varies. For a given S_{lat} in Fig. 3, S'_{lat} will be larger in the circular section than in the rectangular section except when the sliding plane is at the centre in which case they are equal. Hence P_{IC} will occur earlier in the circular section than in the rectangular section that is the build up of confinement stress in the circular section will be more rapid in the circular section than in the rectangular section but their peak values will be the same. Hence basing the analysis of a circular section on the section at B-B_1 in Fig. 3(a) will give a slightly conservative design as it will underestimate the build up of confinement stress but importantly it still gives the correct ultimate confinement. The same argument can be applied to yielding P_{yld} and fracture P_{fr} that is basing the analysis on a section at B-B_1 in Fig. 3(a) will underestimate the build up of the confinement but give the correct maximum value.

From the above, it can be seen that much of the mechanics for rectangular sections [35] can be applied directly to circular sections and only where they diverge will it be explained in detail in this paper.

Confinement Mechanism

The confinement mechanism for generating the passive concrete σ/ε is described qualitatively. This procedure first requires the active concrete σ/ε.

Actively Confined Concrete

Consider the circular cylinder in Fig. 5 that is subjected to an axial stress σ_{ax} and a lateral confining stress σ_{conf}. Prior to the occurrence of sliding, the longitudinal strain ε_m induced by σ_{ax} is a material strain that applies throughout the cylinder height L_{def} and ε_m is size-independent of L_{def}.

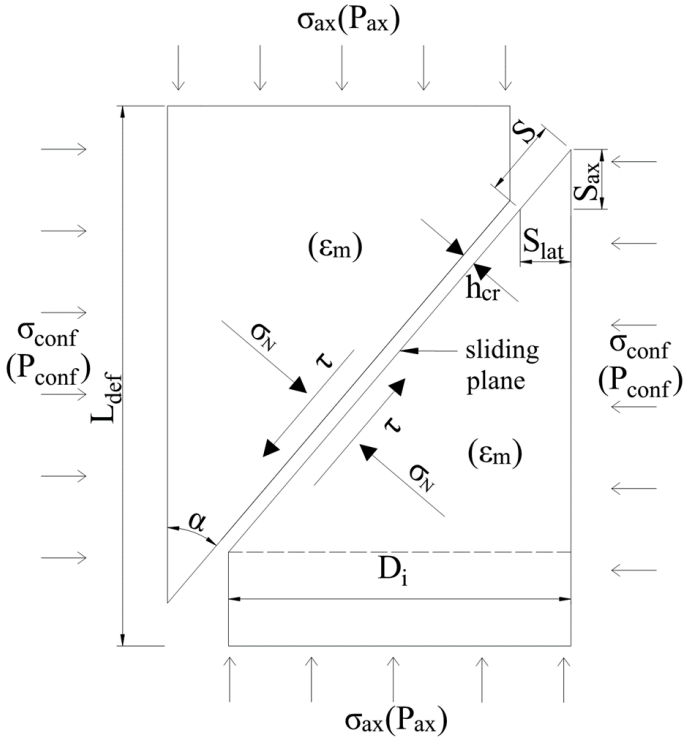

Fig. 5 Actively confined cylinder

With the gradual increase of σ_{ax} in Fig. 5, a sliding plane forms eventually with a slip S and inclination α as shown. The vertical component of the slip S_{ax} will cause the longitudinal contraction of concrete which is a size-dependent equivalent strain ε_S of S_{ax}/L_{def}. Consequently, the total axial strain ε_{ax} when sliding occurs, is comprised of the size-independent material strain ε_m and size-dependent sliding strain ε_S. If lateral confinement reinforcement such as stirrups, tubes or wraps are present, the lateral component of slip S_{lat} would be resisted by these reinforcements going into tension. This tensile resistance from the lateral confinement is balanced by lateral compression of the concrete along the sliding plane of the same magnitude.

The shear sliding plane in Fig. 5 is subjected to a normal stress σ_N and a shear stress τ that are resolved from the forces that induce the axial stress σ_{ax} and lateral confining stress σ_{conf}.

The relationship between σ_N, the shear capacity τ_m, slip S and crack width h_{cr} is referred to as the shear friction material property [27, 28, 31, 39, 40]. However h_{cr} is an order of magnitude smaller than S such that h_{cr} can be ignored which is also a conservative assumption [31, 41]. The relationship is shown in Fig. 6 where: V_u is the shear capacity at the onset of sliding; the shear capacity τ_{mx} can be determined for a given slip S_x and normal stress σ_{Nx}; for a constant σ_N, the shear capacity τ_m reduces as the slip S increases.

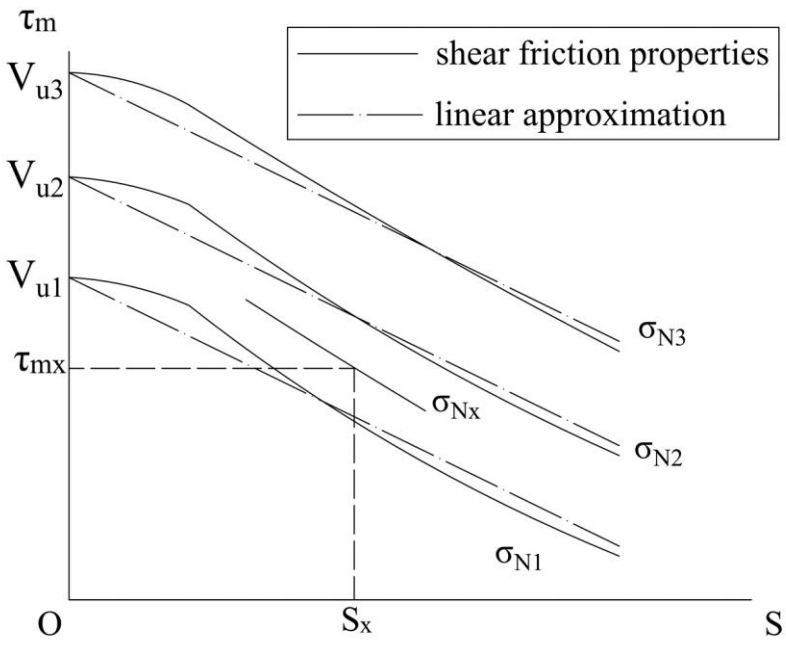

Fig. 6 Shear-Friction material properties

Consider the active stress/strain of concrete as shown in Fig. 7. Sliding occurs at (f_{c0}, ε_{c0}) for unconfined concrete and at (f_{cc}, ε_{cc}) for confined concrete. Prior to the occurrence of sliding, the axial strain is the material strain ε_m which is a material property and can be directly measured by strain gauges. Once sliding occurs, the axial stress σ_{ax} starts to reduce due to slip S and the axial strain ε_{ax} is comprised of material strain ε_m and the additional sliding strain ε_S. This descending branch can be derived from shear friction material properties as shown in Fig. 6 where, from the axial stress σ_{ax} in Fig. 5 and lateral confining stress σ_{conf}, the shear stress τ_{mx} and normal stress σ_{Nx} can be quantified. From these values, the slip S_x in Fig. 6 can be determined and consequently the sliding strain ε_S in Fig. 7 and subsequently one point on the descending branch.

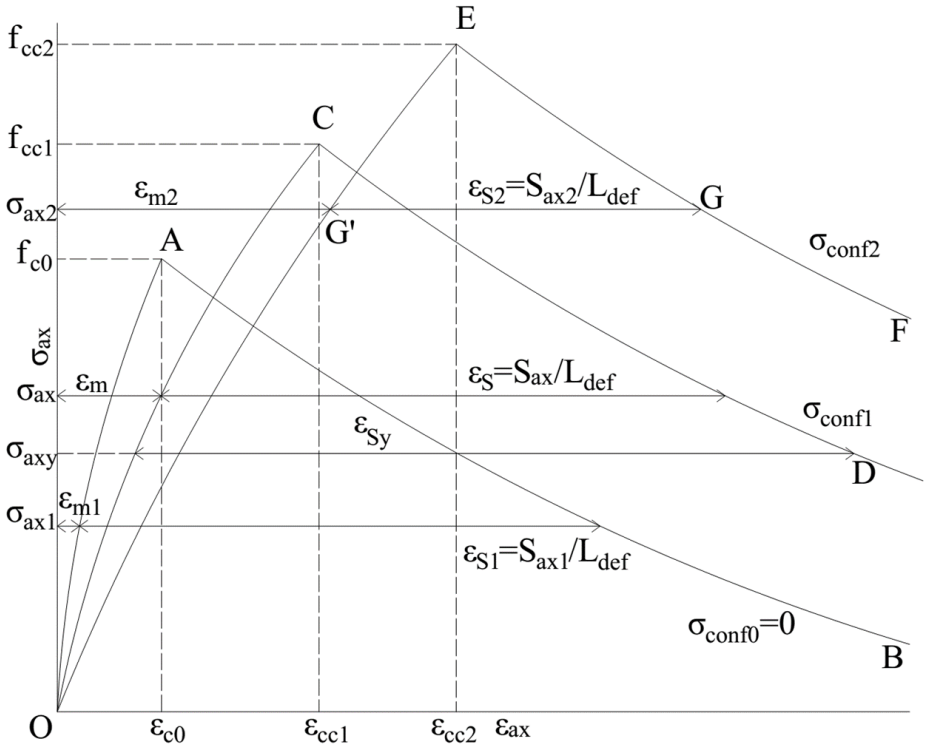

Fig. 7 Theoretical stress/strain of actively confined concrete

As an example, consider the active σ/ε O-E-F in Fig. 7 at a confining stress σ_{conf2}. The point G' at (ε_{m2}, σ_{ax2}) on the ascending branch O-E has a material strain ε_{m2}. The strain of the point G at the same axial stress σ_{ax2} on the descending branch E-G-F is comprised of the material strain ε_{m2} and the sliding strain $\varepsilon_{S2} = S_{ax2}/L_{def}$, where S_{ax2} is the vertical component of slip and L_{def} is the specimen height.

Passively Confined Concrete

Consider the circular cylinder in Fig 8 with lateral confinement reinforcement which can be internal stirrups, external wraps or a tube. The diameter of the transverse reinforcement is D_{ci}. Prior to the occurrence of sliding, the lateral confinement reinforcement has to all intents and purposes no deformation; consequently there is no confinement force nor the associated lateral confining stress. Increasing the axial stress will eventually cause sliding and the lateral component of the slip S_{lat} will cause the deformation of the confinement reinforcement and subsequently a confinement force P_{conf}.

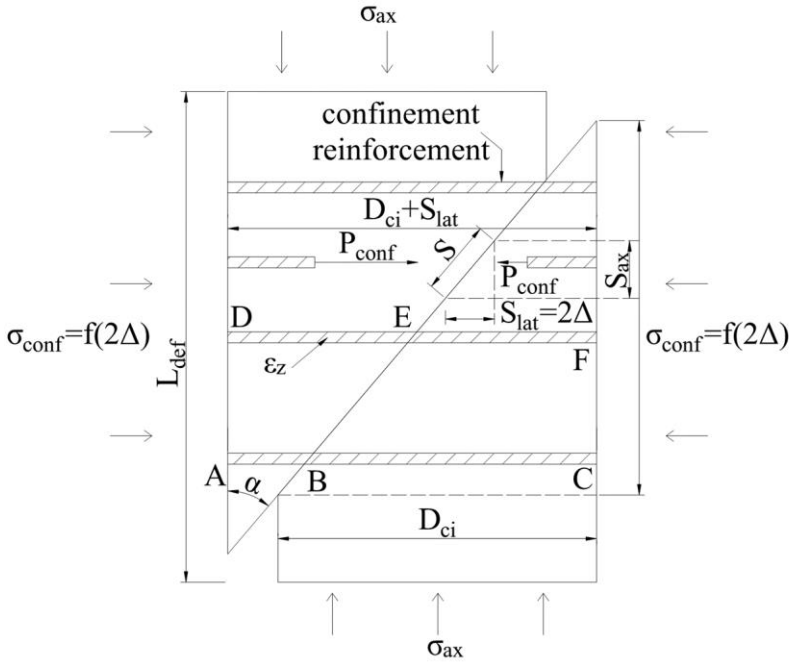

Fig. 8 Confinement force and deformation of passively confined concrete

It has been explained previously using Figs. 3 and 4 that P_{conf} will cause a constant confinement pressure σ_{conf} on the sliding plane in Fig. 2. Furthermore in Fig. 3(a), S'_{lat} will overestimate S_{lat} and, therefore, it is reasonable to assume S_{lat} equals S'_{lat} to give a safe solution. In Fig. 8, S_{lat} can be visualised as the sum of the crack face slips at both sides of the sliding plane and is referred to as 2Δ. The partial-interaction mechanics of intermediate-crack (IC) debonding [33, 34, 42-44] depends on the bond-slip material property τ_B/δ between the confinement reinforcement and adjacent concrete [38, 45-47]. From which, the relationship between the confinement force P_{conf} and crack face slip Δ can be determined and subsequently $S_{lat} = 2\Delta$. Hence, for a given slip S of the sliding plane in Fig. 2, the horizontal component of slip S_{lat} can be employed to derive the confinement force P_{conf} in Fig. 4 and, subsequently, the lateral confining stress σ_{conf} from Eq. 1. The sliding strain ε_S in Fig. 7 can be determined from the vertical component of slip S_{ax} and it is a question of finding or fixing σ_{ax} at which this occurs. For instance, for a lateral confining stress σ_{conf1}, the active stress/strain O-C-D in Fig. 7 can be constructed as described previously. For a given slip S, the vertical component of slip S_{ax} can be quantified and subsequently the sliding strain ε_{Sy}; this horizontal dimension ε_{Sy} is then fitted within the ascending branch O-C and descending branch C-D to fix σ_{axy} and consequently point D.

When there is no interface bond between the reinforcement and the concrete or when IC debonding is complete such that there is no interface bond, then the strain in the confinement reinforcement in Fig. 8 is constant at ε_z. Furthermore by symmetry in Fig. 4(a), this reinforcement is anchored or does not slip at points A and A_1 such that each deformation S'_{lat} is accommodated by strains within the tube of length $\pi D_{ci}/2$. As mentioned previously in terms of the build up of confinement, for a slightly conservative design it will be assumed that S'_{lat} equals S_{lat}. Hence for a given confinement reinforcement strain ε_z, the lateral component of slip S_{lat} for a circular cylinder equals $\pi\varepsilon_z D_{ci}/2$ and the sliding strain ε_{Sy} can be determined for $S_{lat} = \pi\varepsilon_{Sy} D_{ci}/2$. Then the analysis above to determine σ_{axy} in Fig. 7 applies by substituting this ε_{Sy}.

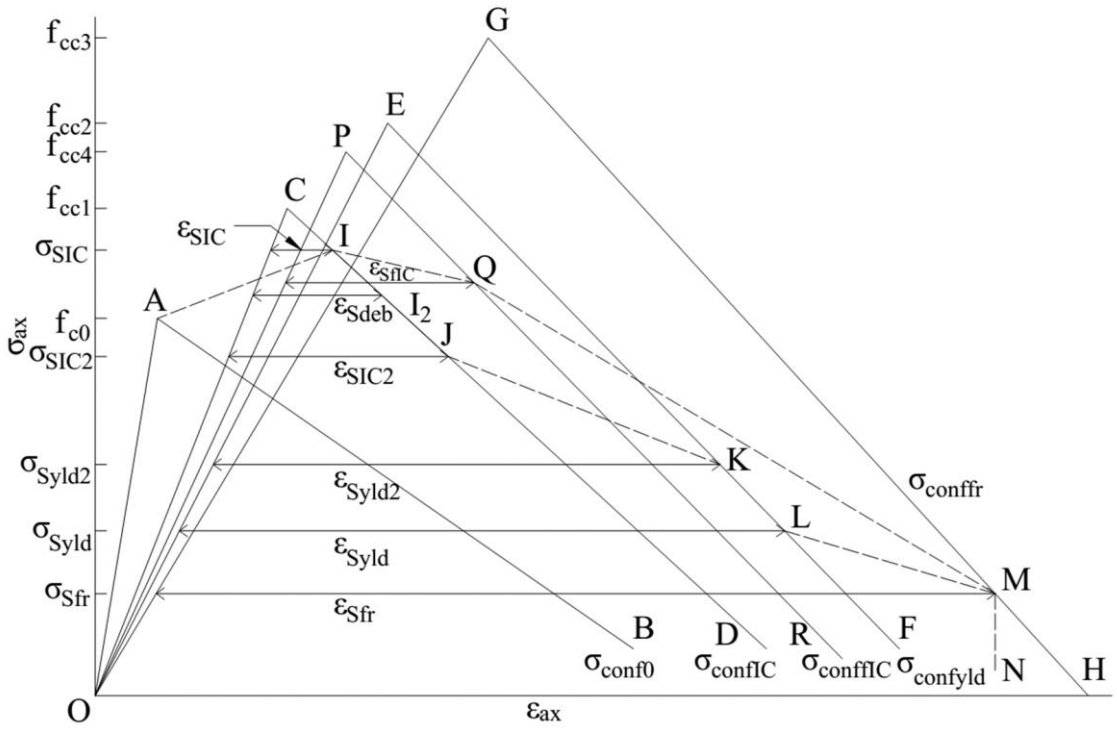

Fig. 9 Theoretical stress-strain of passively confined concrete

Let us now consider the construction of the passive stress/strain in Fig. 9 for the circular cylinder in Fig. 8. The descending branches in Fig. 9 are simplified as straight lines for ease of explanation. Let us start with the active stress/strain O-A-B in Fig. 9 for $\sigma_{conf0} = 0$ which can be constructed as described previously. Similarly, the active stress/strain O-C-D can be constructed at the IC debonding resistance P_{IC} at the lateral confining stress σ_{confIC} when the strain of the confinement reinforcement in the debonded region equals ε_{IC} [33]. The active stress/strain O-E-F can be constructed at the yield capacity P_{yld} and lateral confining stress

$\sigma_{confyld}$. Confinement reinforcement starts to yield at a strain ε_{yld2} and completes at ε_{yld}. Finally at the fracture capacity P_{fr}, the active stress/strain O-G-H can be constructed for lateral confining stress σ_{conffr} at a reinforcement strain ε_{fr}.

Prior to the occurrence of the sliding plane, slip S equals zero such that the confinement reinforcements do not have a deformation and consequently they are ineffective. The loading path will follow the ascending branch O-A in Fig. 9 for the unconfined concrete. Sliding commences at the peak point A. Slip gradually increases, which will cause an increase in the confinement reinforcement force P_{conf} until it reaches P_{IC} at a crack face slip Δ_{IC} and lateral confining stress σ_{confIC}. Hence S_{lat} equals $2\Delta_{IC}$ and the sliding strain ε_{SIC} can be determined. This ε_{SIC} can be fitted within the active stress/strain O-C-D at σ_{confIC} as shown to fix point I and quantify σ_{SIC}. Similarly, at the end of debonding and still at P_{IC}, the reinforcement strain equals ε_{IC} [33] such that $S_{lat} = \varepsilon_{IC}\pi D_{ci}/2$ and subsequently the sliding strain ε_{SIC2}. Hence the point J can be fixed by fitting this ε_{SIC2} within O-C-D for σ_{confIC} and subsequently the axial stress σ_{SIC2} can be determined. At the onset of yielding, the confinement reinforcement strain equals ε_{yld2} and subsequently $S_{lat} = \varepsilon_{yld2}\pi D_{ci}/2$ at the yield capacity P_{yld} and subsequently the lateral confining stress $\sigma_{confyld}$. This $S_{lat} = \varepsilon_{yld2}\pi D_{ci}/2$ can determine the sliding strain ε_{Syld2} and consequently the axial stress σ_{Syld2} at point K. Similarly, yielding ends at a reinforcement strain ε_{yld} and $S_{lat} = \varepsilon_{yld}\pi D_{ci}/2$ which can determine point L. Finally the confinement reinforcement fractures at the reinforcement rupture strain ε_{fr} at the confinement force P_{fr}. From which $S_{lat} = \varepsilon_{fr}\pi D_{ci}/2$ and lateral confining stress σ_{confr} can be determined and subsequently the sliding strain ε_{Sfr} and axial stress σ_{Sfr} at point M. It is worth noting that when the sliding strain is larger than O-H in Fig. 9, it means there is not enough capacity and the concrete cylinder has failed already before reaching this point.

When debonding occurs, the loading path of the passive stress/strain in Fig. 9 will follow O-A-I-J-K-L-M. If yielding does not occur then the loading path will follow O-A-I-J-M. If there is no bond, the loading path will follow O-A-L-M and so on. More points on the loading path can be fixed by taking more confinement forces such as at $P_{IC}/2$ or $P_{yld}/2$, which makes the passive stress/strain more accurate.

Quantification of Active Stress/Strain

The passive confinement mechanism has been described in the previous section; specific equations for quantifying this mechanism are given in this and the following section. Where the mechanics requires material properties, examples are given. However the mechanics does not depend on these specific material properties nor in the form that they are given and as such they could be replaced by the reader with more convenient, suitable or appropriate values. It is worth noting that the type of concrete sliding plane depends on the slenderness ratio. Short cylinders that have a slenderness ratio less than two may fail due to the formation of a circumferential wedge [17, 35, 48]. For larger slenderness ratios, sliding is likely to occur with a single sliding plane as shown in Fig. 8 and this will be investigated first as it is more likely to occur in practice and gives a lower bound to that of the circumferential wedge [35]. However an adjustment for the circumferential wedge will be given later.

The concrete active stress/strain such as in Fig. 7 is derived here from the partial interaction shear friction material properties of Hao [35] as follows.

Shear Friction Properties

The peak stresses f_{cc} in Fig. 7 can be derived from the shear-friction material properties in Fig. 6. The shear-stress capacity τ_m shown as the unbroken lines can be simplified to the linear approximations as follows

$$\tau_m = (A\sigma_N + B)S + C\sigma_N + D \tag{2}$$

where *A*, *B*, *C* and *D* are coefficients of the unconfined concrete strength f_{c0}. The following is an example of the linear approximation derived by Hao [49].

When $\sigma_N < \sigma_{N0}$, where σ_{N0} is the normal stress at the peak axial stress f_{c0} of unconfined concrete, then

$$\tau_m = [(0.00112 f_{c0} - 0.337)\sigma_N - 0.000784 f_{c0}^2 + 0.0152 f_{c0} + 0.556]S + 1.50\sigma_N + 0.105 f_{c0} \tag{3}$$

and

$$\sigma_{N0} = f_{c0} \sin^2 \alpha \tag{4}$$

When $\sigma_{N0} \leq \sigma_N < 3\sigma_{N0}$, then

$$\tau_m = [(0.00112 f_{c0} + 0.0636)\sigma_N - 0.000784 f_{c0}^2 - 0.0620 f_{c0} + 0.556]S + 0.498\sigma_N + 0.298 f_{c0} \tag{5}$$

And when $\sigma_N \geq 3\sigma_{N0}$, then

$$\tau_m = \left[\left(\frac{A_H}{2.5} - 0.199\right)\sigma_N + \frac{B_H}{2.5} - 0.119 f_{c0}\right]S + 0.498\sigma_N + 0.298 f_{c0} \tag{6}$$

where the parameters A_H and B_H are the following functions of the unconfined concrete strength f_{c0}

$$A_H = (1.229 f_{c0} - 0.577 f_{c0} A_\tau - B_\tau) / (1.345 f_{c0}) \tag{7}$$

$$B_H = -0.527 f_{c0} + 0.824 f_{c0} A_\tau + 1.429 B_\tau \tag{8}$$

in which the parameters A_τ and B_τ are given by

$$A_\tau = 0.00281 f_{c0} + 0.657 \tag{9}$$

$$B_\tau = -0.00196 f_{co}^2 + 0.143 f_{c0} + 1.39 \tag{10}$$

Ascending Branch

The peak stress f_{cc} and the strain ε_{cc} at f_{cc}, such as at points C and E in Fig. 7, are functions of the lateral confining stress σ_{conf} as follows [35]

$$f_{cc} = \frac{\sigma_{conf} \sin\alpha \cos\alpha + C\sigma_{conf} \cos^2 \alpha + D}{\sin\alpha \cos\alpha - C \sin^2 \alpha} \tag{11}$$

$$\varepsilon_{cc} = \varepsilon_{c0}[1 + A_0(\frac{\sigma_{conf}}{f_{c0}})] \tag{12}$$

where C and D are coefficients that are the same as those in Eq. (2), A_0 is a coefficient that equals 13.9 and where the unconfined concrete strain ε_{c0} at f_{c0} is

$$\varepsilon_{c0} = 1.74 \times 10^{-6} f_{c0} + 2.41 \times 10^{-3} \tag{13}$$

in which f_{c0} is in MPa.

The ascending branch of the active stress/strain in Fig. 7 can now be obtained [50, 51] by substituting f_{cc} and ε_{cc} from Eqs. (11) and (12) into

$$\sigma_{ax} = f_{cc} \frac{\frac{\varepsilon_{ax}}{\varepsilon_{cc}} r_c}{r_c - 1 + \left(\frac{\varepsilon_{ax}}{\varepsilon_{cc}}\right)^{r_c}} \tag{14}$$

where r_c is the following ductility factor

$$r_c = \frac{E_c}{E_c - \frac{f_{cc}}{\varepsilon_{cc}}} \tag{15}$$

in which the concrete elastic modulus E_c in MPa can be taken as [52]

$$E_c = 3320\sqrt{f_{c0}} + 6900 \tag{16}$$

For ease of analysis, the ascending branch of active stress/strain in Fig. 7 can be linearised as

$$\varepsilon_{ax} = \sigma_{ax} \frac{\varepsilon_{cc}}{f_{cc}} \tag{17}$$

where f_{cc} and ε_{cc} can be obtained from Eqs. (11) and (12).

Descending Branch

For a given lateral confining stress σ_{conf} and a slip S in Fig. 5, the axial stress σ_{ax} of the descending branch can be written as [35]

$$\sigma_{ax} = \frac{\sigma_{conf} \sin\alpha \cos\alpha + AS\sigma_{conf} \cos^2\alpha + BS + C\sigma_{conf} \cos^2\alpha + D}{\sin\alpha \cos\alpha - AS \sin^2\alpha - C \sin^2\alpha} \tag{18}$$

where A, B, C and D are coefficients in Eq. (2).

The vertical component S_{ax} of the slip S in Fig. 5 divided by the specimen height L_{def} gives the sliding strain ε_S that is

$$\varepsilon_S = \frac{S \cos\alpha}{L_{def}} \tag{19}$$

Adding the additional material strain ε_m in Fig. 7 from Eq. (17) gives the following total axial strain ε_{ax}

$$\varepsilon_{ax} = \sigma_{ax} \frac{\varepsilon_{cc}}{f_{cc}} + \frac{S \cos\alpha}{L_{def}} \tag{20}$$

Substituting a specific slip S_1 for a specific confinement σ_{conf1} into Eq. (18) gives the axial stress σ_{ax1}. Substituting S_1 and σ_{ax1} into Eq. (20) gives the axial strain ε_{ax1} for σ_{ax1}. Hence one point on the descending branch at (σ_{ax1}, ε_{ax1}) for the confinement σ_{conf1} has been obtained and the process is repeated to construct the descending branch.

Quantification of Passive Stress/Strain

As explained previously using Fig. 3(a), a slightly conservative design can be based on the section where the sliding plane crosses the centre such as at B-B_1 in Fig. 3(a) and which is shown in Fig. 10. When the sliding crack of width S_{lat} first forms, interface bond shear stresses τ_B form on either side of the crack over a length L_{crt} as shown. These shear stresses induce a shear force P_{conf} which is balanced by the confinement force of equal magnitude. As S_{lat} is increased, and assuming yield or fracture of the reinforcement does not occur, the bond forces reach their maximum value which is referred to as the intermediate crack (IC) debonding resistance [33, 36, 38, 53, 54]. The force at which this occurs is referred to as P_{IC} which induces a reinforcement strain ε_{IC} and occurs at an interface lateral slip S_{lat} of Δ_{IC}. These parameters depend on the bond-slip properties as follows.

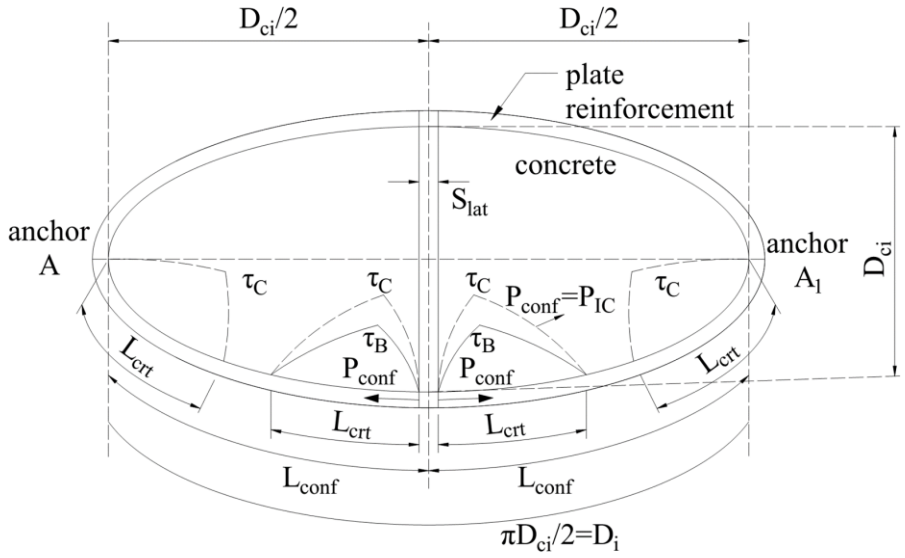

Fig. 10 Confinement lengths at both sides of the sliding plane

IC Debonding

Any appropriate bond-slip material property can be used. As an example, consider the bilinear bond-slip material properties O-A-B in Fig. 11.

For flat plate reinforcement, the parameters can take the following values [38]

$$\tau_{B\max} = (0.802 + 0.078\phi_f) f_{c0}^{0.6} \tag{21}$$

$$\delta_1 = 0 \tag{22}$$

$$\delta_{\max} = \frac{0.976\phi_f^{0.526}}{0.802 + 0.078\phi_f} \tag{23}$$

in which the units are in mm and N and where φ_f is the aspect ratio of the interface debonding plane which can be taken approximately as the inverse of the width of the plate b_f also in mm. It is worth noting that the plate reinforcement width b_f should be no more than 100 mm as this is the maximum of the plate reinforcement width in the database of Seracino et al. [38] used to derive P_{IC} in Eq. (26).

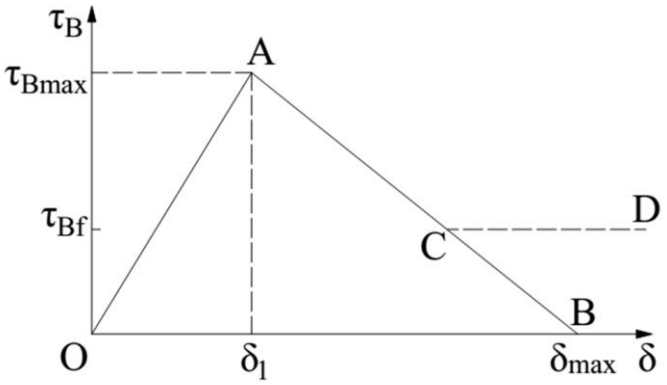

Fig. 11 Bond-Slip material properties

It is also worth noting that the lateral expansion of concrete will induce a confining stress across the curved bonded interface in Fig. 10 which may enhance the bond [55] derived from flat plates and, hence, the above will be on the conservative side.

The maximum bond force is given by [33, 37, 38]

$$P_{IC} = \sqrt{\tau_{B\max}\delta_{\max}}\sqrt{L_{per}E_rA_r} \tag{24}$$

where E_r and A_r are the elastic modulus and cross-sectional area of the confinement reinforcement and L_{per} is b_f and P_{IC} occurs at a half crack width that is a lateral slip $S_{lat}/2$ of

$$\Delta_{IC} = \delta_{\max} \tag{25}$$

As an example, for plate reinforcement the IC debonding can be written as [38]

$$P_{IC} = 0.85\phi_f^{0.25} f_{c0}^{0.33} \sqrt{L_{per} E_r A_r} \tag{26}$$

The minimum length of confinement reinforcement required to develop P_{IC} is referred to as L_{crt} as shown in Fig. 10 and can be expressed as [38]

$$L_{crt} = \frac{\pi}{2\lambda} \tag{27}$$

where

$$\lambda = \sqrt{\frac{\tau_{B\max} L_{per}}{\delta_{\max} E_r A_r}} \tag{28}$$

As previously explained using Fig. 3(a), by symmetry points A and A_1 in Fig. 10 can be considered as anchor points such that the length of the confinement reinforcement either side of the sliding plane is L_{conf} as shown. Hence the maximum bond force P_{IC} can be attained when $L_{crt} < L_{conf}$. Furthermore, the length of a fully debonded plate as shown in Fig. 10 is given by

$$D_i = \frac{\pi D_{ci}}{2} \tag{29}$$

Hence when there is no bond or the confinement reinforcement has been fully debonded, the confinement reinforcement strain is constant at ε_z such that S_{lat} is $\varepsilon_z D_i$ which is $\varepsilon_z \pi D_{ci}/2$.

Interaction between Slip and Confinement

As S_{lat} in Fig. 10 is gradually increased, the bond stresses τ_B build up. When $L_{crt} < L_{conf}$, then P_{IC} can be achieved but the reinforcement may yield at P_{yld} or fracture at P_{fr} prior to

debonding. Should debonding occur at P_{IC} at the bond stresses τ_C, then the distribution of the bond stresses τ_C move away from the sliding plane to the anchor points as shown whilst the confinement force P_{IC} remains constant. After which, the anchor points A and A_1 take over such that, for all intents and purposes, the reinforcement is completely debonded over the length D_i at a strain ε_{IC}. Any further increases in S_{lat} may lead to yield at a strain ε_{yld} over D_i or fracture at a strain ε_{fr}. When $L_{crt} > L_{conf}$ in Fig. 10, then P_{IC} cannot be achieved so that debonding over the length D_i cannot occur in which case the confinement force is limited by yield P_{yld} or fracture P_{fr}. It is a question of determining S_{lat} for these possible scenarios or cases [35].

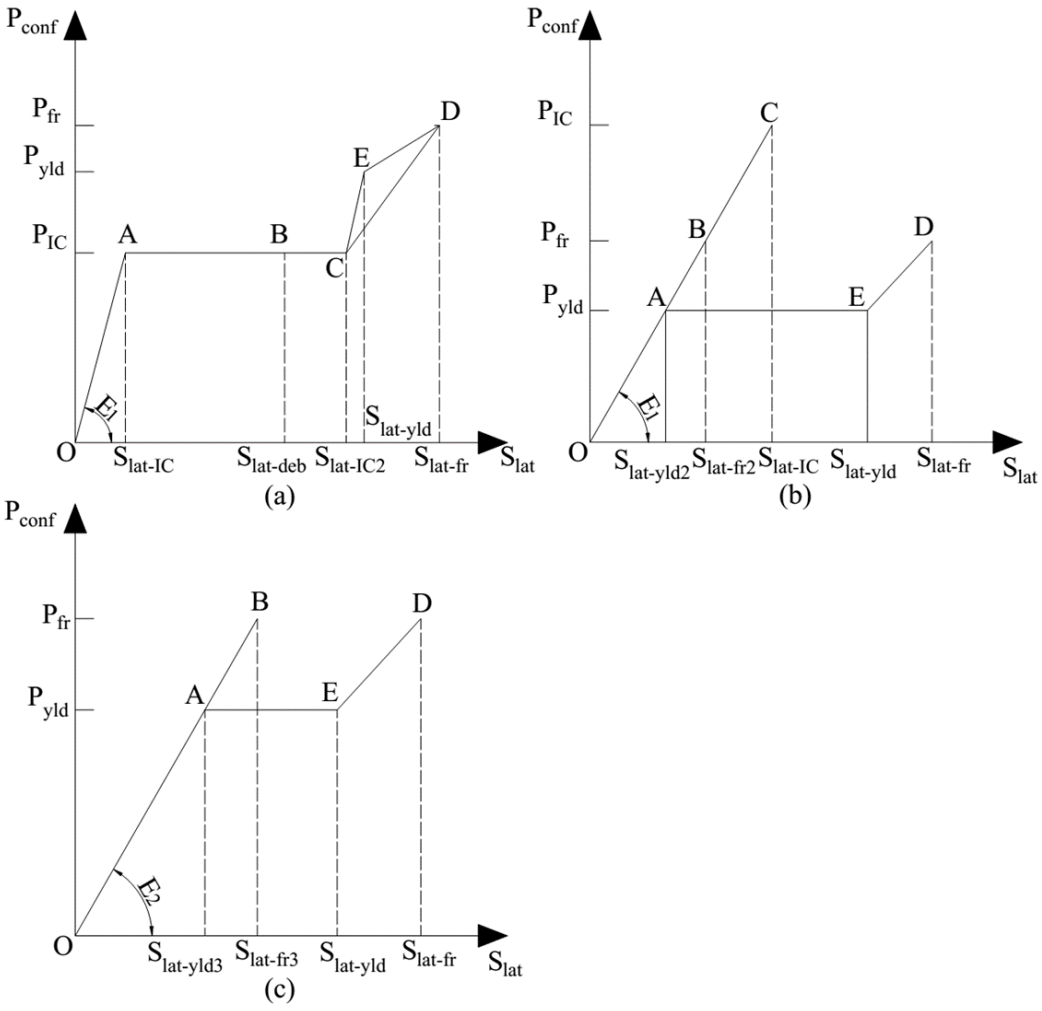

Fig. 12 P_{conf} and S_{lat} relationship for: (a) debonding prior to fracture or yield and $L_{crt} \leq L_{conf}$; (b) fracture or yield without debonding and $L_{crt} \leq L_{conf}$; (c) $L_{crt} > L_{conf}$

Case 1: $L_{conf} \geq L_{crt}$; $P_{IC} < P_{yld}$; $P_{IC} < P_{fr}$

The critical points for the case when P_{IC} is less than P_{fr} or P_{yld} and $L_{conf} \geq L_{crt}$ is summarised in Fig. 12(a). The reinforcement will debond at the crack width and force coordinates (S_{lat-IC}, P_{IC}) at point A. Then the bond stress distributions τ_C in Fig. 10 move to the anchor points which is point B in Fig. 12(a) at ($S_{lat-deb}$, P_{IC}), and then they completely debond at ($S_{lat-IC2}$, P_{IC}) at point C. After which, the confinement reinforcement may either yield at ($S_{lat-yld}$, P_{yld}) at point E and then fracture at point D (S_{lat-fr}, P_{fr}) or directly fracture at point D. The slips at which they occur are as follows [35]:

$$S_{lat-IC} = 2\Delta_{IC} \tag{30}$$

$$S_{lat-deb} = 2\Delta_{IC} + \varepsilon_{IC}(D_i - 2L_{crt}) \tag{31}$$

$$S_{lat-IC2} = \varepsilon_{IC} D_i \tag{32}$$

$$S_{lat-yld} = \varepsilon_{yld} D_i \tag{33}$$

$$S_{lat-fr} = \varepsilon_{frac} D_i \tag{34}$$

where L_{crt}, D_i and Δ_{IC} can be obtained from Eqs. (27), (29) and (25).

Case 2: $L_{conf} \geq L_{crt}$; $P_{IC} \geq P_{yld}$; $P_{IC} \geq P_{fr}$

The crack widths when P_{IC} is more than the fracture capacity P_{fr} or the yield capacity P_{yld} and when $L_{conf} \geq L_{crt}$ are shown in Fig. 12(b). In this case, debonding does not occur. The confinement reinforcement may either directly fracture at ($S_{lat-fr2}$, P_{fr}) at point B, or yield at ($S_{lat-yld2}$, P_{yld}) at point A and then completely yield at ($S_{lat-yld}$, P_{yld}) at point E and ultimately fracture at (S_{lat-fr}, P_{fr}) at point D. From Hao [35]

$$S_{lat-yld2} = 2\Delta_{IC} \frac{P_{yld}}{P_{IC}} \tag{35}$$

$$S_{lat-fr2} = 2\Delta_{IC}\frac{P_{fr}}{P_{IC}} \tag{36}$$

Case 3: $L_{conf} < L_{crt}$

The variation in crack widths when $L_{conf} < L_{crt}$ is shown in Fig. 12(c); it is similar to the previous case in Fig. 12(b). The only difference is that the confinement reinforcement may yield at ($S_{lat\text{-}yld3}$, P_{yld}) at point A or fracture at ($S_{lat\text{-}fr3}$, P_{fr}) at point B. The lateral components of slip S_{lat} and confinement force P_{conf} at points E and D are the same as those in Fig. 12(b) where from Hao [35]

$$S_{lat-yld3} = \frac{P_{yld}}{\lambda E_r A_r}\left[\frac{2\sinh(D_i\lambda)}{\cosh(D_i\lambda)+1}\right] \tag{37}$$

$$S_{lat-fr3} = \frac{P_{fr}}{\lambda E_r A_r}\left[\frac{2\sinh(D_i\lambda)}{\cosh(D_i\lambda)+1}\right] \tag{38}$$

where D_i can be obtained from Eq. (29). It is worth remembering that the crack is assumed to occur in the middle of the cross-section as in Fig. 10 to achieve a conservative solution [35]. Hence the confinement length L_{conf} equals the perimeter of the quadrant that is $\pi D_{ci}/4$. The parameter λ in Eqs. (37) and (38) can be expressed as [56]

$$\lambda = \sqrt{\beta k} \tag{39}$$

where the cylinder parameter β and bond-slip stiffness k can be written as

$$\beta = L_{per}\left(\frac{1}{E_r A_r} + \frac{1}{E_c A_c}\right) \tag{40}$$

$$k = \frac{\tau_{B\max}}{\delta_1} \tag{41}$$

where L_{per} can be taken as b_f and where A_c is the cross-section area of concrete which interacts with the reinforcement in the tension stiffening analysis. It should be noted that for plate reinforcement, the area of the concrete A_c is much larger than that of the reinforcement A_r such that $1/E_cA_c$ in Eq. (40) can be assumed to be zero [44].

Lateral confining stress σ_{conf}

The lateral confining stress σ_{conf} can be derived from Eq. (1) by substituting the lateral confinement force per unit depth of reinforcement for P_{conf}. This is shown in Fig. 13(a) for a cylinder with stirrups where P_{st} is the confining force in a single stirrup that is spaced at S_S. In which case, the confinement per unit depth is

$$P_{st1} = \frac{P_{st}}{S_S} \tag{42}$$

For a concrete infilled tube as in Fig. 13(b), the confinement per unit depth is

$$P_{pl1} = \frac{P_{pl}}{b_f} \tag{43}$$

where P_{pl} is the confinement force in the tube of depth b_f. The forces P_{st1} and P_{pl1} can be substituted for P_{conf} in Eq. (1) to quantify σ_{conf}.

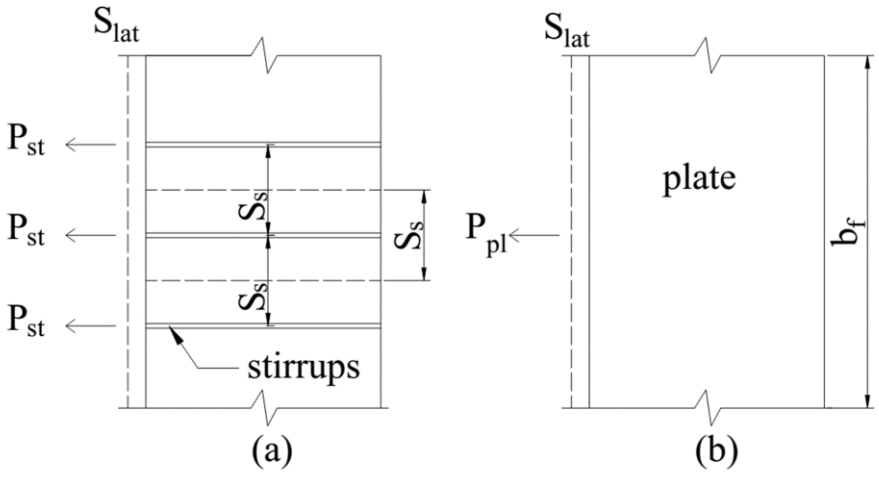

Fig. 13 Lateral confining force from (a) stirrups (b) plate

Equivalent strain ε_S and axial stress σ_S

For a given slip *S*, the sum of the crack face slips at both sides of the sliding plane S_{lat} and the confinement force P_{conf} can be determined from Fig. 12. Subsequently, the lateral confining stress σ_{conf} can be obtained from Eqs. (42) or (43) and (1). From these values, the axial stress σ_S can be obtained from [35]

$$\sigma_S = \frac{\sigma_{conf} \sin\alpha\cos\alpha + \left(A\frac{S_{lat}}{\sin\alpha} + C\right)\sigma_{conf}\cos^2\alpha + B\frac{S_{lat}}{\sin\alpha} + D}{\sin\alpha\cos\alpha - \sin^2\alpha\left(A\frac{S_{lat}}{\sin\alpha} + C\right)} \tag{44}$$

Furthermore, S_{lat} used in Eq. (44) can be employed to derive the following sliding strain ε_S

$$\varepsilon_S = \frac{S\cos\alpha}{L_{def}} = \frac{S_{lat}}{\tan\alpha L_{def}} \tag{45}$$

Adding the addition material strain from Eq. (17) gives the following axial strain ε_{ax}

$$\varepsilon_{ax} = \sigma_S \frac{\varepsilon_{cc}}{f_{cc}} + \frac{S_{lat}}{\tan\alpha L_{def}} \tag{46}$$

where σ_S can be obtained from Eq. (44) and f_{cc} and ε_{cc} can be obtained from Eqs. (11) and (12) by substituting the lateral confining stress σ_{conf} from Eq. (1).

Summary

For a given key point in Fig 12: S_{lat} and the confinement force P_{conf} as well as slip *S* can be determined; the confinement force P_{conf} can be substituted into Eqs. (42) or (43) and (1) to quantify the lateral confining stress σ_{conf}; substituting σ_{conf} and S_{lat} into Eq. (44) gives the axial stress σ_S; substituting σ_{conf} into Eqs. (11) and (12) gives f_{cc} and ε_{cc}, which as well as S_{lat} and σ_S can be substituted into Eq. (46) to give the axial strain ε_{ax}. Consequently, the axial

stress and strain of one key point in Fig. 9 on the passive stress/strain is fixed and, similarly, the axial stress and strain of other key points in Fig. 9 can be determined.

Circumferential Failure Type

The theoretical approach assuming a single sliding mechanism [35, 48] has been described above. However, when the aspect ratio of the circular cylinders tested was small failure due to circumferential wedges [57] may have occurred. The only difference between these two failure types in the proposed approach is the following peak stress f_{cccir} of the active stress/strain from Eq. (11) and the axial stress σ_{Scir} of the passive stress/strain from Eq. (44) [35]

$$f_{cccir} = \frac{2\sigma_{conf}\sin\alpha\cos\alpha + 2C\sigma_{conf}\cos^2\alpha + D}{\sin\alpha\cos\alpha - C\sin^2\alpha} \tag{47}$$

$$\sigma_{Scir} = \frac{2\sigma_{conf}\sin\alpha\cos\alpha + \left(A\frac{S_{lat}}{\sin\alpha} + C\right)2\sigma_{conf}\cos^2\alpha + B\frac{S_{lat}}{\sin\alpha} + D}{\sin\alpha\cos\alpha - \sin^2\alpha\left(A\frac{S_{lat}}{\sin\alpha} + C\right)} \tag{48}$$

The other procedures are the same as that of the single-sliding failure.

Parametric Study

Effect of Bond Material Properties

As mentioned previously, the lateral expansion of the encased concrete will induce a confining stress across the curved bonded interface in Fig. 10 which may enhance the bond. To determine the effect of this bond enhancement, a parametric study of the FRP reinforced specimen SCP-4-2 [10] is conducted using the proposed approach with the circumferential failure type. The variation O-A-B-C-D in Fig. 12(a) applies.

In the previous analysis, the bilinear bond-slip material properties, that is the variation O-A-C-B in Fig. 11, was applied which means that the friction bond stress τ_{Bf} equals zero. However, the confining stress across the curved bonded interface may enhance the friction bond stress τ_{Bf} [55]. In this section, the effect of the friction component of bond τ_{Bf} in Fig. 11 for the case in Fig. 12(a) is investigated.

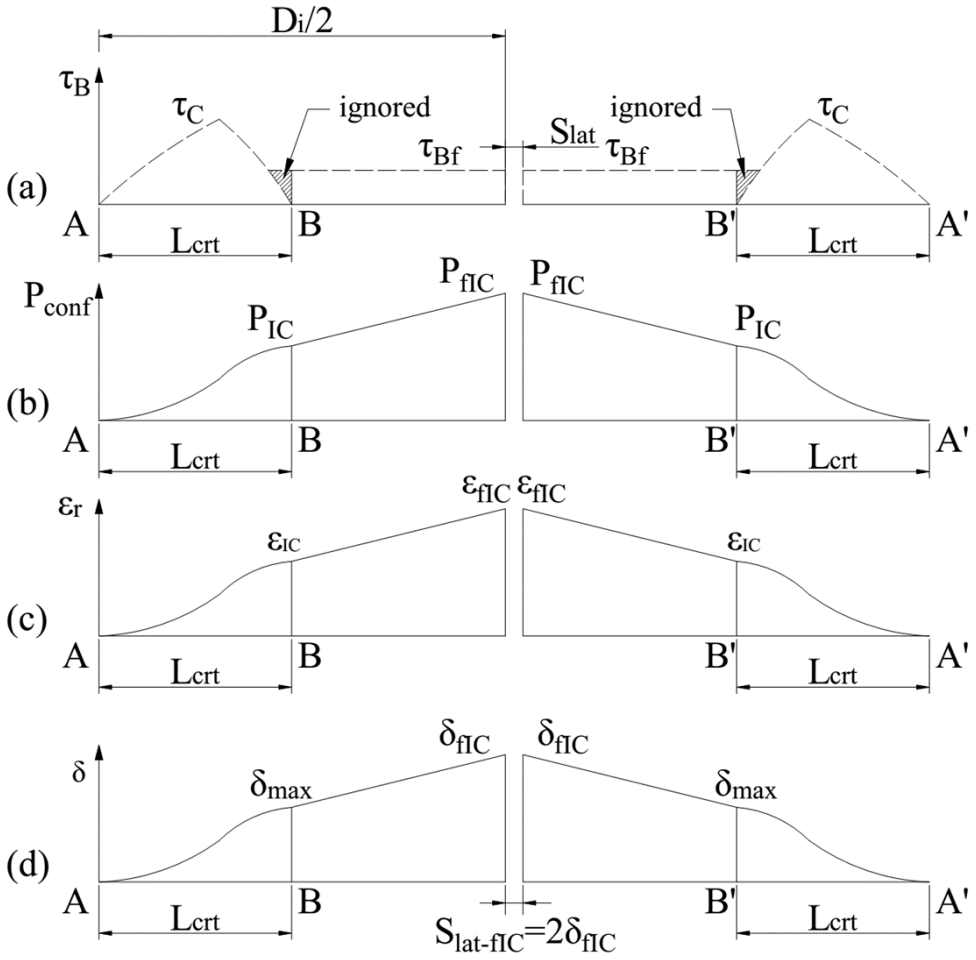

Fig. 14 Distribution of τ_B, P_{conf}, ε_r and δ along D_i

As explained previously by using Fig. 3(a), a slightly conservative assumption is made by using the sliding plane that crosses the centre as shown in Fig. 10. Consider the distribution of bond stress τ_B in Fig. 14(a), confinement force P_{conf} in Fig. 14(b), strain ε_r in Fig. 14(c) and slip δ in Fig. 14(d) along the arch A-A' in Fig. 10 when the bond stress τ_C has been developed to the anchor point A or A' as shown in Fig. 14(a). The shaded bond stress is ignored for ease of analysis and which also gives a slightly conservative assumption. Hence the confinement force, strain and slip at points B and B' equal P_{IC}, ε_{IC} and δ_{max} respectively.

The friction component of bond τ_{Bf} will enhance the confinement force to P_{flC} which can be written as

$$P_{flC} = P_{IC} + \tau_{Bf} L_{per} (\frac{D_i}{2} - L_{crt}) \tag{49}$$

the crack face slip δ_{flC} can be written as

$$\delta_{flC} = \delta_{\max} + \frac{P_{flC} + P_{IC}}{2E_r A_r} (\frac{D_i}{2} - L_{crt}) \tag{50}$$

and consequently the crack width $S_{lat\text{-}flC}$ as

$$S_{lat-flC} = 2\delta_{flC} = 2\delta_{\max} + \frac{P_{flC} + P_{IC}}{2E_r A_r} (D_i - 2L_{crt}) \tag{51}$$

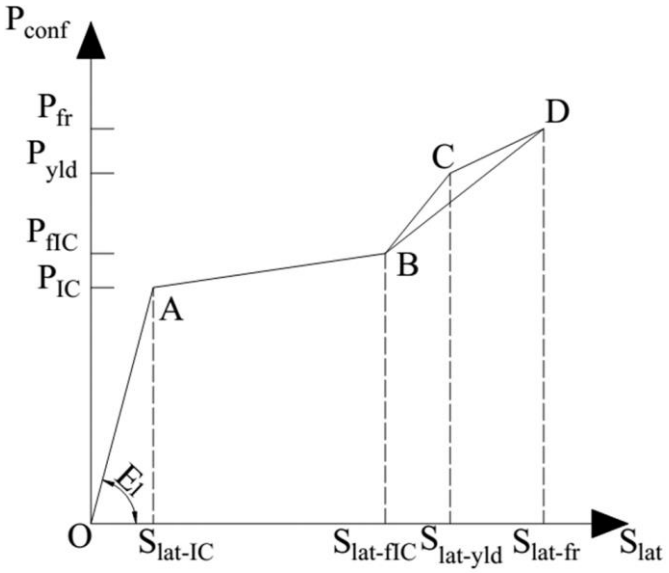

Fig. 15 P_{conf} and S_{lat} relationship for debonding prior to fracture or yield and $L_{crt} \leq L_{conf}$ allowing for τ_{Bf}

The variation O-A-B-C-D that normally applies for FRP reinforced specimens in Fig. 12(a) is updated as shown in Fig. 15. From the variation at point B in Fig. 15, the axial stress and strain can be derived from Eqs. (44) and (46) respectively that is at point Q in Fig. 9. This

point is located on the additional active stress/strain O-P-R in Fig. 9 for confinement $\sigma_{conffIC}$ at P_{flC} from Eq. (49). Hence the loading path of the passive stress/strain in Fig. 9 follows O-A-I-Q-M-N. The corresponding passive stress/strains for specimen SCP-4-2 has been plotted in Fig. 16 where the friction component of bond τ_{Bf} varies. The friction component can increase the strength after debonding at point I and when $\tau_{Bf} = 0.6\tau_{max}$, there is no apparent step change and the loading path follows an ascending branch such as I-M. As there is no available model to quantify τ_{Bf}, in the following validation part, τ_{Bf} is assumed to equal $0.4\tau_{max}$ as an example and this requires further research [58, 59].

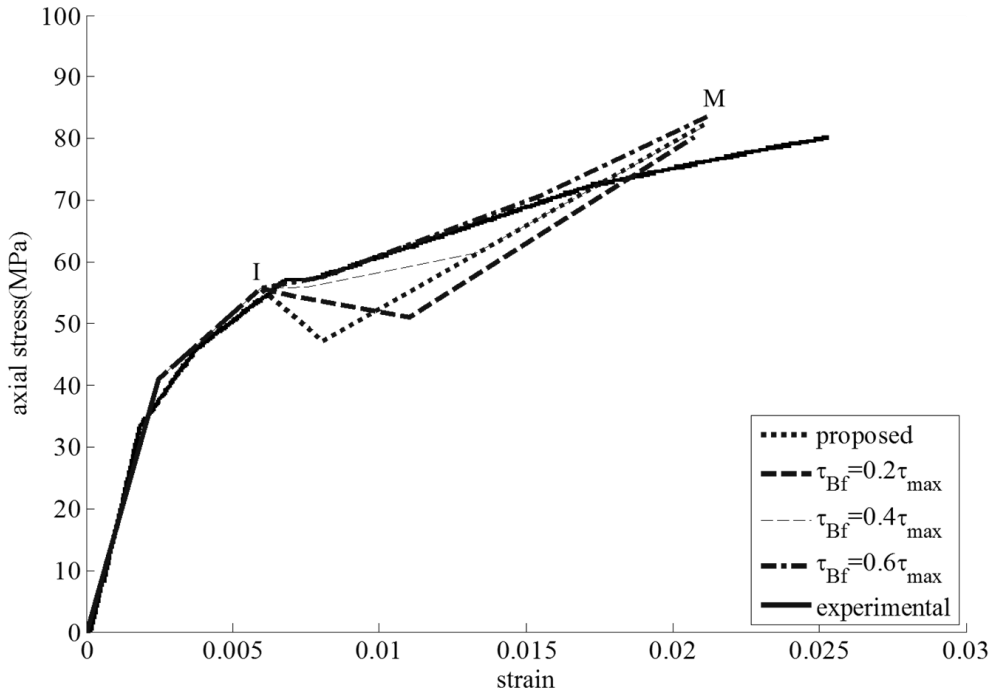

Fig. 16 Parametric study of specimen SCP-4-2

Effect of Cylinder Diameter D_{ci}

A parametric study is conducted to investigate the effect of the cylinder diameter D_{ci} for specimens reinforced with either FRP wrap or a steel tube. Specimen details are given in Appendix 2. The general behaviour is first described followed by a quantification based on the partial interaction theory developed previously.

General Behaviour

The FRP reinforced cases are shown in Fig. 17, Fig. 18, Fig. 19 and Fig. 20. In Fig. 17, the confinement stress σ_{conffr} at fracture of the FRP (P_{fr}) is maintained constant for varying specimen diameters that is P_{fr} is changed with diameter to ensure σ_{conffr} is constant. In the remaining figures, the confinement stress σ_{confIC} at IC debonding (P_{IC}) is held constant. The passive stress/strain follows O-A-I-J-M such as in Fig. 17 where: sliding occurs at point A; confinement reinforcements start to debond at point I; completely debonds at point J; and fracture occurs at point M. Some passive stress/strains end at a point N such as O-A-I_5-N_5 in Fig. 17; this is because at the next point after point N, the sliding strain ε_S is larger than O-H in Fig. 9 which means there is not enough shear capacity along the sliding plane to fracture the FRP. For some cases that fail before the occurrence of debonding at point I, such as the case O-A-M_1 in Fig. 18, the confinement reinforcement fractures first as the fracture capacity P_{fr} is less than the IC debonding resistance P_{IC} that is the case in Fig. 12(b).

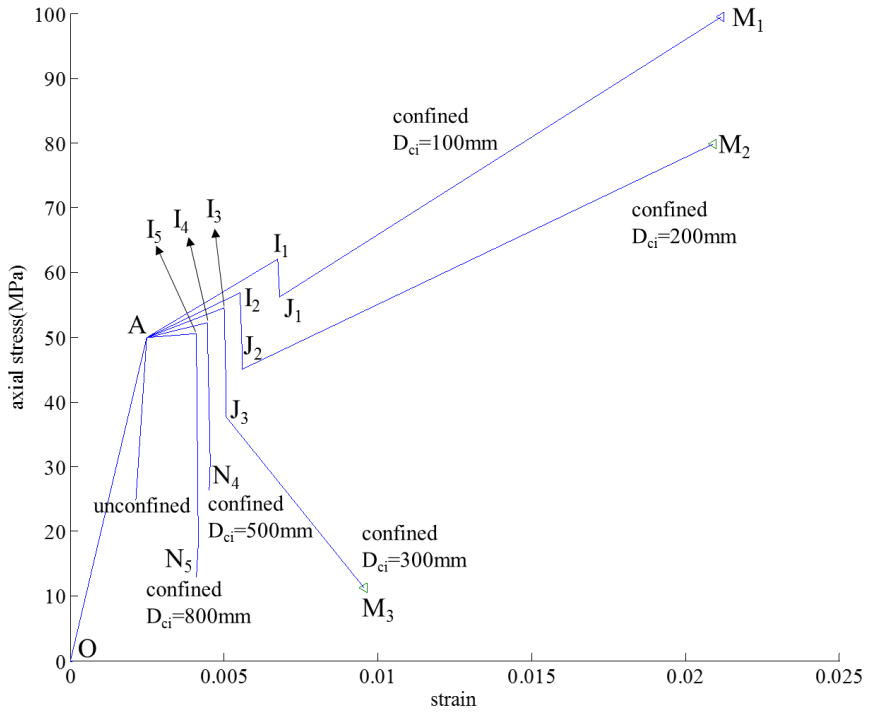

Fig. 17 Effect of diameter D_{ci} when σ_{conffr} is constant (FRP reinforced)

It can be seen in Fig. 17 that design based on the confinement at FRP fracture can lead to large variability in the passive stress/strain with the ductility reducing as the specimen diameter increases. In contrast, design based on confinement at IC debonding in Figs. 18 to

20 has little variability except at fracture and ductility increases with increasing diameter and confinement stress.

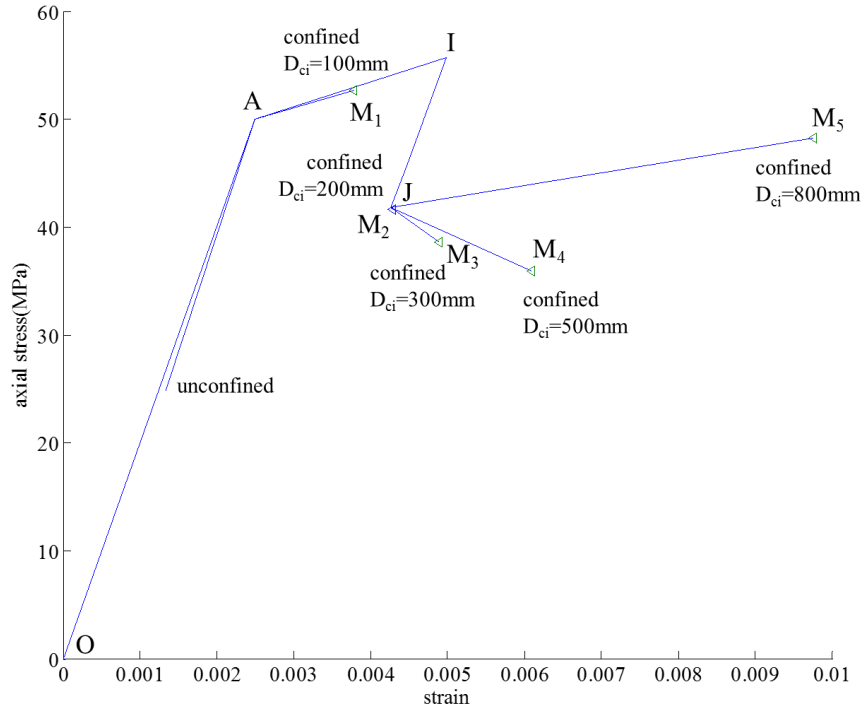

Fig. 18 Effect of diameter D_{ci} when σ_{confIC} is constant at 3.91MPa (FRP reinforced)

It is worth noting that in this parametric study it is assumed that FRP will fail at the material rupture strain. Hence, substituting the fracture capacity P_{fr} into Eqs. (42) or (43) and (1) gives the lateral confining stress at fracture σ_{conffr}; then substituting this σ_{conffr} and the lateral component of slip $S_{lat\text{-}fr}$ at fracture from Eq. (34) into Eq. (44) and Eq. (46) gives the following axial stress σ_{Sfr} and axial strain ε_{axfr} at fracture

$$\sigma_{Sfr} = \frac{\sigma_{conffr}\sin\alpha\cos\alpha + \left(A\frac{\varepsilon_{frac}D_i}{\sin\alpha} + C\right)\sigma_{conffr}\cos^2\alpha + B\frac{\varepsilon_{frac}D_i}{\sin\alpha} + D}{\sin\alpha\cos\alpha - \sin^2\alpha\left(A\frac{\varepsilon_{frac}D_i}{\sin\alpha} + C\right)} \tag{52}$$

$$\varepsilon_{axfr} = \sigma_{S-fr}\frac{\varepsilon_{cc}}{f_{cc}} + \frac{\varepsilon_{frac}D_i}{\tan\alpha L_{def}} \tag{53}$$

which are the co-ordinates of the points M in Figs. 17 to 20 that is a measure of the extent or ductility of the passive stress/strain.

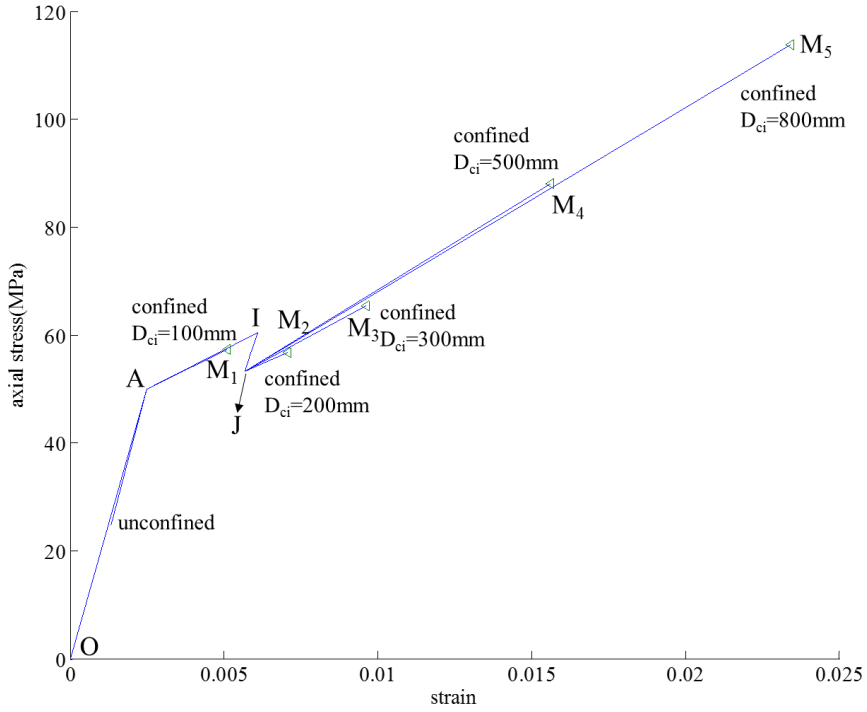

Fig. 19 Effect of diameter D_{ci} when σ_{confIC} is constant at 5.53MP (FRP reinforced)

For the steel tube reinforced cases in Fig. 21, Fig. 22 and Fig. 23, the confinement stress at yield is held constant. The passive stress/strain follows O-A-L, which is also the case in O-A-L in Fig. 9 where the confinement reinforcements yield at point L. It can be seen that basing the design on the confinement at yield produces a wide variation in the concrete ductility with ductility reducing with increasing diameter.

Variation in Diameter

Specimens designed with the same confinement at fracture

In Fig. 17, the diameter D_{ci} is varied whilst the lateral confining stress at fracture σ_{conffr} is held constant (series D_{s1} in Appendix 2). The fracture force P_{fr1} per unit depth can be obtained from $f_p t_{FRP}$ where f_p and t_{FRP} are the fracture capacity and FRP thickness. Substituting P_{fr1} into Eq. (1) gives $\sigma_{conffr} = 2f_p t_{FRP}/D_{ci}$. The ratio of σ_{conffr} for two specimens

of diameter $D_{ci\text{-}S}$ and $D_{ci\text{-}M}$ are written as follows where the subscripts S and M have been used to distinguish between the specimens

$$\frac{\sigma_{conffr-S}}{\sigma_{conffr-M}} = \frac{(2 f_{p-S} t_{FRP-S}) / D_{ci-S}}{(2 f_{p-M} t_{FRP-M}) / D_{ci-M}} \tag{54}$$

If it is assumed that the fracture capacity of the FRP f_p and the lateral confining stresses at fracture σ_{conffr} are the same for the two specimens, then Eq. (54) becomes

$$\frac{t_{FRP-S}}{t_{FRP-M}} = \frac{D_{ci-S}}{D_{ci-M}} \tag{55}$$

which means that to ensure that the confinement stresses σ_{conffr} at fracture are the same, the FRP thickness ratio should be directly proportional to that of the specimen diameters. Most current design-oriented approaches [8, 16, 21, 60] design for σ_{conffr} without considering the size-effect. For instance, when σ_{conffr} is constant and D_{ci} varied, these approaches are assumed to give the same passive stress/strains which is not the case as can be seen in Fig. 17. It would appear that as most specimens in the databases [8, 16] have a small diameter, deriving the stress/strain empirically from these small specimens may overestimate the ductility for large cylinders.

Specimens designed with the same confinement at IC debonding

In Figs. 18 to 20: the lateral confining stress σ_{confIC} at the IC debonding resistance P_{IC} is held constant; the diameters D_{ci} are varied; and the triangular marks are where the specimen fails due to fracture of the confinement reinforcements.

Let us first consider the case in Fig. 18 which is at a small confinement σ_{confIC} of 3.91MPa. The specimens reach their peak stress at the start of IC debonding at point I such that σ_{confIC} controls the strength. As can be seen in Fig. 18, when σ_{confIC} is constant then the ductility, that is the ultimate strain at the Δ points, increases with increasing D_{ci}.

Figures 19 and 20 show that at relatively high confinements σ_{confIC}, the ductility increases with increasing diameter D_{ci}. This is in contrast to those in Fig. 17 where σ_{conffr} is constant

and the ductility decreases with increasing D_{ci}. Substituting $A_r = b_f t_{FRP}$ into Eq. (26) gives the IC debonding resistance P_{IC}. Substituting the confinement force per unit depth $P_{IC1} = P_{IC}/b_f$ into Eq. (1) gives the lateral confining stress σ_{confIC} at P_{IC}

$$\sigma_{confIC} = \frac{1.7\phi_f^{0.25} f_{c0}^{0.33} \sqrt{L_{per} E_r b_f t_{FRP}}}{b_f D_{ci}} \tag{56}$$

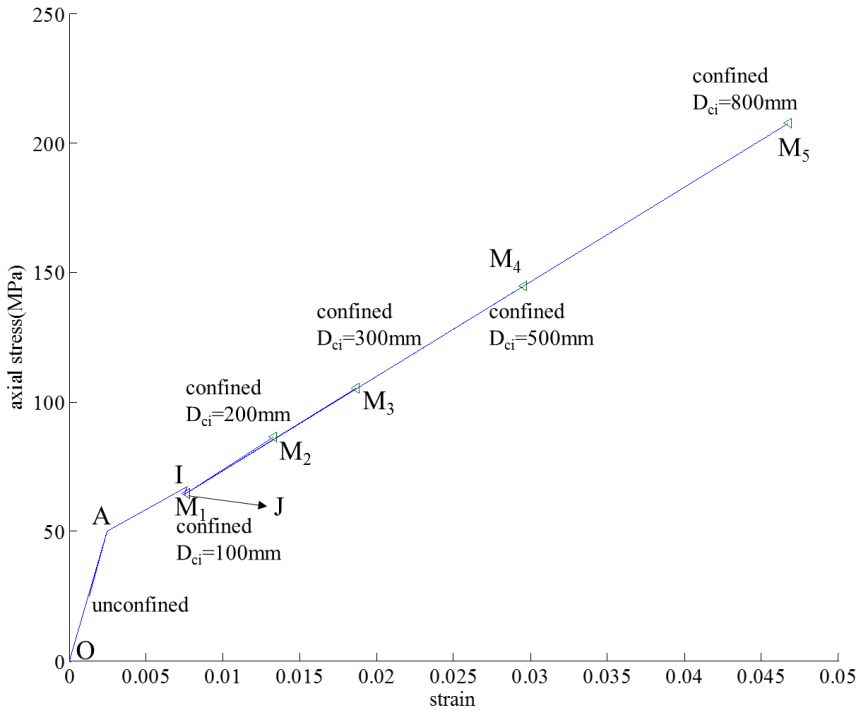

Fig. 20 Effect of diameter D_{ci} when σ_{confIC} is constant at 7.82MPa (FRP reinforced)

The ratio of σ_{confIC} for two specimens is therefore

$$\frac{\sigma_{confIC-S}}{\sigma_{confIC-M}} = \frac{\left(1.7\phi_f^{0.25} f_{c0}^{0.33} \sqrt{L_{per} E_r b_f t_{FRP-S}}\right) / \left(b_f D_{ci-S}\right)}{\left(1.7\phi_f^{0.25} f_{c0}^{0.33} \sqrt{L_{per} E_r b_f t_{FRP-S}}\right) / \left(b_f D_{ci-M}\right)} \tag{57}$$

where the subscripts S and M distinguish between the specimens. When these two specimens have the same unconfined strength f_{c0} and FRP elastic modulus E_r, then the ratio of the FRP thicknesses t_{FRP} to achieve the same lateral confining stresses at debonding σ_{confIC} becomes from Eq. (57)

$$\frac{t_{FRP-S}}{t_{FRP-M}} = \frac{D_{ci-S}^2}{D_{ci-M}^2} \tag{58}$$

which means that to ensure that the IC confining stresses σ_{confIC} are the same, the FRP thickness ratio should be directly proportional to the square of that of the specimen diameters.

Specimens designed with the same confinement at yield

In Figs. 21 to 23: the concrete is encased in a steel tube; the lateral confining stress $\sigma_{confyld}$ at the yield capacity P_{yld} is constant; and the diameter D_{ci} varies at 100 mm, 200 mm, 300 mm, 500 mm and 800 mm (SD_{s2}, SD_{s3} and SD_{s4} series in Appendix 2). It can be seen that when $\sigma_{confyld}$ is constant and D_{ci} increases then the ductility decreases. When $\sigma_{confyld}$ is constant, the relationship between the diameters and reinforcement thickness is the same as the fracture case as illustrated by Eqs. (54) and (55); hence they can be applied by substituting yield capacity f_y and $\sigma_{confyld}$ for fracture capacity f_p and σ_{confrr} respectively. Hence deriving a design-oriented approach from these small-diameter specimen tests based on $\sigma_{confyld}$ without considering the effect of the diameter D_{ci} [61] may overestimate the ductility for large cylinders.

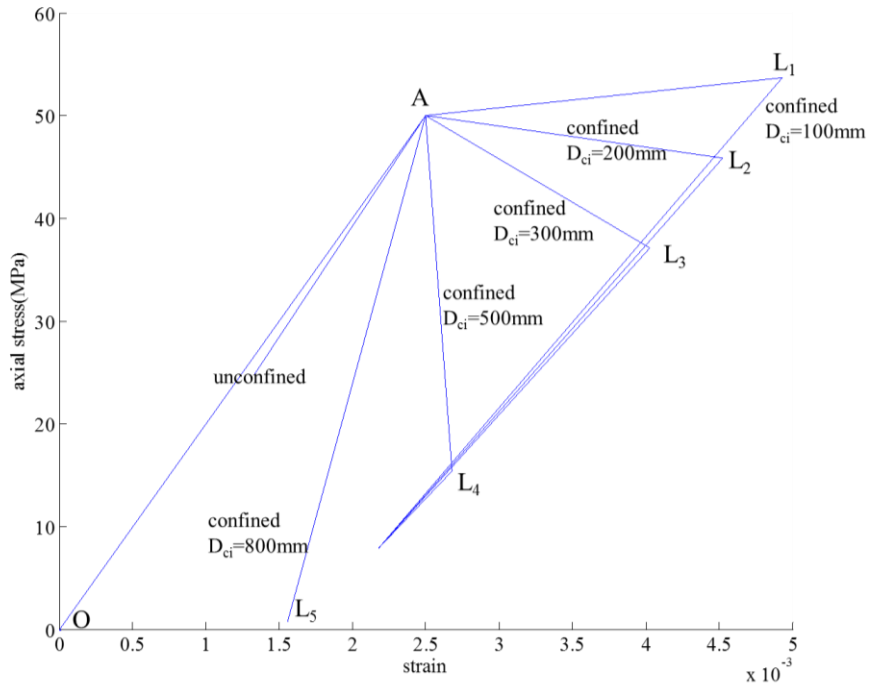

Fig. 21 Effect of diameter D_{ci} when $\sigma_{confyld}$ is constant at 4MPa (steel tube reinforced)

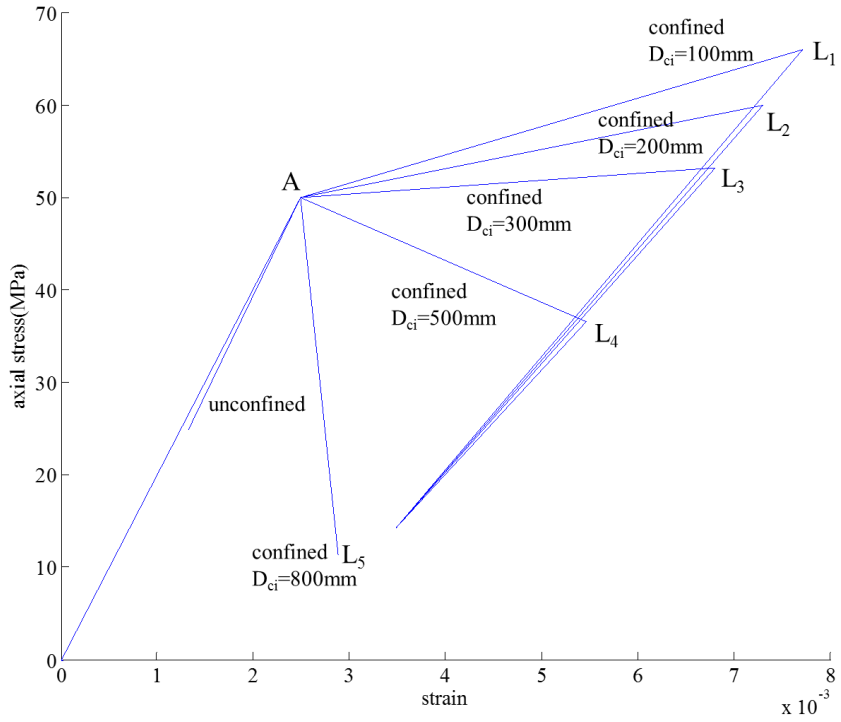

Fig. 22 Effect of diameter D_{ci} when $\sigma_{confyld}$ is constant at 8MPa (steel tube reinforced)

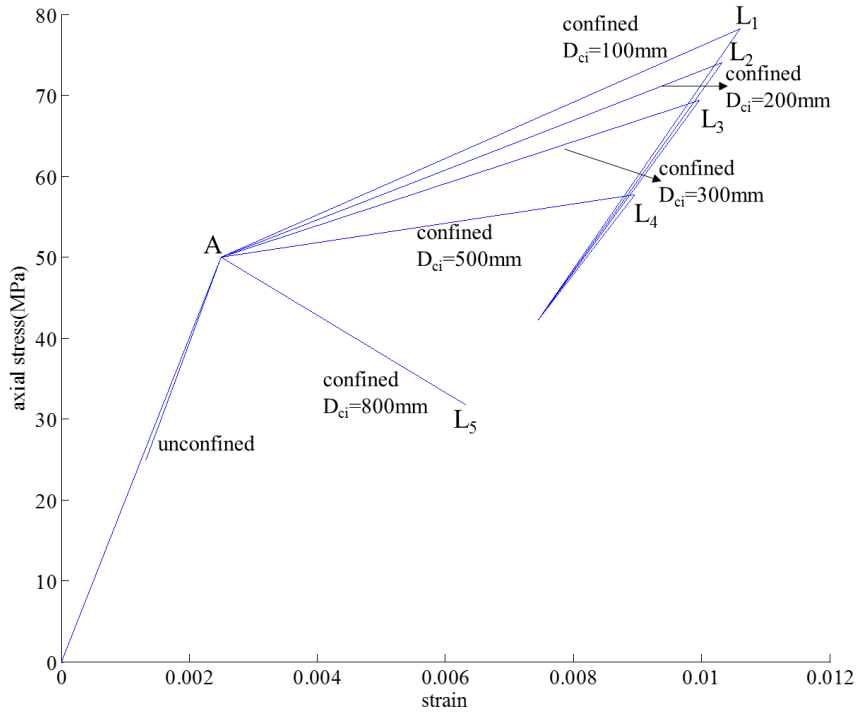

Fig. 23 Effect of diameter D_{ci} when $\sigma_{confyld}$ is constant at 12MPa (steel tube reinforced)

Validation of Confinement Model

The proposed approach has been compared with tests on FRP wrapped circular cylinders [10, 15, 57, 62-70] and those with stirrups [71, 72] that were tested under concentric load. Details of the simulated specimens are given in Appendix 3. Validation with more specimens are given elsewhere [73].

The experimental results are compared with the proposed approach assuming both a single-sliding and a circumferential failure type to give theoretical bounds to the approach. It is worth noting that the strains were measured within the gauge length L_{gl} which will be substituted for L_{def} in Eq. (46) to derive the passive axial strain within the gauge length.

Example of Stress/Strain Derivation

As an example, the approach is applied to the circular cylinder specimen SCP-4-2 by Song et al. [10] for the case of a circumferential failure type as follows.

1. The critical length L_{crt} from Eq. (27) equals 50.1 mm and is less than the perimeter of the quadrant that is $L_{conf} = \pi D_{ci}/4 = 118$ mm. From Eq. (26), P_{IC} for a 100 mm width of plate equals 24,400 kN such that $P_{IC1} = 244$ kN/mm from Eq. (43) which on substituting into Eq. (1) gives $\sigma_{confIC} = 3.25$ MPa. Fracture capacity for a $b_f = 1$mm width of plate can be obtained from $P_{fr1} = b_f f_p t_{FRP} = 1222$ kN, where t_{FRP} is the plate thickness and f_p is the fracture strength. As $L_{crt} < L_{conf}$ and $P_{IC1} < P_{fr1}$, then the variation in Fig. 15 applies. The loading path will follow O-A-I-Q-M in Fig. 9 also shown in Fig. 24 and which will now be determined.
2. Let us start by deriving the active stress/strain O-C-I for $\sigma_{confIC} = 3.25$ MPa. The axial stress and strain at the peak point C are $f_{cccir\text{-}C} = 58.3$ MPa and $\varepsilon_{cc\text{-}C} = 0.00522$ which can be obtained from Eqs. (47) and (12) respectively by substituting σ_{confIC}. The lateral component of slip S_{lat} of point I, that is $S_{lat\text{-}IC}$, can be obtained from Eq. (30) and equals 0.213 mm. The axial stress σ_S and strain ε_{ax} of point I can be obtained by substituting σ_{confIC} and $S_{lat\text{-}IC}$ into Eqs. (44) and (46) which gives 55.7 MPa and 0.00597 respectively. Linking points O, C and I in Fig. 24 gives the active stress/strain O-C-I for σ_{confIC}.

3. Consider the active stress/strain O-P-Q for $\sigma_{conffIC}$ in Fig. 24 where $\sigma_{conffIC}$ = 5.94 MPa is derived by substituting the confinement force P_{fIC} from Eq. (49) into Eqs. (1) and (43).The axial stress and strain at peak point P, $f_{cccir\text{-}P}$ = 72.6 MPa and $\varepsilon_{cc\text{-}P}$ = 0.00748, are derived from Eqs. (47) and (12) respectively by substituting $\sigma_{conffIC}$. The lateral component of slip S_{lat} of point Q that is $S_{lat\text{-}fIC}$ can be obtained from Eq. (51) and equals 1.53 mm. The axial stresses σ_S and strain ε_{ax} of point Q can be obtained by substituting $S_{lat\text{-}fIC}$ and $\sigma_{conffIC}$ into Eqs. (44) and (46) which gives 61.5MPa and 0.0133 respectively. Linking points O, P and Q in Fig. 24 gives the active stress/strain O-P-Q for $\sigma_{conffIC}$.
4. Let us now determine the active stress/strain O-G-M in Fig. 24 for σ_{conffr}. In practice, it has been found [10, 62] that FRP confinement reinforcement cannot reach its material rupture strain in tests, that is it cannot reach its material fracture stress f_p. Consequently, the fracture capacity P_{fr2} will be quantified from the experimentally recorded rupture strain ε_{fr2} = 0.0107 such that P_{fr2} for b_f = 1 mm equals $b_f t_{FRP} E_{FRP} \varepsilon_{fr2}$ which comes to 754kN. Substituting P_{fr2} into Eqs. (43) and (1) gives the lateral confining stress σ_{conffr} = 10.6 MPa, which can be substituted into Eqs. (47) and (12) to derive $f_{cccir\text{-}G}$ = 94.6 MPa and $\varepsilon_{cc\text{-}G}$ = 0.0110 at the peak point G in Fig. 24. From Eq. (34) $S_{lat\text{-}fr}$ at fracture at point M equals 2.53 mm, which with σ_{conffr} can be substituted into Eq. (44) to obtain σ_S = 82.0 MPa. Substituting $S_{lat\text{-}fr}$, $f_{cc\text{-}G}$, $\varepsilon_{cc\text{-}G}$ and σ_S into Eq. (46) gives the axial strain ε_{ax} at point M that is 0.0210. Linking points O, G, and M gives the active stress/strain O-G-M for σ_{conffr}.
5. At point A in Fig. 24, the axial stress f_{c0} and strain ε_{c0} obtained from Eq. (13) equal 40.9 MPa and 0.00248 respectively. Linking points O-A-I-Q-M gives the passive stress-strain.

With regard to the stirrup reinforced concrete cylinders in Fig. 25, the case in Fig. 12(c) applies as $L_{crt} > L_{conf}$. The passive stress/strain O-A-K-F in Fig. 9 applies. After the onset of sliding at point A, the confinement reinforcement yields at point K. The strain hardening effect of stirrups is ignored to give a conservative solution so the remaining path follows K-F.

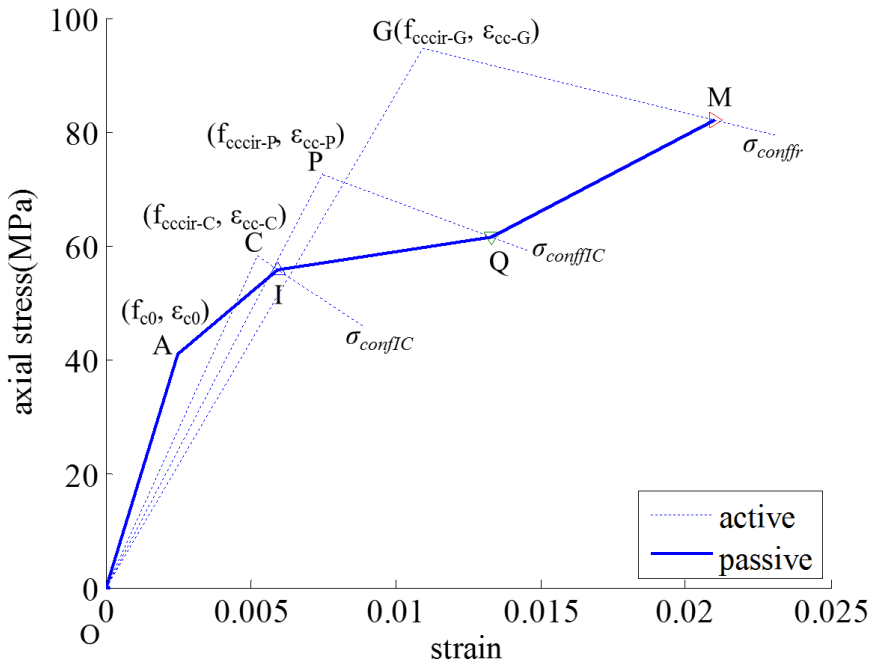

Fig. 24 Theoretical analysis of specimen SCP-4-2

Comparison with Published Experimental Results and Approaches

The comparisons for stirrup reinforced specimens is shown in Fig. 25 where the proposed approach is compared with the experimental results and with Mander's approach [2]. It can be seen that the proposed approach for a circumferential failure type gives reasonable correlation after the initial ascending branch when concrete softening starts and passive confinement commences to improve the ductility.

The design-oriented approach proposed by Lam and Teng [6] and Wei and Wu [74] for FRP confined concrete are shown in Fig. 26; the stress/strain is comprised of a parabolic ascending branch O-A and linear ascending branch A-B. In this approach, the peak axial stress f_{cc} and strain ε_{cc} at point B are empirically derived from a large database of test observations. However, this approach does not consider the size-dependent effect of sliding nor debonding between concrete and confinement reinforcement nor the gauge length L_{gl}. This approach is compared with the proposed approach and experimental results in Fig. 27, Fig. 28, Fig. 29 and Fig. 30. There is reasonable correlation with the circumferential failure type after concrete softening commences, that is there is reasonable correlation in predicting the beneficial effects of the ductility of passively confined concrete.

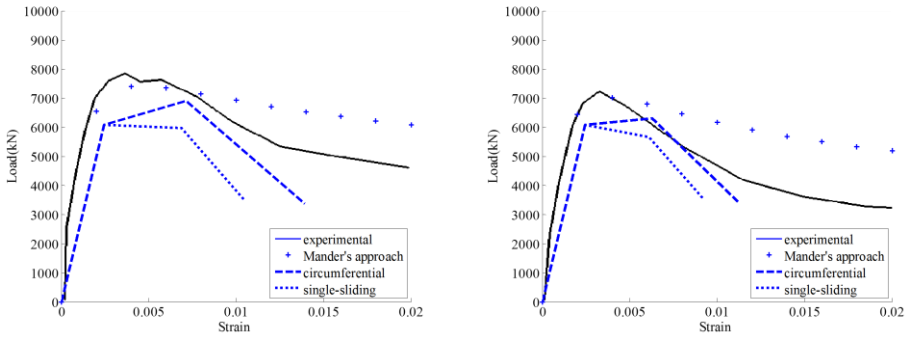

(a)

(b)

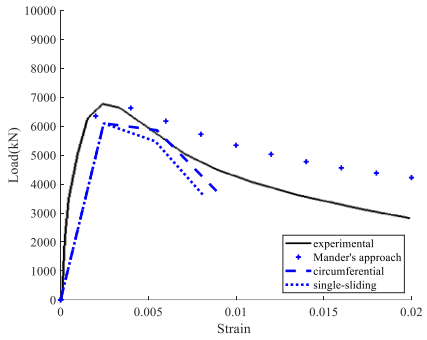

(c)

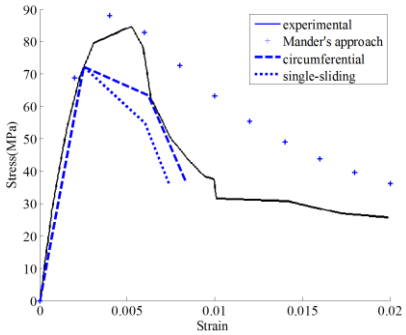

(d)

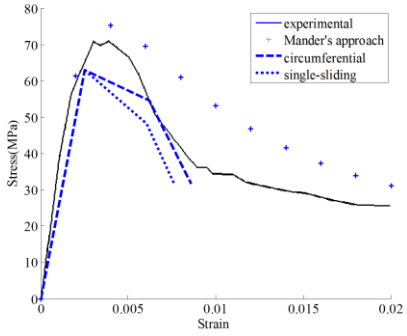

(e)

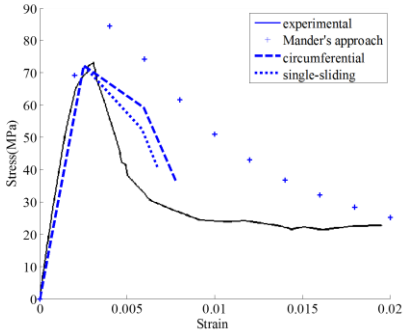

(f)

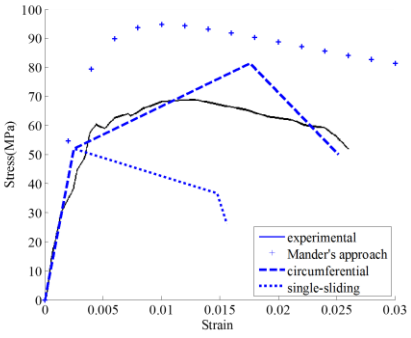

(g)

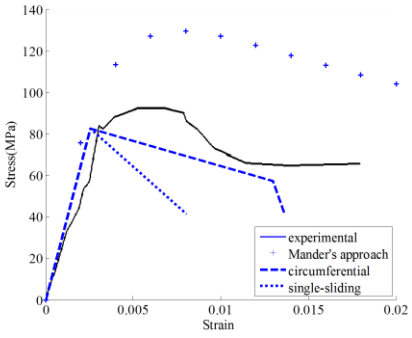

(h)

Fig. 25 Validation with stirrups reinforced specimens (slenderness ratio ≥ 3): (a) 2; (b) 3; (c) 4; (d) 9B; (e) 12A; (f) 12B; (g) 6HB; (h) 6HC;

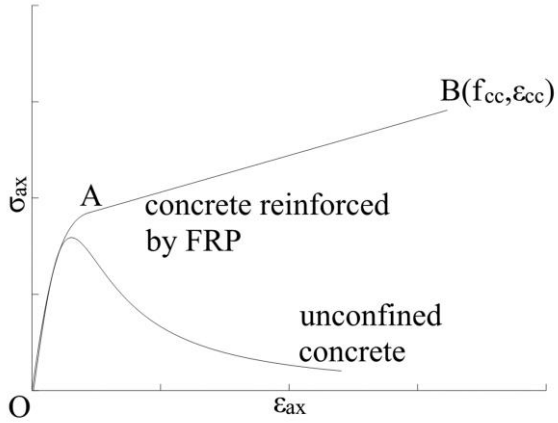

Fig. 26 Teng's and Wu's approach for FRP confined concrete

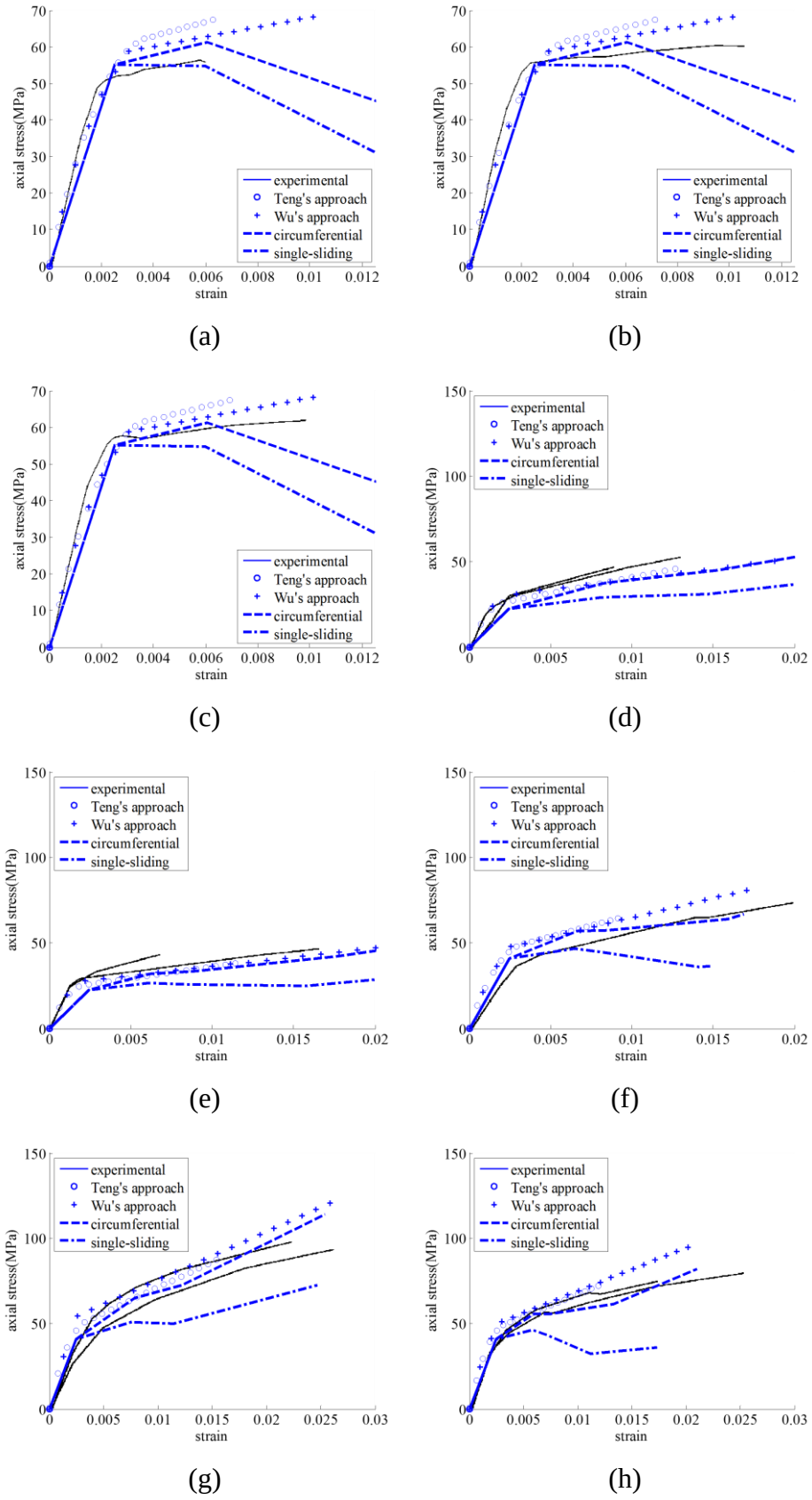

Fig. 27 Validation with FRP reinforced specimens (slenderness ratio ≥ 3): (a) N-0.2T-5R-1; (b) N-0.2T-5R-2; (c) N-0.2T-5R-3; (d) SCP-1-1; (e) SCP-2-1; (f) SCP-3-1 (g) SCP-3-2 (h) SCP-4-2

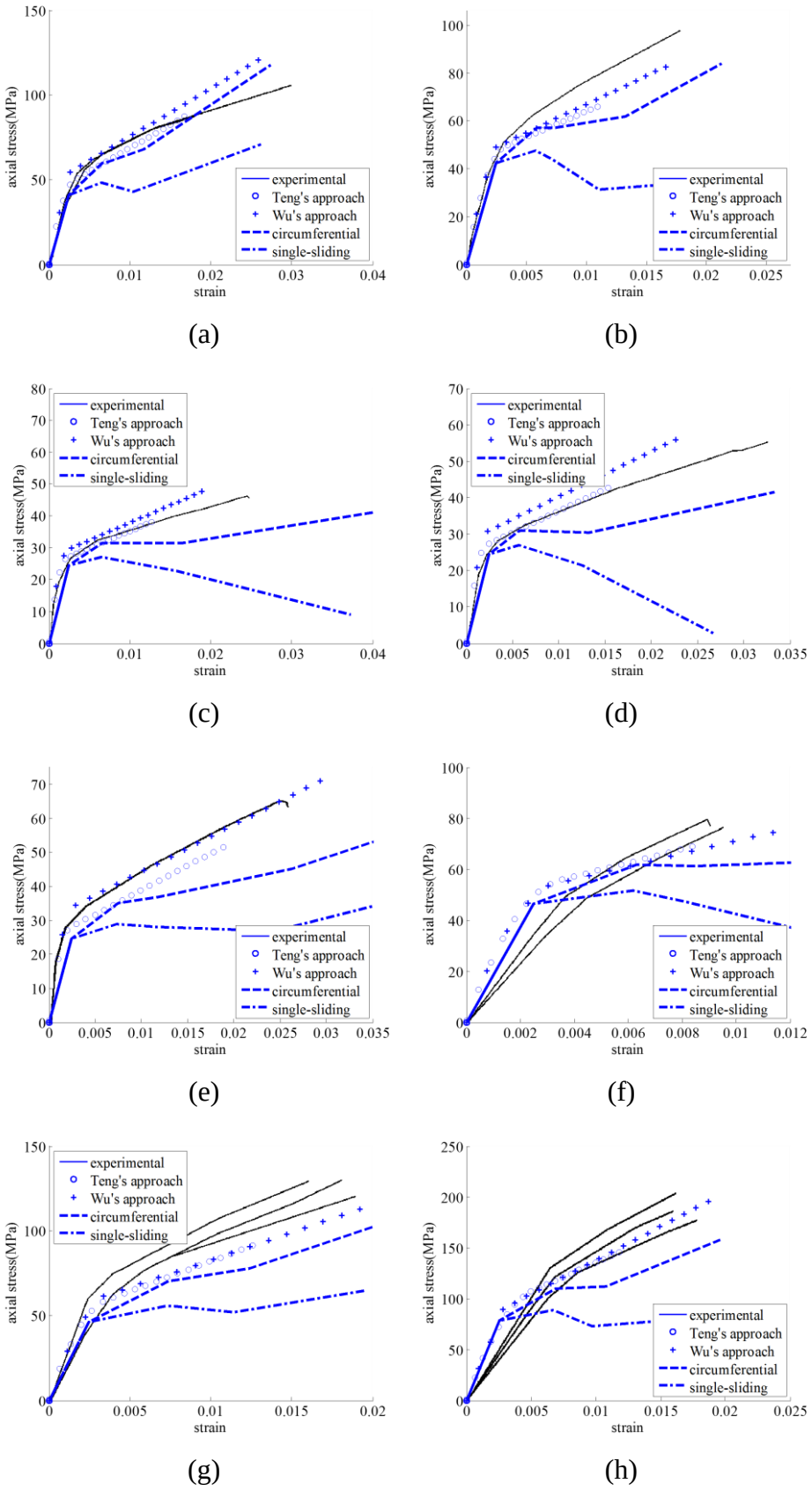

Fig. 28 Validation with FRP reinforced specimens (slenderness ratio ≥ 3): (a) SCP-4-3; (b) C20; (c) C2H0L1M; (d) C1H0L2M; (e) C1H0L2; (f) LC1; (g) LC2; (h) MC3

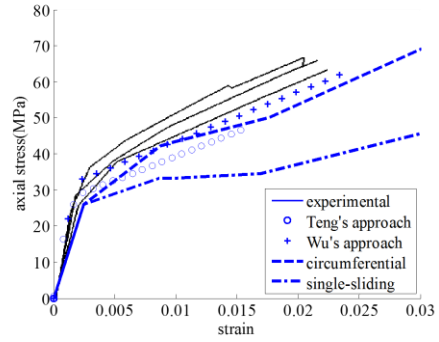

(a)

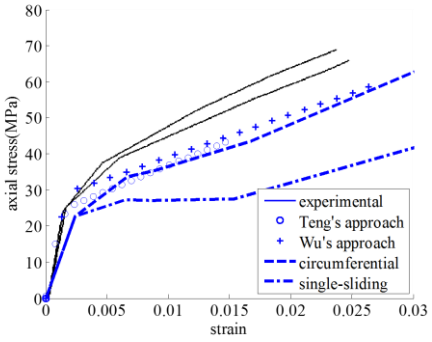

(b)

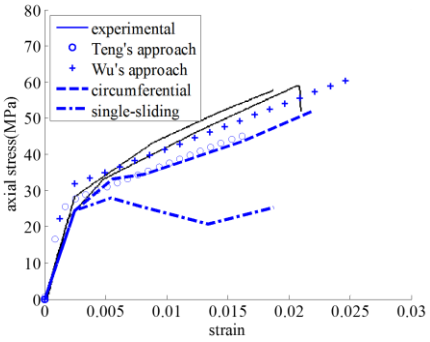

(c)

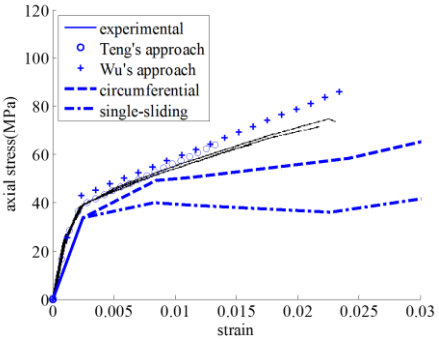

(d)

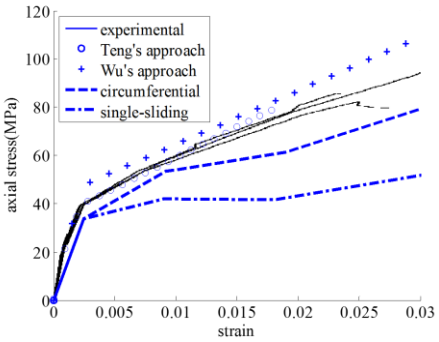

(e)

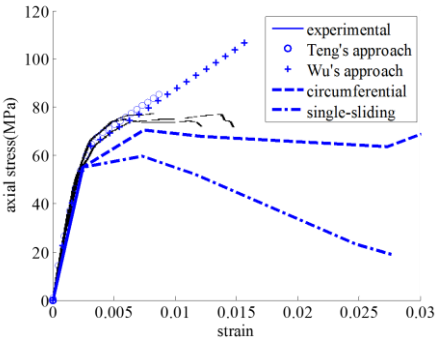

(f)

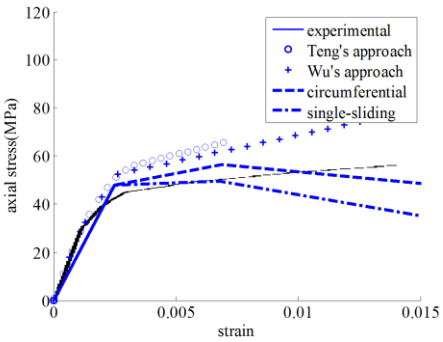

(g)

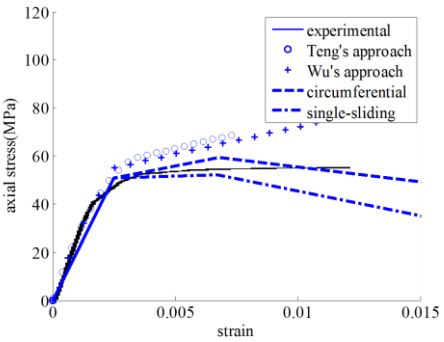

(h)

Fig. 29 Validation with FRP reinforced specimens (slenderness ratio < 3): (a) CC-S; (b) CC-M; (c) CC-L; (d) L2; (e) L3; (f) H2; (g) M1L1; (h) M2L1

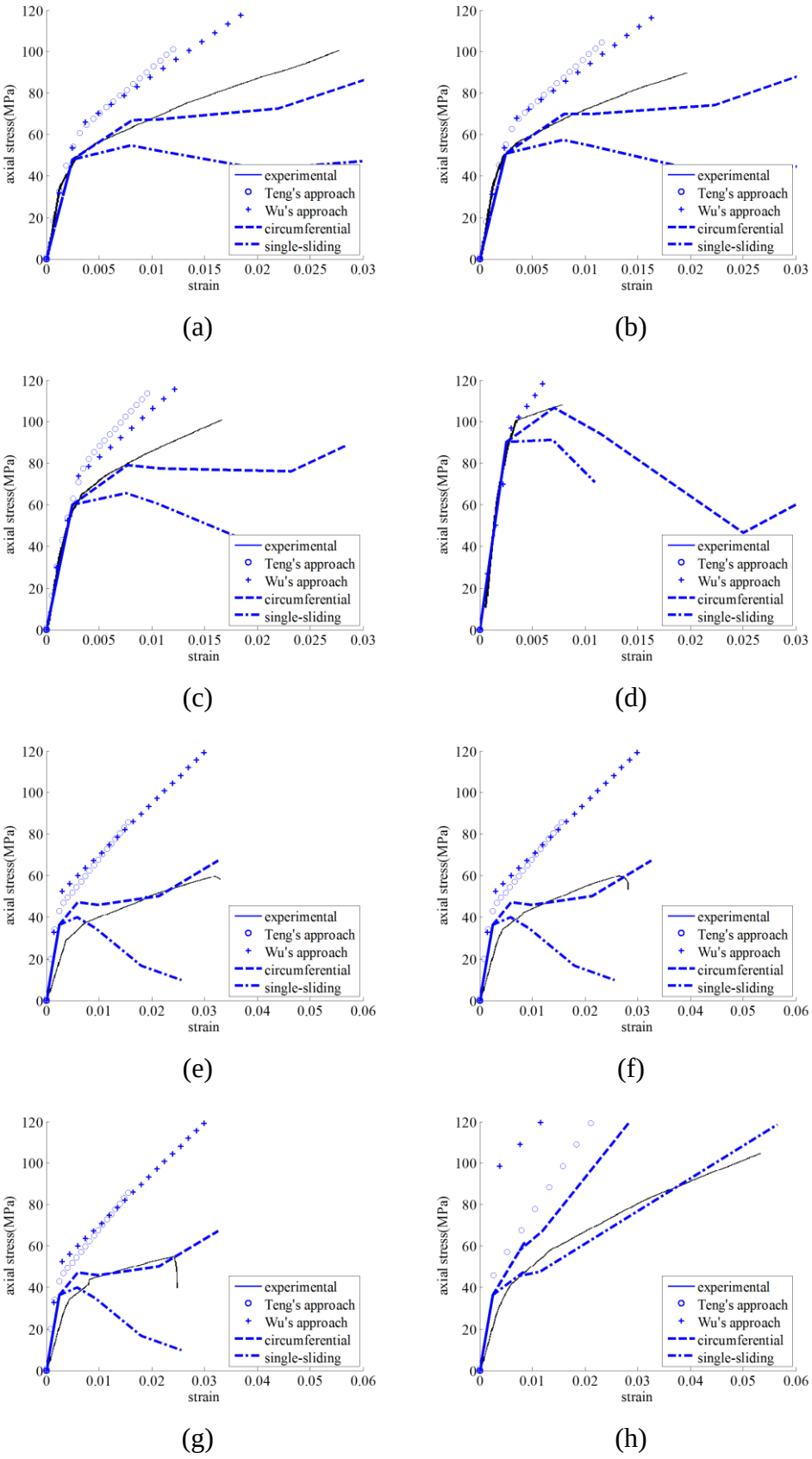

Fig. 30 Validation with FRP reinforced specimens (slenderness ratio < 3): (a) M1L3; (b) M2L3; (c) M3L3; (d) M5L3; (e) E04; (f) E05; (g) E08; (h) E14

Conclusions

A partial-interaction mechanics procedure has been proposed for quantifying the passive stress/strain relationship of encased concrete within circular sections. The procedure uses the partial-interaction bond-slip material property of the encasement and the partial-interaction shear friction material property of the sliding plane. Consequently, it does not rely on member testing and can derive the passive concrete stress/strain for any type of encasement that is stirrups, tubes or wraps, with any geometric variation of the circular section and the concrete can be encased both internally and/or externally such that the confinement varies within the section. The procedure allows for intermediate crack debonding, yield should it occur, fracture of the confinement reinforcement and it also identifies the sequences in which these critical points occur.

Closed form solutions for deriving the passive stress/strain are given. The mechanics model has been compared with published tests on FRP wrapped or stirrup reinforced circular RC sections and with two published semi-empirical approaches which shows that it can simulate the change in ductility with good correlation. These closed form solutions can be used to generate the concrete passive stress/strain from material properties only, that is without the need for member testing, and for any circular cross-section for direct use in design.

A parametric study illustrates the importance of the cylinder size on the concrete passive stress/strain, which is an effect which is normally ignored in current design rules and consequently may give unsafe solutions particularly in practical large-size members. Useful rules of thumb are also developed in the parametric study: to quantify the limit to the ductility of the concrete that is the concrete stress and strain at reinforcement fracture; and to increase the FRP or steel wrap thickness in proportion to the square of the cylinder diameter to maintain concrete ductility.

Appendix 1. Notation

The following symbols are used in this paper:

A, B, C, D, A_H,	=	coefficients of unconfined concrete strength f_{c0} in linear shear friction properties

B_H, A_τ, B_τ		
A_c	=	cross-section area of concrete which interacts with reinforcement in tension stiffening analysis
A_r	=	total cross-section area of reinforcement in tension stiffening analysis
b_f	=	width of reinforcement plate
D_{ci}	=	diameter of circular cylinder
D_i	=	height within confined area of rectangular cylinder or perimeter of a semi-circle for circular cylinder
d_l	=	diameter of longitudinal reinforcement
d_s	=	diameter of stirrups
E_c	=	elastic modulus of concrete
E_{FRP}	=	elastic modulus of FRP
E_r	=	elastic modulus of reinforcement plate
E_1	=	stiffness of P_{conf}/S_{lat} relationship that is equal to $P_{IC}/(2\Delta_{IC})$
E_2	=	stiffness of P_{conf}/S_{lat} relationship from multi-crack analysis
f_{c0}	=	peak strength of unconfined concrete from cylinder tests
f_{cc}	=	peak strength of confined concrete by assuming single sliding failure
f_{cccir}	=	peak strength of confined concrete by assuming circumferential failure
f_{cu}	=	ultimate stress
f_p	=	fracture stress of FRP
$f_{y\text{-}l}$	=	yield capacity of longitudinal reinforcement
$f_{y\text{-}s}$	=	yield capacity of stirrups.
h_{cr}	=	separation of shear-sliding plane interface
k	=	bond-slip stiffness in tension stiffening analysis
k_e	=	arching-effect coefficient
L_{conf}	=	length of confinement reinforcement
L_{crt}	=	critical length which is the minimum length required to achieve the maximum debond force
L_{def}	=	height of specimen

L_{gl} = gauge length

L_{per} = total length of potential debonding failure plane of reinforcement in tension stiffening analysis

P_{ax} = axial load applied to concrete cylinder

P_{conf} = confinement force from confinement reinforcement

P_{fIC} = confinement force when bond stress τ_C is developed to plate end allowing for τ_{Bf}

P_{fr} = fracture capacity of confinement reinforcement

P_{fr2} = confinement force at ε_{fr2}

P_{IC} = debond force of confinement reinforcement

P_{pl} = confinement force from plate reinforcement along the shear failure plane

P_{st} = confinement force from one leg of stirrups

P_{yld} = yield capacity of confinement reinforcement

r = radius of cross-section of circular cylinder

r_c = ductility factor of confined concrete

S = slip displacement

S_{ax} = vertical component of slip S

S_{lat} = lateral component of slip S

S'_{lat} = sum of crack face slips at both sides of sliding plane

$S_{lat\text{-}deb}$ = lateral component of slip when debond developed to plate ends

$S_{lat\text{-}fIC}$ = lateral component of slip at P_{fIC} when $L_{crt}<L_{conf}$ and $P_{IC}<P_{fr}$

$S_{lat\text{-}fr}$ = lateral component of slip when confinement reinforcement starts to fracture when $L_{crt}<L_{conf}$ and $P_{IC}<P_{fr}$

$S_{lat\text{-}fr2}$ = lateral component of slip when confinement reinforcement starts to fracture when $L_{crt}<L_{conf}$ and $P_{IC}>P_{fr}$

$S_{lat\text{-}fr3}$ = lateral component of slip when confinement reinforcement starts to fracture when $L_{crt}>L_{conf}$

$S_{lat\text{-}IC}$ = lateral component of slip at commencement of IC debonding

$S_{lat\text{-}IC2}$ = lateral component of slip when confinement reinforcement is fully debonded

$S_{lat\text{-}yld}$ = lateral component of slip when reinforcement starts to yield when $L_{crt}<L_{conf}$ and $P_{IC}<P_{yld}$

$S_{lat\text{-}yld2}$	=	lateral component of slip when reinforcement starts to yield when $L_{crt}<L_{conf}$ and $P_{IC}>P_{yld}$
$S_{lat\text{-}yld3}$	=	lateral component of slip when confinement reinforcement starts to yield when $L_{crt}>L_{conf}$
S_s	=	stirrups spacing
$S\#$	=	specimen reference number
t	=	tube thickness
t_{FRP}	=	FRP thickness
V_u	=	shear stress at the commencement of crack widening
α	=	failure angle of concrete cylinder
β	=	cylinder parameter in tension stiffening analysis
Δ	=	slip of confinement reinforcement at crack face
Δ_{IC}	=	slip of confinement reinforcement at crack face when debond starts
δ	=	slip between reinforcement and adjacent concrete
δ_{fIC}	=	crack face slip at P_{fIC}
δ_{max}	=	δ when τ_B reduces to zero
δ_1	=	δ at τ_{Bmax}
ε_{ax}	=	axial strain when axial stress is equal to σ_{ax}
ε_{c0}	=	strain at f_{c0} for unconfined concrete
ε_{cc}	=	strain at f_{cc} for confined concrete
$\varepsilon_{cc\text{-}max}$	=	strain at σ_{max} of passive stress/strain
ε_{cu}	=	strain at f_{cu} of passive stress/strain
ε_{fIC}	=	Reinforcement strain at crack face at P_{fIC}
ε_{fr}	=	confinement reinforcement strain at P_{fr}
ε_{fr2}	=	average lateral fracture strain of reinforcement recorded in the experiments
ε_{IC}	=	confinement reinforcement strain at P_{IC}
ε_m	=	material strain of concrete
ε_r	=	confinement reinforcement strain
ε_S	=	sliding strain caused by slip S
ε_{Sdeb}	=	sliding strain at $S_{lat\text{-}deb}$
ε_{Sfr}	=	sliding strain at $S_{lat\text{-}fr}$

ε_{SIC} = sliding strain at $S_{lat\text{-}IC}$

ε_{SIC2} = sliding strain at $S_{lat\text{-}IC2}$

ε_{Syld} = sliding strain at $S_{lat\text{-}yld}$

ε_{Syld2} = sliding strain at $S_{lat\text{-}yld2}$

ε_{yld} = confinement reinforcement strain at $S_{lat\text{-}yld}$

ε_{yld2} = confinement reinforcement strain at $S_{lat\text{-}yld2}$

ε_z = confinement reinforcement strain when debonding is complete or when there is no bond

λ = variation in slip parameter

σ = axial stress

σ_{ax} = axial stress applied to concrete

σ_{conf} = lateral confining stress applied on concrete

σ_{conffr} = lateral confining stress from confinement reinforcement at P_{fr}

$\sigma_{conffIC}$ = lateral confining stress from confinement reinforcement at P_{fIC}

σ_{confIC} = lateral confining stress from confinement reinforcement at P_{IC}

$\sigma_{confyld}$ = lateral confining stress from confinement reinforcement at P_{yld}

σ_{conf0} = lateral confining stress of unconfined concrete and equals zero

σ_{max} = maximum axial stress of passive stress/strain

σ_N = confining stress normal to single-sliding plane

σ_{N0} = normal stress at f_{c0} for unconfined concrete

σ_S = axial stress of passively confined concrete by assuming single-sliding failure

σ_{Scir} = axial stress of passively confined concrete by assuming circumferential failure

σ_{Sdeb} = axial stress at $S_{lat\text{-}deb}$

σ_{Sfr} = axial stress at $S_{lat\text{-}fr}$

σ_{SIC} = axial stress at $S_{lat\text{-}IC}$

σ_{SIC2} = axial stress at $S_{lat\text{-}IC2}$

σ_{Syld} = axial stress at $S_{lat\text{-}yld}$

σ_{Syld2} = axial stress at $S_{lat\text{-}yld2}$

τ = shear stress along single-sliding plane

τ_B = bond stress existing between reinforcement and concrete

τ_{Bf} = friction component of bond

τ_{Bmax} = maximum τ_B

τ_C = bond stress at P_{IC}

τ_m = shear-friction material capacity

φ_f = aspect ratio of interface failure plane

Appendix 2. Specimens Details in Parametric Study

Table 2.1 FRP wrapped specimens

S#	L_{def} (mm)	D_{ci} (mm)	f_{c0} (MPa)	t_{FRP} (mm)	E_{frp} (Gpa)	f_p (MPa)	σ_{confIC}/f_{c0}	σ_{conffr}/f_{c0}
D_{sl}-S1	900	100	50.0	0.400	240	3000	0.1211	0.480
D_{sl}-S2	900	200	50.0	0.800	240	3000	0.0857	0.480
D_{sl}-M	900	300	50.0	1.200	240	3000	0.0699	0.480
D_{sl}-L1	900	500	50.0	2.000	240	3000	0.0542	0.480
D_{sl}-L2	900	800	50.0	3.200	240	3000	0.0428	0.480
D_{s2}-S1	2400	100	50.0	0.100	400	1000	0.0782	0.040
D_{s2}-S2	2400	200	50.0	0.400	400	1000	0.0782	0.080
D_{s2}-M	2400	300	50.0	0.900	400	1000	0.0782	0.120
D_{s2}-L1	2400	500	50.0	2.500	400	1000	0.0782	0.200
D_{s2}-L2	2400	800	50.0	6.400	400	1000	0.0782	0.320
D_{s3}-S1	2400	100	50.0	0.200	400	1000	0.1106	0.080
D_{s3}-S2	2400	200	50.0	0.800	400	1000	0.1106	0.160
D_{s3}-M	2400	300	50.0	1.800	400	1000	0.1106	0.240
D_{s3}-L1	2400	500	50.0	5.000	400	1000	0.1106	0.400
D_{s3}-L2	2400	800	50.0	12.80	400	1000	0.1106	0.640
D_{s4}-S1	2400	100	50.0	0.400	400	1000	0.1564	0.160
D_{s4}-S2	2400	200	50.0	1.600	400	1000	0.1564	0.320
D_{s4}-M	2400	300	50.0	3.600	400	1000	0.1564	0.480
D_{s4}-L1	2400	500	50.0	10.00	400	1000	0.1564	0.800
D_{s4}-L2	2400	800	50.0	25.60	400	1000	0.1564	1.280

Table 2.2 Steel encased specimens

S#	L_{def} (mm)	D_{ci} (mm)	f_{c0} (MPa)	t_{steel} (mm)	E_{steel} (Gpa)	f_y (MPa)	$\sigma_{confyld}/f_{c0}$
SD_{s2}-S1	2400	100	50.0	0.50	200	400	0.080
SD_{s2}-S2	2400	200	50.0	1.00	200	400	0.080
SD_{s2}-M	2400	300	50.0	1.50	200	400	0.080
SD_{s2}-L1	2400	500	50.0	2.50	200	400	0.080
SD_{s2}-L2	2400	800	50.0	4.00	200	400	0.080
SD_{s3}-S1	2400	100	50.0	1.00	200	400	0.160
SD_{s3}-S2	2400	200	50.0	2.00	200	400	0.160
SD_{s3}-M	2400	300	50.0	3.00	200	400	0.160
SD_{s3}-L1	2400	500	50.0	5.00	200	400	0.160
SD_{s3}-L2	2400	800	50.0	8.00	200	400	0.160
SD_{s4}-S1	2400	100	50.0	1.50	200	400	0.240
SD_{s4}-S2	2400	200	50.0	3.00	200	400	0.240
SD_{s4}-M	2400	300	50.0	4.50	200	400	0.240
SD_{s4}-L1	2400	500	50.0	7.50	200	400	0.240
SD_{s4}-L2	2400	800	50.0	12.00	200	400	0.240

where t_{steel} is the steel tube thickness and E_{steel} is the steel tube modulus.

Appendix 3. Specimens Details in Validation

Table 3.1 Details of published FRP reinforced specimen whose aspect ratio is equal to or larger than three

S#	Ref.	L_{gl} (mm)	L_{def} (mm)	D_{ci} (mm)	f_{c0} (MPa)	t_{FRP} (mm)	E_{frp} (Gpa)	f_p (MPa)
N-0.2T-5R-1	Vincent et al [62]	175	750	150	55.2	0.200	128.5	2390
N-0.2T-5R-2	Vincent et al [62]	175	750	150	55.2	0.200	128.5	2390
N-0.2T-5R-3	Vincent et al [62]	175	750	150	55.2	0.200	128.5	2390
SCP-1-1	Song et al [10]	300	300	100	22.4	0.150	237	4073
SCP-2-1	Song et al [10]	450	450	150	22.4	0.150	237	4073
SCP-3-1	Song et al [10]	300	300	100	40.9	0.150	237	4073
SCP-3-2	Song et al [10]	300	300	100	40.9	0.300	237	4073
SCP-4-2	Song et al [10]	450	450	150	40.9	0.300	237	4073
SCP-4-3	Song et al [10]	450	450	150	40.9	0.450	237	4073
C20	Carrazedo et al [63]	450	450	150	42.5	0.340	209	2720
C2H0L1M	Wang et al [70]	204	612	204	24.5	0.167	240	4340
C1H0L2M	Wang et al [70]	305	915	305	24.5	0.334	240	4340
C1H0L2	Wang et al [69]	204	612	204	24.5	0.334	240	4340
LC1	Wu et al [57]	300	300	100	46.4	0.286	118	2060
LC2	Wu et al [57]	300	300	100	46.4	0.572	118	2060
MC3	Wu et al [57]	300	300	100	78.5	0.858	118	2060

where *S#* is the specimen reference number.

Table 3.2 Details of published FRP reinforced specimen whose aspect ratio is less than three.

S#	Ref	L_{gl} (mm)	L_{prsm} (mm)	D_{ci} (mm)	f_{c0} (MPa)	t_{FRP} (mm)	E_{FRP} (GPa)	f_p (MPa)
CC-S	Liang et al [66]	200	200	100	25.9	0.167	245.0	3248
CC-M	Liang et al [66]	400	400	200	22.7	0.334	245.0	3248
CC-L	Liang et al [66]	600	600	300	24.5	0.501	245.0	3248
L2	Xiao et al [67]	152	305	152	33.7	0.762	105.0	1577
L3	Xiao et al [67]	152	305	152	33.7	1.143	105.0	1577
H2	Xiao et al [67]	152	305	152	55.2	0.762	105.0	1577
M1L1	Almusallam [68]	150	300	150	47.7	1.300	27.0	540
M2L1	Almusallam [68]	150	300	150	50.8	1.300	27.0	540
M1L3	Almusallam [68]	150	300	150	47.7	3.900	27.0	540
M2L3	Almusallam [68]	150	300	150	50.8	3.900	27.0	540
M3L3	Almusallam [68]	150	300	150	60.0	3.900	27.0	540
M5L3	Almusallam [68]	150	300	150	90.3	3.900	27.0	540
E04	Nanni et al [65]	300	300	150	36.3	0.600	72.6	3240
E05	Nanni et al [65]	300	300	150	36.3	0.600	72.6	3240
E08	Nanni et al [65]	300	300	150	36.3	0.600	72.6	3240
E14	Nanni et al [65]	300	300	150	36.3	2.400	72.6	3240

Table 3.3 Details of published stirrups reinforced specimen whose aspect ratio is equal to or larger than three

S#	Ref.	L_{gl}	D_{ci}	cover	f_{c0}	d_l	$f_{y\text{-}l}$	d_s	S_s	$f_{y\text{-}s}$
		(mm)	(mm)	(mm)	(MPa)	(mm)	(MPa)	(mm)	(mm)	(MPa)
2	Mander [71]	450	438.00	25.0	28.0	16.0	275	12.0	69.0	275
3	Mander [71]	450	438.00	25.0	28.0	16.0	275	12.0	103	275
4	Mander [71]	450	440.00	25.0	28.0	16.0	275	10.0	119	275
9B	Li et al [72]	300	204.00	15.0	72.3	12.0	443	6.00	50.0	445
12A	Li et al [72]	300	204.00	15.0	63.0	12.0	443	6.00	65.0	445
12B	Li et al [72]	300	204.00	15.0	72.3	12.0	443	6.00	65.0	445
6HB	Li et al [72]	300	203.60	15.0	52.0	12.0	443	6.40	50.0	1318
6HC	Li et al [72]	300	203.60	15.0	82.5	12.0	443	6.40	50.0	1318

where cover is the cover thickness, d_l is the diameter of longitudinal reinforcement, $f_{y\text{-}l}$ is the yield capacity of longitudinal reinforcement, d_s is the diameter of stirrups and $f_{y\text{-}s}$ is the yield capacity of stirrups.

Acknowledgements

The first author would like to acknowledge the financial support of the China Scholarship Council.

References

[1] Bing L, Park R, Tanaka H. Stress-strain behavior of high-strength concrete confined by ultra-high-and normal-strength transverse reinforcements. ACI Structural Journal. 2001;98:395-406.
[2] Mander JB, Priestley MJ, Park R. Theoretical stress-strain model for confined concrete. Journal of Structural Engineering. 1988;114:1804-26.
[3] Toutanji H, Deng Y. Performance of concrete columns strengthened with fiber reinforced polymer composite sheets. Advanced Composite Materials. 2001;10:159-68.
[4] Toutanji HA. Stress-strain characteristics of concrete columns externally confined with advanced fiber composite sheets. ACI Materials Journal. 1999;96:397-404.
[5] Purba BK, Mufti AA. Investigation of the behavior of circular concrete columns reinforced with carbon fiber reinforced polymer (CFRP) jackets. Canadian Journal of Civil Engineering. 1999;26:590-6.
[6] Lam L, Teng J. Design-oriented stress–strain model for FRP-confined concrete. Construction and Building Materials. 2003;17:471-89.
[7] Kumutha R, Vaidyanathan R, Palanichamy M. Behaviour of reinforced concrete rectangular columns strengthened using GFRP. Cement and Concrete Composites. 2007;29:609-15.
[8] Lam L, Teng J. Design-oriented stress-strain model for FRP-confined concrete in rectangular columns. Journal of Reinforced Plastics and Composites. 2003;22:1149-86.
[9] Wang Z, Wang D, Smith ST, Lu D. CFRP-confined square RC columns. I: Experimental investigation. Journal of Composites for Construction. 2011;16:150-60.
[10] Song X, Gu X, Li Y, Chen T, Zhang W. Mechanical behavior of FRP-strengthened concrete columns subjected to concentric and eccentric compression loading. Journal of Composites for Construction. 2012;17:336-46.

[11] Al-Salloum YA. Influence of edge sharpness on the strength of square concrete columns confined with FRP composite laminates. Composites Part B: Engineering. 2007;38:640-50.
[12] Harajli MH. Axial stress–strain relationship for FRP confined circular and rectangular concrete columns. Cement and Concrete Composites. 2006;28:938-48.
[13] Du M, Jin L, Du X, Li D. Size effect tests of stocky reinforced concrete columns confined by stirrups. Structural Concrete. 2017;18:454-65.
[14] Jin L, Du M, Li D, Du X, Xu H. Effects of cross section size and transverse rebar on the behavior of short squared RC columns under axial compression. Engineering Structures. 2017;142:223-39.
[15] Wang Z, Wang D, Smith ST. Size effect of square concrete columns confined with CFRP wraps. Proceedings of the 3rd Asia-Pacific Conference on FRP in Structures, Hokkaido University, Sapporo, Japan2012. p. 2-4.
[16] Ozbakkaloglu T, Lim JC. Axial compressive behavior of FRP-confined concrete: Experimental test database and a new design-oriented model. Composites Part B: Engineering. 2013;55:607-34.
[17] Visintin P, Chen Y, Oehlers D. Simulating the behavior of FRP-confined cylinders using the shear-friction mechanism. Journal of Composites for Construction. 2015;19:04015014.
[18] Wang Z, Wang D, Smith ST, Lu D. CFRP-confined square RC columns. II: Cyclic axial compression stress-strain model. Journal of Composites for Construction. 2011;16:161-70.
[19] Silva MA, Rodrigues CC. Size and relative stiffness effects on compressive failure of concrete columns wrapped with glass FRP. Journal of Materials in Civil Engineering. 2006;18:334-42.
[20] Jiang T, Teng J. Analysis-oriented stress–strain models for FRP–confined concrete. Engineering Structures. 2007;29:2968-86.
[21] Teng J, Huang Y, Lam L, Ye L. Theoretical model for fiber-reinforced polymer-confined concrete. Journal of Composites for Construction. 2007;11:201-10.
[22] Becque J, Patnaik AK, Rizkalla SH. Analytical models for concrete confined with FRP tubes. Journal of Composites for Construction. 2003;7:31-8.
[23] Mirmiran A, Shahawy M. A new concrete-filled hollow FRP composite column. Composites Part B: Engineering. 1996;27:263-8.

[24] Marques SPC, Marques DCdSC, Lins da Silva J, Cavalcante MAA. Model for analysis of short columns of concrete confined by fiber-reinforced polymer. Journal of Composites for Construction. 2004;8:332-40.
[25] Chun S, Park H. Load carrying capacity and ductility of RC columns confined by carbon fiber reinforced polymer. Proceeding, 3rd Int Conf on Composites in Infrastructure: Univ. of Arizona San Francisco; 2002;1-12.
[26] Harmon TG, Ramakrishnan S, Wang EH. Confined concrete subjected to uniaxial monotonic loading. Journal of Engineering Mechanics. 1998;124:1303-9.
[27] Mattock AH, Hawkins NM. Shear transfer in reinforced concrete-recent research. PCI Journal. 1972;17:55-75.
[28] Mattock AH. Shear transfer in concrete having reinforcement at an angle to the shear plane. Special Publication. 1974;42:17-42.
[29] Chen Y, Visintin P, Oehlers D. Concrete shear-friction material properties: Derivation from actively confined compression cylinder tests. Advances in Structural Engineering. 2015;18:1173-85.
[30] Chen Y, Zhang T, Visintin P, Oehlers D. Concrete shear-friction material properties: application to shear capacity of RC beams of all sizes. Advances in Structural Engineering. 2015;18:1187-98.
[31] Haskett M, Oehlers DJ, Ali MM, Sharma SK. Evaluating the shear-friction resistance across sliding planes in concrete. Engineering Structures. 2011;33:1357-64.
[32] Haskett M, Oehlers DJ, Mohamed Ali M, Wu C. Yield penetration hinge rotation in reinforced concrete beams. Journal of Structural Engineering. 2009;135:130-8.
[33] Yuan H, Wu Z, Yoshizawa H. Theoretical solutions on interfacial stress transfer of externally bonded steel/composite laminates. Doboku Gakkai Ronbunshu. 2001;2001:27-39.
[34] Lu X, Teng J, Ye L, Jiang J. Bond–slip models for FRP sheets/plates bonded to concrete. Engineering Structures. 2005;27:920-37.
[35] Hao X. Generation of stress-strain relationship of passively reinforced rectangular concrete prisms. School Report, School of Civil, Environmental and Mining Engineering, The University of Adelaide, Australia. 2018.
[36] Oehlers DJ, Haskett M, Wu C, Seracino R. Embedding NSM FRP plates for improved IC debonding resistance. Journal of Composites for Construction. 2008;12:635-42.
[37] Yuan H, Teng J, Seracino R, Wu Z, Yao J. Full-range behavior of FRP-to-concrete bonded joints. Engineering Structures. 2004;26:553-65.

[38] Seracino R, Raizal Saifulnaz M, Oehlers D. Generic debonding resistance of EB and NSM plate-to-concrete joints. Journal of Composites for Construction. 2007;11:62-70.
[39] Haskett M, Oehlers D, Ali MM, Sharma S. The shear friction aggregate interlock resistance across sliding planes in concrete. Magazine of Concrete Research. 2010;62:907-24.
[40] Walraven J, Reinhardt H. Theory and experiments on the mechanical behaviour of cracks in plain and reinforced concrete subjected to shear loading. HERON, 26 (1A), 1981;5-68.
[41] Chen Y, Visintin P, Oehlers D. Extracting Size-Dependent Stress–Strain Relationships from FRP-Confined Concrete Cylinders for Varying Diameters and Heights. Journal of Materials in Civil Engineering. 2015;28:04015182.
[42] Haskett M, Oehlers DJ, Ali MM. Local and global bond characteristics of steel reinforcing bars. Engineering Structures. 2008;30:376-83.
[43] Visintin P, Oehlers D, Muhamad R, Wu C. Partial-interaction short term serviceability deflection of RC beams. Engineering Structures. 2013;56:993-1006.
[44] Ali MM, Oehlers D, Griffith M, Seracino R. Interfacial stress transfer of near surface-mounted FRP-to-concrete joints. Engineering Structures. 2008;30:1861-8.
[45] Lin X, Zhang Y. Evaluation of bond stress-slip models for FRP reinforcing bars in concrete. Composite Structures. 2014;107:131-41.
[46] Haskett M, Ali MM, Oehlers D, Wu C. Influence of bond on the hinge rotation of FRP plated beams. Advances in Structural Engineering. 2009;12:833-43.
[47] Zhang T, Visintin P, Oehlers DJ. Partial-interaction tension-stiffening properties for numerical simulations. Advances in Structural Engineering. 2017;20:812-21.
[48] Ali MM, Oehlers D, Griffith M. The residual strength of confined concrete. Advances in Structural Engineering. 2010;13:603-18.
[49] Hao X. Mechanics of extracting shear-friction properties from actively confined cylinder tests. School Report , School of Civil, Environmental and Mining Engineering, The University of Adelaide, Australia. 2017.
[50] Visintin P, Chen Y, Oehlers D. Size dependent axial and lateral stress strain relationships for actively confined concrete. Advances in Structural Engineering. 2015;18:1-20.
[51] Popovics S. A numerical approach to the complete stress-strain curve of concrete. Cement and Concrete Research. 1973;3:583-99.

[52] A.C.I Committee. State-of-the-Art report on high-strength concrete. Farmington Hills, Michigan. 1992.
[53] Rashid R, Oehlers D, Seracino R. IC debonding of FRP NSM and EB retrofitted concrete: Plate and cover interaction tests. Journal of Composites for Construction. 2008;12:160-7.
[54] Wu Z, Yuan H, Niu H. Stress transfer and fracture propagation in different kinds of adhesive joints. Journal of Engineering Mechanics. 2002;128:562-73.
[55] Chen C, Sui L, Xing F, Li D, Zhou Y, Li P. Predicting bond behavior of HB FRP strengthened concrete structures subjected to different confining effects. Composite Structures. 2018;187:212-25.
[56] Sturm AB, Visintin P, Oehlers DJ. Time-dependent serviceability behavior of reinforced concrete beams: Partial interaction tension stiffening mechanics. Structural Concrete. 2018;19:508-23.
[57] Wu H-L, Wang Y-F, Yu L, Li X-R. Experimental and computational studies on high-strength concrete circular columns confined by aramid fiber-reinforced polymer sheets. Journal of Composites for Construction. 2009;13:125-34.
[58] Wu Y-F, Liu K. Characterization of mechanically enhanced FRP bonding system. Journal of Composites for Construction. 2013;17:34-49.
[59] Wu Y-F, He L, Bank L. Bond-test protocol for plate-to-concrete interface involving all mechanisms. Journal of Composites for Construction. 2015;20:04015022.
[60] Teng J, Lam L. Behavior and modeling of fiber reinforced polymer-confined concrete. Journal of Structural Engineering. 2004;130:1713-23.
[61] Ellobody E, Young B. Design and behaviour of concrete-filled cold-formed stainless steel tube columns. Engineering Structures. 2006;28:716-28.
[62] Vincent T, Ozbakkaloglu T. Influence of slenderness on stress-strain behavior of concrete-filled FRP tubes: experimental study. Journal of Composites for Construction. 2014;19:04014029.
[63] Carrazedo R, de Hanai JB. Concrete Prisms and Cylinders Wrapped by FRP Loaded in Compression with Small Eccentricities. Journal of Composites for Construction. 2016;21:04016115.
[64] Wang Y-f, Wu H-l. Size effect of concrete short columns confined with aramid FRP jackets. Journal of Composites for Construction. 2010;15:535-44.
[65] Nanni A, Bradford NM. FRP jacketed concrete under uniaxial compression. Construction and Building Materials. 1995;9:115-24.

[66] Liang M, Wu Z-M, Ueda T, Zheng J-J, Akogbe R. Experiment and modeling on axial behavior of carbon fiber reinforced polymer confined concrete cylinders with different sizes. Journal of Reinforced Plastics and Composites. 2012;31:389-403.
[67] Xiao Y, Wu H. Compressive behavior of concrete confined by carbon fiber composite jackets. Journal of Materials in Civil Engineering. 2000;12:139-46.
[68] Almusallam TH. Behavior of normal and high-strength concrete cylinders confined with E-glass/epoxy composite laminates. Composites Part B: Engineering. 2007;38:629-39.
[69] Wang ZY, Wang DY, Lu DG. Behavior of Large-Scale Circular and Square RC Columns Confined with Carbon Fiber-Reinforced Polymer under Uniaxial Compression. Advanced Materials Research: Trans Tech Publ; 2011. p. 3686-93.
[70] Wang Z, Wang D, Smith ST, Lu D. Experimental testing and analytical modeling of CFRP-confined large circular RC columns subjected to cyclic axial compression. Engineering Structures. 2012;40:64-74.
[71] Mander JB. Seismic design of bridge piers. 1983. Ph.D. dissertation, University of Canterbury.
[72] Li B, Park R, Tanaka H. Stress-strain behavior of high-strength concrete confined by ultra-high-and normal-strength transverse reinforcements. ACI Structural Journal. 2001;98:395-406.
[73] Hao X. Generation of stress-strain relationship of passively reinforced circular concrete cylinders. School Report, School of Civil, Environmental and Mining Engineering, The University of Adelaide, Australia. 2018.
[74] Wei Y-Y, Wu Y-F. Unified stress–strain model of concrete for FRP-confined columns. Construction and Building Materials. 2012;26:381-92.

Chapter 4— Flexural Analysis

Introduction

This chapter contains the journal paper below. This paper first shows how the passive stress/strain derived in Chapter 3 from concentrically loaded confined prisms can be used in a flexural analysis. The passive stress/strain is then simplified to a rectangular concrete stress block suitable for design. Closed-form solutions to quantify the ductility of passively confined concrete beams are then derived.

List of Manuscripts

Hao, X, Visintin, P and Oehlers, DJ (2019) Closed Form Solutions for Quantifying the Ductility of Concrete Beams with Passively Restrained Concrete. Submitted to *Journal of Structural Engineering*

Statement of Authorship

Statement of Authorship

Title of Paper	Closed Form Solutions for Quantifying the Ductility of Concrete Beams with Passively Restrained Concrete
Publication Status	☐ Published ☐ Accepted for Publication ☑ Submitted for Publication ☐ Unpublished and Unsubmitted w ork w ritten in manuscript style
Publication Details	Hao, X, Visintin, P and Oehlers, DJ (2019) Closed Form Solutions for Quantifying the Ductility of Concrete Beams with Passively Restrained Concrete. Submitted to *Journal of Structural Engineering*

Principal Author

Name of Principal Author (Candidate)	Xinkai Hao		
Contribution to the Paper	Developed the model, interpreted data, wrote manuscript		
Overall percentage (%)	70%		
Certification:	This paper reports on original research I conducted during the period of my Higher Degree by Research candidature and is not subject to any obligations or contractual agreements with a third party that would constrain its inclusion in this thesis. I am the primary author of this paper.		
Signature		Date	21/10/2019

Co-Author Contributions

By signing the Statement of Authorship, each author certifies that:

i. the candidate's stated contribution to the publication is accurate (as detailed above);

ii. permission is granted for the candidate in include the publication in the thesis; and

iii. the sum of all co-author contributions is equal to 100% less the candidate's stated contribution.

Name of Co-Author	Phillip Visintin		
Contribution to the Paper	Supervised work progress, help modelling and revising manuscript		
Signature		Date	21/10/2019

Name of Co-Author	Deric John Oehlers		
Contribution to the Paper	Supervised work progress, help modelling and revising manuscript		
Signature		Date	21/10/19

Please cut and paste additional co-author panels here as required.

Closed Form Solutions for Quantifying the Ductility of Concrete Beams with Passively Restrained Concrete

X. Hao[1], P. Visintin[2] and D. J. Oehlers[3]

Abstract

The ductility of a beam is important in reinforced concrete member design at the ultimate limit state, especially in resisting dynamic loads such as those from earthquakes or blasts. Concrete confinement reinforcement, such as stirrups or tubes, are widely used in structures and can significantly enhance the ductility of concrete beams. However, this confinement effect is normally ignored in current design standards, limiting the ability to design specifically for ductility or to estimate the ductility of existing structures. In this paper, a novel concrete passive stress/strain relationship based on the application of partial interaction and shear friction theories is simplified to a rectangular stress block for flexural analyses. This confined concrete stress block is then applied to quantify the moment/rotation of a hinge where both the confinement of the concrete and hinge lengths are quantified through mechanics.

Keywords: concrete confinement; passive stress/strain; partial interaction; reinforced concrete beams; ductility; moment/rotation; closed form solutions

Introduction

Experimental research has broadly illustrated that inclusion of confinement reinforcement, such as internal stirrups or external plates or tubes, can enhance the strength and, especially, the ductility of concrete members (Lopes et al. 2012; Mansur et al. 1997; Rashid and Mansur 2005). While widely investigated in research, concrete confinement is often ignored in practical applications (ACI 2014; Fib. 2010) resulting in an under prediction of member strength, but more importantly, member ductility. For instance, over-reinforced beams are not recommended in practical design because of a lack of member ductility when the concrete is unconfined (ACI 2014; Australia Standard 2009; Fib. 2010). However, allowing

for the influence of concrete confinement may allow the beam to behave in a ductile way and to achieve a higher moment capacity (Mansur et al. 1997).

Traditional approaches for predicting member strength and ductility are based on full-interaction moment/curvature analyses (M_{ax}/χ), that is they assume that plane sections remain plane and that there is no slip between the longitudinal or transverse reinforcement and adjacent concrete (Hognestad 1951). Further, at the ultimate limit state a rectangular stress block is applied to idealise the distribution of concrete compressive stresses at an assumed maximum concrete strain. As a result of these assumptions traditional approaches:

1. Rely on empirical factors to quantify the hinge length and member ductility despite significant challenges in their general definition and calibration (Attard and Stewart 1998; Hognestad 1951; Rajagopalan and Everard 1976; Tan and Nguyen 2005);
2. Ignore the size dependency of the concrete stress/strain behaviour, which is known to result in reduced member ductility as member size increases (Du et al. 2017; Jin et al. 2017; Silva and Rodrigues 2006; Thériault et al. 2004); and
3. Ignore the influence of concrete confinement, which increases member ductility at all member sizes, but is a phenomena which is itself size dependent (ACI 2014; Fib. 2010; Hognestad 1951).

In the traditional beam flexural analysis, non-linear unconfined concrete stress/strain relationships are simplified to simplified stress blocks which may be either rectangular (Whitney 1937), bilinear (Jensen 1943), or parabolic (Mensch 1914). The rectangular concrete stress block is widely accepted by codes due to its ease of application (ACI 2014; Australia Standard 2009; Fib. 2010) where parameters α and γ determine the magnitude and position of the simplified rectangular stress block. However, these empirically derived parameters have the following drawbacks. Firstly, they are empirically derived from unconfined-concrete-beam regions (Kaar et al. 1978; Rajagopalan and Everard 1976) but are often used for the design of confined regions (ACI 2014). As a result, their application may underestimate the strength and, more importantly, the ultimate strain of concrete ε_{cu} (Mansur et al. 1997), meaning designers are not able to utilise the higher capacity and ductility afforded by concrete confinement. Secondly, the controlling parameters α and γ are known to be affected by member size, but this effect is not typically quantified (Yi et al. 2002).

In this paper, a new rectangular stress block is quantified based on the application of the fundamental mechanisms of shear friction and partial-interaction theories. It is shown that with this approach the rectangular stress block can be made size-dependent and can explicitly allow for passive confinement which is limited by either yielding, fracture or debonding of the confining reinforcement. Having defined the rectangular stress block it can be utilised either directly in traditional strain-based analysis approaches, or alternatively, as shown here, it can incorporate into displacement based analysis approaches and closed form solution to predict member ductility is proposed.

Passive Concrete σ/ε

The confinement mechanism for deriving the passive stress/strain has been described for rectangular prisms (Hao 2018b) and for circular cylinders (Hao 2018a). This mechanism will be described qualitatively in this section starting with the active stress/strain mechanism followed by the passive mechanism which will then be quantified.

Active Stress/Strain

Consider the actively confined rectangular concrete prism in Fig. 1(a) that has a potential sliding plane F-N. The prism in Fig. 1(a) is subjected to an axial stress σ_{ax} and lateral hydraulic stress σ_{conf}. Here a rectangular prism is shown in Fig. 1(a), but the approach described can also be applied to a circular cross-section. Before the occurrence of sliding, the axial strain is a material strain ε_m and is independent of the size of the deformed length L_{def}. The axial stress σ_{ax} is gradually increased until the sliding plane F-N forms which then has a slip S and inclination α_s. The axial component of the slip S_{ax} will cause contraction of the concrete prism and subsequently a size-dependent equivalent axial strain $\varepsilon_S = S_{ax}/L_{def}$. The shear sliding plane F-N is subjected to shear stress τ and normal stress σ_N along and normal to the shear failure plane resolved from the components of force from σ_{ax} and σ_{conf}. The relationship between shear stress τ, normal stress σ_N, slip S and crack width h_{cr} is referred to as the shear friction material properties (Mattock 1974; Mattock and Hawkins 1972). As the lateral component of the crack width h_{cr} is much smaller than S_{lat} it is ignored in practice giving a slightly conservative assumption (Haskett et al. 2010a; Haskett et al. 2011).

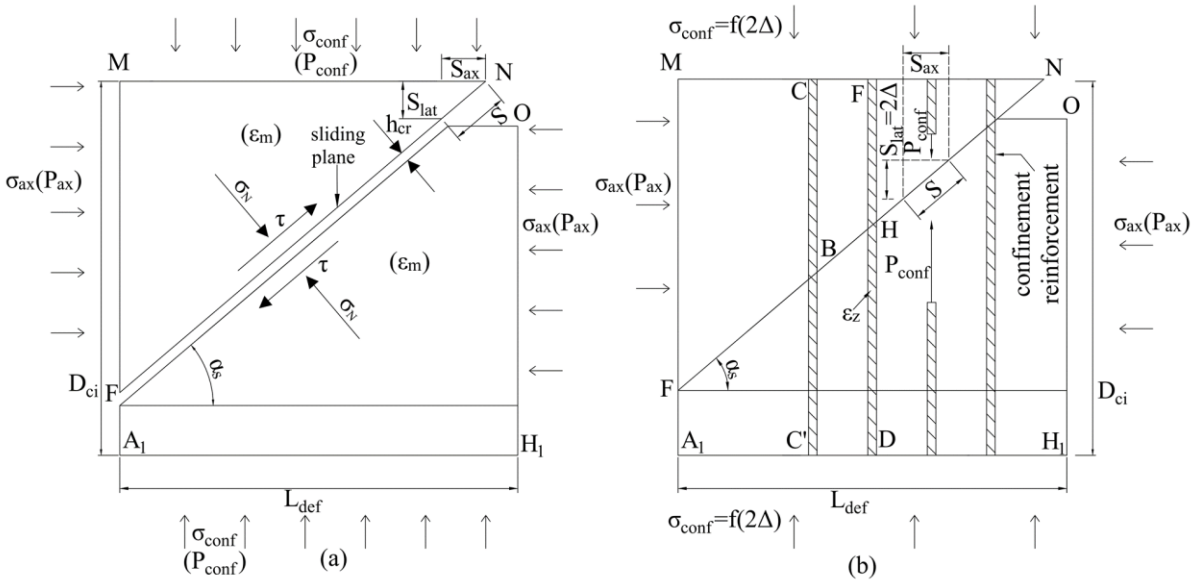

Fig. 1 (a) Actively confined concrete (b) passively confined concrete

Let us first consider the active stress/strain properties which are required in the following section on the passive stress/strain. The active stress/strain O-A-B in Fig. 2 is for the unconfined concrete that is $\sigma_{conf0} = 0$. As an example (although the following applies to any confinement), consider the laterally confined case O-P_1-E-F where the lateral confinement is $\sigma_{confyld}$. On application of load, sliding occurs at point A (ε_{c0}, f_{c0}) for the unconfined concrete and at point E (ε_{cc2}, f_{cc2}) for the confined concrete. Prior to the formation of a sliding plane, the axial strain is the size-independent material strain ε_m. Sliding occurs with a reduction of the axial stress, and the axial strain is comprised of the size-independent material strain ε_m and size-dependent sliding strain ε_S such as point P at a confinement $\sigma_{confyld}$. Then for a given axial stress σ_{ax} and lateral confinement σ_{conf}, the τ and σ_N in Fig. 1(a) can be determined (Ali et al. 2010). From these values, slip S can be derived and subsequently the sliding strain ε_S allowing for the definition of the descending branch of active stress/strain relationship.

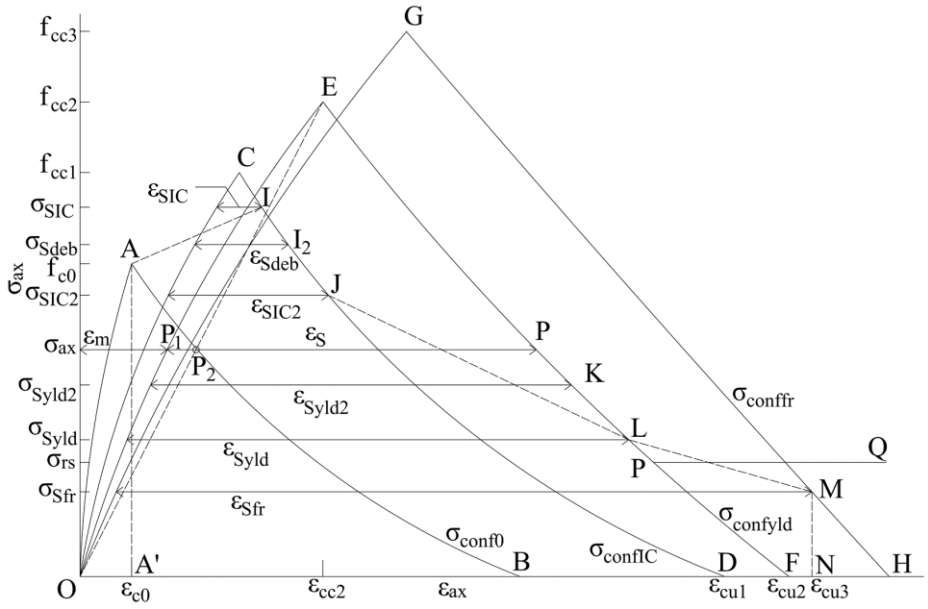

Fig. 2 Passive stress/strain

Passive Stress/Strain

Consider the passively restrained rectangular prism in Fig. 1(b) which is laterally reinforced by either stirrups, tubes, plates or a combination of them. This prism has the same dimensions and potential sliding plane F-N as that in Fig. 1(a) and is under a concentric load P_{ax} and axial stress σ_{ax}. The diameter or width of the cross-section within the transverse reinforcement is D_{ci}. Prior to the formation of the sliding plane, the lateral confinement reinforcement does not have any significant deformation and, subsequently, neither a confinement force nor an associated lateral confining stress. Increase the axial stress until the occurrence of sliding. The lateral slip component S_{lat} is resisted by the lateral reinforcement by the confinement force P_{conf} and subsequently the lateral confinement stress σ_{conf}. It has been illustrated that for circular cross-sections when the confinement force P_{conf} is constant along the confinement reinforcement, then the corresponding lateral confining stress σ_{conf} is constant along the shear sliding plane (Hao 2018a). In Fig. 1(b), S_{lat} can be visualized as the sum of the crack face slips Δ at both sides of the sliding plane that is 2Δ. The confinement reinforcement behaviour P_{conf}/Δ can be determined from partial-interaction mechanics (Haskett et al. 2008; Yuan et al. 2004) and subsequently the relationship P_{conf}/S_{lat} can be derived. Hence for a given slip S, P_{conf} can be derived from P_{conf}/S_{lat} properties, and then σ_{conf} can be derived from P_{conf} from which the active stress/strain can be determined.

From slip *S*, the sliding strain ε_S can be derived and is fitted within the active stress/strain to fix points on the passive stress/strain (Hao 2018b).

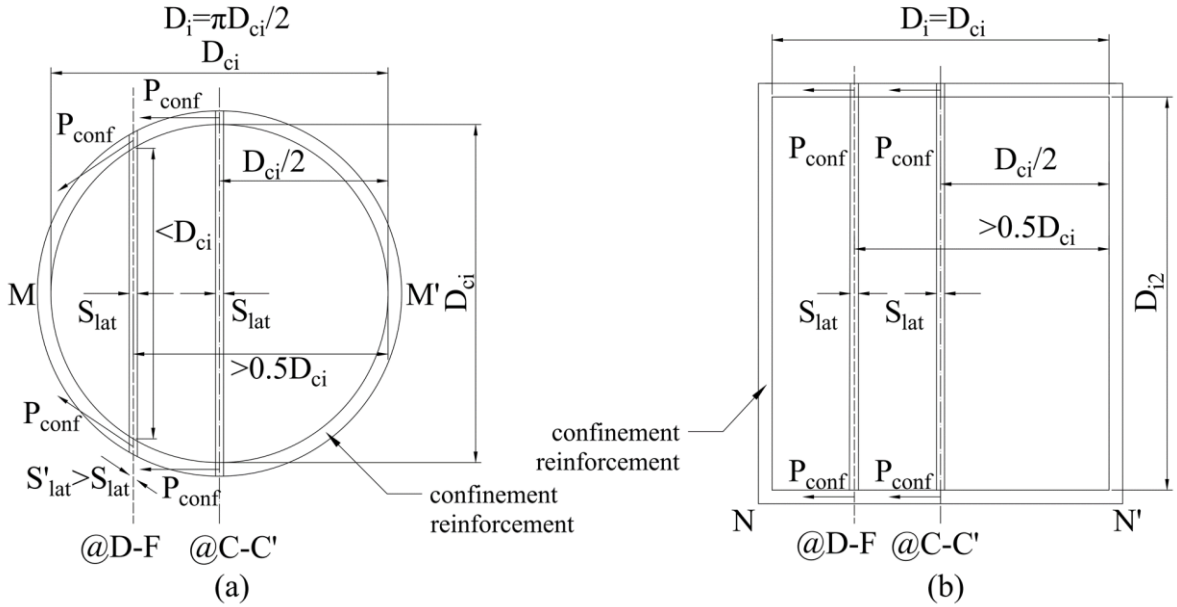

Fig. 3 Confinement mechanism in circular and rectangular sections

Consider the cross-section of the cylinder in Fig. 3(a) or that of the rectangular prism in Fig. 3(b). The sliding plane can be either at the centre at plane C-C' in Fig. 1(b) or off-centre at plane D-F. For the circular section in Fig. 3(a), the confinement force P_{conf} depends on the tangential component of S_{lat} that is S'_{lat}. However, it has been illustrated that it is reasonable to assume that S_{lat} equals S'_{lat} to give a safe solution (Hao 2018a). The confinement reinforcement is assumed to be anchored: at points M and M' in Fig. 3(a) due to symmetry about M-M'; or at points N and N' in Fig. 3(b) due to the right angle bends. Hence when there is no bond or debonding is completed, strain of the confinement reinforcement is constant at ε_Z along the confinement reinforcement length D_i and consequently the lateral component of slip S_{lat} equals $D_i\varepsilon_Z$. For circular cylinders in Fig. 3(a), D_i equals the length of the perimeter of the semi-circle. For rectangular prisms in Fig. 3(b), it equals the section width D_{ci}.

Let us now derive the passive stress/strain in Fig. 2. For this, first derive the active stress/strain O-A-B for σ_{conf0} that is the unconfined case. Then O-C-D for the IC debonding resistance P_{IC} which induces a reinforcement strain ε_{IC} and the consequential lateral

confining stress σ_{confIC} at P_{IC}; P_{IC} is described and quantified in the Appendix B. The active stress/strain O-E-F in Fig. 2 can be constructed for the yield capacity P_{yld} and lateral confining stress $\sigma_{confyld}$ at P_{yld}. Similarly, the active stress/strain O-G-H can be constructed for the fracture capacity P_{fr} and lateral confining stress σ_{conffr} at P_{fr}.

Prior to the occurrence of sliding, the confinement reinforcement does not deform so the passive stress/strain follows O-A in Fig. 2 at $\sigma_{conf0} = 0$. Sliding occurs at point A and slip gradually increases until IC debonding occurs that is at the confinement force P_{IC} and lateral component of slip $S_{lat\text{-}IC}$ from which the effective strain ε_{SIC} can be determined and consequently point I. At the end of debonding and still at P_{IC}, S_{lat} equals $S_{lat\text{-}IC2}$ which is $\varepsilon_{IC}D_i$ and consequently ε_{SIC2} can be determined to give point J. From similar analyses, the confinement reinforcement may yield at P_{yld} at point L then fracture at P_{fr} at point M or directly fracture at point M without yielding at point L. When debonding does not occur, the confinement reinforcement may either yield at point K then completely yield at point L and ultimately fracture at point M or directly fracture at point M without yielding at point L. When the confinement reinforcement does not fracture, after completely yielding at point L, the loading path follows L-F. The ultimate strain ε_{cu} may be either at point D when the longitudinal reinforcement fails at debonding, or at point F for longitudinal reinforcement that fails due to yielding, or at point N for longitudinal reinforcement that fails due to fracture at point M as shown. It is worth noting that for stirrup reinforced prisms under concentric load, it is found that the axial stress will not be lower than a specific strength which is the minimum axial stress and is referred to as the residual stress σ_{rs} (Li et al. 2001) and shown in the ordinate. For instance, should the confinement reinforcement yield at point P in Fig. 2, then the axial stress may be kept constant at the residual stress σ_{rs} such that it follows the path P-Q.

Quantification of Passive Stress/Strain

Quantification of Key Points

The full quantification of the passive stress/strain through closed form solutions has been given elsewhere (Hao 2018b) and for completeness is summarised in Appendix B. Figure 2

shows the key points in the passive stress/strain for four confinements: that is zero confinement that occurs prior to the onset of sliding; that at the onset and completion of IC debonding; that at yield prior to and after debonding; and that at fracture. A specific confinement may not occur and other confinements may be considered such as at a strain between that at yield and fracture to make the analysis more accurate.

Table 1. Loading path for different cases in Fig. B3

Loading path in Fig. 2	Confinement reinforcement behaviour	Equation to give S_{lat}	Scenarios in Fig. B3
①	②	③	④
O-A-I-I_2-J-L-M	debond then yield then fracture	Eqs.(38) to (42)	$L_{conf} \geq L_{crt}$; $P_{IC} < P_{yld}$; $P_{IC} < P_{fr}$
O-A-I-I_2-J-M	debond then fracture	Eqs.(38), (39), (40) and (42)	$L_{conf} \geq L_{crt}$; $P_{IC} < P_{yld}$; $P_{IC} < P_{fr}$
O-A-M	fracture directly	Eq. (44)	$L_{conf} \geq L_{crt}$; $P_{IC} \geq P_{yld}$; $P_{IC} \geq P_{fr}$
O-A-K-L-M	yield then fracture	Eqs. (43), (41) and (42)	$L_{conf} \geq L_{crt}$; $P_{IC} \geq P_{yld}$; $P_{IC} \geq P_{fr}$
O-A-M	fracture directly	Eq. (46)	$L_{conf} < L_{crt}$
O-A-K-L-M	yield then fracture	Eqs. (45), (41) and (42)	$L_{conf} < L_{crt}$

Bearing in mind that the lateral strains ε_S in Fig. 2 are a function of the lateral slip S_{lat}, Fig. B3 shows diagrammatically all the slip paths that can occur. Possible sequences of these slip paths are given in Table 1, their scenarios summarised and the closed form equations for deriving them listed. The key points with corresponding equations are also given in Table 2 for ease of analysis. Finally the procedure is shown as a flow chart in Fig. 4 where it can be seen that central to the whole analysis is the derivation of the lateral slip S_{lat}.

Table 2. S_{lat} of all key points in Fig. 2

Key point in Fig. 2	S_{lat}	Equation to give S_{lat}	P_{conf}	σ_{conf}	Scenario
①	②	③	④	⑤	⑥
A	0		0	0	
I	$S_{lat\text{-}IC}$	Eq. (38)	P_{IC}	σ_{confIC}	$L_{conf} \geq L_{crt}$; $P_{IC} < P_{yld}$; $P_{IC} < P_{fr}$
I_2	$S_{lat\text{-}deb}$	Eq. (39)	P_{IC}	σ_{confIC}	$L_{conf} \geq L_{crt}$; $P_{IC} < P_{yld}$; $P_{IC} < P_{fr}$
J	$S_{lat\text{-}IC2}$	Eq. (40)	P_{IC}	σ_{confIC}	$L_{conf} \geq L_{crt}$; $P_{IC} < P_{yld}$; $P_{IC} < P_{fr}$
K	$S_{lat\text{-}yld2}$	Eq. (43)	P_{yld}	$\sigma_{confyld}$	$L_{conf} \geq L_{crt}$; $P_{IC} \geq P_{yld}$; $P_{IC} \geq P_{fr}$
K	$S_{lat\text{-}yld3}$	Eq. (45)	P_{yld}	$\sigma_{confyld}$	$L_{conf} < L_{crt}$
L	$S_{lat\text{-}yld}$	Eq. (41)	P_{yld}	$\sigma_{confyld}$	
M	$S_{lat\text{-}fr}$	Eq. (42)	P_{fr}	σ_{conffr}	
M	$S_{lat\text{-}fr2}$	Eq. (44)	P_{fr}	σ_{conffr}	$L_{conf} \geq L_{crt}$; $P_{IC} \geq P_{yld}$; $P_{IC} \geq P_{fr}$
M	$S_{lat\text{-}fr3}$	Eq. (46)	P_{fr}	σ_{conffr}	$L_{conf} < L_{crt}$

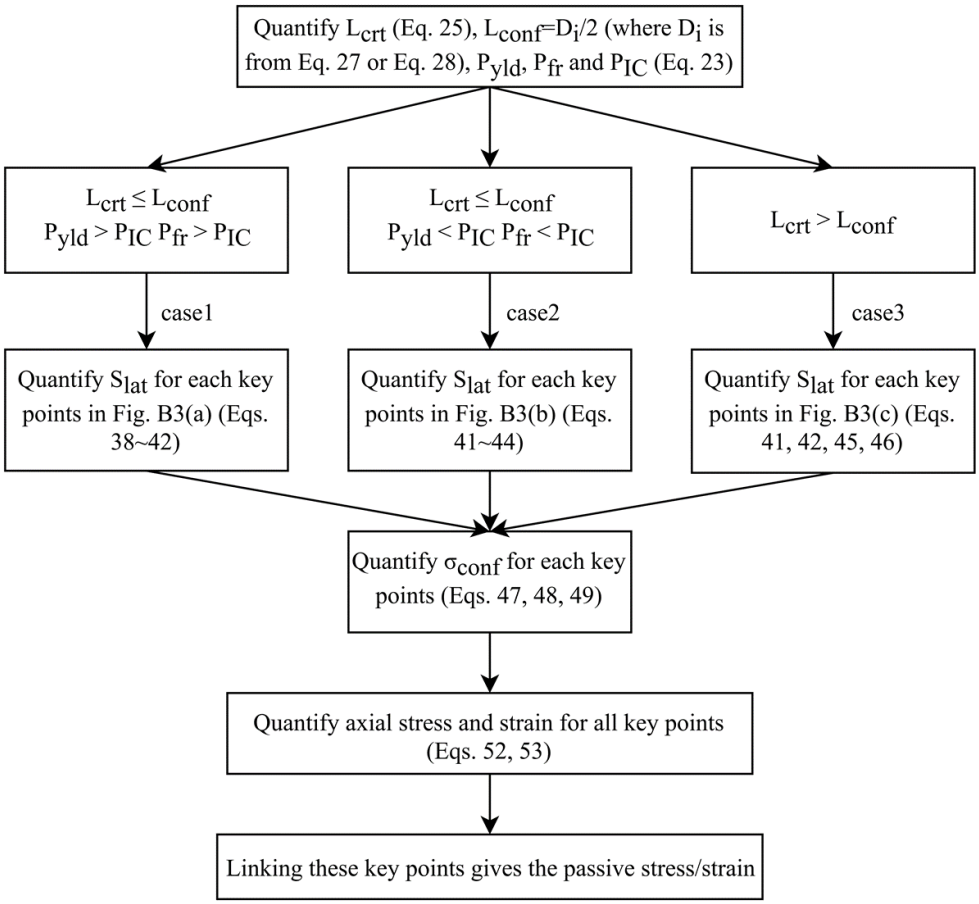

Fig. 4 Flowchart to derive passive stress/strain

Rectangular Stress Block

Having quantified the key points of the passive stress/strain through the procedures outlined in Fig. 4, the form is now simplified to that of a rectangular stress block (Hognestad 1951). The application in a flexural analysis will be described later.

Area and Centroid of the Stress Block

Consider the arbitrary passive stress/strain O-A-K-L-F in Fig. 2 where each key point has coordinates (x_i, y_i). These are also shown in Fig. 5 where point P at (x_{ci}, y_{ci}) is the centroid of the stress block O-A-K-L-F. The coordinates (x_i, y_i) are derived from Eqs. (52) and (53) through Fig. 4 and Appendix B. The area A_{rec} of the polygon O-A-K-L-F in Fig. 5 and the x-coordinate of the polygon centroid x_{ci} are (Bourke 1988)

$$A_{rec} = \frac{1}{2}\sum_{i=0}^{N-1}(x_i y_{i+1} - x_{i+1} y_i) \tag{1}$$

$$x_{ci} = \frac{1}{6A_{rec}}\sum_{i=0}^{N-1}(x_i + x_{i+1})(x_i y_{i+1} - x_{i+1} y_i) \tag{2}$$

where N is the number of key points and x_N and y_N are equals x_0 and y_0 respectively. Take the stress block O-A-K-L-F in Fig. 5 as an example, when N equals five, the coordinate (x_5, y_5) in Eqs. (1) and (2) is assumed to equal (x_0, y_0) as shown (Bourke 1988).

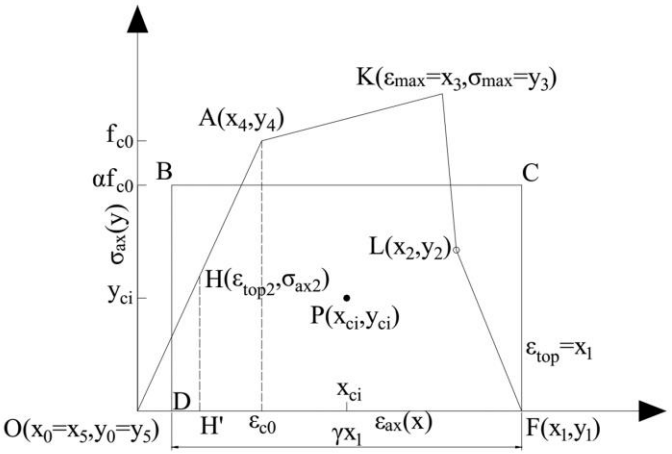

Fig. 5 Rectangular simplification of passive stress/strain

α and γ Parameters

The stress block O-A-K-L-F in Fig. 5 is simplified to the rectangular stress block D-B-C-F with the same area and x-coordinate of the centroid. The width and length of the rectangular stress block are αf_{c0} and γOF where OF equals the maximum strain of the stress block ε_{top} which equals x_1 as shown. From the geometry, parameter γ is

$$\gamma = \frac{DF}{OF} = \frac{2(x_1 - x_{ci})}{x_1} \tag{3}$$

where x_{ci} can be obtained from Eq. (2). From the geometry, α is derived as follows

$$\alpha f_{c0} = \frac{A_{rec}}{\gamma x_1} \tag{4}$$

$$\alpha = \frac{A_{rec}}{f_{c0} \gamma x_1} \tag{5}$$

where A_{rec} can be obtained from Eq. (1). Substituting γ from Eq. (3) into Eq. (5) gives

$$\alpha = \frac{A_{rec}}{2(x_1 - x_{ci}) f_{c0}} \tag{6}$$

Examples of α and γ Derivation

Parameters α and γ will be derived for the stirrup reinforced beam B4-1.5C from tests by Mansur et al. (1997); the details are given in Table 3. The passive stress/strain is derived first and then α and γ.

Table 3. Details of stirrup reinforced beam

S#	Ref.	L_a (mm)	D_0 (mm)	D_{02} (mm)	f_{c0} (MPa)	$f_{y\text{-}l}$ (MPa)	S_s (mm)	$\sigma_{confyld}$ (MPa)	ρ_S
B2-2.6C	Mansur et al 1997	1000	250	170	76.3	550	40.0	6.02	0.0231
B4-3.5C	Mansur et al 1997	1000	250	170	76.3	550	30.0	8.03	0.0462
B4-2.6C	Mansur et al 1997	1000	250	170	81.7	550	40.0	6.02	0.0462
B4-1.5C	Mansur et al 1997	1000	250	170	82.2	550	70.0	3.44	0.0462
B4-2.6L	Mansur et al 1997	1000	250	170	73.0	550	40.0	6.02	0.0462
B4-0.0C	Mansur et al 1997	1000	250	170	72.9	550	-	0.00	0.0462
C4-0.0C	Mansur et al 1997	1000	250	170	89.1	550	-	0.00	0.0462
D4-0.0C	Mansur et al 1997	1000	250	170	105.3	550	-	0.00	0.0462
B312	Rashid et al 2005	2400	400	250	72.8	460	100	3.76	0.0295
B313	Rashid et al 2005	2400	400	250	72.8	460	66.7	5.64	0.0295
S1B0	Giduquio et al 2012	900	300	200	23.9	531	190	1.07	0.0101
S2B2	Giduquio et al 2012	900	300	200	30.9	596	90.0	2.19	0.0101
S2B3	Giduquio et al 2012	900	300	200	31.1	596	45.0	4.38	0.0101

Note: S# = specimen reference number; $f_{y\text{-}l}$ = yield capacity of longitudinal reinforcement; ρ_S = longitudinal tensile reinforcement ratio.

Passive Stress/Strain

From Fig. 4 and Appendix B, the passive stress/strain of the stirrup reinforced prism is plotted in Fig. 6. The passive stress/strain depends on the deformed length L_{def} of the prism as in Fig. 1 which depends on the length of the hinge in the RC beam; this will be assumed to be 259 mm as will be explained later in the beam analysis. The concrete strength f_{c0} equals 82.2 MPa which can be substituted into Eq. (31) to give axial strain ε_{c0} = 0.00255 at f_{c0}. Hence sliding occurs at point A in Fig. 6 that has coordinates (ε_{c0} = 0.00255, f_{c0} = 82.2). The confinement reinforcement yields at point C where the lateral confining stress at yield $\sigma_{confyld}$ = 3.44MPa as obtained from Eq. (47) by substituting the yield capacity of the stirrups P_{yld} = 15.6 kN. The critical length L_{crt} from Eq. (25) equals 1292 mm which is larger than the confinement length $L_{conf} = D_i/2$ = 102 mm. Hence the variation in Fig. B3(c) applies. The lateral component of slip at the onset of yield $S_{lat\text{-}yld3}$ from Eq. (45) equals 0.162 mm. Substituting $\sigma_{confyld}$ = 3.44 MPa and $S_{lat\text{-}yld3}$ = 0.431 mm into Eqs. (52) and (53) gives the axial stress 66.9 MPa and axial strain $\varepsilon_{ax\text{-}yld}$ 0.00632 at point C in Fig. 6 that is the onset of yielding. The strain hardening effect is ignored, hence, after yielding at point C, the confinement force and stress $\sigma_{confyld}$ is unchanged. With regard to point D, substituting the axial stress σ_S = 0 MPa into Eq. (52) and rearranging gives the slip at point D of $S_{lat\text{-}D}$ = 1.47 mm. Substituting $\sigma_{confyld}$ = 3.44 MPa, $S_{lat\text{-}D}$ = 1.47 mm and σ_S = 0 MPa into Eq. (53) gives the axial strain at point D which is also the ultimate strain ε_{cu} = 0.0118. At point E, axial strain equals 1.5ε_{cu} = 0.0177 and axial stress equals zero. Hence, all the coordinates of the key points O, A, C, D and E have been derived. The additional point E at a strain of 1.5ε_{cu} is not required in design but will be used in the ensuing validation to following the rapidly descending branch of the strength.

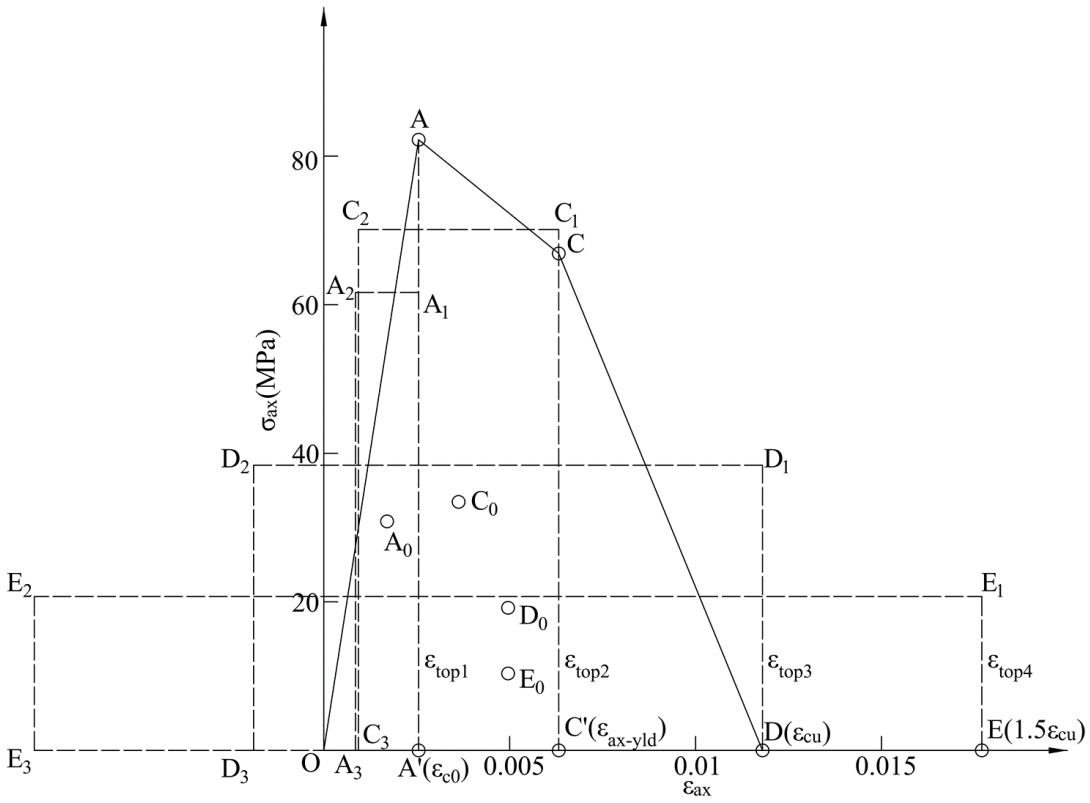

Fig. 6 Rectangular simplification of passive stress/strain of specimen B4-1.5C and L_{def} = $0.5S_{cr}$

Parameters in Flexural Analysis

In this section, α and γ are derived for the stress blocks in Fig. 6 of O-A-A' at the onset of sliding, O-A-C-C' at the onset of yield and O-A-C-D and at the ultimate strain. These stress blocks have the same abscissa of the centroid A_0, C_0 and D_0 with their corresponding rectangular stress blocks A_1-A_2-A_3-A', C_1-C_2-C_3-C' and D_1-D_2-D_3-D respectively. For instance, the stress block O-A-A' has the same abscissa of the centroid A_0 with the simplified rectangular stress block A_1-A_2-A_3-A'. Furthermore, the maximum strain of these stress blocks is also known because the strain of all the key points has been derived. For instance when the stress block O-A-A' is developed, then the maximum strain of the stress block ε_{top1} equals ε_{c0}.

The coordinates of points O, A and A', derived previously, are substituted into Eqs. (1) and (2) to give the area of the polygon O-A-A' which is A_{rec} = 0.1048 and the abscissa of the polygon centroid x_{ci} = 0.00170. From which the parameters α = 0.750 and γ = 0.667 can be

obtained from Eqs. (6) and (3) and, subsequently, the rectangular stress block A_1-A_2-A_3-A' as well as the centroid A_0 can be determined from the definitions of α and γ.

With regard to the stress blocks O-A-C-C' and O-A-C-D in Fig. 6, ε_{top} equals strains at point C' and D with $\varepsilon_{top2} = \varepsilon_{ax\text{-}yld}$ and $\varepsilon_{top3} = \varepsilon_{cu}$ as shown. Similar to the procedure for the derivation of α and γ of the stress block O-A-A', α and γ can be derived from Eqs. (6) and (3); for stress block O-A-C-C', α equals 0.852 and γ equals 0.853 and for stress block O-A-C-D, α equals 0.467 and γ equals 1.16.

The stress block O-A-C-D-E in Fig. 6 is developed to validate the descending branch of the strength and this is not required in design and only in the validation. Similar to the previous description, this stress block is simplified to the rectangular stress block E_1-E_2-E_3-E and parameters α equals 0.252 and γ equals 1.44 from Eqs. (6) and (3).

Segmental Flexural Analysis

In this section, the parameters α and γ are used in a flexural analysis of rectangular sections for both strength and ductility. The results of α and γ can be applied directly to a circular cross-section.

Passive Concrete Confinement in Beams

It will be shown that the concrete stress/strain that is derived from passively confined concentrically loaded prisms as in Fig. 1(b), where the strain profile is uniform, can be applied directly to the concrete in flexurally loaded beams in Fig. 7 where the strain profile varies linearly.

The prismatic section M-N-O-H_1-A_1 in Fig. 1(b) is shown in the beam in Fig. 7(a) where the sliding plane is N-F and the cross section and passive restraints are in Fig. 7(b). Let the prism in Fig. 7(a) be subjected to a uniform axial stress σ_{ax} along its depth M-F-A_1. The prism is sliced into n segments of equal depth $S_{1\text{-}n}$ such that the sliding plane within each segment is passively restrained by identical elements $E_{1\text{-}n}$. Each portion of the sliding plane is shown in

Fig. 8 where $\sigma_{ax1\text{-}n} = \sigma_{ax}$. It can be seen that the sliding planes are identically restrained such that as the axial stress σ_{ax} is varied, the behaviour along each sliding plane can be considered to be identical. Now let us apply a varying axial stress along the depth M-F-A_1 in Fig. 7(a) as occurs in a flexural analysis such that each segment in Fig. 8 has a different axial stress but within the segment the axial stress is uniform. The behaviour of each individual segment is identical to that which would have been obtained from a prism test for the corresponding axial stress.

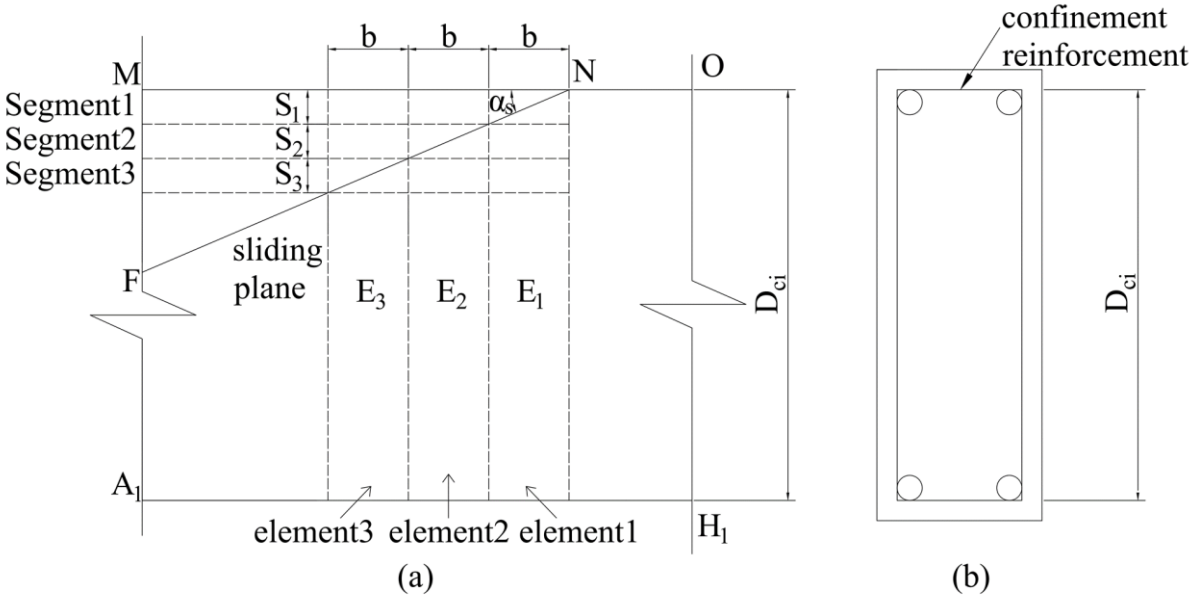

Fig. 7 Lateral reinforced prism

Hence to allow for the variation in the axial stress in a segmental analysis of a beam, each segment and each element in Fig. 8 are considered to act individually.

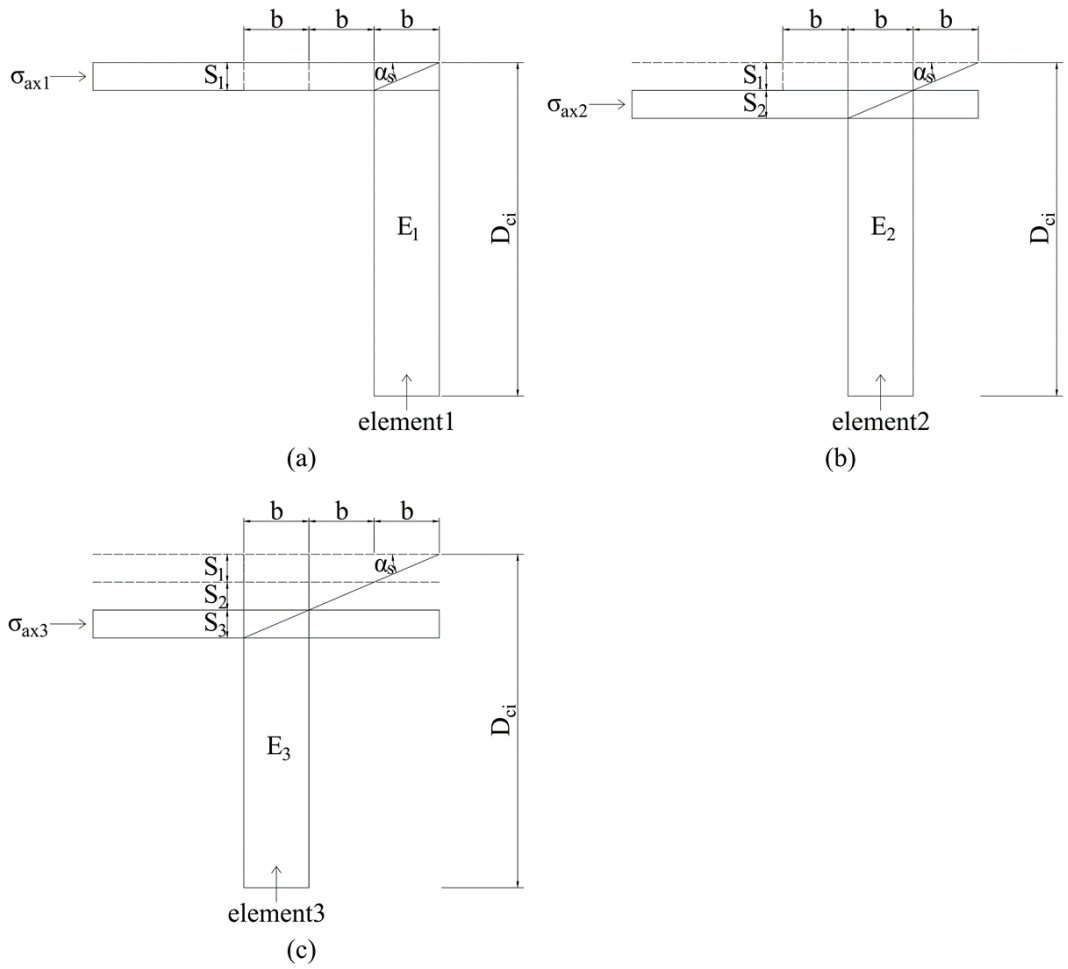

Fig. 8 Elements of lateral reinforced prism from Fig. 7

Segmental Analysis

It has been shown that the passive stress/strain derived from prisms can be applied directly to beams. This passive stress/strain has also been simplified to rectangular stress blocks which will now be used in the segmental analysis of beams. As the segmental analysis has been described in detail elsewhere (Oehlers et al. 2012; Oehlers et al. 2011; Oehlers et al. 2017; Visintin et al. 2012a; Visintin et al. 2013; Visintin et al. 2012b), it is summarised here and the closed form solution will be derived later.

Consider the half of a stirrup reinforced beam under four-point bending in Fig. 9(a). It is symmetric about the plane A'-A_2 and has the rectangular cross-section in Fig. 9(b). The beam is subjected to a shear load P_{ax} and a moment M_{ax}. The load P_{ax} is gradually increased

until flexural cracks and a wedge form. Consider the possible wedge locations A'-E'-E and A'-F'-F which have the same inclination α_s as shown (Visintin et al. 2012b). The deformation or hinge length L_{def} equals $(n+0.5)S_{cr}$ in which n is an integer and S_{cr} is the crack spacing (Visintin et al. 2012b). The integer n is chosen such that L_{def} just encompasses the wedge length L_{wdg}: such as $L_{def1} = S_{cr}/2$ to cover wedge A'-E'-E which has a length L_{wdg1}; or $L_{def2} = S_{cr} + S_{cr}/2$ to cover wedge A'-F'-F which has a length L_{wdg2} (Visintin et al. 2012b). In summary, the deformation or hinge length L_{def} for the moment/rotation analysis is chosen to just cover the maximum wedge length L_{wdg}.

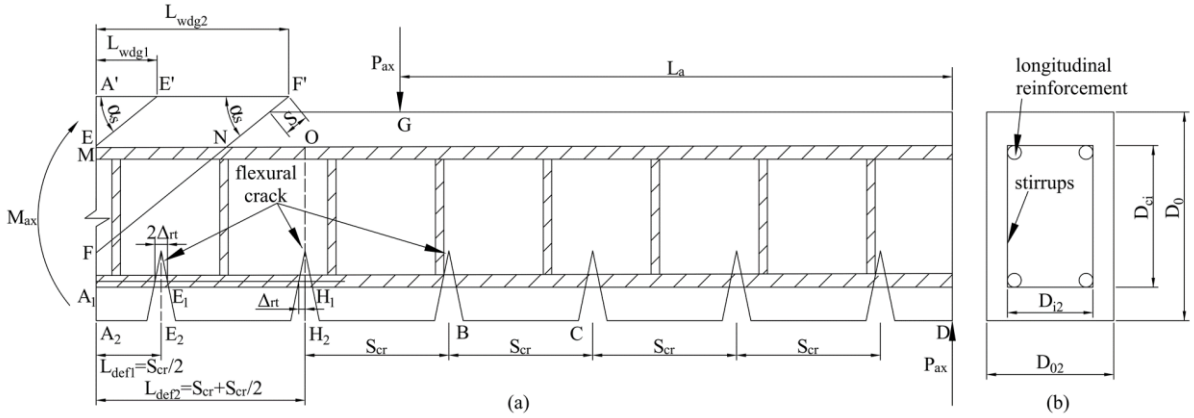

Fig. 9 Half of the reinforced beam under four point bending

Consider, as an example, the segment in Fig. 10(a) that has a hinge length $L_{def} = S_{cr}/2$ and which is subjected to a moment M_{ax} that causes an Euler-Bernoulli rotation θ (Visintin et al. 2012a; Visintin et al. 2012b) such that the displacement profile is linear as in Fig. 10(b). Consequently, the strain profile is linear as in Fig. 10(c) and subsequently the stress in the compressive and tensile longitudinal reinforcement σ_{rc} and σ_{rt} in Fig. 10(d) can be determined. From the peak concrete strain in the linear strain profile in Fig. 10(c) can be determined the concrete rectangular stress block as previously explained. Consider the passive stress/strain O-A-K-L-F in Fig. 5 which is simplified to the rectangular block C-F-D-B which is also shown in Fig. 10(d). This rectangular stress block has a width of αf_{c0} and a length of γd_{NA} where d_{NA} is the neutral axis depth in Fig. 10(a). As occurs in practice, the concrete cover in the compression zone is assumed to spall off as in Fig. 10(f).

From Figs. 10(d) and (f), the compressive force in the concrete is

$$P_{conc} = \alpha f_{c0} \gamma d_{NA} D_{i2} \tag{7}$$

where D_{i2} is the width the cross-section of the confined concrete as in Fig. 10(f). For the longitudinal tensile reinforcement, the stress is obtained from partial interaction theory that gives the relationship between the reinforcement force P_{rt} and crack face slip Δ_{rt} (Visintin et al. 2012b) where Δ_{rt} is derived from the linear deformation profile in Fig. 10(b). The force in the longitudinal compressive reinforcement P_{rc} can be obtained from its strain. Hence when the displacement profile is determined, P_{rt} and P_{rc} can be determined. In the ensuing validation only reinforcement yield is considered, that is reinforcement fracture or debonding are not considered. Furthermore strain hardening is ignored to achieve a conservative solution.

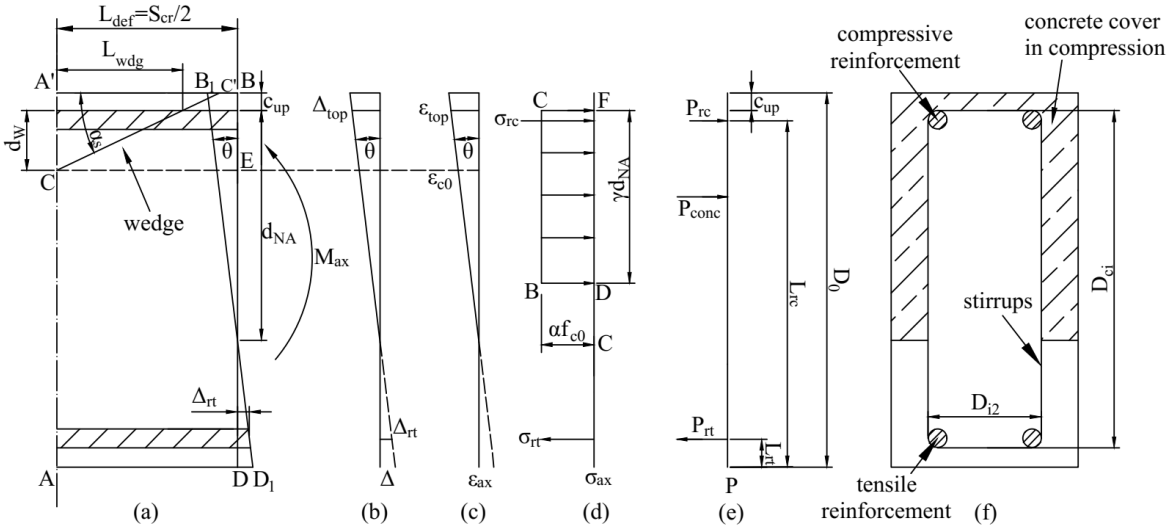

Fig. 10 Segmental analysis when L_{def} equals $0.5S_{cr}$: (a) segment; (b) displacement profile; (c) strain profile; (d) stress profile; (e) force profile; (f) cross-section

When concrete softening occurs, then the maximum strain in the rectangular stress block that controls the key points is shown as an ε_{top} in Fig. 6. Hence the deformation of the top fibre of the confined concrete Δ_{top} in Fig. 10(b) is

$$\Delta_{top} = \varepsilon_{top} L_{def} \tag{8}$$

The iterative approach applied in the segmental analysis is described first and the closed form solution will be given later. For a specific ε_{top} that is for a specific key point in the passive stress/strain, Δ_{top} can be determined from Eq. (8). It is then a question of guessing the neutral axis depth d_{NA} that is by pivoting about Δ_{top}. This fixes the deformation profile in Fig. 10(b) from which the strain, stress and force profiles in Figs. 10(c) to (e) can be derived. The neutral axis depth d_{NA} is varied until longitudinal equilibrium is achieved after which the moment M_{ax} can be derived. When concrete softening does not occur as in under-reinforced beams, then the pivotal point is now Δ_{rt} in Fig. 10(b) when the tension reinforcement yields and the analysis proceeds as before.

Hinge Length Quantification

The hinge or segment length L_{def} in Fig. 10(a) must encompass L_{wdg}. The minimum length of L_{def} equals $S_{cr}/2$ where S_{cr} is given by Zhang et al. (2014) as

$$S_{cr} = 29.1\left(\frac{A_r}{A_c}\right)^{0.207}\left[\frac{(1+\alpha)\, f_{ct} A_c \delta_1^{\alpha_1}}{\tau_{B\max} L_{per}\left(\sqrt{2}\right)^{\alpha_1}}\right]^{\frac{1}{1+\alpha_1}} \tag{9}$$

in which in a tension stiffening analysis: L_{per} is the total length of the debonding failure plane of the tensile reinforcement which equals the perimeter of the reinforcement: A_c is the cross-section area of concrete which interacts with the reinforcement; A_r is the cross-section area of reinforcement; τ_{Bmax} and δ_1 are shown in Fig. B1 and quantified in Appendix B; the coefficient α_1 is set as 0.4; and f_{ct} is the concrete tensile capacity which can be taken as follows (Iravani 1996) and in which f_c is in MPa

$$f_{ct} = 0.59\sqrt{f_c} \tag{10}$$

The wedge depth d_w in Fig. 10(a) can be derived by assuming that concrete cover spalls off from the geometry of the strain profile in Fig. 10(b) as follows

$$d_w = d_{NA} - d_{NA}\frac{\varepsilon_{c0}}{\varepsilon_{top}} \tag{11}$$

where the strain at level C-E in Fig. 10(c) equals ε_{c0}. Hence the wedge length in Fig. 10(a) equals

$$L_{wdg} = (d_{NA} - d_{NA}\frac{\varepsilon_{c0}}{\varepsilon_{top}}) / \tan\alpha \tag{12}$$

Should the derived L_{wdg} be larger than $S_{cr}/2$, then L_{def} should be increased by S_{cr} to $1.5S_{cr}$ as in Fig. 9 for L_{wdg2} such that the size dependent passive stress/strain in Figs. 2 and 6 are now for length $1.5S_{cr}$. The segmental analysis proceeds as explained previously bearing in mind that, as can be seen in Fig. 9, the total deformation of the tensile reinforcement within the hinge length, that is the total crack face slip, is now $3\Delta_{rt}$. Should L_{wdg} exceed $1.5S_{cr}$, the procedure is repeated by increasing deformed length L_{def} by S_{cr} until L_{def} covers the wedge length L_{wdg}.

Closed Form Solution

A closed form solution for the beam B4-1.5C from tests by Mansur et al. (1997) is given in detail in Appendix C as an example. The main steps are summarised as follows.

1. The passive stress/strain and rectangular stress block, such as those shown in Fig. 6, have been derived previously. Hence for these stress blocks, the parameters α and γ as well as the strain of the top fibre of the confined concrete ε_{top} are known.
2. The cross-section of the specimen B4-1.5C is shown in Fig. 11(f) and the hinge of the beam in Fig. 11(a). The hinge length L_{def} is chosen to cover L_{wdg} from Eq. (12). For a neutral axis depth d_{NA}, the displacement profile and strain profile can be determined as a function of d_{NA}. The rectangular concrete stress block is determined as shown in the stress profile in Fig. 11(d) and the concrete force P_{conc} is obtained from Eq. (7) which is also a function of d_{NA}.
3. From the displacement profile the force in longitudinal reinforcement P_{rt1} and P_{rt2} are derived as a function of d_{NA} from Eq. (57) or (58). Substituting the derived P_{conc},

P_{rt1} and P_{rt2} into the force equilibrium from Eq. (65) in Fig. 11(e), d_{NA} can be solved and then the following rotation θ and moment M_{ax} can be determined

$$\theta = \frac{\Delta_{top}}{d_{NA}} \tag{13}$$

$$M_{ax} = P_{conc}(D_0 - c_{up} - \frac{\gamma d_{NA}}{2}) - P_{rt1}L_{rt1} - P_{rt2}L_{rt2} \tag{14}$$

where c_{up} is the cover in Fig. 11(a), Δ_{top} can be determined from Eq. (8), P_{rt1} and P_{rt2} are tensile reinforcement forces as shown in Fig. 11(e) and L_{rt1} and L_{rt2} are their lever arms as shown.

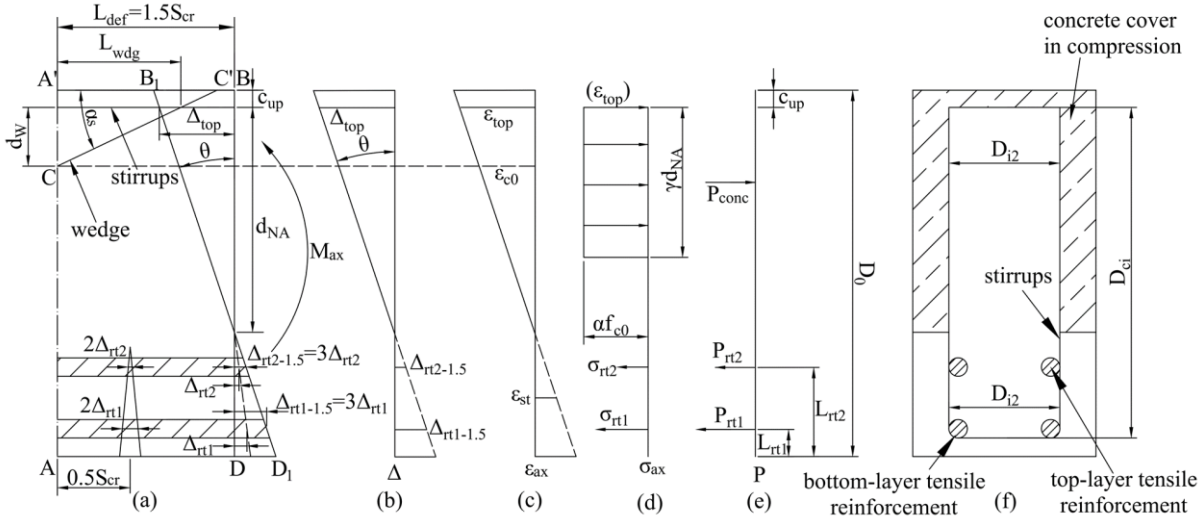

Fig. 11 Segmental analysis of specimen B4-1.5C when L_{def} equals $1.5S_{cr}$: (a) segment; (b) displacement profile; (c) strain profile; (d) stress profile; (e) force profile; (f) cross-section

For an under-reinforced beam, the pivot point is the displacement when all the tensile reinforcement has yielded. The derivation of the moment/rotation about this pivotal point follows. Consider the segmental analysis in Fig. 11. At the pivotal point, the crack face slip Δ_{rt2} in Fig. 11(a) equals Δ_{yld} which is the crack face slip when the longitudinal tensile reinforcement starts to yield and can be quantified from Eq. (59). Hence, when the neutral axis depth d_{NA} is guessed as well as $\Delta_{rt2} = \Delta_{yld}$ in Fig. 11(a), the displacement profile and strain profile can be determined as a function of d_{NA}. Softening normally does not occur and

the triangular concrete stress block O-H-H' in Fig. 5 is developed. For this triangular concrete stress block the resultant force and its lever arm are obtained as a function of d_{NA} from geometry. Having determined the concrete force, the other procedures to derive the moment/rotation is the same as that of an over-reinforced beam.

Idealisation of the Ductility

Derivation of Moment/Rotation from Experiments

There are several methods of quantifying the ductility of a beam such as by using: the traditional full-interaction moment/curvature (M_{ax}/χ); or the partial-interaction moment/rotation (M_{ax}/θ) where, for example, the moment/rotation can be employed in the moment redistribution analysis (Haskett et al. 2010b; Haskett et al. 2009; Visintin and Oehlers 2016); or the load/mid-deflection (P_{ax}/Δ_m). In this research, moment/rotation is used to measure the beam ductility which is extracted from experimental load/mid-deflections as follows.

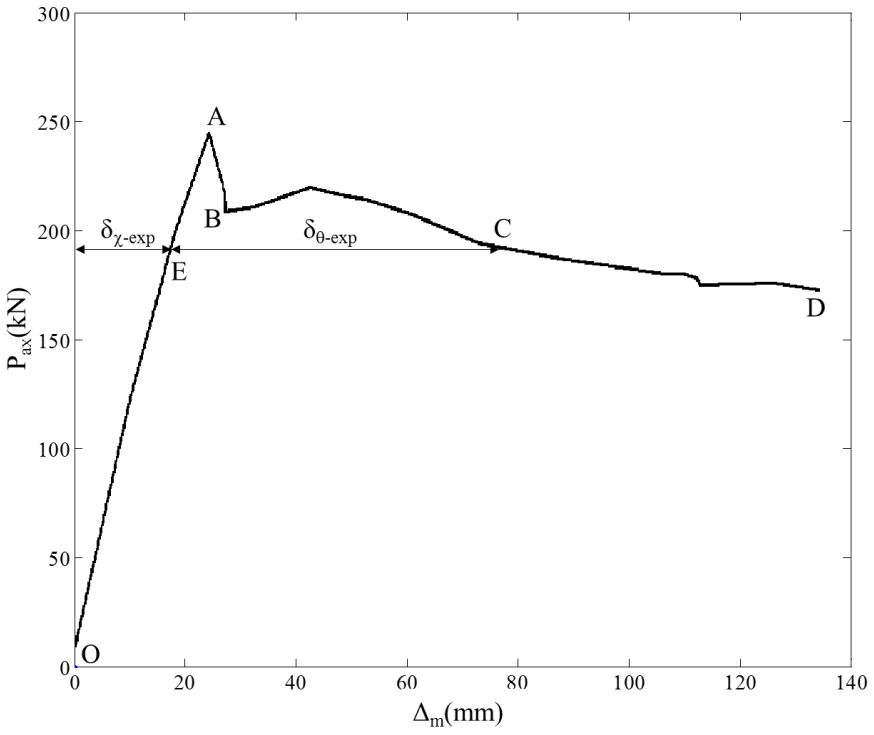

Fig. 12 Load/Mid-deflection (P_{ax}/Δ_m) of specimen B4-3.5C

The load/mid-deflection of the passively confined beam B4-3.5C by Mansur et al. (1997) is shown in Fig. 12. Before the formation of the wedge, the mid-deflection $\delta_{\chi\text{-}exp}$ can be obtained by integrating the continuous curvature along the beam. After the formation of the wedge at point A in Fig. 12, it is assumed that all of the concrete cover above the neutral axis spalls off due to the formation of the wedge; this degree of spalling is probably an overestimation and is therefore a conservative assumption. The spalling causes a sudden reduction of the shear load P_{ax} to point B (Giduquio et al. 2015; Mansur et al. 1997). After which, the mid-deflection, such as that at point C, is comprised of the deflection outside the hinge region $\delta_{\chi\text{-}exp}$ and that due to the rotation of the hinge $\delta_{\theta\text{-}exp}$. These components of the deflection are also shown in Figs. 13(a) and (b) where L_b is the length of the beam.

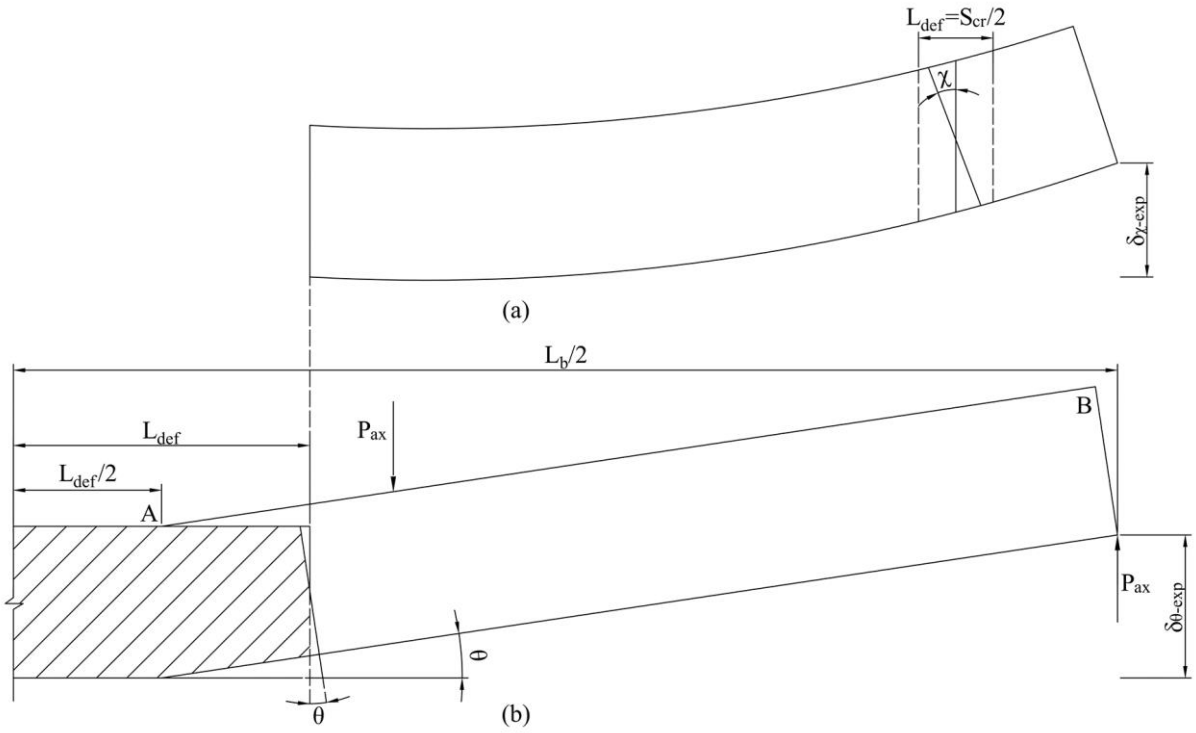

Fig. 13 Mid-Deflection of a beam due to (a) curvature in the non-wedge region (b) rotation of the wedge

The hinge region, which is shown hatched in Fig. 13(b), has a rotation of θ. For ease of analysis, the pivot is assumed to occur at the middle point of the hinge region at point A. Consequently, the deflection due to rotation $\delta_{\theta\text{-}exp}$ is given by $\theta_{exp}(L_b/2\text{-}L_{def}/2)$. Rearranging gives the rotation of the hinge as

$$\theta_{\exp} = \frac{\delta_{\theta-\exp}}{(L_b / 2 - L_{def} / 2)} \tag{15}$$

Because in Fig. 13 the deformed length $L_{def} << L_b$, the effect of the pivot position is small. The remaining component of the deflection $\delta_{\chi\text{-}exp}$ is determined by integrating the curvature outside the hinge region as in Fig. 13(a). The moment/rotation of the hinge can now be obtained from Fig. 12 by converting the ordinate to the moment in the hinge and the abscissa to the rotation using Eq. (15).

It is worth noting that the concrete cover above the neutral axis is assumed to spall off, as in Fig. 10(f), only in the hinge region and after the formation of the wedge at point A in Fig. 12. Consequently the mid-deflection due to the wedge $\delta_{\theta\text{-}exp}$ in Fig. 13(b) is derived from the cross-section without concrete cover that is θ_{exp} is based on a cross-section without concrete cover. In contrast, the concrete cover does not spall off outside the hinge region in Fig. 10(f) through the whole loading process; thus while unloading P_{ax}/Δ_m follows A-O in Fig. 12 that is the load/deflection of beam with concrete cover. Having derived the moment/rotation from experimental load/mid-deflection, let us now consider the derivation of a theoretical moment/rotation.

Idealised Theoretical Moment/Rotation

Key points on the theoretical moment/rotation for over-reinforced and under-reinforced beams will be described qualitatively.

Over-Reinforced Beam

The analysis of an over-reinforced beam is summarised in Fig. 14. Four distributions of the concrete stress block with increasing applied strain profiles are shown in Figs. 14(b) to (e). The concrete cover shown hatched in Fig. 14(a) is assumed to spall off in the compressive region after the onset of concrete softening. The neutral axis A-A' in Fig. 14(a) corresponds to the stress block in Fig. 14(b) and applies to point A in Fig. 15. Whereas the neutral B-B' in Fig. 14(a) is for the stress block in Fig. 14(e) that corresponds to point E in Fig. 15. The

moment/rotation from a continuous segmental analysis is plotted as the solid line in Fig. 15 where the concrete stress block controls the flexural behaviour of the beam as not all the tensile reinforcement may have yielded or fractured. The five key points linking O-A-B-D-E with a dashed line give a simplified moment/rotation for which closed form solutions will be described in the next section by taking specimen B4-1.5C (Mansur et al. 1997) as an example.

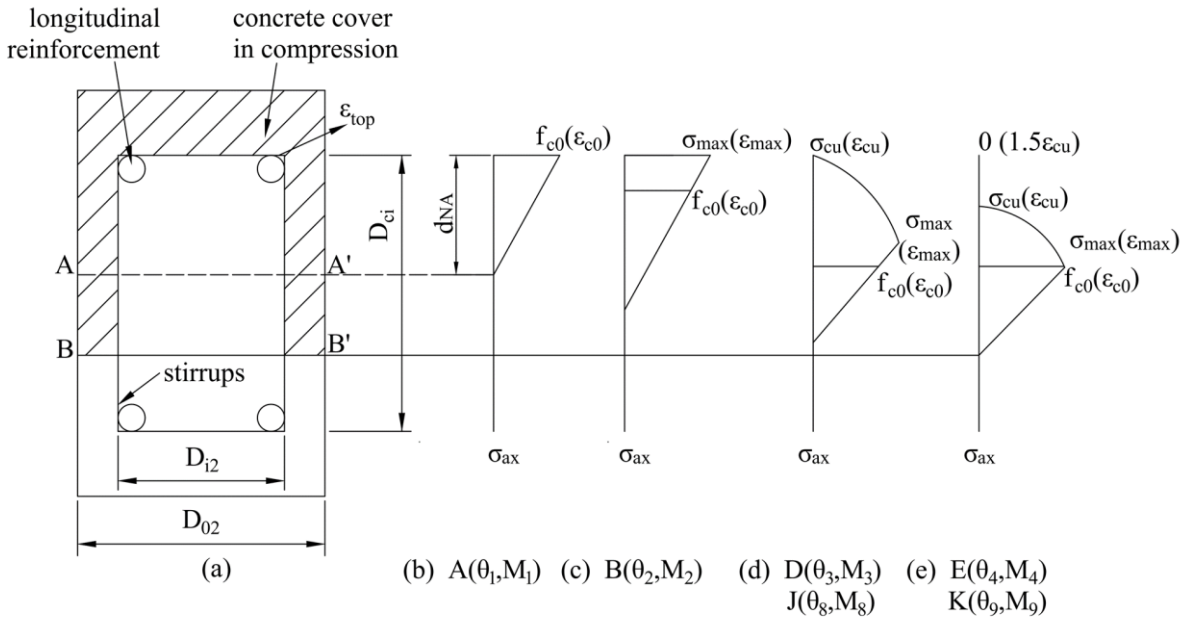

Fig. 14 Cross section of the beam (a) and different stress blocks are developed (b, c, d, and e)

At point A at (θ_1, M_1) in Fig. 15, the strain of the top fibre of the confined concrete, ε_{top} in Fig. 14(a), equals ε_{c0} that is the strain at the unconfined strength f_{c0} in Fig. 5 and in Fig. 14(b). At point B (θ_2, M_2) in Fig. 15, ε_{top} is the strain at the maximum of the passively confined concrete after sliding shown as point K (ε_{max}, σ_{max}) in Fig. 5 and in Fig. 14(c). After point B in Fig. 15, the slope of moment/rotation changes rapidly. Further development of the concrete stress block gives point C at the maximum moment M_{max} where either the moment lever arm or the force in the reinforcement reaches its maximum. Then at point D at (θ_3, M_3), the passive stress/strain is fully developed as in Fig. 14(d). After which, there is usually a rapid loss of moment capacity due to a reduced lever arm such as in Fig. 14(e) which is at point E in Fig. 15 at (θ_4, M_4). The difference between the moments M_2, M_3 and M_{max} is normally within a few percentage points so closed form solutions will only be determined

for: (θ_1, M_1) and (θ_2, M_2) to give the ascending branch and (θ_3, M_3) to quantify the ductility. With regard to point E, it is not required in design but it gives a point as the strength reduces in the validation.

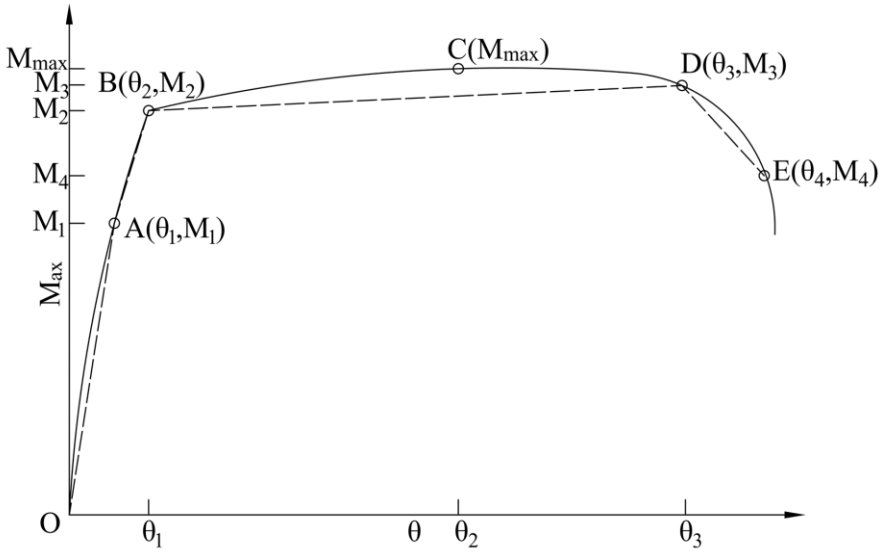

Fig. 15 Moment/Rotation of over-reinforced beam

Under-Reinforced Beam

The idealised moment/rotation of an under-reinforced beam is shown in Fig. 16 where the behaviour of the longitudinal reinforcement controls the flexural behaviour. There are several scenarios to consider: the longitudinal reinforcement may either fracture prematurely leading to no ductility at point G (θ_5, M_5); or yield at point H (θ_6, M_6); and then fracture at I (θ_7, M_7); or yield at H after which the concrete stress block is fully developed at point J (θ_8, M_8) which is the case shown in Fig. 14(d); after which the moment capacity rapidly reduces due to the reduction of the moment lever arm at point K in Fig. 16 at (θ_9, M_9) which is the case shown in Fig. 14(e). Hence for beams that fail due to fracture of the longitudinal reinforcement, closed form solutions are required for points G, H and I in Fig. 16 at (θ_5, M_5), (θ_6, M_6) and (θ_7, M_7). For beams that do not fail due to fracture but are governed by yield of the longitudinal reinforcement, closed form solutions are required for points H and J at (θ_6, M_6) and (θ_8, M_8). Point K is not required in design but will be used in the following validation.

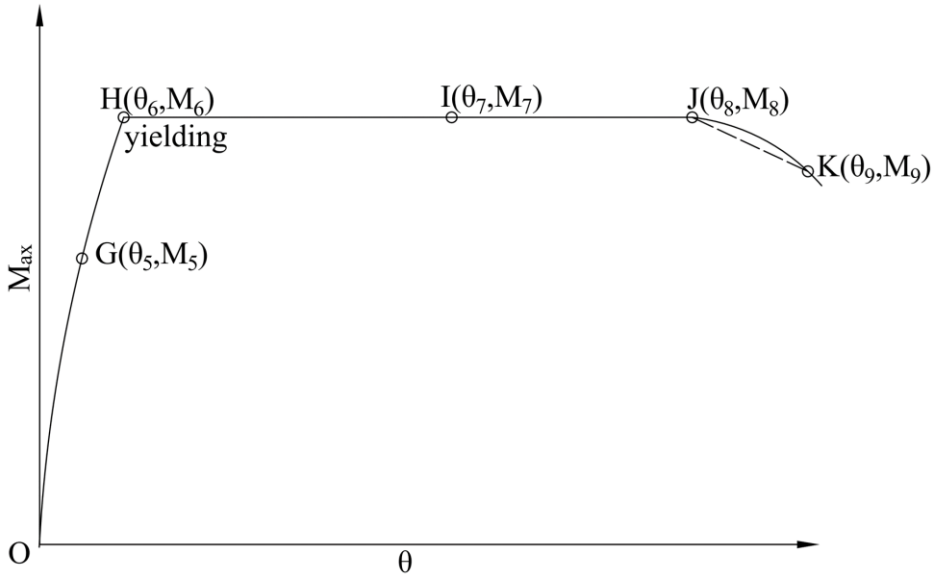

Fig. 16 Moment/Rotation of under-reinforced beam

Validation

Figure 17 compares six different segmental analyses that were applied to the over-reinforced beam B4-1.5C by Mansur et al. (1997). The experimental results of the ductility plateau were obtained from the load/deflection plots as explained using Fig. 13. In cases 1 to 3 in Fig. 17, the theoretical ascending branch of the passive stress/strain was assumed to be linear using Eq. (35). The results of the first three cases are obtained from the proposed closed form solution described in this paper.

1. The first case assumes that all the concrete is unconfined and that there is no spalling or concrete cover loss to give a lower bound.
2. The second case allows for the effect of the confinement reinforcement but without considering the residual stress σ_{rs} in Fig. 2 that is $\sigma_{rs} = 0$. It also assumes that concrete cover in the compressive region, shown in the hatched area in Fig. 14(a), spalls off.
3. The third case is the same as the second case but includes the residual stress σ_{rs} from Eq. (54) giving a reasonably good correlation with the experimental results along the ductile plateau.

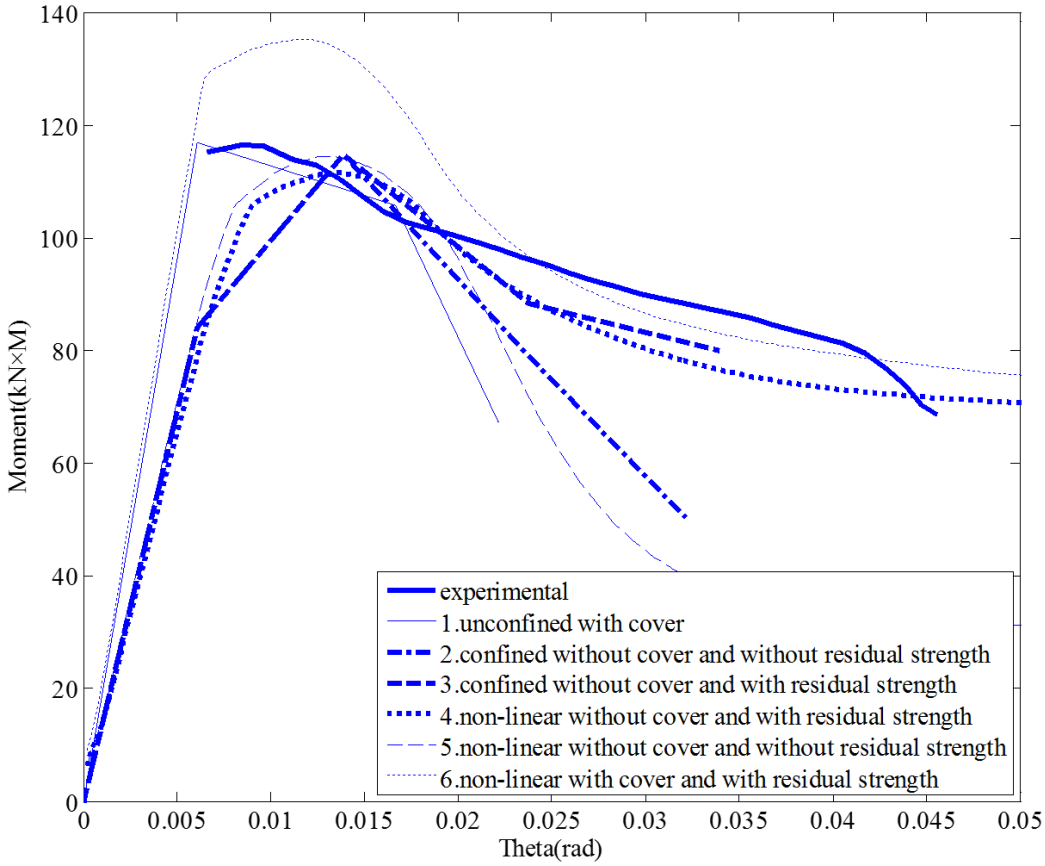

Fig. 17 Moment/Rotations of specimen B4-1.5C

In cases 4 to 6 in Fig. 17, the passive stress/strain has the non-linear ascending branch from Eq. (32) and the results are obtained from a numerical model described elsewhere (Visintin et al. 2012b).

4. The fourth case is the same as the third case except that the linear ascending branch is replaced with a more accurate non-linear form from Eq. (32) giving better correlation at the onset of sliding or softening and good correlation along the ductility plateau.
5. The fifth case is the same as the second case except that the passive stress/strain has the non-linear ascending branch. Once again giving better correlation at the onset of sliding.
6. The sixth case is the same as the fourth case except that the concrete cover in the compressive region does not spall off. This gives a very unconservative result stressing the importance of allowing for spalling.

Compared with Code Approach

Closed form solutions have been compared with published test results by Rashid and Mansur (2005) and Mansur et al. (1997) in Figs. 18 and 19, as well as by Lopes et al. (2012) in Fig. 20. These specimens were either over-reinforced or under-reinforced beams reinforced with lateral confining steel reinforcement; details of these specimens are in Table 3. The second case above, which uses a linear ascending branch without residual stress and with concrete spalling, has been used as it gives a conservative result as well as case 3 that allows for the residual stresses. The results have also been compared with a standard approach for strength referred to as the code approach (Warner et al. 1998) which does not quantify the ductility.

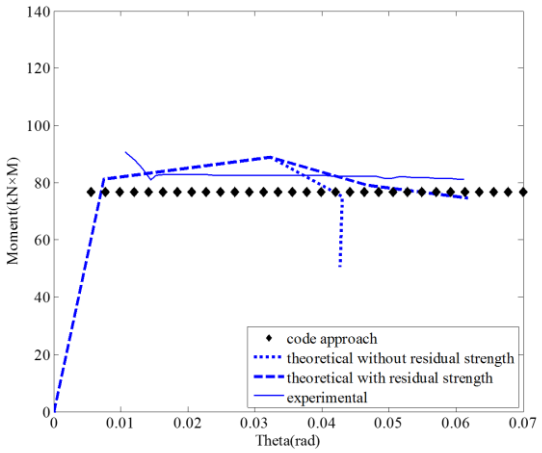

(a)

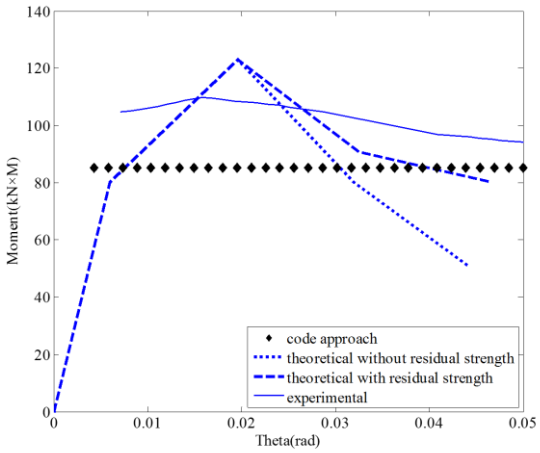

(b)

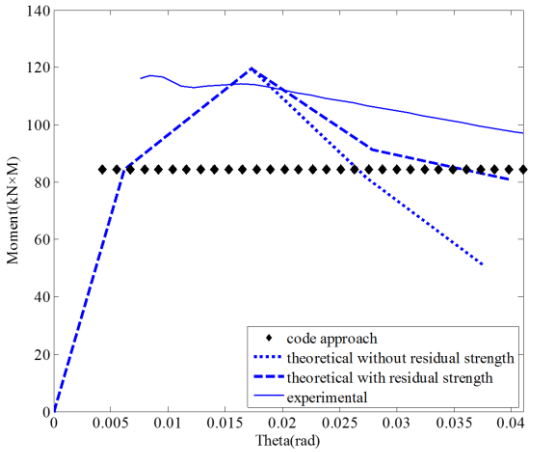

(c)

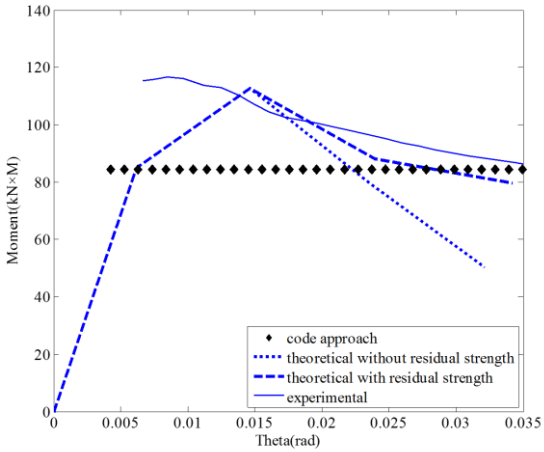

(d)

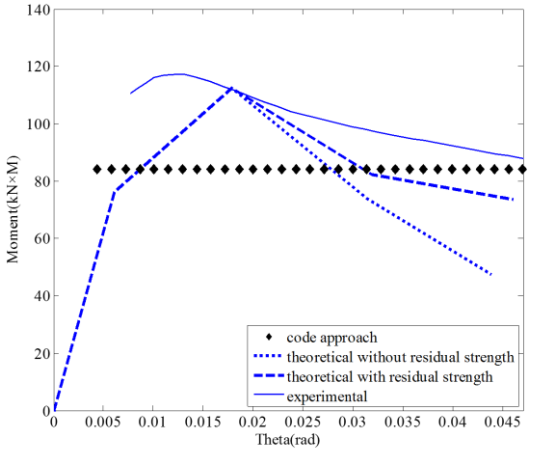

(e)

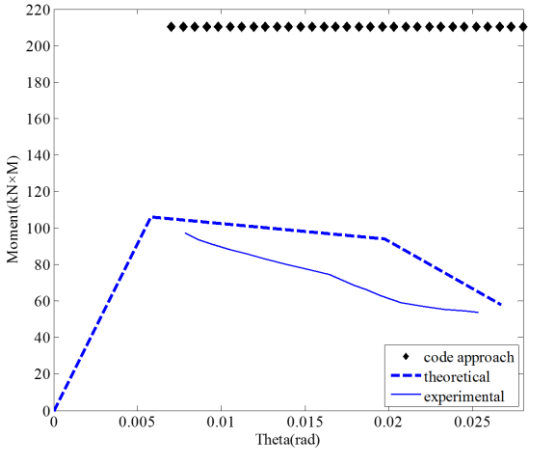

(f)

Fig. 18 Moment/Rotations of over-reinforced beam with specimen number: (a) B2-2.6C; (b) B4-3.5C; (c) B4-2.6C; (d) B4-1.5C; (e) B4-2.6L; (f) B4-0.0C;

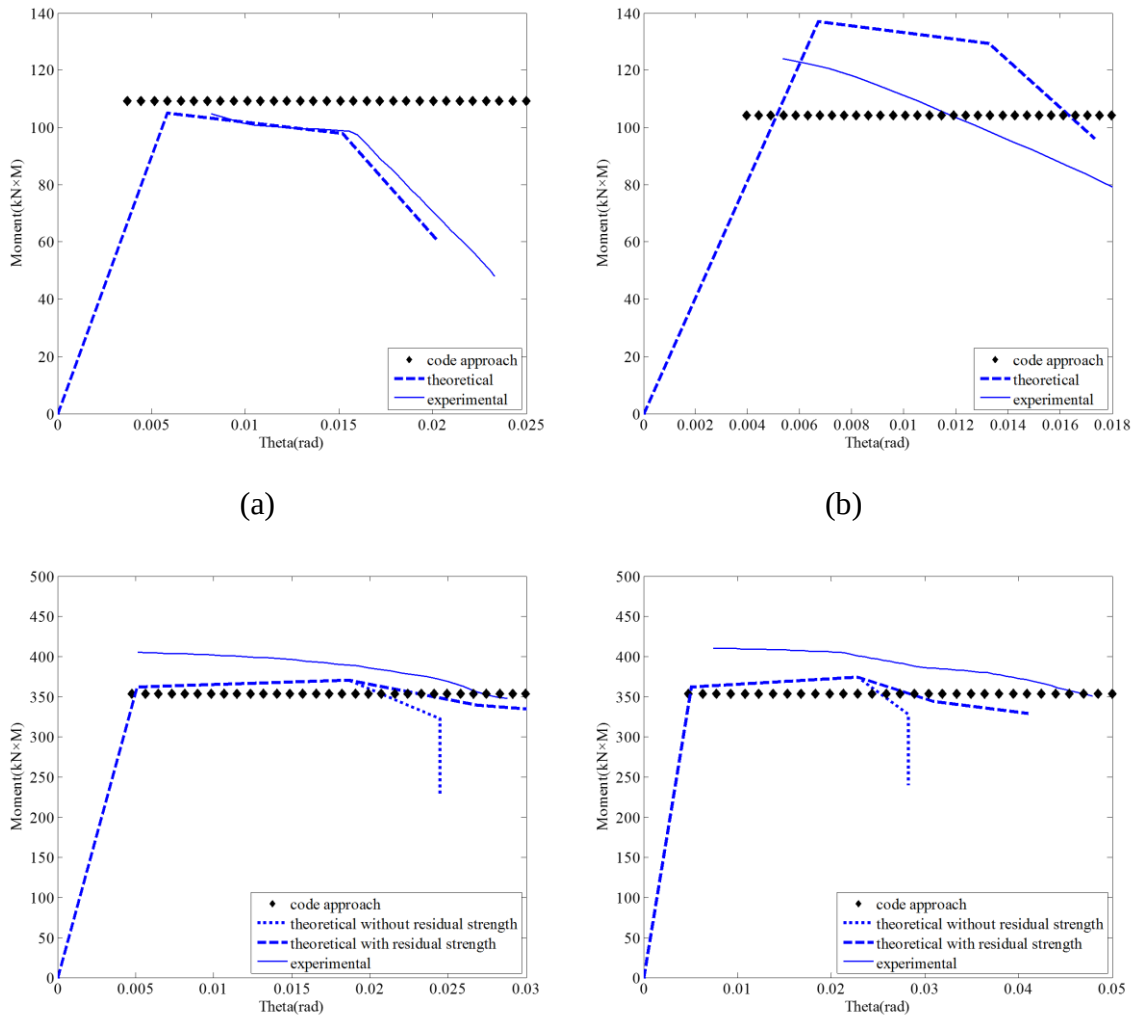

Fig. 19 Moment/Rotations of over-reinforced beam with specimen number: (a) C4-0.0C; (b) D4-0.0C: (c) B312; (d) B313

In Figs. 18 to 20, the 'theoretical without residual strength' that is the second case in Fig. 17 gives, in general, a lower bound to the ductility. With regard to the 'theoretical with residual strength' case that is the third case in Fig. 17, the ductility is in good correlation with the experimental moment/rotation. The passive stress/strain block at point B in Fig. 17 for different levels of confinement reinforcement (B4-3.5C, B4-2.6C, B4-1.5C and B4-0.0C in Table 3) are shown in Fig. 21 and corresponding simplified rectangular stress block is shown in Fig. 22. The experimental moment/rotations of these specimens are also shown in Fig. 23 and corresponding 'theoretical with residual strength' cases are shown in Fig. 24. It can clearly be seen that the confinement reinforcement can enhance ductility for over-reinforced

beams. Using code rectangular stress block in Fig. 22 for confined concrete may give conservative solution.

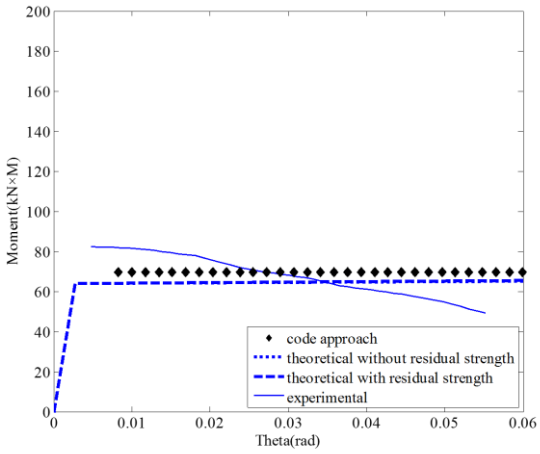

(a)

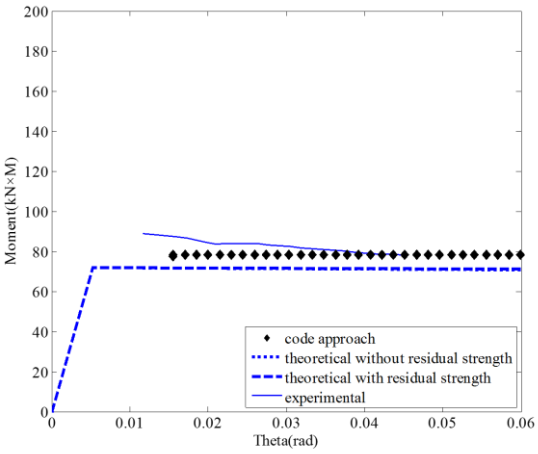

(b)

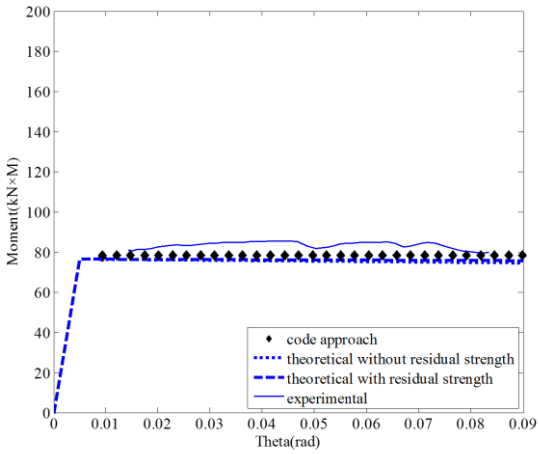

(c)

Fig. 20 Moment/Rotations of under-reinforced beam with specimen number: (a) S1B0; (b) S2B2; (c) S2B3

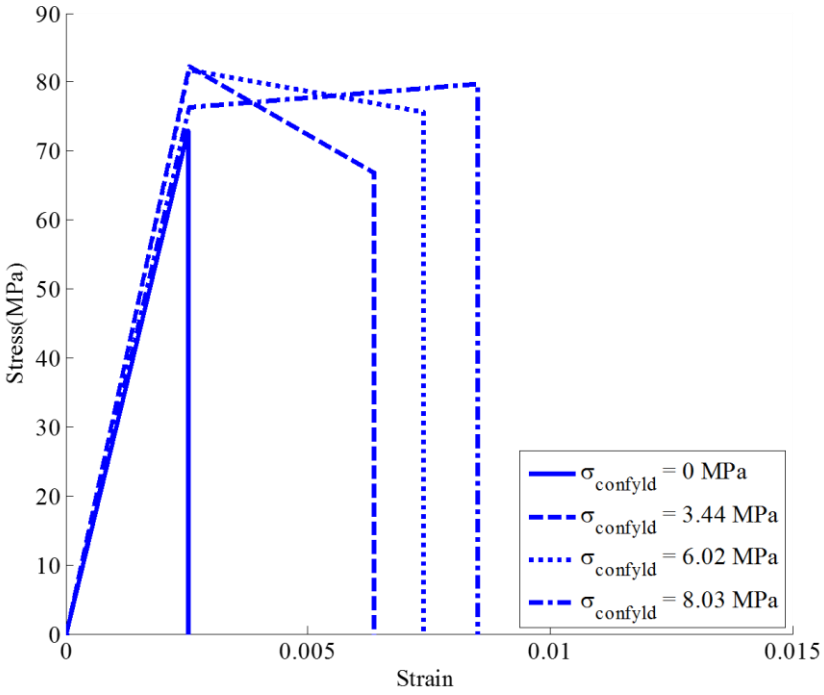

Fig. 21 Effect of confinement on passive stress/strain

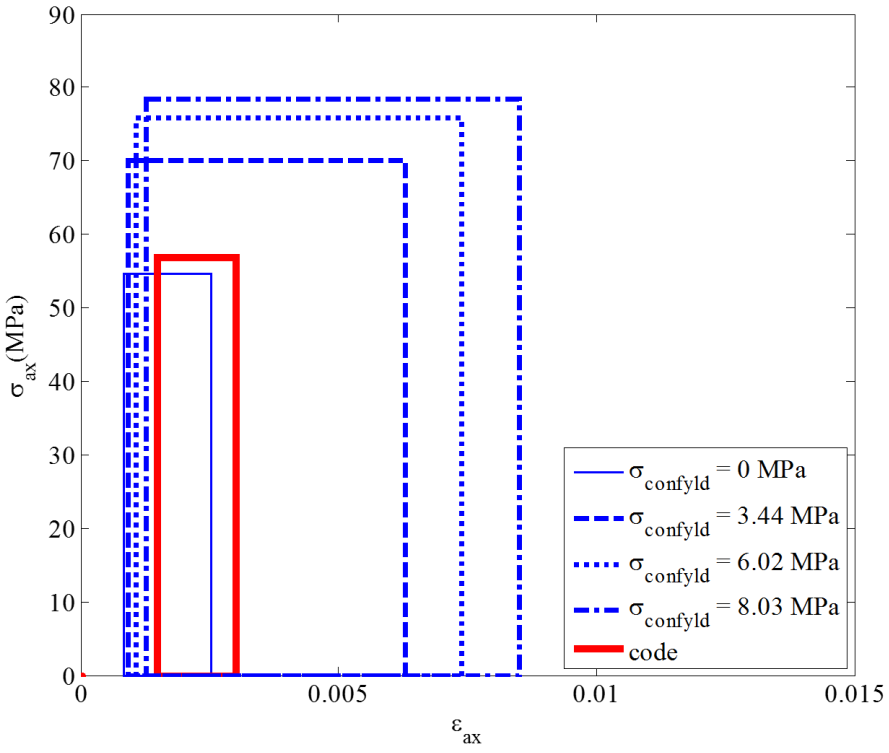

Fig. 22 Effect of confinement on rectangular stress block

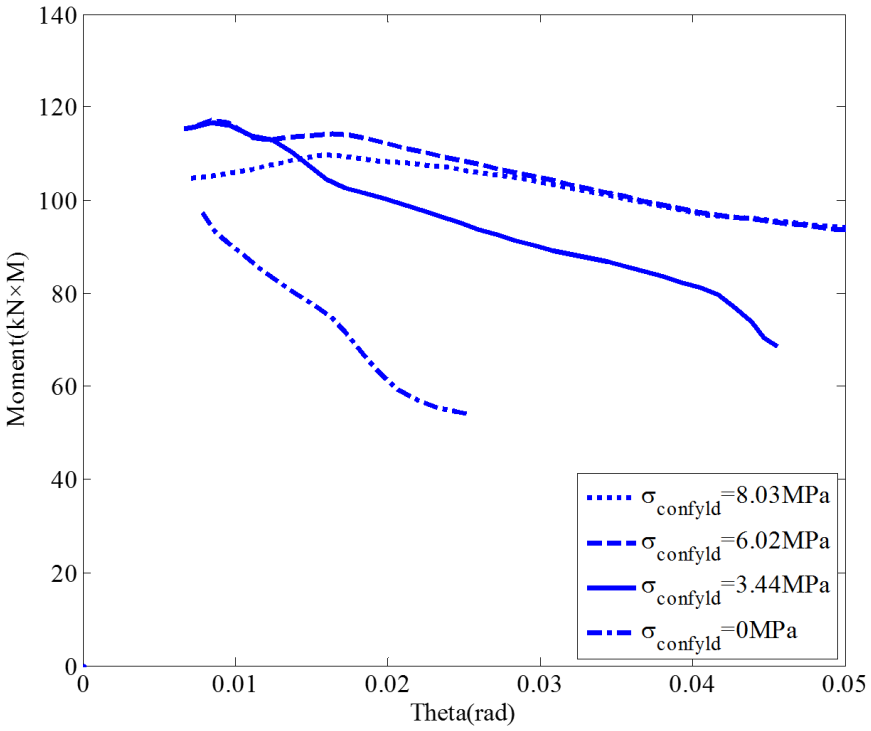

Fig. 23 Effect of confinement on experimental moment/rotations

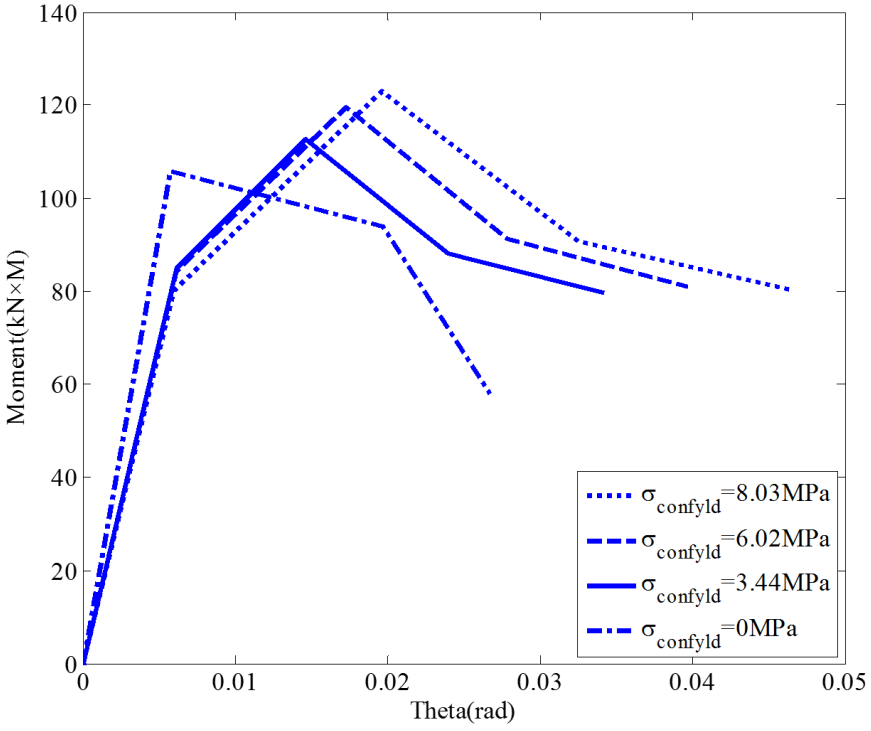

Fig. 24 Effect of confinement on theoretical moment/rotations

Compared with Karthik's Approach

The proposed rectangular concrete stress/strain block is compared with that proposed by Karthik and Mander (2010) (which also allows for concrete confinement) for specimen B4-3.5C in Fig. 25 and specimen B4-1.5C in Fig. 26 and details of these specimen are shown in Table 3. It shows that the main difference between these two stress blocks is the ductility at large rotation such as that at points D and E in Fig. 15. This difference in ductility likely arises because Karthik and Mander's work is based on a size-independent stress/strain relationship and from the application of the empirical hinge length proposed by Sawyer (1965). Figures 27 and 28 compare Karthik and Mander's M/θ with the case 'theoretical with residual strength' as well as the experimental M/θ_{exp} of confined concrete beams in Figs. 18 to 20; the empirically derived rotation of the hinge θ_{exp} is obtained from Eq. (15). It is shown in Eq. (15) that the hinge length L_{def} may affect θ_{exp} but it also has been described previously this effect is small and can be ignored.

Importantly, it is found when applying Karthik and Mander's full-interaction approach, that two layers of tensile longitudinal reinforcement in Fig. 11(f) are yielded, while from proposed approach the top-layer tensile reinforcement is not yielded, and this results in a significant variation in the predicted strength for all specimens shown in Fig. 27.

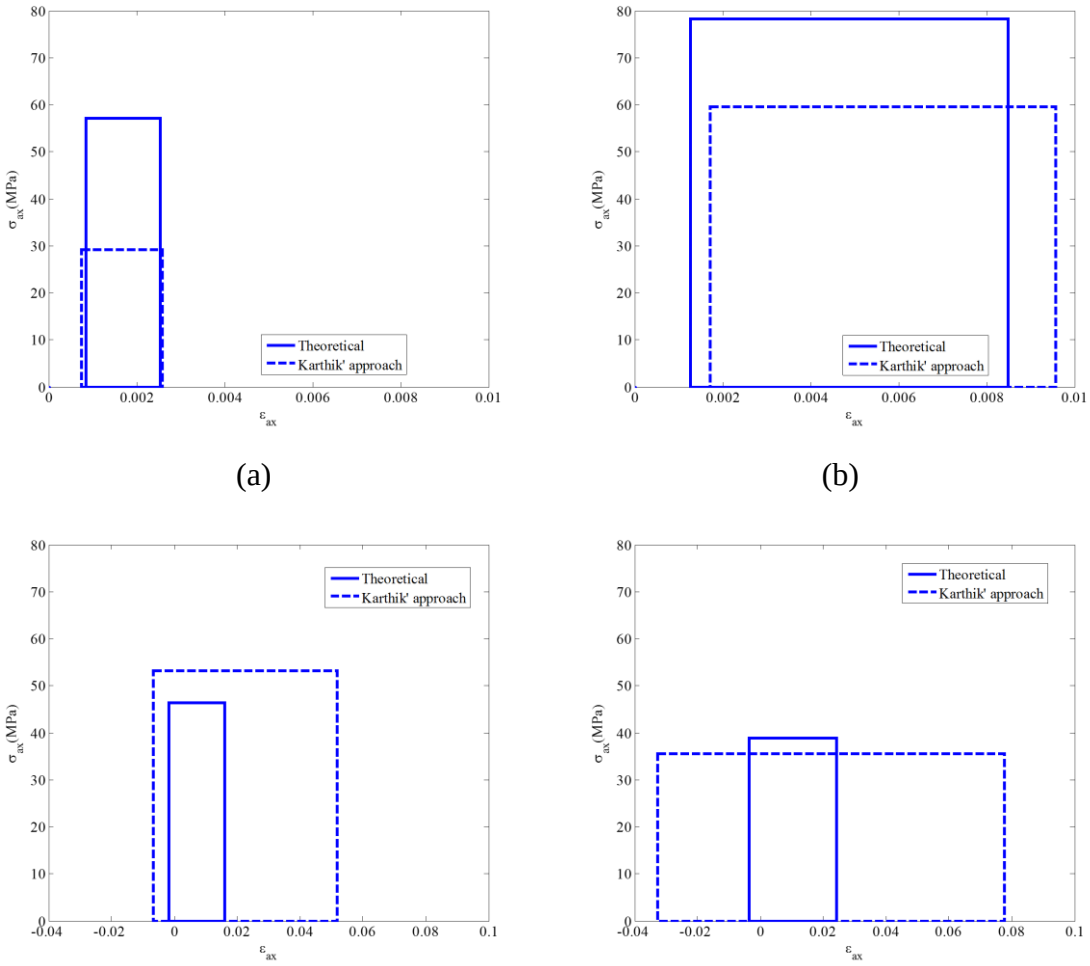

Fig. 25 Rectangular concrete stress block for specimen B4-3.5C for point in Fig. 15: (a) point A; (b) point B; (c) point D; (d) point E

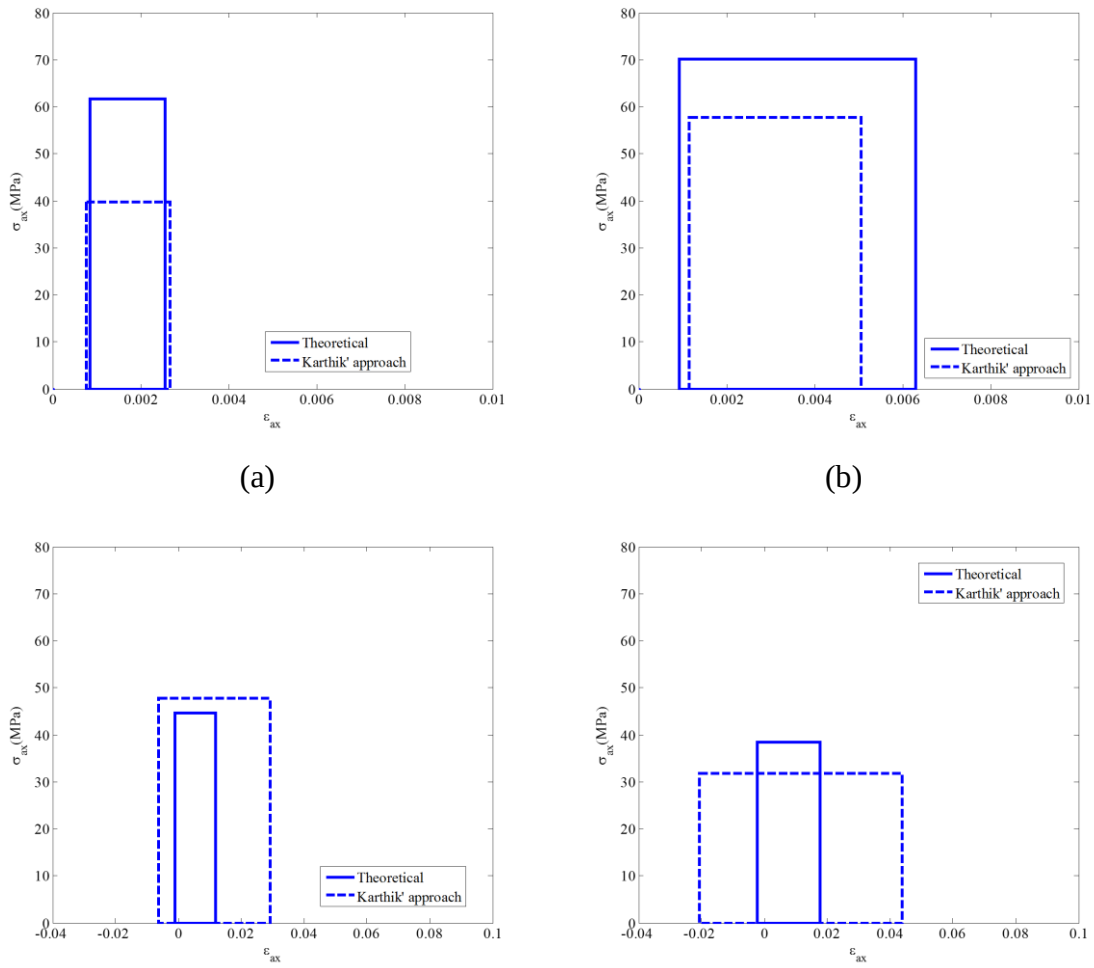

Fig. 26 Rectangular concrete stress block for specimen B4-1.5C for point in Fig. 15: (a) point A; (b) point B; (c) point D; (d) point E

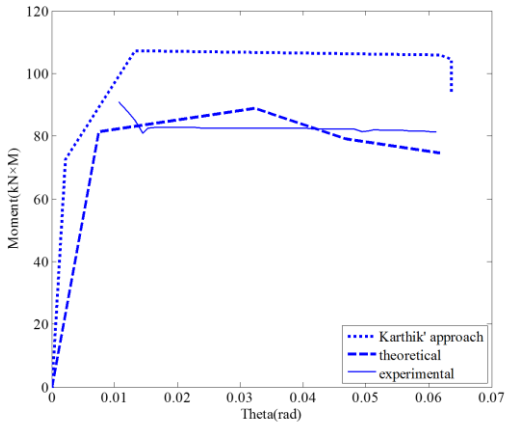

(a)

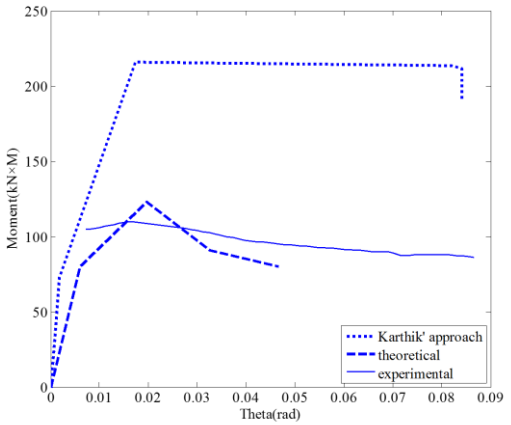

(b)

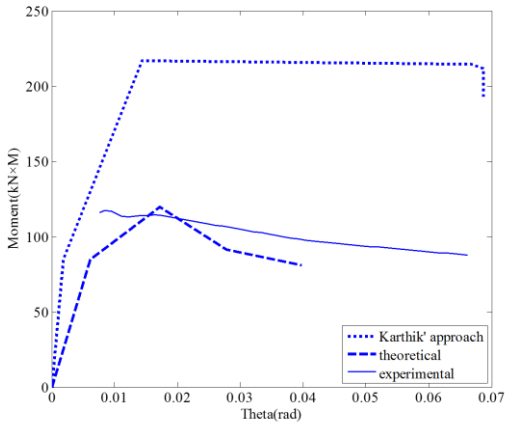

(c)

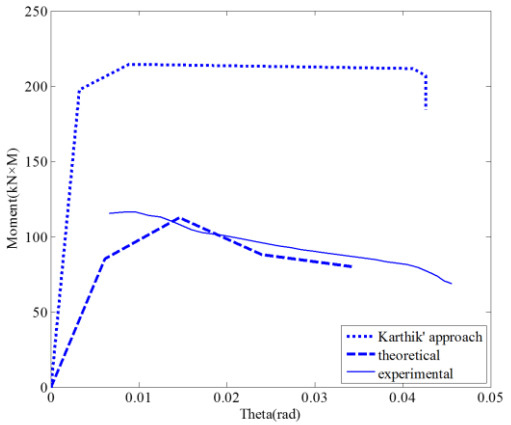

(d)

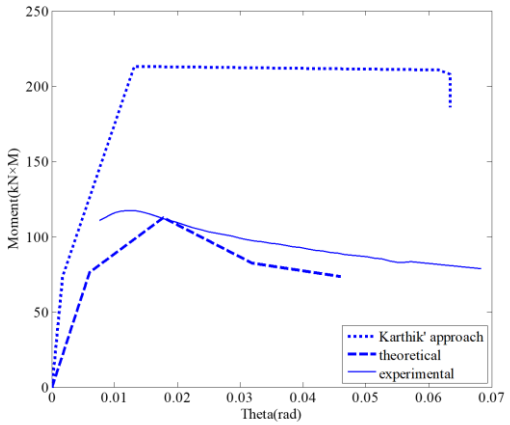

(e)

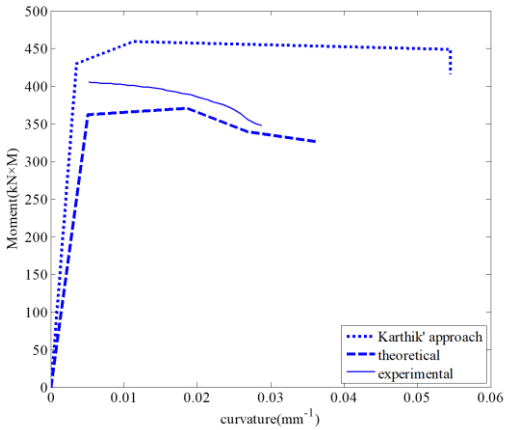

(f)

Fig. 27 Moment/Rotations of over-reinforced confined beam with specimen number: (a) B2-2.6C; (b) B4-3.5C; (c) B4-2.6C; (d) B4-1.5C; (e) B4-2.6L; (f) B312;

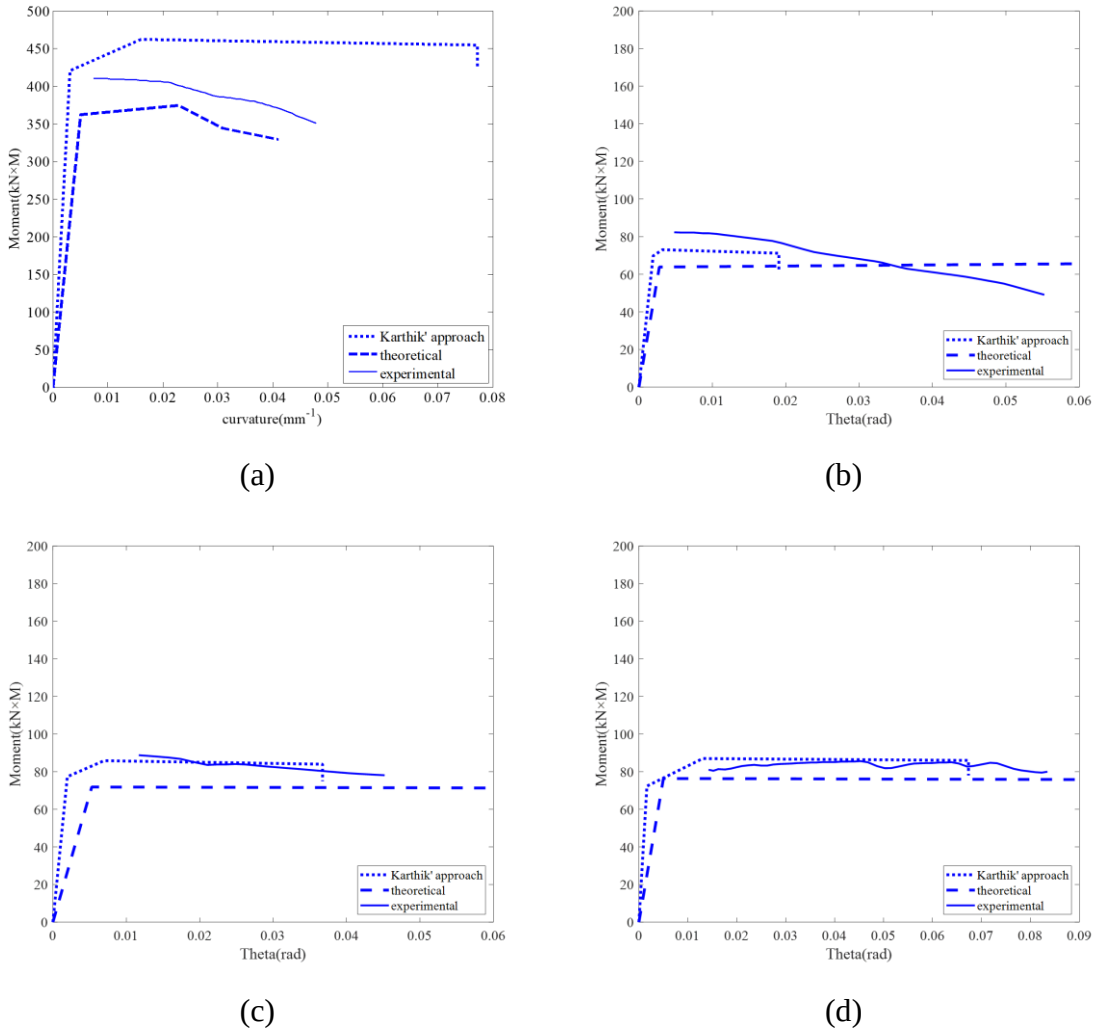

Fig. 28 Moment/Rotations of over-reinforced confined beam (a) B313; and under-reinforced confined beam (b) S1B0; (c) S2B2; (d) S2B3

Conclusions

A mechanics based approach has been described to quantify the concrete passive stress/strain in prisms due to lateral confinement of the concrete from stirrups, tubes and wraps. It has been shown that this passive stress/strain from prisms can be used directly in RC beam analyses. Furthermore, this passive stress/strain has been simplified to a rectangular stress block that is suitable for beam analyses not only for strength but also ductility.

The concrete rectangular passive stress/strain has been used in a segmental analysis of over-reinforced and under-reinforced RC beams with stirrups. It has been shown that there are three key points in quantifying the moment/rotation and consequently the load/deflection behaviour which are: the moment/rotation at the onset of concrete softening which helps quantify the ascending moment/rotation branch; the moment/rotation at the maximum strength of the passively restrained concrete which helps quantify the moment capacity; and the moment/rotation when the passive stress/strain is fully developed which quantifies the ductility. Closed form solution to give moment/rotation of a hinge for these three key points have been derived and are compared with test data extracted from load/deflection test data of fourteen under-reinforced and over-reinforced beams with good correlation.

Appendix A. Notation

The following symbols are used in this paper:

A_c	=	cross-section area of concrete which interacts with reinforcement in tension stiffening analysis
A_r	=	cross-section area of reinforcement
b_f	=	width of reinforcement plate
D_{ci}	=	depth of confined cross-section
D_i	=	confinement reinforcement length
D_{i2}	=	width of confined cross-section
D_0	=	beam depth
D_{02}	=	beam width
d_l	=	longitudinal reinforcement diameter
d_{NA}	=	depth of neutral axis
d_W	=	wedge depth
E_c	=	elastic modulus of concrete

E_r	=	modulus of reinforcement
f_{cc}	=	peak strength of confined concrete by assuming single sliding failure
f_{ct}	=	tensile capacity of concrete
f_{c0}	=	peak strength of unconfined concrete from cylinder tests
$f_{y\text{-}l}$	=	yield capacity of longitudinal reinforcement
h_{cr}	=	separation of shear-sliding plane interface
k	=	bond-slip stiffness in tension stiffening analysis
L_a	=	shear span
L_b	=	half-length of beam
L_{crt}	=	critical length which is the minimum length required to achieve the maximum debond force
L_{def}	=	deformed length
L_{per}	=	total length of potential debonding failure plane of reinforcement in tension stiffening analysis
L_{wdg}	=	wedge length
M_{ax}	=	moment
M_{max}	=	maximum moment
P_{ax}	=	shear load
P_{conc}	=	compressive concrete force
P_{conf}	=	confinement force from reinforcement
P_{fr}	=	fracture capacity of reinforcement
P_{IC}	=	debond force of confinement reinforcement
P_{pl}	=	confinement force from plate reinforcement along shear failure plane

P_{plb} = confinement force in tube of depth b_f

P_{pl1} = confinement force per unit depth from plate

P_{rc} = force in longitudinal compressive reinforcement

P_{rt} = force in longitudinal tensile reinforcement

P_{st} = confinement force from one leg of stirrups

P_{st1} = confinement force per unit depth from stirrups

P_{yld} = yield capacity of confinement reinforcement

r_c = ductility factor of confined concrete

S = slip displacement

S_{ax} = axial component of slip

S_{cr} = crack spacing

S_{lat} = lateral component of slip S

$S_{lat\text{-}deb}$ = lateral component of slip when debond developed to plate ends

$S_{lat\text{-}fIC}$ = lateral component of slip at P_{fIC} when $L_{crt}<L_{conf}$ and $P_{IC}<P_{fr}$

$S_{lat\text{-}fr}$ = lateral component of slip when confinement reinforcement starts to fracture when $L_{crt}<L_{conf}$ and $P_{IC}<P_{fr}$

$S_{lat\text{-}fr2}$ = lateral component of slip when confinement reinforcement starts to fracture when $L_{crt}<L_{conf}$ and $P_{IC}>P_{fr}$

$S_{lat\text{-}fr3}$ = lateral component of slip when confinement reinforcement starts to fracture when $L_{crt}>L_{conf}$

$S_{lat\text{-}IC}$ = lateral component of slip at commencement of IC debonding

$S_{lat\text{-}IC2}$ = lateral component of slip when confinement reinforcement is fully debonded

$S_{lat\text{-}yld}$ = lateral component of slip when reinforcement starts to yield when $L_{crt}<L_{conf}$ and $P_{IC}<P_{yld}$

$S_{lat\text{-}yld2}$ = lateral component of slip when reinforcement starts to yield when $L_{crt}<L_{conf}$ and $P_{IC}>P_{yld}$

$S_{lat\text{-}yld3}$ = lateral component of slip when confinement reinforcement starts to yield when $L_{crt}>L_{conf}$

S_s = stirrup spacing

$S\#$ = specimen reference number

S'_{lat} = tangential component of S_{lat}

x_{ci} = x-coordinate of polygon centroid

y_{ci} = y-coordinate of polygon centroid

α = parameter in beam flexural analysis to determine the magnitude of simplified rectangular stress block

α_s = inclination of failure plane

β = cylinder parameter in tension stiffening analysis

γ = parameter in beam flexural analysis to determine the position of simplified rectangular stress block

θ = rotation of wedge

θ_1 = rotation of wedge of segment with L_{def} equal to $S_{cr}/2$

Δ = crack face slip

Δ_{al} = total crack face slip of segment

Δ_{fr} = crack face slip at fracture of longitudinal tensile reinforcement

Δ_{IC} = slip of confinement reinforcement at crack face when debond starts

Δ_m = mid-deflection

Δ_{rc} = crack face slip of longitudinal compressive reinforcement

Δ_{rt} = crack face slip of longitudinal tensile reinforcement when $L_{def} = 0.5S_{cr}$

$\Delta_{rt\text{-}1.5}$ = crack face slip of longitudinal tensile reinforcement when L_{def} = $1.5S_{cr}$

Δ_{top} = deformation at top fibre of confined concrete

Δ_{top1} = deformation at top fibre of confined concrete of segment with L_{def} equal to $S_{cr}/2$

Δ_{yld} = crack face slip at onset of yielding of longitudinal tensile reinforcement

δ = slip between reinforcement and adjacent concrete

δ_{max} = δ when τ_B reduces to zero

$\delta_{\theta\text{-}exp}$ = deflection due to rotation of wedge

$\delta_{\chi\text{-}exp}$ = deflection outside hinge region

δ_1 = δ at τ_{Bmax}

ε_{ax} = axial strain when axial stress is equal to σ_{ax}

ε_{cc} = strain at f_{cc} for confined concrete

ε_{cu} = ultimate strain when residual strength is ignored and axial stress decrease to zero

ε_{c0} = strain at f_{c0} for unconfined concrete

ε_{fr} = confinement reinforcement strain at P_{fr}

ε_{IC} = confinement reinforcement strain at P_{IC}

ε_m = material strain of concrete

ε_{max} = strain at σ_{max}

ε_S = sliding strain caused by slip S

ε_{Sdeb} = sliding strain at $S_{lat\text{-}deb}$

ε_{Sfr} = sliding strain at $S_{lat\text{-}fr}$

ε_{SIC} = sliding strain at $S_{lat\text{-}IC}$

ε_{SIC2} = sliding strain at $S_{lat\text{-}IC2}$

ε_{st} = average strain in longitudinal tensile reinforcement

ε_{Syld} = sliding strain at $S_{lat\text{-}yld}$

ε_{Syld2} = sliding strain at $S_{lat\text{-}yld2}$

ε_{top} = strain of top fibre of confined concrete

ε_{yld} = confinement reinforcement strain at $S_{lat\text{-}yld}$

ε_z = confinement reinforcement strain when debonding is complete or when there is no bond

ρ_S = longitudinal tensile reinforcement ratio

σ_{ax} = axial stress

σ_{conf} = lateral confining stress applied on concrete

σ_{conffr} = lateral confining stress from confinement reinforcement at P_{fr}

σ_{confIC} = lateral confining stress from confinement reinforcement at P_{IC}

$\sigma_{confyld}$ = lateral confining stress from confinement reinforcement at P_{yld}

σ_{conf0} = lateral confining stress of unconfined concrete and equals zero

σ_{conpl} = lateral confining stress of from plate reinforcement

σ_{const} = lateral confining stress of from stirrups

σ_{cu} = ultimate stress at ε_{cu}

σ_{cu2} = stress at $1.5\varepsilon_{cu}$

σ_{max} = maximum axial stress of key points of passive stress/strain after the onset of sliding

σ_N = confining stress normal to single-sliding plane

σ_{N0} = normal stress at f_{c0} for unconfined concrete

σ_{rc} = stress in longitudinal compressive reinforcement

σ_{rs} = residual strength

σ_{rt} = stress in longitudinal tensile reinforcement

σ_S = axial stress of passively confined concrete by assuming single-sliding failure

σ_{Sdeb} = axial stress at $S_{lat\text{-}deb}$

σ_{Sfr} = axial stress at $S_{lat\text{-}fr}$

σ_{SIC} = axial stress at $S_{lat\text{-}IC}$

σ_{SIC2} = axial stress at $S_{lat\text{-}IC2}$

σ_{Syld} = axial stress at $S_{lat\text{-}yld}$

σ_{Syld2} = axial stress at $S_{lat\text{-}yld2}$

τ = shear stress along single-sliding plane

τ_B = bond stress existing between reinforcement and concrete

τ_{Bmax} = maximum τ_B

τ_C = bond stress at P_{IC}

τ_m = shear-friction material capacity

Appendix B. Quantification of Passive Stress/Strain

The confinement mechanism that induces the concrete passive stress/strain described previously in qualitative terms is now quantified. The whole procedure has been described elsewhere (Hao 2018b) and only a summary is given here. As the concrete in beams softens due to a single sliding plane (Visintin et al. 2012b), this will be applied in the ensuing analyses.

Partial Interaction Properties and Behaviours

Shear Friction Properties

The shear-stress capacity τ_m can be simplified in the following linear form (Hao 2017)

$$\tau_m = (A\sigma_N + B)S + C\sigma_N + D \tag{16}$$

where σ_N is the stress normal to the sliding plane and the coefficients *A*, *B*, *C* and *D* are functions of the unconfined concrete strength f_{c0}. As an example, the following were derived by Hao (2017).

When $\sigma_N < \sigma_{N0}$, where σ_{N0} is the normal stress at the peak axial stress f_{c0} of unconfined concrete and which is given by

$$\sigma_{N0} = f_{c0} \sin^2 \alpha_s \tag{17}$$

where α_s is the sliding angle as shown in Fig. 1(a) and is assumed to equal 26^o (Ali et al. 2010; Jensen 1975; Mattock and Hawkins 1972; Visintin et al. 2015) then

$$\tau_m = [(0.00112 f_{c0} - 0.337)\sigma_N - 0.000784 f_{c0}^2 + 0.0152 f_{c0} + 0.556]S + 1.50\sigma_N + 0.105 f_{c0} \tag{18}$$

When $\sigma_{N0} \leq \sigma_N < 3\sigma_{N0}$, then

$$\tau_m = [(0.00112 f_{c0} + 0.0636)\sigma_N - 0.000784 f_{c0}^2 - 0.0620 f_{c0} + 0.556]S + 0.498\sigma_N + 0.298 f_{c0} \tag{19}$$

Bond/Slip and IC Debonding

Any appropriate bond-slip material property can be used. Consider the bilinear bond-slip in Fig. B1 as an example. For stirrups, the parameters in Fig. B1 have the following values (Haskett et al. 2008)

$$\tau_{B\max} = 2.5\sqrt{f_{c0}} \tag{20}$$

$$\delta_1 = 1.5\text{mm} \tag{21}$$

$$\delta_{\max} = 15\text{mm} \tag{22}$$

where f_{c0} is in MPa. The IC debonding resistance P_{IC} (Ali et al. 2008) is

$$P_{IC} = \sqrt{\tau_{B\max}\delta_{\max}}\sqrt{L_{per}E_rA_r} \tag{23}$$

which occurs at a crack face slip Δ_{IC} that is also $S_{lat\text{-}IC}/2$ and where

$$\Delta_{IC} = \delta_{\max} \tag{24}$$

The critical length required to develop the debonding resistance P_{IC} (Ali et al. 2008) is

$$L_{crt} = \frac{\pi}{2\lambda} \tag{25}$$

where the parameter λ is

$$\lambda = \sqrt{\frac{\tau_{B\max}L_{per}}{\delta_{\max}}\left(\frac{1}{E_rA_r} + \frac{1}{E_cA_c}\right)} \tag{26}$$

The length of the fully debonded confinement reinforcement D_i in Fig. 3 for a rectangular prism is

$$D_i = D_{ci} \tag{27}$$

and for a circular prism is

$$D_i = \frac{\pi D_{ci}}{2} \tag{28}$$

Hence when no bond exists or the confinement reinforcement has been fully debonded, the strain in confinement reinforcement is constant along D_i at ε_Z such that $S_{lat} = \varepsilon_Z D_i$.

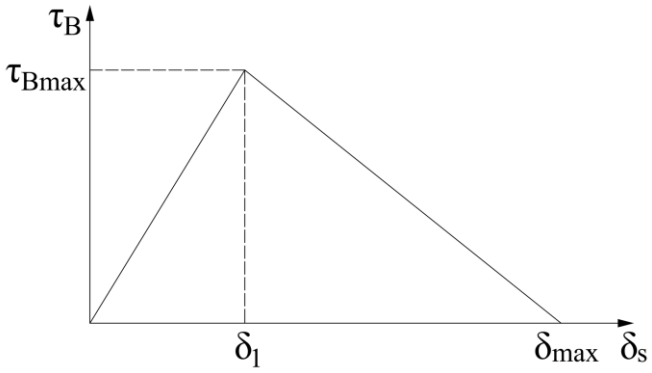

Fig. B1 Bond slip material properties

Quantification of Active Stress/Strain

Ascending Branch

The following peak stress f_{cc}, such as those at points C, E and G in Fig. 2, are functions of the lateral confining stress σ_{conf} (Hao 2018b)

$$f_{cc} = \frac{\sigma_{conf} \sin\alpha_s \cos\alpha_s + C\sigma_{conf} \cos^2\alpha_s + D}{\sin\alpha_s \cos\alpha_s - C\sin^2\alpha_s} \tag{29}$$

where the strain ε_{cc} at f_{cc} is (Visintin et al. 2015)

$$\varepsilon_{cc} = \varepsilon_{c0}[1 + A_0(\frac{\sigma_{conf}}{f_{c0}})] \tag{30}$$

in which A_0 is a coefficient that equals 13.9 and where the unconfined concrete strain ε_{c0} at f_{c0} is

$$\varepsilon_{c0} = 1.74\times10^{-6} f_{c0} + 2.41\times10^{-3} \tag{31}$$

where f_{c0} is in MPa. The ascending branch of the active stress/strain such as O-P_1-E in Fig. 2 (Popovics 1973) is

$$\sigma_{ax} = f_{cc} \frac{\frac{\varepsilon_{ax}}{\varepsilon_{cc}} r_c}{r_c - 1 + \left(\frac{\varepsilon_{ax}}{\varepsilon_{cc}} \right)^{r_c}} \tag{32}$$

where r_c is the following ductility factor

$$r_c = \frac{E_c}{E_c - \frac{f_{cc}}{\varepsilon_{cc}}} \tag{33}$$

in which the concrete elastic modulus E_c in MPa can be taken as (ACI 1992)

$$E_c = 3320\sqrt{f_{c0}} + 6900 \tag{34}$$

For ease of analysis, the ascending branch O-P_1-E of the active stress/strain in Fig. 2 can be linearised to O-P_2-E as

$$\varepsilon_{ax} = \sigma_{ax} \frac{\varepsilon_{cc}}{f_{cc}} \tag{35}$$

where f_{cc} and ε_{cc} can be obtained from Eqs. (29) and (30).

Descending Branch

For a given lateral confining stress σ_{conf} and slip S in Fig. 1(a), the following axial stress σ_{ax} is derived from the shear friction material properties (Hao 2018b)

$$\sigma_{ax} = \frac{\sigma_{conf} \sin\alpha_s \cos\alpha_s + AS\sigma_{conf} \cos^2\alpha_s + BS + C\sigma_{conf} \cos^2\alpha_s + D}{\sin\alpha_s \cos\alpha_s - AS \sin^2\alpha_s - C \sin^2\alpha_s} \tag{36}$$

The axial strain ε_{ax} can be written as (Hao 2018b)

$$\varepsilon_{ax} = \sigma_{ax} \frac{\varepsilon_{cc}}{f_{cc}} + \frac{S \cos\alpha_s}{L_{def}} \tag{37}$$

where f_{cc} and ε_{cc} can be obtained from Eqs. (29) and (30).

Quantification of Passive Stress/Strain

A slightly conservative assumption is made in that the sliding plane crosses the centre, such as plane C-B-C' in Fig. 1(b), which is shown in Figs. B2(a) and (b) for a rectangular and circular prism respectively (Hao 2018a; Hao 2018b). After the onset of sliding, the lateral component of slip S_{lat} in Fig. 1(a) will cause the bond stress τ_B as shown which induces a shear force P_{conf} and which is balanced by a confinement force of equal magnitude. As S_{lat} increases, the bond stress may build up to the maximum value τ_C and, subsequently, a maximum confinement force due to bond P_{IC} should yield or fracture not occur. This P_{IC} is referred to as the intermediate crack debonding resistance (Seracino et al. 2007; Yuan et al. 2001) which occurs at a crack face slip Δ_{IC} that depend on the bond-slip material properties.

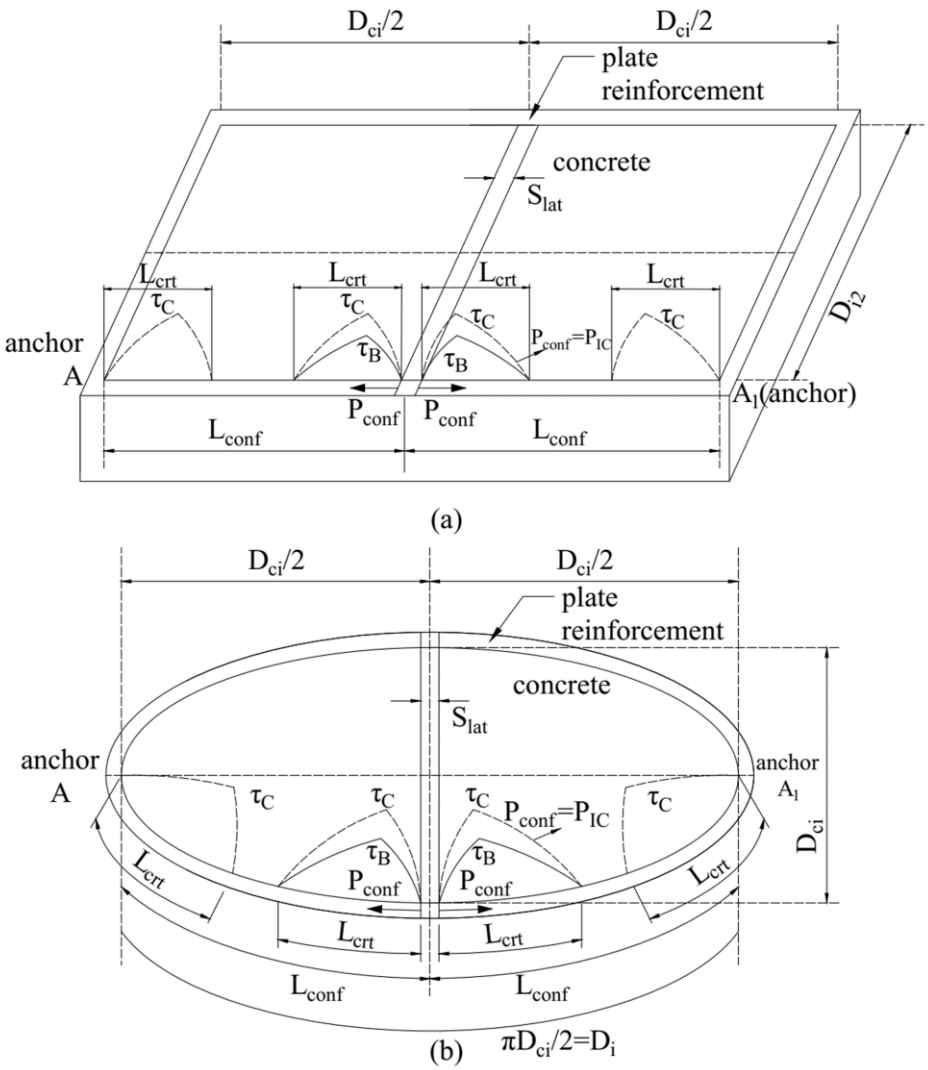

Fig. B2 Development of bond stress for (a) rectangular section (b) circular section

Lateral Extension due to Sliding S_{lat}

As S_{lat} in Fig. B2 gradually increases, the bond stress τ_B builds up over the critical length L_{crt}. When L_{crt} is less than confinement reinforcement length L_{conf}, the bond stress τ_B can be fully developed to τ_C when P_{IC} is less than the yield capacity P_{yld} or fracture capacity P_{fr}. Any further increase in S_{lat} causes the bond stress block to move away from the sliding plane towards the anchor points A or A_1 whilst the confinement force remains at P_{IC}. After completely debonding, the strain in the debonded reinforcement equals ε_{IC} and any further increase in S_{lat} may lead to a yield strain ε_{yld} or fracture strain ε_{fr} over D_i. When L_{crt} is larger than L_{conf}, debonding does not occur and the confinement reinforcement may directly yield

at P_{yld} or fracture at P_{fr}. For all these scenarios, S_{lat} will be derived as below; full details are shown elsewhere (Hao 2018b).

Case 1: $L_{conf} \geq L_{crt}$; $P_{IC} < P_{yld}$; $P_{IC} < P_{fr}$

The P_{conf}/S_{lat} relationship for the case where P_{IC} is less than P_{yld} or P_{fr} and $L_{conf} \geq L_{crt}$ is shown in Fig. B3(a). The reinforcement debonds at ($S_{lat\text{-}IC}$, P_{IC}) at point A. Then the fully developed bond stress τ_C in Fig. B2 moves towards the anchor points at ($S_{lat\text{-}deb}$, P_{IC}) at point B in Fig. B3(a) after which the reinforcement completely debonds at ($S_{lat\text{-}IC2}$, P_{IC}) at point C. The confinement reinforcement may either yield at ($S_{lat\text{-}yld}$, P_{yld}) at point E and then fracture at ($S_{lat\text{-}fr}$, P_{fr}) at point D or directly fracture at point D. For these points S_{lat} is given as follows (Hao 2018b)

$$S_{lat-IC} = 2\Delta_{IC} \qquad (L_{conf} \geq L_{crt};\ P_{IC} < P_{yld};\ P_{IC} < P_{fr}) \tag{38}$$

$$S_{lat-deb} = 2\Delta_{IC} + \varepsilon_{IC}(D_i - 2L_{crt}) \qquad (L_{conf} \geq L_{crt};\ P_{IC} < P_{yld};\ P_{IC} < P_{fr}) \tag{39}$$

$$S_{lat-IC2} = \varepsilon_{IC} D_i \qquad (L_{conf} \geq L_{crt};\ P_{IC} < P_{yld};\ P_{IC} < P_{fr}) \tag{40}$$

$$S_{lat-yld} = \varepsilon_{yld} D_i \tag{41}$$

$$S_{lat-fr} = \varepsilon_{frac} D_i \tag{42}$$

where L_{crt}, D_i for rectangular prisms and cylinders, and Δ_{IC} can be obtained from Eqs. (25), (27), (28) and (24) respectively.

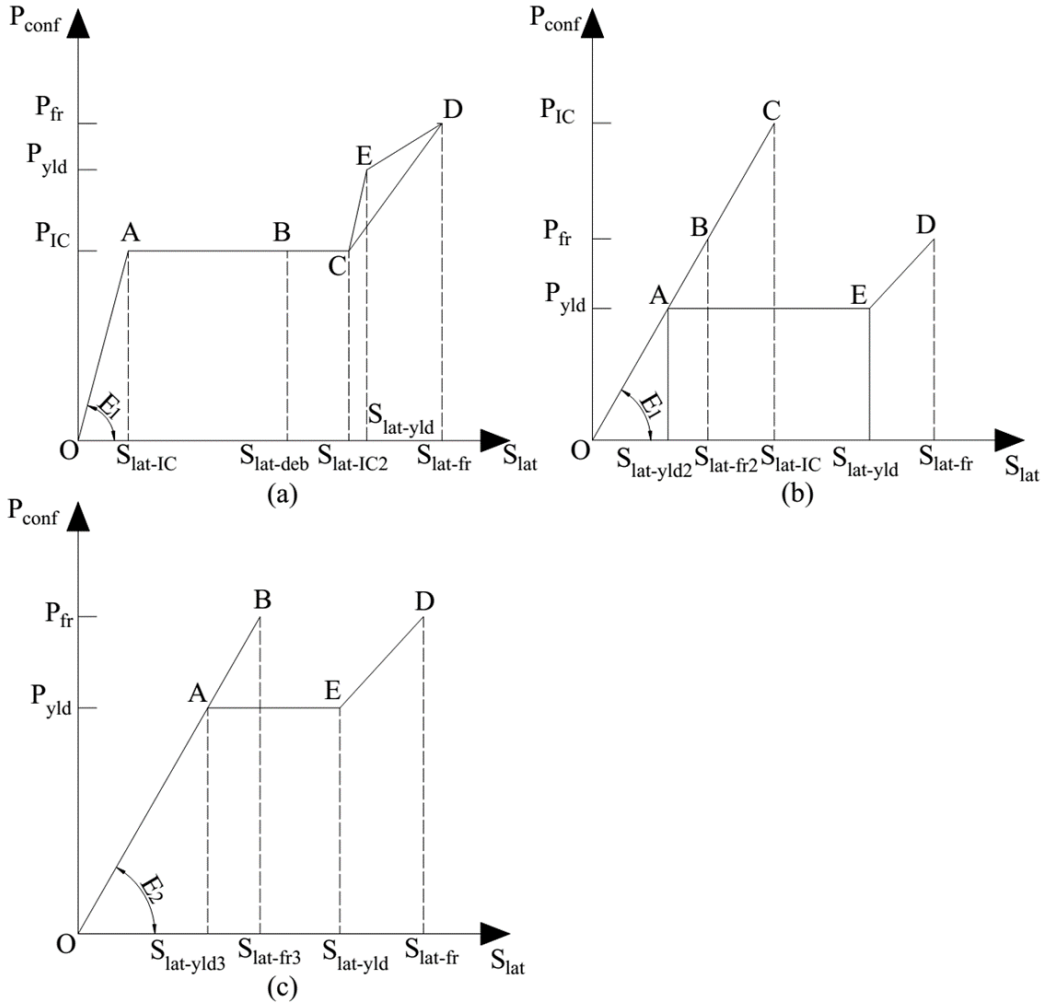

Fig. B3 P_{conf} and S_{lat} relationship for: (a) debonding prior to fracture or yield and $L_{crt} \leq L_{conf}$; (b) fracture or yield without debonding and $L_{crt} \leq L_{conf}$; (c) $L_{crt} > L_{conf}$

Case 2: $L_{conf} \geq L_{crt}$; $P_{IC} \geq P_{yld}$; $P_{IC} \geq P_{fr}$

When $L_{conf} \geq L_{crt}$ and the IC debonding resistance is larger than the yield capacity P_{yld} or fracture capacity P_{fr}, debonding does not occur and the P_{conf}/S_{lat} behaviour is shown in Fig. B3(b). The confinement reinforcement may: either yield at ($S_{lat\text{-}yld2}$, P_{yld}) at point A; then completely yield at ($S_{lat\text{-}yld}$, P_{yld}) at point E; and ultimately fracture at ($S_{lat\text{-}fr}$, P_{fr}) at point D; or directly fracture at ($S_{lat\text{-}fr2}$, P_{fr}) at point B. From Hao (2018b)

$$S_{lat-yld\,2} = 2\Delta_{IC}\frac{P_{yld}}{P_{IC}} \qquad (L_{conf} \geq L_{crt};\ P_{IC} \geq P_{yld};\ P_{IC} \geq P_{fr}) \tag{43}$$

$$S_{lat-fr2} = 2\Delta_{IC}\frac{P_{fr}}{P_{IC}} \qquad (L_{conf} \geq L_{crt};\ P_{IC} \geq P_{yld};\ P_{IC} \geq P_{fr}) \tag{44}$$

where Δ_{IC} and P_{IC} can be obtained from Eqs. (24) and (23) respectively.

Case 3: $L_{conf} < L_{crt}$

When $L_{conf} < L_{crt}$, debonding does not occur as shown in Fig. B3(c). This case is similar to the previous Case 2 in Fig. B3(b). The only difference is that $S_{lat\text{-}yld2}$ at point A and $S_{lat\text{-}fr2}$ at point B are replaced by the following $S_{lat\text{-}yld3}$ and $S_{lat\text{-}fr3}$ as shown in Fig. B3(c) (Hao 2018b).

$$S_{lat-yld3} = \frac{P_{yld}}{\lambda E_r A_r}\left[\frac{2\sinh(D_i\lambda)}{\cosh(D_i\lambda)+1}\right] \qquad (L_{conf} < L_{crt}) \tag{45}$$

$$S_{lat-fr3} = \frac{P_{fr}}{\lambda E_r A_r}\left[\frac{2\sinh(D_i\lambda)}{\cosh(D_i\lambda)+1}\right] \qquad (L_{conf} < L_{crt}) \tag{46}$$

where D_i can be obtained from either Eq. (27) for rectangular prisms or Eq. (28) for cylinders. The parameter λ in Eqs. (45) and (46) can be obtained from Eq. (60).

Lateral Confining Stress

The lateral confining stress from stirrup reinforcement σ_{const} and plate reinforcement σ_{conpl} for rectangular prisms have been derived elsewhere and can be written as (Hao 2018b)

$$\sigma_{const} = \frac{2P_{st}}{S_s D_{i2}} \tag{47}$$

$$\sigma_{conpl} = \frac{2P_{pl}\tan\alpha}{D_{ci}D_{i2}} \tag{48}$$

where S_s is the stirrup spacing, D_{i2} is the length of the cross-section length within transverse reinforcement as shown in Fig. 3(b), P_{st} is the confinement force from one leg of the stirrups and P_{pl} is the confinement force from a plate acting along the whole sliding plane.

With regard to cylinders, the lateral confining stress σ_{conf} be written as (Hao 2018a)

$$\sigma_{conf} = \frac{2P_{conf}}{D_{ci}} \tag{49}$$

Then σ_{const} or σ_{conpl} can be derived by substituting the following confinement force per unit depth from stirrups P_{st1} or plate P_{pl1} for P_{conf} in Eq. (49)

$$P_{st1} = \frac{P_{st}}{S_S} \tag{50}$$

$$P_{pl1} = \frac{P_{plb}}{b_f} \tag{51}$$

where P_{plb} is the confinement force in the tube of depth b_f.

Axial Stresses σ_S and Strains ε_{ax} at Key Points

For an arbitrary key point in Fig. B3, the confinement force P_{conf} and S_{lat} can be obtained as described above. The lateral confining stress σ_{conf} can be derived from either Eq. (47), (48) or (49) by substituting the confinement force P_{conf}. Then σ_{conf} and S_{lat} can be substituted into following equations to derive the axial stress σ_S and axial strain ε_{ax} (Hao 2018b)

$$\sigma_S = \frac{\sigma_{conf} \sin\alpha_s \cos\alpha_s + \left(A\frac{S_{lat}}{\sin\alpha_s} + C \right)\sigma_{conf} \cos^2\alpha_s + B\frac{S_{lat}}{\sin\alpha_s} + D}{\sin\alpha_s \cos\alpha_s - \sin^2\alpha_s \left(A\frac{S_{lat}}{\sin\alpha_s} + C \right)} \tag{52}$$

$$\varepsilon_{ax} = \sigma_S \frac{\varepsilon_{cc}}{f_{cc}} + \frac{S_{lat}}{\tan \alpha_s L_{def}} \tag{53}$$

Hence the axial stress and strain for each key point in Fig. B3 can be derived such as those shown in Fig. 2 and linking these key points gives the passive stress/strain.

The residual stress σ_{rs} as shown in Fig. 2 for stirrup reinforced prisms is written as follows (Li et al. 2001)

$$\sigma_{rs} = 0.4\sigma_{\max} \tag{54}$$

The whole procedure is summarized in Fig. 4.

Appendix C. Example of a Beam Analysis

Specimen B4-1.5C by Mansur et al. (1997) will be analysed for the second case in Fig. 17 which uses a linear ascending branch of the passive stress/strain without residual stress and with concrete spalling. The passive stress/strain parameters α and γ in the flexural analysis for each key point in Figs. 15 and 16 have been derived previously. Specimen B4-1.5C which is over-reinforced has two layers of tensile reinforcement as in Fig. 11(f). From compatibility in Fig. 11(b), the deformation in the tensile reinforcement layers are

$$\Delta_{rt1-1.5} = \Delta_{top} \frac{(D_0 - L_{rt1} - d_{NA})}{d_{NA}} \tag{55}$$

$$\Delta_{rt2-1.5} = \Delta_{top} \frac{(D_0 - c_{up} - L_{rt2} - d_{NA})}{d_{NA}} \tag{56}$$

where L_{rt1} and L_{rt2} are shown in Fig. 11(e). First assume that the deformed length L_{def} in Fig. 11(a) is $1.5S_{cr}$ such that L_{def} encompasses an interior crack as shown; this assumption will be checked later. Full details of each step of the analysis are as follows.

Point A in Fig. 15

The deformed length in Fig. 11(a) is L_{def} = 1.5S_{cr} = 259mm where S_{cr} is from Eq. (9). The concrete stress block is O-A-A' in Fig. 6 and for the equivalent rectangular stress block the parameters α and γ are 0.750 and 0.667 respectively as derived previously. The deformation at the top fibre Δ_{top} = 0.661 mm is obtained from Eq. (8). The analysis consists of pivoting about Δ_{top} in Fig. 11(b) and finding the neutral axis depth d_{NA} in which equilibrium is achieved in Fig. 11(e).

For a given or fixed value of d_{NA}, the forces in Fig. 11(e) can be derived as follows. The concrete force P_{conc} is obtained by substituting d_{NA} as well as parameters α and γ into Eq. (7). As can be seen in Figs. 11(a) and (b), the deformation required to determine the force in the tensile reinforcement for L_{def} = 1.5S_{cr} are Δ_{rt1} = $\Delta_{rt1\text{-}1.5}$/3 or Δ_{rt2} = $\Delta_{rt2\text{-}1.5}$/3. The relationship between the tensile reinforcement force P_{rt} and Δ_{rt} is bilinear as follows (Zhang et al. 2017)

$$P_{rt} = \Delta_{rt} \frac{P_{yld}}{\Delta_{yld}} \qquad (\Delta_{rt} < \Delta_{yld}) \tag{57}$$

$$P_{rt} = P_{yld} \qquad (\Delta_{rt} \geq \Delta_{yld}) \tag{58}$$

where before the yield of tensile reinforcement, P_{rt} is obtained from Eq. (57) and after yielding P_{rt} is kept constant at P_{yld} that is from Eq. (58) and Δ_{yld} = 0.222 mm can be derived from the following (Sturm et al. 2018)

$$\Delta_{yld} = \frac{P_{yld}}{\lambda E_r A_r} \tanh\left(\frac{\lambda S_{cr}}{2}\right) \tag{59}$$

where λ is

$$\lambda = \sqrt{\beta k} \tag{60}$$

and where the prism parameter β and bond-slip stiffness k can be expressed as

$$\beta = L_{per}\left(\frac{1}{E_r A_r} + \frac{1}{E_c A_c}\right) \tag{61}$$

$$k = \frac{\tau_{B\max}}{\delta_1} \tag{62}$$

where E_c is concrete modulus and E_r is modulus of reinforcement.

However, P_{rt} cannot be directly obtained from Δ_{rt} as the relationship between them is bilinear from Eqs. (57) and (58) so the solution is given as follows. Firstly, assume that the two layers of tensile longitudinal reinforcement are not yielded. It has been illustrated previously that before yielding P_{rt} is obtained from Eq. (57) and after yielding P_{rt} is from Eq. (58). Then as the tensile longitudinal reinforcement are assumed to be not yielded, the following force in two-layer tensile reinforcement P_{rt1} and P_{rt2} as shown in Fig. 11(e) can be obtained from Eq. (57)

$$P_{rt1} = \Delta_{top}\frac{(D_i - c_{up} - L_{rt1} - d_{NA})}{3d_{NA}}\frac{P_{yld}}{\Delta_{yld}} \tag{63}$$

$$P_{rt2} = \Delta_{top}\frac{(D_i - c_{up} - L_{rt2} - d_{NA})}{3d_{NA}}\frac{P_{yld}}{\Delta_{yld}} \tag{64}$$

Equilibrium in Fig. 11(e) is

$$P_{conc} - P_{rt1} - P_{rt2} = 0 \tag{65}$$

Substituting Eqs. (63) and (64) as well as P_{conc} from Eq. (7) into Eq. (65) and solving for the neutral axis depth gives d_{NA} = 107 mm and consequently the force P_{conc} = 599 kN, P_{rt1} = 424 kN and P_{rt2} = 174 kN from Eqs. (7), (63) and (64) respectively. Previously, it had been assumed that the two layers of tensile reinforcement had not yielded and whether this assumption is correct will be checked. From compatibility in Fig. 11(a) $\Delta_{rt2\text{-}1.5}$ equals 0.215 mm from Eq. (56) and $\Delta_{rt1\text{-}1.5}$ equals 0.524 mm from Eq. (55). Subsequently, $\Delta_{rt2} = \Delta_{rt2\text{-}1.5}/3$

= 0.0717 mm and $\Delta_{rt1} = \Delta_{rt1\text{-}1.5}/3$ = 0.175 mm which are both smaller than Δ_{yld} = 0.222 mm from Eq. (59) and consequently both have not yielded and previous assumption is correct. The results of the analyses are given in Fig. C1. From geometry the rotation θ from Eq. (13) equals 0.00617 and the moment from Eq. (14) equals 84.9 kN·m.

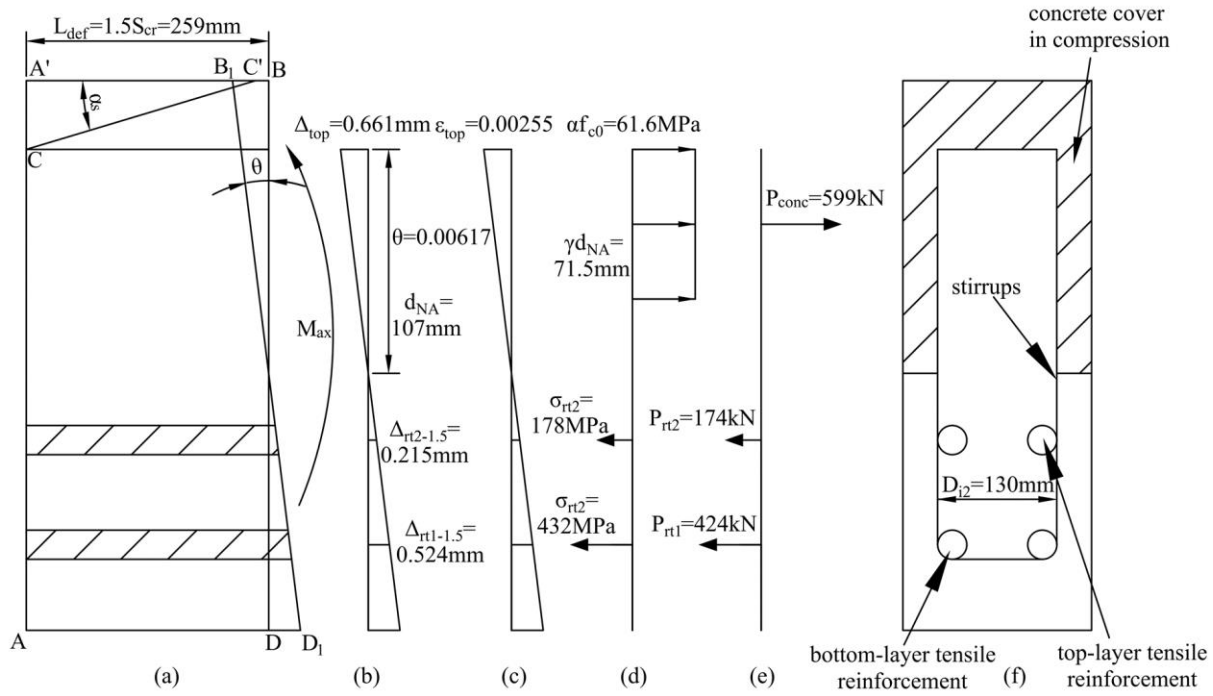

Fig. C1 Segmental analysis of specimen B4-1.5C at point A in Fig. 15 when L_{def} equals 1.5S_{cr}: (a) segment; (b) displacement profile; (c) strain profile; (d) stress profile; (e) force profile; (f) cross-section

Points B and D in Fig. 15

At the next point B in Fig. 15, stress block O-A-C-C' in Fig. 6 is developed for which α = 0.852 and γ = 0.853. The deformation at the top fibre Δ_{top} is obtained from Eq. (8) and equals 1.63 mm. Assuming both layers longitudinal tensile reinforcement have not yielded then substituting P_{rt1} from Eq. (63), P_{rt2} from Eq. (64) and P_{conc} from Eq. (7) into Eq. (65) and solving gives d_{NA} = 122 mm. From compatibility Δ_{rt1} and Δ_{rt2} in Fig. 11(a) equals 0.316 mm and 0.0916 mm. However Δ_{rt1} is larger than Δ_{yld} = 0.222 mm from Eq. (59). Hence the bottom-layer tensile reinforcement yields and has the force $P_{rt1} = P_{yld}$ = 540 kN. Consequently, previous assumption that both layers longitudinal tensile reinforcement have not yielded is incorrect. Substituting $P_{rt1} = P_{yld}$ as well as P_{rt2} from Eq. (64) and P_{conc} from

Eq. (7) into the force equilibrium Eq. (65) gives d_{NA} = 111 mm. Hence the forces can be determined by substituting this d_{NA} = 111 mm to give P_{conc} = 905 kN from Eq.(7), $P_{rt1} = P_{yld}$ = 540 kN and P_{rt2} = 365 kN from Eq. (64). The results are shown in Fig. C2. The rotation and moment can be obtained from Eqs. (13) and (14) which are 113 MPa and 0.0147 respectively.

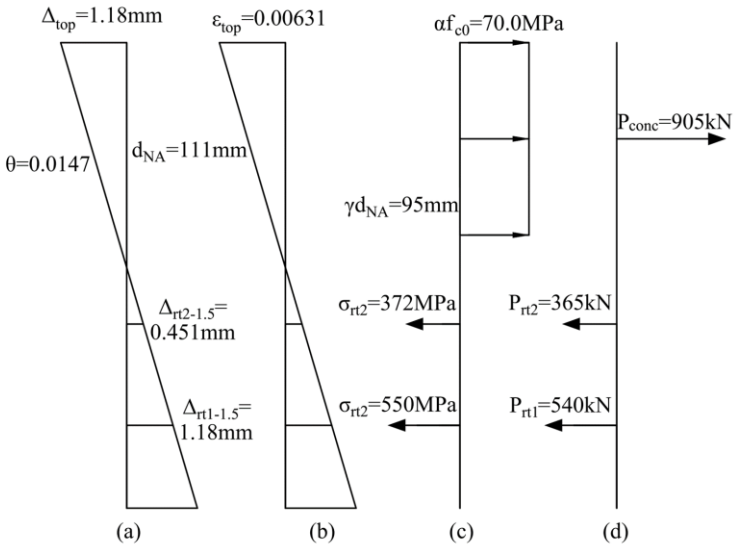

Fig. C2 Segmental analysis of specimen B4-1.5C at point B in Fig. 15 when L_{def} equals 1.5S_{cr}: (a) displacement profile; (b) strain profile; (c) stress profile; (d) force profile

The moment/rotation analysis at points D in Fig. 15 is similar to that at point B. The only different input is the value of parameters α and γ. The results are given in Fig. C3. The top-layer of longitudinal reinforcement has not yielded for all the key points in Fig. 15, hence, this beam is an over-reinforced beam.

It is worth noting that the largest wedge length L_{wdg} from Eq. (12) equals 208 mm at point D in Fig. 15 which is larger than S_{cr}/2 and smaller than 1.5S_{cr}. Hence, the initial assumption at the start of the analyses of L_{def} = 1.5S_{cr} is correct.

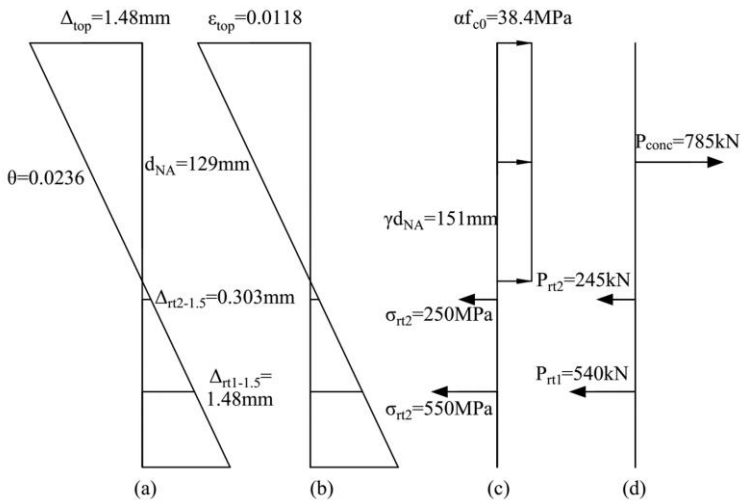

Fig. C3 Segmental analysis of specimen B4-1.5C at point D in Fig. 15 when L_{def} equals 1.5S_{cr}: (a) displacement profile; (b) strain profile; (c) stress profile; (d) force profile

Data Availability Statement

All data, models, and code generated or used during the study appear in the submitted article.

Acknowledgements

The first author would like to acknowledge the financial support of the China Scholarship Council.

References

ACI (American Concrete Institute). (1992). "State-of-the-art report on high-strength concrete." Farmington Hills, Michigan.

ACI (American Concrete Institute). (2014). "Building code requirements for structural concrete." *ACI 318-14*, Farmington Hills, Michigan.

Ali, M. M., Oehlers, D., and Griffith, M. (2010). "The residual strength of confined concrete." *Advances in Structural Engineering*, 13(4), 603-618.

Ali, M. M., Oehlers, D., Griffith, M., and Seracino, R. (2008). "Interfacial stress transfer of near surface-mounted FRP-to-concrete joints." *Engineering Structures*, 30(7), 1861-1868.

Attard, M. M., and Stewart, M. G. (1998). "A two parameter stress block for high-strength concrete." *Structural Journal*, 95(3), 305-317.

Australia Standard. (2009). "Concrete Structures (AS 3600-2009)."

Bourke, P. (1988). "Calculating the area and centroid of a polygon." *Swinburne University of Technology*, 7.

Du, M., Jin, L., Du, X., and Li, D. (2017). "Size effect tests of stocky reinforced concrete columns confined by stirrups." *Structural Concrete*, 18(3), 454-465.

Fib. (The International Federation for Structural Concrete) (2010). "Model Code 2010, final draft." *Bulletin 65/66*, Federation Internationale du Beton, Lausanne, Switzerland.

Giduquio, M. B., Cheng, M.-Y., and Wibowo, L. S. (2015). "High-Strength Flexural Reinforcement in Reinforced Concrete Flexural Members under Monotonic Loading." *ACI Structural Journal*, 112(6).

Hao, X. (2017). "Mechanics of extracting shear-friction properties from actively confined cylinder tests." *School Report* , School of Civil, Environmental and Mining Engineering, The University of Adelaide, Australia.

Hao, X. (2018a). "Generation of stress-strain relationship of passively reinforced circular concrete cylinders." *School Report*, School of Civil, Environmental and Mining Engineering, The University of Adelaide, Australia.

Hao, X. (2018b). "Generation of stress-strain relationship of passively reinforced rectangular concrete prisms." *School Report*, School of Civil, Environmental and Mining Engineering, The University of Adelaide, Australia.

Haskett, M., Oehlers, D., Ali, M. M., and Sharma, S. (2010a). "The shear friction aggregate interlock resistance across sliding planes in concrete." *Magazine of Concrete Research*, 62(12), 907-924.

Haskett, M., Oehlers, D. J., Ali, M., and Wu, C. (2010b). "Analysis of moment redistribution in fiber-reinforced polymer plated RC beams." *Journal of Composites for Construction*, 14(4), 424-433.

Haskett, M., Oehlers, D. J., and Ali, M. M. (2008). "Local and global bond characteristics of steel reinforcing bars." *Engineering Structures*, 30(2), 376-383.

Haskett, M., Oehlers, D. J., Ali, M. M., and Sharma, S. K. (2011). "Evaluating the shear-friction resistance across sliding planes in concrete." *Engineering Structures*, 33(4), 1357-1364.

Haskett, M., Oehlers, D. J., Ali, M. M., and Wu, C. (2009). "Rigid body moment–rotation mechanism for reinforced concrete beam hinges." *Engineering Structures*, 31(5), 1032-1041.

Hognestad, E. (1951). "Study of combined bending and axial load in reinforced concrete members." *University of Illinois. Engineering Experiment Station. Bulletin no. 399*.

Iravani, S. (1996). "Mechanical properties of high-performance concrete." *Materials Journal*, 93(5), 416-426.

Jensen, B. C. (1975). "Lines of discontinuity for displacements in the theory of plasticity of plain and reinforced concrete." *Magazine of Concrete Research*, 27(92), 143-150.

Jensen, V. P. (1943). "The Plasticity Ratio of Concrete and It's Effect on the Ultimate Strength of Beamse." *ACI Journal Proceedings*, 39, 555-584.

Jin, L., Du, M., Li, D., Du, X., and Xu, H. (2017). "Effects of cross section size and transverse rebar on the behavior of short squared RC columns under axial compression." *Engineering Structures*, 142, 223-239.

Kaar, P. H., Hanson, N. W., and Capell, H. (1978). "Stress-strain characteristics of high-strength concrete." *Special Publication*, 55, 161-186.

Karthik, M. M., and Mander, J. B. (2010). "Stress-block parameters for unconfined and confined concrete based on a unified stress-strain model." *Journal of Structural Engineering*, 137(2), 270-273.

Li, B., Park, R., and Tanaka, H. (2001). "Stress-strain behavior of high-strength concrete confined by ultra-high-and normal-strength transverse reinforcements." *ACI Structural Journal*, 98(3), 395-406.

Lopes, A. V., Lopes, S. M., and do Carmo, R. N. (2012). "Effects of the compressive reinforcement buckling on the ductility of RC beams in bending." *Engineering Structures*, 37, 14-23.

Mansur, M., Chin, M., and Wee, T. (1997). "Flexural behavior of high-strength concrete beams." *Structural Journal*, 94(6), 663-674.

Mattock, A. H. (1974). "Shear transfer in concrete having reinforcement at an angle to the shear plane." *Special Publication*, 42, 17-42.

Mattock, A. H., and Hawkins, N. M. (1972). "Shear transfer in reinforced concrete—Recent research." *Pci Journal*, 17(2), 55-75.

Mensch, L. J. (1914). "New-Old Theory of Reinforced Concrete Beams in Bending." *ACI Journal Proceedings*, 10(12), 28-41.

Oehlers, D. J., Ali, M. M., Griffith, M. C., Haskett, M., and Lucas, W. (2012). "A generic unified reinforced concrete model." *Proceedings of the Institution of Civil Engineers-Structures and Buildings*, 165(1), 27-49.

Oehlers, D. J., Haskett, M., Ali, M., Lucas, W., and Muhamad, R. (2011). "Our obsession with curvature in RC beam modelling." *Advances in Structural Engineering*, 14(3), 391-404.

Oehlers, D. J., Visintin, P., Chen, J.-F., Seracino, R., Wu, Y., and Lucas, W. (2017). "Reinforced Concrete Behavior, Research, Development, and Design through Partial-Interaction Mechanics." *Journal of Structural Engineering*, 143(7), 02517002.

Popovics, S. (1973). "A numerical approach to the complete stress-strain curve of concrete." *Cement and concrete research*, 3(5), 583-599.

Rajagopalan, K., and Everard, N. J. "Flexural behavior of high-strength concrete beams." *Journal Proceedings*, 73(9), 517-521.

Rashid, M., and Mansur, M. (2005). "Reinforced high-strength concrete beams in flexure." *ACI Structural Journal*, 102(3), 462-471.

Sawyer, H. A. (1965). "Design of concrete frames for two failure stages." *Special Publication*, 12, 405-437.

Seracino, R., Raizal Saifulnaz, M., and Oehlers, D. (2007). "Generic debonding resistance of EB and NSM plate-to-concrete joints." *Journal of Composites for Construction*, 11(1), 62-70.

Silva, M. A., and Rodrigues, C. C. (2006). "Size and relative stiffness effects on compressive failure of concrete columns wrapped with glass FRP." *Journal of Materials in Civil Engineering*, 18(3), 334-342.

Sturm, A. B., Visintin, P., and Oehlers, D. J. (2017). "Time‐dependent serviceability behavior of reinforced concrete beams: Partial interaction tension stiffening mechanics." *Structural Concrete*, 19(2), 508-523.

Tan, T.-H., and Nguyen, N.-B. (2005). "Flexural behavior of confined high-strength concrete columns." *ACI Structural Journal*, 102(2), 198-205.

Thériault, M., Neale, K. W., and Claude, S. (2004). "Fiber-reinforced polymer-confined circular concrete columns: Investigation of size and slenderness effects." *Journal of composites for construction*, 8(4), 323-331.

Visintin, P., Chen, Y., and Oehlers, D. (2015). "Size dependent axial and lateral stress strain relationships for actively confined concrete." *Advances in Structural Engineering*, 18(1), 1-20.

Visintin, P., Oehlers, D., Haskett, M., and Wu, C. (2012a). "Mechanics-based hinge analysis for reinforced concrete columns." *Journal of Structural Engineering*, 139(11), 1973-1980.

Visintin, P., Oehlers, D., Muhamad, R., and Wu, C. (2013). "Partial-interaction short term serviceability deflection of RC beams." *Engineering Structures*, 56, 993-1006.

Visintin, P., Oehlers, D., Wu, C., and Haskett, M. (2012b). "A mechanics solution for hinges in RC beams with multiple cracks." *Engineering Structures*, 36, 61-69.

Visintin, P., and Oehlers, D. J. (2016). "Mechanics‐based closed‐form solutions for moment redistribution in RC beams." *Structural Concrete*, 17(3), 377-389.

Warner, R., Rangan, B., Hall, A., and Faulkes, K. (1998). *Concrete structures*, Addison Wesley Longman.

Whitney, C. S. "Design of reinforced concrete members under flexure or combined flexure and direct compression." *Journal Proceedings*, 33(3), 483-498.

Wu, Y.-F. (2015). "Theorems for flexural design of RC members." *Journal of Structural Engineering*, 142(5), 04015172.

Yi, S.-T., Kim, J.-H. J., and Kim, J.-K. (2002). "Effect of specimen sizes on ACI rectangular stress block for concrete flexural members." *ACI Structural Journal*, 99(5), 701-708.

Yuan, H., Teng, J., Seracino, R., Wu, Z., and Yao, J. (2004). "Full-range behavior of FRP-to-concrete bonded joints." *Engineering structures*, 26(5), 553-565.

Yuan, H., Wu, Z., and Yoshizawa, H. (2001). "Theoretical solutions on interfacial stress transfer of externally bonded steel/composite laminates." *Doboku Gakkai Ronbunshu*, 2001(675), 27-39.

Zhang, T., Visintin, P., and Oehlers, D. (2014). "A semi-mechanical model for tension-stiffening." *Departmental report, No. R*186.

Zhang, T., Visintin, P., and Oehlers, D. J. (2017). "Partial-interaction tension-stiffening properties for numerical simulations." *Advances in Structural Engineering*, 20(5), 812-821.

Chapter 5— Behaviour of Steel Tube Confined Concrete

Introduction

In the journal paper below, the mechanics based closed-form solutions of the passive stress/strain response developed in Chapter 3 for reinforced concrete members are now extended to cover steel tube confined concrete with the additional effect of shrinkage for the first time. These closed-form solutions of the passive stress/strain are then simplified to a rectangular stress block based on the mechanics described in Chapter 4 for application in flexural analyses. Then a parametric study is conducted to investigate the effect of shrinkage on the passive stress/strain response.

List of Manuscripts

Hao, X, Visintin, P and Oehlers, DJ (2019) Mechanical Derivation of the Passive Stress/Strain for Steel Tube Confined Concrete for Design. Submitted to *Journal of Constructional Steel Research*

Statement of Authorship

Statement of Authorship

Title of Paper	Passive Stress/Strain Relationship for the Design of Steel Tube Confined Concrete
Publication Status	☐ Published ☐ Accepted for Publication ☑ Submitted for Publication ☐ Unpublished and Unsubmitted work written in manuscript style
Publication Details	Hao, X, Visintin, P and Oehlers, DJ (2019) Passive Stress/Strain Relationship for the Design of Steel Tube Confined Concrete. Submitted to *Journal of Constructional Steel Research*

Principal Author

Name of Principal Author (Candidate)	Xinkai Hao
Contribution to the Paper	Developed the model, interpreted data, wrote manuscript
Overall percentage (%)	70%
Certification:	This paper reports on original research I conducted during the period of my Higher Degree by Research candidature and is not subject to any obligations or contractual agreements with a third party that would constrain its inclusion in this thesis. I am the primary author of this paper.
Signature	Date 28/10/2019

Co-Author Contributions

By signing the Statement of Authorship, each author certifies that:

i. the candidate's stated contribution to the publication is accurate (as detailed above);

ii. permission is granted for the candidate in include the publication in the thesis; and

iii. the sum of all co-author contributions is equal to 100% less the candidate's stated contribution.

Name of Co-Author	Phillip Visintin
Contribution to the Paper	Supervised work progress, help modelling and revising manuscript
Signature	Date 28/10/19

Name of Co-Author	Deric John Oehlers
Contribution to the Paper	Supervised work progress, help modelling and revising manuscript
Signature	Date 28/10/19

Please cut and paste additional co-author panels here as required.

Passive Stress/Strain Relationship for the Design of Steel Tube Confined Concrete

X. Hao, P. Visintin and D. J. Oehlers

Abstract

The encasement of concrete in steel tubes provides an efficient form of composite steel and concrete construction. As an additional benefit, the steel tube provides passive confinement to the concrete which can increase both the concrete strength and in particular the ductility, thereby, enhancing that of the composite steel and concrete structure. The difficulty in utilising this additional benefit is in quantifying the passive concrete confinement and, consequently, the concrete passive stress/strain as it depends on the encased concrete size, shape, and material properties such as the concrete shrinkage. This paper derives, through mechanics, the concrete passive stress/strain from the partial-interaction concrete shear-friction properties for any configuration of the composite structure, for any material properties and for any concrete shrinkage. Furthermore, the passive stress/strain relationship is simplified to a rectangular stress block that can be used in standard design approaches to allow for the benefits of concrete confinement in design.

Keywords: confined concrete, steel tube confined concrete (STCC), composite steel and concrete columns

1. Introduction

In the past two decades, steel tubes have been widely used as confinement reinforcement in concrete structures as they can significantly enhance the strength and especially the ductility [1-3]. Most current research approaches focus on concrete filled steel tubular (CFST) prisms where both the concrete and steel tube are simultaneously loaded axially [4-9]. However in practical buildings, this sometimes is not the case as the steel tube does not sustain axial loads [10-12]. In this case, the steel tube only acts as confinement reinforcement and this type of column is referred to as a steel tube confined concrete (STCC) column [11]. Furthermore, STCC columns have several benefits compared with CFST columns as they avoid longitudinal buckling of the steel tube [13, 14] and have a better ductility performance

to resist seismic loads [15]. In this paper, only the concrete in STCC columns under concentric loads will be investigated. However it is worth bearing in mind that the stress/strain of the passively confined concrete that is developed in this research can be applied directly to the analysis of members under flexural load [16].

There are only a limited number of approaches for predicting the behaviour of STCC prisms or columns, as most available approaches focus on CFST prisms. Approaches to predicting the behaviour of STCC prisms can be split mainly into two categories: empirical approaches and numerical approaches.

The former approach treats STCC as a new material and develops the concrete stress/strain from empirical observations. For example, O'Shea et al. [17] applied Mander's equation [18] for stirrup reinforced prisms. O'Shea's approach [17] can only be applied for circular-section specimens and requires the peak stress f_{cc} and strain ε_{cc} at f_{cc} which are derived from regression analyses of O'Shea's test results [19]. The simple form of these approaches makes their application easy. However outside the range of the regressed databases, the accuracy of these approaches may decrease and, furthermore, in these approaches the size effect is not considered. The importance of the size-effect is recognised [20] but there is no available empirical model to quantify it.

In the finite element method which is also a numerical approach, the concrete and steel tube are treated separately and the passive concrete stress/strain is derived from the interaction between them [5, 21]. The procedure is summarized as follows: impose an axial strain from which the lateral strain can be derived from Poisson's ratio and subsequently the lateral confining stress; consequently the concrete element is assumed to be under a triaxial confining stress and from the active stress/strain properties its behaviour can be determined [5, 21]. However, the active stress/strain of concrete used in these numerical approaches normally does not consider the size effect. Furthermore, although these models can give a more accurate prediction of the concentrically loaded behaviour, the complexity of these approaches may hinder their application.

With regard to the effect of shrinkage on the behaviour of STCC prisms, it was found that shrinkage for normal strength concrete can be ignored but for high strength concrete this

effect is critical [1]. Most current approaches to predicting the behaviour of STCC prisms do not allow for shrinkage.

In this paper, an approach is developed to predict the passive stress/strain of concentrically loaded STCC prisms that allows for the size effect and which can incorporate different cross-sectional shapes and shrinkages. This approach is based on fundamental mechanics that uses the shear-friction [22-27] material properties. This fundamental approach has been used elsewhere for prisms confined with stirrups or FRP wraps under either concentric loads [28, 29] or flexural loads [16]. In this paper, the application of this approach specifically to STCC prisms is described and, furthermore, the fundamental mechanics is extended for the first time to allow for the displacements due to shrinkage.

The procedure to construct the concrete passive stress/strain from the shear-friction partial interaction material properties is described and it is shown how to allow for shrinkage in the derivation. This is followed by a validation to compare the proposed approach with published tests and then a parametric study to show the effect of shrinkage on different specimen sizes and concrete strengths.

2. Confinement mechanism

Consider the concrete prism encased in a steel tube of thickness t in Fig. 1(a). The dimension D_{ci} is the width of the prism in the direction of sliding. The deformation length L_{def} is any length of prism that encompasses the sliding plane; for concentrically loaded prisms it is normally the specimen height L_{prsm}. The length L_{def} allows for the size effect of the concrete stress/strain.

In the lateral direction in Fig. 1(a), the concrete shrinks $\varepsilon_{sh}D_{ci}$ such that a void could form between the concrete and tube all around the concrete. It is worth bearing in mind that the gap due to shrinkage is very small [30]. However the shrinkage gap will help reduce the already weak chemical bond such that no bond will be considered.

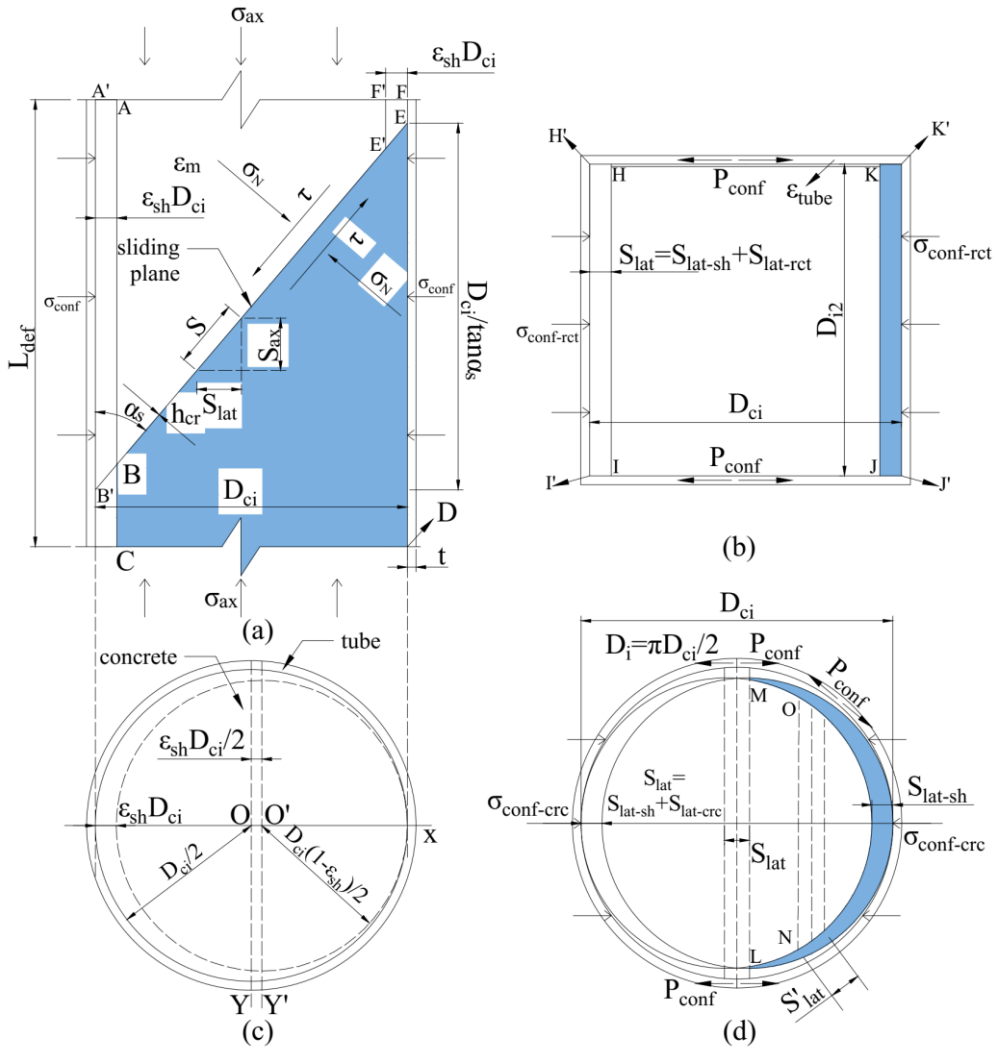

Fig. 1 (a) STCC prisms under concentrically loaded with: (b) rectangualr section or (c, d) circular section

2.1 Behaviour prior to concrete confinement

Prior to loading and after shrinkage and for ease of explanation, the concrete prism is shown as A-B-C-D-E-F in Fig. 1(a). In the direction of potential sliding, the gap due to shrinkage $S_{lat\text{-}sh}$ is

$$S_{lat-sh} = \varepsilon_{sh} D_{ci} \tag{1}$$

which is shown in Fig. 1(a) to the left. Because of the shrinkage gap and prior to sliding, the concrete behaves as unconfined.

An axial displacement that induces an axial stress σ_{ax} and an axial strain in the material ε_m is applied directly to the concrete in Fig. 1(a) until the peak unconfined strength f_{c0} is reached, whereupon, the sliding plane B'-B-E'-E occurs at an angle α_s. Any further increase in the axial displacement causes rigid body sliding along the plane such that the prism above the sliding plane moves from A-B-E-F to A'-B'-E'-F' as shown. The axial component of the slip along the sliding plane S is S_{ax} and the lateral component is S_{lat} such that $S_{ax} = S_{lat}\cot\alpha_s$. Hence the axial component of the strain due to sliding $\varepsilon_S = S_{ax}/L_{def}$, which is the effective axial strain due to sliding, is given by [31, 32]

$$\varepsilon_S = \frac{S_{lat}\cot\alpha_s}{L_{def}} \tag{2}$$

Prior to the shrinkage gap closing, the concrete does not bear onto the tube so the concrete is unconfined such that σ_{conf} in Fig. 1(a) is zero. Hence when the axial stress σ_{ax} is applied in Fig. 1(a) and after sliding, the total axial strain ε_{ax} is comprised of two components that is the material strain ε_m and the additional sliding strain ε_S as shown at level σ_{ax} in Fig. 2.

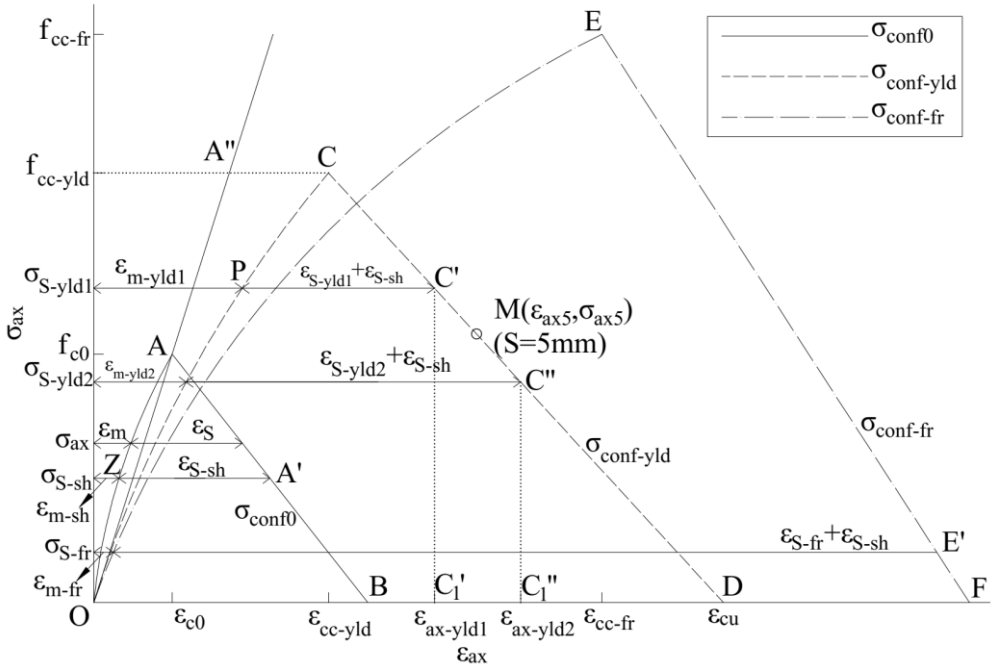

Fig. 2 Passive stress/strain

The lateral component of slip required to close the shrinkage gap is $S_{lat\text{-}sh}$ from Eq. (1). Hence the sliding strain required to close the shrinkage gap $\varepsilon_{S\text{-}sh}$ is obtained by substituting $S_{lat\text{-}sh}$ from Eq. (1) into Eq. (2) to give

$$\varepsilon_{S-sh} = \frac{\varepsilon_{sh} D_{ci} \cot \alpha_s}{L_{def}} \tag{3}$$

This strain is shown at a stress level $\sigma_{S\text{-}sh}$ in Fig. 2 between the ascending branch O-A and descending branch A-B for the unconfined concrete that is at $\sigma_{conf} = 0$. Hence from the known material stress/strain of the unconfined concrete O-A-B in Fig. 2, it is a question of finding the level of $\sigma_{S\text{-}sh}$ at which there is the known strain $\varepsilon_{S\text{-}sh}$ between the ascending and descending branches to give point A'. Point A' being the axial stress σ_{ax} and axial strain ε_{ax} when the shrinkage gap has closed that is the point on the passive stress/strain at the onset of confinement. Hence on applying the axial load in Fig. 1(a), the passive concrete stress/strain path follows O-A-A' in Fig. 2 after which the concrete bears against the tube inducing confinement and its benefits. Once confinement occurs, then the concrete no longer acts as unconfined that is the active stress/strain does not follow the path O-A-B in Fig. 2 but the material properties are enhanced such that the active stress/strain will follow a path such as O-C-D or O-E-F which depends on the confinement stress σ_{conf}.

2.2 Confinement benefit on concrete stress/strain

Once the shrinkage gap has been closed due to sliding in Fig. 1(a), any further increase in axial displacement will cause the concrete prism to bear against the tube causing the tube to go into lateral tension P_{conf} and, consequently, inducing lateral compression σ_{conf} across the concrete tube interface as shown. This is the passive confinement pressure on the concrete which is induced at the concrete tube interface and subsequently across the sliding plane.

2.2.1 Rectangular section

For a rectangular section, the lateral tensile forces in the tube P_{conf} are shown in Fig. 1(b). Both of these forces, that is $2P_{conf}$, passively restrain the sliding action and they act over the width of the sliding plane D_{i2} and depth of the sliding plane $D_{ci}/\tan\alpha_s$ in Fig. 1(a). Should

P_{conf} be defined as the confinement force in the tube, over the depth of the sliding plane that is $D_{ci}/\tan\alpha_s$ in Fig. 1(a), per unit depth of tube, then the lateral confinement pressure across the sliding plane [28] is

$$\sigma_{conf-rct} = \frac{2P_{conf}}{D_{i2}} \tag{4}$$

For a given confinement σ_{conf} from Eq. (4), the active stress/strain, such as for example O-C-D in Fig. 2 when the tube has yielded, can be obtained from the known material properties at that confinement. It is now a question of determining where on C-D this confinement force σ_{conf} starts to act or is acting, bearing in mind that the concrete is only passively restrained that is σ_{conf} is not acting all the time. To determine this, we need to know at which level of axial stress σ_S the effective strain ε_S acts.

Let the strain in the tube along H'-K' and I'-J' in Fig. 1(b) be ε_{tube} so that the lateral expansion of the tube $S_{lat\text{-}rct}$ is

$$S_{lat-rct} = \varepsilon_{tube} D_{ci} \tag{5}$$

which on substituting into Eq. (2) gives the effective strain due to sliding in a rectangular section of

$$\varepsilon_{S-rct} = \frac{\varepsilon_{tube} D_{ci} \cot\alpha_s}{L_{def}} \tag{6}$$

As an example, consider when the confinement pressure is sufficient to cause the steel tube to start to yield laterally that is when σ_{conf} in Fig. 1(a) equals $\sigma_{conf\text{-}yld}$. Let the concrete with this active confinement have the properties O-C-D in Fig. 2. When the strain ε_{tube} in Fig. 1(b) is the steel strain at the start of yielding ε_{yld1}, then the effective strain due to sliding $\varepsilon_{S\text{-}yld1}$ can be obtained from Eq. (6) by substituting $\varepsilon_{tube} = \varepsilon_{yld1}$. There are now two components of the sliding strain as well as the material strain ε_m such that the total strain is given by

$$\varepsilon_{ax} = \varepsilon_m + \varepsilon_{S-sh} + \varepsilon_{S-rct} \tag{7}$$

where on substituting $\varepsilon_{S\text{-}sh}$ and $\varepsilon_{S\text{-}rct}$ from Eqs. (3) and (6) respectively gives

$$\varepsilon_{ax-rct} = \varepsilon_m + \frac{D_{ci}\cot\alpha_s}{L_{def}}(\varepsilon_{tube} + \varepsilon_{sh}) \tag{8}$$

As shown in Fig. 2 at level $\sigma_{S\text{-}yld1}$, the total sliding strain is now that due to the tube $\varepsilon_{S\text{-}yld1}$ and that due to shrinkage $\varepsilon_{S\text{-}sh}$. Once this known strain is fitted between the ascending branch and descending branches for the actively confined concrete at $\sigma_{conf\text{-}yld}$, then this gives both the axial stress at which this occurs $\sigma_{S\text{-}yld1}$ and axial strain $\varepsilon_{ax\text{-}yld1}$ and subsequently point C' of the passive stress/strain. Hence from the start of loading, the concrete passive stress/strain follows the path O-A-A'-C'. Another point between A' and C' could be obtained by repeating the above analysis at a confinement pressure σ_{conf} between zero and that due to yield.

Should the steel have a material yield plateau and have a yield strain or effective yield strain just prior to strain hardening of ε_{yld2}, then substituting ε_{yld2} for ε_{yld1} in the previous analysis gives point C" in Fig. 2. Hence the passive stress/strain follows the path O-A-A'-C'-C". Should $\varepsilon_{S\text{-}yld2}+\varepsilon_{S\text{-}sh}$ exceed O-D then this simply means that the shear friction properties of the concrete [33] along the sliding plane are not strong enough to cause ε_{yld2} that is the concrete strength governs which may be referred to as concrete failure.

The above analysis can be repeated at the steel fracture strain $\varepsilon_{tube} = \varepsilon_{fr}$. The active stress at this confinement is shown as $\sigma_{conf\text{-}fr}$ in Fig. 2. Should the sliding strain $\varepsilon_{S\text{-}fr} + \varepsilon_{S\text{-}sh}$ be greater than O-F, then fracture of the tube does not occur so that the passive stress/strain can be considered to be O-A-A'-C'-C" with a rapid descent. As the fracture strain is normally considerably greater than that of the yield strain, fracture of the tube is unlikely to occur [4].

2.2.2 Circular section

Consider the circular section in Fig. 1(c). The concrete shrinks such that radius of the concrete reduces from $D_{ci}/2$ to $D_{ci}(1\text{-}\varepsilon_{sh})/2$ as shown. For ease of explanation, the concrete cylinder has been placed touching the tube to the right such that the vertical axes of the

concrete O'-Y' is $\varepsilon_{sh}D_{ci}/2$ to the right of the vertical axes of the tube O-Y. On applying an axial load σ_{ax} to the cylinder in Fig. 1(a) and on reaching the unconfined concrete strength f_{c0}, a sliding plane will form. After which, the upper part of the cylinder will move as a rigid body to the left. Sliding will continue until S_{lat} equals $\varepsilon_{sh}D_{ci}$ after which passive confinement will occur. The fundamental mechanism illustrated in Fig. 1(a) is the same for both the rectangular and circular sections. However, there is a slight difference in quantifying the lateral displacements [29].

In the rectangular section in Fig. 1(b), the upper and lower portions of the tube H'-K' and I'-J' provide the confinement force. The angle between these forces and the sliding plane (90^o) is always constant. Hence the confinement pressure is not affected by the level at which the section in Fig. 1(b) is taken in Fig. 1(a). That is an analysis at the mid-depth of the sliding plane in Fig. 1(a) would give the same results as that closer to the ends of the sliding plane. This is not the case for the circular section in Fig. 1(d).

At section O-N in Fig. 1(d), neither the lateral movement that stresses the tube S'_{lat} nor the force in the tube P_{conf} are in line with the direction of sliding. However research has shown [34] that even though the force in the tube is not in line with the sliding plane, it does provide exactly the same confinement. Furthermore an analysis at section L-M, which is equivalent to that in Fig. 1(b) where the sliding plane and force are in line, gives a safe and only slightly conservative solution. Hence the lateral confining stress for a circular section $\sigma_{conf\text{-}crc}$ is [29]

$$\sigma_{conf-crc} = \frac{2P_{conf}}{D_{ci}} \tag{9}$$

The strain in the tube over half the circumference in Fig. 1(d) allows the lateral slip, so Eq. (4) for a rectangular section becomes for a circular section

$$S_{lat-crc} = \frac{\pi\varepsilon_{tube}D_{ci}}{2} \tag{10}$$

and Eq. (6) becomes

$$\varepsilon_{S-crc} = \frac{\pi \varepsilon_{tube} D_{ci} \cot \alpha_s}{2L_{def}} \tag{11}$$

and Eq. (8) becomes

$$\varepsilon_{ax-crc} = \varepsilon_m + \frac{D_{ci} \cot \alpha_s}{L_{def}} \left(\frac{\pi \varepsilon_{tube}}{2} + \varepsilon_{sh} \right) \tag{12}$$

3. Quantification of confinement

The active concrete stress/strain at different confinement levels in Fig. 2 is shown generically in Fig. 3 in terms of the concrete confinement properties (ε_{cc}, f_{cc}) and the idealised maximum slip strain (ε_{cu}, 0) at specific confinements σ_{conf}. Both the ascending branch O-A-P and the descending branch P-R-M are nonlinear. Any active stress/strain [18, 31, 35], preferably with size dependency [31], can be used. For example Appendix B gives approaches based on shear friction material properties that can be applied using closed form or numerical solutions.

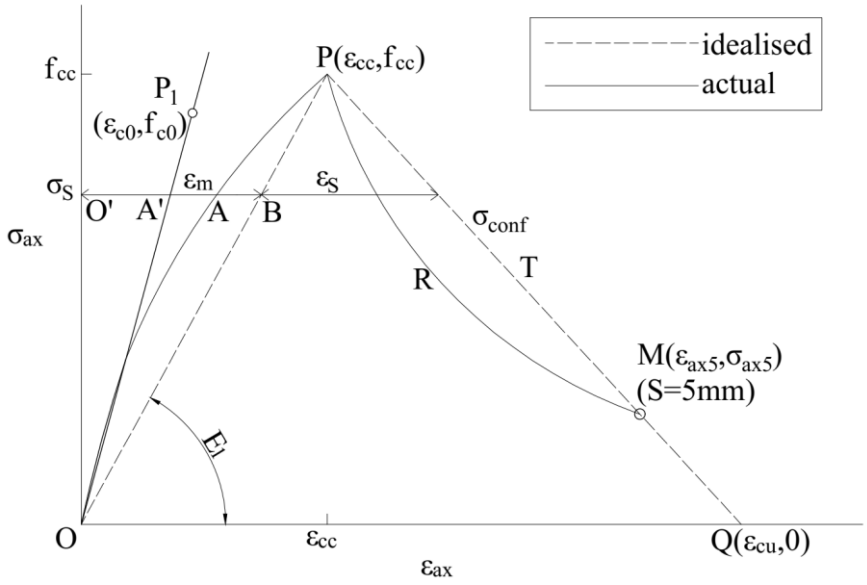

Fig. 3 Active stress/strain

For ease of analysis, the non-linear stress/strain variation in Fig. 3 can be idealised as linear ascending O-B-P and linear descending P-Q. Examples of which are also given in Appendix

B based on shear friction material properties. These linear variations give the following simplified approach to quantifying the passive stress/strain.

The co-ordinates of the bilinear variation O-B-P-Q in Fig. 3 are f_{cc}, ε_{cc} and ε_{cu} where for a concrete with an unconfined concrete strength f_{c0} and lateral confining stress σ_{conf}, f_{cc} is the peak axial stress, ε_{cc} is the strain at f_{cc} and ε_{cu} is the ultimate strain. The bilinear active stress/strain can be determined as follows

$$\begin{aligned} \sigma_{ax} &= \frac{f_{cc}}{\varepsilon_{cc}}\varepsilon_{ax} \qquad (\varepsilon_{ax} < \varepsilon_{cc}) \\ \sigma_{ax} &= f_{cc}\frac{\varepsilon_{ax} - \varepsilon_{cu}}{\varepsilon_{cc} - \varepsilon_{cu}} \qquad (\varepsilon_{ax} \geq \varepsilon_{cc}) \end{aligned} \tag{13}$$

From the geometry of Fig. 3, the sliding strain ε_S is

$$\varepsilon_S = \varepsilon_{cu} - \frac{\varepsilon_{cu}\sigma_S}{f_{cc}} \tag{14}$$

where the sliding strain ε_S consists of two components: the sliding strain due to the tube strain ε_{tube} which is either $\varepsilon_{S\text{-}rct}$ from Eq. (6) for a rectangular section or $\varepsilon_{S\text{-}crc}$ from Eq. (11) for a circular section; plus the sliding strain due to shrinkage $\varepsilon_{S\text{-}sh}$ from Eq. (3). Inserting these two components of ε_S into Eq. (14) gives the axial stress at which the sliding strain is accommodated which for a rectangular cross-section is

$$\sigma_{S-rct} = [\varepsilon_{cu} - \frac{D_{ci}\cot\alpha_s}{L_{def}}(\varepsilon_{tube} + \varepsilon_{sh})]\frac{f_{cc}}{\varepsilon_{cu}} \tag{15}$$

or for a circular cross-section is

$$\sigma_{S-crc} = [\varepsilon_{cu} - \frac{D_{ci}\cot\alpha_s}{L_{def}}(\frac{\pi\varepsilon_{tube}}{2} + \varepsilon_{sh})]\frac{f_{cc}}{\varepsilon_{cu}} \tag{16}$$

The strain at which this occurs can be obtained by substituting σ_S into Eq. (13) to give for the descending branch P-Q in Fig. 3

$$\varepsilon_{ax} = \frac{\sigma_S(\varepsilon_{cc} - \varepsilon_{cu})}{f_{cc}} + \varepsilon_{cu} \tag{17}$$

The procedure is described in Appendix B and summarized in Table 1. For a given strain in the steel tube ε_{tube} in Column 2, the confinement force P_{conf} can be derived and, subsequently, the lateral confining stress σ_{conf} from Eq. (4) or (9) which is shown in Column 3. For this σ_{conf}, the axial stress σ_S in Column 4 can be determined by substituting the given ε_{tube} from Column 2 into Eq. (15) or (16) and, subsequently, the axial strain ε_{ax} in Column 5 from Eq. (17).

Table 1. Coordinates of the stress blocks in Fig. 4 using bilinear active stress/strain

Key points in Fig. 2	ε_{tube}	σ_{conf}	σ_S	ε_{ax}	Coordinates of stress block O-A'-C'-C_1'	Coordinates of stress block O-A'-C'-C"-C_1"	Coordinates of stress block O-A'-C"-C_1"
①	②	③	④	⑤	⑥	⑦	⑧
O	0	0	0	0	(ε_{ax0}, σ_{ax0}), (ε_{ax4}, σ_{ax4})	(ε_{ax0}, σ_{ax0}), (ε_{ax5}, σ_{ax5})	(ε_{ax0}, σ_{ax0}), (ε_{ax4}, σ_{ax4})
A	0	0	f_{c0}	ε_{c0} from Eq.(36)			
A'	0	0	Eq. (15) or (16)	Eq. (17)	(ε_{ax3}, σ_{ax3})	(ε_{ax4}, σ_{ax4})	(ε_{ax3}, σ_{ax3})
C'	ε_{yld1}	$\sigma_{conf\text{-}yld}$	Eq. (15) or (16)	Eq. (17)	(ε_{ax2}, σ_{ax2})	(ε_{ax3}, σ_{ax3})	
C"	ε_{yld2}	$\sigma_{conf\text{-}yld}$	Eq. (15) or (16)	Eq. (17)		(ε_{ax2}, σ_{ax2})	(ε_{ax2}, σ_{ax2})
C_1'	ε_{yld1}	$\sigma_{conf\text{-}yld}$	Eq. (15) or (16)	Eq. (17)	(ε_{ax1}, σ_{ax1})		
C_1"	ε_{yld2}	$\sigma_{conf\text{-}yld}$	Eq. (15) or (16)	Eq. (17)		(ε_{ax1}, σ_{ax1})	(ε_{ax1}, σ_{ax1})
E'	ε_{fr}	$\sigma_{conf\text{-}fr}$	Eq. (15) or (16)	Eq. (17)			

4. Rectangular stress block

The above analysis has explained how in Fig. 2 the points A', at the onset of confinement, C', at the onset of yield, and C", at the completion of yield, can be derived from the active concrete stress/strain. Hence the concrete passive stress/strain can be approximated as the multilinear variation O-A-A'-C'-C" followed by a rapid decent. To simplify the analysis, this can be approximated to O-A'-C'-C". Flexural analyses [16] have shown that: using the stress block O-A'-C'-C_1' in Fig. 4(a), that is limiting the concrete strain to that at the peak concrete strength, can give a good approximation of the flexural capacity; and, furthermore, using the stress block O-A'-C'-C"-C_1" in Fig. 4(b), that is limiting the strain to that at the completion of yield, can give a good approximation of the flexural ductility. A further simplification of the stress block O-A'-C'-C"-C_1" in Fig. 4(b) is the stress block O-A'-C"-

C_1" in Fig. 4(c). To allow for a standard flexural analysis, these multilinear stress blocks have been further simplified to rectangular stress blocks as follows.

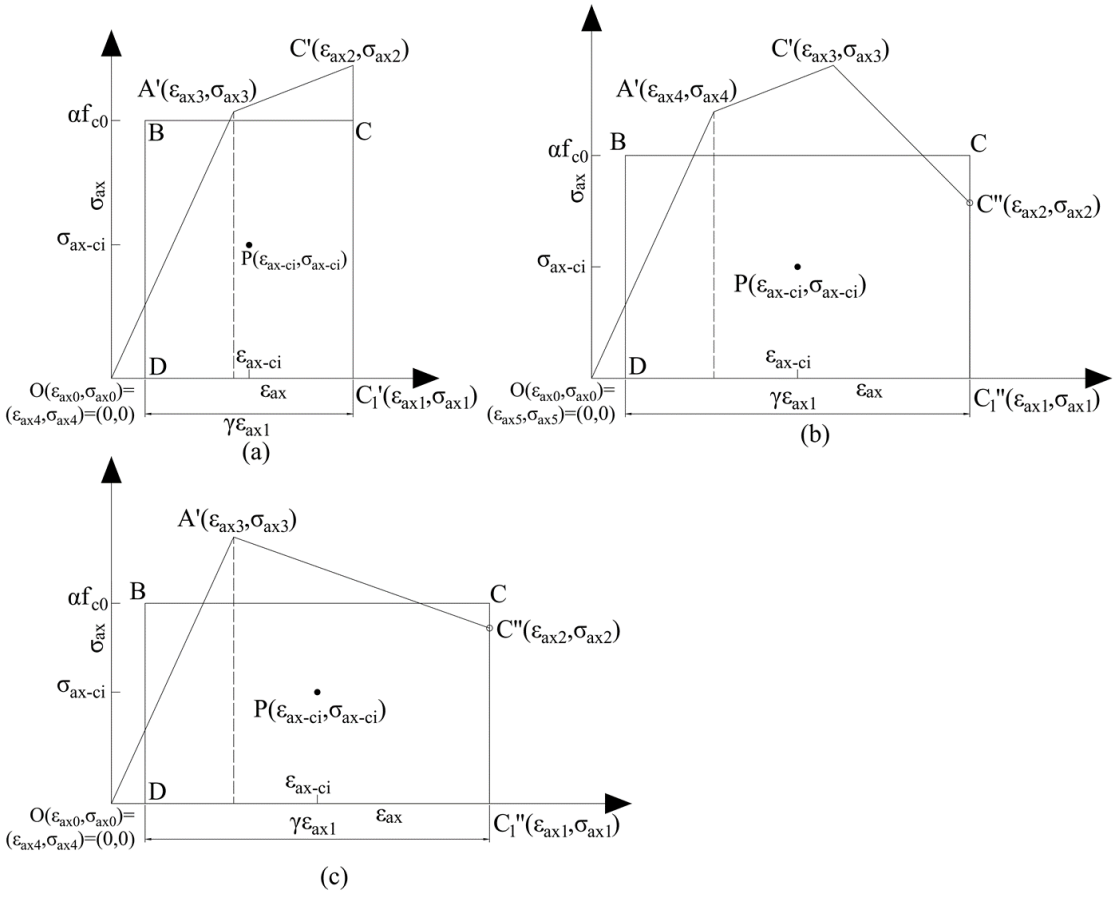

Fig. 4 Conrete stress block for analysis of: (a) strength; (b) ductility; (c) simplified ductility

4.1 Derivation of rectangular stress blocks

The derivation of key points of the passive stress/strain has been given in Appendix B and summarised in Table 1. It has been explained previously that: at key point A' in Column 1 in Table 1 confinement starts; at key point C' the confinement reinforcement yields; and at key point C", yield is completed. Other key points including C_1' and C_1" as shown in Fig. 4 have the same abscissae with C' and C" respectively and are located on the x-axis. To determine the rectangular stress block, the coordinates of the vertexes of the original stress block are required and these vertexes are the key points in Column 1. These coordinates are assumed to be numbered in the order of their occurrence along the stress block's perimeter in the anticlockwise order. Take stress block O-A'-C'-C_1' in Fig. 4(a) as an example, the

first point is fixed at the origin O in Fig. 4(a) at (ε_{ax0}, σ_{ax0}) at (0, 0). The next points at (ε_{ax1}, σ_{ax1}), (ε_{ax2}, σ_{ax2}) and (ε_{ax3}, σ_{ax3}) are defined at points C_1', C' and A' respectively in anticlockwise order of the stress block which is shown in Column 6 in Table 1. Then the area of the stress block is given by

$$A_{rec} = \frac{1}{2}\sum_{i=0}^{N-1}\left[\varepsilon_{axi}\sigma_{ax(i+1)} - \varepsilon_{ax(i+1)}\sigma_{axi}\right] \tag{18}$$

and the abscissa of the centroid by

$$\varepsilon_{ax-ci} = \frac{1}{6A_{rec}}\sum_{i=0}^{N-1}(\varepsilon_{axi} + \varepsilon_{ax(i+1)})\left[\varepsilon_{axi}\sigma_{ax(i+1)} - \varepsilon_{ax(i+1)}\sigma_{ax}\right] \tag{19}$$

where N is the number of key points [36]. It is worth noting that substituting the maximum value for N into Eqs. (18) and (19) gives an undefined point (ε_{axN}, σ_{axN}). Take stress block O-A'-C'-C_1' in Fig. 4(a) as an example, when substituting N = 4 into Eqs. (18) and (19), the coordinate (ε_{ax4}, σ_{ax4}) is not defined as described previously and this point is assumed to be the same as (ε_{ax0}, σ_{ax0}) at (0, 0) [36].

To determine the simplified rectangular stress block with the same area A_{rec} and the same abscissa of the centroid as the original stress block, parameters α and γ are required; these two parameters determine the width and length of this rectangular stress block which equals αf_{c0} and $\gamma\varepsilon_{ax1}$ respectively [16]. They have been derived elsewhere [16] and can be written as

$$\alpha = \frac{A_{rec}}{2(\varepsilon_{ax1} - \varepsilon_{ax-ci})\, f_{c0}} \tag{20}$$

$$\gamma = \frac{2(\varepsilon_{ax1} - \varepsilon_{ax-ci})}{\varepsilon_{ax1}} \tag{21}$$

where A_{rec} and $\varepsilon_{ax\text{-}ci}$ are obtained from Eqs. (18) and (19). Take the stress block O-A'-C'-C_1' in Fig. 4(a) as an example. It is simplified to the rectangular stress block D-B-C-C_1' and they have the same area A_{rec} and the same abscissa of the centroid that is $\varepsilon_{ax\text{-}ci}$ at point P [16].

4.2 Stress block for analysis of strength

The concrete passive stress block for strength O-A'-C'-C_1' in Fig. 2 which is shown in Fig. 4(a) is simplified to the rectangular stress block D-B-C-C_1'. The coordinates of the stress block O-A'-C'-C_1' have been described as an example previously and substituting these coordinates in Column 6 in Table 1 into Eqs. (18) and (19) gives

$$A_{rec} = \frac{1}{2}\left[\varepsilon_{ax1}\sigma_{ax2} + \varepsilon_{ax2}\sigma_{ax3} - \varepsilon_{ax3}\sigma_{ax2}\right] \tag{22}$$

$$\varepsilon_{ax-ci} = \frac{(\varepsilon_{ax1} + \varepsilon_{ax2})\varepsilon_{ax1}\sigma_{ax2} + (\varepsilon_{ax2} + \varepsilon_{ax3})(\varepsilon_{ax2}\sigma_{ax3} - \varepsilon_{ax3}\sigma_{ax2})}{3\left(\varepsilon_{ax1}\sigma_{ax2} + \varepsilon_{ax2}\sigma_{ax3} - \varepsilon_{ax3}\sigma_{ax2}\right)} \tag{23}$$

and then the parameters α and γ can be obtained from Eqs. (20) and (21) respectively.

4.3 Stress block for analysis of ductility

Consider the stress block O-A'-C'-C"-C_1" in Fig. 2 for analysis of ductility which is shown in Fig. 4(b) where it is simplified to the rectangular stress block D-B-C-C_1" [16].

Similarly to the coordinates of the key points in Column 6 in Table 1, the coordinates of the stress block O-A'-C'-C"-C_1" are shown in Column 7 in Table 1.These coordinates are used in Eqs. (18) and (19) and numbered along the stress block's perimeter in an anticlockwise order where the first point at (ε_{ax0}, σ_{ax0}) is fixed at the origin O in Fig. 4(a). Substituting the coordinates of the stress block O-A'-C'-C"-C_1" in Column 7 in Table 1 into Eqs. (18) and (19) gives

$$A_{rec} = \frac{1}{2}\left[\varepsilon_{ax1}\sigma_{ax2} + \varepsilon_{ax2}\sigma_{ax3} - \varepsilon_{ax3}\sigma_{ax2} + \varepsilon_{ax3}\sigma_{ax4} - \varepsilon_{ax4}\sigma_{ax3}\right] \tag{24}$$

$$\varepsilon_{ax-ci} = \frac{(\varepsilon_{ax1}+\varepsilon_{ax2})\varepsilon_{ax1}\sigma_{ax2} + (\varepsilon_{ax2}+\varepsilon_{ax3})(\varepsilon_{ax2}\sigma_{ax3} - \varepsilon_{ax3}\sigma_{ax2}) + (\varepsilon_{ax3}+\varepsilon_{ax4})(\varepsilon_{ax3}\sigma_{ax4} - \varepsilon_{ax4}\sigma_{ax3})}{3\left(\varepsilon_{ax1}\sigma_{ax2} + \varepsilon_{ax2}\sigma_{ax3} - \varepsilon_{ax3}\sigma_{ax2} + \varepsilon_{ax3}\sigma_{ax4} - \varepsilon_{ax4}\sigma_{ax3}\right)} \quad (25)$$

and subsequently the parameters α and γ from Eqs. (20) and (21) respectively.

For simplification, stress block O-A'-C'-C"-C_1" in Fig. 4(b) can be simplified to stress block O-A'-C"-C_1" in Fig. 4(c). The coordinates of this case are similar to that of the previous stress block O-A'-C'-C"-C_1" shown in Column 7 in Table 1 and the only difference is that coordinate of point C' is removed as shown in Column 8 in Table 1. Substituting these coordinates of stress block O-A'-C"-C_1" in Column 8 in Table 1 into Eq. (18) and (19) gives

$$A_{rec} = \frac{1}{2}\left[\varepsilon_{ax1}\sigma_{ax2} + \varepsilon_{ax2}\sigma_{ax3} - \varepsilon_{ax3}\sigma_{ax2}\right] \quad (26)$$

$$\varepsilon_{ax-ci} = \frac{(\varepsilon_{ax1}+\varepsilon_{ax2})\varepsilon_{ax1}\sigma_{ax2} + (\varepsilon_{ax2}+\varepsilon_{ax3})(\varepsilon_{ax2}\sigma_{ax3} - \varepsilon_{ax3}\sigma_{ax2})}{3\left(\varepsilon_{ax1}\sigma_{ax2} + \varepsilon_{ax2}\sigma_{ax3} - \varepsilon_{ax3}\sigma_{ax2}\right)} \quad (27)$$

and subsequently parameters α and γ from Eqs. (20) and (21) respectively.

5. Validation

The above theoretical approach has been compared with sixteen concentrically loaded circular and rectangular specimens with normal strength concrete. As the effect of shrinkage has been found to be negligible in normal strength concrete specimens [1], shrinkage has been ignored in this validation. However the effect of shrinkage will be studied in detail in the ensuing parametric study.

Four closed-form solutions from Appendix B are compared with the experimental results of concentrically loaded STCC circular cylinders [11, 19] in Figs. 5 to 6 and those with rectangular cross-sections [11] in Fig. 7. Details of the specimens are shown in Table 2. The closed-form solutions in Figs. 5 to 7: use a non-linear descending branch for the active

stress/strain that is derived from linear shear friction properties [33]; assume either a single sliding failure or a circumferential failure as derived in Appendix B; assume either no-interaction between the steel tube and concrete or full-interaction such that they act together with the same total axial strain. The passive stress/strains in Figs. 5 to 7 are labelled as follows: 'E' for the experimental stress/strain from the tests; 'S' for the theoretical approach in which a single sliding failure plane is assumed; 'C' when a circumferential failure type is assumed; 'SB' when the theoretical approach assumes both a single sliding failure and full-interaction between the concrete and steel tube; and 'CB' when the approach assumes both a circumferential failure type and full-interaction between concrete and steel tube.

Table 2 Details of STCC Prisms in Validation

S#	Ref.	Section	L_{def} (mm)	D_{ci} (mm)	f_{c0} (MPa)	t (mm)	f_{yld} (MPa)	$\sigma_{confyld}/f_{c0}$
S10CL80C	[19]	circular	665	188	56.4	0.86	211	0.034
S12CL80C	[19]	circular	662	188	56.4	1.13	186	0.040
S10CL50C	[19]	circular	658	188	38.2	0.86	211	0.050
S12CL50C	[19]	circular	657	188	38.2	1.13	186	0.059
S20CL80C	[19]	circular	656	186	56.4	1.94	256	0.095
S20CL50C	[19]	circular	660	186	38.2	1.94	256	0.140
A-CTRC-3d	[11]	circular	600	196	59.4	2.00	263	0.090
A-CTRC-2d	[11]	circular	630	204	59.4	3.00	254	0.126
A-CTRC-5d	[11]	circular	630	204	59.4	3.00	346	0.137
A-CTRC-4d	[11]	circular	630	204	42.4	3.00	254	0.171
A-CTRC-1d	[11]	circular	450	144	59.4	3.00	254	0.178
A-STRC-3d	[11]	rectangular	600	196	59.4	2.00	263	0.090
A-STRC-5d	[11]	rectangular	630	206	42.4	2.00	263	0.120
A-STRC-2d	[11]	rectangular	630	204	59.4	3.00	254	0.126
A-STRC-4d	[11]	rectangular	630	204	42.4	3.00	254	0.171
A-STRC-1d	[11]	rectangular	450	144	59.4	3.00	254	0.178

Note: S# is the specimen number and f_{yld} is the yield strength of steel tube.

Four numerical approaches from Appendix B are also compared with the above experimental results for circular section specimens in Figs. 8 to 9 and for rectangular sections in Fig. 10. In addition, they are also compared with O'Shea's approach [17], that was derived for circular section prisms only, in Figs. 8 to 9. These numerical approaches use a non-linear active stress/strain and non-linear shear friction properties. The passive stress/strains in Figs.

8 to 10 are labelled in the same way as those in Figs. 5 to 7 with the addition of O'Shea's approach [17] which is labelled 'O'.

In the sets of figures in Figs. 5-10, the confinement stress $\sigma_{conf\text{-}yld}/f_{c0}$ increases from the first of the set of figures labelled (a) onwards. It can be seen in each of these sets of figures that the correlation between the experimental results and the theoretical model with full interaction labelled SB or CB improves with increasing confinement σ_{conf}. This is because the confinement pressure increases the bond between the concrete and tube such that full interaction is more likely to occur. In addition from previous research it was shown that for rectangular cross-sections, single sliding failure is more likely to occur [28, 37, 38] and for circular sections circumferential failure more likely [29, 39, 40]. Hence, single sliding failure is recommended for rectangular sections as also suggested by the results in Fig. 10. In contrast, circumferential failure is recommended for circular cross sections such as suggested by the results in Figs. 8 and 9. Furthermore, it is worth noting that the two specimens in Figs. 5(a) and (b) had almost the same properties and only a slight difference in the lateral confining stress ($\sigma_{conf\text{-}yld}/f_{c0}$ equals 0.034 and 0.040 respectively). However, when compared with the experimental stress/strain, the closed-form solutions show poor correlation in Fig. 5(a) and good correlation in Fig. 5(b) which indicates the scatter of the experimental results.

In general there is good correlation with the numerical model labelled C in Figs. 8-10 in which there is no bond between the concrete and the steel tube and, furthermore, in which a circumferential sliding plane is assumed as might occur for specimens of this size. Allowing for full-interaction, that is the numerical model labelled CB, does increase the strength slightly and may lead on occasion to better correlation with the test results. However, it is felt that this bond should not be relied upon in design as it does occasionally lead to an unconservative results as in Figs. 10(b), 10(d) and 10(e) where it would appear that the bond had broken down. As would be expected, the numerical models in Figs. 8-10 give a better correlation with the test results than the simplified closed form solutions in Figs. 5-7. However these simplified closed form solutions do in general give a lower bound, that is a safe approximation, and are more convenient to use in design.

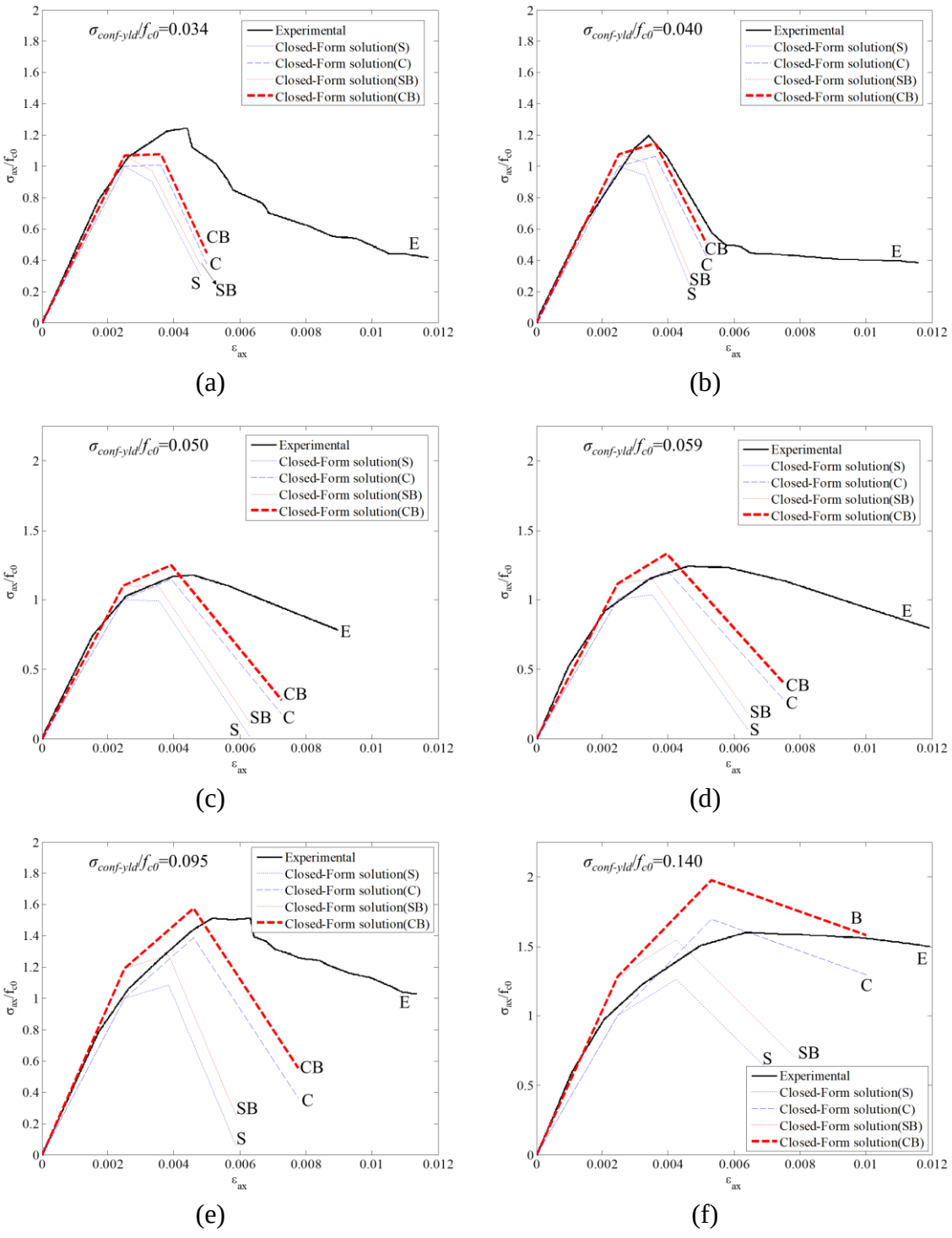

Fig. 5 Closed-Form solution of STCC circular cylinders with specimen number: (a) S10CL80C (b) S12CL80C (c) S10CL50C (d) S12CL50C (e) S20CL80C (f) S20CL50C

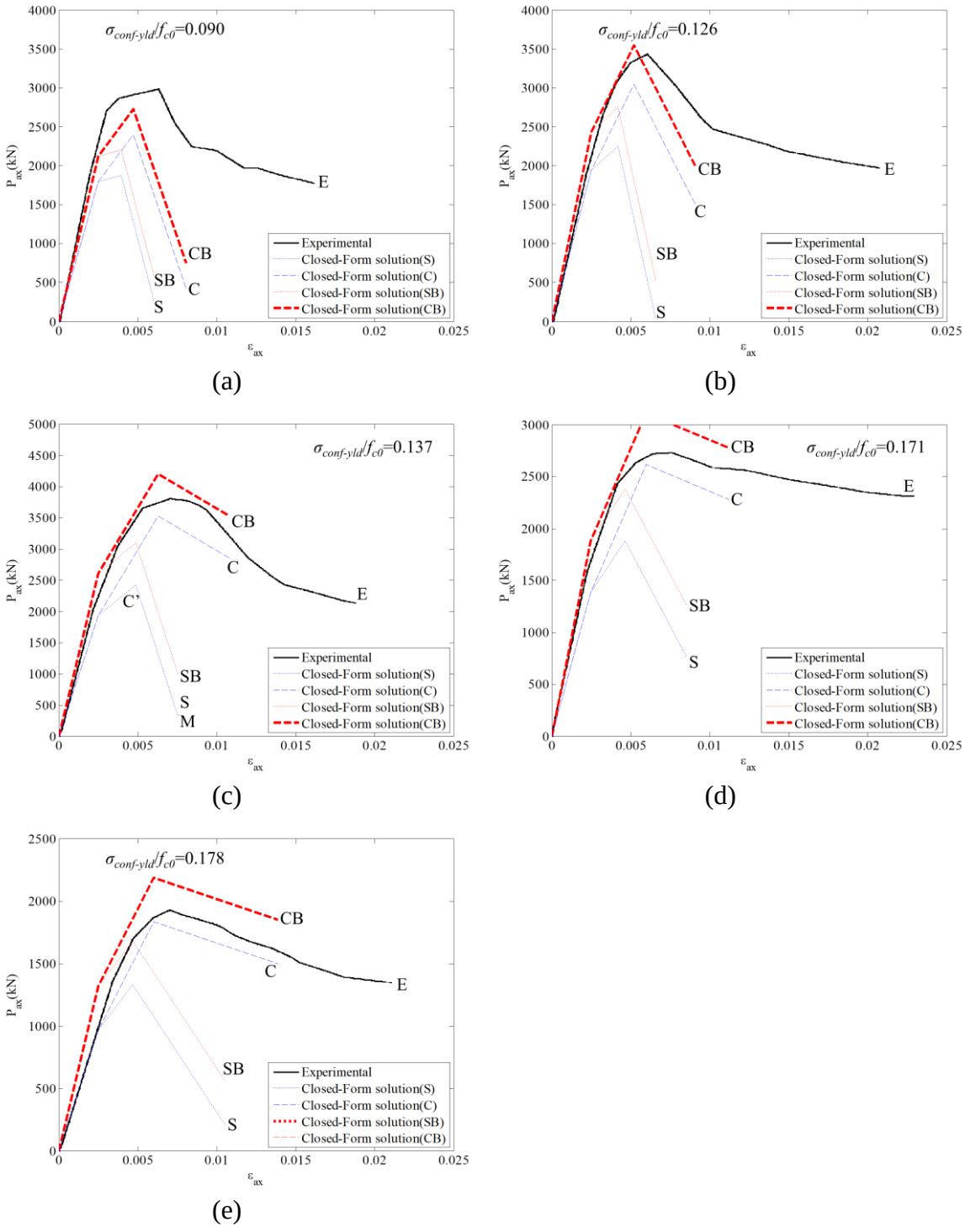

Fig. 6 Closed-Form solution of STCC circular cylinders with specimen number: (a) A-CTRC-3d (b) A-CTRC-2d (c) A-CTRC-5d (d) A-CTRC-4d (e) A-CTRC-1d

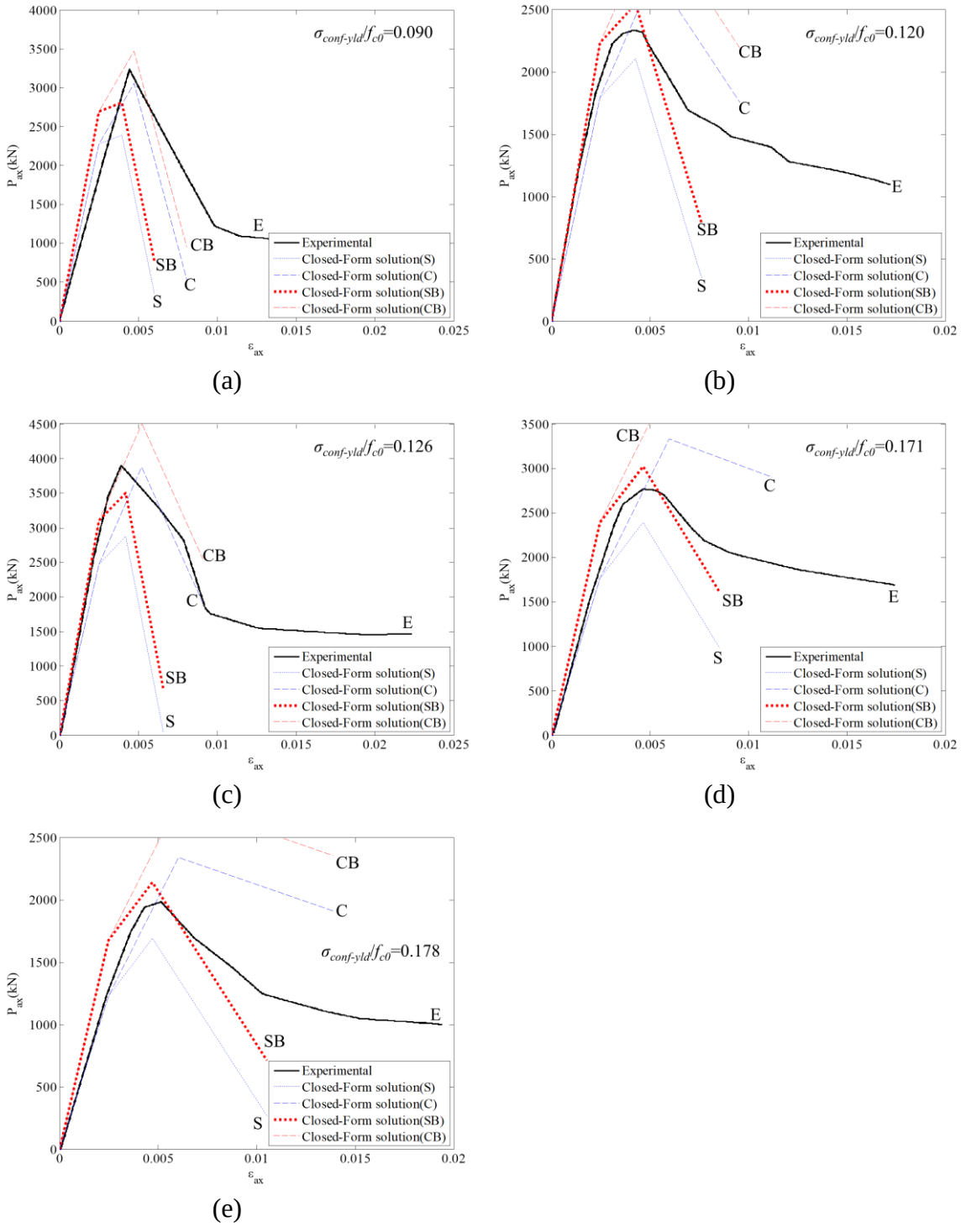

Fig. 7 Closed-Form solution of STCC rectangular prisms with specimen number: (a) A-STRC-3d (b) A-STRC-5d (c) A-STRC-2d (d) A-STRC-4d (e) A-STRC-1d

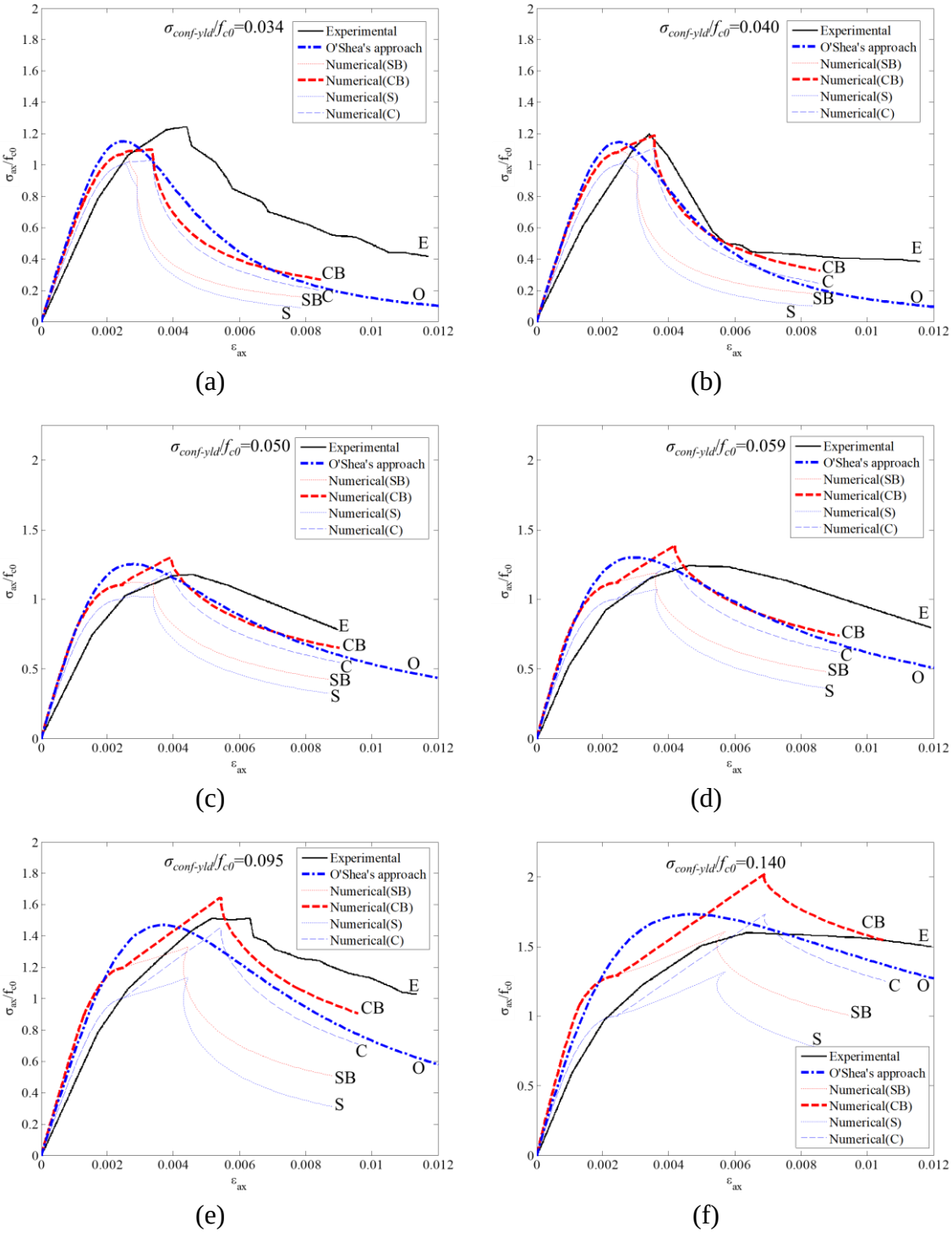

Fig. 8 Numerical model to simulate STCC circular cylinders with specimen number: (a) S10CL80C (b) S12CL80C (c) S10CL50C (d) S12CL50C (e) S20CL80C (f) S20CL50C

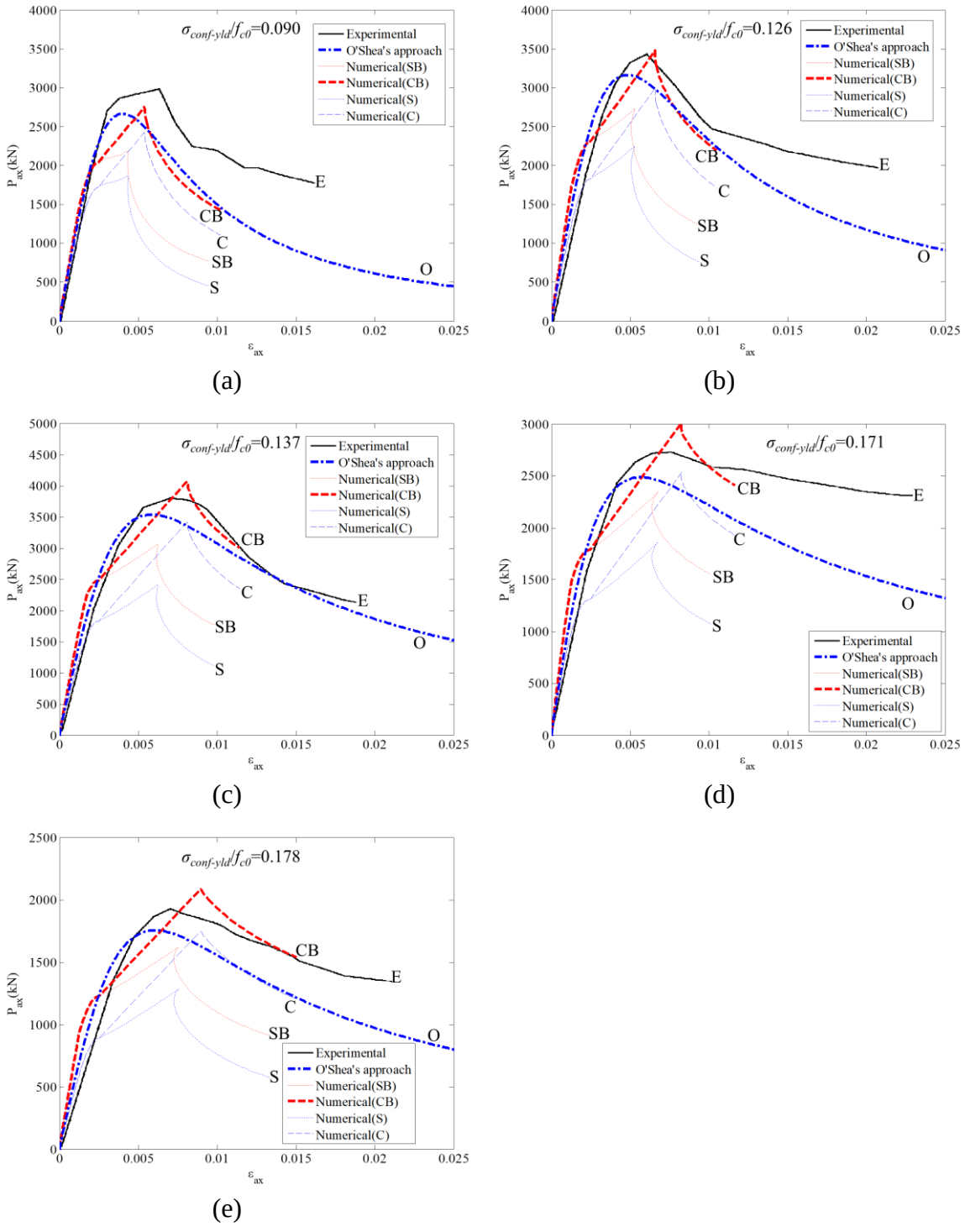

Fig. 9 Numerical model to simulate STCC circular cylinders with specimen number: (a) A-CTRC-3d (b) A-CTRC-2d (c) A-CTRC-5d (d) A-CTRC-4d (e) A-CTRC-1d

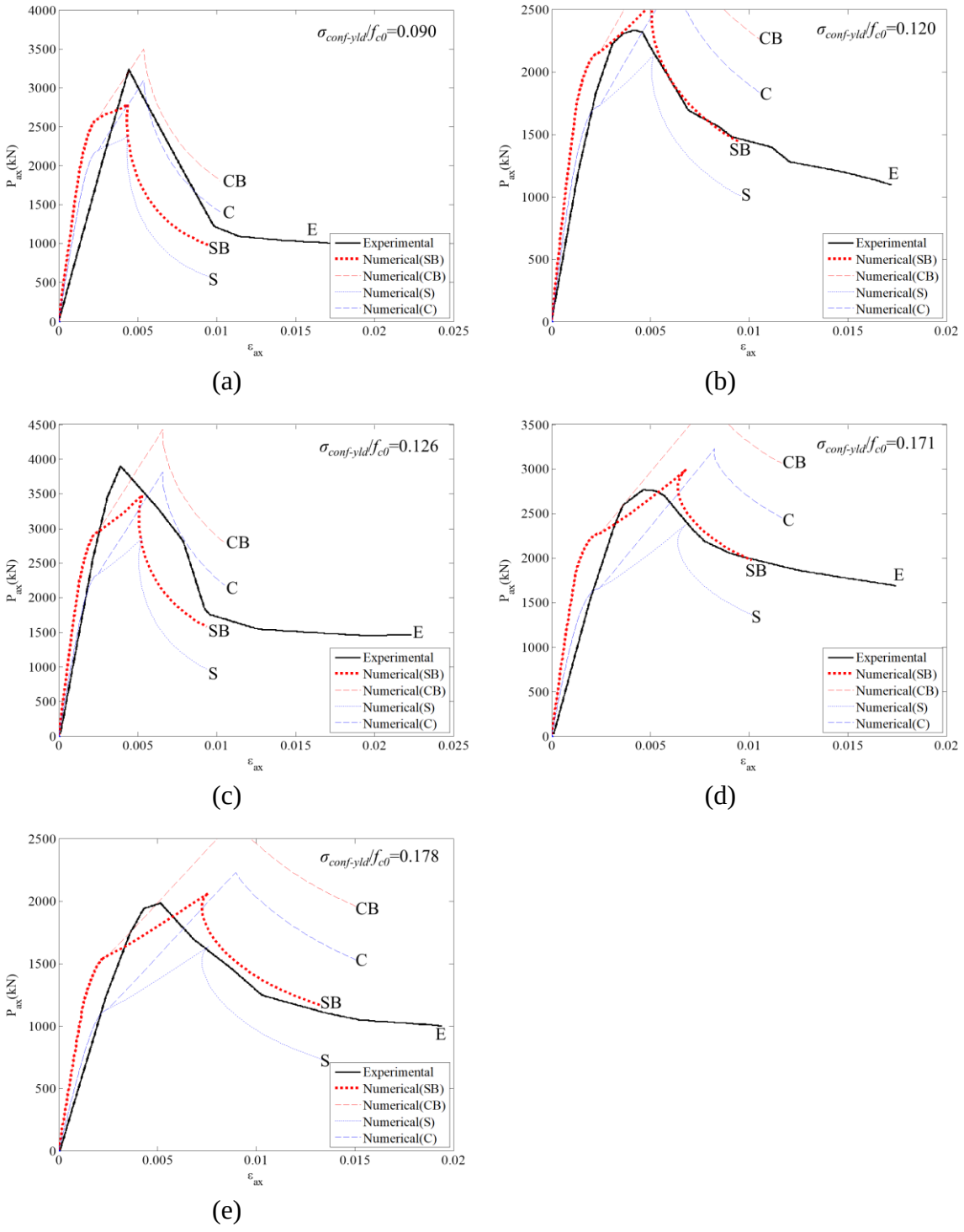

Fig. 10 Numerical model to simulate STCC rectangular prisms with specimen number: (a) A-STRC-3d (b) A-STRC-5d (c) A-STRC-2d (d) A-STRC-4d (e) A-STRC-1d

6. Parametric study

In the following parametric study: only the cases in Fig. 4(a) for strength and in Fig. 4(b) for ductility are investigated; the passive stress/strain is derived using linear shear friction properties which results in a non-linear descending branch of the active stress/strain; and a single sliding failure type is used. The procedure is derived in Appendix B and in Table 4 and is similar to that summarised in Table 1. The only difference is that for the key points in Column 1 after the occurrence of sliding, the axial stress σ_S in Column 4 is obtained from Eq. (46) or (48) and the axial strain ε_{ax} in Column 5 is obtained from Eq. (47) or (49). Details of the specimens in this parametric study are shown in Table 3.

Table 3. Details of STCC Prisms in Parametric Study

S#	Figure number	Section	ε_{sh} με	L_{def} (mm)	D_{ci} (mm)	f_{c0} (MPa)	t (mm)	f_{yld} (MPa)	$\sigma_{conf\text{-}yld}/f_{c0}$
$D_{ci}100$	Figs.11,12	circular	0	300	100	60	2	300	0.200
$D_{ci}100$	Figs.11,12	circular	500	300	100	60	2	300	0.200
$D_{ci}100$	Figs.11,12	circular	1000	300	100	60	2	300	0.200
$D_{ci}300$	Figs.11,12	circular	0	900	300	60	6	300	0.200
$D_{ci}300$	Figs.11,12	circular	500	900	300	60	6	300	0.200
$D_{ci}300$	Figs.11,12	circular	1000	900	300	60	6	300	0.200
$f_{c0}30$	Figs.13,14	circular	0	900	300	30	3	300	0.200
$f_{c0}30$	Figs.13,14	circular	500	900	300	30	3	300	0.200
$f_{c0}30$	Figs.13,14	circular	1000	900	300	30	3	300	0.200
$f_{c0}90$	Figs.13,14	circular	0	900	300	90	9	300	0.200
$f_{c0}90$	Figs.13,14	circular	500	900	300	90	9	300	0.200
$f_{c0}90$	Figs.13,14	circular	1000	900	300	90	9	300	0.200
$D_{ci}100$	Fig.15	circular	1000	300	100	60	2	300	0.200
$D_{ci}200$	Fig.15	circular	1000	600	200	60	4	300	0.200
$D_{ci}300$	Fig.15	circular	1000	900	300	60	6	300	0.200

Note: figure number is where the figure is shown.

Table 4. Coordinates of the stress blocks in Fig. 4 using non-linear descending branch of active stress/strain and linear shear friction properties

Key points in Fig. 2	ε_{tube}	σ_{conf}	σ_S	ε_{ax}	Coordinates of stress block O-A'-C'-C_1'	Coordinates of stress block O-A'-C'-C"-C_1"	Coordinates of stress block O-A'-C"-C_1"
①	②	③	④	⑤	⑥	⑦	⑧
O	0	0	0	0	(ε_{ax0}, σ_{ax0}), (ε_{ax4}, σ_{ax4})	(ε_{ax0}, σ_{ax0}), (ε_{ax5}, σ_{ax5})	(ε_{ax0}, σ_{ax0}), (ε_{ax4}, σ_{ax4})
A	0	0	f_{c0}	ε_{c0} from Eq.(36)			
A'	0	0	Eq. (46) or (48)	Eq. (47) or (49)	(ε_{ax3}, σ_{ax3})	(ε_{ax4}, σ_{ax4})	(ε_{ax3}, σ_{ax3})
C'	ε_{yld1}	$\sigma_{conf\text{-}yld}$	Eq. (46) or (48)	Eq. (47) or (49)	(ε_{ax2}, σ_{ax2})	(ε_{ax3}, σ_{ax3})	
C"	ε_{yld2}	$\sigma_{conf\text{-}yld}$	Eq. (46) or (48)	Eq. (47) or (49)		(ε_{ax2}, σ_{ax2})	(ε_{ax2}, σ_{ax2})
C_1'	ε_{yld1}	$\sigma_{conf\text{-}yld}$	Eq. (46) or (48)	Eq. (47) or (49)	(ε_{ax1}, σ_{ax1})		
C_1"	ε_{yld2}	$\sigma_{conf\text{-}yld}$	Eq. (46) or (48)	Eq. (47) or (49)		(ε_{ax1}, σ_{ax1})	(ε_{ax1}, σ_{ax1})
E'	ε_{fr}	$\sigma_{conf\text{-}fr}$	Eq. (46) or (48)	Eq. (47) or (49)			

Figure 11 shows the results of the analysis for strength as in Fig. 4(a). The results in Fig. 11(a) and Fig. 11(c) are for a 100 mm diameter specimen and those in Fig. 11(b) and Fig. 11(d) for a 300 mm specimen. It can be seen that varying the shrinkage strain over a very wide range from zero to 1000 με only has a relatively minor effect on the passive stress/strains in Figs. 11(a) and (b) and, consequently, that in the rectangular stress blocks in Figs. 11(c) and (d). However, comparing the passive stress/strains with the unconfined stress/strain shows a very significant increase in both strength and ductility that is the beneficial effect of confinement. Figure 12 shows the results for the analysis for ductility in Fig. 4(b). Once again shrinkage has only a minor effect on the stress blocks and confinement a huge beneficial effect on both the strength and ductility. A comparison of Fig. 11(b) with Fig. 12(c) shows only a minor change for the large diameter specimen (300 mm) which is in contrast to the major change between Fig. 11(a) and Fig. 12(a) for the small diameter specimen (100 mm). Hence the benefits of confinement increase with reducing diameter.

In Fig. 13, the strength of the concrete is changed from 30 MPa in Figs. 13(a) and (c) to 90 MPa in Figs. 13(b) and (d) in this analysis for strength. It can be seen that shrinkage has little effect on the low strength concrete but causes a significant reduction in the strength and ductility of the high strength concrete. A similar outcome can be seen in the ductility analysis in Fig. 14. It can also be seen in both the strength and confinement analyses that the confinement substantially increases both the strength and ductility.

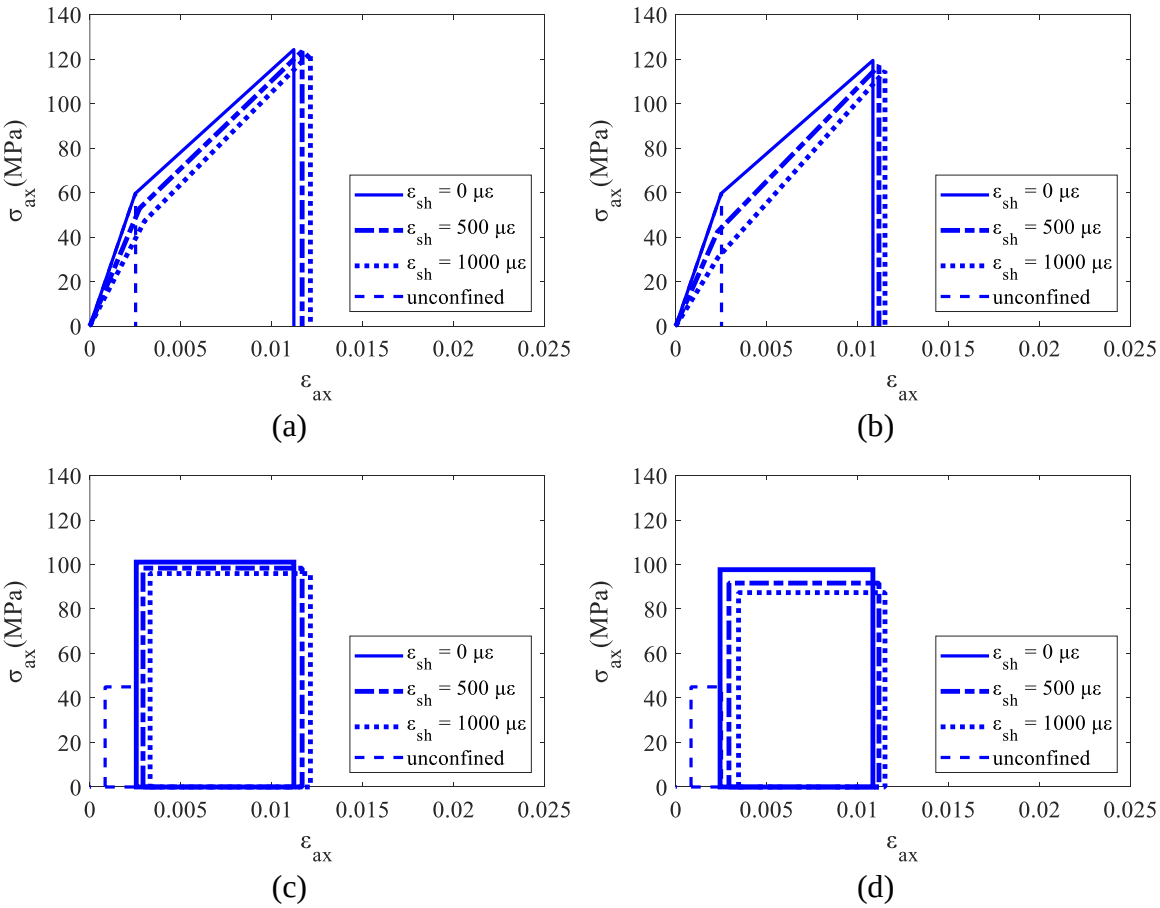

Fig. 11 (a) Strength;100 mm (b) Strength;300 mm (c) Strength;100 mm (d) Strength;300 mm

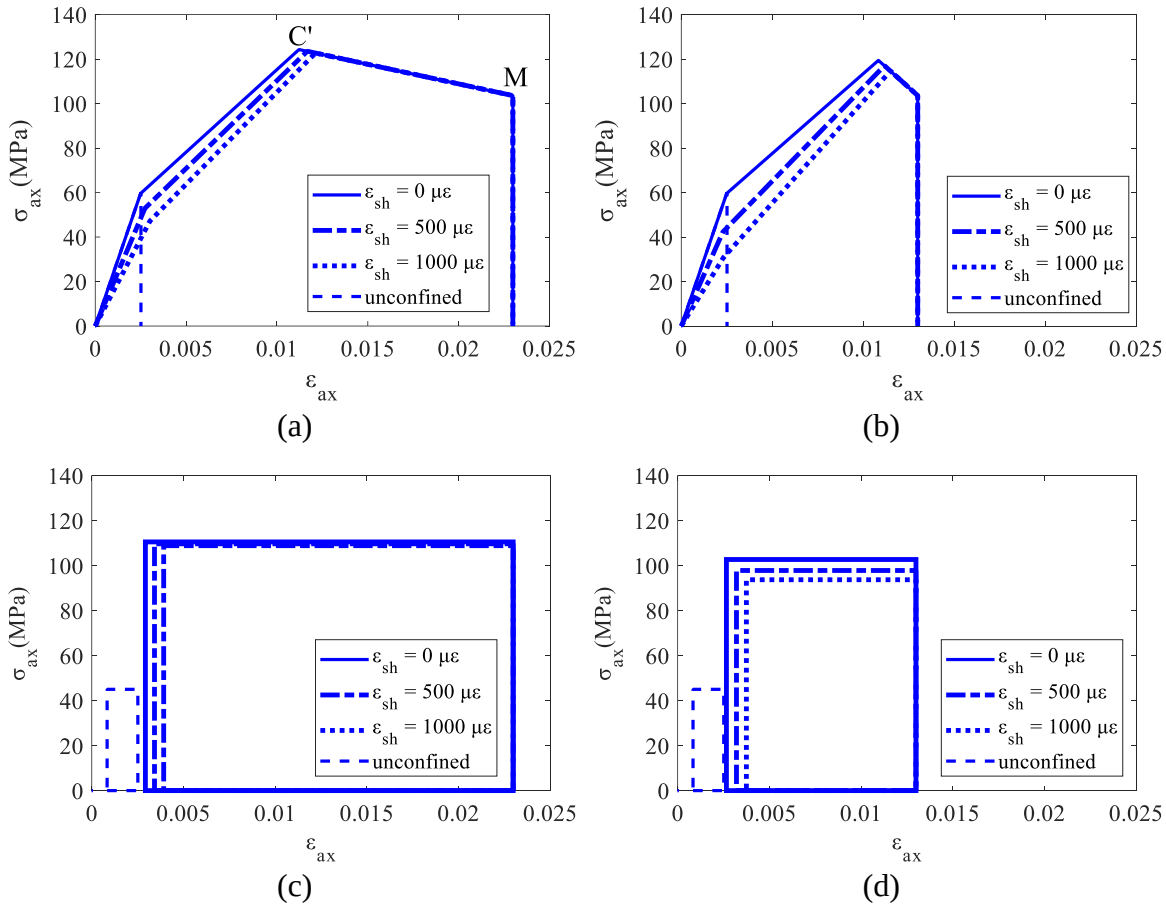

Fig. 12 (a) Ductility; 100 mm (b) Ductility; 300 mm (c) Ductility; 100 mm (d) Ductility; 300 mm

In Fig. 15, the specimen diameter was varied from 100 mm to 300 mm and a large shrinkage strain of 1000 με was imposed. It can be seen that a substantial change in shrinkage has only a minor effect on the strength analysis in Figs. 15(a) and (c). However it has a significant effect on the ductility in Figs. 15(b) and (d) where it can be seen that the beneficial effects of confinement reduce significantly with increasing diameter. Once again, the strength and ductility are significantly increased with confinement.

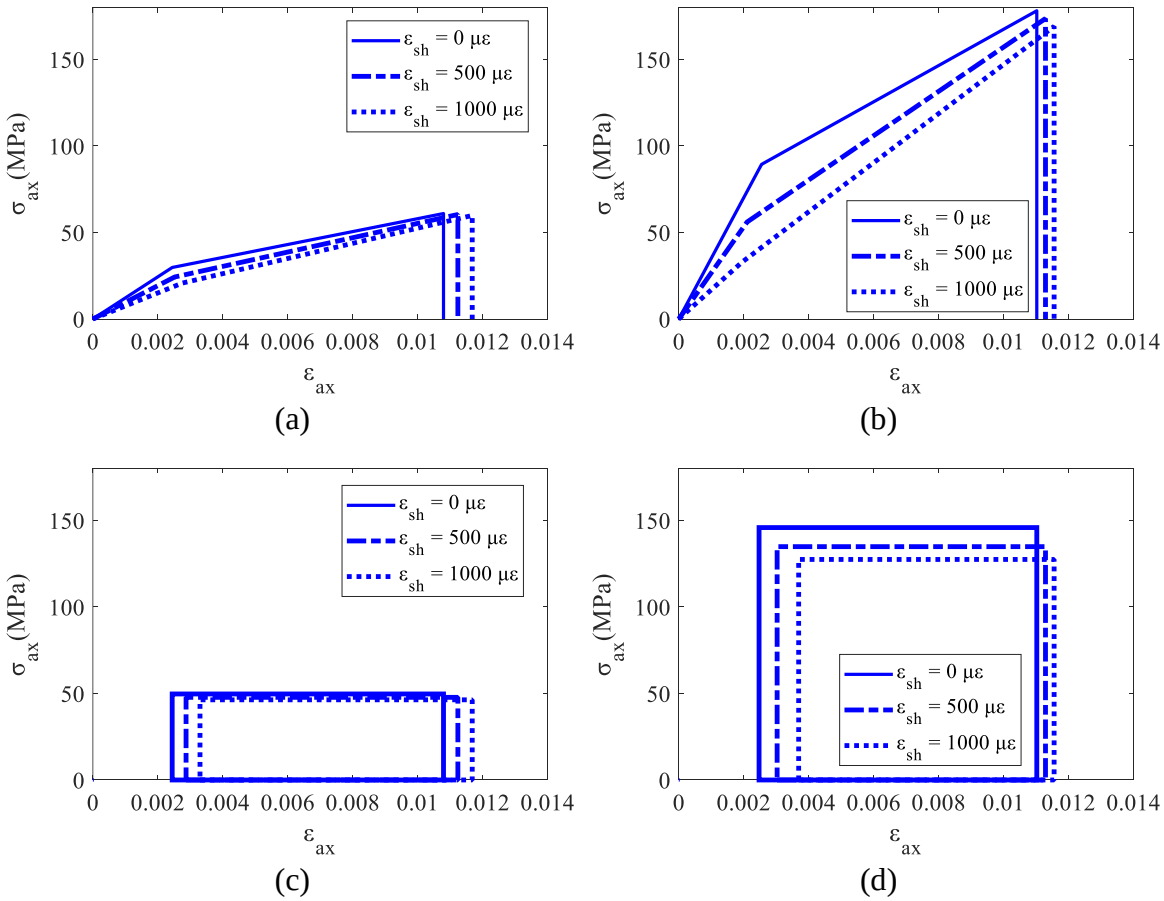

Fig. 13 (a) Strength; 30 MPa (b) Strength; 90 MPa (c) Strength; 30 MPa (d) Strength; 90 MPa

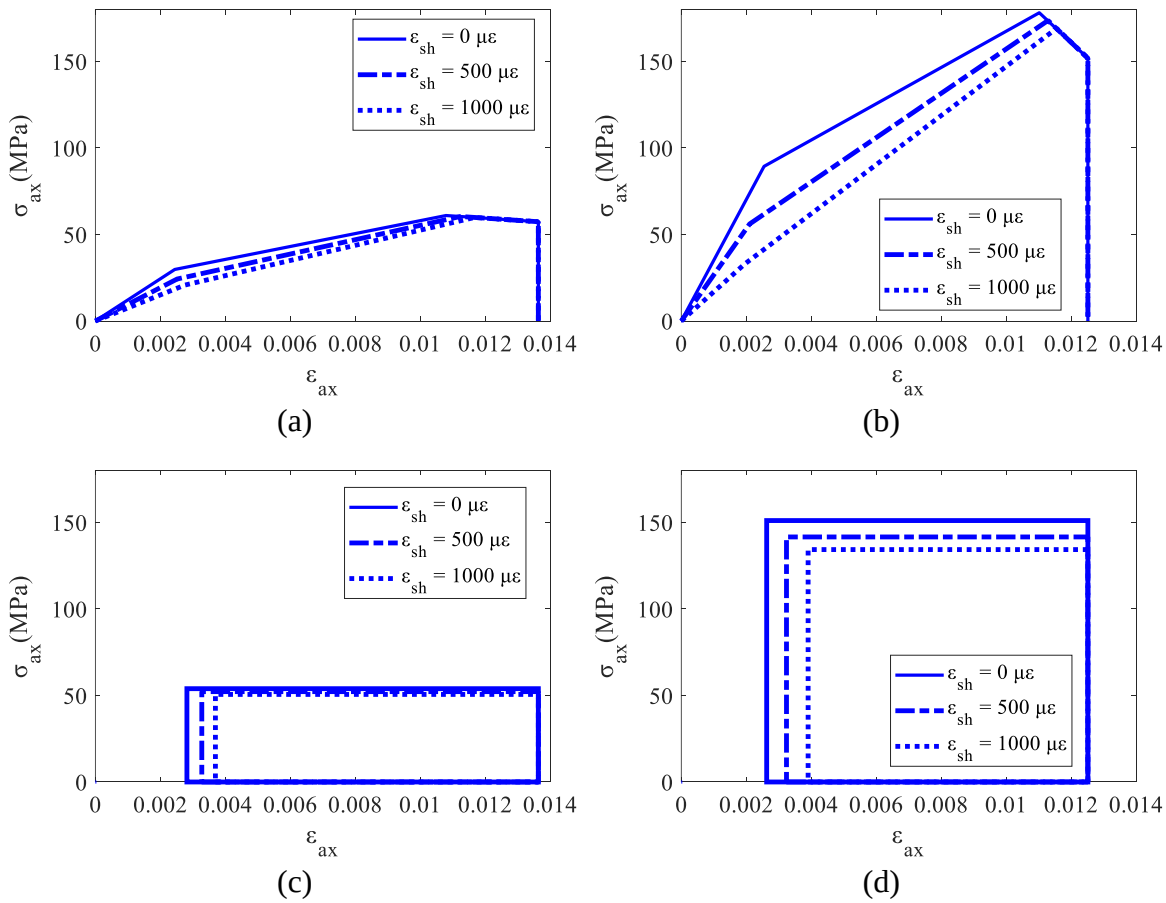

Fig. 14 (a) Ductility; 30 MPa (b) Ductility; 90 MPa (c) Ductility; 30 MPa (d) Ductility; 90 MPa

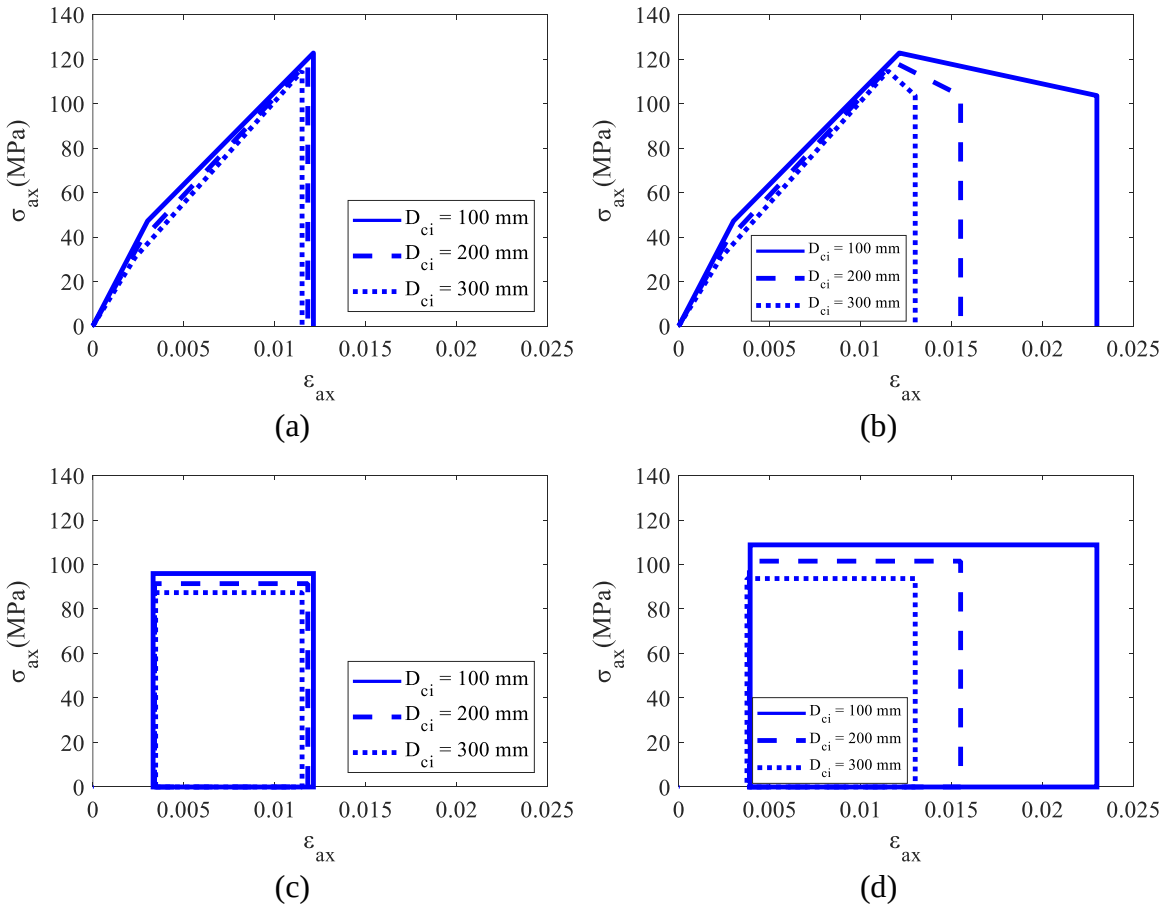

Fig. 15 (a) Strength (b) Ductility (c) Strength (b) Ductility

7. Conclusion

A procedure has been developed to quantify the passive concrete stress/strain of concrete encased in steel tubes which allows for any configuration of the composite steel and concrete member and for the effects of concrete shrinkage. The analysis requires the active stress/strain properties of the confined concrete. These properties can be determined directly from tests on confined concrete or as shown in this paper from the shear/friction properties of the concrete which are readily available or relatively easy to obtain experimentally. The procedure does not depend on member level testing and can be applied to both circular and rectangular sections.

A numerical shear/friction analysis technique is described to derive the passive stress/strain properties which have then been simplified to provide closed form solutions for the passive

stress/strain. These in turn have been further simplified into rectangular stress blocks convenient for standard design approaches for composite steel and concrete members subjected to both flexure and axial loads. These passive stress/strains have then been compared with sixteen test results of members with circular or rectangular sections. Confinement varied from 5% to 23% of the unconfined concrete strength. The numerical approach gave good correlation with the test results. It was shown how full interaction could be achieved particularly with high confinements but that the bond required for full interaction could not be relied upon. The closed form solutions were shown to give a lower bound to the strengths and ductility as would be expected and, hence, are suitable for a safe design,

A parametric study was then used to determine the influence of shrinkage and confinement on specimens up to 300 mm width. It was shown that confinement substantially increases both the concrete strength and ductility but the beneficial effects of confinement reduce with increasing specimen diameter. Furthermore shrinkage has little effect on the behaviour of normal strength concrete but a substantial effect on high strength concrete in which the benefits of confinement reduce with increasing shrinkage.

Appendix A. Notation

The following symbols are used in this paper:

A_{rec}	=	area of the stress block
D_{ci}	=	depth or diameter of confined cross-section
D_{i2}	=	width of confined cross-section
E_c	=	elastic modulus of concrete
f_{cc}	=	peak strength of confined concrete by assuming single sliding failure
f_{cccir}	=	peak strength of confined concrete by assuming circumferential wedge failure
$f_{cc\text{-}yld}$	=	f_{cc} for lateral confining stress at yield $\sigma_{conf\text{-}yld}$
$f_{cc\text{-}fr}$	=	f_{cc} for lateral confining stress at fracture $\sigma_{conf\text{-}fr}$
f_{c0}	=	peak strength of unconfined concrete from cylinder tests

f_{yld}	=	yield strength of steel tube
h_{cr}	=	separation of shear-sliding plane interface
L_{def}	=	deformed length
L_{prsm}	=	specimen height
P_{ax}	=	axial load
P_{conf}	=	confinement force from reinforcement acting along the whole sliding plane
P_{fr}	=	fracture capacity of reinforcement
P_{yld}	=	yield capacity of confinement reinforcement
r_c	=	ductility factor of confined concrete
S	=	slip displacement
S_{ax}	=	axial component of slip
S_{lat}	=	lateral component of slip S
$S_{lat\text{-}crc\text{-}all}$	=	total lateral component of slip to cause sliding strain for circular section
$S_{lat\text{-}crc}$	=	lateral expansion of circular section tube
$S_{lat\text{-}fr}$	=	lateral component of slip when confinement reinforcement starts to fracture
$S_{lat\text{-}rct}$	=	lateral expansion of rectangular section tube
$S_{lat\text{-}rct\text{-}all}$	=	total lateral component of slip to cause sliding strain for rectangular section
$S_{lat\text{-}sh}$	=	lateral component of slip to close the shrinkage gap
$S_{lat\text{-}yld1}$	=	lateral component of slip when reinforcement starts to yield
$S_{lat\text{-}yld1}$	=	lateral component of slip at the end of reinforcement yielding
$S\#$	=	specimen reference number
S'_{lat}	=	tangential component of S_{lat}
t	=	steel tube thickness
α	=	parameter in beam flexural analysis to determine the magnitude of simplified rectangular stress block
α_s	=	sliding angle
γ	=	parameter in beam flexural analysis to determine the position of simplified rectangular stress block
ε_{ax}	=	axial strain when axial stress is equal to σ_{ax}

ε_{ax5} = axial strain at S = 5 mm

$\varepsilon_{ax\text{-}ci}$ = x-coordinate of stress block centroid

$\varepsilon_{ax\text{-}crc}$ = ε_{ax} for circular section

$\varepsilon_{ax\text{-}rct}$ = ε_{ax} for rectangular section

$\varepsilon_{ax\text{-}yld1}$ = axial strain at the onset of tube yielding

$\varepsilon_{ax\text{-}yld2}$ = axial strain at the end of tube yielding

ε_{cc} = strain at f_{cc} for confined concrete

$\varepsilon_{cc\text{-}fr}$ = strain at $f_{cc\text{-}fr}$

$\varepsilon_{cc\text{-}yld}$ = strain at $f_{cc\text{-}yld}$

ε_{cu} = ultimate strain for confined concrete

ε_{c0} = strain at f_{c0} for unconfined concrete

ε_{fr} = confinement reinforcement strain at P_{fr}

ε_{m} = material strain of concrete

$\varepsilon_{m\text{-}fr}$ = material strain at fracture

$\varepsilon_{m\text{-}sh}$ = material strain to close shrinkage gap

$\varepsilon_{m\text{-}yld1}$ = material strain at the onset of yielding

$\varepsilon_{m\text{-}yld2}$ = material strain at the end of yielding

ε_{S} = sliding strain caused by slip S

$\varepsilon_{S\text{-}crc}$ = sliding strain due to tube strain in a circular section

$\varepsilon_{S\text{-}fr}$ = sliding strain at fracture

$\varepsilon_{S\text{-}rct}$ = sliding strain due to tube strain in a rectangular section

$\varepsilon_{S\text{-}sh}$ = sliding strain to close shrinkage gap

$\varepsilon_{S\text{-}yld1}$ = sliding strain at the onset of yielding

$\varepsilon_{S\text{-}yld2}$ = sliding strain at the end of yielding

ε_{sh} = shrinkage strain

ε_{tube} = strain in tube

ε_{yld1} = tube strain at the onset of tube yielding

ε_{yld2} = tube strain at the end of tube yielding

σ_{ax} = axial stress

σ_{ax5} = axial stress at S = 5 mm

σ_{conf} = lateral confining stress applied on concrete

$\sigma_{conf\text{-}crc}$ = lateral confining stress for circular section

$\sigma_{conf\text{-}fr}$ = lateral confining stress from confinement reinforcement at P_{fr}

$\sigma_{conf\text{-}rct}$	=	lateral confining stress for rectangular section
$\sigma_{conf\text{-}yld}$	=	lateral confining stress from confinement reinforcement at P_{yld}
σ_{conf0}	=	lateral confining stress of unconfined concrete and equals zero
σ_N	=	confining stress normal to single-sliding plane
σ_{Ncir}	=	confining stress normal to circumferential wedge
σ_{N0}	=	normal stress at f_{c0} for unconfined concrete
σ_S	=	axial stress of passively confined concrete by assuming single-sliding failure
σ_{Scir}	=	axial stress of passively confined concrete by assuming circumferential failure
$\sigma_{S\text{-}fr}$	=	axial stress at fracture
$\sigma_{S\text{-}g}$	=	guessed axial stress
$\sigma_{S\text{-}sh}$	=	axial stress to close shrinkage gap
$\sigma_{S\text{-}yld1}$	=	axial stress at the onset of tube yielding
$\sigma_{S\text{-}yld2}$	=	axial stress at the end of tube yielding
τ	=	shear stress along single-sliding plane
τ_{cir}	=	shear stress along circumferential wedge
τ_m	=	shear-friction material capacity

Appendix B. Quantification of confinements based on shear friction material properties

The passive stress/strain is quantified using shear friction material properties. Full details that were originally developed for reinforced concrete elements are described elsewhere [28]. These are adapted here specifically for STCC prisms.

B.1 Shear friction properties

The crack width h_{cr} in Fig. 1(a) is ignored as its contribution to both the axial and lateral strains is small compared with that due to S to give a slightly conservative assumption [22, 24]. The material interaction between σ_N, τ and S, as in Fig. B1, are the shear friction material properties [22, 42, 43]. The non-linear shear friction property τ_m in Fig. B1 is a function of

the confining stress normal to the sliding plane σ_N, slip S and the unconfined concrete strength f_{c0} [27] that is

$$\tau_m = f(\sigma_N; S; f_{c0}) \tag{28}$$

which can be derived from actively confined cylinder tests [33, 42, 43]. These non-linear variations can be linearized to the following form [33] also shown in Fig. B1

$$\tau_m = (A\sigma_N + B)S + C\sigma_N + D \tag{29}$$

where A, B, C and D are coefficients of unconfined concrete strength f_{c0}. As an example, the following linear shear friction properties were derived by Hao [33]:

when $\sigma_N < \sigma_{N0}$, where

$$\sigma_{N0} = f_{c0} \sin^2 \alpha_s \tag{30}$$

and in which α_s is the sliding angle as shown in Fig. 1(a) and is assumed to equal 26^o [31, 44-46], then

$$\tau_m = [(0.00112 f_{c0} - 0.337)\sigma_N - 0.000784 f_{c0}^2 + 0.0152 f_{c0} + 0.556]S + 1.50\sigma_N + 0.105 f_{c0} \tag{31}$$

when $\sigma_{N0} \leq \sigma_N < 3\sigma_{N0}$, then

$$\tau_m = [(0.00112 f_{c0} + 0.0636)\sigma_N - 0.000784 f_{c0}^2 - 0.0620 f_{c0} + 0.556]S + 0.498\sigma_N + 0.298 f_{c0} \tag{32}$$

which was derived for slips S less than 5 mm [33, 43] which is, therefore, the limit to the application of this equation.

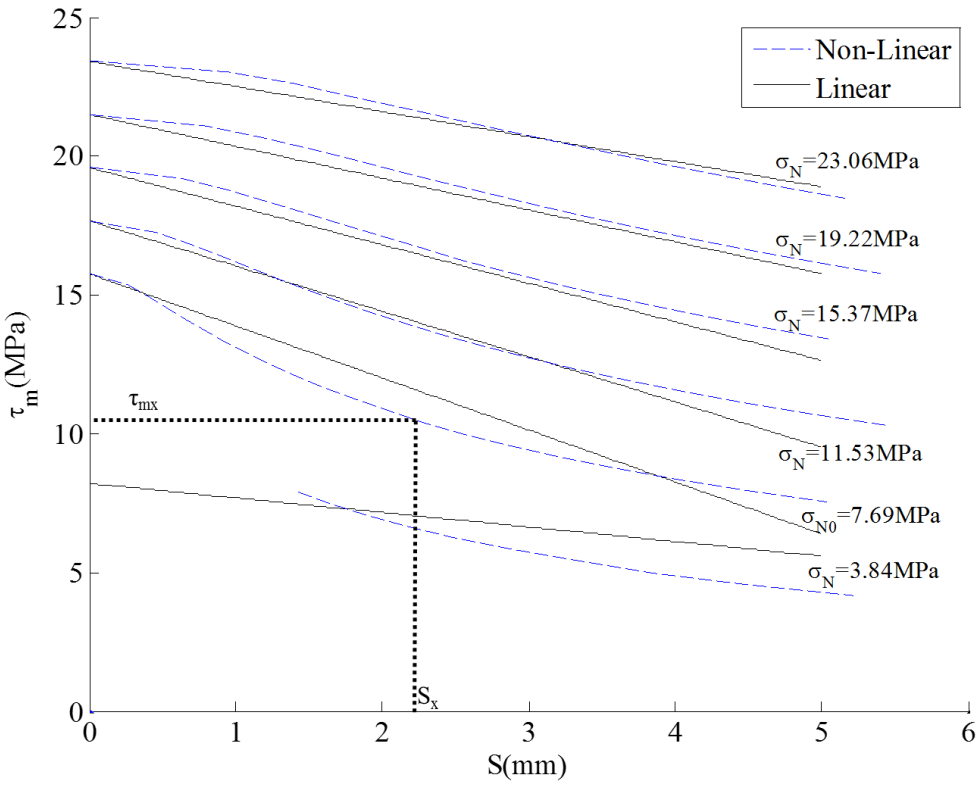

Fig. B1 Shear friction material properties for f_{c0} = 40MPa

B.2 Closed-Form solutions of active stress/strain

This closed-form solution uses a linear ascending branch of the active stress/strain that is O-B-P in Fig. 3 and the non-linear descending branch P-R-M derived from the linear shear friction properties from Eqs. (31) and (32) such as those shown in Fig. B1.

B.2.1 Linear ascending branch

The non-linear ascending branch of the active stress/strain O-A-P is linearized to O-B-P as shown in Fig. 3. However, the material strain O'-B from the linearized O-B-P may overestimate the material strain O'-A from the non-linear ascending branch O-A-P. Hence, the unconfined ascending branch O-A'-P_1 is used to derive the material strain O'-A' to give a safe solution for the ductility where P_1 is at (ε_{c0}, f_{c0}). Hence from Fig.3, the linear ascending branch is given by

$$\varepsilon_{ax} = \sigma_{ax} \frac{\varepsilon_{c0}}{f_{c0}} \tag{33}$$

in which ε_{c0} can be obtained from Eq. (36).

B.2.2 Linear descending branch

To derive the linear descending branch, the coordinates of point P in Fig. 3, that is ε_{cc} and f_{cc}, can be taken as follows [28]

$$f_{cc} = \frac{\sigma_{conf} \sin\alpha_s \cos\alpha_s + C\sigma_{conf} \cos^2\alpha_s + D}{\sin\alpha_s \cos\alpha_s - C\sin^2\alpha_s} \tag{34}$$

where C and D are the same as those in Eq. (29) and the strain ε_{cc} at f_{cc} is [31]

$$\varepsilon_{cc} = \varepsilon_{c0}[1 + A_0(\frac{\sigma_{conf}}{f_{c0}})] \tag{35}$$

where A_0 is equal to 13.9, f_{c0} is in MPa and ε_{c0} is a function of f_{c0} as follows

$$\varepsilon_{c0} = 1.74\times10^{-6} f_{c0} + 2.41\times10^{-3} \tag{36}$$

in which f_{c0} is in MPa. The ultimate strain ε_{cu} in Fig. 3 is also required to construct the linear descending branch. Consider point M where the slip S equals 5 mm, which is the maximum slip that can be used for the shear friction material properties in Eqs. (31) and (32). Substituting σ_{conf} and S = 5 mm into Eqs. (40) and (41) gives the axial stress σ_{ax5} and strain ε_{ax5} respectively which can be substituted into the following geometry equation to give the ultimate strain ε_{cu}

$$\varepsilon_{cu} = \frac{f_{cc}\varepsilon_{ax5} - \sigma_{ax5}\varepsilon_{cc}}{f_{cc} - \sigma_{ax5}} \tag{37}$$

after which the linear descending branch P-M-Q can be constructed by linking points P and Q.

B.2.3 Non-Linear descending branch

Along the sliding plane B'-E in Fig. 1(a), the confining stress σ_N and shear stress τ are resolved from the axial stress σ_{ax} and lateral confining stress σ_{conf} as follows [33, 45]

$$\tau = (\sigma_{ax} - \sigma_{conf}) \sin\alpha_s \cos\alpha_s \tag{38}$$

$$\sigma_N = \sigma_{ax} \sin^2\alpha_s + \sigma_{conf} \cos^2\alpha_s \tag{39}$$

Setting the shear stress τ from Eq. (38), that is from mechanics, to equal the shear stress material capacity τ_m from Eq. (29) gives the axial stress σ_{ax} as a function of slip S and the lateral confining stress σ_{conf} as follows [28]

$$\sigma_{ax} = \frac{\sigma_{conf} \sin\alpha_s \cos\alpha_s + AS\sigma_{conf} \cos^2\alpha_s + BS + C\sigma_{conf} \cos^2\alpha_s + D}{\sin\alpha_s \cos\alpha_s - AS \sin^2\alpha_s - C \sin^2\alpha_s} \tag{40}$$

The axial strain ε_{ax} at σ_{ax} can be obtained from the sum of the material strain ε_m and sliding strain

$$\varepsilon_{ax} = \varepsilon_m + \frac{S \cos\alpha_s}{L_{def}} \tag{41}$$

in which ε_m is from Eq. (33). Substituting a series of slips S into Eq. (40) and (41) gives the non-linear descending branch P-R-M in Fig. 3.

B.3 Closed-Form solutions of passive stress/strain

B.3.1 Passive stress/strain using linear descending branch of active stress/strain

This simplified bilinear approach has been described previously in the main text. The axial stress can be obtained from Eq. (15) or (16) and the axial strain from Eq. (17) where f_{cc}, ε_{cc} and ε_{cu} are obtained from Eqs. (34), (35) and (37). The whole procedure is summarised in Table 1. For the key points in Column 1: sliding occurs at point A in Fig. 2; confinement starts at point A'; the confinement reinforcement yields at point C' and yielding ends at point C"; and the confinement reinforcement fractures at point E'. The strain in the tube ε_{tube} is shown in Column 2 in Table 1 and the lateral confining stress σ_{conf} is shown in Column 3 which are substituted into the equations in Columns 4 and 5 to give the axial stress σ_S and strain ε_{ax}.

B.3.2 Passive stress/strain using non-linear descending branch of active stress/strain

For a lateral component of slip S_{lat} and for the lateral confining stress σ_{conf} from Eq. (4) or (9), substituting $S = S_{lat}/\sin\alpha_s$ into Eq. (40) and (41) gives the following axial stress σ_S and strain ε_{ax} [28]

$$\sigma_S = \frac{\sigma_{conf}\sin\alpha_s\cos\alpha_s + \left(A\frac{S_{lat}}{\sin\alpha_s} + C\right)\sigma_{conf}\cos^2\alpha_s + B\frac{S_{lat}}{\sin\alpha_s} + D}{\sin\alpha_s\cos\alpha_s - \sin^2\alpha_s\left(A\frac{S_{lat}}{\sin\alpha_s} + C\right)} \tag{42}$$

$$\varepsilon_{ax} = \varepsilon_m + \frac{S_{lat}}{\tan\alpha_s L_{def}} \tag{43}$$

where ε_m is from Eq. (33). As described previously, the following lateral components of slip S_{lat} are comprised of that due to shrinkage from Eq. (1) and that due to the tube strain from Eq. (5) or (10), that is for a rectangular cross-section

$$S_{lat-rct-all} = \varepsilon_{sh}D_{ci} + \varepsilon_{tube}D_{ci} \tag{44}$$

and for a circular cross-section

$$S_{lat-crc-all} = \varepsilon_{sh}D_{ci} + \frac{\pi\varepsilon_{tube}D_{ci}}{2} \tag{45}$$

These can be substituted into Eqs. (42) and (43) to give the axial stress and strain as a function of ε_{tube} which for a rectangular cross-section is

$$\sigma_{S-rct} = \frac{\sigma_{conf} \sin\alpha_s \cos\alpha_s + \left[A\frac{(\varepsilon_{tube}+\varepsilon_{sh})D_{ci}}{\sin\alpha_s} + C \right] \sigma_{conf} \cos^2\alpha_s + B\frac{(\varepsilon_{tube}+\varepsilon_{sh})D_{ci}}{\sin\alpha_s} + D}{\sin\alpha_s \cos\alpha_s - \sin^2\alpha_s \left[A\frac{(\varepsilon_{tube}+\varepsilon_{sh})D_{ci}}{\sin\alpha_s} + C \right]} \quad (46)$$

$$\varepsilon_{ax-rct} = \varepsilon_m + \frac{(\varepsilon_{tube}+\varepsilon_{sh})D_{ci}\cot\alpha_s}{L_{def}} \quad (47)$$

and for a circular cross-section is

$$\sigma_{S-crc} = \frac{\sigma_{conf} \sin\alpha_s \cos\alpha_s + \left[A\frac{(\pi\varepsilon_{tube}/2+\varepsilon_{sh})D_{ci}}{\sin\alpha_s} + C \right] \sigma_{conf} \cos^2\alpha_s + B\frac{(\pi\varepsilon_{tube}/2+\varepsilon_{sh})D_{ci}}{\sin\alpha_s} + D}{\sin\alpha_s \cos\alpha_s - \sin^2\alpha_s \left[A\frac{(\pi\varepsilon_{tube}/2+\varepsilon_{sh})D_{ci}}{\sin\alpha_s} + C \right]} \quad (48)$$

$$\varepsilon_{ax-crc} = \varepsilon_m + \frac{(\pi\varepsilon_{tube}/2+\varepsilon_{sh})D_{ci}\cot\alpha_s}{L_{def}} \quad (49)$$

where the material strain ε_m is obtained from Eq. (33).

The whole procedure is summarised in Table 4 where substituting ε_{tube} from Column 2 and σ_{conf} from Column 3 into the equations in Columns 4 and 5 gives the axial stress and strain of the key points in Column 1. This procedure is similar to that summarized in Table 1; the only difference are the equations in Columns 4 and 5 to derive the axial stress and strain. It is worth noting that the points on the descending branch derived from linear shear friction properties from Eqs. (31) and (32) have a maximum slip S = 5 mm at point M in Fig. 2. Hence, the descending branch of the passive stress/strain using the linear shear friction properties from Eqs. (31) and (32) in the validation and parametric study are derived by linking C'-M in Fig. 2, where at point C' the confinement reinforcement yields and M is the

maximum strain point. As an example, these are the limits to the closed form solutions in Fig. 6(c) and the analyses Fig. 12(a).

B.4 Passive Stress/Strain from Numerical Model

The way to construct the passive stress/strain numerically will be described in this section. Firstly, the non-linear shear friction properties, such as those shown in Fig. B1 which were derived from actively confined cylinder tests [33], are used in this numerical model. Secondly, the following non-linear ascending branch [31, 35], such as O-P-C in Fig. 2, is used

$$\sigma_{ax} = f_{cc} \frac{\frac{\varepsilon_{ax}}{\varepsilon_{cc}} r_c}{r_c - 1 + \left(\frac{\varepsilon_{ax}}{\varepsilon_{cc}} \right)^{r_c}} \tag{50}$$

where f_{cc} and ε_{cc} are obtained from Eqs. (34) and (35) and in which the ductility factor r_c is

$$r_c = \frac{E_c}{E_c - \frac{f_{cc}}{\varepsilon_{cc}}} \tag{51}$$

where the concrete elastic modulus E_c in MPa is

$$E_c = 3320\sqrt{f_{c0}} + 6900 \tag{52}$$

Finally, the axial stress σ_S is obtained from iterative steps. The steps have been described in details elsewhere [33] and are summarised in Fig. B2 as follows:

1. Before the occurrence of sliding, the loading path follows the non-linear unconfined ascending branch O-Z-A in Fig. 2 which is obtained from Eq. (50) by substituting f_{c0} and ε_{c0} for f_{cc} and ε_{cc} respectively [31, 35]. With regard to a point after the occurrence of sliding at point A in Fig. 2, guess an axial stress $\sigma_{S\text{-}g}$ and impose a slip S_x. For the imposed

slip S_x, S_{lat} equals $S_x\tan\alpha_s$ and when $S_x\tan\alpha_s$ is less than $S_{lat\text{-}sh}$ from Eq. (1), there is no confinement and P_{conf} equals zero. When $S_x\tan\alpha_s$ is larger than the $S_{lat\text{-}sh}$, $S_x\tan\alpha_s$ can be substituted for $S_{lat\text{-}all}$ in Eq. (44) or (45) and rearranged to give ε_{tube} and from which the confinement force P_{conf} can be obtained. Substituting P_{conf} into Eq. (4) or (9) gives the lateral confining stress σ_{conf}. Then the shear stress τ from mechanics and the normal stress σ_N can be obtained by substituting $\sigma_{S\text{-}g}$ and σ_{conf} into Eqs. (38) and (39).

2. The nonlinear shear friction properties for a concrete with f_{c0} = 40 MPa are given in Fig. B1; for a given confining stress σ_N normal to the sliding plane, when a slip S is imposed, then the shear friction material capacity τ_m can be determined. As an example, from the non-linear shear friction material properties derived from actively confined cylinder tests [33] from Eq. (28) and shown in Fig. B1, S_x is imposed and σ_N is obtained from Eq. (39) and then τ_{mx} is obtained.

4. If the shear stress τ from mechanics, that is from Eq. (38), is not equal to the shear capacity τ_m from step 2, then the guessed axial stress $\sigma_{S\text{-}g}$ will be changed. The whole procedure will be iterated until the shear stress τ equals the shear capacity τ_m and then the axial stress σ_S equals $\sigma_{S\text{-}g}$. Then for the imposed slip S_x, the axial stress $\sigma_S = \sigma_{S\text{-}g}$ is derived, and from Eq. (47) or (49) the strain ε_{ax} can be obtained. It is worth noting that for the numerical model described in this section, the material strain ε_m in Eq. (47) or (49) is obtained from the non-linear ascending branch of the active stress/strain from Eq. (50); for instance, ε_m in Fig. 3, that is O'A, is obtained from the non-linear ascending branch O-A-P. Furthermore, if there is no solution to σ_S, this simply means that there is not enough capacity to resist the applied load.

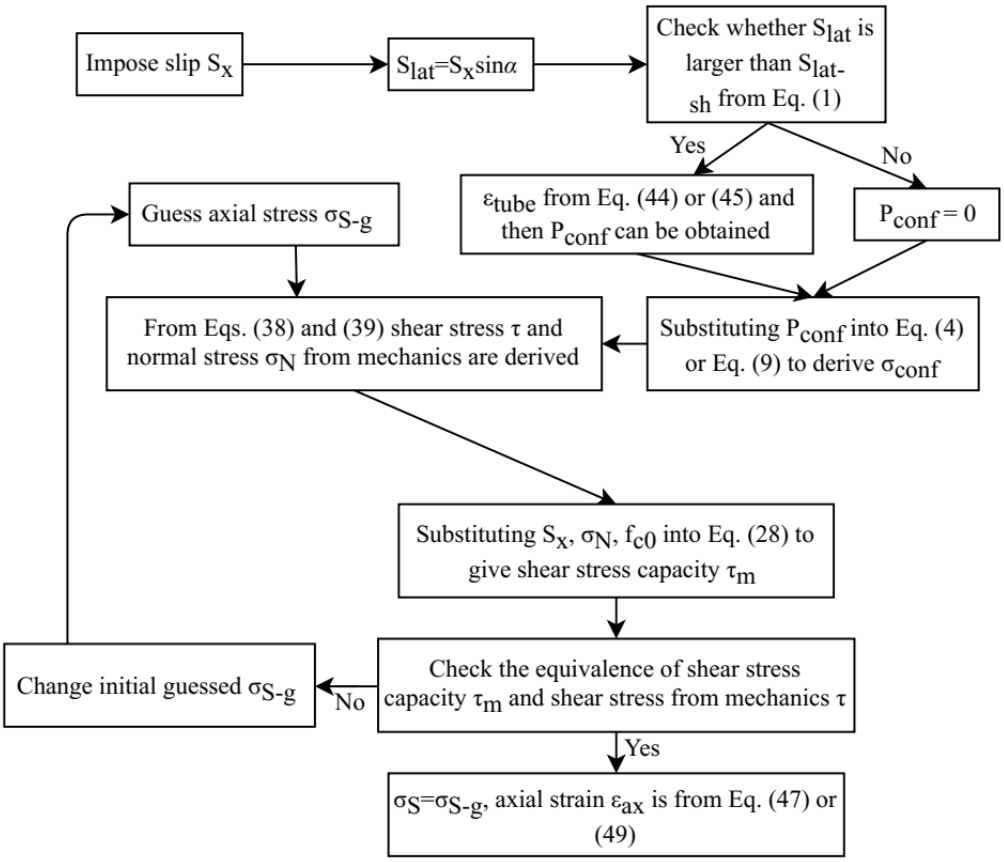

Fig. B2 Flowchart of to derive passive stress/strain numerically

B.5 Different Failure Types

The theoretical approach described above assumes a single sliding mechanism [41]. However, the circular cylinder may fail due to the formation of circumferential wedges [41, 47]. The difference between these two failure types is the following peak stress f_{cccir} of the actively confined concrete from Eq. (34) and the axial stress σ_{Scir} of the passively confined concrete from Eq. (42) [28]

$$f_{cccir}=\frac{2\sigma_{conf}\sin\alpha_s\cos\alpha_s+2C\sigma_{conf}\cos^2\alpha_s+D}{\sin\alpha_s\cos\alpha_s-C\sin^2\alpha_s} \tag{53}$$

$$\sigma_{Scir}=\frac{2\sigma_{conf}\sin\alpha_s\cos\alpha_s+\left(A\frac{S_{lat}}{\sin\alpha_s}+C\right)2\sigma_{conf}\cos^2\alpha_s+B\frac{S_{lat}}{\sin\alpha_s}+D}{\sin\alpha_s\cos\alpha_s-\sin^2\alpha_s\left(A\frac{S_{lat}}{\sin\alpha_s}+C\right)} \tag{54}$$

Furthermore and for the circumferential failure type, the shear stress τ from Eq. (38) and the normal stress σ_N from Eq. (39) become the following [28, 48]

$$\tau_{cir} = (\sigma_{ax} - 2\sigma_{conf})\sin\alpha_s \cos\alpha_s \tag{55}$$

$$\sigma_{Ncir} = \sigma_{ax}\sin^2\alpha_s + 2\sigma_{conf}\cos^2\alpha_s \tag{56}$$

B.6 Summary

When the linear descending branch of the active stress/strain is used, substituting ε_{tube} from Column 2 in Table 1 and the lateral confining stress σ_{conf} from Column 3 into Eqs. (17) and (15) or (16) gives the axial strains and stresses of the key points in Column 1.

When the non-linear descending branch of the active stress/strain and the linear shear friction properties are used, then the derivation of the closed-form solutions of the key points in Fig. 2 is summarised in Table 4. The loading path follows O-A-A'-C'-C"-E'. For these key points, substituting ε_{tube} from Column 2 and the lateral confining stress σ_{conf} from Column 3 into the equations in Columns 4 and 5 gives the axial stress and strain when assuming a single sliding failure. When the circumferential wedge is assumed to occur, then f_{cccir} of the actively confined concrete from Eq. (34) and the axial stress σ_{Scir} of the passively confined concrete from Eq. (42) are obtained from Eqs. (53) and (54) respectively.

With regard to the numerical model, the non-linear shear friction properties and the non-linear active stress/strains are used. The main step is summarised in Fig. B2 for a single sliding failure. When the circumferential wedge is assumed to occur, then f_{cccir}, τ_{cir} and σ_{Ncir} are obtained from Eqs. (53), (55) and (56) respectively instead of Eqs. (34), (38) and (39).

Acknowledgements

The first author would like to acknowledge the financial support of the China Scholarship Council.

References

[1] G. Giakoumelis, D. Lam, Axial capacity of circular concrete-filled tube columns, Journal of Constructional Steel Research 60(7) (2004) 1049-1068. https://doi.org/10.1016/j.jcsr.2003.10.001

[2] A.H. Varma, J.M. Ricles, R. Sause, L.-W. Lu, Seismic behavior and design of high-strength square concrete-filled steel tube beam columns, Journal of Structural Engineering 130(2) (2004) 169-179. https://doi.org/10.1061/(ASCE)0733-9445(2004)130:2(169)

[3] L.-H. Han, The influence of concrete compaction on the strength of concrete filled steel tubes, Advances in Structural Engineering 3(2) (2000) 131-137. https://doi.org/10.1260/1369433001502076

[4] K. Sakino, H. Nakahara, S. Morino, I. Nishiyama, Behavior of centrally loaded concrete-filled steel-tube short columns, Journal of Structural Engineering 130(2) (2004) 180-188. https://doi.org/10.1061/(ASCE)0733-9445(2004)130:2(180)

[5] E. Ellobody, B. Young, Design and behaviour of concrete-filled cold-formed stainless steel tube columns, Engineering Structures 28(5) (2006) 716-728. https://doi.org/10.1016/j.engstruct.2005.09.023

[6] B. Chen, Z. Lai, Q. Yan, A.H. Varma, X. Yu, Experimental behavior and design of CFT-RC short columns subjected to concentric axial loading, Journal of Structural Engineering 143(11) (2017) 04017148. https://doi.org/10.1061/(ASCE)ST.1943-541X.0001879

[7] T. Ekmekyapar, B.J. Al-Eliwi, Experimental behaviour of circular concrete filled steel tube columns and design specifications, Thin-Walled Structures 105 (2016) 220-230. https://doi.org/10.1016/j.tws.2016.04.004

[8] D. Lam, L. Gardner, Structural design of stainless steel concrete filled columns, Journal of Constructional Steel Research 64(11) (2008) 1275-1282. https://doi.org/10.1016/j.jcsr.2008.04.012

[9] Y. Wei, C. Jiang, Y.-F. Wu, Confinement effectiveness of circular concrete-filled steel tubular columns under axial compression, Journal of Constructional Steel Research 158 (2019) 15-27. https://doi.org/10.1016/j.jcsr.2019.03.012

[10] J. Liu, S. Zhang, X. Zhang, L. Guo, Behavior and strength of circular tube confined reinforced-concrete (CTRC) columns, Journal of Constructional Steel Research 65(7) (2009) 1447-1458. https://doi.org/10.1016/j.jcsr.2009.03.014
[11] J. Liu, X. Zhou, Behavior and strength of tubed RC stub columns under axial compression, Journal of Constructional Steel Research 66(1) (2010) 28-36. https://doi.org/10.1016/j.jcsr.2009.08.006
[12] J. Yang, J. Wang, X. Wang, L. Cheng, Z. Wang, Compressive Behavior of Circular Tubed Steel-Reinforced High-Strength Concrete Short Columns, Journal of Structural Engineering 145(9) (2019) 04019086. https://doi.org/10.1061/(ASCE)ST.1943-541X.0002361
[13] Q. Yu, Z. Tao, W. Liu, Z.-B. Chen, Analysis and calculations of steel tube confined concrete (STCC) stub columns, Journal of Constructional Steel Research 66(1) (2010) 53-64. https://doi.org/10.1016/j.jcsr.2009.08.003
[14] L.-H. Han, H. Qu, Z. Tao, Z.-F. Wang, Experimental behaviour of thin-walled steel tube confined concrete column to RC beam joints under cyclic loading, Thin-walled structures 47(8-9) (2009) 847-857. https://doi.org/10.1016/j.tws.2009.03.001
[15] R.S. Aboutaha, R. Machado, Seismic resistance of steel confined reinforced concrete (SCRC) columns, The Structural Design of Tall Buildings 7(3) (1998) 251-260. https://doi.org/10.1002/(SICI)1099-1794(199809)7:3<251::AID-TAL112>3.0.CO;2-J
[16] X. Hao, Fundamental mechanics for simulating and quantifying the benefits of concrete confinement in RC beams, School Report, School of Civil, Environmental and Mining Engineering, The University of Adelaide, Australia, (2019).
[17] M.D. O'Shea, R.Q. Bridge, Design of circular thin-walled concrete filled steel tubes, Journal of Structural Engineering 126(11) (2000) 1295-1303. https://doi.org/10.1061/(ASCE)0733-9445(2000)126:11(1295)
[18] J.B. Mander, M.J. Priestley, R. Park, Theoretical stress-strain model for confined concrete, Journal of structural engineering 114(8) (1988) 1804-1826. https://doi.org/10.1061/(ASCE)0733-9445(1988)114:8(1804)
[19] M.D. O'Shea, R.Q. Bridge, Tests on circular thin-walled steel tubes filled with medium and high strength concrete, Australian civil engineering transactions 40 (1998) 15-27.
[20] Y. Wang, P. Chen, C. Liu, Y. Zhang, Size effect of circular concrete-filled steel tubular short columns subjected to axial compression, Thin-Walled Structures 120 (2017) 397-407. https://doi.org/10.1016/j.tws.2017.09.010

[21] H.-T. Hu, C.-S. Huang, M.-H. Wu, Y.-M. Wu, Nonlinear analysis of axially loaded concrete-filled tube columns with confinement effect, Journal of Structural Engineering 129(10) (2003) 1322-1329. https://doi.org/10.1061/(ASCE)0733-9445(2003)129:10(1322)
[22] M. Haskett, D.J. Oehlers, M.M. Ali, S.K. Sharma, Evaluating the shear-friction resistance across sliding planes in concrete, Engineering Structures 33(4) (2011) 1357-1364. https://doi.org/10.1016/j.engstruct.2011.01.013
[23] W. Lucas, D. Oehlers, M. Ali, Formulation of a shear resistance mechanism for inclined cracks in RC beams, Journal of Structural Engineering 137(12) (2011) 1480-1488. https://doi.org/10.1061/(ASCE)ST.1943-541X.0000382
[24] M. Haskett, D. Oehlers, M.M. Ali, S. Sharma, The shear friction aggregate interlock resistance across sliding planes in concrete, Magazine of Concrete Research 62(12) (2010) 907-924. https://doi.org/10.1680/macr.2010.62.12.907
[25] A.H. Mattock, N.M. Hawkins, Shear transfer in reinforced concrete-recent research, PCI Journal 17(2) (1972) 55-75.
[26] L. Johal, Shear transfer in reinforced concrete with moment or tension acting across the shear plane, PCI Journal (1975) 76-93.
[27] J. Walraven, H. Reinhardt, Theory and experiments on the mechanical behaviour of cracks in plain and reinforced concrete subjected to shear loading, HERON, 26 (1A), (1981) 5-68.
[28] X. Hao, Generation of stress-strain relationship of passively reinforced rectangular concrete prisms, School Report, School of Civil, Environmental and Mining Engineering, The University of Adelaide, Australia, (2018).
[29] X. Hao, Generation of stress-strain relationship of passively reinforced circular concrete cylinders, School Report, School of Civil, Environmental and Mining Engineering, The University of Adelaide, Australia, (2018).
[30] Y. Wang, Y. Geng, G. Ranzi, S. Zhang, Time-dependent behaviour of expansive concrete-filled steel tubular columns, Journal of Constructional Steel Research 67(3) (2011) 471-483. https://doi.org/10.1016/j.jcsr.2010.09.007
[31] P. Visintin, Y. Chen, D. Oehlers, Size dependent axial and lateral stress strain relationships for actively confined concrete, Advances in Structural Engineering 18(1) (2015) 1-20. https://doi.org/10.1260/1369-4332.18.1.1
[32] Y. Chen, P. Visintin, D. Oehlers, U. Alengaram, Size-dependent stress-strain model for unconfined concrete, Journal of Structural Engineering 140(4) (2013) 04013088. https://doi.org/10.1061/(ASCE)ST.1943-541X.0000869

[33] X. Hao, Mechanics of extracting shear-friction properties from actively confined cylinder tests, School Report, School of Civil, Environmental and Mining Engineering, The University of Adelaide, Australia, (2017).
[34] B. Kyle, S. Harrison, S. Alexander, S. Philip, A mechanics-based approach to quantifying the ductility of reinforced concrete members with passive confinement of stirrups and FRP wraps, School Report, School of Civil, Environmental and Mining Engineering, The University of Adelaide, Australia, (2015).
[35] S. Popovics, A numerical approach to the complete stress-strain curve of concrete, Cement and concrete research 3(5) (1973) 583-599. https://doi.org/10.1016/0008-8846(73)90096-3
[36] P. Bourke, Calculating the area and centroid of a polygon, Swinburne University of Technology, (1988) 7.
[37] R. Basset, S. Uzumeri, Effect of confinement on the behaviour of high-strength lightweight concrete columns, Canadian Journal of Civil Engineering 13(6) (1986) 741-751. https://doi.org/10.1139/l86-109
[38] K.-N. Hong, S.-H. Han, S.-T. Yi, High-strength concrete columns confined by low-volumetric-ratio lateral ties, Engineering Structures 28(9) (2006) 1346-1353. https://doi.org/10.1016/j.engstruct.2006.01.010
[39] Z. Wang, D. Wang, S.T. Smith, Size effect of square concrete columns confined with CFRP wraps, Proceedings of the 3rd Asia-Pacific Conference on FRP in Structures, Hokkaido University, Sapporo, Japan, (2012) 2-4.
[40] H.-L. Wu, Y.-F. Wang, L. Yu, X.-R. Li, Experimental and computational studies on high-strength concrete circular columns confined by aramid fiber-reinforced polymer sheets, Journal of Composites for Construction 13(2) (2009) 125-134. https://doi.org/10.1061/(ASCE)1090-0268(2009)13:2(125)
[41] Y. Chen, Quantifying the compressive ductility of concrete in RC members through shear friction mechanics, Ph.D. dissertation, The University of Adelaide, (2015). http://hdl.handle.net/2440/95248
[42] Y. Chen, T. Zhang, P. Visintin, D. Oehlers, Concrete shear-friction material properties: application to shear capacity of RC beams of all sizes, Advances in Structural Engineering 18(8) (2015) 1187-1198. https://doi.org/10.1260/1369-4332.18.8.1187
[43] Y. Chen, P. Visintin, D. Oehlers, Concrete shear-friction material properties: Derivation from actively confined compression cylinder tests, Advances in Structural Engineering 18(8) (2015) 1173-1185. https://doi.org/10.1260/1369-4332.18.8.1173

[44] B.C. Jensen, Lines of discontinuity for displacements in the theory of plasticity of plain and reinforced concrete, Magazine of Concrete Research 27(92) (1975) 143-150. https://doi.org/10.1680/macr.1975.27.92.143
[45] M.M. Ali, D. Oehlers, M. Griffith, The residual strength of confined concrete, Advances in Structural Engineering 13(4) (2010) 603-618. https://doi.org/10.1260/1369-4332.13.4.603
[46] A.H. Mattock, N.M. Hawkins, Shear transfer in reinforced concrete—Recent research, Pci Journal 17(2) (1972) 55-75.
[47] Z.-w. Yu, F.-x. Ding, C. Cai, Experimental behavior of circular concrete-filled steel tube stub columns, Journal of Constructional Steel Research 63(2) (2007) 165-174. https://doi.org/10.1016/j.jcsr.2006.03.009
[48] P. Visintin, Y. Chen, D. Oehlers, Simulating the behavior of FRP-confined cylinders using the shear-friction mechanism, Journal of Composites for Construction 19(6) (2015) 04015014. https://doi.org/10.1061/(ASCE)CC.1943-5614.0000573

Chapter 6— Conclusions and Further Research

Summary and Conclusions

Confinement reinforcement can enhance the strength and ductility of concrete structures. This thesis presents the development of a mechanics-based model to predict both the stress/strain behaviour and the flexural behaviour of passively confined concrete. This model is directly based on fundamental partial interaction shear-friction and bond-slip material properties and can incorporate: different types of the confinement reinforcement; different shapes of the cross-section; different types of reinforcement; different specimen sizes; different concrete strengths; and different loading conditions that includes concentric loads and flexural loads. As only the material properties are required in this model which can be obtained from simple material tests, there is no need for member testing and this approach can be easily extended to new types of confinement reinforcement reinforced concrete members. Corresponding closed-form solutions are given which can be used for design purpose.

The closed-form equations of the confinement mechanisms are introduced first for both rectangular and circular cross-sections for all possible scenarios of the confinement reinforcement that is debonding, yield, fracture or combinations of these; hence these equations can be applied to all kinds and types of available confinement reinforcement such as external plates or internal stirrups. Then shear friction material properties are derived from actively confined cylinder tests as well as shear-sliding tests that are based on a large database and then these properties are simplified to a linear form which can be used in the ensuing derivation of the closed-form solutions of the proposed approach. The active stress/strain is then constructed to validate the linear approximation with good correlation. After which, the required bond-slip material properties for FRP and steel plates as well as for FRP and steel rebars are summarised and simplified to a bilinear model.

Having gathered all the required material properties, a mechanics-based model to give the stress/strain of passively confined concrete is derived for both rectangular and circular cross-section prisms respectively. The specimen height and diameter or side length of the cross-

section as well as different scenarios of confinement reinforcement are considered in this approach. Closed-form solutions for this model are proposed for design purposes. Closed-form solutions of the proposed approach are compared with published test data of concrete prisms reinforced by either FRP or stirrups with good correlation. Hence, the proposed approach can predict the passive stress/strain behaviour well and can be used for design purposes. A parametric study has been conducted to show the effect of size. It is shown that available empirical approaches that were derived from small-size specimens may be unsafe for practical use in large size concrete structures.

Closed-form solutions of the passive stress/strain have been derived and then their application in a flexural analysis is described. Firstly it is shown how the passive stress/strain can be applied in a flexural analysis and then the passive stress/strain is simplified to a rectangular stress block. Using this rectangular stress block in a segmental analysis, closed-form solutions of the moment/rotation of the beam are derived for three key points which are: at the onset of concrete softening; at the maximum strength of the passively confined concrete; and when the passive stress/strain is fully developed. Then the derived moment/rotation is compared with test data extracted from experimental load/deflections with good correlation. Consequently, the proposed closed-form solutions can quantify the ductility of passively confined concrete beams allowing for confinement and can be used in design.

The proposed approach is then extended to steel tube confined concrete to give passive stress/strains which can also incorporate the shrinkage effect. Derived passive stress/strains are then simplified to rectangular stress blocks which can be used in flexural analyses. This is followed by a parametric study which shows the effect of shrinkage on the passive stress/strain with regard to strength and to ductility.

In summary, this thesis describes a mechanics-based model that is based on partial interaction bond-slip and shear friction material properties. This model can predict the stress/strain and flexural behaviour of passively confined concrete to quantify the strength and, more importantly, the ductility of concrete prisms restrained by confinement reinforcement.

Further Research Directions

The following directions are suggested to improve the accuracy of the proposed approach:

1: Shear friction material properties derived in this thesis are limited by the assumption that the maximum slip is five millimetres. Although the validation shows a five millimetre limit is sufficient for most current concrete members, when better shear friction material properties are developed, they can be applied to improve the accuracy of the proposed approach.

2: Bond slip material properties are derived from pull-out tests where the confining stress normal to the interface between the concrete and reinforcement is zero which is not the case for members with circular cross-sections. Although from the validation, it is shown that based on this assumption the proposed model gives good correlation with experimental results, when better bond-slip material properties are developed, they can be applied in the proposed approach to increase accuracy.

3: The proposed approach can be applied to different types of concrete such as ultra-high performance concrete or sea sand concrete when the shear friction material properties for these new types of concrete are developed. The proposed approach can also be easily extended to concrete members reinforced by new types of confinement reinforcement such as double skin composite confinement.